

*MSc Dujearic-Stephane Kouao*  
*Institute of Fluid-Flow Machinery, Polish Academy of Sciences*

**Processing and diagnostics of semitransparent photoelectrodes  
based on titania for energy conversion applications**

Doctoral dissertation  
Institute of Fluid-Flow Machinery, Polish Academy of Sciences

Supervisor:  
PhD DSc Eng. Katarzyna Siuzdak Professor of IMP PAN

*Gdańsk, September 2024*

## Acknowledgements

I would like to express my sincere gratitude to my supervisor, PhD DSc Eng. Katarzyna Siuzdak, prof. IMP PAN for guiding me throughout my studies. I am grateful for all the knowledge and support I received from her during my PhD studies.

I would like to thank the National Science Centre of Poland for the financial support of the CEUS-UNISONO project No. 2020/02/Y/ST8/00030 in which I participated as a PhD student.

Thanks to PhD DSc Katarzyna Grochowska, Prof. Vitezslav Stranak, PhD Petr Sezemsky, MSc Radka Šimerová, Prof. Ondřej Kylián, PhD Jan Hanuš, Prof. Mateusz Śmietana and MSc Eng. Emil Piłula, all members of CEUS-UNISONO project for their help in substrates fabrication, measurements and contribution to manuscripts preparation and all the received remarks.

I would also like to thank PhD DSc Eng. Mirosław Sawczak, prof. IMP PAN, PhD DSc Eng. Emerson Coy, prof. UAM, PhD DSc Eng. Jakub Karczewski, prof. PG, PhD Agnieszka Kramek, MSc Justyna Gumieniak, MSc Eng. Franciszek Skiba for the assistance in measurements for manuscripts preparation.

I would like to express my gratitude to PhD DSc Agata Szczeszak for guiding me and sharing her knowledge during my training in hydrothermal synthesis of nanomaterials at the Department of Rare Earths, Faculty of Chemistry, Adam Mickiewicz University, Poznań.

Thanks to Kpanna Api, my parents Akaffou Apo Edithe and Atse Kouao Hyacinthe, family and friends for their daily support.

This dissertation was supported by

CEUS-UNISONO project entitled: “Semitransparent titania nanostructures on complex geometry surfaces for enhanced light harvesting and sensing” financed by National Science Centre in Poland, project no. 2020/02/Y/ST8/00030.



The work was carried out in the Laboratory of Functional Materials, Department of Physical Aspects of Ecoenergy, Centre of Plasma and Laser Engineering, Institute of Fluid-Flow Machinery, Polish Academy of Sciences.

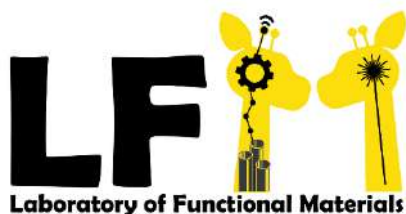


## Table of contents

1	Abstract .....	6
2	Streszczenie .....	7
3	List of abbreviations .....	8
4	Literature and background.....	11
4.1	General introduction.....	11
4.2	Fabrication of anodic semitransparent TiO <sub>2</sub> nanotubes.....	16
4.2.1	Deposition methods of Ti film onto transparent conducting oxides.....	18
4.2.2	Anodization .....	20
4.3	Different morphologies of the titania nanotubes .....	27
4.4	Effect of annealing on the crystalline phase of titania.....	30
4.5	Modification techniques of the semitransparent tubular layer .....	32
4.6	Introduction to MXene .....	34
4.6.1	Synthesis of MXene .....	34
4.7	Photoelectrochemical activity of TiO <sub>2</sub> functionalized with Ti <sub>3</sub> C <sub>2</sub> T <sub>x</sub> MXene.....	37
4.8	Laser ablation method .....	39
5	Objectives and Hypotheses.....	41
6	Methods .....	44
6.1	Introduction .....	44
6.2	Magnetron sputter method.....	44
6.3	Sputtering conditions of indium tin oxide (ITO) layer, TiO <sub>2</sub> interlayer and Ti films onto planar substrates .....	46
6.3.1	Sample preparation for layer sputtering .....	46
6.3.2	Deposition conditions of the different layers i.e. ITO layer, TiO <sub>x</sub> interlayer and Ti film onto planar substrates (i.e. onto one side or onto the two side of the substrates).....	47
6.4	Anodization setup.....	51
6.5	Analytical Methods .....	51
6.5.1	Electron microscopy .....	52
6.5.2	Energy dispersive X-rays (EDX) for elemental analysis.....	57
6.5.3	X-ray photoelectron spectroscopy .....	58
6.5.4	X-ray diffraction.....	61
6.5.5	Raman spectroscopy .....	63
6.5.6	UV-vis absorption spectroscopy.....	65
6.5.7	Fourier transform infrared spectroscopy .....	66
6.6	Electrochemical and photoelectrochemical characterisation methods .....	67
6.6.1	Cyclic voltammetry .....	69



6.6.2	Linear sweep voltammetry .....	71
6.6.3	Electrochemical impedance spectroscopy .....	73
6.6.4	Mott-Schottky analysis .....	77
6.6.5	Intensity-modulated photocurrent spectroscopy (IMPS).....	80
6.6.6	Incident-photon-to-current efficiency (IPCE) .....	82
6.6.7	Photoluminescence (PL) measurements .....	84
7	Results .....	86
7.1	Fabrication of semitransparent aligned and spaced titania nanotubes.....	88
7.2	Anodization of Ti films sputtered onto the substrate of complex geometries .....	123
7.3	Anodization of TiAg alloy films deposited onto ITO-glass .....	146
7.4	Semitransparent electrode based on aligned nanotubes for methylene blue sensing .....	180
7.5	Functionalization of semitransparent tubular layer with laser-treated MXene .....	194
8	General conclusion .....	233
9	Scientific achievements .....	237
10	Authors contribution statement .....	243
11	Bibliography .....	266

## 1 Abstract

This PhD dissertation focuses on the fabrication and characterization of semitransparent substrates overgrown by titania material. The applicability of the fabricated material as a potential photoanode for efficient light conversion and optoelectrochemical sensing was also investigated. The general approach adopted in this work towards fabricating the semitransparent material consists first of the sputtering of Ti film onto indium tin oxide (ITO) coated glass substrate followed by anodizing of the deposited film. Optimization of the anodization parameters was carried out to obtain highly ordered, semitransparent layers composed of aligned or spaced nanotubes on planar substrates. Next, the tubular morphology was formed on the both sides of planar substrates using an anodization setup equipped with a suitable sample holder allowing each side to be anodized independently. The influence of the distribution of the tubes, i.e. aligned, when outer walls are adjacent to each other, and spaced on some distance, on the photoactivity of the fabricated double-sided materials was studied. Aligned nanotubes were also obtained out of Ti film sputtered onto optical fiber. Anodization was carried out in the system where Ti covered fiber was placed between two platinum meshes. The transparent layer of nanotubes was obtained on the optical fiber owing to the optimization of the distance between the platinum meshes. The presence of tubular layer onto the optical fiber plays important role in determination of the refractive index in liquid medium. It should be underlined that semitransparent materials are less efficient than those fabricated onto Ti foil in terms of light conversion. However, the improvement of the quantum efficiency of the semitransparent tubular layers through their modification can be carried out. To reach this, the incorporation of silver within the nanotubular layers was proposed. This aim was realized by the formation of aligned and spaced nanotubes out of TiAg films with different Ag content (i.e., 1.7, 3.5, and 5 % Ag content, the rest is Ti) deposited onto ITO coated glass substrate. Energy dispersive X-ray analysis revealed for the aligned tubular architecture the preservation of 60 % of the Ag content in the sputtered TiAg layer after the anodization. A three-fold increase in the incident photon-to-current conversion efficiency (IPCE) for the aligned nanotubes out of the TiAg films containing 3.5 % of Ag was obtained with respect to the bare titanium dioxide layer with the same tubular architecture. The quantum efficiency of the tubular layer was also increased through its functionalization with  $\text{Ti}_3\text{C}_2\text{T}_x/\text{TiO}_2$  heterostructures. The heterostructures were synthesized via laser annealing of  $\text{Ti}_3\text{C}_2\text{T}_x$  frozen suspension. The nanotube layer integrated with  $\text{Ti}_3\text{C}_2\text{T}_x/\text{TiO}_2$  demonstrated about ten time increase in the IPCE compared to the bare substrate. The main outcome of this work is the development of fabrication procedures of semitransparent ordered nanostructures and their functionalization that can contribute to the development of solar powered devices and optoelectrochemical sensors.

## 2 Streszczenie

Niniejsza rozprawa doktorska dotyczy wytwarzania i diagnostyki półprzezroczystych podłoży z ditlenkiem tytanu. Zbadano również możliwość zastosowania wytworzonego materiału jako potencjalnej fotoanody przeznaczonej do wydajnej konwersji światła i czujnika optoelektrochemicznego. Podejście zastosowane w tej pracy w celu otrzymywania materiału półprzezroczystego polega najpierw na napyłaniu warstwy Ti na podłoże szklane pokryte tlenkiem indy i cyny (ITO), a następnie anodyzacji takiej warstwy. Przeprowadzono optymalizację parametrów procesu anodyzacji by uzyskać wysoce uporządkowane półprzezroczyste warstwy składające się z przylegających do siebie i rozstawionych na pewną odległość nanorurek na płaskich podłożach. Następnie, nanostruktury rurkowe utworzono po obu stronach płaskich podłoży z użyciem zestawu do anodyzacji wyposażonego w odpowiedni chwytak na próbki umożliwiający prowadzenie anodyzacji niezależnie dla każdej ze stron. Zbadano wpływ rozmieszczenia nanorurek na podłożu, które mogą do siebie przylegać ściankami zewnętrznymi lub być rozstawione na pewną odległość względem siebie, na fotoaktywność wytworzonych materiałów. Przylegające nanorurki otrzymano także z warstwy tytanowej napyłonej na światłowód. Anodyzowanie przeprowadzono w układzie, w którym światłowód z warstwą Ti umieszczono pomiędzy dwiema siatkami platynowymi. Dzięki dobraniu odległości pomiędzy platynowymi siatkami otrzymano przezroczystą warstwę przylegających nanorurek. Warstwa nanorurek odgrywała istotną rolę w wyznaczeniu współczynnika załamania światła dla cieczy, w której zanurzono czujnik światłowodowy. Należy mieć jednak na uwadze fakt, że materiały półprzezroczyste nie umożliwiają na prowadzenie tak wydajnej fotokonwersji jak te wytworzone na folii tytanowej. Można jednak doprowadzić do poprawy wydajności kwantowej półprzezroczystych warstw nanorurek dzięki ich modyfikacji. By to osiągnąć, zaproponowano wprowadzenie srebra do warstw z nanorurek. Cel ten zrealizowano poprzez utworzenie przylegających i rozstawionych warstw nanorurek na drodze anodyzacji warstw TiAg o różnej zawartości Ag (tj. 1,7, 3,5 i 5% Ag, a resztę stanowi Ti), osadzonych na podłożu szklanym pokrytym ITO. Analiza rentgenowska z dyspersją energii wykazała, że w przypadku warstwy przylegających nanorurek 60 % Ag z napyłonej warstwy TiAg pozostało w warstwie. Uzyskano trzykrotny wzrost wydajności kwantowej fotokonwersji (IPCE) dla nanorurek otrzymanych z warstw TiAg zawierających 3,5 % Ag w porównaniu z warstwą ditlenku tytanu o tym samym sposobie rozmieszczenia nanorurek na podłożu. Wydajność kwantową fotokonwersji dla warstwy nanorurek zwiększono również poprzez jej funkcjonalizację heterostrukturami  $\text{Ti}_3\text{C}_2\text{T}_x/\text{TiO}_2$ . Heterostruktury wytworzono poprzez obróbkę wiązką laserową zamrożonej zawiesiny  $\text{Ti}_3\text{C}_2\text{T}_x$ . Warstwa nanorurek wraz z  $\text{Ti}_3\text{C}_2\text{T}_x/\text{TiO}_2$  wykazała ok. dziesięciokrotny wzrost IPCE w porównaniu z niemodyfikowanym podłożem. Głównym rezultatem tych prac jest opracowanie procedur wytwarzania półprzezroczystych uporządkowanych nanostruktur i ich funkcjonalizacji, które mogą przyczynić się do rozwoju zasilanych energią słoneczną i czujników optoelektrochemicznych.

### 3 List of abbreviations

A	Absorbance
CV	Cyclic Voltammetry
LSV	Linear Sweep Voltammetry
CPE	Constant phase element
EIS	Electrochemical Impedance Spectroscopy
ITO	Indium Tin Oxide
FTO	fluorine-doped Tin Oxide
TNT	Titania Nanotubes
QCM	Quartz Crystal Microbalance
TCO	Transparent conducting oxide
EQC	Electric Equivalent Circuit
SEM	Scanning Electron Microscopy
TEM	Transmission Electron Microscopy
EDX	Energy Dispersive X-rays
XPS	X-ray Photoelectron Spectroscopy
XRD	X-ray diffraction
IMPS	Intensity-Modulated Photocurrent Spectroscopy
IPCE	Incident-Photon-to-Current Efficiency
FTIR	Fourier Transform Infrared Spectroscopy

#### Notations

FA	side overgrown with aligned nanotubes
FS	side overgrown with spaced nanotubes
F1	side 1 of the symmetric electrode
F2	side 2 of the symmetric electrode
NT(A)-ITO-NT(A)	ITO overgrown with aligned nanotubes on the both sides
NT(S)-ITO-NT(S)	ITO overgrown with spaced nanotubes on the both sides
NT(A)-ITO-NT(S)	one side of the ITO is overgrown with aligned nanotubes and the other with spaced nanotubes
PEC	Photoelectrochemical
UV-vis	Ultraviolet – visible
PL	Photoluminescence

## Symbols and units

C	Space charge capacitance [F]
e	Electron charge [C]
E	Applied potential [V]
E°	Formal Potential [V]
E <sub>g</sub>	Band gap energy [eV]
E <sub>fb</sub>	Flat band potential [V]
F	Frequency of the AC signal [Hz]
K	Boltzmann constant [JK <sup>-1</sup> ]
H	Planck constant [Js]
M	Number of parameters of the Powell algorithm [-]
N <sub>D</sub>	Donor density [cm <sup>-3</sup> ]
N <sub>A</sub>	Acceptor density [cm <sup>-3</sup> ]
N	Number of points in the Powell algorithm [-]
N <sub>t</sub>	Nanotubes per unit area [cm <sup>-2</sup> ]
P <sub>M</sub>	Parameters of the Powell algorithm [-]
Q	Capacitance for n =1 [Ω <sup>-1</sup> cm <sup>-2</sup> s <sup>n</sup> ]
r <sub>a</sub>	Amplitude weighting [-]
r <sub>c</sub>	Constant parameter [-]
R <sub>ct</sub>	Charge transfer resistance at the semiconductor/electrolyte interface [Ω]
R <sub>s</sub>	Series resistance [Ω]
T	Temperature [K]
W <sub>or</sub>	Warburg coefficient [Ωcm <sup>-2</sup> s <sup>0.5</sup> ]
W <sub>oc</sub>	Warburg coefficient [s <sup>0.5</sup> ]
Z	Impedance [Ω]
Z''	Imaginary part of the impedance [Ω]
Z'	Real part of the impedance [Ω]
i	Current [A]
i <sub>p</sub>	Peak current [A]
j	Current density [A cm <sup>-2</sup> ]
t	Time [unit depending on the time scale]
E <sub>F</sub>	Fermi level [eV]

## **Greek**

$\varepsilon$	Relative permittivity [-]
$\varepsilon_0$	Permittivity of the free space [Fcm <sup>-1</sup> ]
$\omega$	Angular frequency [rads <sup>-1</sup> ]
$\chi^2$	fitting errors [-]
$\alpha$	Absorption coefficient [cm <sup>-1</sup> ]
$\nu$	photon frequency [Hz]
$\Phi$	Work function

## 4 Literature and background

### 4.1 General introduction

The continuous warming of the climate due to the intensive use of the fossil-based resources is becoming preoccupant. In this regard, scientists are working together to determine responsibilities for climate action.<sup>1</sup> The ambition is to limit the increase in global mean temperature to below 1.5 °C per year.<sup>1</sup> It is therefore urgent to gradually reduce the high dependence on fossil resources in favour of renewable and sustainable energy resources. Among others, sunlight is the largest source of green energy for the planet. Indeed,  $4.3 \times 10^{20}$  J of solar energy hits the Earth in an hour.<sup>2</sup> This energy is larger than the annual global energy consumption, which is estimated to  $4.1 \times 10^{20}$  J.<sup>2</sup> Therefore, the energy delivered by the sun in one hour is sufficient to cover the annual global energy demand.<sup>2</sup> However, one of the major issues for the usage of this abundant and freely available energy from sunlight is its efficient harvesting and conversion.<sup>3</sup> Up to now a plenty of devices and processes were proposed, utilizing solar radiation to provide heat or electricity around the globe. Among others there exist already huge solar cell farms and series of solar panels present on the roofs, photocatalytic reactors used for the pollution removal, solar collectors and even outdoor photoactive paintings. Nevertheless, still many efforts should be undertaken to increase the efficiency of those processes not only via upgrading the construction of the device, but also some works still need to be focused onto the element that is responsible for the efficient light capture. The synthesis and/or the modification of new photoactive structure requires a number of optimisation stages. Additionally, if the photoactive material is planned to be used as an electrode, the method of stable immobilisation should be developed to avoid leakages at the current collector/active material interface. Thus, research in the field of novel electrode materials is strongly related with huge effort put on the processing procedures that guarantee construction of the device exhibiting high light harvesting.

Realizing that the manipulation of the photoelectrode nanostructure can bring substantial changes in its activity under irradiation, I focused my research on exploring processing of titania. This material is considered as one of the most promising candidate for highly efficient photoconversion device, especially for third generation solar cells and photo assisted water splitting. Despite titanium dioxide exhibits strong absorption capabilities in ultraviolet light that covers only 5 % of total sun radiation, it can be easily doped or modified by other materials to gain activity also in the visible range.<sup>4</sup> Moreover, depending on the fabrication process, various titania nanostructures characterized by highly developed surface area with controllable morphologies can be produced. The structure of the photoanode

is composed of: (a) a supporting conducting substrate i.e. the current collector and (b) the photoactive layer i.e. the semiconductor material (e.g.,  $\text{TiO}_2$  or  $\text{TiO}_2$  modified with other heteroatoms). The most commonly used support substrates are Ti foil,<sup>5</sup> screen printed carbon electrodes, glass coated with transparent conducting oxide substrates (TCO-glass),<sup>6</sup> flexible polymer substrate (e.g. 4,4'-oxydiphenylene-pyromellitimide known as kapton) covered by conducting oxide layer.<sup>7</sup> The photoelectrode can be obtained by physical or chemical deposition of the photoactive layer on the platform that is responsible for charge collection. An alternative method of fabricating the photoelectrode is based on growing the active material directly on the support substrate. In this case a titanium material that can be in the form of metallic foil, thick plate or wire as well as Ti film deposited on conducting substrates is anodically etched leading to the formation of the photoactive nanostructure. The fabricated photoelectrode can be semitransparent depending on the optical properties of the support substrate. Typically, the semitransparent electrode is obtained when a transparent material (e.g. glass or TCO-glass) is used as the support. The advantage of using a semitransparent electrodes in the photoelectrochemical (PEC) or photovoltaic (PV) devices as compared to the opaque one is that the incident light can pass through this photoelectrode (owing to its transparency features) to excite the semiconductor.<sup>8</sup> In this way more electron-hole pairs can be generated and in consequence the photoconversion efficiency can be improved.<sup>8</sup> Since semitransparent titania-based photoanodes gain more and more attention, particular emphasis has been put to the precise control of the morphologies of titania and further modification of its structure and surface. One can distinguish  $\text{TiO}_2$  nanostructures with various morphologies including the layers composed of nanoparticles and one-dimensional such as nanofibers,<sup>9</sup> nanowires,<sup>10</sup> nanorods,<sup>11</sup> or nanotubes,<sup>6</sup> that grow perpendicular to the substrate surface and were already applied in PEC and PV devices.<sup>12</sup> Comparing to the layers formed by nanoparticles, the one-dimensional titania nanomaterials exhibit straightforward charge percolation.<sup>6</sup> Indeed, although titania nanoparticles are still widely used for the fabrication of photoelectrodes the boundaries between the randomly distributed nanoparticles in the packed layer hamper the effective transport of electrons, thus promoting the recombination processes at the grain boundaries.<sup>13,14</sup> Among different forms of one-dimensional titania mentioned above, the nanotubular form is the most appealing morphology due to its relatively large surface area resulting from the contribution of both the outer and inner surfaces of the tubes. This means that not only the outer area, as in the case of wires is available for the electrochemical process but also the inner area of the nanotubes as well.<sup>15</sup> In addition, the nanotube arrays can be obtained directly out of the Ti film deposited onto stable substrate by anodic oxidation method. Taking into account



numerous samples that are required for the optimisation procedure and further characterisation using the variety of methods on the laboratory scale as well as the potential commercialisation and easy repeatability, a simple fabrication method of the photoelectrode based on titania is widely considered.

In general, the architecture of the TiO<sub>2</sub> nanotubes (TNT) is strictly related with the anodization conditions, namely with electrolyte composition, water content and its temperature as well as the distance between electrodes and applied potential. Owing to the changes in the anodization procedure, the nanotubes can be closely-packed arranged (**Figure 1 (a)**), or clearly visible spaces could be present between the tubes (**Figure 1 (b)**).

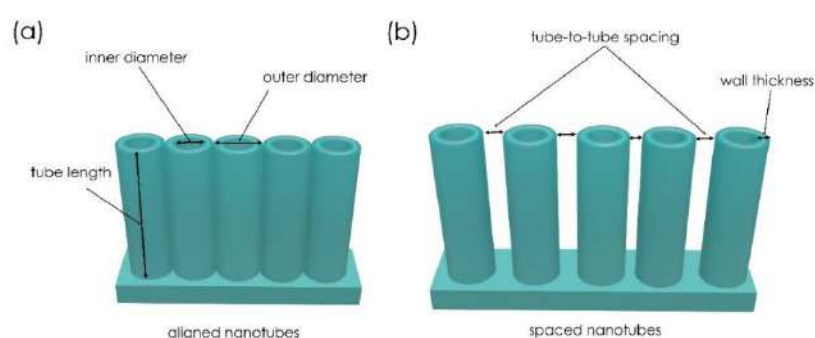


**Figure 1.** Schematic representation of the aligned and spaced TNT architectures.

It is common in the literature that the close-packed nanotubes are often labelled as aligned TNT and the loose-packed nanotubes are frequently recognized as spaced TNT. Those two terms, namely, aligned TNT and spaced TNT come from the vocabulary common in this research area. Taking into account the time line of titania nanotubes development, the close-packed TNT were first synthesized by the anodic oxidation of titanium by Assefpour et al.<sup>16</sup> After that moment, the term “aligned” appeared in literature focused on titanium dioxide nanotubes and is widely used to indicate that the anodic nanotubes are oriented in the direction perpendicular to the substrate surface and the outer wall of one tube touches to the outer wall of the adjacent nanotube.<sup>17,18</sup> Regarding spaced TNT architecture, it is worth to note that they offer additional paths for the electrolyte infiltration by adjusting the space between the tubes that is beneficial for ions storage from electrolyte.<sup>19</sup> In addition, the optimization of the tube-to-tube spacing can affect the decoration of the outer surface of the nanotubes.<sup>20</sup> However, the tubes density i.e. the number of tubes per unit area decreases with increasing the tube-to-tube spacing. This leads to a reduction in the specific active surface available for the photoelectrochemical reaction. Nevertheless, the control of nanotubes arrangement in nanoscale provides a variety of

possibilities regarding their further modifications. More detailed description of both architectures as well as the anodization conditions is provided in the next subsections. After presenting the semitransparent photoelectrodes based on titania nanotubes and describing the different tubular architectures, the methods already reported targeting to augment the photoelectrochemical and electrochemical activities of these semitransparent materials are discussed. For each approach, a concise description of the proposed method and its limitations are provided to clearly show the new aspects developed in the study.

In general, the efficiency of light conversion into current of the pristine single-sided semitransparent anodic titania nanotubes is low (only 7 %).<sup>21</sup> This results from the semitransparency and the wide bandgap of titania. The term single-sided electrode indicates that the active material (e.g.  $\text{TiO}_2$ ) is present only on one side of the support substrate. Therefore, the strategy to take advantage of both the harvesting and the conversion of the incident light from the two sides of the planar substrate has been also explored. Two different synthesis approaches to produce the double-sided semitransparent titania nanotubes photoelectrode have been reported in the literature. According to one fabrication path, the double-sided electrode is fabricated by juxtaposing two different single-sided semitransparent titania nanotube photoelectrodes back to back.<sup>22</sup> However, in this method, the use of two glass substrates instead of one increases the cost of the photoanode system and make the tandem electrode heavy. In addition, the presence of the material which acts as glue to hold the two electrodes together can absorb or disperse a part of the incident light. In the other approach, titania nanotubes were first obtained by anodizing Ti foils.<sup>23</sup> Then, the tubular layers were gently detached from the anodized Ti foil and transferred onto the two sides of the ITO-glass.<sup>23</sup> However, the nanotube layers can be dislocated into several parts during their removal from the Ti foil. In addition, this method is time-consuming as it involves several steps.<sup>24</sup> In consequence, the problem of large-scale production of this photoelectrodes may arise. Unlike the two already known methods, in this work the feasibility to fabricate the double-sided semitransparent titania nanotubes electrode by anodizing independently the two sides of the planar substrate is investigated. An anodization setup equipped with a special sample holder has been used for this purpose. The experimental setup is presented in the section dedicated to the details of anodization method (subsection 4.2.2). The proposed synthesis approach, and used in this work made it possible to effectively control the architectures of the nanotubes on the both sides of the planar substrate. As evidence, the asymmetric photoelectrodes where one side of the electrode is covered by aligned nanotubes and the other one, by spaced nanotubes have been successively synthesized. The two symmetric photoanodes consisting of (a) aligned

nanotubes onto both sides, and (b) spaced nanotubes on both sides were synthesized as well. Investigation on the photoactivity properties of the as-synthesized double-sided electrodes is shown in the results section.

Another strategy of modifying the tubular layer with heteroatoms has also been reported to further increase its conversion efficiency. In this regards, not pure but Ti alloys films such as TiNb,<sup>25</sup> TiCo,<sup>26</sup> TiFe,<sup>27,28</sup> TiMo<sup>29</sup>, TiW,<sup>30</sup> TiCu,<sup>31</sup> TiAg<sup>32</sup> are typically sputtered onto the TCO and subsequently anodized to obtain well dispersed heteroatom within the anodic tubular layer. An increase of the conversion efficiency of about 11 % was reported for the tubular layer formed out of the TiCu alloy film.<sup>31</sup> However, only the aligned TNT architecture was grown out of the alloy films that limits some further modifications. No work was conducted to investigate the feasibility to grow the spaced TNT architecture out of deposited Ti alloy films and then used them as a platform for further modifications. In this study, both single-sided semitransparent spaced TNT and aligned TNT were obtained by anodizing the deposited TiAg alloys onto indium tin oxide coated glass. Then, the influence of the silver content in the deposited alloy films on both the formation of the spaced TNT architectures and the physico-chemical and photoelectrochemical properties of the fabricated nanotubes were investigated.

The modification of the tubular layer can be also realized by depositing noble metal (e.g. Au<sup>33</sup>, AuPt<sup>34</sup>, Ru<sup>35</sup>) on top of the nanotubes. However, the high cost of noble metals is a concern for large-scale production of such photoelectrodes. The recent works reported by Lemos et al,<sup>36</sup> He et al,<sup>37</sup> and Khatun et al.<sup>38</sup> have revealed that the conversion efficiency of dye-sensitized solar cells using photoanode based on titania can be significantly increased up to 30 % by decorating the titania layer with two-dimensional transition metal carbides (e.g. Ti<sub>3</sub>C<sub>2</sub>T<sub>x</sub> known as MXenes) Therefore, Ti<sub>3</sub>C<sub>2</sub>T<sub>x</sub> can be explored as a promising candidate as alternative to the noble metals. Following promising features of MXenes, TiO<sub>2</sub>/Ti<sub>3</sub>C<sub>2</sub>T<sub>x</sub> heterojunctions have been produced through various in-situ treatments, i.e. laser ablation treatment,<sup>39,40</sup> plasma treatment,<sup>41</sup> hydrothermal,<sup>42</sup> or temperature annealing.<sup>43</sup> The benefit of synthesizing TiO<sub>2</sub>/Ti<sub>3</sub>C<sub>2</sub>T<sub>x</sub> heterostructure is to take advantage of the synergistic effects between the outstanding electrical conductivity as well as the good light absorption ability of Ti<sub>3</sub>C<sub>2</sub>T<sub>x</sub> MXenes<sup>44</sup> and the excellent photoactivity of TiO<sub>2</sub>. Thus, the TiO<sub>2</sub>/Ti<sub>3</sub>C<sub>2</sub>T<sub>x</sub> can act as an electrochemical catalyst capable to raise the performance of the semiconductor photoelectrodes. In this work the feasibility to convert Ti<sub>3</sub>C<sub>2</sub>T<sub>x</sub> MXenes into TiO<sub>2</sub>/Ti<sub>3</sub>C<sub>2</sub>T<sub>x</sub> heterostructure via laser ablation method is investigated. Then, a strategy is elaborated to integrate the as-synthesized TiO<sub>2</sub>/Ti<sub>3</sub>C<sub>2</sub>T<sub>x</sub> heterojunction into the semitransparent tubular layer of the photoanode. The detailed description of the laser ablation strategy used in this work as

well as the investigation on the photoactivity of the as-synthesized electrodes is presented in the results section.

This section provided detailed explanations on the different steps involved in the fabrication of the semitransparent anodic titania nanotubes. The physical coating methods reported for the deposition of Ti film onto TCO-glass, which are subsequently anodized, are presented. The anodization method and the different anodic tubular architectures are described as well.

## 4.2 Fabrication of anodic semitransparent $\text{TiO}_2$ nanotubes

The first step in the PhD works was the optimisation of the anodization procedure to reach well organized semitransparent titania nanotubes of various spatial arrangements. The steps involved in the whole fabrication process are shown in **Figure 2**.

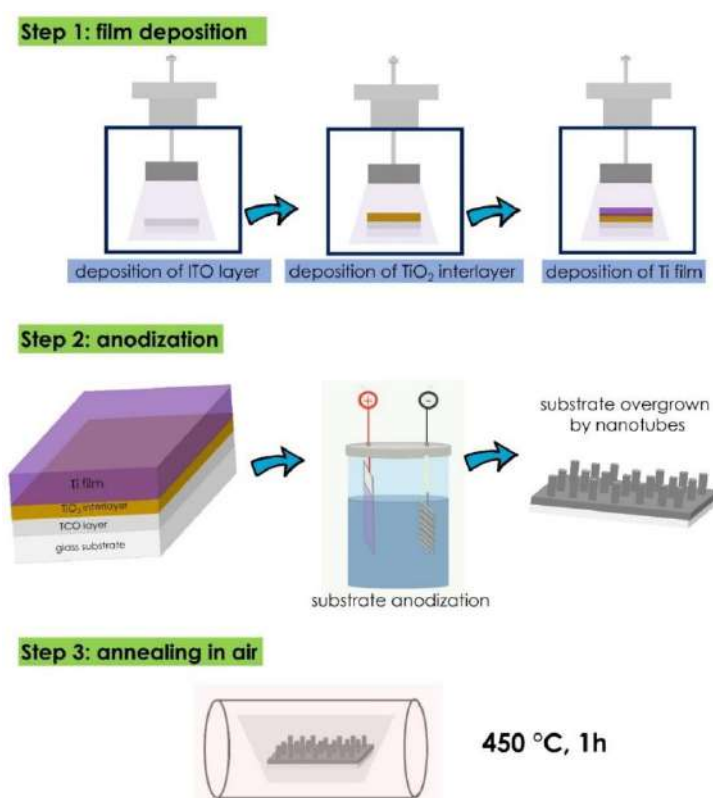


**Figure 2.** Schematic of the steps of the synthesis process: (1) deposition of the film (i.e. TCO,  $\text{TiO}_2$  interlayer and Ti film) followed by (2) the anodization and subsequent, (3) annealing of the as-anodized materials.

As shown in **Figure 2** the fabrication procedure requires not only the elaboration of the anodization process but also the preparation stages crucial for the successful synthesis. The

sample after the deposition step (i.e. step 1) is composed of three different layers, namely TCO, TiO<sub>2</sub> and Ti layers, consecutively deposited onto the glass substrate. The glass substrate serves as a stable support during sputtering and also its surface should be cleaned before. The role of each deposited layer (namely, TCO and TiO<sub>2</sub> layers) related with the quality of the tubular oxide layer (i.e. in obtaining a cracks-free tubular oxide layer) during the anodization process is explained in this subsection. Due to its relatively low electrical resistance (sheet resistance  $\approx 10 \text{ } \Omega$ )<sup>45</sup>, the TCO layer plays the role of current collector both during the anodization of the substrate and during the electrochemical and photoelectrochemical testing of the anodized material.<sup>45</sup> Due to that any performed process must therefore not lead to their damage. As shown in **Figure 2** (in step 2), a TiO<sub>2</sub> interlayer concatenates the sputtered Ti film and the TCO layer, which improves the adhesion between the Ti film and the TCO.<sup>46</sup> The presence of this transition layer is crucial to obtain semitransparent material with cracks-free tubular oxide layer.<sup>47,48</sup> Indeed, the anodization of substrates in the glass/TCO/Ti configuration, i.e. without the TiO<sub>2</sub> transition layer between the TCO layer and the Ti film, resulted in the detachment of the tubular oxide layer from the substrate during the anodization process.<sup>47,48</sup> This spontaneous removal of the tubular layer from the substrate occurs due to the release of oxygen molecules at the TCO surface, resulting from the contact of the electrolyte with the highly conductive TCO layer. As shown in **Figure 3**, the release of oxygen formed at the electrolyte/TCO electrode interface is evident from the analysis of current-time profiles recorded by Kim et al.<sup>47</sup> during the anodization of TCO/Ti and TCO/NTO/Ti substrates, where Nb-doped TiO<sub>2</sub> (NTO) acts as the transition layer between the TCO layer and the Ti film.

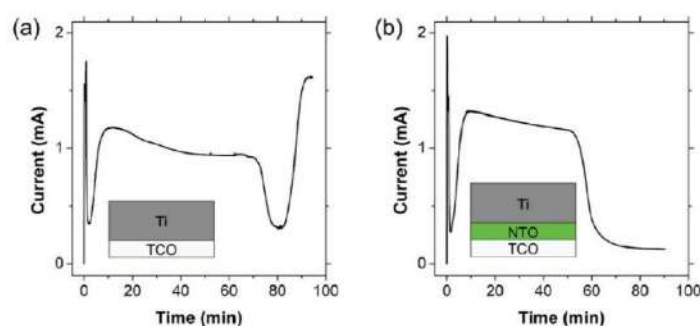


**Figure 3.** Anodization current as a function of time of substrates: (a) without and (b) with NTO interlayer between the TCO and the deposited Ti film. (Reprinted with the permission from reference<sup>47</sup>).

The release of the gas bubbles can be also seen on the anodized area of the sample by the naked eye during the anodization. As it can be seen in **Figure 3**, after 80 minutes, the

anodization current of the TCO/NTO/Ti sample becomes constant whereas, in the case of the TCO/Ti sample, an abrupt increase in the anodization current occurs. This sudden increase in current is associated with the oxidative degradation of the TCO layer with concomitant release of oxygen gas at its surface due to the contact with the electrolyte. This leads to the delamination of the tubular oxide layer.<sup>47,48</sup> Similar sudden increase in the anodization current shown in **Figure 3 (a)** accompanied of the detachment of the tubular layer have been also observed by Krumpmann et al.<sup>48</sup> during the anodization of TCO/Ti substrate. To solve this problem, Krumpmann et al.<sup>48</sup> proposed to stop the anodization process before the complete transparency of the substrates in order to avoid the contact between the electrolyte and the TCO layer. However, the transparency of the anodized substrate is an important parameter, especially for photoelectrochemical devices. Thus, the introduction of the protective TiO<sub>2</sub> thin film as the interface between the TCO layer and the Ti film seems to be the most simple and suitable way to achieve regular formation of the semitransparent nanotubes with cracks-free tubular oxide layer. In addition, the oxidative degradation of the current collector (i.e. TCO) leads to a significant increase in the electrical resistance of the TCO after the anodization of the substrate.<sup>47,48</sup> This will obviously lead to the poor performance during the electrochemical and photoelectrochemical test.

In this work the deposition configuration shown in **Figure 2** (i.e. glass/TCO/TiO<sub>2</sub>/Ti) was adopted for the preparation of the samples for further modifications. After discussing the role of the TCO and TiO<sub>2</sub> layers in the glass/TCO/TiO<sub>2</sub>/Ti deposition configuration, the next subsection will be dedicated to the description of the different deposition methods utilized to form metal and metal oxide films.

#### 4.2.1 Deposition methods of Ti film onto transparent conducting oxides

The magnetron sputtering technique was used for the deposition of both Ti film and Ti alloy films onto indium tin oxide coated glass (ITO-glass). This task was carried out by our partners from Czech Republic: University of South Bohemia in Ceske Budejovice and Charles University in Prague within the cooperation established for the realization of CEUS-UNISONO project 2020/02/Y/ST8/00030. Another method, namely electron beam evaporation has been also reported by other researchers for the deposition of Ti film that was subsequently anodized. For example, the electron beam evaporation technique was used in the works of Mor et al.,<sup>49</sup> Kim et al.,<sup>50</sup> Krysa et al.,<sup>51</sup> Heljo et al.,<sup>52</sup> Kim et al.,<sup>53</sup> and Chappanda et al.<sup>54</sup> for the deposition

of the Ti film onto quartz glass, fluorine-doped tin oxide (FTO), ITO and Si substrates, and then the deposited films were anodized for the fabrication of TiO<sub>2</sub> nanotubes.

In this subsection, a comparative study based on the literature regarding the mechanical, morphological and electrical properties of Ti films deposited onto TCO produced by electron beam evaporation and magnetron sputtering is presented, since those features are strongly related with the performance of the obtained electrode materials. The SEM images, reported by Mor et al.<sup>49</sup>, shown in **Figure 4** indicate that the titanium film obtained by magnetron sputtering deposition is more smooth and compact than the loosely packed granular film produce by electron beam evaporation.<sup>49</sup>

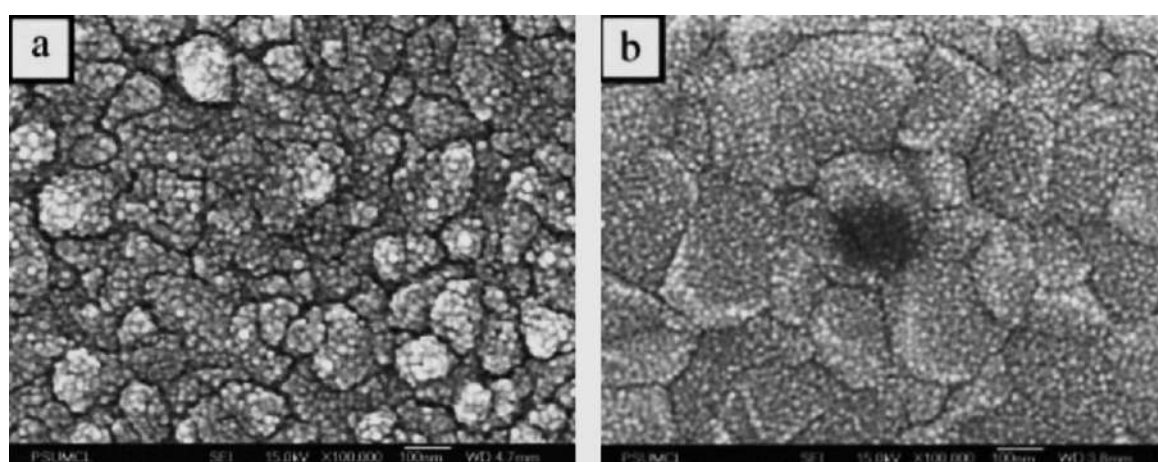


**Figure 4.** Morphology of Ti film deposited onto glass substrate by (a) the electron beam evaporation and (b) RF magnetron sputtering. (Reprinted with the permission from reference<sup>49</sup>).

Investigations on the mechanical properties such as the hardness and the reduced modulus of the deposited Ti films using these two methods (i.e. magnetron sputtering and electron beam evaporation) have demonstrated that the sputtered film exhibits greater hardness and reduced modulus of  $3.4 \pm 0.4$  GPa and  $141 \pm 5$  GPa, respectively, comparing to those of the evaporated Ti films (i.e.  $3.0 \pm 0.3$  GPa and  $115 \pm 6$  GPa).<sup>51</sup> Those relatively poor mechanical properties of the evaporated Ti films can be explained by the large amount of pinholes generated in the deposited film using the electron beam evaporation method (shown in **Figure 5 (a)**).<sup>51</sup>

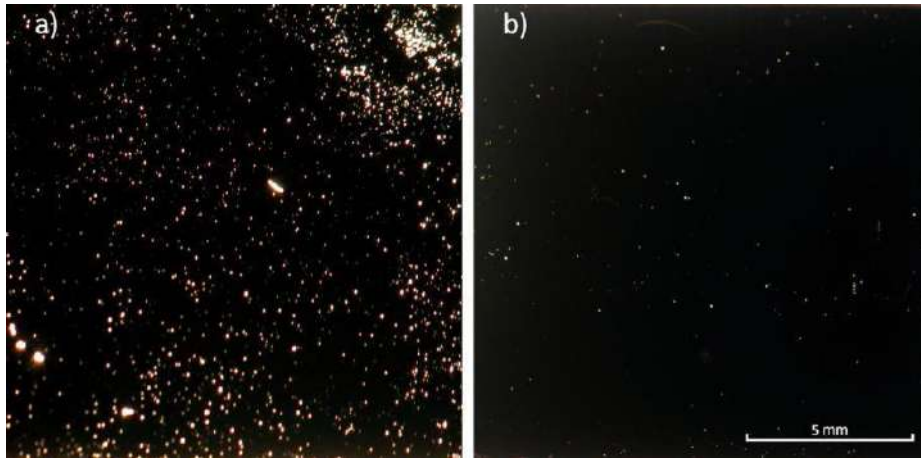


**Figure 5.** Optical microscope image of the deposited Ti film onto glass substrate by (a) the electron beam evaporation and (b) RF magnetron sputtering.

(Reprinted with the permission from reference <sup>51</sup>).

Moreover, both Krysa et al.<sup>51</sup> and Mor et al.<sup>49</sup> have reported the presence of cracks over the oxide tubular layers after anodizing the evaporated Ti films. These works have also shown that the sputtered Ti film is more dense compared to the evaporated one, which is crucial to obtain well-ordered and cracks-free oxide tubular layers after anodization.<sup>55</sup> Furthermore, a comparative study conducted by Arshi et al.<sup>56</sup> on the electrical resistivity (four-point probe technique) of Ti film deposited by magnetron sputtering and electron beam evaporation methods revealed that the sputtered Ti films exhibit approximately 5 times lower electrical resistivity than the evaporated film. The good conductivity of the deposited Ti layer is another important parameter that facilitate the anodization process.

These results gathered by other groups also supports the utilization of magnetron sputtering technique in this work. The working principle of the magnetron sputtering method is described in detail in the method section.

#### 4.2.2 Anodization

Metals such as magnesium, aluminium and titanium and their alloys have light weight, low density and high strength-to-weight ratio.<sup>57</sup> Those features are considered as very attractive for industrial applications. However, local corrosion occurs on the surface of these metals when exposed to aggressive external environments, for example solutions containing chemicals such as chlorides or sulfates.<sup>58</sup> In 1857, Buff discovered that an oxide layer grow on the surface of the aluminium metal immersed in an aqueous solution when the metal is positively polarized.<sup>59</sup> The discovery of this phenomenon gave rise to a new coating method called “anodization”. The



name anodizing was proposed because this phenomenon occurs when aluminium is used as an anode in the electrochemical cell.<sup>58</sup> Material properties, including hardness, corrosion and abrasion resistance, can be improved by anodizing metals in appropriate electrolytes.<sup>58</sup> Thus, by the early 1920s, the anodizing method was widely used in industry to protect seaplane parts from corrosive seawater.<sup>58</sup> In addition, a tubular oxide layer can be also obtained through anodization out of the metal foil under specific anodization conditions.

This subsection has a two main objectivities:

- presentation of synthesis generations of anodic TiO<sub>2</sub> nanotubes,
- description of different mechanisms proposed to explain the anodic growth of the tubular oxide layer.

### Anodic TiO<sub>2</sub> nanotubes and their generations

Anodization is a simple method that yields more reproducible results in obtaining directly oxide tubular layers out of Ti foil<sup>60</sup> or Ti film deposited onto TCO.<sup>61</sup> Titania based materials produced after the anodization can exhibit highly ordered and well-defined vertically oriented nanotubes uniformly distributed over the surface of the TCO. The reliability of the anodization method lies in its effectiveness to control the geometric features of the tube, namely the tube length, wall thickness, pore diameter as well as the tube-to-tube spacing. Anodization can be carried out in two<sup>61</sup> or three<sup>62</sup> electrode cell system or even in bipolar orientation, when the Ti is immersed in the electrolyte but is not connected directly to the external circuit. The anodization setups for two or three-electrode system are presented in **Figure 6**.

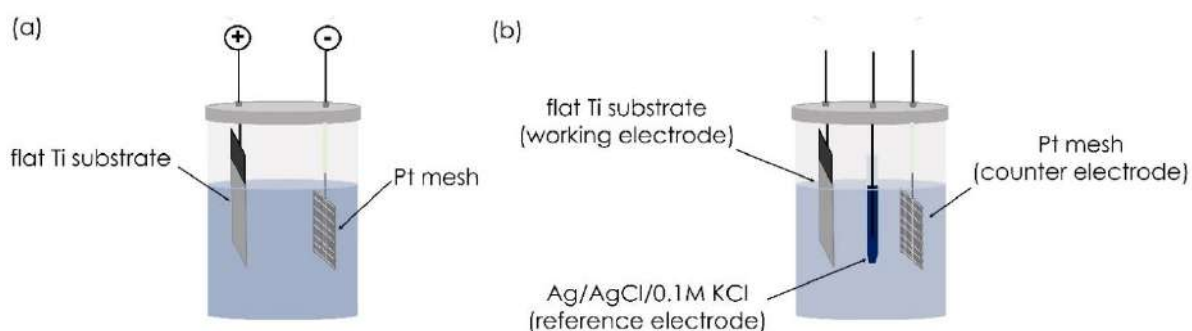


**Figure 6.** Electrochemical cell used for the anodization in (a) 2-electrode arrangement and (b) 3-electrode arrangement.

For two-electrode system, the Ti film deposited on TCO (or Ti foil) and a platinum mesh (or graphite rod) are connected to the positive and negative terminals of the power supply

(**Figure 6 (a)**). In the case of the three-electrode system, the Ti substrate, platinum mesh, and Ag/AgCl act as working, counter, and reference electrodes, respectively, as shown in **Figure 6 (b)**. The sample holder for the Ti film deposited on TCO used in this work dedicated for the synthesis of the double sided electrode is presented in **Figure 7**.

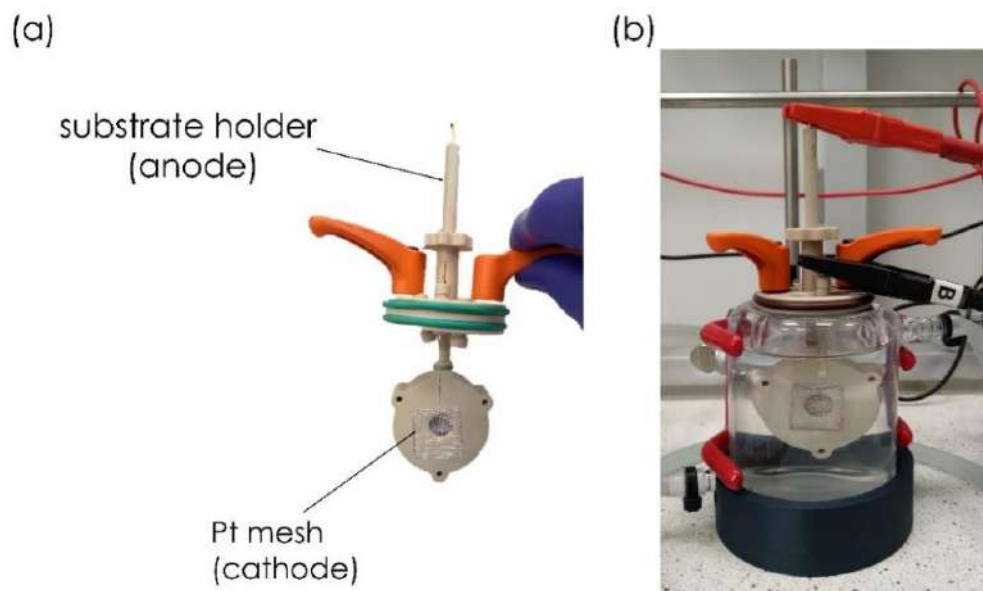


**Figure 7.** Part of electrochemical setup used for the anodization of the single-sided and the double-sided samples in (a) image of the substrate holder together with Pt mesh, (b) image of the anodization cell.

The anodic growth of nanotubular arrays of  $\text{TiO}_2$  can be classified into three synthesis generations depending on the chemical nature of the used electrolyte. The first synthesis generation of  $\text{TiO}_2$  nanotubes was produced in acid electrolyte based on a the mixture of  $\text{H}_2\text{CrO}_4$  and HF by Assefpour-Dezfuly et al.<sup>16</sup> in 1984. Nanotubes with an average tube length of about 500 nm were achieved. However, for the practical application of these materials as photoelectrodes, the thickness of the nanotubes layer must be relatively long for the efficient absorption of the incident light.<sup>63</sup> As explained by Zhao et al.,<sup>63</sup> to increase the efficiency of photoelectrodes based on titanium nanotubes, the length of the tube must be greater than the penetration length of the incident light. Later, other researchers such as Gong et al.<sup>64</sup> and Mor et al.<sup>65</sup> attempted to produce longer nanotubes by optimizing the concentration of HF in the electrolyte. Unfortunately, their approaches were unsuccessful. In general, the presence of HF in the electrolyte results in faster formation as well as dissolution rates of the  $\text{TiO}_2$  oxide layer at the top, thereby limiting the length of the nanotubes. The use of weak inorganic acid based

electrolytes, i.e. buffered KF or NaF aqueous solutions, has been proposed by Cai et al.<sup>66</sup> as an alternative to the acidic based electrolyte. Indeed, Cai et al.<sup>66</sup> obtained a tubular layer with an average tube length 10 times longer than that obtained with the acidic solution of HF. This achievement gave rise to the second synthesis generation of TiO<sub>2</sub> nanotubes. Although buffered aqueous solutions can produce relatively long nanotubes, the high water content of these electrolytes introduces another problem. Indeed, it has been demonstrated that the increase in water content in electrolytes also can lead to a rapid chemical dissolution of the formed oxide.<sup>67</sup> Therefore, to obtain a tubular layer with an average tube length even in the millimeter range, the water content must be reduced. This is the basic concept that initiated the exploration of the range of organic electrolytes such as glycerol, ethylene glycol, diethylene glycol, triethylene glycol and dimethyl sulfoxide. The era of the use of these organic electrolytes introduced the third generation of TiO<sub>2</sub> nanotubes. In general, compared to the inorganic buffer solutions, much longer and smoother tubes can be grown in viscous organic electrolytes. The viscosity of the organic solution is an important parameter that strongly affects the ionic mobility in the electrolyte.<sup>62</sup> TiO<sub>2</sub> nanotube array of 1 mm in length has been reported by Paulose et al.<sup>68</sup> by using ethylene glycol based electrolyte containing 0.6 wt% NH<sub>4</sub>F in 3.5 vol % H<sub>2</sub>O.

### **Growth mechanism of self-organized anodic nanotubes**

The anodic growth mechanism of titanium nanotubes is still not fully clear. This section discusses two models mostly evoked in the literature, namely field-assisted dissolution theory and oxygen bubble model to explain the formation of tubular morphology during the anodization process.

#### *Field-assisted dissolution theory*

Hoar and Mott were the first who propose the “field-assisted dissolution theory” to explain the mechanism of anodic formation of porous alumina films.<sup>69</sup> Later, the field-assisted dissolution theory was also used to describe the anodic formation of porous or tubular oxide layer obtained out of Ti in electrolyte containing fluorine ions. This explanation remains until now the most cited one to describe the anodic growth of porous or tubular oxides layers out of other metals such as Ti,<sup>70</sup> Sn,<sup>71</sup> Zr<sup>72</sup> and Nb<sup>73</sup>. According to field-assisted dissolution theory, the formation of the tubular layer results from the dynamic equilibrium between the growth rate of the oxide layer at the metal/oxide interface and its chemical dissolution occurring at the oxide/electrolyte interface. Three steps can be distinguished in process described by the field-assisted dissolution theory i.e.:

- (I) field-assisted oxidation of Ti metal,
- (II) field-assisted dissolution, and
- (III) chemical dissolution (or etching) of TiO<sub>2</sub> by fluoride ions.

Each step i.e. (I), (II) and (III) in the anodization timeline is indicated in the **Figure 8**.

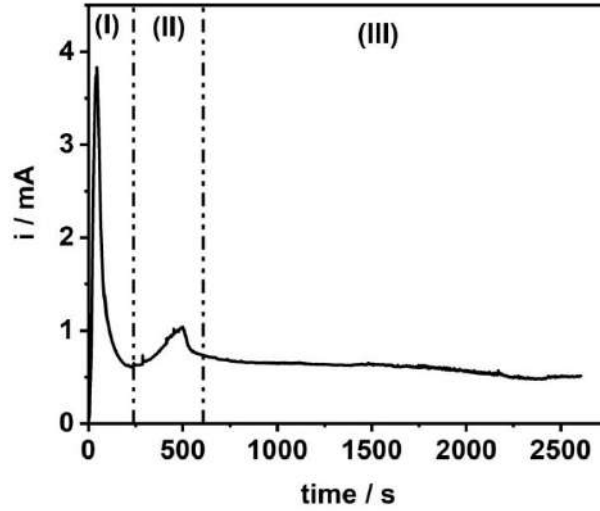


**Figure 8.** Anodization current as a function of time recorded during the anodization of Ti film deposited onto ITO-glass in ethylene glycol-based electrolyte mixed with 0.27 M NH<sub>4</sub>F, 1 M H<sub>3</sub>PO<sub>4</sub>, and 5 vol% H<sub>2</sub>O at 60 V.

Step (I), field-assisted oxidation of Ti: the chemical reactions between Ti and the anions: O<sup>2-</sup> and OH<sup>-</sup> arising from the dissociation of water in the electrolyte, due to the applied electric field leads to the formation of a barrier oxide layer at the Ti/electrolyte interface as described in equations (1) to (4).



The formation of the barrier oxide layer leads to a decrease of the current as show in the step (I) (**Figure 8**).

In step (II), the field-assisted dissolution occurs and the Ti<sup>4+</sup> ions are transported from the bulk metal towards the electrolyte due to the applied voltage, where they dissolve and form a titanium hexafluoride complex with the fluorine ions according to the equation (5). The

migration of the  $Ti^{4+}$  in the electrolyte leads to a slight increase in the current as shown in **Figure 8**.



Then, in step (III), chemical dissolution of  $TiO_2$  by fluoride ions occurs. During this step, the etching of the formed oxide layer by the fluorine ions trapped at the  $TiO_2$ /electrolyte interface leads to the formation of pits. These pits play the role of pore embryos forming centres. The conversion of the porous layer to the tubular structure occurs when the rate of growth of the oxide layer and the rate of dissolution of the oxide layer reach the equilibrium state (equations (6) and (7)).



This competition between the growth of the  $TiO_2$  oxide layer and its dissolution by fluoride ions is crucial for the formation of the tubular structure. At this stage, the current undergoes a steady state as shown in step (III) **Figure 8**.

### ***Oxygen bubble model***

Although field-assisted dissolution theory is frequently evoked to explain the anodic formation of  $TiO_2$  nanotubes, this theory cannot explain the appearance of gaps between tubes, which lead to the laterally spaced nanotubes architecture.<sup>74</sup> Furthermore, as required by field-assisted dissolution theory, the formation of the anodic tubular nanostructure results from the dynamic equilibrium between the growth rate of the oxide layer at the  $Ti/TiO_2$  interface and its chemical dissolution at the  $TiO_2$ /electrolyte interface caused by fluoride ions. However, the work of Yu et al.<sup>75</sup> revealed that  $TiO_2$  oxide stops growing at the bottom while its chemical dissolution continues. That is an evidence against the traditional field-assisted dissolution theory. In addition, Lu et al.<sup>76</sup> and Fahim et al.<sup>77</sup> have obtained tubular layer by anodizing Ti in fluorine-free electrolyte. Furthermore, the current-time curve recorded during anodization by Fahim et al.<sup>77</sup> in  $H_2SO_4$  solution was similar to those obtained also in a fluorine-containing electrolyte. This achievement demonstrated that the presence of the fluorine ions is not essential for the initiation of the formation of the pore embryos as is considered as critical factor in the field-assisted dissolution theory according to the equation (6) and (7). The oxygen bubble model was proposed by Zhu et al.<sup>78</sup> to explain the formation of a porous or tubular layer in a fluorine-free electrolyte. Unlike field-assisted dissolution theory, the oxygen bubble model states that

the initiation of pore formation results from the evolution of oxygen anions trapped within the oxide layer during its growth.<sup>78</sup> The series of steps involved in this model can be well understood from the scheme presented in **Figure 9**.

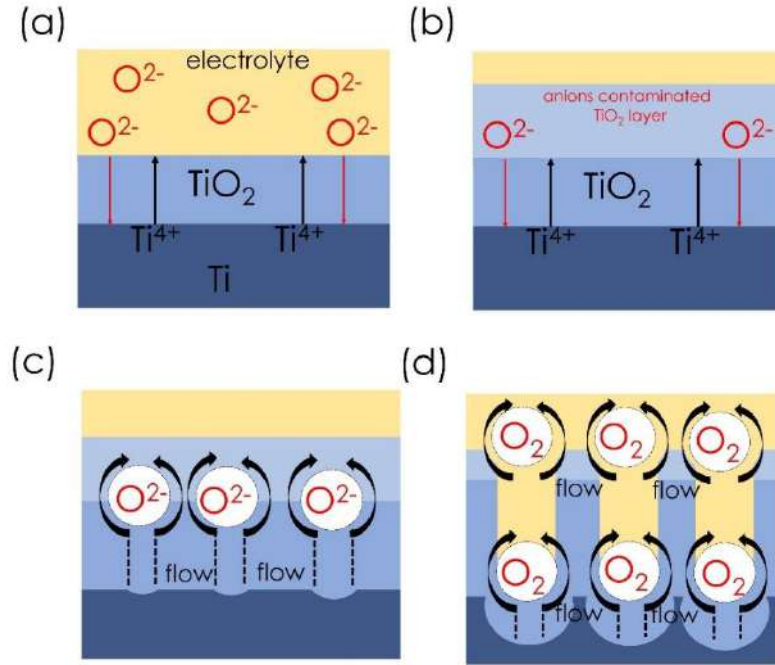


**Figure 9.** The nanotubes growth diagram according to the oxygen bubble model.

(a) Formation of the barrier oxide layer. (b) Formation of the anion-contaminated oxide layer near the electrolyte. (c) Formation of hemispherical shape for pores bottom. (d) Upward growth of the tube wall due to the volumetric expansion of oxygen.

In this model, the formation of the barrier oxide layer results from the ionic current (i.e., the migration of  $\text{Ti}^{4+}$  and  $\text{O}^{2-}$  ions), as shown in **Figure 9 (a)**.<sup>74,78</sup> As the oxide barrier layer grows, nearby  $\text{O}^{2-}$  ions are inevitably trapped inside the  $\text{TiO}_2$  layer, leading to an anion-contaminated layer near the electrolyte (**Figure 9 (b)**).<sup>74,78</sup> Since the electrodes are connected to the power supply, the electric current oxidizes the  $\text{O}^{2-}$  ions to  $\text{O}_2$  gas (**Figure 9 (c)**) and the release of oxygen gas takes place in the barrier oxide layer.<sup>74,78</sup> The pressure due to the  $\text{O}_2$  gas within the oxide layer leads to the appearance of hemispherical nanostructures at the  $\text{TiO}_2/\text{Ti}$  interface.<sup>74,78</sup> The increase in pressure initiates the formation of embryonic pores within the layer contaminated by the anions.<sup>74,78</sup> The nanotubes grow due to the upward volumetric expansion of the  $\text{O}_2$  gas toward the  $\text{TiO}_2/\text{electrolyte}$  interface where it is released (**Figure 9 (d)**).<sup>74,78</sup>

### 4.3 Different morphologies of the titania nanotubes

This section presents two titania nanotubes architectures that have been synthesized in this work namely, aligned and spaced nanotubes. In general, the tubular layers produced using both acid electrolyte containing fluorine ions (first generation) and the buffered KF or NaF aqueous solutions (second generation) i.e. by adjusting the pH of the solution at a desired value, have a closely packed, known as aligned TNT, architecture. Similar tightly packed nanotubes were also obtained using a mixture of organic solutions based electrolyte (e.g. glycerol,<sup>79</sup> ethylene glycol,<sup>79</sup> sodium carboxymethyl cellulose,<sup>80</sup> and 1-butyl-3-methylimidazolium tetrafluoroborate<sup>81</sup>) with fluorine salts enabling formation of third generation titania nanotubes. However, among all already listed organic electrolyte, Niu et al.<sup>79</sup> have shown that the average length of the nanotubes obtained in ethylene glycol is roughly 2 times longer than that produced in glycerol solution. Macak et al.<sup>62</sup> also have reported anodic TiO<sub>2</sub> nanotubes with a length of 1.6  $\mu\text{m}$  in ethylene glycol electrolyte compared to 1.3  $\mu\text{m}$ -long in glycerol solution. Although sodium carboxymethyl cellulose is cheaper organic compound than glycol electrolyte and glycerol, only nanotubes with a length of 450 nm have been reported by Mohamed et al.<sup>82</sup> when Ti anodization was carried out in sodium carboxy methylcellulose solution. The optimization of the anodization conditions for the growth of the tubular structure in the ionic liquid (i.e. 1-butyl-3-methylimidazolium tetrafluoroborate) electrolyte enabled to reach tube length of only 650 nm.<sup>81</sup> On the contrary, 1 mm-long TiO<sub>2</sub> nanotubes were achieved by Paulose et al.<sup>68</sup> in ethylene glycol based electrolyte. The results showed that TiO<sub>2</sub> nanotubes produced in an ethylene glycol-based electrolyte are much longer comparing to those obtained in the other organic electrolytes. The possibility to obtain longer nanotubes is very important since as common for photoactive nanostructures, the photoelectrochemical and electrochemical activity of anodic TiO<sub>2</sub> nanotubes strongly depends on their active surface area. Because tube length is directly correlated to the active surface area of the tubular layer (i.e., the area of all the inner and outer walls), material performance can be optimized by the manipulation of length of the nanotubes. Taking into account already published data, in this work ethylene glycol was also used as organic electrolyte. The morphology of aligned nanotubes (top and cross-section images) architecture is presented in **Figure 10**.

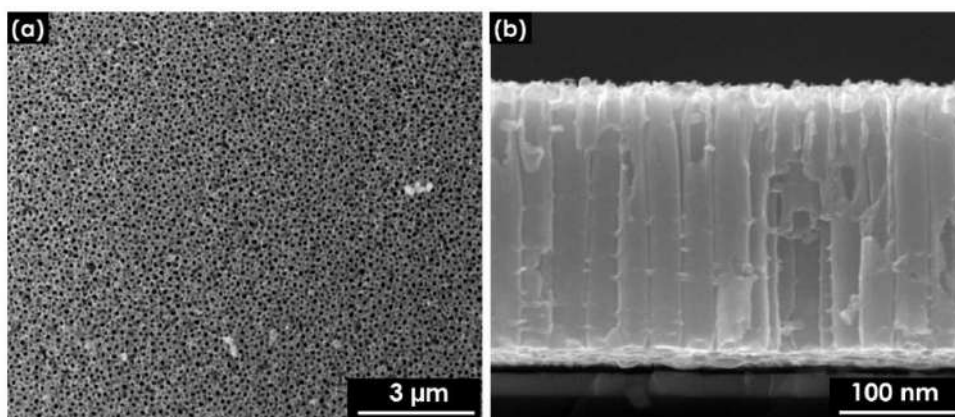


**Figure 10.** SEM (a) top image and (b) cross-section image of aligned TiO<sub>2</sub> nanotubes obtained from Ti film anodized in ethylene glycol-based electrolyte mixed with 0.27 M NH<sub>4</sub>F, 1 M H<sub>3</sub>PO<sub>4</sub>, and 5 vol% H<sub>2</sub>O at 60 V.

Later on, the work of Ozkan et al.,<sup>83,84</sup> Nguyen et al.,<sup>85</sup> Niu et al.<sup>79</sup> and Zhang et al.<sup>19</sup> showed that not only tube geometry (i.e. length, wall thickness, and pore diameter) is sensitive to electrolyte composition, but also the distance between the tubes. As evidence, anodizing Ti in organic electrolytes such as diethylene glycol, triethylene glycol, and dimethyl sulfoxide leads to a tubular layer with clearly visible gaps between the tubes. This tube-to-tube distance can reach up to few hundred nanometres.<sup>19,83–85</sup> Controlling the tube-to-tube spacing will obviously be a simple way to provide more additional channels for electrolyte penetration through the tubular layer. The advantage of tube-to-tube spacing control is not only limited to electrochemical storage devices such as fuel cells, Li-ion batteries, supercapacitors which required high porosity to store ions but for light harvesting application as well. In fact, adjusting the gaps between the tubes will also allow decorating the outer surface of the nanotubes with for example plasmonic nanoparticles, which can increase the photoactivity of these materials being beneficial for application in solar cells. Ruiquan et al.<sup>86</sup> explained the appearance of regular spaces between individual nanotubes, which leads to the spaced titania nanotubes architecture, by using the oxygen bubble model. The schematic diagrams of the formation of the space between individual nanotubes according to the oxygen bubble model proposed by Ruiquan et al.<sup>86</sup> are shown in **Figure 11**. As given in step (II) of **Figure 11**, the release of oxygen gas, confined within the oxide barrier layer during the step (I), leads to the formation of the porous structure. In stage (III), the pressure of the oxygen bubbles at the bottom of the pores causes the expansion of the oxide barrier layer. The appearance of the space between the tubes results from the repulsive forces induced between neighbouring cells during the expansion of the oxide layer and the distribution of the electric field at the pore bases.



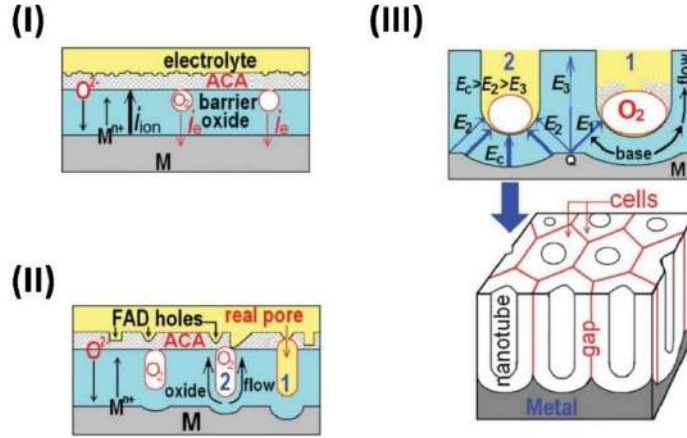


**Figure 11.** Schematic diagrams of the formation of gaps between individual nanotubes according to the oxygen bubble mold model.  
(Reprinted with the permission from reference.<sup>86</sup>)

In this work, the anodization of the Ti film in diethylene glycol made it possible to obtain the loosely packed structure of nanotubes by adjusting the water content in the electrolyte and the fluorine ion concentration. The feasibility of growing laterally spaced nanotubes using both triethylene glycol and dimethyl sulfoxide has not been studied in this work. The example of the surface morphology of spaced nanotubes architecture obtained in diethylene glycol electrolyte is presented in **Figure 12**.

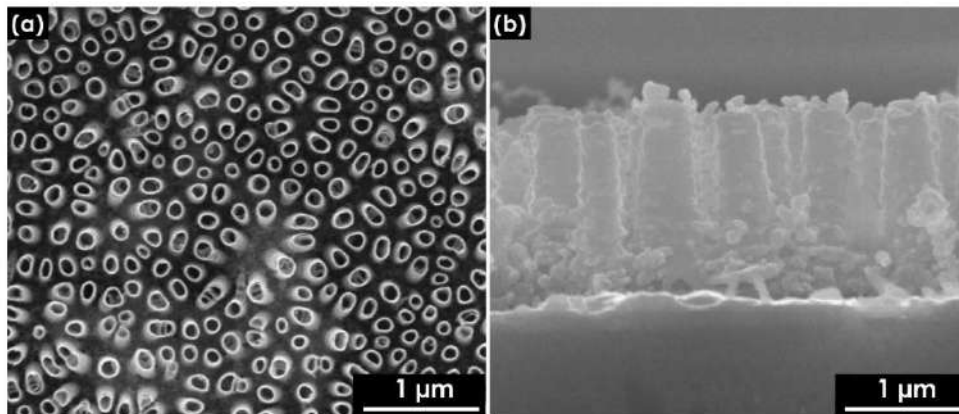


**Figure 12.** High resolution SEM (a) top image of spaced  $TiO_2$  nanotubes showing visible gaps between nanotubes, and (b) cross-section image of the anodized sample obtained out of Ti film anodized in diethylene glycol electrolyte mixed with 0.15 M  $NH_4F$ , 0.5 M  $HF$ , and 7 vol%  $H_2O$  at 40 V.

#### 4.4 Effect of annealing on the crystalline phase of titania

According to results provided by Aiempanakit et al.<sup>87</sup> Bjelajac et al.<sup>61,88</sup> and Vadla et al.<sup>7</sup> after anodizing the Ti film, like in the case of anodized titanium foil the obtained oxide layer is amorphous. In general, the photoactivity of such amorphous materials is low due to the disordered local atomic arrangement of their microstructures.<sup>89–91</sup> This disordered amorphous microstructure will hamper the percolation of charges leading to a substantial increase of the electron–hole recombination rate.<sup>89–91</sup> Therefore, a nearly perfect titania microstructure (i.e. crystalline one) is required to facilitate the percolation of electrons.<sup>89,92</sup> The amorphous layer obtained after the anodization of the Ti film must be transformed into a crystalline phase of titania to expect good photoconversion efficiencies. The three different crystalline phases of titania can be distinguished in nature: anatase, brookite and rutile. The set of parameters for the crystal structure of the polymorphic phase (i.e. anatase, brookite and rutile phases) of titania are set in **Table 1**.

**Table 1.** The parameters known for the different crystal structures of titania.<sup>93,94</sup>

parameters	anatase	brookite	rutile
crystal structure	tetragonal	orthorhombic	tetragonal
Ti-O bond length (Å)	1.949 (4) 1.980 (2)	1.87 – 2.04	1.937 (4) 1.965 (2)
O-Ti-O bond angle	81.2 ° 90.0 °	77.0 ° – 105 °	77.7 ° 92.6 °
lattice constant (Å)	a = b = 4.5936 c = 2.9587	a = 9.184 b = 5.447 c = 5.154	a = b = 3.784 c = 9.515
space group	I4 <sub>1</sub>	pbca	P4 <sub>2</sub>
density (g cm <sup>-3</sup> )	4.13	3.99	3.79

Those various polymorphic phase of titania can be obtained by an appropriate treatment of its amorphous phase, including soaking in hot water,<sup>95</sup> laser annealing,<sup>96</sup> solvothermal,<sup>7</sup> and thermal annealing in air.<sup>61</sup> For example, as shown in **Figure 13**, anatase titania has been obtained by irradiating the amorphous titania for one minute by a 532 nm-laser beam (10× objective) with a laser power of 75 W mm<sup>-2</sup>.<sup>96</sup> The increase of the laser power to 275 W mm<sup>-2</sup>

led to a mixture of anatase and rutile phase, whereas, the further raise of the laser power up to  $445 \text{ W mm}^{-2}$  fully transformed the initial anatase phase to rutile one.

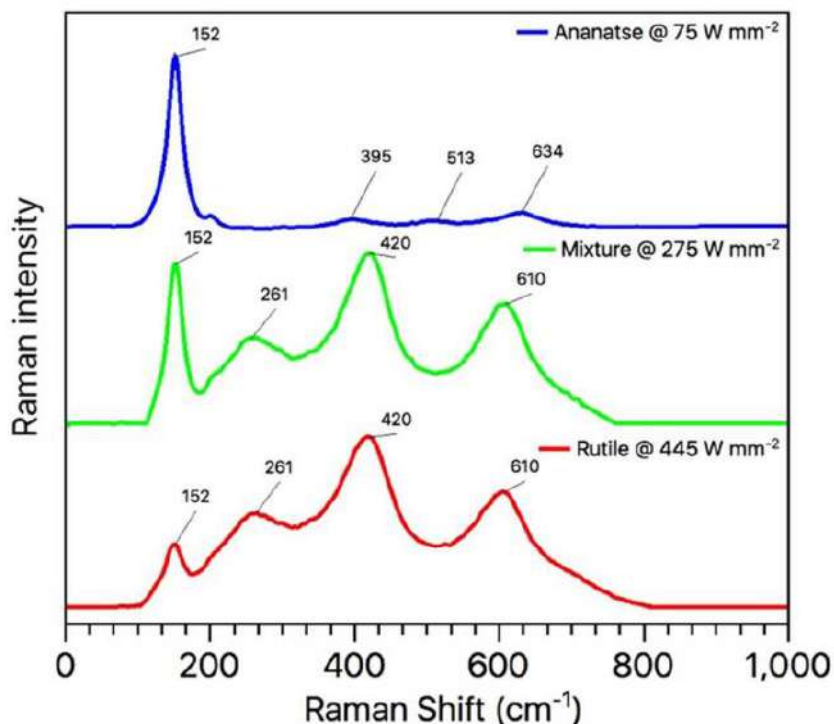


**Figure 13.** Raman spectra of titania material irradiated with 532 nm-laser beam at different laser power. (Reprinted with the permission from reference. <sup>96</sup>)

Among the different titania crystalline phases, the rutile phase of titania is the most thermodynamically stable one.<sup>97</sup> Lebedev et al.<sup>98</sup> have shown that the rutile phase can be detected after annealing in the air amorphous titania by slow heating (e.g.  $5 \text{ }^{\circ}\text{C/min}$ ) to  $500 \text{ }^{\circ}\text{C}$  or by fast heating (<e.g.  $5 \text{ }^{\circ}\text{C/min}$ ) to  $600 \text{ }^{\circ}\text{C}$ .<sup>98</sup> However, those relatively high temperatures can cause the destruction of the ordered tubular layer. Indeed, Shivaram et al. <sup>99</sup> have observed under scanning electron microscope signs of degradation of the tubular layer after annealing the sample at  $500 \text{ }^{\circ}\text{C}$ . In addition, the collapse of the titania nanotubes have been reported for the annealing temperature of  $600 \text{ }^{\circ}\text{C}$ .<sup>61</sup> Unlike to the rutile phase, anatase titania can be obtained at relatively low temperature even at  $230 \text{ }^{\circ}\text{C}$  by solvothermal.<sup>7</sup> The complete transformation of amorphous titania (nanotube arrays) to anatase by annealing of the titania sample in air at  $350 \text{ }^{\circ}\text{C}$  was also reported.<sup>45</sup> In addition, anatase nanotubes obtained after the annealing of the amorphous sample at  $450 \text{ }^{\circ}\text{C}$ , have shown an increase in the photoresponse about 100 times

higher comparing to the amorphous sample.<sup>89</sup> The brookite phase is the most instable one and difficult to synthesize.<sup>100</sup> To avoid the thermal degradation of the organized tubular layers all anodized samples in this work were annealed at 450 °C for an hour to convert them into the anatase titania.

The mechanism of the anatase TiO<sub>2</sub> crystal formation out of the amorphous TiO<sub>2</sub> was proposed by Zhang et al.<sup>101</sup> and Wu et al.<sup>95</sup> First the anatase TiO<sub>2</sub> nucleates through atomic rearrangements occurring at the interface between the amorphous titania particles.<sup>101,102</sup> When the anatase phase is nucleated, rapid conversion of two adjacent amorphous particles to a single anatase crystal occurs.<sup>101</sup> The anatase particles continuously grow by redistribution of atoms from an amorphous titania particle onto an existing anatase particle.<sup>101,103</sup>

#### **4.5 Modification techniques of the semitransparent tubular layer**

In this section the information regarding the various modification methods commonly applied for semitransparent anodic tubular oxide layers is summarized. In general, two approaches are the most frequently reported, concerning mostly their surface region or also their interior, manipulating inside their atomic structure. The first one is based on the decoration of the tubular oxide layer with an adequate amount of metal nanoparticles such as Au<sup>33</sup>, AuPt<sup>34</sup>, Ru<sup>35</sup>. The transparency of materials synthesized by anodic oxidation of a Ti film already deposited on TCO coated glass is of paramount importance. In particular, for photoelectrochemical and optoelectrochemical devices (e.g., dye-sensitized solar cells or electrochromic devices) semitransparent electrodes are required. In fact, the semitransparency allows incident light to pass through the TCO coated glass and be absorbed by the photoactive material. In this regard, semitransparent tubular oxide layers should be modified in a way that does not reduce significantly their optical transparency. The presence of the tubular oxide layer on the TCO coated glass, already is responsible for some reduction of the light transmittance across the entire substrate. This loss depends on the thickness of the nanotube layer developed on the TCO coated glass as well as the interface present between nanotubes and TCO. For example, Li et al.<sup>33</sup> reported transmittances of 80 % for FTO coated glass and 71 % for semitransparent substrates obtained by anodizing a 500 nm thick Ti film deposited on FTO (i.e. a transmittance loss was of about 9 %). Then, additional transmittance loss is present when the semitransparent tubular layer is modified with other, guest material. In fact, as shown by Li et al.<sup>33</sup> in **Figure 14**, further modification of the tubular layer with a 19.4 nm thick layer of gold nanoparticles sputtered on top of the nanotubes layer resulted in a significant transmittance loss of about 40 % compared to that of the layer of pristine semitransparent TNT.

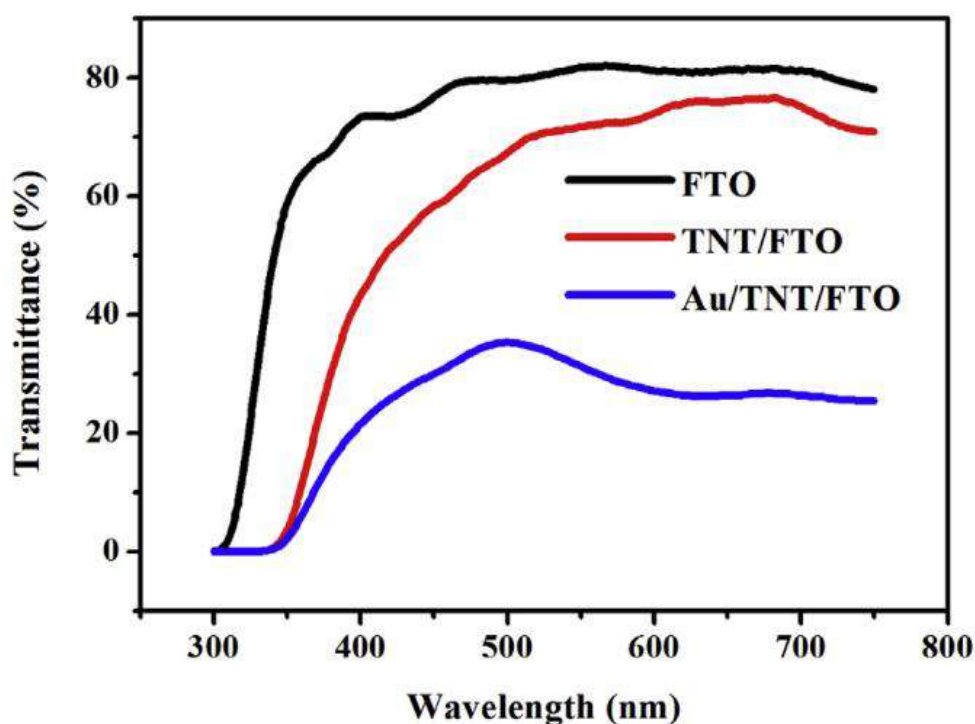


**Figure 14.** Transmittance of FTO coated glass, anodic titania nanotubes grown onto FTO coated glass and 19.4 nm thick gold film deposited on top of the tubular layer.  
(Reprinted with the permission from reference <sup>33</sup>).

Another issue reported for the deposition of heteroatoms on top of the tubular layer is the complete coverage of the entire surface on the top of TNT, thus blocking the pores<sup>104,105</sup>. The opaque nanoparticle layer can prevent a substantial incident light to reach the photoactive material. This will obviously drop the photoactivity of the material.

The second approach that considers changes in the bulk of titania nanotubes, is based on the growth of the tubular oxide layer out of Ti alloy film deposited onto TCO coated glass substrate. For the already reported works, titanium and heteroatoms (X) such as Nb,<sup>25</sup> Co,<sup>26</sup> Fe,<sup>27,28</sup> Mo<sup>29</sup>, W,<sup>30</sup> Cu,<sup>31</sup> Ag<sup>32</sup> were used as targets for the deposition of TiX alloy films on the TCO substrate by cosputtering method. Then, anodization of the formed alloy was carried out to produce uniform nanotube arrays with well dispersed heteroatoms in the tubular layer. However, it should be underlined that this method can lead to a significant loss of the amount of the heteroatoms present in the initial alloy film during the etching process. In addition, excessive heteroatoms content in alloy films can inhibit the formation of the tubular structure during the anodization. Herein, the latter approach was employed for the synthesis of semitransparent titania nanotubes out of titanium-silver alloy films. Comparing to mentioned

approaches I undertook efforts to decorate semitransparent tubular oxide layer with laser treated titania carbide known as MXene. The next section provides an introduction to MXene with a particular focus on its catalytic performance, especially reported for titania material modified with  $Ti_3C_2T_x$  MXene.

## 4.6 Introduction to MXene

### 4.6.1 Synthesis of MXene

Transition metal carbides/carbonitrides/nitrides known as MXenes are two-dimensional materials. The general formula of MXenes is  $M_{n+1}X_nT_x$ , where “M” stands for a transition metal (Sc, Ti, Zr, Hf, V, Nb, Ta, Cr, or Mo), “X” is carbon or nitrogen, and  $n = 1-4$ , and  $T_x$  element represents surface terminations (i.e. -O, -OH, or -F), respectively.<sup>106</sup> The synthesis procedure of MXenes covers (a) the selective etching of their corresponding MAX phase precursors, followed by (b) the physical or chemical delamination of the resultant product after the etching process. The MAX phases are chemical compounds with a stacked layered structure having a hexagonal lattice symmetry (space group  $P6(3)/mmc$ ).<sup>107</sup> The general formula of MAX phases is  $M_{n+1}AX_n$ , where “A” represents an element from groups III–VI of the periodic table (Al, Ga, In, Tl, Si, Ge, Sn, Pb, P, As, Bi, S, or Te). Typically, in  $M_{n+1}AX_n$  the M-X bonds are covalent bonds, whereas the M-A bonds are weak metallic bonds.<sup>108</sup> The low strength of the M-X bond facilitates the selective removal of the “A” layers in  $M_{n+1}AX_n$  to obtain  $M_{n+1}X_n$  stacked accordion-like multilayers. Strategies including HF etching, alkali etching and electrochemical etching have been explored for the removal of the “A” layers in  $M_{n+1}AX_n$ . Among these methods, HF etching still remains the most used technique for the synthesis of stacked multilayer MXenes. Indeed, various types of multilayered MXene sheets with open accordion morphology such as  $Ti_3C_2T_x$ ,<sup>109</sup>  $V_2CT_x$ ,<sup>110</sup>  $Nb_2CT_x$ ,<sup>111</sup>  $Nb_4C_3T_x$ ,<sup>112</sup>  $Ta_4C_3T_x$ ,<sup>113</sup>  $Mo_2TiC_2T_x$ ,<sup>114</sup>  $Mo_4VC_4T_x$ ,<sup>115</sup> have been synthesized by HF etching. For the particular case of titanium aluminium carbide MAX phase the HF etching mechanism proposed by Gogotsi and Barsoum et al.<sup>109</sup> is summarized as followed:

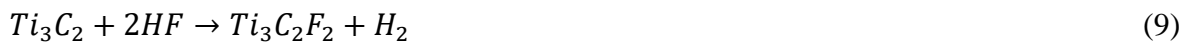


**Figure 15** shows the morphology of  $\text{Ti}_3\text{C}_3\text{T}_x$  MXene with the open space between neighbouring nanosheets.

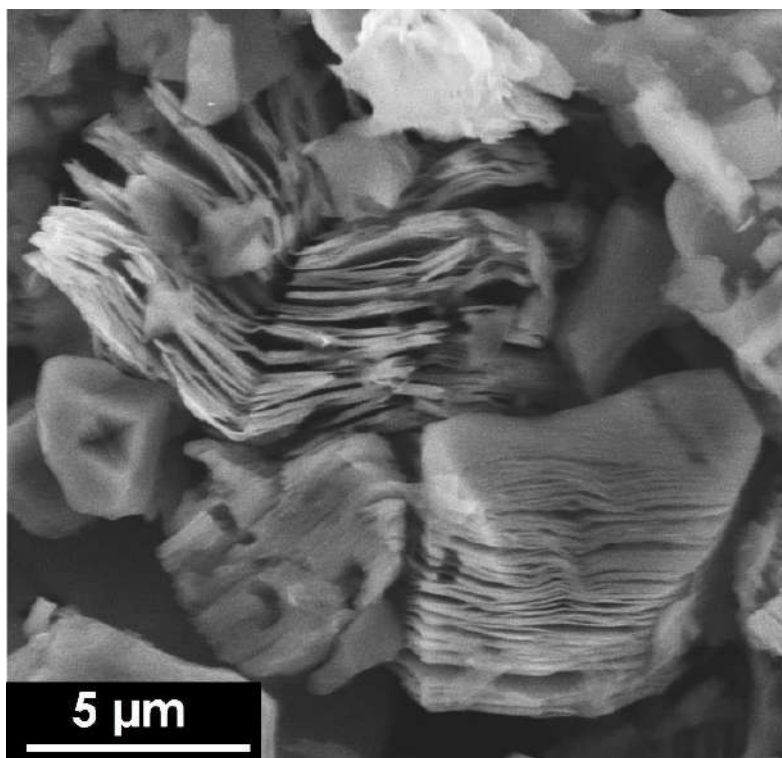


**Figure 15.** SEM image of  $\text{Ti}_3\text{C}_3\text{T}_x$  MXene.

Although the “A” layer is very reactive with fluorine ions, which facilitates its removal from  $\text{M}_{n+1}\text{AX}_n$  in a concentrated solution of HF, the high toxicity and corrosive activity of fluorine-containing reagents lead to considerable safety and environmental concerns.<sup>116,117</sup> In this regard, alkali etching has been also explored to take into account the trend of green chemistry and clean production of MXene. The works of Xie et al.<sup>118</sup> and Li et al.<sup>119</sup> have revealed that both NaOH and KOH have also good ability in the removal of the aluminium layer in  $\text{Ti}_3\text{AlC}_2$ . However, the high reactivity of the hydroxides group with aluminium leads to the formation of contaminant  $\text{Al}(\text{OH})_3$  over the MXene surface. Although the use of alkaline salts as etchants is environmentally friendly and cost effective, the purity level of the MXene product is a concern. A strategy based on the thermal treatment of MXene dispersed in 1 M  $\text{H}_2\text{SO}_4$  solution was proposed by Xie et al.<sup>118</sup> to reduce aluminium hydroxide impurities from  $\text{Ti}_3\text{C}_2\text{T}_x$  after NaOH etching. As shown in **Figure 16** Li et al.<sup>119</sup> optimized both the temperature and the NaOH concentration to significantly reduce the  $\text{Al}(\text{OH})_3$  contaminant from the MXene.



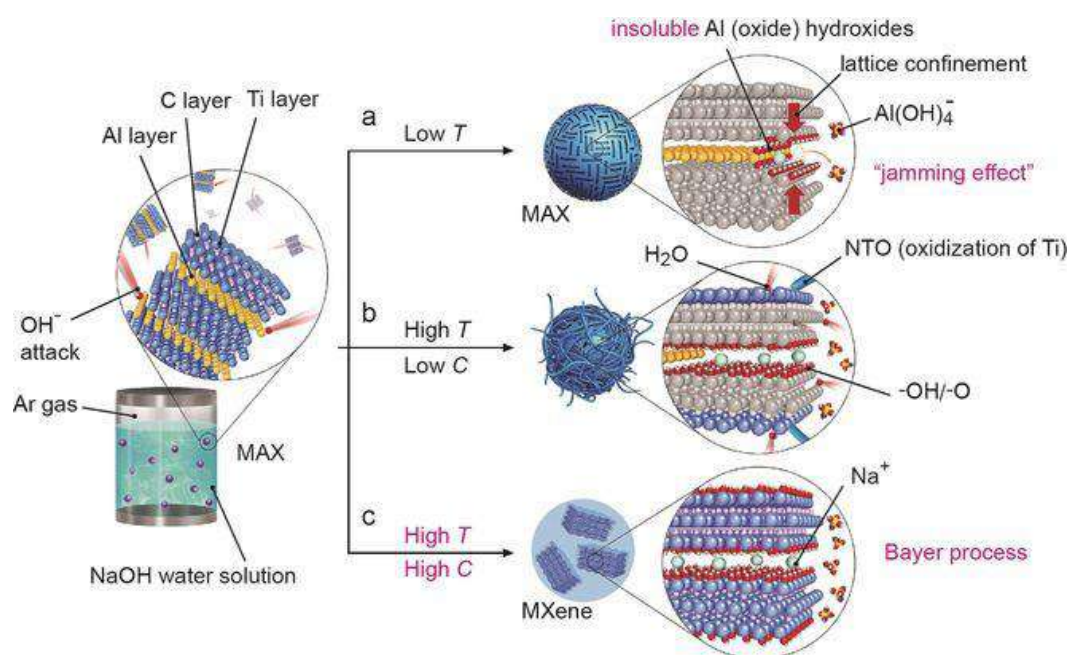


**Figure 16.** Influence of the temperature and the concentration of NaOH on the purity of the MXene. (Reprinted with the permission from reference <sup>119</sup>).

Electrochemical etching method consists of the removal of the “A” layer in the MAX phase in NaCl or HCl solutions under an applied voltage. Here, the bulk  $\text{Ti}_3\text{AlC}_2$ <sup>120</sup> or MAX phase coated onto conducting substrate<sup>121</sup> acts as the working electrode. This method has demonstrated its effectiveness in etching the aluminium layer from different MXene including  $\text{Ti}_3\text{AlC}_2$ ,<sup>120</sup>  $\text{Ti}_2\text{AlC}$ ,<sup>122</sup>  $\text{V}_2\text{AlC}$ ,<sup>123</sup>  $\text{Cr}_2\text{AlC}$ .<sup>123</sup> However, the use of this method leads to the formation of carbide derived carbon from the MAX phase on the surface of produced MXene. Unfortunately this hinders the subsequent etching of the MAX precursor and results in a low yield of MXene.<sup>121</sup>

In general, after the removal the “A” layer in the MAX phase by using HF, alkali or electrochemical etching the resultant MXene exhibit stacked accordion-like multilayers morphology. It has been proven that the delamination of the  $\text{M}_{n+1}\text{X}_n\text{T}_x$  multilayers into single-layered  $\text{M}_{n+1}\text{X}_n\text{T}_x$  MXene can remarkably raise both their electrical conductivity and hydrophilicity comparing to their multilayered counterparts.<sup>124</sup> Therefore, particular attention has been put to elaborate an efficient and simple chemical or physical method for the delamination of the multilayered materials into single-layer or few-layer MXene. The frequently used approach consists of the dispersion of the multilayered MXene in organic or



alkali solution (e.g. dimethyl sulfoxide, N,N-dimethylformamide, tetrabutylammonium hydroxide, hydroxyl choline, and n-butylamine) followed by its continuous stirring. This allows the intercalation of organic molecules or alkali cations between the MXene sheets to weaken the van der Waals forces between layers and widen the interlayer spacing. Then the delamination of the multilayered materials is achieved by either vigorous handshaking or ultrasonic treatment.

In this work  $\text{Ti}_3\text{C}_2\text{T}_x$  have been synthesised and then treated via laser ablation method for further modification of the semitransparent titania nanotubes. The achievements already reported regarding the photoelectrochemical activity of semitransparent titania modified by  $\text{Ti}_3\text{C}_2\text{T}_x$  MXene are summarized in the following section.

#### 4.7 Photoelectrochemical activity of $\text{TiO}_2$ functionalized with $\text{Ti}_3\text{C}_2\text{T}_x$ MXene

$\text{Ti}_3\text{C}_2\text{T}_x$  have found a wide range of applications as summarized in **Figure 17**.

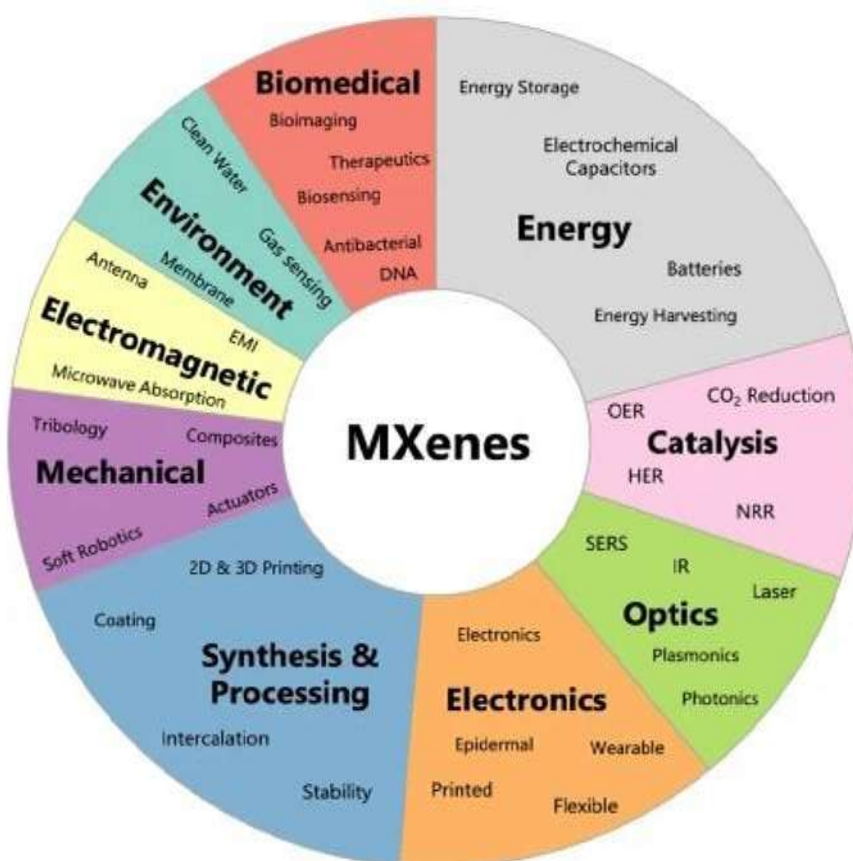


**Figure 17.** The pie chart showing various sectors in which MXene is explored. Reprinted with the permission from reference <sup>125</sup>

In the case of solar energy harvesting devices, since  $\text{Ti}_3\text{C}_2\text{T}_x$  is not a photoactive material, strategies have been found to use  $\text{Ti}_3\text{C}_2\text{T}_x$  as a decorating agent for the modification of a photoactive material such as  $\text{TiO}_2$  to increase its electrical conductivity. This initiative was motivated by looking for alternative catalysts to noble metals (i.e. Au and Ag) to increase the electrochemical and photoelectrochemical activity of semiconductor materials. Different research groups, namely Colin-Ulloa et al.<sup>126</sup>, Khatun et al.<sup>38</sup> and Jehad et al.<sup>127</sup> showed experimentally that, similarly to noble metals,  $\text{Ti}_3\text{C}_2\text{T}_x$  MXene also exhibits plasmonic effect under visible and near-IR light. The absorption spectra of  $\text{Ti}_3\text{C}_2\text{T}_x$  MXene reported by Khatun et al.<sup>38</sup> is presented in **Figure 18**.

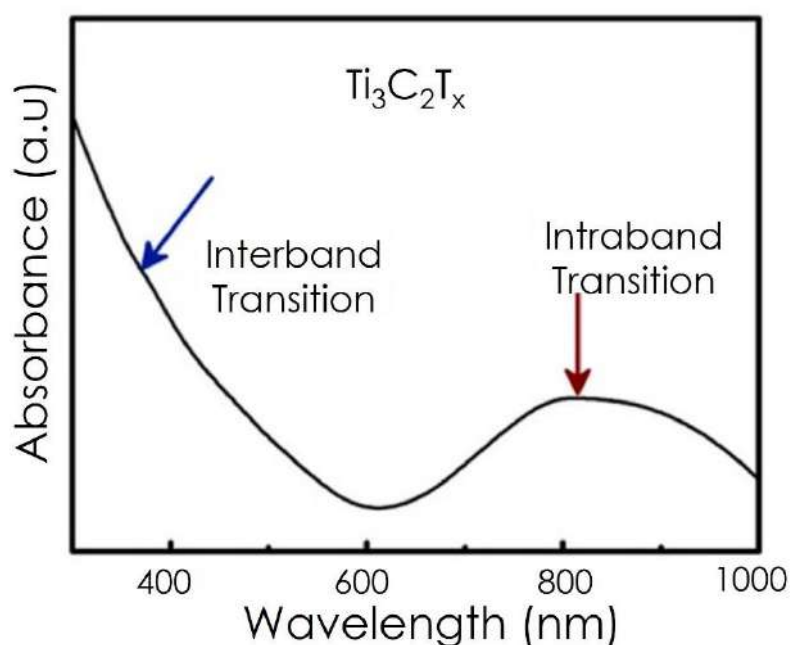


**Figure 18.** Absorbance spectra of  $\text{Ti}_3\text{C}_2\text{T}_x$  MXene.  
(Reprinted with the permission from reference.<sup>38</sup>)

Therefore, attempts have been undertaken to functionalize the photoactive semiconductor  $\text{TiO}_2$  with  $\text{Ti}_3\text{C}_2\text{T}_x$ . This was done to obtain  $\text{TiO}_2/\text{Ti}_3\text{C}_2\text{T}_x$  heterojunction material with improved performance compared to pristine  $\text{TiO}_2$ . As evidence Zheng et al.<sup>42</sup> and Zhang et al.<sup>128</sup> have shown that  $\text{TiO}_2/\text{Ti}_3\text{C}_2\text{T}_x$  heterostructure materials exhibit narrower band gaps than the bare titania. The decoration of  $\text{TiO}_2$  with only 0.075 wt %  $\text{Ti}_3\text{C}_2\text{T}_x$  has led to an increase in the power conversion efficiency of dye-sensitized solar cells (DSSC) of about 20 %.<sup>36</sup> Similarly, He et al.<sup>37</sup> have reported a high power conversion efficiency of about 30 %

under UV-vis light for a photoelectrode based on  $\text{TiO}_2/\text{Ti}_3\text{C}_2\text{T}_x$ . The advantage of the presence of the  $\text{Ti}_3\text{C}_2\text{T}_x$  in the heterojunction is effectively explained as follows: (a) as illustrated in **Figure 19**, first collective electronic excitations (i.e. the plasmonic effect) occur at the  $\text{TiO}_2/\text{Ti}_3\text{C}_2\text{T}_x$  interface. Then, the generated electrons are injected into the band conduction of the  $\text{TiO}_2$  semiconductor, thus compensating for the electron-hole recombination losses (b). The excellent electrical conductivity of  $\text{Ti}_3\text{C}_2\text{T}_x$  resulting from its semi-metallic properties facilitates the migration of the photogenerated electrons towards the output terminal of the devices, thereby reducing electron-hole recombination.

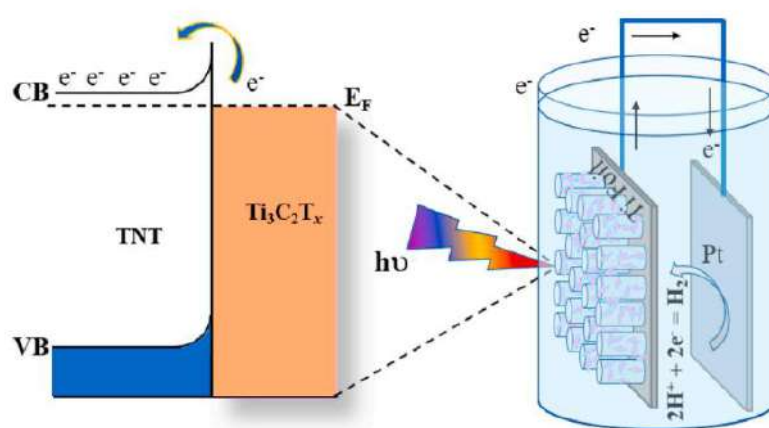


**Figure 19.** Schematic of band diagram for the  $\text{TiO}_2/\text{Ti}_3\text{C}_2\text{T}_x$  heterostructure.  
(Reprinted with the permission from reference.<sup>38</sup>)

Unlike the works mentioned above, in this doctoral work, in-situ formation of  $\text{TiO}_2$  sphere/ $\text{Ti}_3\text{C}_2\text{T}_x$  was achieved through laser ablation of frozen  $\text{Ti}_3\text{C}_2\text{T}_x$  solution. Then, the functionalization of semitransparent anodic titania nanotubes with the as prepared heterostructure has remarkably raised the electrochemical and photoelectrochemical performances of semiconductor tubular structures. This study paves the way towards the usage of  $\text{TiO}_2/\text{Ti}_3\text{C}_2\text{T}_x$  as promising decorating agent to boost the photoactivity of semiconducting and semitransparent oxides. The finding of this work will be described in details in the results section. The laser ablation method is introduced in the next section.

#### 4.8 Laser ablation method

There are many synthesis methods reported for the production of nanoparticles including sol-gel, co-precipitation, hydrothermal, solvothermal, high-energy ball milling. However, there also exist processing procedures utilising laser beam like laser ablation that is a straightforward

and rapid synthesis route for the generation of nanoparticles.<sup>129</sup> This method involves usage of target that is irradiated by the laser beam and is the source of the new nanomaterial. The target can be either in form of powder sometimes pressed as a pellet and or thin film deposited on to a flat substrate (e.g. glass substrate,<sup>130,131</sup> sapphire substrate,<sup>130</sup> and silicon substrate<sup>130</sup>) immersed in a solvent (e.g. in methanol <sup>132</sup>, ethanol <sup>133</sup> or in water <sup>134</sup>). Compared to the other methods, the laser ablation does not need multiple-step synthesis procedure as in the chemical methods (i.e. sol-gel method, co-precipitation method) or long reaction time at high temperature (i.e. in hydrothermal, solvothermal).<sup>129</sup> Indeed, the nanoparticles can be obtained within few minutes. The properties of the generated particles during the laser ablation including shape, size, size distribution and composition can be optimized by adjusting the laser parameters such as wavelength, pulse repetition rate, pulse width, and laser fluence.<sup>129</sup> As described by Semaltianos et al.<sup>129</sup> the steps involved in the mechanism of the particle generation differ depending on whether the ablation is performed in air or in a liquid environment.

Firstly, considering the case when the laser ablation is performed in air (or in other gas atmosphere), the steps of the formation of the particles are described as following. In the first step the interaction of the intense laser beam with the target material results in delivering high power to a small area of the target. This leads to the ejection of species in the form of an energetic and dense luminescent plume from the surface of the material.<sup>129</sup> In the second step (2), the plume expands and compresses locally the background gas, resulting in the generation of a shockwave at the plume/background gas interface.<sup>129</sup> Then, in the step number (3), a few microseconds after expansion, the material species at the plume/background gas interface lose their energy. This causes a deceleration of the material species present in the plume/background gas interface. The process of deceleration leads to the formation of an inverse pressure gradient at the plume/background gas interface. As the consequence the pressure in plume/background gas interface has become greater than the pressure inside the plume. Then an internal shockwave is generated and travels from the plume/background interface towards the centre of the plume.<sup>129</sup> Finally, in the step 4, the internal shock wave propagates inside the volume of the plume by reflection at the plume/gas interface. During this stage, the material species cooled, leading to condensation, nucleation, and clustering of the plume species with the formation of nanoparticles.<sup>129</sup>

Similar to the ablation in air, when the ablation is carried out in the liquid, in the first step, the plasma plume is created upon illuminating the target by light, followed by the generation of the shockwave at the plume/background liquid interface in the second step.<sup>129</sup> In step three, chemical reactions can take place inside the plume and the liquid, but also at the

plume/liquid interface.<sup>129</sup> The illustration of the different steps is presented in the **Figure 20**. In this work  $\text{TiO}_2/\text{Ti}_3\text{C}_2\text{T}_x$  heterostructure was synthesized by laser ablation of  $\text{Ti}_3\text{C}_2\text{T}_x$ . Details of the laser ablation mechanism proposed in this work is provided in results section.

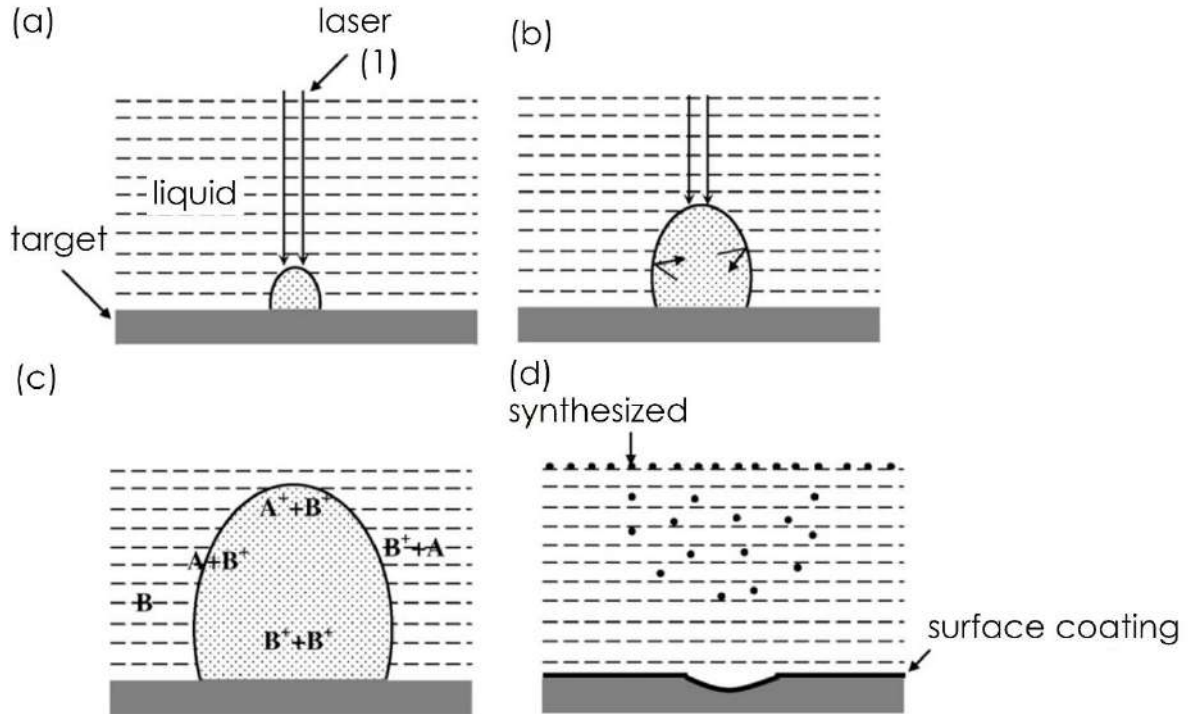


**Figure 20.** Illustration of the steps in generation of nanoparticles via laser ablation in liquid. (a) Generation of the laser induced plume at the liquid/target interface. (b) Expansion of the plume in the liquid. (c) Possible interactions between the species from the solvent and the material. (d) Condensation of the plasma plume in the liquid leading to the generation of the nanoparticles. (Reprinted with the permission from reference.<sup>135</sup>)

## 5 Objectives and Hypotheses

Semitransparent devices for solar-driving process gain more and more importance in industry and society. Nowadays we observe the popularity of the smart and small electronic devices including wearables, like watches, bands and even on-body sensors that are mostly powered by outer source. Taking into account the multifunctions as well as long working hours of such devices their frequent charging is required. As an alternative semitransparent solar cell integrated with such device is proposed, that can be placed directly on the display or just the area exposed to the daylight. Such idea is along with the promotion of the decarbonization of energy systems and improvement of the energy sustainability. This way we can take advantage of the solar light which anyway irradiates the device. Among others, the materials used for its

construction should not only exhibit high degree of semitransparency but have to be able to perform photoconversion to provide the charge to the device. In addition, such semitransparent photoelectrode materials are important elements in optoelectrochemical sensors gaining interest in the monitoring systems, where also the optical signal readout is crucial. Therefore, researches on the fabrication and characterization of semiconductor nanostructures developed on semitransparent materials are of fundamental importance.

Related to this, the main objective of this work is focused on the optimization process of semitransparent material that can be formed via methods that are already utilized on the technological scale however the selection of proper processing parameters is essential. Due to that I focused my works during PhD realization onto the semitransparent layers composed of nanotubes formed by the anodization of titanium films obtained by magnetron sputtering. The main objective of my work was to elaborate the series of the processing parameters resulting in highly ordered titania nanotubes exhibiting different spatial arrangement (aligned and spaced) on various substrates, their complex characterisation of their morphology, structure, optical properties as well as their applicability as photoanodes for efficient light conversion and optoelectrochemical sensing. Realizing that pure titanium dioxide exhibits wide bandgap enabling absorption of UV light, its modification is needed to utilize efficiently light from the part of the visible radiation but to preserve some degree of semitransparency. Due to that the aim also concerns formation of the titania doped with silver and heterojunction with  $\text{Ti}_3\text{C}_2\text{T}_x/\text{TiO}_2$  as a decorating agent affecting both optical and electric properties.

This main ambitious aim can be subdivided into the following specific objectives:

- a) Optimization of anodizing parameters resulting in the fabrication of semitransparent substrate overgrown by highly ordered and crack-free aligned and spaced tubular layers and characterisation of their optical properties and morphological features.
- b) Elaboration of the anodization strategies enabling the formation of the tubular layer on both sides of the planar substrates as well as on the surface of optical fiber out of the sputtered titanium films.
- c) Diagnostic of the physicochemical properties of the prepared double-sided materials to bring understanding of the influence of the nanotubes architecture on the photoactivity of these photoanodes.
- d) Fabrication of semitransparent substrate overgrown by highly ordered and crack-free aligned and spaced tubular layers out of titanium-silver alloy films and diagnostics of their photoconversion properties.

- e) Preparation of the series of semitransparent materials based on ordered titania nanotubes for the verification as promising surface-enhanced Raman spectroscopy (SERS) platforms and optical sensors.
- f) Elaboration of the laser assisted fabrication procedure of  $\text{Ti}_3\text{C}_2\text{Tx}/\text{TiO}_2$  heterostructure as efficient noble-metal free catalyst used further as a decorating agent for the semitransparent titania nanotubes.
- g) Development of a new deposition strategy towards integration of as-synthesized semitransparent tubular layer with the  $\text{Ti}_3\text{C}_2\text{Tx}/\text{TiO}_2$  in order to improve the photoresponse of electrode material.
- h) Complex diagnostics of formed heterojunction covering morphology, structure and electrochemical and photoelectrochemical performance including also investigation of the incident photon-to-current conversion efficiency.

**Herein, I would like to list the major four hypotheses that motivated me to perform research work.**

**Hypothesis 1:** The optimization of the anodization conditions will allow to form semitransparent ordered titania nanotubes with aligned or spaced architecture out of Ti film sputtered onto the transparent conductive oxide substrate.

**Hypothesis 2:** Effective control of the tubular morphology on the both sides of the planar substrate will offer efficient and sequential light harvesting.

**Hypothesis 3:** It will be possible to fabricate uniform semitransparent layers of aligned or spaced titania nanotubes with well dispersed heteroatoms in titania via anodization of Ti alloy films. Obtained semitransparent materials will exhibit superior light harvesting properties comparing to the bare tubular layers.

**Hypothesis 4:** It will be possible to increase the incident photon-to-current conversion efficiency of the anodic tubular layer through its functionalization with laser treated MXenes.

## 6 Methods

### 6.1 Introduction

Sputtered Ti and Ti alloy films onto TCO substrates were anodized under different anodization conditions to produce aligned or spaced nanotubes out of the deposited Ti (or Ti alloy) films. Various characterization techniques have been utilized to study the physicochemical properties of anodized materials. The deposition of Ti films and Ti alloys on TCO substrates was carried out by foreign scientific partners involved in the realisation of CEUS-UNISONO project no 2020/02/Y/S8/00030. Those research groups are from Czech Republic: University of South Bohemia in Ceske Budejovice and Charles University in Prague and are experts in the deposition of metallic and oxides layers on different substrates like plane glass and optical fibres. Members of those groups provided details of their deposition procedure that together with the optimized anodization process form the overall description of the samples fabrication. Nevertheless, this work has contributed to optimize the deposition process that enables fabrication of the ordered titania nanotubes. In this section the deposition procedures, as well as the experimental setups, including the anodization unit, and the different techniques used for the complex material analysis are described.

### 6.2 Magnetron sputter method

Both direct current (DC) magnetron sputtering and radio frequency (RF) magnetron sputtering were employed during realization of this PhD thesis. In general, comparing to other physical deposition techniques known for the physical deposition of thin film (e.g. spray pyrolysis and electron beam evaporation), DC and RF magnetron sputtering have the advantages of high deposition rate and good reproducibility.<sup>136</sup> In fact, the idea of the magnetron sputtering technique is to increase the sputtering rate by increasing the ionization of the atomic gas in the chamber to hit the target. Briefly, permanent magnets are placed below the target material. The presence of permanent magnets creates a magnetic field in the vicinity of the target. The magnetic field confines electrons close to the target. This increases the ionization of the argon atoms in the chamber, thus, enabling more ions to bombard the target. The deposition of films is carried out by ejection of the constituent species of the film from the target held at the cathode by ion bombardment, and afterwards deposition on the substrate located in the vicinity. The magnetron sputtering process is presented in **Figure 21**.



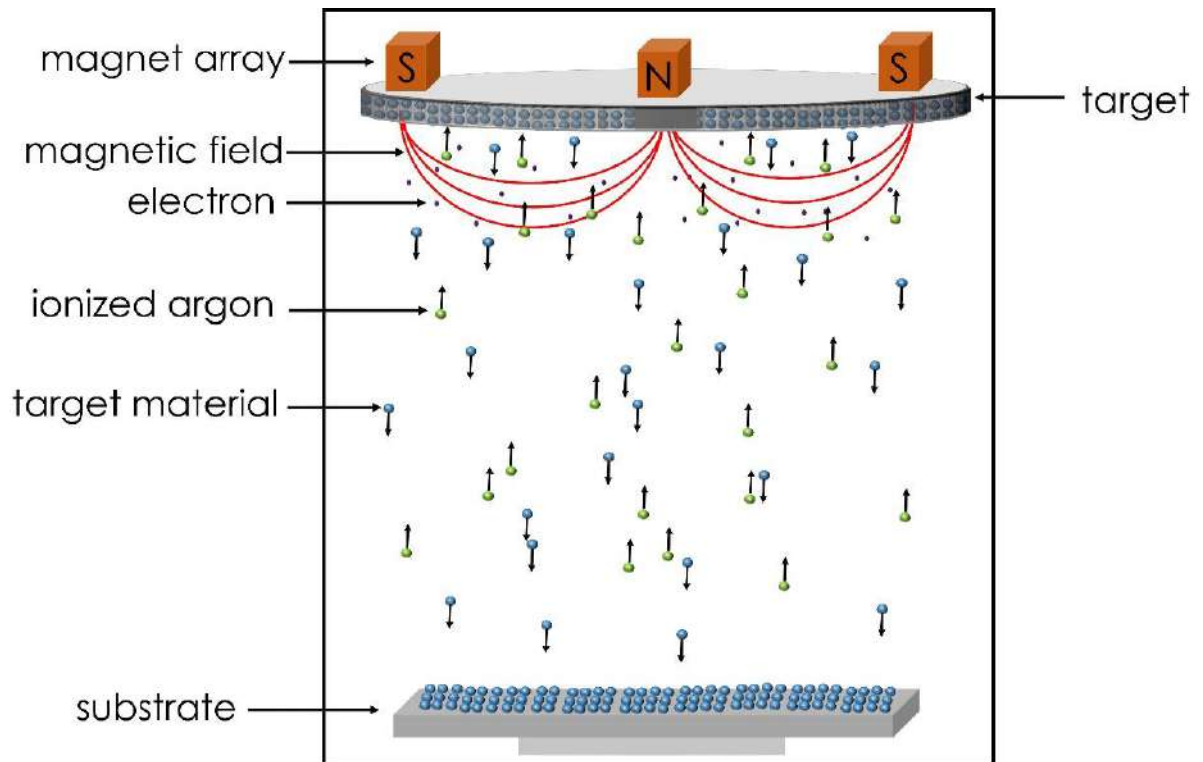


**Figure 21.** Scheme of the magnetron sputtering process.

The top and side images of the magnetron sputtering gun are presented in **Figure 22**.

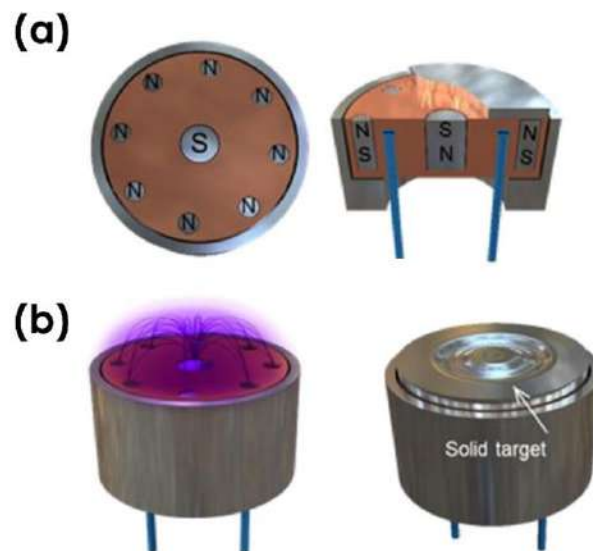


**Figure 22.** (a) Top and side view schematics of magnetron sputtering gun with magnets.

(b) image of the magnetron sputtering gun with its magnetic field and solid target. <sup>137</sup>

(under CC BY licence).

Typically, DC magnetron sputtering is only used for the deposition of conductive films (e.g. metal films or alloy films), where the high conductivity of the target materials can prevent charge build-up on its surface.<sup>138</sup> For the deposition of dielectric films (i.e. insulating films), the application of an alternating voltage is necessary to overcome the build-up of positive charge at the surface of the target.<sup>138</sup> Due to that RF sputtering was elaborated to overcome this issue.

Insulating film deposition by RF sputtering can be understood as follows. A negative potential is applied to the target during the negative half-cycle of the alternating voltage. This allows the target to be bombarded by positive ions. Since the target is an insulating material, these positive charges accumulate on its surface during the positive half-cycle.<sup>138</sup> Later, along the positive half of the cycle of the alternating voltage, a large number of electrons accumulate near the target, thereby neutralizing the positive charges built-up on its surface.<sup>138</sup> As was already mentioned, one can take advantage from RF sputtering both for the deposition of both conductive films as well as non-conductive films.

### **6.3 Sputtering conditions of indium tin oxide (ITO) layer, TiO<sub>2</sub> interlayer and Ti films onto planar substrates**

#### **6.3.1 Sample preparation for layer sputtering**

Rectangular silica glass microscopic slides (Menzel Glaeser) with dimension of  $15 \times 26 \text{ mm}^2$  (or  $15 \times 10 \text{ mm}^2$ ) were used as supports for deposition of films. First, the glass substrates were successively cleaned in the following order: acetone, distilled water, isopropanol, distilled water, ethanol and deionized water in an ultrasonic bath cleaning. Afterwards, the surface of the samples were exposed to plasma environment under ultra-high vacuum condition (UHV). The UHV chamber is equipped with magnetron sputtering gun(s). The deposition of the ITO layer, TiO<sub>x</sub> interlayer and Ti film were carried out in the same UHV chamber. The different components of the deposition chamber are presented in **Figure 23**. The plasma cleaning was realized by applying a negative bias of 200 V to the glass substrate in a mixed reactive gas (Ar/O<sub>2</sub> = 6/20) at a pressure of 3.5 Pa, propagating an RF (Advanced Energy Cesar, 13.56 MHz, 30 W) discharge for 10 minutes. After this process the gas present inside the chamber was evacuated through a primary dry scroll, and a base-pressure of  $6 \times 10^{-6} \text{ Pa}$  is ensured in the chamber by a secondary turbomolecular pump for film deposition.

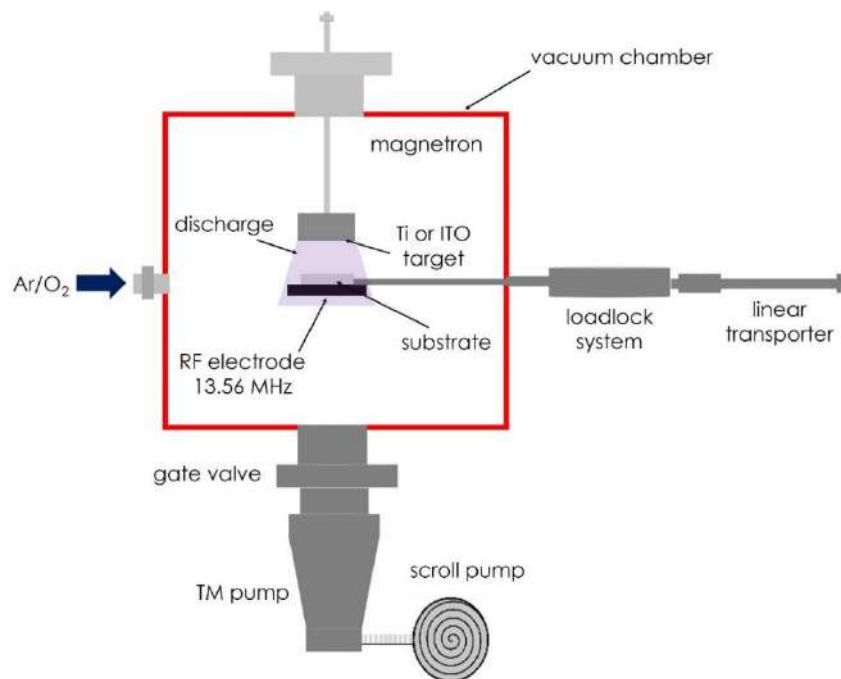


**Figure. 23.** Scheme of experimental arrangement for the deposition of the films (TM: Turbomolecular).

### 6.3.2 Deposition conditions of the different layers i.e. ITO layer, TiO<sub>x</sub> interlayer and Ti film onto planar substrates (i.e. onto one side or onto the two side of the substrates)

#### Sputtering conditions of the ITO layer

In the same UHV chamber just after the plasma cleaning, a 100 nm thick layer of ITO was sputtered onto the glass substrate. The deposition was carried out by RF magnetron sputtering with a gun diameter of 3 inches (Kurt J. Lesker Company). The substrate was placed at a distance of 160 mm from the magnetron gun. The composition of the ITO target used for the deposition was In<sub>2</sub>O<sub>3</sub>/SnO<sub>2</sub> = 90/10 wt% with a purity grade of 99.99% (Testbourne Ltd). The substrate was fed by a RF power of 150 W with a self-negative bias of 160 V. The deposition was carried out in an argon atmosphere at 1 Pa with a continuous flow rate of 25 sccm. The growth of the ITO film was realized in situ and monitored in real time by a quartz crystal microbalance (QCM) to obtain at every attempt 100 nm thick layer uniformly deposited onto the glass substrate. The deposition lasted 11 minutes. After the formation of ITO coating, it was annealed at 500 °C for 1 hour to improve its optical and electrical properties.

### **Sputtering conditions of the TiO<sub>x</sub> interlayer**

The deposition of the TiO<sub>x</sub> interlayer was carried out by DC magnetron sputtering. A Ti target with a diameter of 3 inches, thickness of 4 mm and a purity grade of 99.3% produced by Bibus Metals was used. The substrate was placed 60 mm from the magnetron gun. The magnetron was fed by a dc power supply (Kurt J. Lesker, DC01 BP) supplying a constant current of 600 mA. The deposition was carried out in a mixed atmosphere of Ar/O<sub>2</sub> = 6/20, at a constant pressure of 0.5 Pa for one minute. The thickness of the deposited TiO<sub>x</sub> interlayer is about 5 nm.

### **Sputter conditions of the Ti film**

The main Ti film was deposited by DC magnetron sputtering using the same Ti target as for the deposition of the TiO<sub>x</sub> interlayer. For this deposition, a constant current of 600 mA, and a power of 226 W were supplied by the dc power supply. The deposition was carried out in Ar atmosphere (flow rate: 6 sccm) at a pressure of 0.12 Pa. The sputtering rate was controlled by the by quartz microbalance. In this work Ti films with different thickness i.e. 500 nm, 540 nm and 1000 nm were deposited to verify which thickness will be the most optimal for fabrication of titania nanotubes of different morphology. **Figure 24** shows the image of the sample after the deposition of films onto one side of the substrate.

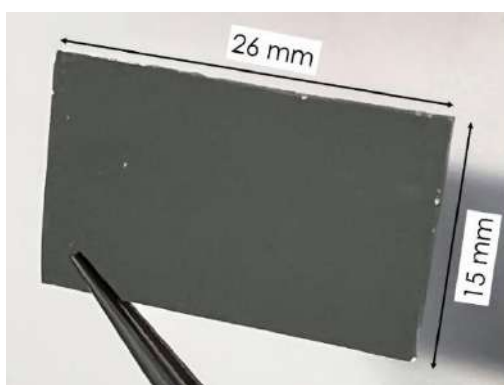


**Figure 24.** Photography of 500 nm thick layer deposited onto ITO-coated glass.

In the case of the double-sided Ti/TiO<sub>x</sub>/ITO/TiO<sub>x</sub>/Ti samples the same steps for the deposition of the ITO layer, TiO<sub>x</sub> interlayer and Ti film were done onto the two sides of the glass substrate. The realization was that first all layers were deposited onto one side and afterwards the substrate was flipped and the same stack of layers was deposited on the other side.

### Sputtering conditions of the TiAg alloy films

First, ITO layer and  $\text{TiO}_x$  interlayer were deposited onto the glass substrate according to the procedure described above. Afterwards, the TiAg alloy film was deposited by co-sputtering technique i.e. both Ti and Ag targets were used for the sputtering and two magnetron guns were placed in the UHV chamber, as shown in **Figure 25**, one containing the 3" Ti target (Bibus Metals, 99.3% purity) and the second containing the 3" Ag target (Kurt J. Lessker, 99.99% purity).

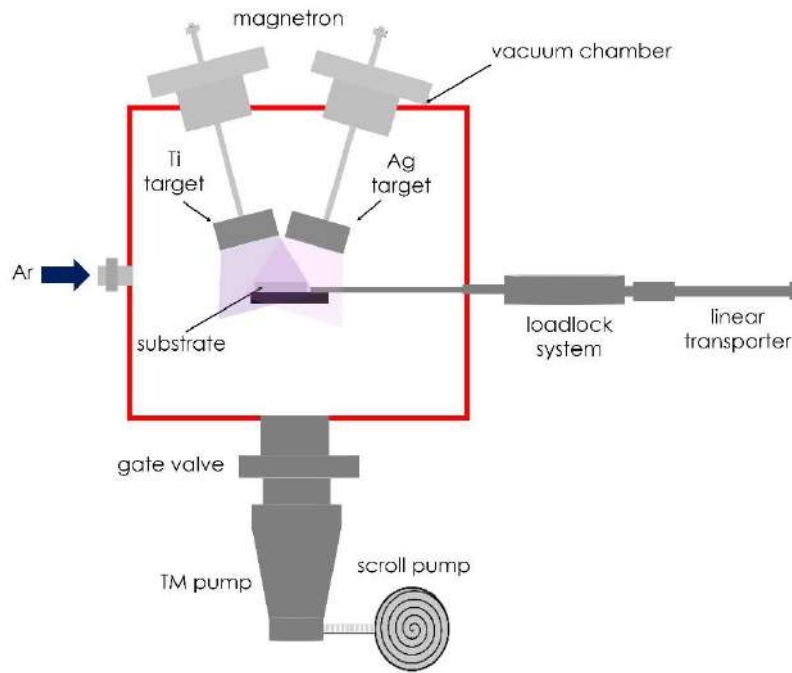


**Figure 25.** Scheme of experimental arrangement for the cosputtering of the alloy films.

The deposition was carried out in an Ar atmosphere at a pressure of 0.125 Pa. The Ti target is powered by DC power (232 W), while the amount of the Ag in the deposited film is controlled by the DC power supplied to the Ag target. For example, 1.7, 3.5 and 5 % silver contents in the deposited TiAg film were obtained by supplying a power of 9, 20 and 30 W, respectively, to the Ag target.

### Sputter conditions of Ti film onto optical fibers

The steps involved in the fabrication of the optical fiber structure used in this work are illustrated in **Figure 26**.

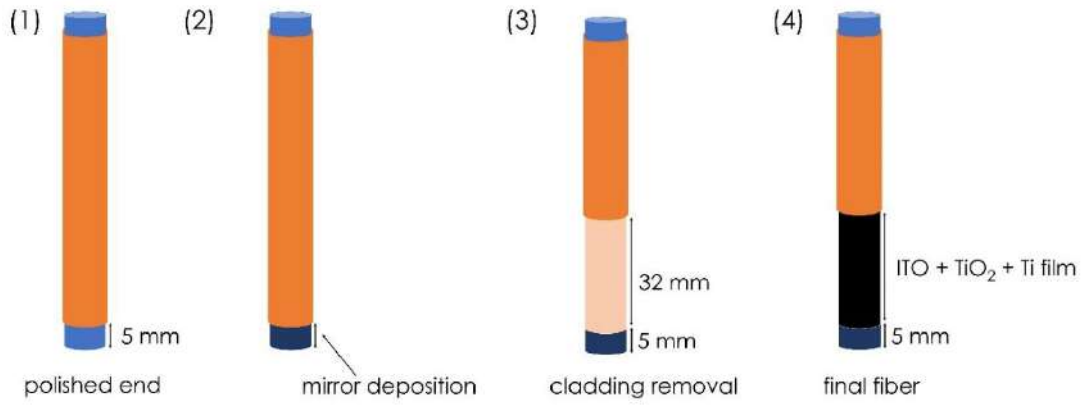


**Figure 26.** Steps of the fabrication of optical fiber coated with Ti film.

A 150 mm long multimode optical fiber with a core diameter of 400  $\mu\text{m}$  was used as the starting substrate. First, one end of the fiber (about 5 mm long) was polished. Then, a thin layer of silver was sputtered onto the polished terminal part of the fiber by DC magnetron sputtering for 2 min under argon atmosphere at 1 Pa and using 3" Ag target. The fiber was placed at a distance of 65 mm from the magnetron gun and the DC power delivered was 130 W. This deposited layer acts as a mirror, which allows the fiber to operate in the reflective mode. Then the mirror was covered with a protective layer of  $\text{TiO}_2$ . This is to avoid contact between the mirror and the electrolyte during the anodization process. The deposition of the  $\text{TiO}_2$  layer is carried out by DC magnetron sputtering for 6 min under an  $\text{O}_2/\text{Ar}$  mixture atmosphere (with a ratio of 1/3) at 0.4 Pa and using Ti 3" target. The fiber was placed at a distance of 50 mm from the magnetron gun and the DC power delivered was 350 W. Then, 32 mm of the polymer coating was removed from the end part coated with silver, as shown in step (3) in **Figure 26**. Then, the surface of the fiber core was cleaned with acetone and isopropanol. Finally, the substrate obtained in step (3) (**Figure 26**) was used as a support for the successive deposition of an ITO layer of 70 nm thickness, a  $\text{TiO}_2$  transition layer of 5 nm thickness and then Ti film of 370 nm thickness. The deposition of the ITO layer is carried out by RF magnetron sputtering for 25 min under an argon atmosphere at 0.2 Pa and using 3" ITO target. The magnetron gun was placed 16 cm from the fiber and the RF power delivered was 150 W. The  $\text{TiO}_2$  was deposited by DC magnetron sputtering (3" Ti target) for 2 min under an  $\text{O}_2/\text{Ar}$  mixture atmosphere (with a ratio of 6/1) at 0.4 Pa. Then, the flow of oxygen was stopped, leading to the deposition of only Ti film in the same conditions. **Figure 27** shows the images of the obtained fiber coated with Ti film.

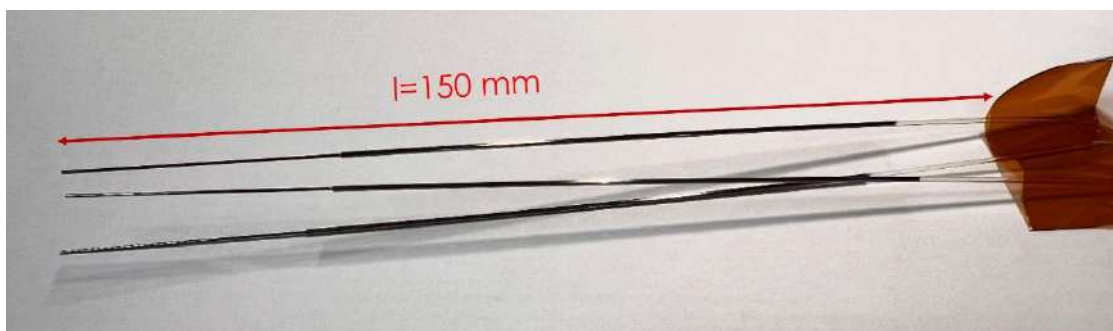


**Figure. 27.** Image of the fabricated optical fibers (core diameter of 400  $\mu\text{m}$ ).

#### 6.4 Anodization setup

The anodization unit utilized in this work is composed of four components, namely:

- (a) a power supply to maintain a constant dc voltage at the electrodes immersed in the electrolyte,
- (b) a computer to monitor the dc voltage through a LabVIEW program. For all carried out anodization processes the voltage was increased to an established value at a rate of  $0.1 \text{ Vs}^{-1}$  and then held until the substrate became semitransparent,
- (c) a two-electrode arrangement was used where Pt mesh was the cathode and ITO-glass coated with Ti film was the anode,
- (d) a thermostat connected to the anodization cell through a cooling jacket allows the control of the temperature of the whole setup.

The pictures of the anodization cells used in this work are already presented in **Figure 6** and **Figure 7** in the section 4.2.2. The one in **Figure 7** is used for the fabrication of both single-sided and double-sided semitransparent nanotubes. This cell enables only the area of 10.5 mm in diameter to be anodized, while the other parts of the sample are isolated from the electrolyte.

#### 6.5 Analytical Methods

It should be noted that the deposited Ti films are directly anodized without any pre-treatment. Except the optical fibres, after the anodization, the samples were annealed in air at 450  $^{\circ}\text{C}$  for an hour. Morphological information of samples are obtained using a scanning electron microscope (SEM). The microstructure of the samples (i.e. the prepared MXenes before and after laser ablation) was analysed also by transmission electron microscope (TEM). The chemical composition of the materials was analysed using energy dispersive X-rays (EDX), which provides elemental analysis information. The chemical states analysis was carried out

using X-ray photoelectron spectroscopy (XPS). The crystal structure investigation was carried out with X-ray diffraction (XRD) technique. The vibrational modes present in the synthesized materials were investigated by Raman spectroscopy. The absorption properties of the bare and modified tubular oxide layer were analysed using UV-vis spectrophotometer.

The synthesized materials were used as working electrodes for electrochemical and photoelectrochemical tests. Electrochemical measurements such as cyclic voltammetry (CV), electrochemical impedance spectroscopy (EIS) and Mott-Schottky analysis were carried out as well as photoelectrochemical testing including: linear sweep voltammetry (LSV), intensity-modulated photocurrent spectroscopy (IMPS), quantum efficiency measurements i.e. incident-photon-to-current efficiency (IPCE) and photoluminescence (PL) measurements.

In this section, the fundamental physics underlying all techniques used to characterize the samples is discussed in details. The working principles of the different measurement instruments are also described.

### 6.5.1 Electron microscopy

Optical microscopy is most commonly used to take the image of various objects. This microscope utilizes illumination of the specimen with visible light. However, this microscope has a limit resolution of  $\frac{\lambda}{2NA}$ , where  $\lambda$  is wavelength and NA is the numerical aperture of the instrument.<sup>139</sup> As the visible light used in the light microscope has a limited range of wavelengths between 400 nm and 700 nm, this microscope has not the ability to distinguish objects and features smaller than approximately 0.1  $\mu\text{m}$ .<sup>140</sup> To obtain an image of an object smaller than 0.1  $\mu\text{m}$ , other apparatus operating on the basis of the interaction between the electron and the matter are explored, including scanning electron microscope and transmission electron microscope.

Elastic and/or inelastic scattering can occur upon collision of an incident beam of electrons with the sample surface.<sup>140</sup> Elastic scattering occurs when the incident electron also known as primary electron strikes the sample target and changes its incident direction with the same wavelength (i.e. elastically scattered electron does not transfer its energy to the target material during a collision).<sup>140</sup> In the case of an inelastic scattering, the scattered electron changes its incident direction with a longer wavelength compared to that of the primary electron.<sup>140</sup> This implies that the primary electron has lost a part of its energy during the interaction with the sample. This leads the sample to release other particles at different angles.



**Figure 28** shows how different signals can be detected upon the electron-matter interaction during e.g. morphology inspection using SEM.

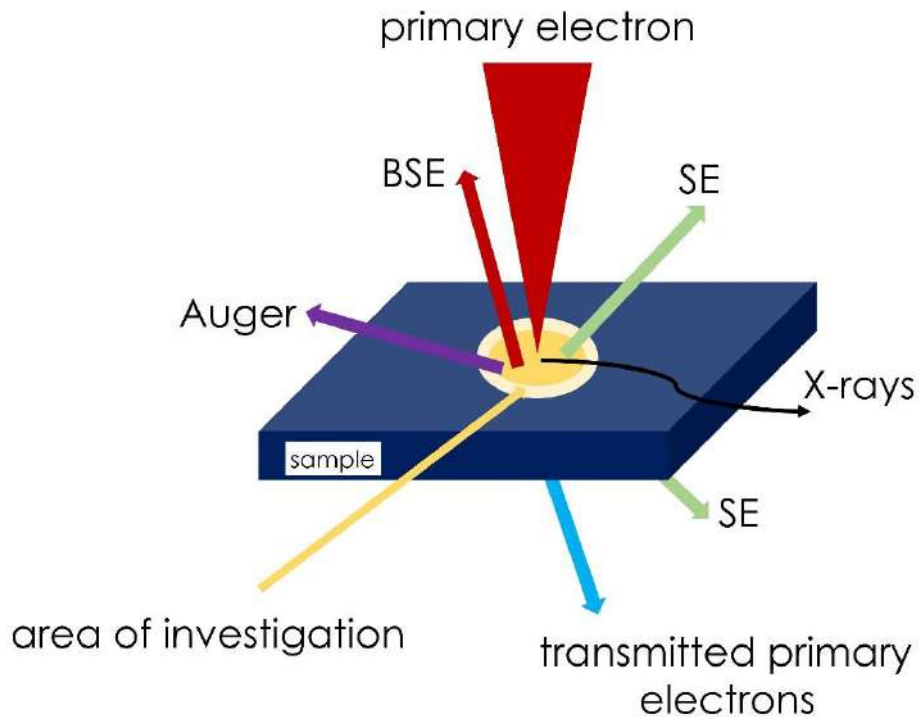


**Figure 28** Various signals generated during the electron - matter interaction during SEM inspection. (BSE: backscattered electrons; SE: secondary electrons).

Those signals provide information about the topography and chemical composition of the sample. As shown in **Figure 28**, the probable signals that can be detected upon the collision of the electron with the atoms present in the sample are: the secondary electrons, backscattered electrons, characteristic X-rays, Auger, and transmitted primary electron. Among others, two types of signals such as backscattered electrons and secondary electrons are responsible for the formation of the image in the case of scanning electron microscope. The secondary electrons result from the inelastic interactions between the electron beam and the sample. This signal originates from the atoms in the sample, whereas backscattered electrons arise from elastic collisions of electrons with the sample, which result only in a change in the trajectories of the primary electrons.

For the characterisation of the morphology of obtained samples two types of the electron microscopes were utilized: scanning and transmission electron ones. Regarding scanning electron microscope, the core components are depicted in **Figure 29**.

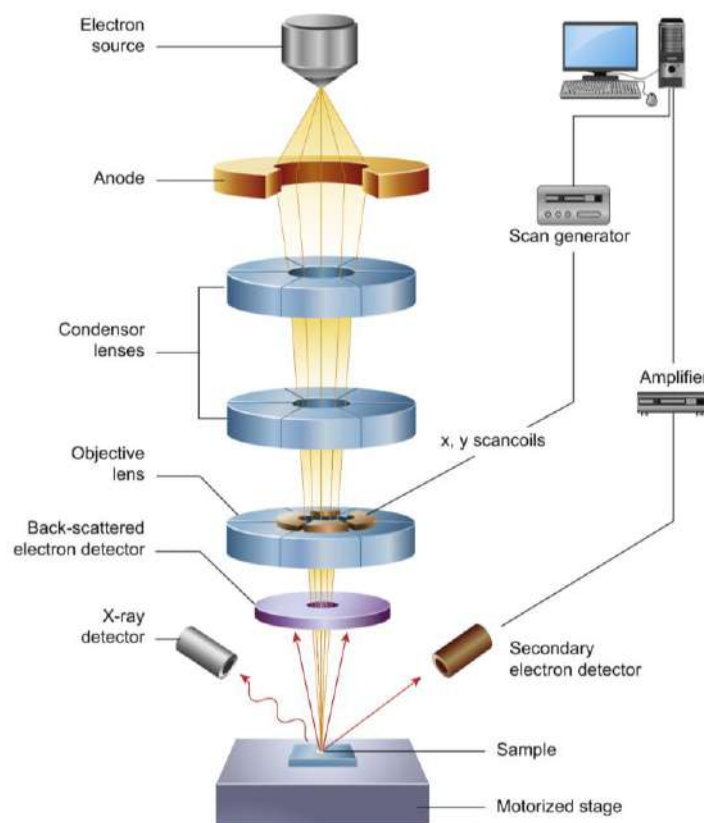


**Figure 29.** Schematic diagram of the core of a scanning electron microscope.

(Reprinted with permission from reference <sup>140</sup>)

The electrons generated at the electron gun (by heating a tungsten filament) are accelerated by the anode, usually with an accelerating voltage of 1 to 30 kV, and pass through two condenser lenses. The first condenser is responsible for narrowing the beam across its aperture by removing high-angle electrons from the incident electron beam. Then, the next condenser lens further eliminates the high-angle electrons from the beam to form a coherent and tight electron beam. The coils present on the objective lens aperture scan the beam for a period of time set by the operator (i.e. the scan speed) and then focus the scanning beam on the part of the surface sample on which the image is taken. As the electron beam hits the surface of the sample, different signals are emitted from the specimen. Among others, the signal emitted in the form of secondary electrons is detected by an electronic devices connected to the microscope. This signal is then amplified and displayed as an image on a cathode ray tube. The obtained image stays therefore as a distribution map of the intensity of the secondary electron signal that is emitted from the scanned area of the specimen. The backscattered electrons collected at the detector are proportional to the average atomic number of the target material.<sup>141</sup>

This signal supports improvement of the contrast of the image. The images appear brighter for the higher average atomic number (Z) than those of low average Z. Depending on the model of SEM, this instrument can have a magnification of up to  $\times 1000000$ <sup>142</sup> and can achieve resolutions of the order of 1 to 20 nm.

Top view and cross sectional images of the samples were performed by:

(a) PhD DSc Eng Jakub Karczewski, prof. PG - Faculty of Applied Physics and Mathematics, Institute of Nanotechnology and Materials Engineering, Gdańsk University of Technology, Narutowicza 11/12 St., 80-233 Gdańsk, Poland.

Used equipment: Quanta FEG 250 (FEI) Schottky field-emission scanning electron microscopy instrument equipped with a secondary Everhart-Thornley electron detector with a beam accelerating voltage of 10 kV.

(b) PhD Jan Hanuš from Faculty of Mathematics and Physics, Charles University, V Holesovickach 2, 18000 Prague 8, Czech Republic.

Used equipment: JSM-7200F (JEOL) scanning electron microscopy instrument operated in secondary electron mode.

(c) Prof. Ondřej Kylián from Faculty of Mathematics and Physics, Charles University, V Holesovickach 2, 180 00 Prague 8, Czech Republic.

Used equipment: JSM-7200F (JEOL) scanning electron microscopy instrument operated in secondary electron mode.

(d) MSc Eng Franciszek Skiba from Faculty of Electronics and Informatics, Gdańsk University of Technology, Narutowicza 11/12 St., 80-233 Gdańsk, Poland.

Used equipment: Phenom XL microscope Thermo Fisher Scientific.

I was also responsible for imaging of the surface morphology of the samples using SEM (Hitachi SU3500) present at IMP PAN and I analysed the images using ImageJ software.

It is important to note that a vacuum condition is necessary in the chamber to avoid static charge build-up on the sample surface during the electron beam scanning. Hence, samples must be well dried before imaging. Otherwise, water will vaporize in the vacuum chamber. For top-view images, a piece of copper tape with conducting glue was used to stick the sample to the stage providing this way the electrical connection between the sample surface and the table. For the cross section images, 10 nm-thin gold film was deposited on the sample to improve the conductivity of the layer. Other important parameters such as stigmatism, working distance, acceleration voltage and condenser lens current can also be adjusted by the operator during measurements to improve image quality.

The analysis of the micro- and nanostructure of the material can be investigated also using a transmission electron microscope. The main components and their arrangement in a transmission electron microscope are shown in the **Figure 30**.

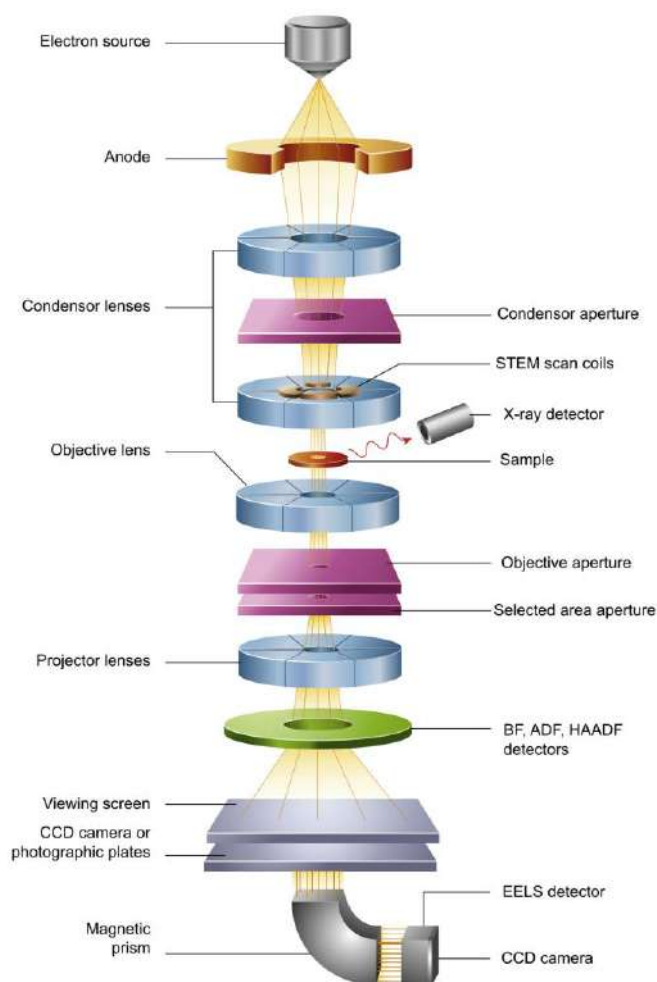


**Figure 30.** Schematic diagram of the core of a transmission electron microscope. CCD: Charge-Coupled Device; BF: Bright Field; ADF: Annular Dark Field; HAADF: High-Angle Annular Dark-Field; EELS: Electron Energy Loss Spectroscopy.

Reprinted with permission from reference <sup>140</sup>.

Unlike the SEM microscope, the TEM microscope includes electrostatic lenses placed above and below the samples and can have 10 times higher resolution than for SEM. Electrons are accelerated using the voltage of 80 to 300 kV, (i.e. roughly 10 times higher than that required for SEM microscope) to provide them with sufficient energy to pass through the material. <sup>140</sup> The condenser lenses arranged sequentially along the path of the incident electron enable to

eliminate high-angle electrons. Thus, they control the diameter and convergence of the primary electrons onto the sample.<sup>140</sup> The transmitted electrons from the sample pass through two lenses i.e. objective lens and the projector lens. The transmitted electron beam passing through the objective aperture is focused to form a diffraction pattern. Then this diffraction pattern is magnified as it passes through the projector lens to the detection system.

TEM images of the fabricated samples in this thesis were taken by:

PhD DSc Eng. Emerson Coy, prof. UAM, from NanoBioMedical Centre (Adam Mickiewicz University, Wszechnicy Piastowskiej 3 St., 61-614 Poznań).

Used equipment: ARM 200F (JEOL) transmission electron microscopy instrument operated at 200 eV, equipped with an energy-dispersive X-ray spectrometer (EDX).

I was taking part in the analysis of the obtained images.

### 6.5.2 Energy dispersive X-rays (EDX) for elemental analysis

As already discussed above, the different signals emitted by the sample during its interaction with the high energy electron provide information not only about the topography of the sample but the chemical composition. In EDX mode, the X-rays energies released from the samples can be detected and give information about elemental composition and atomic mapping of the sample. The generation of the characteristic X-ray is depicted in **Figure 31**.

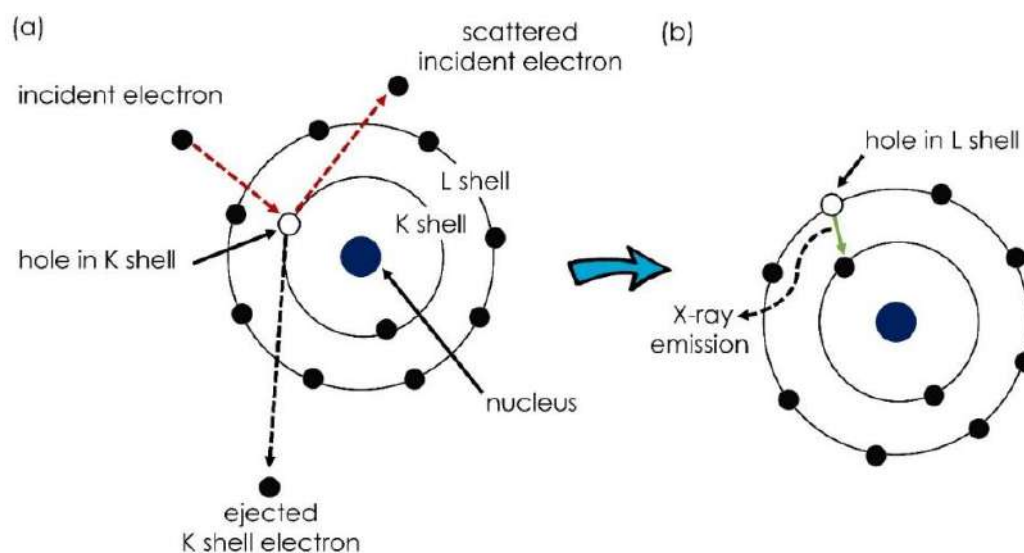


**Figure 31.** (a) Creation of the hole in the inner lower-energy shell upon collision with the incident electron. (b) Release of X-ray upon the transition of the electron from the outer higher-energy level to the inner lower-energy shell.

As shown in **Figure 31**, the incident electron hits the sample and knocks off an electron from the K shell, leaving a hole. Subsequently, a transition of the other electron from the outer shell, L shell, to the K shell occurs. This transition of the electron from the outer higher-energy to the inner lower-energy shell is accompanied by the release of X-ray energy. Each chemical element has a unique characteristic X-ray emission energy. Therefore, the elemental analysis of the specimen is possible by recording the characteristic energy of X-ray spectrum accompanied with the analysis of its intensity. A silicon drift detector measures the X-ray spectrum of the sample and the qualitative (i.e. type of chemical elements) and quantitative (i.e. percentage) analyses of each chemical element present in the material are carried out using a software.

EDX spectra of the samples were recorded by:

(a) PhD DSc Eng. Emerson Coy, prof. UAM, from NanoBioMedical Centre, Adam Mickiewicz University, Wszechnicy Piastowskiej 3 St., 61-614 Poznań, Poland.

Used equipment: JEOL SDD (silicon drift detector) connected to the ARM 200F (JEOL) transmission electron microscopy instrument.

(b) PhD Jan Hanuš from Faculty of Mathematics and Physics, Charles University, V Holesovickach 2, 18000 Prague 8, Czech Republic.

Used equipment: JEOL SDD (silicon drift detector) connected to the JSM-7200F (JEOL) scanning electron microscopy instrument.

I was responsible for the analysis of the obtained EDX spectra.

### 6.5.3 X-ray photoelectron spectroscopy

The principle of X-ray photoelectron spectroscopy (XPS) is based on the photoelectric effect. Photoemission occurs when an atom absorbs the energy of an incident photon ( $h\nu$ ), causing the emission of electrons of discrete energy, namely photoelectron. The photoelectric effect process is illustrated in **Figure 32 (a)**. The ejected electron from the sample is detected by the spectrometer and then the measurement of its energy is based on the energy level diagram (**Figure 32 (b)**). The electron escapes from the core level orbitals upon absorption of the incident photon leading to the photoionization of the atom:



It is important to mention that the photoelectron is only emitted if the incident photon has an energy greater than the binding energy of the atom.

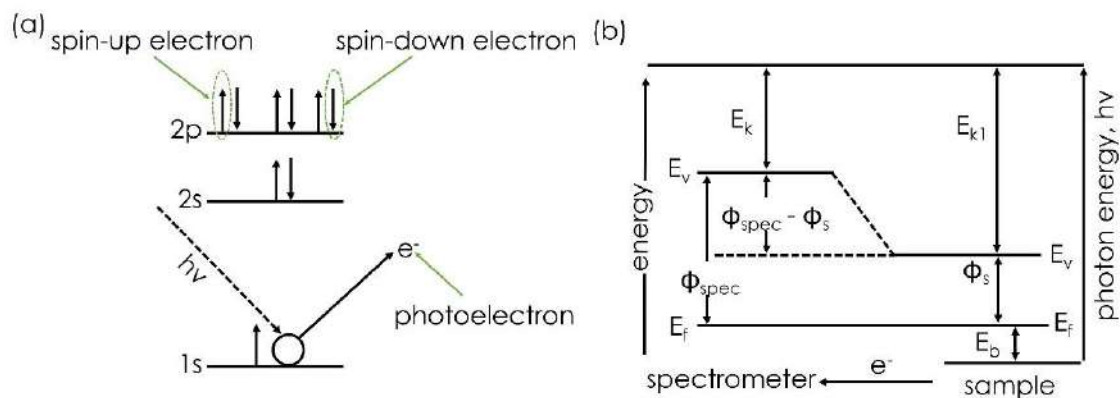


**Figure 32.** (a) Photoemission process.

(b) Energy level diagram for XPS binding energy measurements.

The determination of both the kinetic energy of the photoelectron and the binding energy of the atom from the energy level diagram is explained as follows, the sample and the spectrometer housing are electrically connected so that both have the same reference for measuring the energy of the electron. This energy reference shown in **Figure 32 (b)** is called the Fermi level ( $E_F$ ). The incident photon with the energy  $h\nu$  ejects the photoelectron towards the vacuum level ( $E_V$ ). As shown in **Figure 32 (b)**, the kinetic energy of the photoelectron on the surface of the sample can be determined basing on the equation:

$$E_k = E_{k1} - (\phi_{spec} - \phi_s) \quad (13)$$

where  $E_{k1}$  is the energy of the photoelectron relative to the vacuum level,  $\phi_{spec}$  is the work function of the spectrometer and  $\phi_s$  is the work function of the sample. The work function is defined as the energy required to remove electron from the Fermi to vacuum level. The binding energy ( $E_b$ ) of the material can be determined as well from the energy diagram according to the equation:

$$h\nu = E_b - E_k + \phi_{spec} \quad (14)$$

Regarding the XPS instrument, the analysis chamber presents five main components including a photon source (i.e., the anode), electromagnetic lenses, an electrostatic hemispherical analyser, and a detector (**Figure 33**).

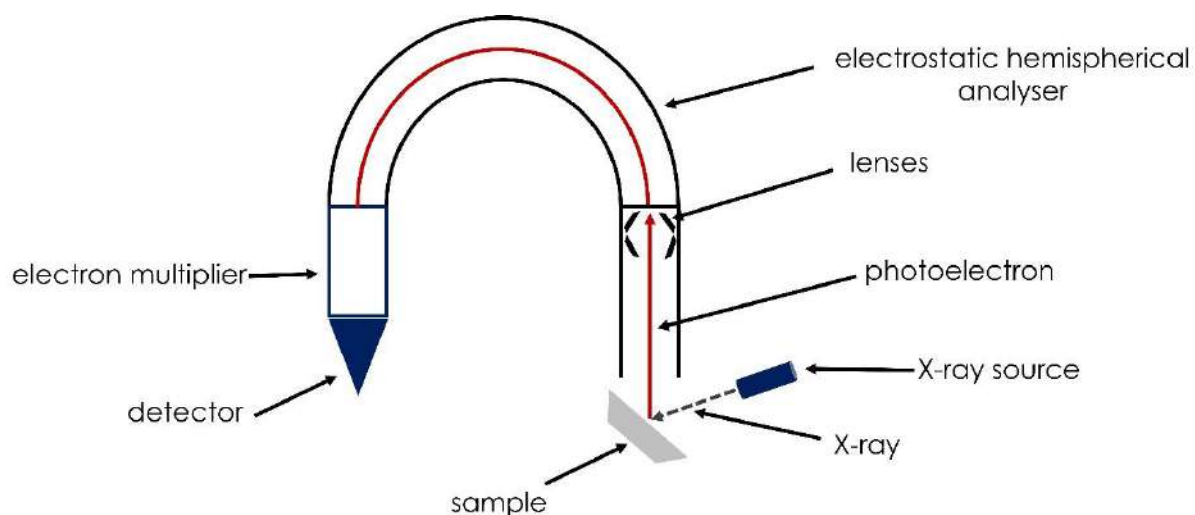


**Figure 33.** Schematic of the XPS analysing chamber.

The anode in the X-ray source is generally made of aluminium and is bombarded by electrons accelerated with an energy of 15 keV. When the electron strikes the aluminium, X-rays are emitted according to the same process described in **Figure 31**. The emitted photon focuses on the samples and allows the photoelectron to be ejected. The electromagnetic lenses converge the photoelectrons towards the entrance slit of the hemispherical analyser. This enables the deflection of the photoelectrons with a specific angle, which depends on the width of the slit as well as the radius of the hemisphere. Then the photoelectrons are collected by a detector, usually called a channeltron. The detector is usually a tube whose interior is covered with a material capable of releasing a large number of electrons when an electron strikes its surface. This is to amplify the output signal of the XPS. The nomenclature of detected peaks found on XPS spectra is given according to the orbital ( $l = 0, 1, 2, \dots$ ) from which the electron emanates and denoted as s, p, d, f... The spin quantum number ( $s$ ) taking value of  $\pm 1/2$  and the total momentum  $j$  ( $j = l \pm s$ ) of the photoelectrons for example Ti ( $2p_{3/2}$ ) and Ti ( $2p_{1/2}$ ) indicate that in both cases the photoelectron is emitted from the orbital p (i.e.  $l = 1$ ) of the Ti atom, total momentum is  $3/2$  for Ti ( $2p_{3/2}$ ) and  $1/2$  for Ti ( $2p_{1/2}$ ), and by using the formula  $j = l \pm s$ , the spin of the emitted electron is  $1/2$  for Ti ( $2p_{3/2}$ ) and  $-1/2$  for Ti ( $2p_{1/2}$ ). This spectroscopic technique allows analysis of the surface composition, chemical state and material chemistry of a few outermost 10 nm atomic layers.

In the case of the materials prepared in this thesis XPS spectra were recorded by

- (a) PhD Jan Hanuš from Faculty of Mathematics and Physics, Charles University, V Holesovickach 2, 18000 Prague 8, Czech Republic.



Used equipment: Thermo Scientific K-Alpha X-ray Photoelectron Spectrometer equipped with a hemispherical analyzer (Phoibos 100, Specs) and an Al K $\alpha$  X-ray source (1486.6 eV, 200 W, Specs).

(b) PhD Agnieszka Kramek, PhD student Justyna Gumieniak from The Faculty of Mechanics and Technology, Rzeszów University of Technology, Kwiatkowskiego 4 St., 37-450 Stalowa Wola, Poland.

Used equipment: Thermo Scientific K-Alpha X-ray Photoelectron Spectrometer. The samples were irradiated with low-energy X-ray radiation (Al K $\alpha$  = 1486.7 eV).

I took part in the analysis of the obtained spectra.

#### 6.5.4 X-ray diffraction

As shown in **Figure 34**, an X-ray diffractometer has three main components, namely the X-ray source, the specimen holder and the X-ray detector.

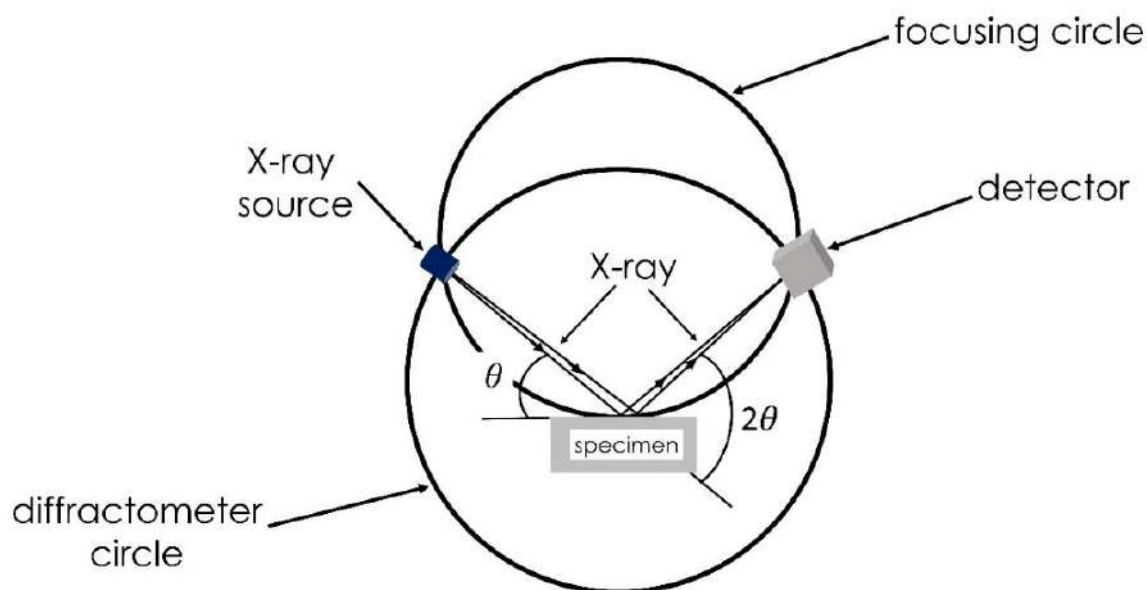


**Figure 34.** Geometry of an X-ray diffractometer.

All components are placed on the circumference of a circle known as focusing circle. The emission of X-rays inside the source follows the same steps as shown in **Figure 31**. X-rays are emitted by directing a beam of electrons to the target material at a high voltage. The value of the accelerating voltage depends on the target materials. For example, a voltage of 40 kV is applied when copper is used as the target. The specimen consists of a thin layer of the active material deposited on a glass microscope slide being a non-diffracting substrate. First, the

incident X-ray beam hits the sample. If the incoming incident beam and the scattered X-ray beam have the same wavelength, constructive interference occurs. As the consequence, the scattered X-rays are diffracted in directions depending on the nature of the crystalline sample. The relation between the wavelength of the X-rays and the spacing of the atomic planes is governed by Bragg's law:

$$n\lambda = 2d \sin \theta \quad (15)$$

where  $\theta$  is the angle between the plane of the specimen and the incident X-ray, and  $d$  is defined as inter-atomic spacing.

As shown in **Figure 34**, the angle between the direction of the incident X-ray and the the diffracted X-ray is  $2\theta$ . The direction of the diffracted X-rays defined by the Miller index (hkl) and the position of the signals found on the diffraction patterns for anatase (JCPDS Card no. 21-1272) and rutile (JCPDS Card no. 21-1276) phase of titania as well as the reported values of the d-spacing are summarized in **Table 2** and **3**.

**Table 2.** Miller indices (hkl), d spacing, and corresponding diffraction angle for anatase phase of titania.<sup>143</sup>

<b>hkl</b>	<b>d / nm</b>	<b>2 <math>\theta</math> / degree</b>
101	3.5163	25.308
103	2.4307	36.950
004	2.3786	37.790
112	2.3322	38.571
200	1.8921	48.046
105	1.7001	53.884
211	1.6662	55.071
213	1.4931	62.112
204	1.4808	62.690
116	1.642	68.754
220	1.3379	70.302
215	1.2646	75.051
301	1.2505	76.049

**Table 3.** Miller indices, d spacing, and corresponding diffraction angle for rutile phase of titania.<sup>143</sup>

<b>hkl</b>	<b>d / nm</b>	<b>2 <math>\theta</math> / degree</b>
110	3.2477	27.440
101	2.4875	36.078
200	2.2965	39.196
111	2.1873	41.239
210	2.0541	44.049
211	1.6874	54.323
220	1.6239	56.634
002	1.4795	62.750
310	1.4524	64.057
301	1.3598	69.001
112	1.3464	69.795
311	1.3038	72.425
202	1.2437	76.534
212	1.2005	79.827

In this work, X-ray diffraction patterns of the samples were recorded by:  
PhD DSc Eng. Jakub Karczewski, prof. PG from Faculty of Applied Physics and Mathematics,  
Institute of Nanotechnology and Materials Engineering, Gdańsk University of Technology,  
Narutowicza 11/12 St., 80-233 Gdańsk, Poland.

Used equipment: Bruker D2 Phaser 2nd generation using CuK $\alpha$  radiation and a LynxEye XE-T detector.

I took part in the analysis of the obtained data.

### 6.5.5 Raman spectroscopy

In the Raman spectrometer the monochromatic light emitted by the laser is focused on the sample and detector is responsible for collection of the scattered light. In general, the majority of photons generated by the excitation source are scattered elastically i.e. they are simply deviated from their incident directions with the same frequency as the incident light  $\nu_0$ . This is called Rayleigh scattering. However, a small number of incident photons, approximately 1/1000000, are scattered inelastically with a frequency of  $\nu_0 \pm \nu_m$ , causing the molecules of the

sample to vibrate with the frequency of  $\nu_m$ . This is described as Raman scattering. We consider Stokes or anti-Stokes scattering when the incident photon is scattered with the frequencies  $\nu_0 - \nu_m$  or  $\nu_0 + \nu_m$ . The vibrational frequency of the molecules of the sample i.e.  $\nu_m$  is measured as a shift from the frequency of the incident light ( $\nu_0$ ) by using a Raman spectrometer. Therefore, the recorded Raman shift is a direct measure of the vibrational energies of the molecules constituting the sample. **Figure 35** illustrates Raman and Rayleigh scattering. In Rayleigh scattering, after collision with the photon, the molecule is excited to a virtual state and then drops to its ground state. In Raman scattering, the molecule can take or lose energy from the photon during interaction with laser light.

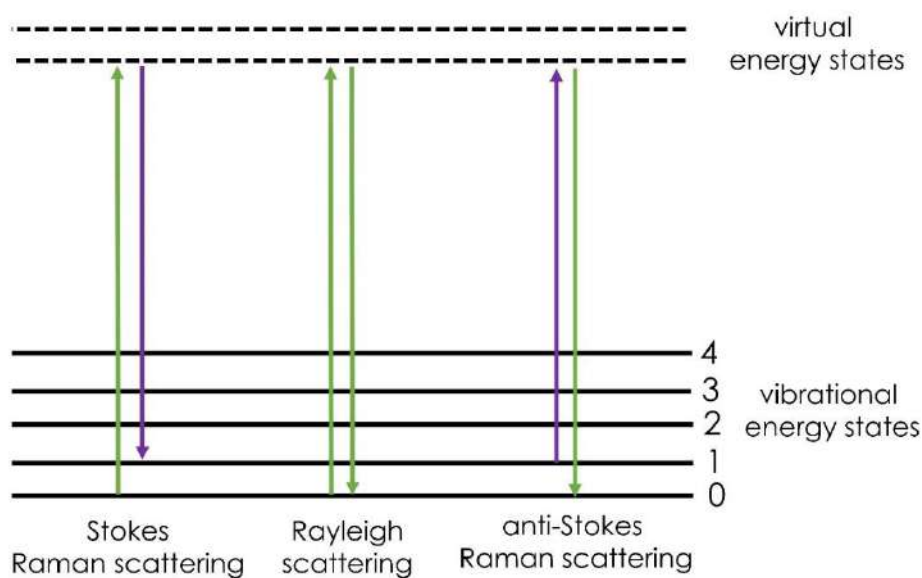


**Figure 35.** Indication of the three different forms of scattering  
i.e. Rayleigh, Stokes and anti-Stokes scattering.

Raman spectrum of anatase phase of  $\text{TiO}_2$  exhibits active bands located at  $144 \text{ cm}^{-1}$ ,  $197 \text{ cm}^{-1}$ ,  $399 \text{ cm}^{-1}$ ,  $516 \text{ cm}^{-1}$  and  $639 \text{ cm}^{-1}$ , which correspond to  $E_{g(1)}$ ,  $E_{g(2)}$ ,  $B_{1g}$ ,  $A_{1g} + B_{1g}$  and  $E_{g(3)}$  modes, respectively.<sup>144</sup> Rutile phase of titanium dioxide is characterized by four active modes at  $143 \text{ cm}^{-1}$  ( $B_{1g}$ ),  $447 \text{ cm}^{-1}$  ( $E_{1g}$ ),  $612 \text{ cm}^{-1}$  ( $A_{1g}$ ) and  $826 \text{ cm}^{-1}$  ( $B_{2g}$ ).<sup>144</sup>

In this work I was responsible for the Raman measurements to identify the vibrational modes present in the synthesized samples. Raman measurements were carried out at room temperature using a Raman spectrometer (Renishaw) equipped with two different lasers as the excitation source operating at: 514 nm or 785 nm. For the measurements carried out with the 514 nm laser source operating at 10 % of its total power (50 mW), the exposure time was 10 s

and a 50× objective was used. The spectra were recorded in the range from 100 to 2000  $\text{cm}^{-1}$ . In the case of measurements performed with the 785 nm laser used as the excitation source, the laser was operating at 1 % of its total power (500 mW) while the spectra were registered in the range from 100 to 1000  $\text{cm}^{-1}$  using 20× objective.

### 6.5.6 UV-vis absorption spectroscopy

The UV-vis spectrophotometer works based on the interaction between monochromatic light and matter. When a sample absorbs light of particular wavelength, the molecules inside the sample vibrate due to a change of their electronic state. Thus, qualitative and quantitative analysis can be performed to reveal the optical properties of the sample. The essential components of a UV-vis spectrophotometer include (a) a source (UV and visible), (b) a monochromator, (c) a sample container/holder - in the most cases it is cuvette, and the (iv) a photodetector. Generally, a tungsten lamp is used for the emission of light in the wavelengths between 330 and 900 nm, while a deuterium lamp is used for the emission of light in the wavelength range from 160 to 450 nm that covers the ultraviolet region. All the most important elements of spectrophotometer are shown in **Figure 36**.

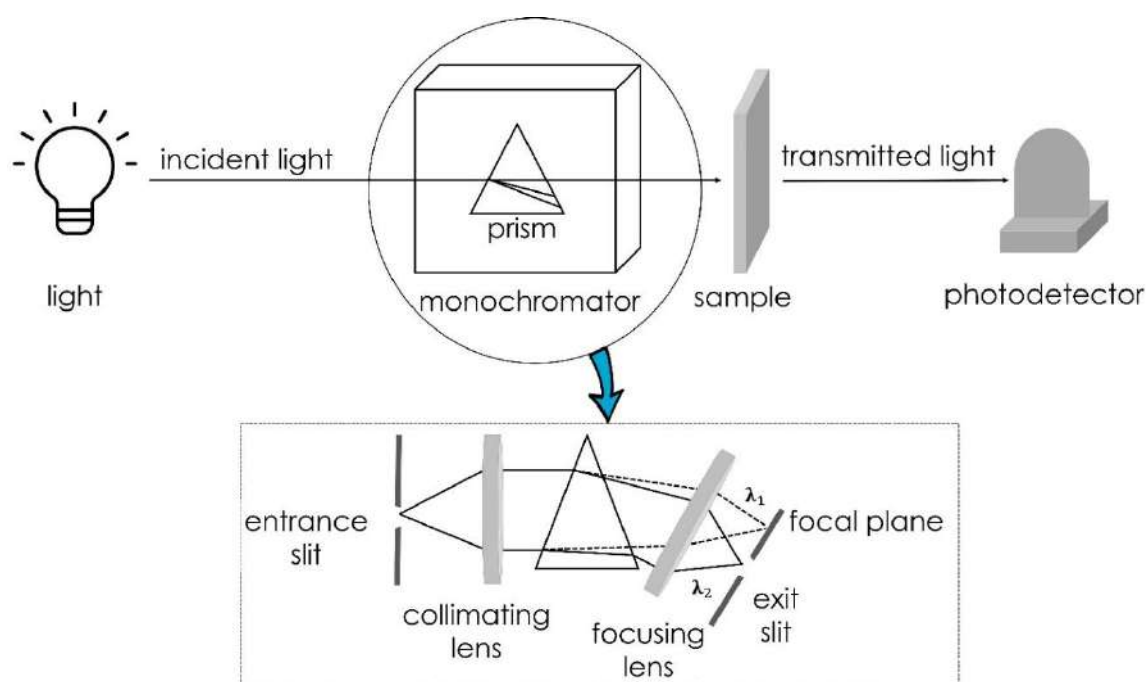


**Figure 36.** Schematic diagram of UV-vis spectrophotometer.

In short, polychromatic radiation is collimated by the lens after entering through the entrance slit of the monochromator. Then, the wavelengths are separated into their individual

components as they pass through the prism. The focal plane allows only radiation of a single wavelength to run out of the monochromator and reach the sample. The fraction of light is transmitted through the sample, if it is semitransparent, and then collected at the detector. The detector converts the light energy into electrical impulse that is collected and further analysed by the software. The absorbance is then determined as the logarithm of the ratio of incident light ( $I_{in}$ ) to transmitted light ( $I_{out}$ ) and given by the equation:

$$A = \log(I_{in}/I_{out}) \quad (16)$$

In this work I was responsible for the measurements of the absorbance spectra for the planar samples and their analysis. The measurements were carried out using spectrophotometer Lambda 35 Perkin-Elmer operating at a scanning speed of  $120 \text{ nm min}^{-1}$  with slit width of 2 nm. The spectra were recorded in the wavelength range of 320–900 nm.

#### 6.5.7 Fourier transform infrared spectroscopy

Fourier transform infrared spectroscopy (FTIR) is an analysis technique used for determining the chemical bonds present in the sample. This method is based on the interaction between infrared light (i.e. light with a wavelength between 780 nm and 1 mm) and matter. Light with specific IR frequencies is absorbed when illuminating the sample. These frequencies are either removed from the original IR beam or transmitted to the upstream detector with an intensity much lower than that of the incident beam. This brings atoms in the sample to the constant vibration. There are six different vibrational modes that can occur namely, the symmetric stretch, the antisymmetric stretch, the deformation or bending vibration, rocking, twisting, and wagging. The main component of the FTIR equipment is the interferometer as shown in **Figure 37**. Roughly, 50 % of the incident IR light is reflected towards a stationary mirror by the beam splitter. The other 50 % of light is transmitted towards the movable mirror (**Figure 37**). Both beams are reflected by the mirrors (i.e. stationary mirror and movable mirror) to the beam splitter where they recombine and interfere. The difference in path length between those two light beams at the beam splitter is called the retardation. The interference is recorded by the detector and converted into a digital signal. Due to constantly changing position of the moveable mirror, the dependency of the interference on the retardation is recorded and converted into a recorded electric signal. This interference is known as the interferogram. A specific software transforms the obtained digital signal into a plot of absorbance against wavenumber by Fourier transformation.

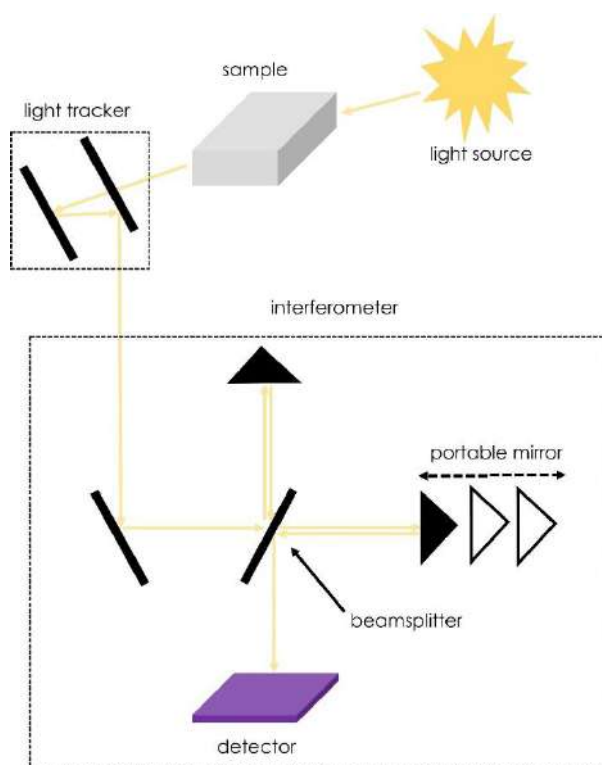


**Figure 37.** The scheme of FTIR spectrometer with its main components.

FTIR spectra were recorded by: Prof. PhD DSc Eng. Anna Dołęga from Department of Inorganic Chemistry, Gdańsk University of Technology, Narutowicza 11/12 St, 80-233 Gdańsk, Poland.

Used equipment: Nicolet iS50 FT-IR spectrometer. The instrument is equipped with a diamond single-reflection Special Quest ATR accessory. The measurement was performed in the wavenumber range of  $3500\text{--}400\text{ cm}^{-1}$ . The recorded spectra were analysed using OMNIC software.

I was responsible for the analysis of the obtained data.

## 6.6 Electrochemical and photoelectrochemical characterisation methods

The electrochemical and photoelectrochemical activities of the fabricated semitransparent electrodes were studied using cyclic voltammetry, linear sweep voltammetry, and electrochemical impedance spectroscopy techniques. The setup dedicated for the measurements is composed of an Autolab PGSTAT302N potentiostat-galvanostat system (Methrom,) connected to a three-electrode electrochemical cell with a quartz window depicted in **Figure 38**.

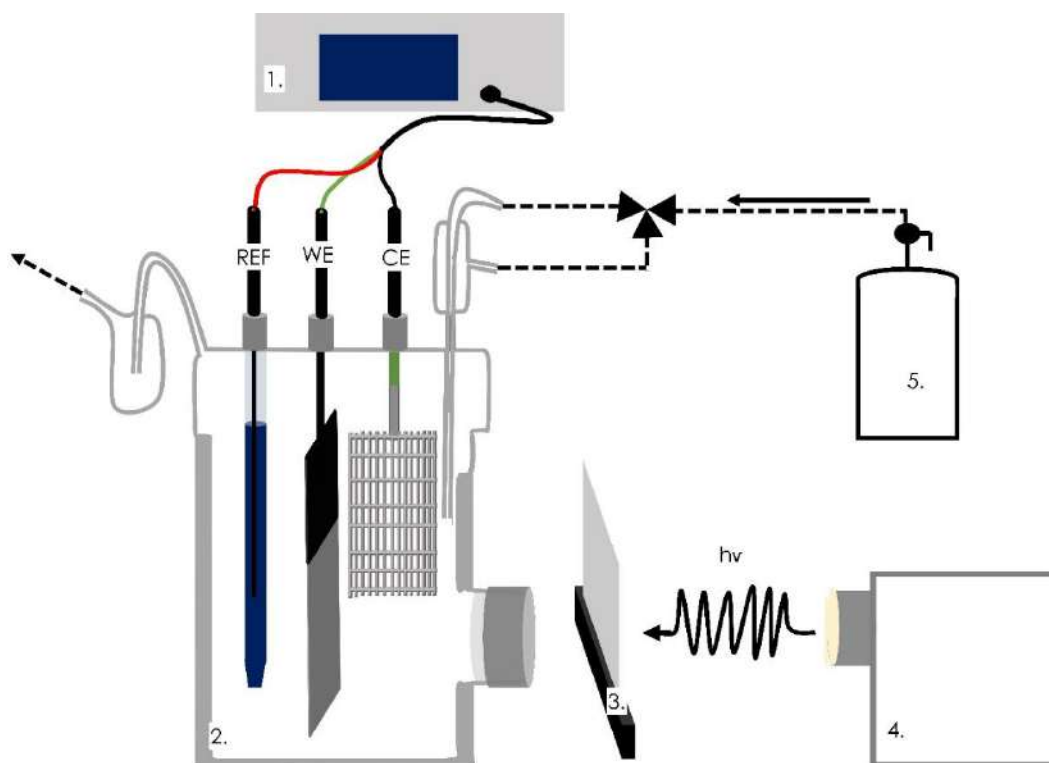


**Figure 38.** Schematic illustration of the measurement setup. (REF: reference electrode; WE: working electrode; CE: counter electrode; 1. electrochemical workstation: potentiostat-galvanostat; 2. electrochemical cell; 3. cut-off optical filter; 4. xenon lamp as solar simulator; 5. argon gas bottle.

The electrochemical cell consists of:

- platinum mesh (Pt) as the counter electrode,
- Ag/AgCl/0.1 M KCl as the reference electrode,
- the semitransparent titania nanotube substrates as a working electrode,
- 0.5 M Na<sub>2</sub>SO<sub>4</sub> electrolyte in which electrodes were immersed.

Prior to each measurement, the electrolyte was deaerated by argon gas flow for 30 min. During the experimental measurements the flow of argon was kept above the electrolyte to hamper the access of oxygen to the electrolyte. For the photoelectrochemical measurements a xenon lamp simulator (Osram XBO 150), with a light intensity of 100 mW/cm<sup>2</sup> was used as the light source. Incident light calibration was performed by adjusting the distance between the light source and the electrochemical cell by using a calibrated reference cell (RERA solution). The characteristics of the used reference cell are: material: silicon, calibration value: 64.7 mV. The measurements carried out in the visible region were conducted by placing a cut-off optical filter (AM 1.5 Filter,  $\lambda > 420$  nm, Schott) between the light source and the electrochemical cell, as



shown in **Figure 38**. It is worth mentioning that for both types of measurements: electrochemical and photoelectrochemical measurements, the same setup presented in **Figure 38** was used. The only difference was that during the electrochemical test carried out in darkness, sample was not exposed to the light originating from solar simulator.

Other photoelectrochemical tests such as intensity-modulated photocurrent spectroscopy (IMPS), quantum efficiency measurements i.e. incident-photon-to-current efficiency (IPCE) and photoluminescence (PL) measurements were carried out as well. Information about the equipment used for the IMPS, IPCE and PL measurements is provided in the subsections **6.5.5**, **6.5.6** and **6.5.7**, respectively.

Those subsections aim to provide clear explanation on key parameters investigated in each method, as well as the description of the principle of those techniques.

### 6.6.1 Cyclic voltammetry

Cyclic voltammetry (CV) technique provides important information such as the thermodynamics of redox reaction, kinetics of heterogeneous electron-transfer reactions, the potential window of the electrode, the adsorption or diffusion processes of the active material.<sup>145</sup> The reaction of the electrodes during CV measurement involves different elementary steps. Those steps include the transfer of electrons at the electrode and/or the adsorption of species on the electrode and/or the transfer of mass in the electrolyte. In particular, when the electron transfer process predominates over the mass transfer process, that is, the rate of electron transfer is sufficiently higher than that of mass transfer, the electrode reaction is called reversible.<sup>146</sup> In this case the electrode potential is expressed by the Nernst equation:

$$E = E^0 + \frac{RT}{nF} \ln\left(\frac{C_O}{C_R}\right) \quad (16)$$

where  $E^0$  is the formal potential,  $R$  is the gas constant,  $T$  is temperature in K,  $n$  is the stoichiometric number of electrons involved in the process,  $F$  is the Faraday constant,  $C_O$  is the concentration of the oxidant and  $C_R$  is the concentration of the reductant. The formal potential is a measure of the potential of a cell where both oxidised and reduced species are present at equal concentration (i.e. average midpoint potential of cathodic and anodic peak potential).<sup>147</sup>

During cyclic voltammetry measurements, the potential of the working electrode (i.e., TNT grown on the glass substrates) is varied linearly with respect to time at a scan rate  $v$  forward to a switching potential, at which point the potential is swept in reverse direction at the same rate (**Figure 39**).

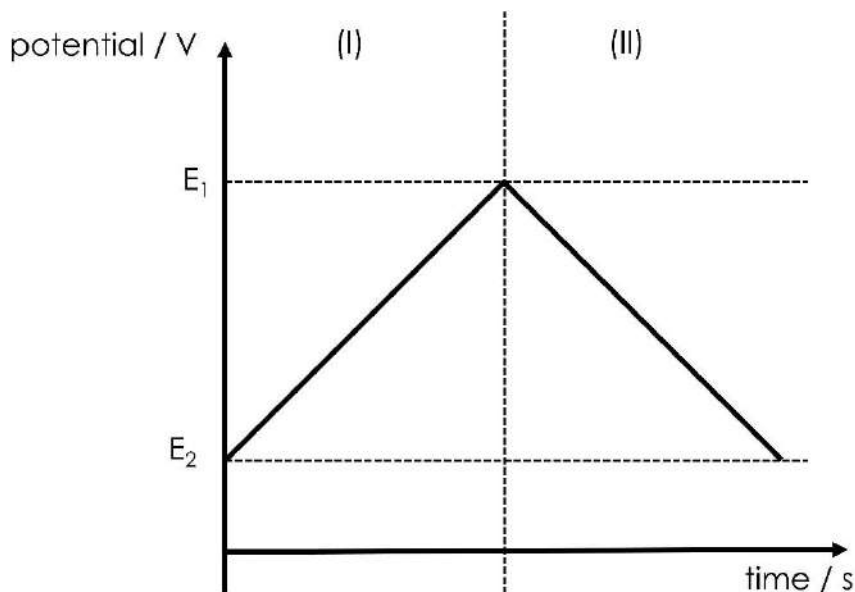


**Figure 39.** Potential applied to the cell versus time during (I) forward scan; (II) reverse scan.

The current response is recorded and plotted as a function of the applied potential to obtain the voltammetry cycle. The scan rate defines how fast the potential of the working electrode is changed. A faster scan leads to the decrease in the size of the diffusion layer<sup>148</sup> and in consequence the capacitive current decreases.<sup>148</sup> Indeed, at higher scan rates the ions in the electrolyte do not have sufficient time to fill both the outer and inner pore surfaces of the electrodes.<sup>149</sup> In this work on the basis of the already reported works and preliminary measurements, 50 mVs<sup>-1</sup> was selected for the CV measurements. CV test were carried out in 0.5 M Na<sub>2</sub>SO<sub>4</sub> electrolyte. In particular for TNT grown out of TiAg film, CV was also performed in 0.5 M Na<sub>2</sub>SO<sub>4</sub> containing 10 mM K<sub>3</sub>Fe(CN)<sub>6</sub> to study the kinetics of the [Fe(CN)<sub>6</sub>]<sup>3-/4-</sup> redox couple at the electrodes by using Randles-Sevcik equation:

$$i_p = 0.4463FAC_0\sqrt{\frac{FDv}{RT}} \quad (17)$$

where  $i_p$  is the peak current,  $R$  is the gas constant,  $T$  is temperature in K,  $A$  is the electrode surface area in cm<sup>2</sup>,  $F$  is the Faraday constant,  $C_0$  is the concentration of the redox species in mol cm<sup>-3</sup>,  $D$  is the diffusion coefficient in cm<sup>2</sup> s<sup>-1</sup> and  $v$  is the scan rate in V s<sup>-1</sup>.<sup>146</sup>

In general, this analysis is conducted first by recording the CV at different scan rates, then plotting the peak current  $i_p$  as a function of the square root of the scan rate  $v$ . An illustration is shown in **Figure 40** for ITO coated glass electrode. In general two cases can be observed. If the plot shows a linear increase of the peak current density  $j_p$  with  $v^{1/2}$ , as it is in **Figure 40 (b)**.

This implies that the kinetic of the ferricyanide species is predominantly under diffusion control, and the diffusion coefficients are determined using the equation (17).<sup>150</sup> Whereas, if the curve  $j_p$  vs.  $v^{1/2}$  does not show any linear relation it indicates that the electron transfer occurs by surface adsorbed species.<sup>148</sup>

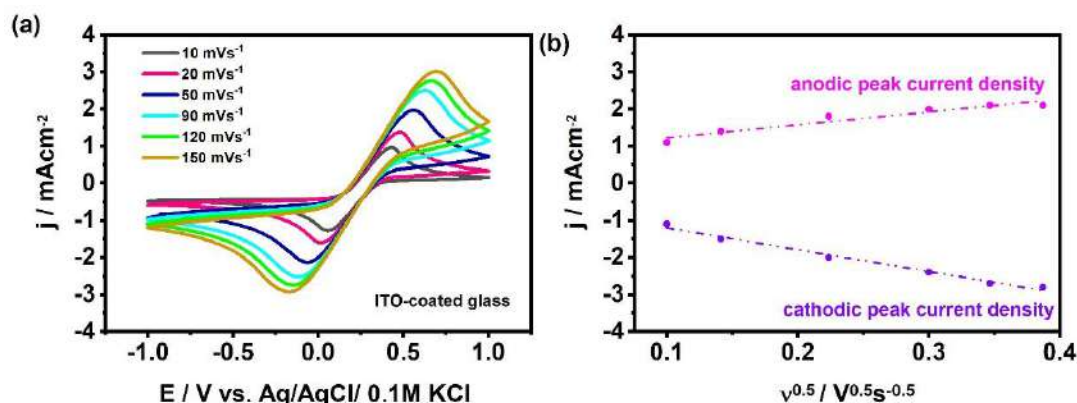


**Figure 40.** (a) Voltammogram of bare ITO-coated glass in 0.5 M Na<sub>2</sub>SO<sub>4</sub> + 10 mM K<sub>3</sub>Fe(CN)<sub>6</sub> recorded within the scan rate range of 10 - 150 mV s<sup>-1</sup>.  
(b) corresponding plot of peak current density vs.  $v^{1/2}$ .

### 6.6.2 Linear sweep voltammetry

In this technique, similar to the CV measurements, the potential of the working electrodes is varied linearly with respect to time and the current that flows in response to the change in potential is recorded. However, during LSV measurements the potential is only scanned in one direction, i.e. the potential is swept either to the anodic or to the cathodic direction, depending on the investigated process. In this work, LSV technique was used to characterise the photoactivity of the synthesized materials. The photoresponse tests were carried out by recording the LSV curves for the working electrodes under chopped light irradiation. Chopped irradiation means that the electrode was exposed to light and then kept in dark, while each step lasts established time (I used 5 s). The principle of this measurement is explained as followed, when the light illuminates the photoactive material (i.e., the light turns on), the recorded current density increases to a maximum value, reaches saturation level and then returns to the initial, dark current value when the light is off. The photocurrent is determined by subtracting the current density measured under light illumination by the current density in the dark. The shapes of the photocurrent run during on/off actions reported in the literature during LSV measurements are presented in **Figure 41**.

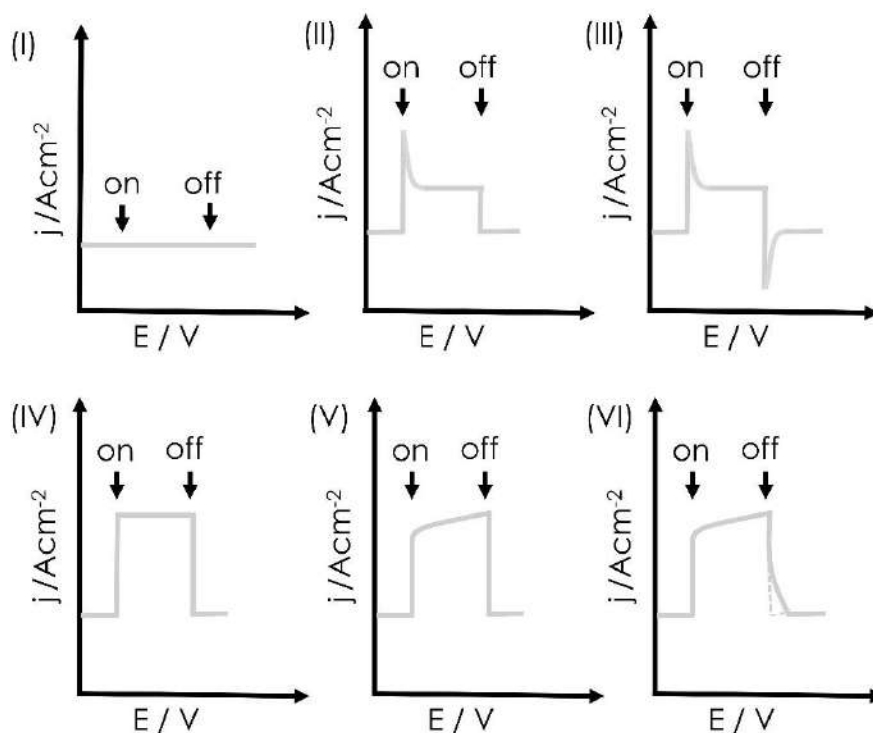


**Figure 41.** Possible options of photocurrent density response for an illuminated semiconductor electrode. On means that the irradiation of the electrode was initiated whereas off means that the exposition of the electrode to irradiation was stopped.

According to the various photoresponse runs given in **Figure. 41**, following situations can occur:

**(I)** When the material is not photoactive, there is no increase in the recorded current density upon turning on the light.

**(II)** Upon turning on the light, the photocurrent exhibits a rapid increase before an exponential drop to reach a steady state photocurrent. Then, the current drops to its basic value when the light is turned off. The occurrence of those spikes is due to the recombination of the photogenerated electrons with the surface-trapped holes.<sup>151</sup>

**(III)** Two spikes can be present during one on/off irradiation cycle, i.e. one when the light is turned on and the other when the light is turned off. The occurrence of the spike observed when the light is turned on is explained as followed: the photogenerated holes are trapped at the semiconductor/electrolyte interface under illumination. Then, once the light is turned off, these holes are oxidized, resulting in a sharp peak before the current returns to its background level.<sup>152</sup>

(IV) There are no spikes when light is turned on and/ or off. This almost rectangular shape of the photocurrent suggests that there is no recombination of electrons with holes and the number of recombination centres in the material is very limited. This case is considered as the most desired for the fabricated photoelectrode.

(V) When turning on the light, one can observe a rapid rise followed by a slower increase in the photocurrent to reach the maximum value. This slow dynamic of the photocurrent to reach the steady state is associated with the presence of trap filling phenomena, i.e. trapping/detrapping processes.<sup>89,153</sup>

(VI) When the exposition of the material to light is stopped, the longer photocurrent tail is seen. This shape is attributed to the time required for the charges to be detrapped after the light is turned off.<sup>154</sup>

### 6.6.3 Electrochemical impedance spectroscopy

Electrochemical impedance spectroscopy technique was used in this work for detailed studies of the charge transfer kinetics at the electrode/electrolyte interface. The impedance is defined as the resistance to the passage of an alternating current through the material. In this technique, a stimulus potential  $v(t)$  of amplitude of a few millivolts, thus small alternating potential, is applied to the sample and the alternating current response  $i(t)$  is measured. Small alternating potential (few millivolts) is then applied to the working electrode to ensure the linearity of the current response to the alternating potential.<sup>155</sup> Both, the alternating potential and its current response have the same frequency, but are shifted in phase. The impedance depends on the frequency of the alternating signal applied to the material and is defined by the equation (18):<sup>155</sup>

$$Z = \frac{v(t)}{i(t)} \quad (18)$$

The total impedance can be also given in the complex form (equation 19):

$$Z = Z' + jZ'' \quad (19)$$

where  $Z'$  and  $Z''$  are respectively the real and imaginary part of  $Z$ .

The graphical representation of the imaginary part  $-Z''$  together with the real part  $Z'$  of the impedance is known as the Nyquist plot. The negative sign of the imaginary part of the impedance is simply to keep the Nyquist plot in the first quadrant of the Cartesian plane. Analysis of Nyquist plot can provide information on the kinetics and mass transport at the semiconductor/electrolyte interface as well as the corrosion level of conductive materials. As

shown in **Figure 42**, for the most cases of electrode materials, the corresponding Nyquist spectra consists of two regions, namely the kinetic control region at high frequencies and the mass transfer region at the intermediate and at low frequency regions.<sup>156</sup>

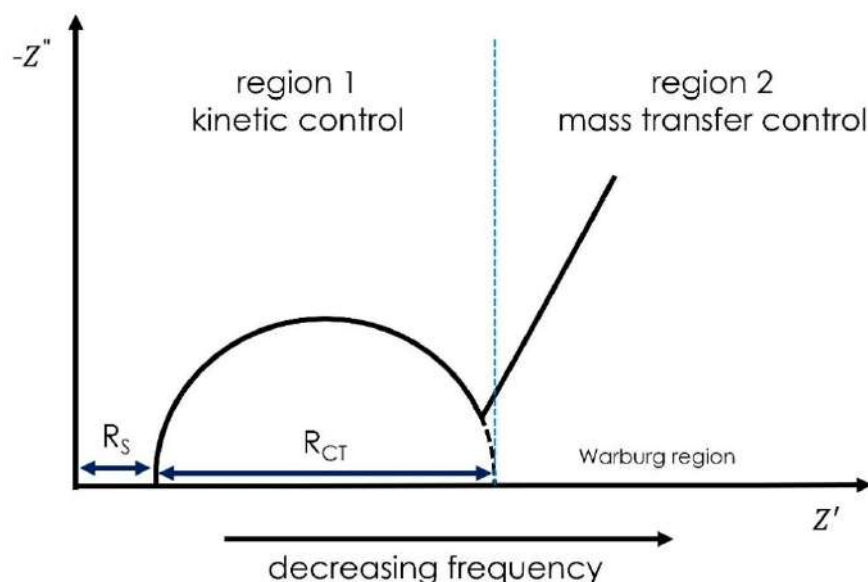


**Figure 42.** Nyquist plot for electrode (with faradic reaction at the electrode/electrolyte interface) with the indication of the key regions, namely, the kinetic control region and the mass transfer region (Reproduced from <sup>156</sup>, under CC BY-NC 3 license).

The physical interpretation of this spectra is carried out according to the electric equivalent circuit (EQC), where each element and the relation between elements represent the electrochemical system feature. In the kinetic control region, the distance from the origin of the cartesian plane to the intercept of the Nyquist plot with the x-axis is assigned to the equivalent series resistance ( $R_s$ ) also known as the internal resistance. This resistance takes into account the resistances of the electrolyte, the electrode, and the contact resistance between the electrode and the current collector.<sup>157</sup> In general, the diameter of the semicircle is attributed to the charge transfer resistance at the semiconductor/electrolyte interface.<sup>157</sup> The charge transfer resistance ( $R_{ct}$ ) represents the insulating features at the electrode/electrolyte interface.<sup>158</sup> This means that  $R_{ct}$  affects the charge separation kinetic at the interface between electrode surface and the electrolyte.<sup>159</sup> The lower values of charge transfer resistance indicate fast electron transfer in this region. It is worth mentioning that although one semicircle is usually obtained, it is also possible to obtain not ideally hemispheric shape of the spectrum as well as two or more semicircles at lower frequencies can be present. This indicates that different electrochemical processes contribute to the overall charge transport at the electrode/electrolyte interface. For

example, the presence of the second semicircle in the lower frequency region can be attributed to the adsorption and desorption processes of ions at the electrode/electrolyte interface.<sup>156</sup> As the frequency decreases, the mass transfer process becomes predominant. The non-vertical line at low frequencies is assigned to the ion transport from the electrolyte to the porous electrode layer. This resistance is also known as Warburg impedance.<sup>157</sup> In the EQC, the Warburg diffusion can be described by finite or infinite diffusion models. The infinite model is considered when the distance and time of the diffusion are smaller compared to the dimensions of the system. The Warburg impedance is given by the equation (20)<sup>160</sup>:

$$Z_w = \frac{\sigma\sqrt{2}}{j\omega^{0.5}} \quad (20)$$

where  $\sigma$  is the resistance associated with diffusion as a function of concentration of charge carriers and their diffusion coefficients:

$$\sigma = \frac{RT}{(nF)^2 A \sqrt{2}} \left( \frac{1}{C_{ox} D_{ox}^{0.5}} + \frac{1}{C_{red} D_{red}^{0.5}} \right) \quad (21)$$

where R is the gas constant, T is temperature in K, A is the electrode surface area, F is the Faraday constant,  $C_{ox}$  and  $C_{red}$  are the concentration of the redox species,  $D_{ox}$  and  $D_{red}$  are the diffusion coefficients.<sup>160</sup>

Considering the Warburg diffusion in a finite thickness layer, two situations can be distinguished. In one, the contact at the electrode/electrolyte interface can be reflecting (open) i.e. no mass transfer occurs through this interface from the electrolyte to the electrode. The corresponding Warburg impedance is described by the equation (21)<sup>160</sup>:

$$Z_{wo} = \frac{\sigma\sqrt{2}}{(j\omega)^{0.5}} \coth\left[\frac{L}{D^{0.5}} (j\omega)^{0.5}\right] \quad (21)$$

In the other, there is a mass transfer that occurs across the solid/electrolyte interface from the electrolyte to the electrode. The corresponding Warburg impedance is described by the equation (22):

$$Z_{ws} = \frac{\sigma\sqrt{2}}{(j\omega)^{0.5}} \tanh\left[\frac{L}{D^{0.5}} (j\omega)^{0.5}\right] \quad (22)$$

where L is the finite thickness of the diffusion layer and D is the diffusion coefficient of the mobile charge carrier.

Typically quantitative analysis of the impedance data is realized through the fitting procedure on the basis of the proposed electric equivalent circuit using dedicated software, for

example provided by the producer of potentiostat-galvanostat equipment or other research groups like EIS Analyzer.<sup>161</sup> The fitting of the impedance data enables determination of the magnitude of the equivalent series resistance, charge transfer resistance and the Warburg impedance as well the magnitude of other electrical components present in the EQC and required for the analysis of the electrochemical behaviour of the electrode. As an example the EQC of Randles equivalent circuit model of Nyquist plot for electrodes with conductive surface is depicted in **Figure 43**.

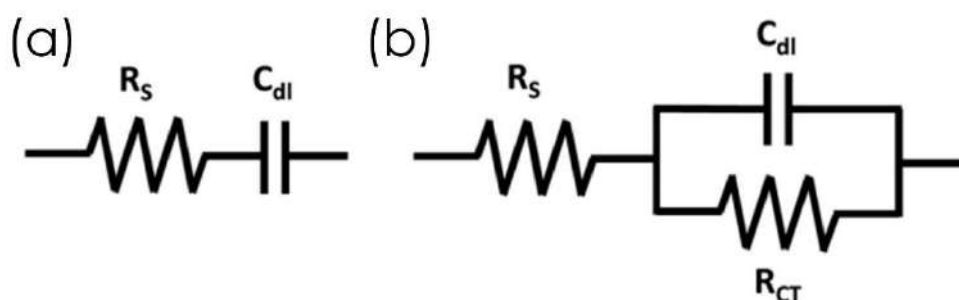


**Figure 43.** The simple models of electric equivalent circuits: (a) without faradic reaction at the electrode/electrolyte interface, (b) with faradic reaction at the electrode/electrolyte interface.

Instead of an ideal capacitor it is common to find a constant phase element (CPE) that is characterized by the equation (23):

$$Z_{CPE} = \frac{1}{(Q(j\omega))^n} \quad (23)$$

where  $\omega$  represents the angular frequency. For  $n = 1$ ,  $Q$  is identified as capacitance.

In this work the fitting of Nyquist plots were done using the EIS Spectrum Analyzer program. The modified Powell algorithm was used with amplitude weighting  $r_a$ :

$$r_a(\omega, P_1 \dots P_M) = r_c^2 / (N - M) \quad (24)$$

where  $N$  is the number of points,  $M$  is the number of parameters,  $\omega$  is the angular frequency,  $P_1 \dots P_M$  are parameters. Parameter  $r_c$  is defined as:

$$r_c^2 = \sum_{i=1}^N \frac{(Z'_i - Z'_{i_{calc}})^2 + (Z''_i - Z''_{i_{calc}})^2}{Z'^2_i + Z'^2_{i_{calc}}} \quad (25)$$



#### 6.6.4 Mott-Schottky analysis

Mott-Schottky analysis is one of the widely used technique for the determination of important parameters of semiconductor, namely the flat-band potential, the donor concentration (n-type semiconductor), or acceptor concentration, (p-type semiconductor). For better understanding the meaning of the flat band potential, it should be related with the Fermi energy. The Fermi energy is one of the features characterizing semiconductors, defined as the highest occupied energy level of a material at absolute zero temperature.<sup>162</sup> When the semiconductor is immersed in the electrolyte, a built-in electric field is generated at the electrode/electrolyte interface. This can result from the charge carrier diffusion between the semiconductor and the electrolyte. The migration of the charge carriers is due to the difference in the work functions of the solid phase (semiconductor) and the liquid phase (electrolyte). The diffusion of the charge carriers at the semiconductor/electrolyte interface occurs until the electrochemical equilibrium between the solid phase and the liquid phase is reached.<sup>163,164</sup> This means that the work function of the electrolyte (i.e., the redox potential of the electrolyte) is equal to the work function of the semiconductor (i.e. the Fermi level).<sup>163,164</sup> The bending of the band edges of the semiconductor takes place in the space charge region due to the built-in electric field. In the case of the n-type semiconductor, electrons migrate from the electrode to the electrolyte, leaving a positive charge in the space charge region. This causes an upward bending of the band edges, whereas for p-type semiconductor, electrons are transferred from the electrolyte to the electrode, thus bending the band edges is present downward. The bending of the band edges can be altered by applying an external bias potential. The required potential that must be applied to the electrode so that no net transfer of charge can occur at the semiconductor/electrolyte interface and, therefore, no band edges bending can occur is defined as flat band potential.<sup>163,164</sup> The effect of varying the applied potential on the band edges of an n-type and p-type semiconductor is depicted in **Figure 44**.

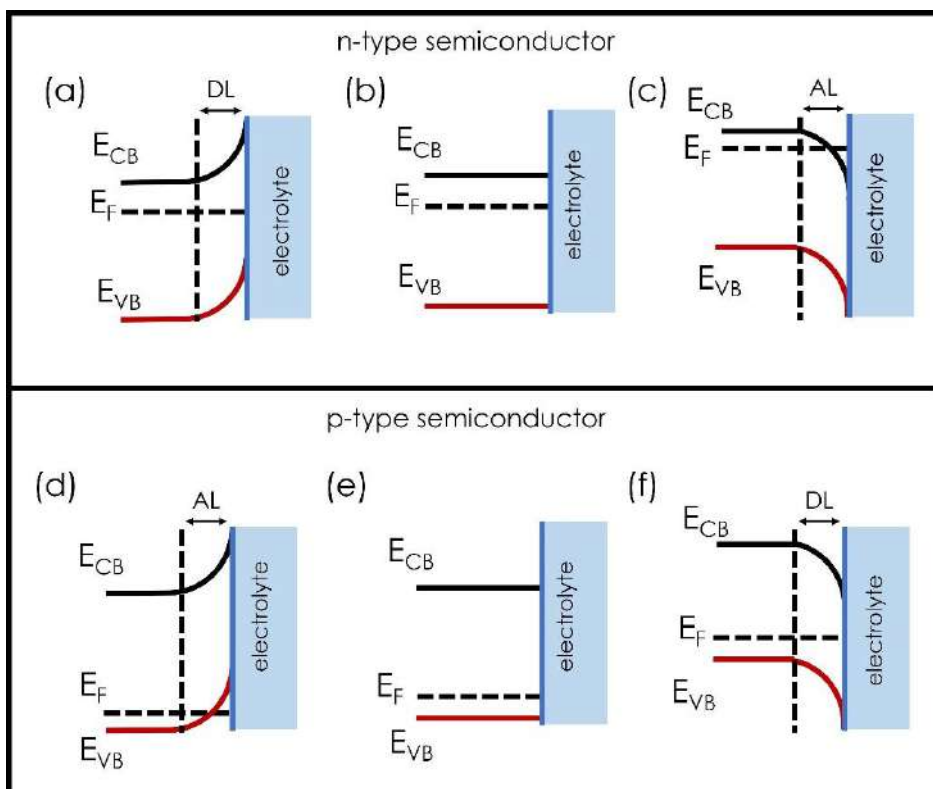


**Figure 44.** Effect of varying the applied potential on the band edges of an n-type semiconductor: (a)  $E > E_{FB}$ , (b)  $E = E_{FB}$ , (c)  $E < E_{FB}$  and for a p-type semiconductor: (d)  $E > E_{FB}$ , (b)  $E = E_{FB}$ , (c)  $E < E_{FB}$ . (DL: depletion layer; AL: accumulation layer).

Since the flat band potential has been defined, its importance in the charge transfer process at the semiconductor/electrode will be now evoked. The discussion will be conducted for the n-type semiconductor, but can be also easily done for the p-type semiconductor using similar explanations as was clearly given by Bott et al.<sup>165</sup>. When a potential is applied to the n-type semiconductor, three different situations that can happen are presented in **Figure 44**. If the applied potential is greater than the flat band potential as presented in **Figure 44 (a)**, the formation of a depletion region occurs at the semiconductor/electrolyte interface. This means that the majority of charge carriers of the n-type semiconductor, i.e. electrons, has been removed from the space charge layer. In consequence, the material will exhibit poor electrical conductivity and the transport of charge carriers at the semiconductor/electrolyte interface will be slow. If the applied potential is equal to the flat band potential i.e. in the situation in **Figure 44(b)**, the semiconductor and the electrolyte are in equilibrium i.e. no charge transfer can occur at the electrode/electrolyte interface. If the applied potential is smaller than the flat band potential, accumulation of electrons occur at the semiconductor/electrolyte interface as

shown in **Figure 44 (c)**. This indicates that more electrons are available to improve the electrical conductivity of the semiconductor. In addition, the charge carrier transfer at the semiconductor/electrolyte interface is faster.

Both the charge carrier density i.e. donor density (for n-type semiconductor) or acceptor density (for p-type semiconductor) and the flat band potential can be determined through Mott-Schottky plot. The Mott-Schottky relation for a n-type semiconductor is given in the equation (26) and for the p-type in the equation (27):

$$C^{-2} = \left(\frac{2}{e\epsilon\epsilon_0 N_D}\right)(V - V_{fb} - \frac{kT}{e}) \quad (26)$$

$$C^{-2} = \left(\frac{2}{e\epsilon\epsilon_0 N_A}\right)(V + V_{fb} - \frac{kT}{e}) \quad (27)$$

where C is the space charge capacitance,  $\epsilon$  is the permittivity of the anatase titania ( $\epsilon = 38$ )<sup>166</sup>,  $\epsilon_0$  ( $8.85 \cdot 10^{-14} \text{ F cm}^{-1}$ ) is the permittivity of free space, e is the electron charge,  $N_D$  and  $N_A$  are the donor and acceptor densities respectively, V is the applied potential,  $V_{fb}$  is the flat band potential, k is the Boltzmann constant, and T is the temperature.<sup>7</sup>

The capacitance for each potential can be then calculated using the equation (28):

$$C = \frac{1}{2\pi f Z''} \quad (28)$$

where f is the frequency of the AC signal, and  $Z''$  is the imaginary part of the impedance. Typically for measurements a relatively high frequency of 1000 Hz is selected. This choice of calculating the capacitance at higher frequency is explained as follows. From a physical point of view, at high frequencies, the electron transport process freezes due to phenomenon known as finite inertia.<sup>167</sup> Thus, the low current detected at high frequencies comes only from the displacement associated with the charge of the geometric capacitance.<sup>167</sup> This implies that at high frequencies, the calculated capacitance approaches a constant value equal to that of the capacitance of geometrical area.<sup>167</sup> By considering the equation (28), the curve  $C^{-2}$  vs. the applied potential is plotted and the flat band potential can be determined as the intersection of the tangent of the linear regions of the curve with the potential axis. An example of the extrapolation of the linear region of the Mott-Schottky plot for semitransparent aligned titania nanotubes grown by anodic oxidation is presented in **Figure 45**.

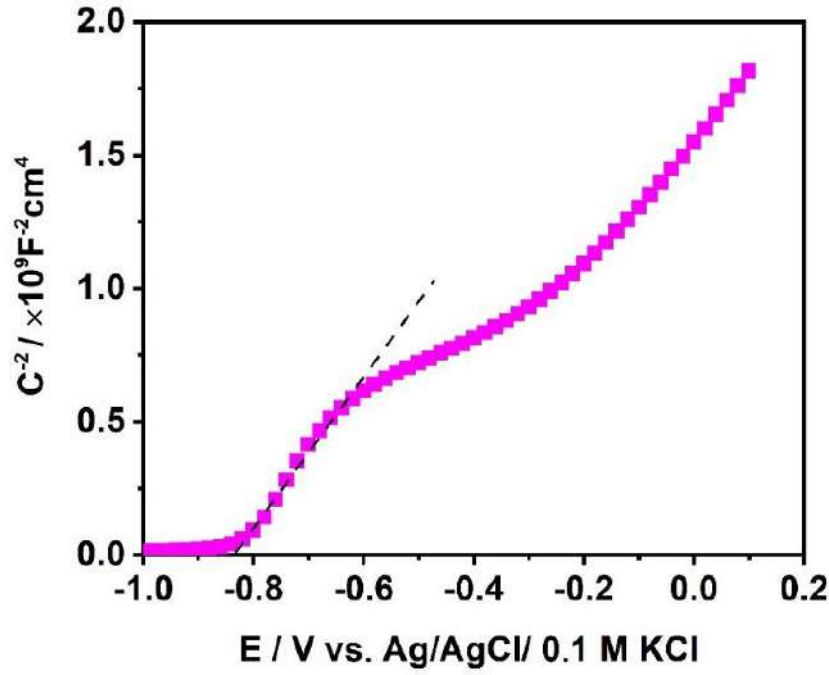


**Figure 45.** Mott-Schottky plot of semitransparent aligned titania nanotubes in 0.5 M Na<sub>2</sub>SO<sub>4</sub>.

The donor density,  $N_D$  is then calculated from the equation (29):<sup>7</sup>

$$N_D = \left( \frac{2}{e\epsilon\epsilon_0} \right) \left( \frac{dE}{dC^2} \right) \quad (29)$$

Another importance of the the flat band potential is it utilization in estimating the edges position of the forbidden band of the semiconductor, i.e. the bottom of the conduction band  $V_{CBM}$  and the top of the valence band  $V_{VBM}$  through the equations (30) and (31):<sup>168</sup>

$$V_{CBM} = V_{fb} + \Delta V - 0.059 \cdot (7 - \text{pH}) \quad (30)$$

$$V_{VBM} = V_{CB} + \frac{E_g}{e} \quad (31)$$

where  $\Delta V = +0.21$  V is the potential of Ag/AgCl pseudoelectrode against normal hydrogen electrode (NHE)<sup>168</sup>,  $e$  is the electron charge, and  $E_g$  the bandgap of the materials.

In this work Mott-Schottky plots were obtained by recording the impedance data ( $Z'$ ,  $-Z''$ ) of the samples in 0.5 M Na<sub>2</sub>SO<sub>4</sub> at a constant frequency of 1 kHz, in the potential range from +0.1 to -1.2 V vs Ag/ AgCl/0.1 M KCl.

### 6.6.5 Intensity-modulated photocurrent spectroscopy (IMPS)

Intensity-modulated photocurrent spectroscopy technique is used to study the charge carriers dynamic in semiconductor electrodes exposed to illumination of given wavelength. In

this technique, a small ac potential perturbation is superimposed onto the DC potential which is applied to the photoelectrode.<sup>169</sup> Then, the electrode is illuminated by a light of modulated intensity. The perturbed photocurrent response due to the modulated incident light intensity is recorded, and plotted as a function of the frequency of the incident light resulting in the formation of IMPS spectrum. Similarly to the total impedance  $Z$  in electrochemical impedance spectroscopy, in the IMPS method, transfer function  $H$  is defined from the resulting photocurrent response. This function stays as the ratio of the light modulation intensity to the recorded alternating photocurrent density.

The light intensity of the incident stimulus  $L(t)$  is described as:

$$L(t) = L + \Delta L \sin(2\pi ft) \quad (32)$$

where  $L$  is the steady-state light intensity (in photons  $\text{cm}^{-2} \text{s}^{-1}$ ),  $\Delta L$  the light modulation amplitude and  $f$  the frequency of the modulated light.<sup>170</sup> The current density response  $J_{ph}(t)$  is in the form:

$$J_{ph}(t) = J + \Delta J \sin(2\pi ft + \varphi) \quad (33)$$

where  $J$  is the response of the steady-state photocurrent density,  $\Delta J$  the amplitude of the alternating photocurrent density and  $\varphi$  the phase difference between the modulated light and the alternating current density. Hence, the transfer function of the system is given by the equation (34)<sup>171</sup>:

$$H = \frac{\Delta J \sin(2\pi ft + \varphi)}{\Delta L \sin(2\pi ft)} \quad (34)$$

However, in the literature, it is common to discuss IMPS results in terms of current density response only instead of transfer function, because according to equation (34) the two quantities are proportional.

The transfer function depends on the frequency of the modulated light. In general, the spectra obtained at the high-frequency modulations are associated with the faster processes (i.e. charge separation and surface recombination processes), whereas the information regarding the slower processes can be found at the low-frequency modulations.<sup>172</sup> At the frequency minimum of the spectrum, the electron - hole separation process predominates over the recombination process. Therefore, at this frequency the average charge transfer time, also known as charge transit time, can be calculated using following equation:<sup>173</sup>

$$\tau = \frac{1}{2\pi f_{min}} \quad (35)$$

The low-frequency loop formed in the quadrant (a) for the p-type photoelectrode (or in the quadrant (e) for the n-type photoelectrode) is associated with the competition between the charge transfer and surface recombination processes (**Figure 46**).<sup>172</sup> Indeed, this loop disappears when the charge transfer rate is much higher than that of surface recombination. The high frequency loops recorded in quadrants (c) and (d) in **Figure 46** (for a p-type photoelectrode), and in the in quadrants (g) and (h) (for an n-type photoelectrode) are related to the time constant of the cell.<sup>172</sup>

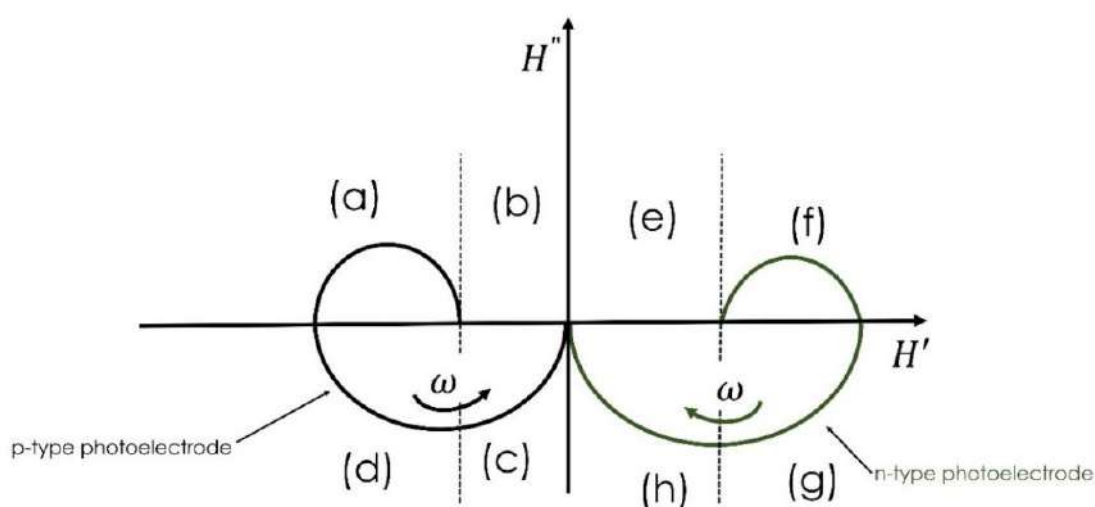


**Figure 46.** The examples of IMPS spectra for a p-type and n-type photoelectrode.

I performed IMPS measurements by using electrochemical spectrometer (Instytut Fotonowy, Poland) connected to a 373 nm LED and a potentiostat. The IMPS spectra were recorded in the light frequency range from 1000 to 0.1 Hz.

#### 6.6.6 Incident-photon-to-current efficiency (IPCE)

Incident photon-to-electron conversion measurements were carried out to track the efficiency of the semitransparent layer depending on the absorbed photon energy corresponding to the particular wavelength reaching the electrode surface. As depicted in **Figure 47** the main components of the IPCE setup includes xenon lamp, lamp controller, optical fiber, monochromator, filter wheel, electrochemical cell and potentiostat. Before the measurement, the light source was calibrated using the silicon photodiode.

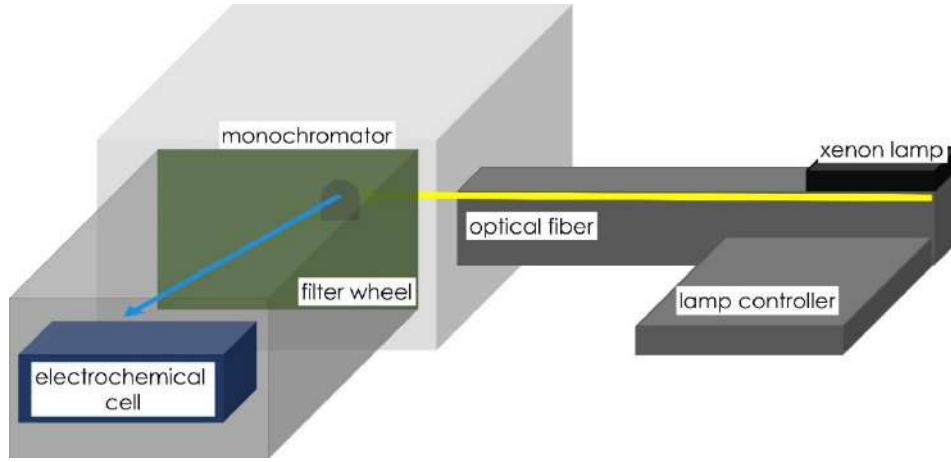


**Figure 47.** Schematic of the IPCE photoelectric spectrometer setup.

During the measurement, the monochromator is responsible for the illumination of the photoelectrode with a single wavelength. For a given wavelength  $\lambda$ , incident photons whose energy is greater than the bandgap of the semiconductor result in the generation of electron-hole pairs. Moreover, not all photogenerated electrons will be collected as the current due to the recombination process occurring in active layer and at the various interfaces. Thus, IPCE ( $\lambda$ ) is expressed as the ratio of the number of effective electrons excited ( $\Delta N$ ) by the photons (and collected in the circuit) to the number of incident photons ( $\Delta P$ ) of the incident light source<sup>174</sup>:

$$\text{IPCE}(\lambda) = \frac{\Delta N}{\Delta P} \quad (36)$$

It can be as also given as:

$$\text{IPCE}(\lambda) = \frac{j}{P} \hbar \omega \quad (37)$$

where  $j$  is the photocurrent density,  $P$  is light intensity and  $\hbar \omega$  is photon energy.

As shown in **Figure 48**, a 3D maps of IPCE can be recorded as well by varying both the wavelength and potential of working electrode.

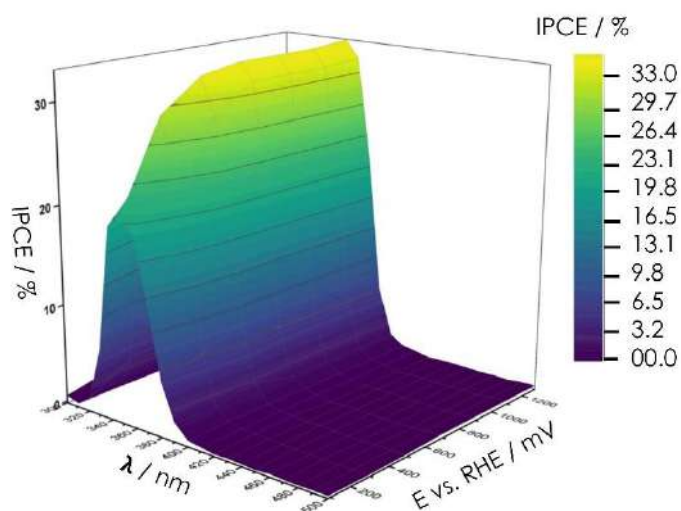


**Figure 48.** IPCE 3D maps recorded for anodic titania nanotubes grown out of Ti foil decorated by Au nanowires within the wavelength range from 300 nm to 500 nm, and varied constant potentials in the range from +0.25 to +1.65 V vs. RHE in a 0.1 M Na<sub>2</sub>SO<sub>4</sub> solution.

RHE: reversible hydrogen electrode. Reproduced from<sup>175</sup>, under CC BY 3 license.

In this work, I was responsible for recording of 3D IPCE maps using for this purpose a photoelectric spectrometer (Instytut Fotonowy, Poland) equipped with quartz window and the set of three electrodes.

#### 6.6.7 Photoluminescence (PL) measurements

Photoluminescence (PL) measurement is another characterization technique for evaluating the light emission of the material upon its excitation. The gathered data can provide information about the rate of electron-hole recombination within the active layer.<sup>176</sup> The system used herein for PL measurements was composed of a SHAMROCK spectrograph - SR-303I-A (Andor Technology), a 450 mW LED excitation light source ( $\lambda = 365$  nm), an ICCD camera for recording fluorescence spectra and an optical filter, FGUV-11 (Thorlabs) with a GG 400 (Schott AG) to eliminate unwanted lighting modes. During the measurement, the 450 mW LED illuminates the material with light of 365 nm wavelength to excite the electrons to higher energy levels. This particular wavelength was selected taking into account the bandgap of titania material (anatase TiO<sub>2</sub>, ca. 3.2 eV) to excite the electron from the valence band to the upper energy level. Then, those photoexcited electrons will be quenched to lower energy levels and recombine with holes. The transition from higher to lower energy levels is accompanied by radiative emission. Different bands can be observed during the radiative electron-hole recombination.<sup>177</sup> For example the red and green bands emission for titania materials have been



already reported.<sup>177</sup> The red band results from the radiative recombination of trapped electrons present on the  $\text{Ti}^{3+}$  or  $\text{Ti}^{4+}$  sites (below the conduction bands) with holes in the valance band ( $h_{\text{VB}}^+ + e_{\text{trapped}}^- \rightarrow h\nu$ ).<sup>178</sup> Whereas the green band is associated to the radiative recombination of electrons with trapped holes ( $e_{\text{CB}}^- + h_{\text{trapped}}^+ \rightarrow h\nu$ ).<sup>178</sup> **Figure 49** shows an example of PL spectra for  $\text{TiO}_2$  material. The illustration of the setup dedicated for the PL measurement is presented in **Figure 50**.

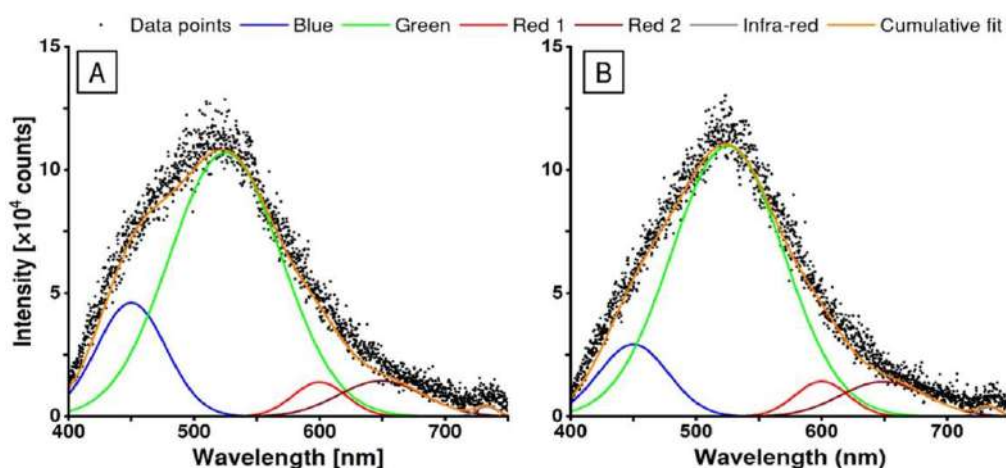


**Figure 49.** Example of deconvoluted photoluminescence spectra for (a) bare spaced  $\text{TiO}_2$  nanotubes, (b) spaced  $\text{TiO}_2$  nanotubes treated with 355 nm laser with  $30 \text{ mJcm}^{-2}$  fluence.

(Reproduced<sup>179</sup> from, under CC BY 4 license.)

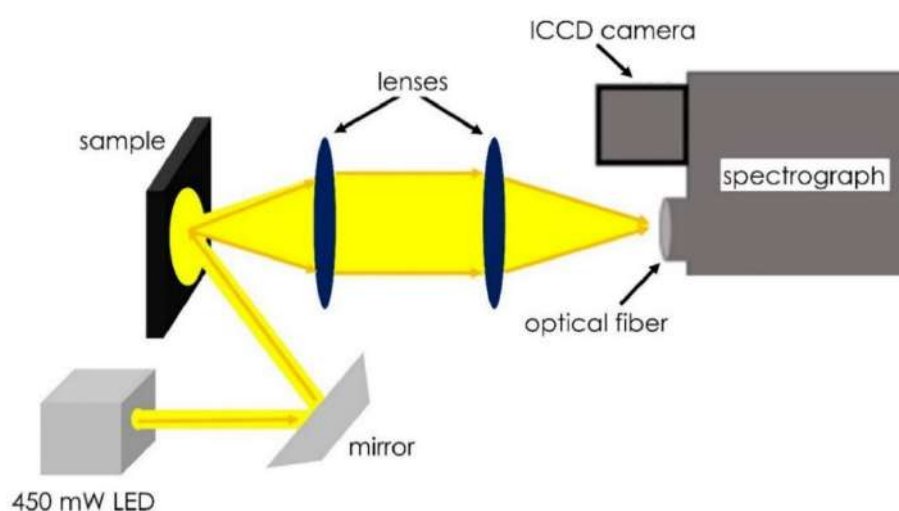


**Figure 50.** Schematic of a PL measurement system.

## 7 Results

The main results gathered during this PhD studies are described in subsections corresponding to the particular articles that I already published. In each part I described the most important information, namely fabrication procedure of the material, its morphology, structure, as well as optical properties, electrochemical and photoelectrochemical performance. I also present here some unpublished data. Despite they were not included in papers in JCR journals, they were crucial for me to undertake the next steps in my scientific path. I also would like to underline that my thesis is a significant part of the realisation of the research plan of CEUS-UNISONO project, n° 2020/02/Y/ST8/00030 supported financially by NCN.

The articles will be labelled A followed by a number for example. A1, A2, A3, A4 and A5.

**A1. Kouao, D.-S.; Grochowska, K.; Siuzdak, K. The Anodization of Thin Titania Layers as a Facile Process towards Semitransparent and Ordered Electrode Material. *Nanomaterials* **2022**, 12 (7), 1131. <https://doi.org/10.3390/nano12071131>. IF = 5.30 / 100 points.**

**A2. Kouao, D.-S.; Hanuš, J.; Kylián, O.; Simerova, R.; Sezemsky, P.; Stranak, V.; Grochowska, K.; Siuzdak, K. Double-Sided Semitransparent Titania Photoelectrode with Enhanced Light Harvesting. *Renewable and Sustainable Energy Reviews* **2024**, 197, 114390. <https://doi.org/10.1016/j.rser.2024.114390>. IF = 16.79 / 200 points.**

**A3. Hanková, A.; Kuzminova, A.; Hanuš, J.; Sezemsky, P.; Simerova, R.; Stranak, V.; Grochowska, K.; Kouao, D.-S.; Siuzdak, K.; Procházka, M.; Košutová, T.; Kylián, O. TiO<sub>2</sub>/Ag Nanostructured Coatings as Recyclable Platforms for Surface-Enhanced Raman Scattering Detection. *Surfaces and Interfaces* **2022**, 35, 102441. <https://doi.org/10.1016/j.surfin.2022.102441>. IF = 6.20 / 70 points.**

**A4. Kouao, D.-S.; Hanuš, J.; Kylián, O.; Simerova, R.; Sezemsky, P.; Stranak, V.; Grochowska, K.; Siuzdak, K. Photoelectrochemical and Electrochemical Activity of Anodic Semitransparent Aligned and Spaced Titania Nanotubes Formed out of Titanium–Silver Alloys. *ACS Applied Nano Materials*. **2024**, 7 (2), 1548–1561. <https://doi.org/10.1021/acsanm.3c04186>. IF = 5.90 / 20 points.**

**A5. Kouao, D.-S.; Grochowska, K.; Stranak, V.; Sezemsky, P.; Gumieniak, J.; Kramek, A.; Karczewski, J.; Coy, E.; Hanus, J.; Kylian, O.; Sawczak, M.; Siuzdak, K. Laser-Treated MXene as an Electrochemical Agent to Boost Properties of Semitransparent**

**Photoelectrode Based on Titania Nanotubes.** ACS Nano **2024**, 18 (14), 10165–10183.  
<https://doi.org/10.1021/acsnano.4c00092>. **IF = 17.1 / 200 points.**

All journals in which listed articles were published are attributed to the mechanical engineering discipline.

**Total sum of IF: 51.29**

**Total sum of point: 590**

### **Structure of the results section**

The results section is composed of five subsections structured as follows:

The first subsection presents the results obtained during the optimization of the anodization process to grow the aligned and the spaced TNT architectures out of the deposited Ti films onto ITO-glass. First, a brief overview of the review article A1 is provided to show the gaps in existing studies in the explored area of semitransparent titania based electrodes. Then, taking into account comments and advices from other reported works, the anodization parameters such as water content in the electrolyte and the applied potential were tuned to obtain crack-free aligned and spaced TNT layers out of the sputtered Ti film. The different steps of the optimization process are described and explained.

After elaborating the optimal anodization conditions resulting in aligned and spaced TNT out of the deposited Ti film onto one side of the planar substrate, the next procedure was optimized, resulting in growth of the tubular layer on the two sides of the planar substrate and on the optical fiber substrate. The physicochemical properties together with the photoelectrochemical performance of the as-prepared double-sided materials are discussed in the second subsection. In this section one can find the description of method resulting in the aligned nanotubes onto the surface of optical fiber. Then such substrate was used by the Prof. M. Śmietana research group from Warsaw University of Technology for opto-electrochemical diagnostics. Owing to the common realisation of CEUS-UNISONO project, herein I show some promising results concerning application of the nanostructured optical fiber for the purpose of label-free sensing.

In general, as has been already underlined in the introduction, the photoactivity of the bare titania layer is relatively low, limited mainly to UV region. Therefore, the functionalization

of the formed nanotubes layer is required to change the electrochemical and the photoelectrochemical activities of the samples. In this regard, in the third subsection I discussed the feasibility to fabricate semitransparent photoelectrodes consisting of aligned and spaced nanotubes obtained out of titanium-silver alloy i.e. TiAg film with different Ag content. Investigations on the electrochemical and photoelectrochemical activities of the semitransparent doped titania layers were carried out as well.

In the fourth subsection, silver nanoislands sputtered onto aligned titania nanotubes (anodically developed onto ITO-glass) acting as sensing layers were discussed. Investigations of the fabricated semitransparent nanotubular/Ag substrate as a potential sensor towards surface-enhanced Raman scattering (SERS) detection of organic pollutant i.e. methylene blue dye (MB) was carried out. To understand the influence of titania morphology onto the SERS enhancement with the use of  $\text{TiO}_2/\text{Ag}$ , two other substrates, namely the planar  $\text{TiO}_2/\text{Ag}$  substrate and the nanoparticle-based  $\text{TiO}_2/\text{Ag}$  substrate were fabricated and their performance towards SERS based detection of MB was investigated as well. The findings of this study are discussed in the fourth subsection. The experiments including SERS were conducted by partner from Charles University in Prague, the group led by doc. RNDr. Ondřej Kylián, Ph.D, also within the cooperation established for the realization of CEUS-UNISONO project 2020/02/Y/ST8/00030.

The fifth section presents the results gathered on the fabrication of a noble metal-free heterostructure material i.e.  $\text{TiO}_2/\text{Ti}_3\text{C}_2\text{T}_x$  obtained by laser ablation method. The feasibility to use for the first time such a heterostructure as a decorating agent for the modification of the semitransparent tubular layer is also investigated. Herein, details on the physicochemical characterization of the laser synthesized  $\text{TiO}_2/\text{Ti}_3\text{C}_2\text{T}_x$  are presented. Among others, major achievements including the photon harvesting properties of the nanotubular titania layer functionalized with  $\text{TiO}_2/\text{Ti}_3\text{C}_2\text{T}_x$  are discussed.

## **7.1 Fabrication of semitransparent aligned and spaced titania nanotubes**

### **Brief overview of the article A1**

#### *Introduction*

The solar conversion efficiency of the nanostructure composed of titania tubular layer is sensitive to the nanotube dimensions, i.e. length, wall thickness, pore diameter. Unlike the sol-gel or the hydrothermal methods, in which the final product is in the form of powder composed of randomly distributed hierarchical tubes exhibiting multimodal lengths (**Figure 51**),<sup>180</sup> the anodic oxidation offers the possibility of controlling both the dimensions and the distribution of the nanotubes already on the stable substrate.

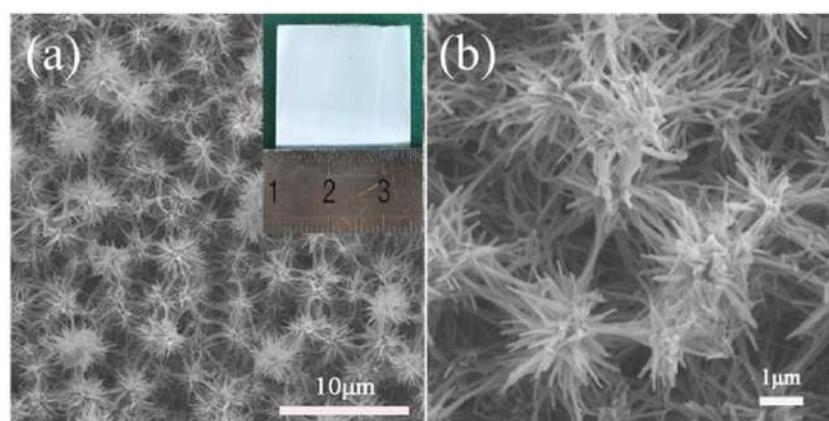


**Figure 51.** Titania nanotubes obtained by hydrothermal method.  
(Reproduced with the permission from reference<sup>180</sup>).

In this regard, one can find in the literature many approaches targeted to the optimization of light conversion efficiency, simply by adjusting the geometry of the tubes (e.g. length and diameter), where light can be trapped. It has even been suggested that the photoconversion efficiency of titania nanotube-based photoanodes increases with the tube length.<sup>181</sup> However, Varghese et al.<sup>21</sup> achieved a photoconversion efficiency of only 7 % with a photoanode based on bare nanotube arrays with the length of 17.6  $\mu\text{m}$ , above which the photoconversion efficiency drops despite the tube length increases. Similarly, Beranek et al.<sup>181</sup> reported a photoconversion efficiency of 6 % for bare nanotubes with a length of 9  $\mu\text{m}$ . They also observed that the conversion efficiency drops drastically for photoanodes with a tube length greater than 9  $\mu\text{m}$ . Therefore, it was not possible to increase the conversion efficiency of the photoanode above 7 % simply by adjusting the tube dimension of the bare photoactive layer. The reason is that the photogenerated electron can be collected efficiently if its diffusion length is greater than the tube length.<sup>15</sup> With increasing tube length, photogenerated electrons must travel for a longer distance to be collected by the current collector.<sup>181,182</sup> This increases the rate of electron-hole recombination within this tubular path. This very short discussion demonstrates

that no significant improvement in the photoactivity of the semitransparent tubular layer can be expected simply by tuning the nanotubes geometry.

Consequently, the first stage of this work was not intended to grow nanotubes with the specific dimensions onto the semitransparent substrate, but to elaborate the procedure towards formation of stable ordered layer with high translucency. In addition, one of the main requirements for the application of the tubular layer in label-free sensing is a smooth and crack-free layer with well-open pores. Therefore, the first objective of the experimental part in my work was to achieve highly ordered crack-free aligned and spaced TNT layers by optimizing the anodization conditions. The set of the anodization conditions are presented and discussed.

*Preliminary unpublished results on synthesis of aligned nanotubes out of Ti film deposited onto ITO-glass*

For the elaboration of the optimized procedure resulting in fabrication of the aligned titania nanotubes the anodization is carried out in ethylene glycol (GE) based electrolyte. Among various anodization parameters, the water content and the applied potential were reported to be the most influencing parameters that substantially affect the tubular morphology<sup>183</sup>. In this work, the water content in the electrolyte is varied from 2 vol% to 25 vol%, and the applied potential is changed between 40 V and 60 V. The anodization process was stopped when the substrate being initially opaque turns transparent. This is the first, visual indication that the transformation of the metallic Ti film into oxide layer occurs. The example of the set of the anodization conditions that I tested are presented in **Table 4**.

**Table 4.** The set of anodization conditions used for the optimisation towards formation of the semitransparent aligned titania nanotube architecture (a: aligned).

sample label	temperature / °C	potential / V	time / s	electrolyte composition			
				[NH <sub>4</sub> F] / M	[H <sub>3</sub> PO <sub>4</sub> ] / M	vol % H <sub>2</sub> O	vol % GE
a-TNT-1	23	40	180	0.27	1	2	98
a-TNT-2	23	50	180	0.27	1	2	98
a-TNT-3	23	60	163	0.27	1	2	98
a-TNT-4	23	40	180	0.27	1	5	95
a-TNT-5	23	50	180	0.27	1	5	95
a-TNT-6	23	60	157	0.27	1	5	95

a-TNT-7	23	40	180	0.27	1	10	90
a-TNT-8	23	50	138	0.27	1	10	90
a-TNT-9	23	60	54	0.27	1	10	90
a-TNT-10	23	40	178	0.27	1	15	85
a-TNT-11	23	50	116	0.27	1	15	85
a-TNT-12	23	60	66	0.27	1	15	85
a-TNT-13	23	40	102	0.27	1	20	80
a-TNT-14	23	40	88	0.27	1	25	75

The inspection of the morphologies was carried out by examining the tubular layer using scanning electron microscopy. **Figure 52** shows the SEM images of the anodized substrates at relatively low water content i.e. 2 vol% and 5 vol%.

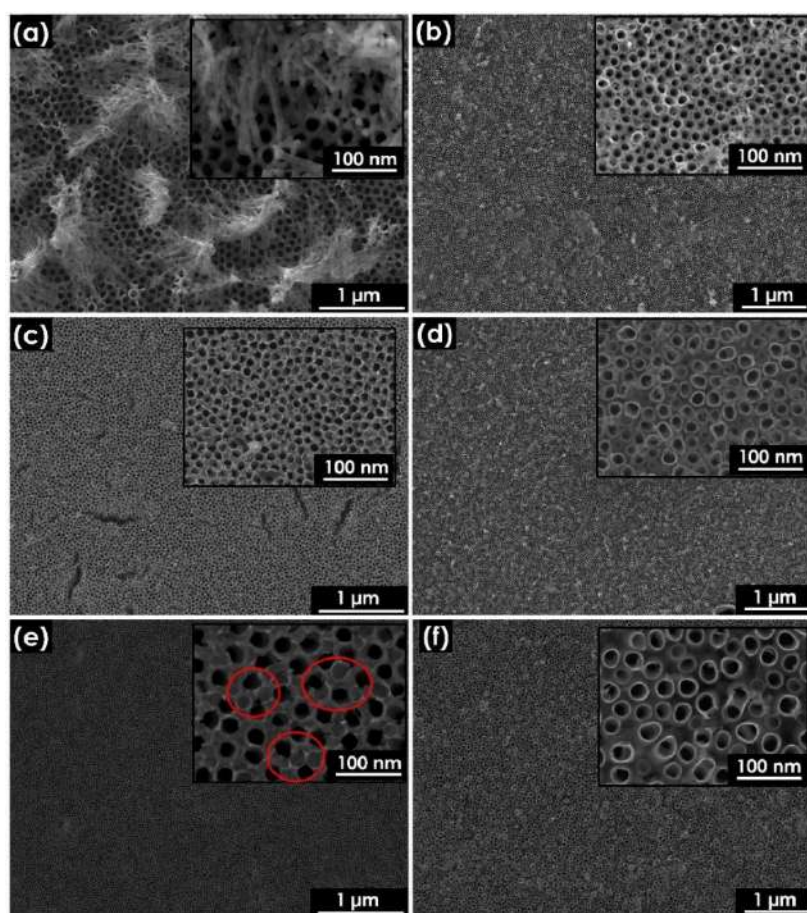


**Figure 52.** SEM images of titania layer (inset: corresponding high resolution images of the prepared materials): (a), (c) and (e)  $\text{TiO}_2$  layers anodized in EG electrolyte containing 2 vol% of water content at the voltage of (a) 40 V, (c) at 50 V, (e) 60 V (some closed end pore are

shown in the red circles see in insert ). In the case of (b), (d) and (f) titanium layers were anodized in EG bath containing 5 vol% of water content at (b) 40 V, (d) at 50 V, (f) 60 V.

Although the SEM image of the sample anodized at 40 V for 2 vol% of water content in the electrolyte shows well visible nanopores, abundant amount of nanograss covers the top surface of the sample (**Figure 52 (a)**). Nanograss is frequently defined in literature as a mixture of collapsed thin tubes and nanoparticles, aggregated on top of the tubular layer.<sup>184</sup> The collapsed thin tubes are visible in the inset in **Figure 52 (a)**. The presence of nanograss on top of the anodized tubular layer at relatively low water content (i.e., 2 vol% or 3 vol%) at 40 V was also reported by Broens et al.<sup>185</sup>, Naduvath et al.<sup>186</sup>, Seçkin et al.<sup>187</sup> and Fraoucene et al.<sup>184</sup> The generation of such grass-like nanostructures results from the high chemical dissolution of the oxide barrier layer due to the high viscosity of the organic solvent based electrolyte.<sup>184–186</sup> Such morphology is not appropriate from the point of view of electrochemical applications, namely as an electrode material, since the nanograss blocks the accessibility of ions inside the nanopores. Two different approaches can be found in literature with some advice how to remove nanograss stacked over the tubular layer. One of them concerns keeping the water content at 2 vol% and increase the applied voltage up to 60 V.<sup>184</sup> **Figure 52 (c)** and **Figure 52 (e)** show the morphologies of the anodized samples at 50 V and 60 V for 2 vol% of H<sub>2</sub>O. The increase in the applied potential in this work to 50 V significantly reduced the formation of those grass-like nanostructures on the top surface of the sample (**Figure 52 (c)**). This removal of the nanograss is explained by the reduction in the high viscosity of the organic solvent (i.e., ethylene glycol) with increasing applied potential, which facilitates the diffusion of ions present in the electrolyte during the anodization, inhibiting the formation of nanograss.<sup>184</sup> The further increase in the applied potential to 60 V leads to a smoother surface. However, the high resolution SEM image shown in **Figure 52 (e)** (see the inset) indicates that still several pores are closed on the top of the tubular nanostructure (shown in the red circles). The other approach refers to the reduction of the viscosity of the organic electrolyte by raising the water content in the electrolyte.<sup>185,186</sup> Accordingly, I increased the water content in the electrolyte to 5 vol%. **Figure 52 (b), (d) and (f)** show that all titanium layers anodized in the electrolyte with 5 vol% of water content exhibit crack-free aligned nanotubes layers regardless the applied potential. The sample anodized at 60 V exhibits a smoother surface compared to those obtained at 40 V and 50 V.



To further investigate the influence of the water content in the electrolyte on the tubular morphology, the water content was increased up to 15 vol%. The surface morphologies of the samples obtained in such conditions are presented in **Figure 53**. All titanium films anodized in the electrolyte with 10 vol% of water exhibit well-ordered and crack-free layers regardless to applied potential (**Figure 53. (a), (c) and (d)**).

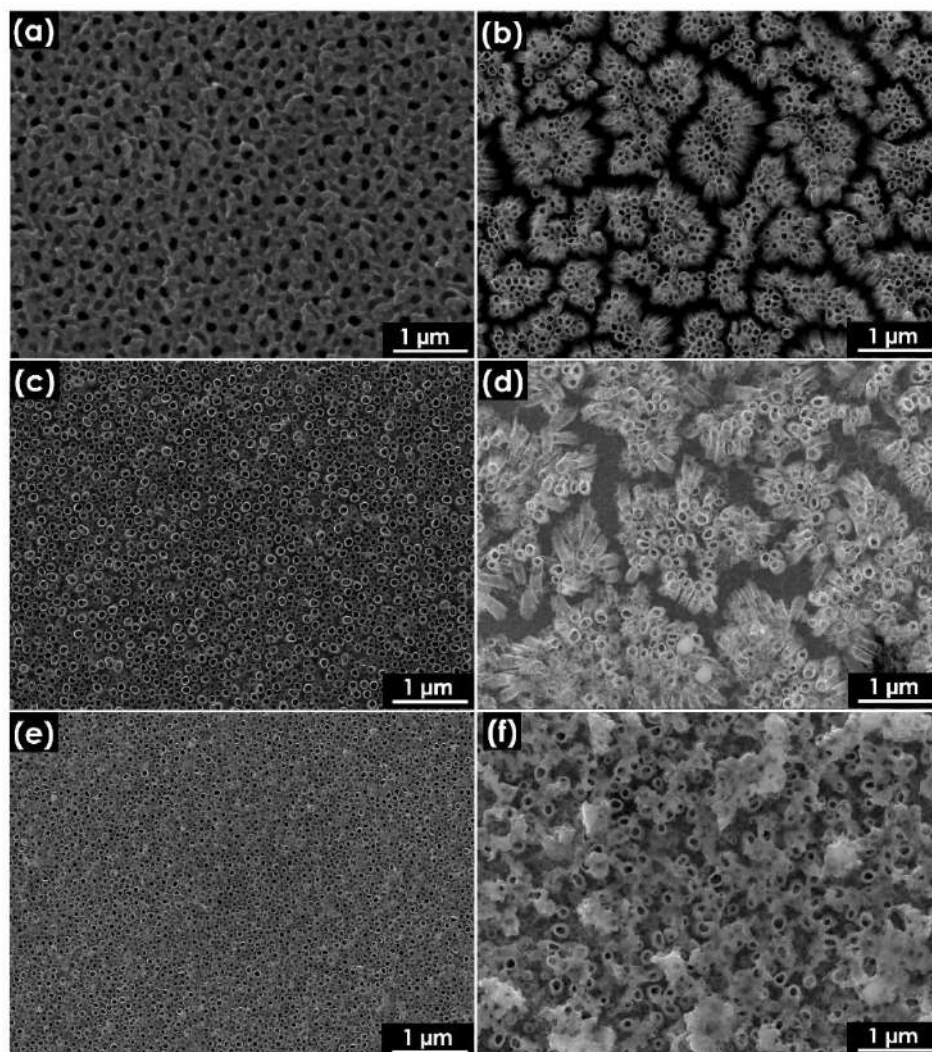


**Figure 53.** SEM images of titania layer (Inset: high resolution images of the prepared materials). (a), (c) and (e)  $\text{TiO}_2$  layers anodized in EG electrolyte containing 10 vol% of water content at (a) 40 V, (c) at 50 V, (e) 60 V. In the case of (b), (d) and (f) Ti layers were anodized in EG bath containing 15 vol% of water content at (b) 40 V, (d) at 50 V, (f) 60 V.

However, by increasing the water content in the electrolyte to 15 vol%, the tubular morphology loses its close-packed, arranged architecture. The nanotubes are aggregated then into several blocks delimited by large tubular oxide layer fractures, leading to an irregular

architecture. In the case of further increase in the water content to 20 vol% the tubular layer looks damaged (**Figure 54(a)**). No nanotube can be detected for 25 vol% of water content (**Figure 54(b)**).

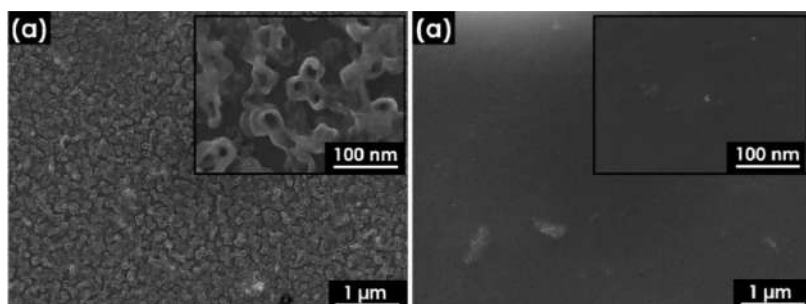


**Figure 54.** SEM images of anodized Ti films. (Inset: corresponding high resolution images of the prepared materials) at 40 V. In the case of (a) 20 vol% and (b) 25 vol% of water content in the electrolyte was present.

Therefore, to achieve well-ordered tubular layer out of the titanium films deposited onto ITO substrate, it was essential to keep the water content between 5 vol% and 10 vol%. **Figure 55** shows the cross section images of the anodized samples at 60 V, for different water content in the electrolyte and the corresponding values of the geometrical features are given in **Table 5**.

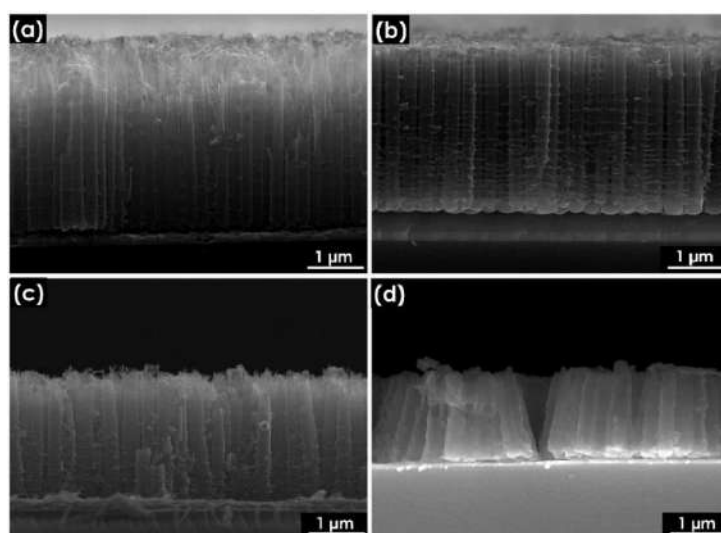


**Figure 55.** Cross section SEM images of anodized Ti films at 60 V in EG electrolyte containing (a) 2 vol%, (b) 5 vol%, (c) 10 vol% and (d) 15 vol% water content.

**Table 5.** The values of the main geometrical parametres (averaged inner diameters and lengths) of obtained titania nanotubes at 60 V for 2 vol % (a-TNT-3), 5 vol% (a-TNT-6), 10 vol% (a-TNT-9) and 15 vol % (a-TNT-12) water content in the electrolyte.

sample label	average length / $\mu\text{m}$	average inner diameter / nm
a-TNT-3	$2.4 \pm 0.03$	$91 \pm 10$
a-TNT-6	$2.1 \pm 0.04$	$120 \pm 19$
a-TNT-9	$1.8 \pm 0.05$	$187 \pm 30$
a-TNT-12	$1.2 \pm 0.07$	$173 \pm 35$

*Synthesis of spaced nanotubes out of Ti film deposited onto ITO-glass*

The anodization leading to the formation of spaced nanotubes was carried out in diethylene glycol (DGE) based electrolyte. The parameters such as the applied potential, the water content in the electrolyte and the concentration of ammonium fluoride were optimized in order to reach the nanotubular structure well distributed over the entire anodized area. One of the exemplary set of anodization conditions that I applied during the optimization of the whole process is given in **Table 6**.

**Table 6.** Anodization conditions for the spaced nanotube architecture (s: spaced).

sample label	temperature / °C	potential / V	time / s	electrolyte composition			
				[NH <sub>4</sub> F] / M	[HF] / M	vol % H <sub>2</sub> O	vol % DGE
s-TNT-1	40	20	60	0.15	1	10	90
s-TNT-2	40	30	52	0.15	1	10	90
s-TNT-3	40	40	43	0.15	1	10	90
s-TNT-4	40	50	35	0.15	1	10	90
s-TNT-5	40	50	41	0.15	0.8	10	90
s-TNT-6	40	20	50	0.15	0.5	7	93
s-TNT-7	40	30	42	0.15	0.5	7	93
s-TNT-8	40	40	44	0.15	0.5	7	93
s-TNT-9	40	50	38	0.15	0.5	7	93

In the first attempt, the water content in the electrolyte was fixed at 10 vol%, and the applied potential was increased from 20 V to 50 V. However, only porous structures were obtained as shown in **Figure 56**. Several collapsed nanotubes are visible on the surface of the sample anodized at 40 V (**Figure 56.(c)**). This indicates that the applied anodization condition is relatively severe. In another attempt the fluorine ions content was reduced by changing the concentration of HF from 1 M to 0.8 M.

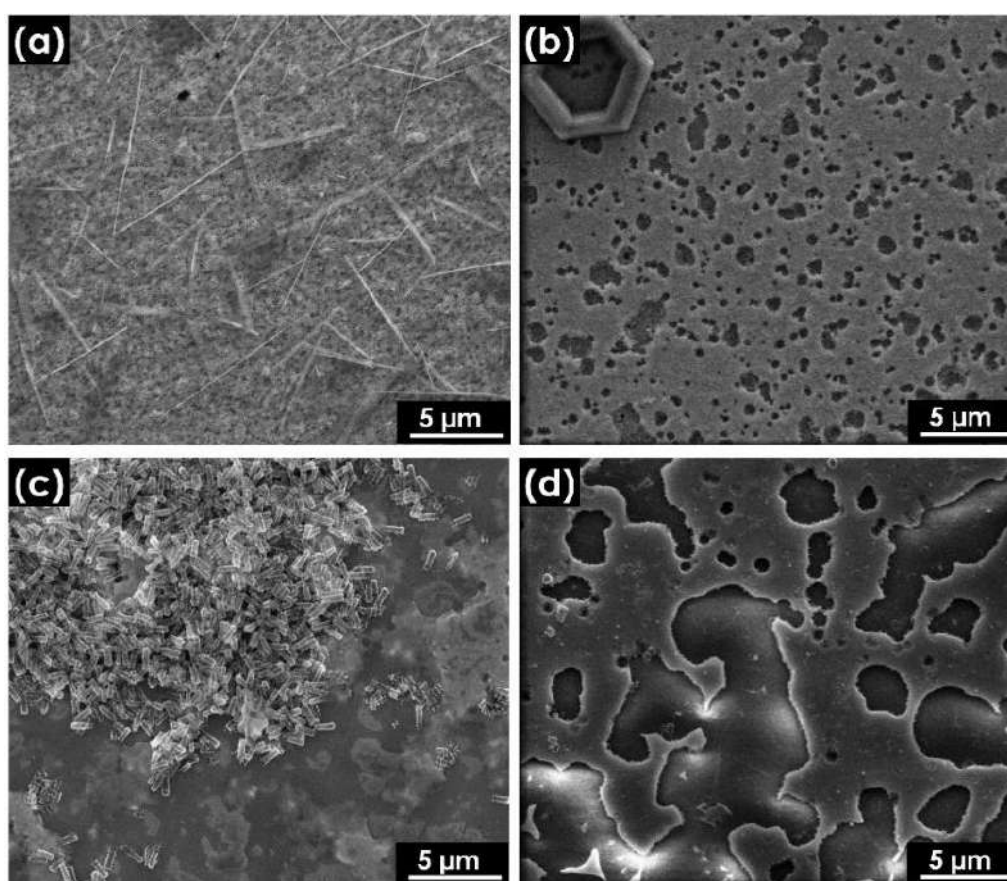


**Figure 56.** SEM top images of anodized Ti films when 10 vol% water content was present in the electrolyte at (a) 20 V, (b) 30 V, (c) 40 V, (d) 50 V.

**Figure 57** shows the SEM image of the material that was obtained with the reduced of the HF concentration to 0.8 M. The presence of the tubular forms (**Figure 57**) made some promise that the efforts were carried out in the proper direction. Although the surface of the sample is not uniform and also porous irregular nanostructures are detected, well-developed nanotubes can be distinguished. The fluorine content was further reduced by changing the concentration of HF from 0.8 M even to 0.5 M.

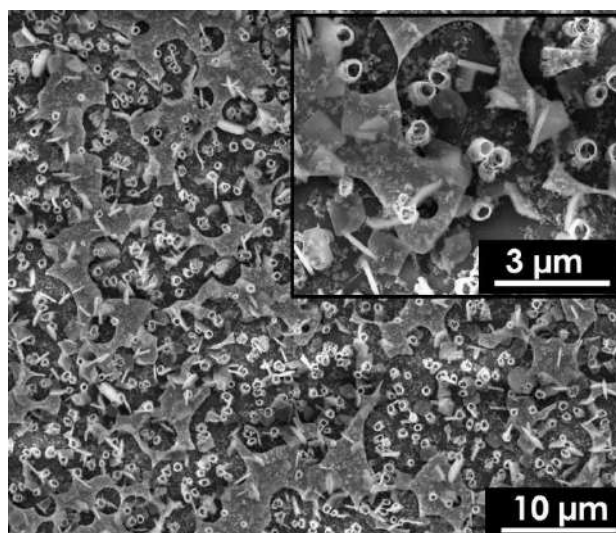


**Figure 57.** SEM top images of anodized Ti films in the electrolyte containing 10 vol% water and 0.8 M HF and at the applied voltage of 50 V.

The water content was also slightly reduced to 7 vol%, and the applied potential was, as in the previous case, increased from 20 V to 50 V. The morphologies of the series of samples are shown in **Figure 58**.

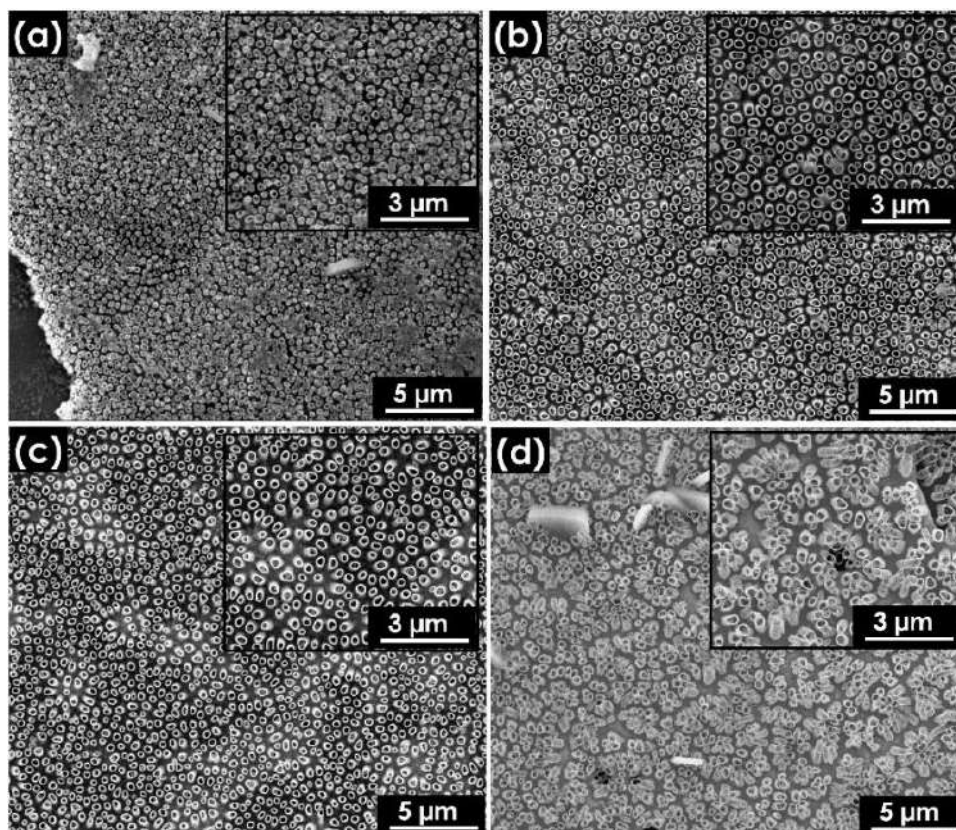


**Figure 58.** SEM images of the top of tubular layer obtained in the electrolyte containing 7 vol% water and 0.5 M HF at the voltage of (a) 20 V, (b) 30 V, (c) 40 V and (d) 50 V.

Well-ordered spaced nanotubes were grown out of Ti film deposited onto ITO-glass when the process was carried out in the electrolyte with 7 vol% water content and 0.5 M HF at the potential below 50 V. The confirmation of the hierarchical arrangements is presented in cross section image of the sample anodized at 40 V in **Figure 59**. The obtained nanotubes have an average length of  $906 \pm 42$  nm with an inner diameter of  $129 \pm 13$  nm.

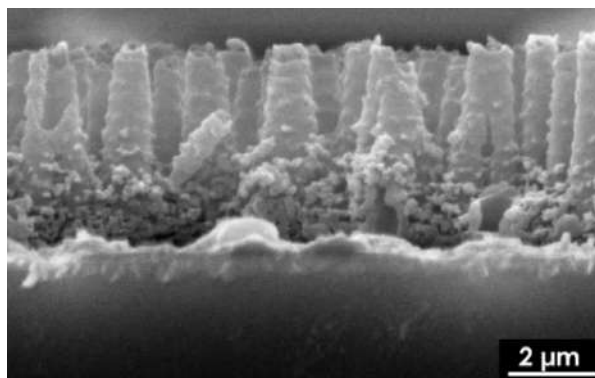


**Figure 59.** Cross section SEM image of spaced nanotubes obtained at 40 V in the electrolyte composed of diethylene glycol mixed with 0.5 M HF, 0.15 M  $\text{NH}_4\text{F}$  and 7 vol% water.

*Problems occurred during optimization of the anodizing process towards the semitransparent layer*

Besides the cases in **Figure 56**, showing that after the anodization no tubular layers were found in the SEM images, other problems also arose during the anodizing process and could be diagnosed even by the naked eye as presented in **Figure 60**.

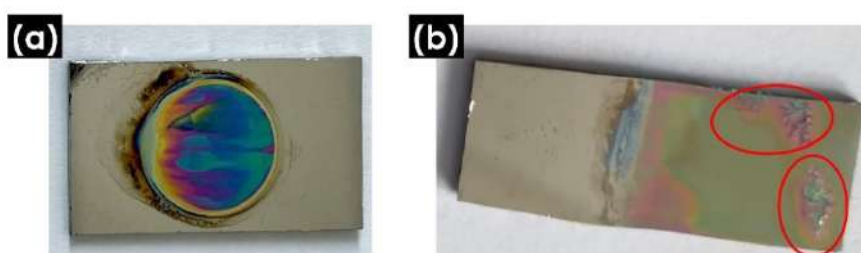


**Figure 60.** Some issues occurred during the optimisation of the anodization process:

- (a) the semitransparency of substrate is not achieved after more than 2 h of anodization in following conditions; electrolyte composition: 0.15 M  $\text{NH}_4\text{F}$ , 0.5 M H, 7 vol %  $\text{H}_2\text{O}$ , 93 vol % DGE; temperature:  $40^\circ\text{C}$ , voltage: 40 V) (b) delamination of Ti layer from the substrate (marked by red circles) during the anodization performed in the following conditions; electrolyte composition: 0.27 M  $\text{NH}_4\text{F}$ , 1 M  $\text{H}_3\text{PO}_4$ , 5 vol %  $\text{H}_2\text{O}$ , 95 vol % GE, temperature:  $23^\circ\text{C}$ , voltage: 60 V.



As shown in **Figure 60**, after more than 2 h of anodization that should lead to the spaced architecture, semitransparency was not reached. On the other hand, for Ti films sputtered under the same conditions onto the ITO glasses, as shown in **Table 6**, the anodization time to obtain the spaced nanotubes does not exceed one hour. In general, the main reason that the opaque bare Ti film did not reach semitransparency, was its poor electrical conductivity. In fact, a good conductivity of the sputtered film is essential to drive the anodization process towards formation of tubular nanostructure and oxidation the Ti film into a semitransparent  $\text{TiO}_2$  layer according to the equations from (1) to (4) provided in subsection 4.2.2. This problem can be also observed during the anodization of TiX alloys (where X is a heterometal) sputtered onto TCO. In this case, a relatively high amount of heterometal in the alloy film may be responsible for the non-transparency of the anodizing substrate. Another problem depicted in **Figure 60 (b)** is delamination of the sputtered Ti film due to its poor adhesion to the ITO/glass substrate.

#### *Structural properties of the tubular layers*

In order to verify the structure of the obtained aligned and spaced  $\text{TiO}_2$  nanotubes grown onto indium tin oxide coated glass before and after the annealing, the Raman spectra were recorded, see **Figure 61**.

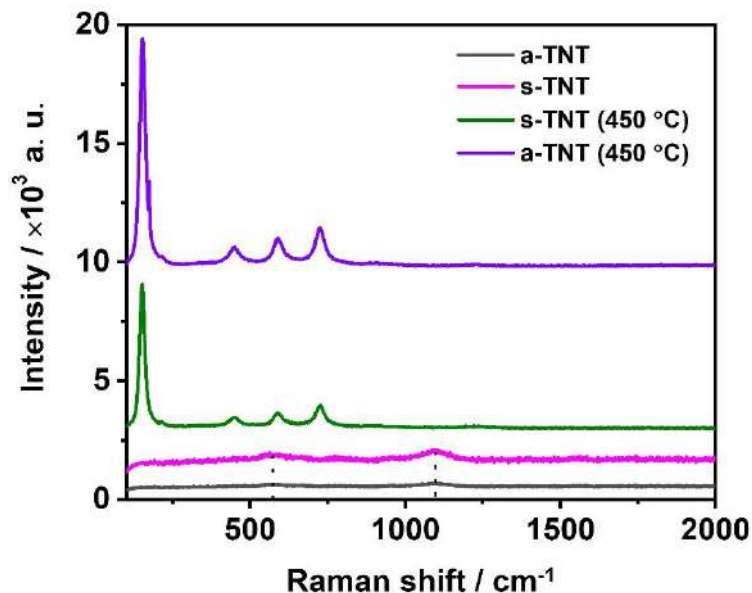


**Figure 61.** Raman spectra of anodized titania films deposited on ITO-glasses: a-TNT: aligned nanotubes, s-TNT: spaced nanotubes, annealed at 450 °C for 2 h.

It is well known that the Raman spectrum of anatase phase of  $\text{TiO}_2$  exhibits active bands located at 144  $\text{cm}^{-1}$ , 197  $\text{cm}^{-1}$ , 399  $\text{cm}^{-1}$ , 516  $\text{cm}^{-1}$  and 639  $\text{cm}^{-1}$ , which correspond to  $E_{g(1)}$ ,  $E_{g(2)}$ ,  $B_{1g}$ ,  $A_{1g} + B_{1g}$  and  $E_{g(3)}$  modes, respectively.<sup>144</sup> Independently on the tubes arrangement, the Raman

spectrum of the TiO<sub>2</sub> layer before calcination shows two not so intense bands with maxima located at 612 and 1050 cm<sup>-1</sup>. The broad band at 610 cm<sup>-1</sup> is assigned to Ti-O stretching in amorphous titania.<sup>188</sup> The peak found at 1050 cm<sup>-1</sup> observed in both spectra results from ITO-glass substrate.<sup>189</sup> The Raman spectra of the calcined aligned and spaced TNT samples present six peaks as it is also shown in **Figure 61**. The peaks located at 144, 197, 399, 516 and 639 cm<sup>-1</sup> are ascribed to E<sub>g(1)</sub>, E<sub>g(2)</sub>, B<sub>1g</sub>, A<sub>1g</sub>+B<sub>1g</sub> and E<sub>g(3)</sub> active modes of the anatase phase.<sup>144</sup> The observed peaks at 610 cm<sup>-1</sup> in the Raman spectra before the calcination disappeared after calcination. This analysis evidences the transformation of the amorphous phase of titania to the anatase phase after annealing of samples at 450 °C.

### *Conclusions*

In summary, the fabrication of the aligned and spaced titania nanotubes via anodization of Ti film deposited onto ITO-glass have been optimized owing to the numerous attempts carried out in various conditions. The selection of the range of the various parameters values used in optimisation process and finally reaching this goal was possible due to the detailed studies of the current state of art regarding anodization of sputtered titanium films. Indeed, some problematic issues took place during the growth of the tubular oxide layer, however they were solved taking into account the comments and advices reported in the literature. The influence of the water content present in the electrolyte on the quality of the tubular layer, i.e. obtaining a crack-free layer with well-open pores, was investigated. The results revealed that for aligned nanotubes, regardless of the applied voltage, water content between 5 vol% and 10 vol% is essential to avoid the formation of nanograin on the sample surface and the aggregation of nanotubes into several regions. In the case of the spaced nanotubes 0.5 M is found to be the optimal concentration of hydrofluoric acid to grow the tubular layer.

The optimized anodization conditions selected for the growth of nanotubes are as following:

- aligned nanotubes: the mixture of ethylene glycol (95 vol%) and water (5 vol%) containing 1 M H<sub>3</sub>PO<sub>4</sub> and 0.27 M NH<sub>4</sub>F at 23 °C, applied voltage of 60 V;
- the spaced nanotubes: the mixture of diethylene glycol (93 %) and water (7%) containing 0.15 M NH<sub>4</sub>F and 0.5 M HF at 23 °C, applied voltage of 40 V.





## Review

# The Anodization of Thin Titania Layers as a Facile Process towards Semitransparent and Ordered Electrode Material

Dujeanic-Stephane Kouao \*, Katarzyna Grochowska and Katarzyna Siuzdak

Centre for Plasma and Laser Engineering, The Szwedowski Institute of Fluid-Flow Machinery, Polish Academy of Science, Fiszerka 14 St., 80-231 Gdańsk, Poland; kgrochowska@imp.gda.pl (K.G.); ksiuzdak@imp.gda.pl (K.S.)

\* Correspondence: dkouao@imp.gda.pl; Tel.: +48-58-522-5298-9

**Abstract:** Photoanodes consisting of titania nanotubes (TNTs) grown on transparent conductive oxides (TCO) by anodic oxidation are being widely investigated as a low-cost alternative to silicon-based materials, e.g., in solar light-harvesting applications. Intending to enhance the optical properties of those photoanodes, the modification of the surface chemistry or control of the geometrical characteristics of developed TNTs has been explored. In this review, the recent advancement in light-harvesting properties of transparent anodic TNTs formed onto TCO is summarized. The physical deposition methods such as magnetron sputtering, pulsed laser deposition and electron beam evaporation are the most reported for the deposition of Ti film onto TCO, which are subsequently anodized. A concise description of methods utilized to improve the adhesion of the deposited film and achieve TNT layers without cracks and delamination after the anodization is outlined. Then, the different models describing the formation mechanism of anodic TNTs are discussed with particular focus on the impact of the deposited Ti film thickness on the adhesion of TNTs. Finally, the effects of the modifications of both the surface chemistry and morphological features of materials on their photocatalyst and photovoltaic performances are discussed. For each section, experimental results obtained by different research groups are evoked.

**Keywords:** Ti film; transparent conductive oxides; electrochemical anodization; interfacial adhesion; titania nanotubes; semitransparent photoelectrode



**Citation:** Kouao, D.-S.; Grochowska, K.; Siuzdak, K. The Anodization of Thin Titania Layers as a Facile Process towards Semitransparent and Ordered Electrode Material. *Nanomaterials* **2022**, *12*, 1131. <https://doi.org/10.3390/nano12071131>

Academic Editor: Gian Andrea Rizzi

Received: 30 January 2022

Accepted: 25 March 2022

Published: 29 March 2022

**Publisher's Note:** MDPI stays neutral with regard to jurisdictional claims in published maps and institutional affiliations.



**Copyright:** © 2022 by the authors. Licensee MDPI, Basel, Switzerland. This article is an open access article distributed under the terms and conditions of the Creative Commons Attribution (CC BY) license (<https://creativecommons.org/licenses/by/4.0/>).

## 1. Introduction

The depletion of fossil-based resources and the continuous warming of the climate have prompted human beings to attach considerable interest to the use of renewable energy resources [1]. Among the various renewable energy sources, the energy from sun that hits the earth in one hour is sufficient to meet the energy demand of the world in a year [2]. The development of low cost and high efficiency photoactive materials is fundamental to leave the dependency of fossil-based resources. Intensive efforts have been devoted to the synthesis of new functional materials with improved light-harvesting capability [3]. For this, various semiconductor oxides with one-dimensional geometry have been synthesised and used as photoactive materials. Among others, titania nanotube arrays obtained onto transparent conductive oxides via anodization process are the most appealing.

TNTs exhibit numerous advantages as compared to titania nanoparticles, or other one-dimensional geometry materials such as nanofibers, nanowires and nanorods. TNTs vertically oriented with an average length in order of micrometer significantly enhance the visible light scattering and absorption [4]. Additionally, electrons transport is much faster along nanotubes as compared to the randomly distributed nanoparticle networks [5,6]. Boundaries between nanoparticles slow the percolation of electrons through the inter-connected nanoparticles, thus promoting electron-hole recombination. Lynch et al. [5] compared the incident photon-to-current conversion efficiency (IPCE) spectra obtained from two photoanodes. One was fabricated by using TiO<sub>2</sub> nanoparticles layer (2 µm thick)

and the other by a TNTs layer with average length of also 2  $\mu\text{m}$ . They noticed that for the same thickness, TNTs based photoanode exhibits IPCE values much higher than that of the nanoparticles. It is well known that the electron diffusion length is a major parameter that decides on the conversion efficiency of the material, and a larger diffusion length than the material geometrical size i.e., nanotube length or nanoparticle layer, leads to higher photoconversion efficiency [7]. The study conducted by Lynch et al. [5] also shown that the electron diffusion length along the nanotubes was approximately 30 times greater than that within the nanoparticle layer. Further increase of the electron diffusion length can be achieved by optimizing both the order, and the geometry of the nanotubes through electrochemical anodization [8]. Other synthesis methods including sol-gel, and hydrothermal lead to a random orientation of nanotubes [9]. As compared to nanofibers, nanorods or nanowires, the nanotube geometry has the highest surface area owing to its additional inner walls [7]. This means that the decoration can be done by incorporating nanoparticles on the outer and inner tube walls. The modification of TNTs can be realized by: (1) immersing the formed TNTs after anodization in the heteroatom solution, (2) thermal post-treatment of the anodized materials with reactive heteroatom gases, (3) anodizing the substrates in electrolyte mixed with heteroatom salts [4]. Recently, titania nanotubes-based materials synthesized by depositing Ti films onto TCO, and subsequent anodization to obtain semitransparent TNTs are widely explored, taking advantage of the synergistic effect between the high ordering degree of TNTs, and the excellent transparency of TCO. This can address the spectral mismatch between the photoanode and the solar incident radiation [3]. For example, a red shift of the absorption edge from 397 nm to 575 nm has been reported by Bjelajac et al. [4] when investigating the absorption spectra of TNTs sensitized with CdS quantum dots grown by anodic oxidation on fluorine doped tin oxide (FTO) considered there as a semitransparent conducting substrate. This indicates a significant improvement in the absorption capacity towards the visible range of the semitransparent material after CdS quantum dots decoration. Moreover, a good transmittance, about 90%, in the visible range was achieved by Paušová et al. [1] after the annealing of TNTs grown on FTO at 500  $^{\circ}\text{C}$ .

Although titania nanotube arrays directly grown onto TCO via anodic oxidation are widely investigated as promising materials for photoelectrochemical applications, such as photocatalysis and solar cells, so far there is no review devoted to describing the fabrication process of these semitransparent materials, and summarizing recent achievements in terms of light-harvesting efficiencies. Such semitransparent materials used as photoelectrodes allow the incident light to pass through the entire electrochemical cell structure. The present review is specially focused on both the synthesis process of semitransparent TNTs formed out of Ti film deposited onto TCO, and the photoconversion properties of these active materials, through the modification of both their surface chemistry, and overall geometry. First, detailed descriptions of the different physical depositions methods are provided. Related to this, the various strategies utilized to improve the adhesion of Ti deposited onto TCO are discussed as well. Then, the anodic growth mechanism of TNTs is discussed through three models, namely field-assisted dissolution, viscous flow and oxygen bubble models. Afterward, the dependency of the deposited Ti thickness on the morphological characteristics and adhesion of the prepared TNTs layer are discussed. In order to discuss the performances of the semitransparent TNTs investigated as active materials in photoelectrochemical systems, the most recent achievement in boosting the photocatalytic and photovoltaic efficiencies of TNTs grown on TCO and other polymer substrates are presented in the last section.

## 2. Description of Deposition Techniques of TCO-Ti: Metal Thin Films

Nowadays, we explore deeply the nanomaterials world [10]. Going towards the nanodimensions we can identify the properties that have not been reported for the macroscale [11]. It may seem strange that having the same chemical formula, like pure gold, silver, titanium dioxide or iron oxide, the control over the morphology can lead to the completely different properties [12]. Despite we have the limited number of abundant elements and easy



accessible compounds; one can produce nanomaterials with unique properties basing on the same substrate. Herein we consider titanium layer that can be such substrate that after special treatment can bring us the highly ordered nanomaterial.

Although, titanium foil exhibits good mechanical stability in macro scale, those properties deteriorate with the downsizing of its thickness due to the phenomenon known as grain size effect [13]. Hence, the miniaturization of materials based on  $\text{TiO}_2$  nanotube arrays grown on Ti foils becomes a challenge since the thickness of Ti foil cannot be reduced indefinitely. To address the issue, various techniques have been utilized to grow well-ordered TNTs onto TCO coated glass. Among others, the as-grown TNTs layer adhesion plays here a crucial role. Transparent conductive oxides, including indium tin oxide (ITO), aluminum zinc oxide (AZO) and indium zinc oxide (IZO) can be synthesized with a thickness of the order of the micrometer, and exhibit good mechanical properties [14]. Moreover, TCO substrates have the advantage of cut-off of the optical transmittance at the near-infrared (NIR) region, and their high optical nonlinearities play a major role in the enhancement of light-harvesting properties of photoelectrodes [15]. Indeed, their conductivity and transparency are explored in the designing of solar cell [16], electrochromic device [17], optoelectronic devices [18], and biosensors [19]. For example, in the back-side illumination set-up of dye-sensitized solar cells, photoanodes consist of a dye-sensitized nanostructured titania grown onto an opaque titanium foil [20]. In this configuration, the light is partially absorbed and reflected onto the platinum layer coating on the counter electrode of the device. This reduces the number of photons available for the photoexcitation of the dye molecules. In general, the back-side illumination dye-sensitized solar cells have low conversion efficiency (7%, [21]) due to the absorption of the incident light by both the counter electrode and the electrolyte [21,22]. In order to reduce this great energy loss, attempt have been conducted either to optimize the thickness of the Pt film coated onto the counter electrode [22], or to replace the traditional iodide/triiodide redox electrolyte by cobalt based redox electrolyte [21]. For example Zhong et al. [22] achieved an efficiency of 4.29% for a deposited Pt film thickness of 2.48 nm. Kim et al. [21] reported a power conversion efficiency of 7%, by replacing the  $\text{I}^-/\text{I}_3^-$  redox couple by a  $[\text{Co}(\text{bpy})_3]^{2+/3+}(\text{PF}_6)_2$  redox couple. They pointed out that the improvement in the back-side illuminated DSSC efficiency was due to the high transmittance of the electrolyte containing the cobalt redox couple. Although the front-side illumination dye-sensitized solar cells demonstrate the best performance [8], two important problems need to be addressed. One is the adhesion of TNTs formed onto TCO, which is important to ensure a good stability of the systems. The second issue is to control the chemical and structural properties of the obtained TNTs. Indeed, these properties rule the charge separation and electron transfer at the TNTs/electrolyte interface. The scheme of dye-sensitized solar cells irradiated under different configurations, namely from the front- and back-side is shown on the Figure 1.

Indium tin oxide and fluorine-doped tin oxide are the widely used TCO substrates in the literature for the fabrication of transparent photoanode based on TNTs [23]. Two different approaches are usually reported for the fabrication of the transparent photoanodes [24].

In one approach, titania nanotube arrays are first grown out of the opaque titanium film, followed by detaching the grown TNTs via selective dissolution of the metal. Thereafter, the free-standing titania nanotubes layers are physically transferred and bonded onto a transparent conducting oxide coated glass. This approach has been successfully utilized for the synthesis of semitransparent photoelectrodes based on TNTs [25,26]. However, the physical or chemical selective detachment out of the metal support can lead to a severe distortion in both the titania nanotubes geometry and microstructure, thereby dropping the charge separation rate. Moreover, during the transfer of the free-standing TNTs onto the TCO, a layer of titania nanoparticles paste is first applied onto the substrate using doctor-blade technique to assure a good adhesion. The numerous grain boundaries within the disordered network of titania nanoparticles layer may also reduce the charge transport rate and diminish the photoelectrode performance [24]. This method has also some limitations regarding the size of the transferred TNTs layer to the TCO.

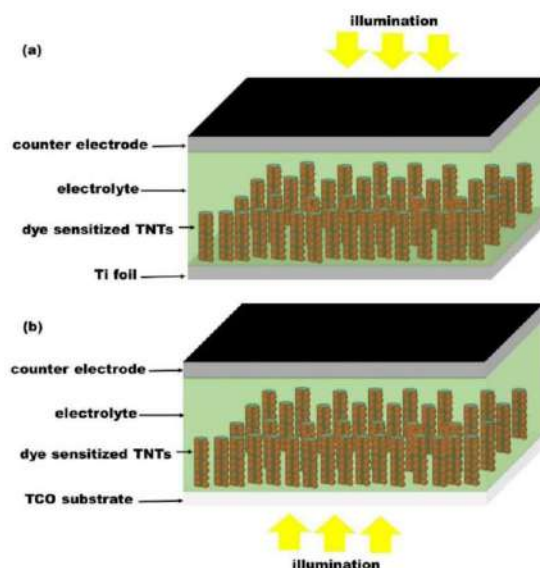


**Figure 1.** Schematic illustration of dye-sensitized solar cells under (a) back-side illumination and (b) front-side illumination.

In the second approach, titanium film is first deposited on the TCO coated substrate, followed by the anodization of the obtained film. In this approach, both the architecture and the adhesion of the TNTs layers strongly depend on the morphology and the adhesion of the titanium layer to the substrate. The temperature of the base is also a key parameter requiring optimization to achieve both a good adhesion of the titanium film to the substrate and an adequate Ti film morphology. A good adhesion is necessary to avoid the delamination of Ti as well as formed TNTs from the TCO during the anodization process and further calcination. Various coating methods have been investigated in the literature, for the deposition of Ti and Ti:X (X = heteroatom other than Ti) thin films onto ITO and FTO. Among them, satisfied adhesion of the Ti or Ti:X layer to the substrate has been reported using physical deposition techniques including radio-frequency (RF), pulsed direct current (DC) sputtering, and pulsed laser deposition (PLD) by adjusting the substrate's temperature in the range of 400–500 °C [27–29].

### 2.1. Magnetron Sputtering

Magnetron sputtering technique including direct current, radio frequency, and high-power impulse magnetron sputtering has been largely used for the deposition of Ti:X onto TCO such as ITO [16,30], and FTO [9,31]. As mentioned earlier, the morphological features of the deposited titanium film including surface roughness, the shape of grains and their size distribution can be also controlled by adjusting the substrate temperature. Figure 2 shows the surface morphology of Ti films deposited onto ITO at room temperature and at 300 °C. One can see that the morphological features of the deposited film change with the increase temperature. The films formed at the 300 °C has much smoother sides than that obtained at room temperature.

Kathirvel et al. [24] sputtered titanium thin film onto fluorine-doped tin oxide via RF deposition technique and investigated the temperature dependency of the surface roughness. The results indicated that the temperature dependency of the surface roughness is not linear. A decrease of the surface roughness from 80 nm to 50 nm has been observed with the increase of the substrate temperature from room temperature up to 200 °C. This is



due to the low density of metal particles at relatively low temperature. Next, an abrupt increase of the surface roughness of 140 nm was observed when the temperature reached 400 °C, leading to the presence of several aggregations of grains and voids. Furthermore, the increase of the substrate temperature from 150 to 450 °C leads to the increase of grain size and the specific surface area of the deposited film [28]. Zelny et al. [28] sputtered titanium layer onto FTO kept at different temperatures from room temperature up to 450 °C, and thereafter they anodized the obtained materials. The results indicated that TNTs film grown out the material prepared at 450 °C exhibits good adhesion without any delamination from the FTO substrate.

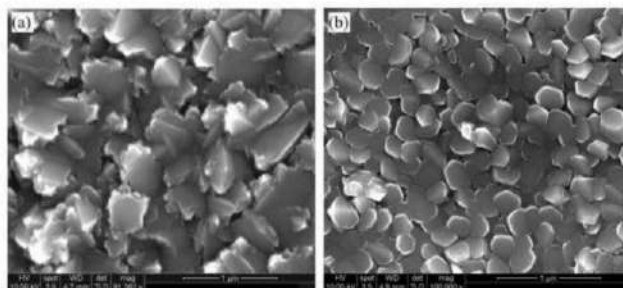


**Figure 2.** Morphology of RF sputtered Ti films on ITO glass (a) at room temperature and (b) at 300 °C. Reprinted with the permission from reference [17].

Another technique that relies on the introduction of a conducting Nb-doped titania layer between the titanium film and the TCO substrate has been used by Kim et al. [27]. It was shown that it can prevent the degradation of the titania nanotube arrays during anodization. A similar method has been explored by Buttner et al. [16] to prepare high performance transparent electrode based on titania nanotube arrays grown on ITO dedicated for solar cells. The deposition of titania thin layer between the Ti film and ITO by RF magnetron sputtering allowed to achieve crack-free and well-ordered architecture of titania nanotubes arrays with tuneable geometry. Krumpmann et al. [32] examined the impact of the titania interlayer placed between Ti film and FTO on the morphological features of the TNTs photoanodes. To achieve the goal, two photoanodes have been prepared. In the first case, TNTs was grown on FTO by anodizing a Ti layer previously sputtered directly onto the FTO. For the second probe, titania layer was first deposited onto FTO, followed by sputtering of Ti film. After anodization, the comparative study was conducted to analyse the morphological properties of both photoanodes. The results indicated that the presence of the compact titania interlayer with a thickness range of 50–100 nm improves the adhesion of Ti film and leads to more regular and homogeneous formation of TNTs.

## 2.2. Electron Beam Evaporation

The electron beam evaporation technique has the advantage of higher deposition rate and lower impurity level and is broadly used as a thin film coating method for the deposition of Ti or Ti:X films onto indium tin oxide [33–35]. Krysa et al. [33] reported that films prepared by using electron beam evaporation have poor adhesion to the TCO, as compared to films deposited by magnetron sputtering. Indeed, a comparative study of the adhesion and morphology of titanium films deposited on FTO have been conducted using both deposition techniques. The results showed that the sputtered Ti film is denser and more compact than the evaporated Ti film. The large amount of pinholes observed on the evaporated film led to a weak adhesion. Moreover, a complete delamination of TNTs layer from FTO was observed in aqueous electrolyte owing to the weak adhesion of the evaporated Ti film. Figure 3 shows the images obtained under optical and scanning electron microscopy for Ti films deposited on FTO prepared by evaporation and magnetron sputtering obtained by Krysa et al. [33].

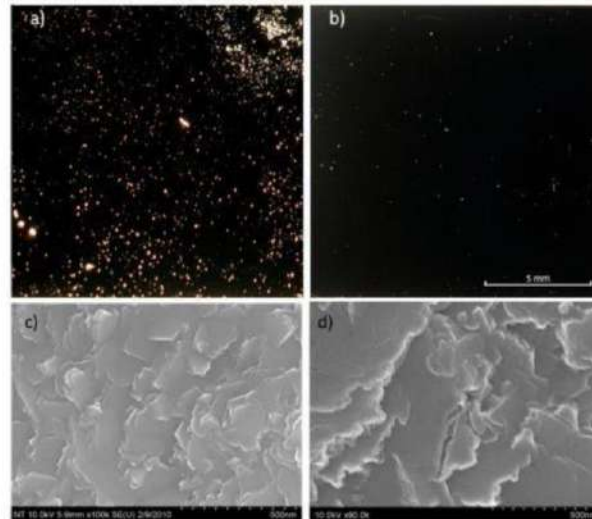


**Figure 3.** Optical microscope image of defects (pinholes) on (a) evaporated and (b) sputtered Ti metal on FTO glass, SEM surface morphology of (c) evaporated and (d) sputtered Ti metal on FTO glass. Reprinted with the permission from reference [33].

### 2.3. Pulsed Laser Deposition

Pulsed laser deposition is a technique that has been also widely utilized for preparing Ti:X layers onto indium tin oxide [29,36]. The morphological features and the electrical properties of Ti:X film deposited onto the TCO can be controlled by varying substrate temperature. Kumi et al. [29] reported that an increase of the substrate temperature to 500 °C leads to an increase in clusters and aggregation of the nanoparticles, which is beneficial to achieve a film with high density and better adhesion. Figure 4 presents the surface morphology the deposited films achieve by Kumi et al. [29].

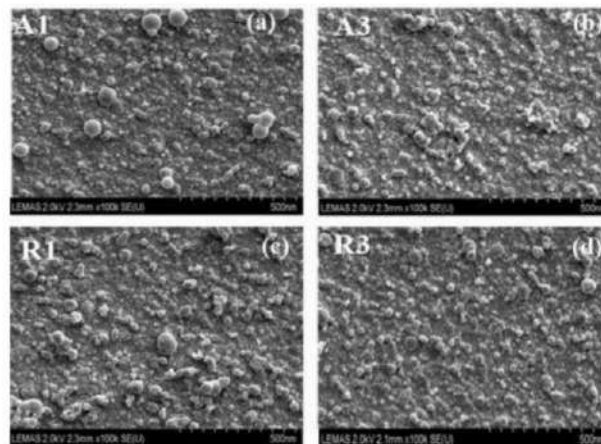


**Figure 4.** Surface morphologies of  $\text{TiO}_2$  thin films deposited onto glass substrate by fs-PLD at various substrate temperatures: (a) [A1 (25 °C)], (b) [A3 (700 °C)] and rutile thin films: (c) [R1 (25 °C)] (d) [R3 (700 °C)]. Reprinted from reference [29] under license CC BY.

### 3. Electrochemical Mechanism of Self-Organized Anodic TNTs

After describing both the physical deposition methods and various strategies investigated to improve the adhesion of Ti films to TCO, this section presents the different models already presented in the literature to explain the mechanism of TNTs formation through anodic oxidation. The growth of TNTs via electrochemical anodization is a simple and highly reproducible technique, enabling control over the geometry of the produced TNTs [4]. Moreover, this method does not need sophisticated facilities. In general, the used electrochemical anodization set-up consists of a positive terminal of the DC power supply connected either to a Ti foil or Ti film deposited onto TCO which, serves as anode, the negative terminal (cathode) that is connected to a platinum foil or graphite rod and cell filled in with an appropriate conductive electrolyte. Figure 5 shows the schematic diagram of the synthesis set-up. It is well known that the pH of the electrolyte and its chemical composition control the growth rate of the porous or tubular layer [37]. The dissolution rate of the developed oxide layer film at the Ti/electrolyte interface depends strongly on the pH of the electrolyte. The barrier layer is easily soluble in acidic electrolyte, whereas, the dissolution rate of the barrier is drastically slower in neutral and basic electrolytes [37].

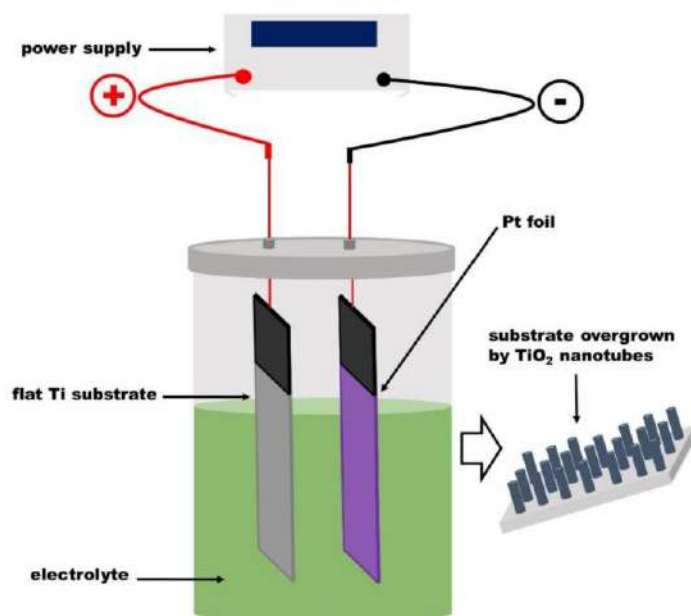


Figure 5. Electrochemical anodization set-up.

#### 3.1. Conventional Field-Assisted Dissolution Theory

Conventional field-assisted dissolution theory is among others the most frequently evoked theory describing the formation mechanism of anodic TNTs in electrolytes containing fluorine ions [38]. Hoar and Mott, first put forward the “field-assisted dissolution” mechanism when investigating the formation of porous anodic oxide films [39]. They proposed that the formation of the porous or tubular structure is associated with the dynamic equilibrium between the growth rate of the oxide layer at the metal/oxide interface and the chemical dissolution of the developed oxide layer at the oxide/electrolyte interface [40]. According to this theory, TNTs are grown by self-organization of the formed TiO<sub>2</sub> layer during the process of electrochemical anodization in three relatively independent steps [41]. Figure 6 illustrates the mechanism occurring in those steps.



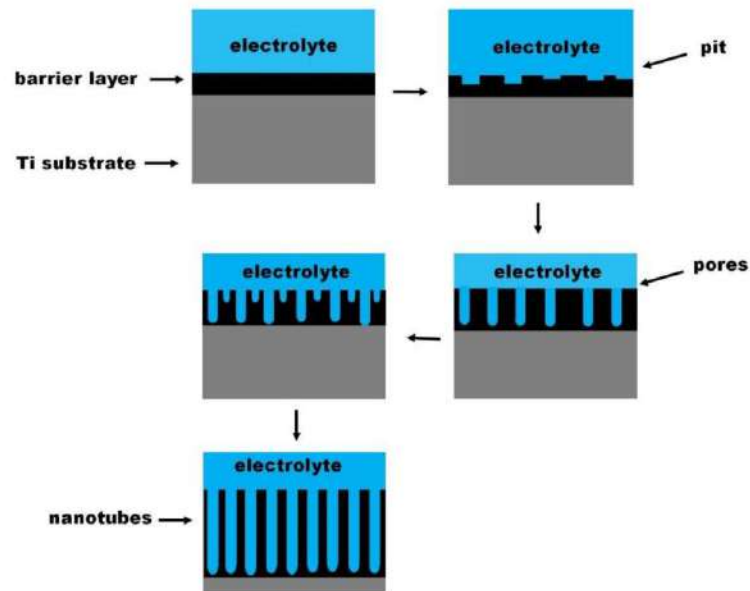


Figure 6. Scheme presenting the stages of TNTs formation by field-assisted dissolution.

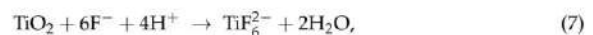
In the first step known as field-assisted oxidation of Ti layer (Equations (1)–(5)),  $O^{2-}$  and  $OH^-$  anions originating from the dissociation of water in the electrolyte interact with the metal (Ti), leading to the growth of the barrier oxide layer ( $TiO_2$ ) at the Ti/electrolyte interface. Additionally, hydrogen evolution takes place at the cathode [37,42].



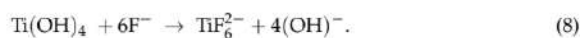
In the second step called field-assisted dissolution of  $Ti^{4+}$  (Equation (6)),  $Ti^{4+}$  ions migrate from the Ti/ $TiO_2$  interface toward the electrolyte where they combine with fluorine ions and dissolve to form titanium hexafluoride complex,  $[TiF_6]^{2-}$ . Simultaneously,  $O^{2-}$  and  $OH^-$  moves through  $TiO_2$  layer toward the Ti/ $TiO_2$  interface and interact with Ti leading to a continued growth of the  $TiO_2$  layer according to the Equations (2)–(4) [37,42].



In the last step the chemical dissolution of both, the formed  $TiO_2$  and Ti by fluorine ions takes place simultaneously at the  $TiO_2$ /electrolyte and Ti/ $TiO_2$  interfaces. The localized etching of the  $TiO_2$  layer leads to the formation of small pits, which act as pore forming centres. The  $TiO_2$  layer growth rate at the metal/oxide interface described by Equations (2)–(4) and the rate of chemical dissolution of the oxide layer and Ti (Equations (6)–(8)) become equal, and the porous structure converts to a tubular layer [37,42].







#### Experimental Evidences against the Field-Assisted Dissolution Theory

Although the field-assisted dissolution theory remains the most popular one to describe the electrochemical mechanism of self-organized TNTs formation, recently, several experimental results have shown its limits. As mentioned above according to the field assisted dissolution theory, the tubular structure is generated due to the dissolution of the oxide layer at  $\text{TiO}_2$ /electrolyte interface by the fluoride ions, driven by the electric field. Hence, the presence of fluoride ions in the electrolyte is crucial to initiate the formation of the porous texture and achieve a tubular structure [43]. However, Fahim et al. [44] achieved a bundles tubular structure of a length of 500 nm in aqueous solution containing only sulphuric acid (fluorine free electrolyte). Similar results have been observed by Lu et al. [45] when anodizing Ti substrate in aqueous solution of silver nitrate (also fluoride ion free electrolyte). The results achieved in both experiments confirm that fluoride ions are not essential for the initiation of the formation of the porous structure. Moreover, Zhou et al. [46] observed experimentally that electrochemical anodization of Ti substrate in organic electrolyte containing fluoride salt, i.e., 0.7 wt% ammonium fluoride ( $\text{NH}_4\text{F}$ ) leads to the formation of a dense barrier oxide ( $\text{TiO}_2$ ) layer at the Ti/electrolyte interface. No tubular structure was obtained.

The mechanism of porous structure initiation by fluoride ions during anodization remains unclear. The theory describes the growth of the oxide layer at the Ti/electrolyte interface as the result of the chemical reaction between the  $\text{O}^{2-}$  and  $\text{OH}^-$  anions produced during the dissociation of water molecules from the electrolyte with the metal. Therefore, an increase of water content in the electrolyte should be an obvious way to increase the growth rate of the  $\text{TiO}_2$  layer, and achieve tubular structure with longer nanotubes [47]. Zhou et al. [47] anodized titanium substrate in ethylene glycol (EG) based electrolyte containing 0.5 wt%  $\text{NH}_4\text{F}$  and 2 wt% or 10 wt%  $\text{H}_2\text{O}$ . They found that the growth rate of the nanotubes layer in 2 wt%  $\text{H}_2\text{O}$  in the electrolyte (240 nm/min) was much faster than that in electrolyte with 10 wt%  $\text{H}_2\text{O}$  (36 nm/min). This unexpected observation contradicts the field-assisted dissolution theory.

This theory has also been called into question by Yu et al. [48] According to the field-assisted dissolution, the barrier oxide layer growth at the Ti/ $\text{TiO}_2$  interface is described by the Equations (2)–(4) and its dissolution at the  $\text{TiO}_2$ /electrolyte interface by the Equations (7) and (8). In order to test this assertion, the authors performed a sequence of three anodizations of Ti substrate to determine the exact location where the  $\text{TiO}_2$  layer grows during the anodization process. Authors expected to observe the porous oxide layer growth only at the Ti/ $\text{TiO}_2$  interface and hemispheres or a tubular structure at the  $\text{TiO}_2$ /electrolyte interface, during the whole process. However, the experimental results were totally different. A flat morphology at Ti/ $\text{TiO}_2$  and  $\text{TiO}_2$ /electrolyte interfaces was observed after the second anodization. This observation clearly indicates that a new barrier oxide layer has been grown on Ti/ $\text{TiO}_2$  and  $\text{TiO}_2$ /electrolyte interfaces simultaneously. The growth of the barrier oxide layer at the two interfaces at the same time contradicts the field-assisted dissolution theory.

The phenomena known as terminated nanotubes has been highlighted by Yu et al. [49]. They demonstrated that there is no dynamic equilibrium between the growth rate of the barrier oxide layer at the metal/oxide interface and the rate of its chemical dissolution at the oxide/electrolyte interface, as suggested by field-assisted dissolution theory. Their results showed that the barrier oxide stops growing whereas its dissolution continues as long as  $\text{O}^{2-}$  and  $\text{OH}^-$  anions interact with Ti at the Ti/ $\text{TiO}_2$  interface, so the bottoms of nanotubes can be sealed, ‘terminated nanotubes’. The bottom of the terminated nanotubes is not in contact with the  $\text{TiO}_2$  wall, as shows in the Figure 7. It has been also reported that field-assisted dissolution theory fails to explain the phenomenon of separation into tubes, i.e., the formation of spaced nanotubes [41]. Therefore, it can be stated that the description of the formation mechanism of TNTs based on field-assisted dissolution theory

is not convincing enough. New models and theories including, oxygen bubbles model [50] and viscous flow model [51] should be more and more explored to elucidate the growth mechanism of TNTs.

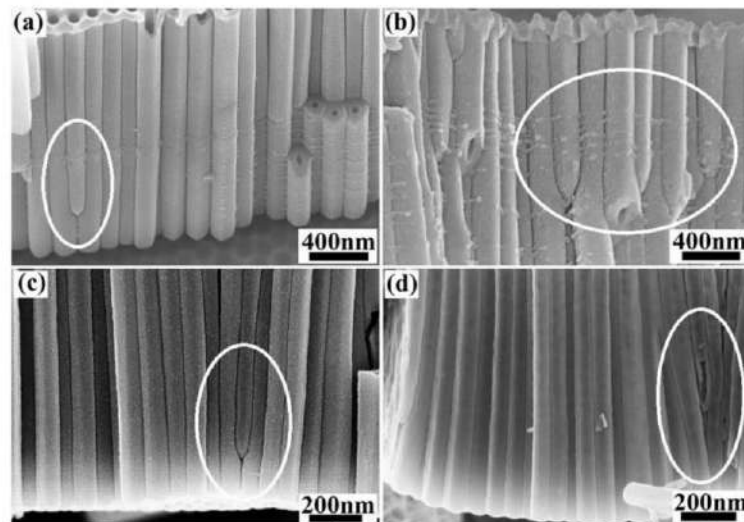


**Figure 7.** SEM images of terminated nanotubes obtained at different voltage, (a) 50 V, (b) 70 V, (c) 40 V and (d) 30 V. Reprinted with the permission from reference [49].

### 3.2. Viscous Flow Model

As described above, field-assisted dissolution theory cannot be regarded as reliable to explain certain phenomenon such as, the formation of spaced nanotubes architecture, and the terminated nanotubes [49,52]. Some experimental works have shown that the dissolution rate of titanium oxide in electrolyte containing fluorine ions is in fact very low [53]. Moreover, there is no obvious quantitative correlation between the dissolution rate of the oxide layer and the anodizing current [52]. In 2006, Skeldon et al. [54] first proposed the viscous flow model to investigate the formation of the tubular structure of alumina. The authors showed that the growth mechanism of the tubular structure is different from that described under the conventional field-assisted dissolution theory. Later in 2008, LeClere et al. [51] used the tracer atom technique to investigate pores formation in anodic titania and pointed out that the generation of the nanotubes can be explained by the viscous flow model. The growth mechanism of the anodic tubular structure according to the viscous flow model is described as follow. First, the barrier oxide is developed due to the migration of the  $Ti^{4+}$  ions outward from the metal and  $O^{2-}$  toward the anode [54]. The oxide layer grows at both interfaces: Ti/oxide and oxide/electrolyte. The incorporation of anions into the oxide layer caused by the electric field induces stress, and in consequence, plastic flow of the oxide is driven [55]. When the stress reaches a maximum, the growth of the oxide layer at the oxide/electrolyte interface stops and pore embryos start to form [55]. The creation of the pores is due to the flow instability caused by spatially non-uniform near-surface compressive stress [55]. The increase of stress from electrostriction assists the stabilisation of the formed pores at the flat oxide/electrolyte interface [54,55].

### 3.3. Oxygen Bubble Model

The oxygen bubble mould model is based on the physical nature of the ionic current and electronic current within the anodic oxide, and was first proposed by Zhu et al. [56]. The applied electric field generates two currents, the ionic current due to the migration of anions and cations in the electrolyte and the electronic current. According to the model, the formation of the barrier oxide layer is due to the contribution of the ionic current, while the electronic current causes the oxygen evolution at the anode and paves way for the formation of the tubular structure [57]. The initiation of pores growth is induced by the oxygen evolution. The formation of the tubular structure is a three-step process.

In the first step, the formation of the barrier oxide layer is driven by the ionic current. The ionic current has two components, the one due to the migration of cations ( $\text{Ti}^{4+}$  ions) and the one due to the anions, i.e.,  $\text{OH}^-$ ,  $\text{O}^{2-}$  ions. At this step, the electronic current is negligible.  $\text{Ti}^{4+}$  cations migrate from Ti to the Ti/electrolyte interface and  $\text{O}^{2-}$  anions from the electrolyte to the Ti/electrolyte interface, where they combine to form  $\text{TiO}_2$ . As the barrier oxide layer is formed, new oxide layers grow at both the Ti/oxide and the electrolyte/oxide interfaces. The barrier oxide layer grows up to the critical thickness and the total current drops dramatically. Anions are inevitably incorporated into  $\text{TiO}_2$  during its formation and this leads to an anion-contaminated layer near the electrolyte [43,52,56].

In the second step, the electronic current increases with the increase of the barrier oxide thickness according to the Equations (9) and (10) proposed by Gong et al. [43] for the electronic and ionic conduction.

$$J_{\text{ions}} = A e^{\frac{\beta U}{d}}, \quad (9)$$

$$J_e = J_0 e^{\alpha d}, \quad (10)$$

$$J_{\text{total}} = J_{\text{ions}} + J_e, \quad (11)$$

where  $J_{\text{ions}}$  is the ionic current density,  $J_e$  is the electronic current density and  $J_{\text{total}}$  is the total current density,  $J_0$  the primary electronic current density during the anodization,  $\alpha$  is the impact ionization coefficient,  $U$  is the applied voltage and  $d$  is the thickness of the barrier oxide layer.  $A$  and  $\beta$  are temperature dependent constants [43].

Hence, when the barrier oxide layer reaches the critical thickness, the total current becomes almost equal to the electronic current. The electronic current causes the oxidation of the  $\text{OH}^-$ ,  $\text{O}^{2-}$  anions incorporated within  $\text{TiO}_2$  layer and oxygen gas evolution takes place. Due to the pressure of the anion-contaminated layer and the electrolyte, oxygen bubbles cannot be released from  $\text{TiO}_2$ /electrolyte interface at once. Thus, the pressure of the oxygen bubbles on the barrier oxide leads to the formation of hemispherical bottoms. Oxygen bubbles generate nanotube embryos within the anion-contaminated layer. Nanotubes thickness grows due to the volumetric expansion of oxygen bubbles through the anion contaminated layer and then oxygen molecules are released at  $\text{TiO}_2$ /electrolyte interface [43,52,56].

In the stage 3, the electrolyte penetrates inside the nanotubes and reaches the bottom of the tubes. New oxide layers still grow due to the ionic current and promote the upward growth of the tube wall. When the bottom of the nanotubes reaches a critical thickness, the total current remains virtually constant [43,52,56]. Figure 8 illustrates the growth process.



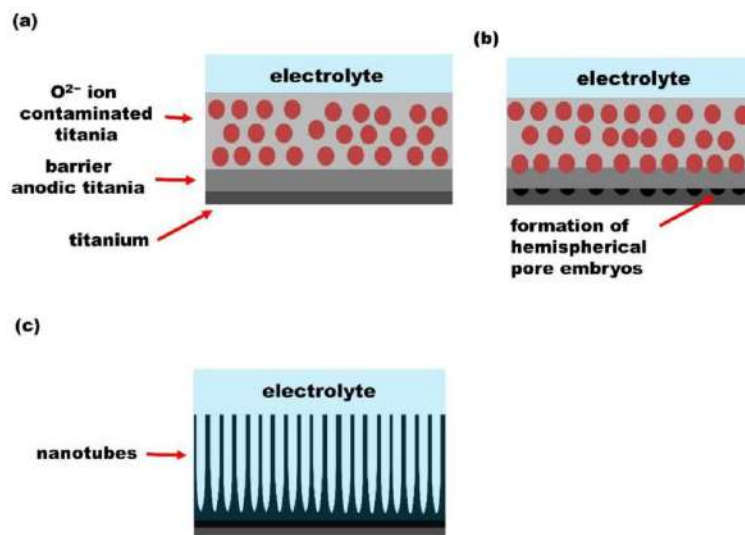


**Figure 8.** Schematic diagram of oxygen bubble model. (a) Formation of the anion-contaminated oxide layer near the electrolyte. (b) Formation of hemispherical shape for pores bottom. (c) Upward growth of the tube wall due to the volumetric expansion of oxygen.

#### 4. Effect of the Deposited Ti Thickness on TNTs Adhesion and Geometry

As already discussed above the substrate temperature during the deposition is considered as one of the most important parameter that should be adjusted to achieve a good adhesion of Ti films to the substrate. However, the works done by Buettner et al. [16], Pausova et al. [1] and Krysa et al. [33] have shown that not only the substrate temperature, but also the morphology of the deposited Ti films play a major role in good adhesion of TNTs layer. This section discusses the impact of the deposited Ti thickness on the geometrical features of anodic semitransparent TNTs. The thickness of the metal must be optimized during the deposition. The morphological features of the prepared anodic TNTs depend on the homogeneity and thickness of the sputtered Ti [33]. The increase of the metal thickness leads to an increase of the internal stress. Thus, a thicker metal layer deposited on the TCO may suffer from the insufficient adhesion [33]. The homogeneity of the deposited Ti film, also is of high importance. The presence of pinholes generated due to the inhomogeneity of the film causes damaging of the tubular structure. Hence, dense and smooth Ti films are required to achieve good quality of ordered structure during anodization [16]. Moreover, the geometrical features, i.e., average diameters and length of nanotubes formed during anodization, can be adjusted on the basis of the initial Ti thickness [16]. Therefore, many studies have focused on the optimization of the thickness of the deposited Ti film to improve the morphological properties of TNTs. Buettner et al. [16] sputter-coated Ti films with different thicknesses, i.e., 170, 340 and 510 nm, on ITO and anodized the fabricated substrates in EG based electrolyte containing 0.5 wt%  $NH_4F$ , 3 wt%  $H_2O$  and 0.5 wt%  $H_3PO_4$  (85%) at 60 V. The results indicated that the developed TNTs layers expanded by a factor of 2.2 with respect to the original sputtered Ti thickness. The optimal initial thickness of Ti is found to be 340 nm, which leads to a good film adhesion and crack-free layer after anodization. The deposited 510 nm Ti film suffers from the formation of cracks during anodization. Cracks identified as are mechanical degradations of the material. Indeed, the presence of cracks causes fragmentation of the layer due to the disintegration of the structure, thus the synthesis of TNTs with crack-free layer is paramount for building photo-electrochemical cells of reproducible properties. The dependency of the tubular length on

the initial Ti film thickness has been also investigated by Paušová et al. [1], when anodizing Ti coated FTO. Their results show that deposited Ti films with a thickness in the range of 100–600 nm have an expansion factor of 1.8 after anodization. And the expansion factor increases up to 2.5 for initial Ti film thickness of 1  $\mu\text{m}$  and above. The authors pointed out that the adhesion of the Ti film with thicknesses above 1  $\mu\text{m}$  needs to be improved. The SEM images (Figure 9) of the anodized samples show that the geometrical features such as wall thickness and pore diameter differ depending on the thickness of the deposited Ti film. As one can observe, the nanotubes are not well-developed for film thickness below 600 nm. The increase of the deposited Ti film thickness leads to poor contact between the tubular structure and the substrate after anodization. Although these works proved the strong dependency of the initial Ti film thickness on the TNTs adhesion and geometry, the anodization parameters, i.e., applied voltage, anodization time, anodization temperature and the electrolyte composition, must be taken into account during the optimization of the geometry of TNTs.

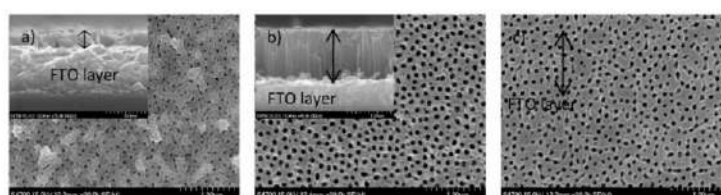


**Figure 9.** SEM images of TNTs grown onto FTO (inset: cross section image) by the anodization of Ti films of thickness of: (a) 100 nm; (b) 600 nm; and (c) 1000 nm. Reprinted from reference [1] under license CC BY.

## 5. Effect of Surface Chemistry and Morphology on Light Harvesting Properties of Semitransparent $\text{TiO}_2$ Nanotubes

Photoactive materials consisting of TNTs grown on TCO have been investigated to address global challenges such as organic pollutant degradation [58], solar-to-electricity conversion [30], and solar-to-hydrogen conversion [59]. The large band gap of  $\text{TiO}_2$ , i.e., 3 eV for rutile and 3.2 eV for anatase phase, is the fundamental drawback of TNTs-based materials. This means that the photocatalytic activation takes place in the ultraviolet region that is only 5% of the solar spectrum [60]. Therefore, it is necessary to broaden the absorption spectrum of  $\text{TiO}_2$  to the visible range (45% of the solar spectrum), e.g., by modifying its nanostructure [60]. For this purpose, the decoration of TNTs by metal or non-metal heteroatoms has been investigated. The incorporation of heteroatoms in the material structure generates inter-band levels between the conduction and valence bands, thus in consequence narrowing the band gap [61]. We focused in here on the recent advances in the enhancement of the light harvesting properties of photoactive materials, prepared by anodization of titanium film deposited on transparent substrates.

### 5.1. Photocatalytic Performance of Transparent Anodic TNTs

Any material that promotes chemical reactions by generating electron-hole pairs in the presence of light is referred as a photocatalyst. One advantage of TCO substrates as compared to Ti film lies in the fact that the TCO constitutes itself a heteroatoms source and allows the decoration of the developed TNTs walls during annealing. This method has been utilised by Bjelajac et al. [9] to prepared tin doped TNTs. The photoactive material was synthesized by anodizing the Ti film deposited on FTO in EG solution containing 0.3 wt%  $\text{NH}_4\text{F}$  and 2 wt%  $\text{H}_2\text{O}$  at 60 V, followed by the calcination of the anodized material at 500  $^\circ\text{C}$ . The band gap of the obtained material was found to be 2.92 eV. The authors ascribed the significant reduction of the band gap as compared to that of the anatase TNTs (3.2 eV) to the diffusion of Sn from FTO into  $\text{TiO}_2$  nanostructure. They pointed out that the dynamic diffusion of Sn from FTO to  $\text{TiO}_2$  occurs for an annealing temperature between

500 and 550 °C, and an increase of the temperature above 600 °C leads to the decrease of the specific surface area because the formed TNTs collapse and the degradation of the crystal structure (anatase phase) is initiated, thus decreasing the photocatalytic activity.

The presence of the  $\text{TiO}_2$ -FTO interface is another advantage over the Ti foil monolayer. Indeed, since the conduction band levels of FTO is lower than that of  $\text{TiO}_2$ , the photogenerated electrons in the conduction band of  $\text{TiO}_2$  are easily injected into FTO, thus reducing the electron-hole recombination [9,62]. Figure 10 illustrates the charge carrier transfer from  $\text{TiO}_2$  to  $\text{SnO}_2$  conduction bands.

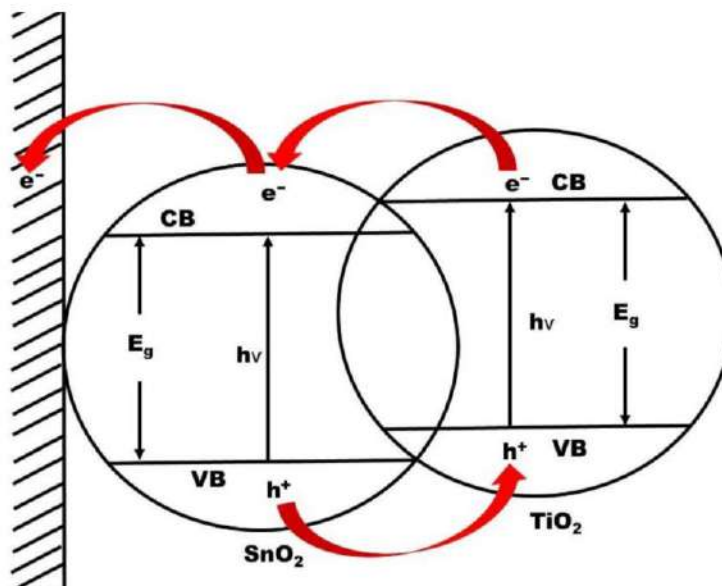


Figure 10. Scheme for charge carrier transfer from  $\text{TiO}_2$  to  $\text{SnO}_2$  conduction bands.

The photocatalytic degradation of Rhodamine B (RhB) dye by photoelectrodes consisting of TNTs grown on transparent substrates such as ceramic spinel ( $\text{MgAl}_2\text{O}_4$ ) and polymeric Kapton film via electrochemical anodization, has been investigated by Petriskova et al. [58]. They compared the performance of the fabricated active materials to those obtained by using Si wafer or Ti foil as substrates. It is well known that ceramics and polymer films have poor electric conductivity. The main objective of their study was to compare the morphology of TNTs formed out on those substrates, i.e., ceramic spinel, Si wafer, polymeric Kapton film, and Ti foil and correlated it with the photocatalytic properties of fabricated photoactive materials in the degradation RhB dye. Ti film (1.5  $\mu\text{m}$  thick) deposited on each substrate by DC-magnetron sputtering was anodized in EG electrolyte bath containing 0.5 wt%  $\text{NH}_4\text{F}$  and 0.2 wt%  $\text{H}_2\text{O}$  for 30 min at 40 V. In Table 1 the geometrical characteristics of prepared TNTs is summarized.

It can be noticed that the morphological features of grown TNTs differ depending on the used substrate. Figure 11 shows the photocatalytic performance of the prepared materials. The results indicate that the photocatalytic response of TNTs increases with geometrical parameters including total surface area, wall thickness and inner or outer diameter of TNTs. The correlation between the photocatalytic response and the length is not clear. According to the authors, the increase of the length of NTs not only promotes electron-hole recombination, but also limits the UV light penetration depth. The above observations suggest that the length is important parameter that must be optimized to achieve high performance photocatalytic activity.



**Table 1.** Geometrical features of TNTs prepared on different substrates: ceramic spinel (M), Si wafer (Si), polymeric Kapton film (K), and Ti foil (Ti). Adapted with permission from Petriskova et al., 2021.

Sample	Inner Diameter (nm)	Outer Diameter (nm)	Wall Thickness (nm)	Length (nm)	Total Tube Surface ( $\mu\text{m}^2$ )
Ti/TNTs	$84 \pm 5$	$146 \pm 9$	31	1222	0.8942
Si/TNTs	$64 \pm 2$	$104 \pm 4$	20	1681	0.8925
K/TNTs	$51 \pm 2$	$95 \pm 5$	22	1443	0.6669
M/TNTs	$57 \pm 1$	$93 \pm 3$	18	1098	0.5217

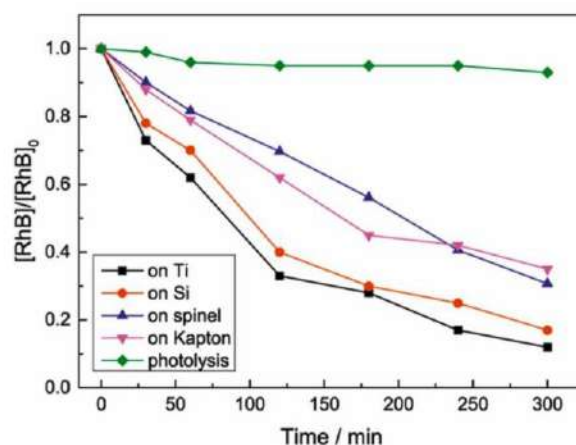


**Figure 11.** Photocatalytic degradation of RhB dye with UVA irradiation by TNTs grown on different substrates, i.e., ceramic spinel, Si wafer, polymeric Kapton film, and Ti foil. Reprinted with the permission from reference [58].

Çırak et al. [31] studied the influence of chromium decoration of  $\text{TiO}_2$  material on its photocatalytic performance. First, un-doped material was synthesized in two-step fabrication process. Ti film was sputtered on FTO substrate, thereafter the deposited Ti film was anodized in EG solution containing 0.4 wt%  $\text{NH}_4\text{F}$ , and 5 wt% deionized water. A Cr-decorated nanoporous transparent electrode was achieved by thermal evaporation of Cr nanoparticles on the anodized material in vacuum for 15 minutes. The photocatalytic performance of both fabricated materials un-doped and Cr-doped photoelectrodes was evaluated by investigating the degradation of Rhodamine B dye within a time interval of 60 min under light illumination. The results indicated that the un-doped photoelectrode could not lead to the complete decomposition the pollutant after 60 min. 27% of the initial concentration of the dye was still remaining as shown in the Figure 12. While the transparent electrode decorated with Cr nanoparticles results in the full decolouration. This excellent performance was ascribed to the presence of Cr nanoparticles.

## 5.2. Photovoltaic Performance of Transparent Anodic TNTs

The direct conversion of sunlight into electricity by using an appropriate semiconducting material is termed as photovoltaic (PV) effect [63]. The photovoltaic cells have three fundamental drawbacks namely, the high cost, low efficiency and their relatively short operating lifetime [64]. Intensive research has been conducted to improve photovoltaic cells efficiencies in a unexpensive manner, in order to further reduce their cost [3]. Dye sensitized solar cells (DSSC) are considered as a cost-effective alternatives to high-cost conventional silicon solar cells [65]. The photoanode is a key component that determines the performance of the cells. Its nanostructure strongly influences the dynamic of charge carriers. TNTs grown on TCO are promising photoanodes, since their geometry can be

controlled to improve the conversion efficiency [5]. Additionally, TCO substrates exhibit high light transmission capacity and good mechanical stability [66]. Aiempnanakit et al. [30] optimized the anodization process of Ti film sputtered on ITO by adjusting both the applied voltage (20–40 V) and the amount of  $\text{NH}_4\text{F}$  (0.4–1.4 wt%), and investigated the dependency of the performance of dye-sensitized solar cells on the anodization conditions. Figure 13 shows the SEM top view and cross sectional images of the closed-packed architecture of as-fabricated TNTs, and Table 2 summarizes the geometrical features i.e., the average length and diameter of TNTs obtained for each anodization conditions and their photo-electron conversion efficiencies.

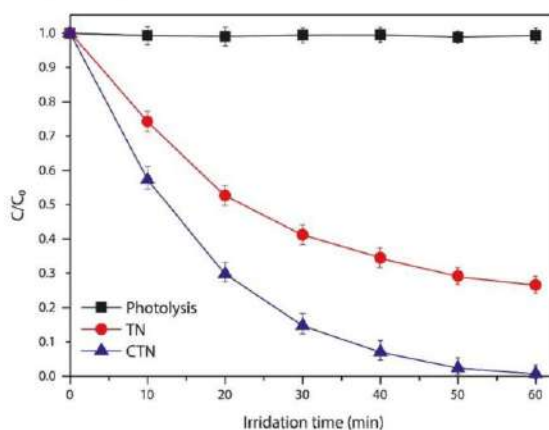


**Figure 12.** Photocatalytic degradation of RhB dye with UVA irradiation by un-doped (TN) and Cr-decorated photoanodes. Reprinted with the permission from reference [31].

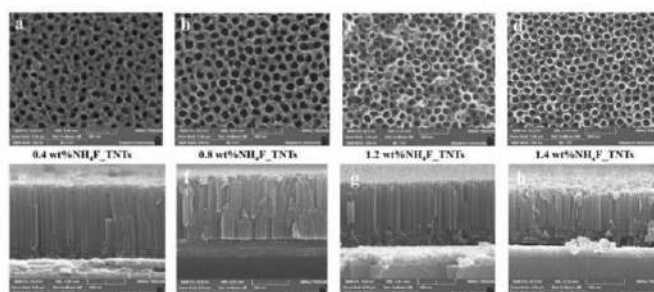


**Figure 13.** SEM images of as-prepared TNTs grown onto ITO. (a–d) Top view images for: (a) 0.4 wt%  $\text{NH}_4\text{F}$ ; (b) 0.8 wt%  $\text{NH}_4\text{F}$ ; (c) 1.2 wt%  $\text{NH}_4\text{F}$ ; (d) 1.4 wt%  $\text{NH}_4\text{F}$ . (e–h) Cross-section images for: (e) 0.4 wt%  $\text{NH}_4\text{F}$ ; (f) 0.8 wt%  $\text{NH}_4\text{F}$ ; (g) 1.2 wt%  $\text{NH}_4\text{F}$ ; (h) 1.4 wt%  $\text{NH}_4\text{F}$ . Reprinted from reference [30] under license CC BY 4.0.

**Table 2.** Average diameter, length and photo-electron conversion efficiencies ( $\eta$ ) of as-prepared TNTs under different conditions. Reprinted from Aiempnanakit et al., 2020, under license CC BY 4.0.

Condition	Diameter (nm)	Length (nm)	$\eta$ (%)
0.4 wt% $\text{NH}_4\text{F}$	$37.4 \pm 4.5$	$961.5 \pm 14.3$	0.17
0.8 wt% $\text{NH}_4\text{F}$	$48.2 \pm 5.1$	$848.8 \pm 19.9$	0.28
1.2 wt% $\text{NH}_4\text{F}$	$51.0 \pm 4.5$	$818.5 \pm 17.1$	0.40
1.4 wt% $\text{NH}_4\text{F}$	$49.2 \pm 4.2$	$575.1 \pm 22.4$	0.29



The results indicate that 1.2 wt% is the optimal amount of fluorine salt to achieve the highest photo-electron conversion efficiency. The solar energy-to-electricity conversion efficiency rises linearly with increasing tube diameter, while it decreases with the NTs length when it exceeds 818.5 nm. Indeed, the tube diameters have significant influence on the surface properties i.e., roughness factor and porosity of the materials. Their play a major role on both the infiltration of both the dye solution and the redox electrolyte hence, affecting the overall efficiency of dye-sensitized solar cells [7]. Kathirvel et al. [24] prepared a photoanode based on TNTs grown on FTO via anodization of Ti film in EG solution containing 0.3 wt%  $\text{NH}_4\text{F}$  and 2 vol% water. The anodized material was annealed at 450 °C for 3 h, and the fabricated DSSC exhibits a conversion efficiency of 1.9%. Then, the authors studied the effect of TNTs surface modification using  $\text{TiCl}_4$  post-treatment on the conversion efficiency. For this purpose the prepared TNTs after anodization was first immerse in 0.2 M  $\text{TiCl}_4$  bath maintained at 70 °C for 30 min, before calcination under the previous condition. An increase of the conversion efficiency to 2.59%, due to  $\text{TiCl}_4$  post-treatment was observed. Further improvement in the conversion efficiency to 2.95% was achieved by using TNTs decorated with  $\text{TiO}_2$  nanorods (TNR) though solvothermal process. Indeed, the TNR decoration of TNTs further increases its surface area and allows more dye adsorption. Figure 14 shows the I–V and IPCE curves of the fabricated DSSCs. The IPCE percentage value increases from 12 to 15% at 530 nm after the post treatment. The nanorod decorated TNTs exhibit the highest IPCE percentage value of 17% at 530 nm.

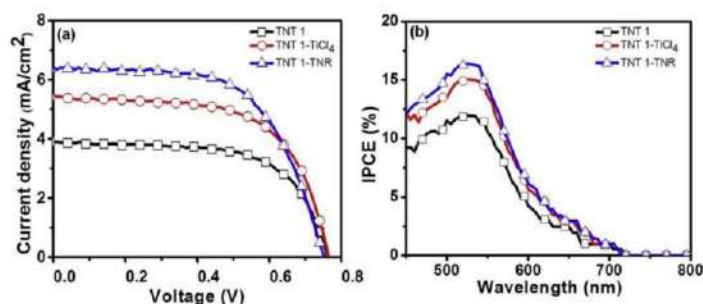


**Figure 14.** (a) Current-voltage curves; and (b) IPCE curves of fabricated DSSCs by using TNTs before and after  $\text{TiCl}_4$  treatment and  $\text{TiO}_2$  nanorods decoration as photoanodes. Reprinted with the permission from reference [24].

Up to now, the best conversion efficiency of DSSC is 14%, and was reported by Kakiage et al. [67]. The photoanode was fabricated by coating FTO with  $\text{TiO}_2$  nanoparticle film, followed by sintering the obtained material at 450 °C. In spite of the efforts made to improve the conversion efficiency of TNTs-based photoanode, only 6.9% has been reached [8]. Considerable efforts still need to be done to improve its performance. Another approach consisting of the anodization of Ti film sputter coated on TCO-coated polymer sheet (plastic) instead of the conventional TCO has been explored by Galstyan et al. [68] to fabricate DSSC with a photoconversion efficiency of 3.31%. This early achievement prompted optimization of the geometry of TNTs directly grown on plastic substrates. Polymer films such as poly (4,4'-oxydiphenylene-pyromellitimide) that is a mixture of two monomers i.e., pyromellitic dianhydride and oxydiphenylene diamine known as Kapton type HN or Kapton type E, which is a mix of pyromellitic dianhydride and biphenyltetracarboxylic acid dianhydride, have been investigated due to their relatively high glass transition temperature  $T_g > 360$  °C [68]. This allows the further annealing of the anodized material at 360 °C to obtain TNTs anatase phase. Vomiero et al. [69] anodized Ti deposited on Kapton HN polyimide sheet in glycerol (GI) bath containing 0.5 wt%  $\text{NH}_4\text{F}$  and 2 M  $\text{H}_2\text{O}$  and the prepared photoanode without calcination exhibited a conversion efficiency of 0.5% which is higher than those obtained by Aiempnakit et al. [30] (0.4%) and Elsanousi et al. [70] (0.43%) by

using calcined TNTs grown on TCO. The performance of the prepared material was further improved by annealing the anodized material at 350 °C for 5 h. A crack-free TNTs layer was obtained over the Kapton substrate with an average length of 6 µm. Constructed DSSC exhibits a photoconversion efficiency of 3.5%, which is an increase of a factor of 7 with respect to its initial value. However, exposing a polymer film at 350 °C for 5 h may affect its mechanical properties. Promising alternative to achieve the crystallization by solvothermal process was proposed by Vadla et al. [71]. Indeed, the solvothermal process allows the crystallization of the materials at temperature at ca. 200 °C as compared to the calcination in air occurring between 350–500 °C. Recently reported morphological characteristics of TNTs grown on TCO or polymer substrates and their conversion efficiency are presented in the Table 3.

**Table 3.** Average diameter, length and solar energy-to-electricity conversion efficiency ( $\eta$ ) of TNTs grown on TCO or polymer substrates.

Electrolyte	Substrate	Length/ $\mu$ m	Tube Diameter/nm	$\eta$ /%	Reference
EG + 0.5 wt% $\text{NH}_4\text{F}$ + 0.2 wt% $\text{H}_2\text{O}$	Kapton	1.4	51	-	[58]
EG + 0.5 wt% $\text{NH}_4\text{F}$ + 0.2 wt% $\text{H}_2\text{O}$	Spinel	1.1	57	-	[58]
EG + 0.5 wt% $\text{NH}_4\text{F}$ + 4 wt% $\text{H}_2\text{O}$	Kapton	1.5	80	-	[71]
EG + 0.4 wt% $\text{NH}_4\text{F}$ + 2 wt% $\text{H}_2\text{O}$	ITO	0.8	51	0.4	[30]
EG + 0.5 wt% $\text{NH}_4\text{F}$ + 3 wt% $\text{H}_2\text{O}$ + 0.5 wt% $\text{H}_3\text{PO}_4$	ITO	0.75	-	0.5	[16]
EG + 0.135 M $\text{NH}_4\text{F}$ + 1.75 vol% $\text{H}_2\text{O}$	FTO	10.4	-	-	[27]
EG + 3 M $\text{NH}_4\text{F}$ + 2 vol% $\text{H}_2\text{O}$	FTO	1.6	70	-	[72]
EG + 0.3 wt% $\text{NH}_4\text{F}$ + 2 wt% $\text{H}_2\text{O}$	FTO	2	60	-	[4]
EG + 0.2 M $\text{NH}_4\text{F}$ + 4 M $\text{H}_2\text{O}$	FTO	2.4	-	-	[1]
EG + 0.3 wt% $\text{NH}_4\text{F}$ + 2 vol% $\text{H}_2\text{O}$	FTO	2	-	2.95	[24]
EG + 0.1 wt% $\text{NH}_4\text{HF}_2$	FTO	12.5	119	-	[73]
EG + 1.5 wt% $\text{NH}_4\text{F}$	Glass	0.4	60	0.43	[70]
EG + 0.3 wt% $\text{NH}_4\text{F}$ + 4 vol% $\text{H}_2\text{O}$	Kapton	5.1	-	-	[74]
GI + 1 wt% $\text{NH}_4\text{F}$ + 1 M $\text{H}_2\text{O}$	Kapton	5	120	3.31	[68]
GI + 0.5 wt% $\text{NH}_4\text{F}$ + 2 M $\text{H}_2\text{O}$	Kapton	6	-	3.5	[69]
DMSO + 2 vol% HF + 4 vol% $\text{H}_2\text{O}$	FTO	20	95	6.9	[8]

The morphological characteristics of TNTs play a major role in the light absorption properties of the material, thus affecting the efficiency of solar cells. For example, Varghese et al. [8] studied the influence of the thickness of the TNTs layers on the incident photon to current conversion efficiencies. For this, the IPCE values of different thicknesses of layers of titanium nanotubes (2.8 to 20 µm) grown on FTO were compared. Their results indicated that the highest IPCE value was obtained with the 20 µm thick nanotube layer. This suggests that the light absorption properties of TNTs-based materials can be improved by increasing the length of the nanotubes. However, the use of thicker titanium nanostructured materials will inevitably cause both the loss of the photoelectrode semitransparency and the increase the internal resistance of solar cells [75]. Moreover, Lynch et al. [5] pointed out that above a titania layer of 5.5 µm thick, the absorption of photons is not sufficient to compensate for the extra losses that occur within longer tubes due to high recombination of electron-hole pairs. Obviously, there is a need to optimize the geometrical features of TNT-based photoelectrodes in order to improve the efficiency of solar cells. In general, the low efficiency of TNT-based DSSCs is due to the extraction losses owing to the high recombination of charge carriers and the optical losses due to both the non-absorption of low-energy photons and the thermalization losses due to absorption of high-energy photons [3]. The active surface of the photoelectrode plays an important role in both the absorption and charge transport properties of the material. Hence, different strategies have been proposed to improve the solar cell efficiency through modification of the TNTs morphology. For example,  $\text{TiCl}_4$  pre- and post-treatments have been suggested to improve the surface properties of the semitransparent materials, thereby increasing the dye loading on the active surface [76]. Moreover, it has been reported that  $\text{TiCl}_4$  post-treatment can increase the electron transfer efficiency and reduce charge recombination [77]. In order



to further improve the solar-to-electricity conversion efficiency of TNT-based photoanodes works should be focused on the synthesis of double-sided photoactive materials prepared by developing TNTs onto both sides of the TCO, or polymer substrates. Such strategy provides increased active surface area of the material. Promising results have been already reported by Chen et al. [78]. Indeed, the TNTs grown on both sides of the substrate can be sensitized by dye molecules. Therefore, the double-sided transparent electrodes (TNTs/TCO/TNTs) can increase the loading amount of dye as compared to the single-sided one (TCO/TNTs). Chen et al. [78] prepared a solar cell by using a double-sided CdS-sensitized TNTs/ITO/TNTs as photoanode. Their results indicated that the fabricated solar cell achieved a photoconversion efficiency of 7.5% under illumination ( $100 \text{ mW/cm}^2$ ). Although the work of Chen et al. [78] is encouraging, the use of double-sided transparent electrodes in DSSCs requires counter electrodes placed on each side of the photoelectrode, and these counter electrodes can absorb a lot of light (at least compared to single-sided electrodes) and thereby reducing the efficiency. Additional efforts still need to be made to improve the light-harvesting performances of the double-sided transparent photoelectrodes through the optimization of their structural properties, that could eventually lead to practical environmental and energy applications.

## 6. Conclusions

TNTs formed out on TCO via anodization have gained much interest during the past decades due to their good performance in light-harvesting. The good mechanical and thermal properties of TCO combined with the outstanding photocatalytic activity of  $\text{TiO}_2$  rendering those functional materials capable to address social challenges, including both environmental and energy production applications. In general, three ways are investigated to improve the conversion efficiency of those photoelectrodes. The first one is to increase the specific surface area of the used materials. For this, the available internal surface in the hollow of TNTs is an advantage. Moreover, the geometry and especially total surface area of TNTs can be optimized by adjusting the anodization parameters. The second way is to minimize the recombination of photogenerated electron-hole. For this objective, additional to highly ordered and vertically oriented nanotubes that increase the electron diffusion length, the  $\text{TiO}_2$ /TCO interface can be explored due to the difference of the conduction band levels of  $\text{TiO}_2$  and TCO. Last, the photo-responsiveness TNTs-based materials can be broaden to visible range through heteroatom-decoration on the tubes walls and inside the hollow as well. In this contribution, recent research progress of TNTs grown on TCO in photocatalyst and photovoltaic applications are summarized. Overall, considerable efforts have been devoted in the synthesis of TNTs formed onto the TCO and the improvement of their photoconversion efficiency. Along with the low solar-conversion efficiency, the long term stability i.e., the operating lifetime of TNTs-based photoactive materials remains an issue of concern. Therefore, studies must focus on the improvement of the adhesion of TNTs to the TCO or polymer substrates. The geometrical features of the developed TNTs including the tube length, wall thickness, tube diameter, and tube-to-tube spacing play an important role in light scattering and transporting photogenerated charge carriers. A clear and convincing model must be developed to explain the anodic oxidation growth mechanism of TNTs, which could allow a good control over its morphological characteristics.

**Author Contributions:** Conceptualization, K.S., K.G. and D.-S.K.; methodology, D.-S.K.; validation, K.S. and K.G.; formal analysis, D.-S.K.; investigation, K.S.; resources, K.S.; writing—original draft preparation, K.S., K.G. and D.-S.K.; visualization, D.-S.K.; supervision, K.S. and K.G.; project administration, K.S.; funding acquisition, K.S. All authors have read and agreed to the published version of the manuscript.

**Funding:** This research was funded by the National Science Centre, Poland, grant number 2020/02/Y/ST8/00030.

**Institutional Review Board Statement:** Not applicable.

**Informed Consent Statement:** Not applicable.

**Data Availability Statement:** No new data were created or analyzed in this study. Data sharing is not applicable to this article.

**Acknowledgments:** Authors acknowledge the financial support received from the National Science Center, Poland via grant no. 2020/02/Y/ST8/00030.

**Conflicts of Interest:** The authors declare no conflict of interest.

## References

1. Paušová, Š.; Kment, Š.; Zlámal, M.; Baudys, M.; Hubička, Z.; Krýsa, J. Transparent Nanotubular TiO<sub>2</sub> Photoanodes Grown Directly on FTO Substrates. *Molecules* **2017**, *22*, 775. [CrossRef] [PubMed]
2. Kabir, E.; Kumar, P.; Kumar, S.; Adelodun, A.A.; Kim, K.-H. Solar energy: Potential and future prospects. *Renew. Sustain. Energy Rev.* **2018**, *82*, 894–900. [CrossRef]
3. Day, J.; Senthilarasu, S.; Mallick, T.K. Improving spectral modification for applications in solar cells: A review. *Renew. Energy* **2019**, *132*, 186–205. [CrossRef]
4. Bjelajac, A.; Petrović, R.; Djokic, V.; Matolin, V.; Vondraček, M.; Dembele, K.; Moldovan, S.; Ersen, O.; Socol, G.; Mihailescu, I.N.; et al. Enhanced absorption of TiO<sub>2</sub> nanotubes by N-doping and CdS quantum dots sensitization: Insight into the structure. *RSC Adv.* **2018**, *8*, 35073–35082. [CrossRef]
5. Lynch, R.P.; Ghicov, A.; Schmuki, P. A Photo-Electrochemical Investigation of Self-Organized TiO<sub>2</sub> Nanotubes. *J. Electrochem. Soc.* **2010**, *157*, G76. [CrossRef]
6. Roy, P.; Kim, D.; Lee, K.; Spiecker, E.; Schmuki, P. TiO<sub>2</sub> nanotubes and their application in dye-sensitized solar cells. *Nanoscale* **2010**, *2*, 45–59. [CrossRef]
7. Sun, L.; Zhang, S.; Sun, X.; He, X. Effect of the Geometry of the Anodized Titania Nanotube Array on the Performance of Dye-Sensitized Solar Cells. *J. Nanosci. Nanotechnol.* **2010**, *10*, 4551–4561. [CrossRef]
8. Varghese, O.K.; Paulose, M.; Grimes, C.A. Long vertically aligned titania nanotubes on transparent conducting oxide for highly efficient solar cells. *Nat. Nanotechnol.* **2009**, *4*, 592–597. [CrossRef]
9. Bjelajac, A.; Petrović, R.; Vujanec, J.; Veltruska, K.; Matolin, V.; Siketic, Z.; Provatas, G.; Jaksic, M.; Stan, G.E.; Socol, G.; et al. Sn-doped TiO<sub>2</sub> nanotubular thin film for photocatalytic degradation of methyl orange dye. *J. Phys. Chem. Solids* **2020**, *147*, 109609. [CrossRef]
10. Huang, L.; Guo, Y.; Peng, Z.; Porter, A.L. Characterising a technology development at the stage of early emerging applications: Nanomaterial-enhanced biosensors. *Technol. Anal. Strateg. Manag.* **2011**, *23*, 527–544. [CrossRef]
11. Rafique, M.; Tahir, M.B.; Rafique, M.S.; Hamza, M. History and fundamentals of nanoscience and nanotechnology. In *Nanotechnology and Photocatalysis for Environmental Applications*; Elsevier: Amsterdam, The Netherlands, 2020; pp. 1–25.
12. Mavridi-Printezi, A.; Menichetti, A.; Guernelli, M.; Montalti, M. Frontispiece: The Photophysics and Photochemistry of Melanin-Like Nanomaterials Depend on Morphology and Structure. *Chem. A Eur. J.* **2021**, *27*, 16309–16319. [CrossRef] [PubMed]
13. Wang, S.; Feng, S.K.; Chen, C.; Liao, B.; Zhong, Z.H.; Li, P.; Cao, L.F. Size effects on tensile properties and deformation mechanism of commercial pure tantalum foils. *Int. J. Refract. Met. Hard Mater.* **2019**, *80*, 161–173. [CrossRef]
14. Boscarino, S.; Crupi, I.; Mirabella, S.; Simone, F.; Terrasi, A. TCO/Ag/TCO transparent electrodes for solar cells application. *Appl. Phys. A* **2014**, *116*, 1287–1291. [CrossRef]
15. Abuelwafa, A.A.; El-sadek, M.S.A.; Elnobi, S.; Soga, T. Effect of transparent conducting substrates on the structure and optical properties of tin (II) oxide (SnO) thin films: Comparative study. *Ceram. Int.* **2021**, *47*, 13510–13518. [CrossRef]
16. Buttner, P.; Döhler, D.; Korenko, S.; Möhrlein, S.; Bochmann, S.; Vogel, N.; Minguez-Bacho, I.; Bachmann, J. Solid state interdigitated Sb<sub>2</sub>S<sub>3</sub> based TiO<sub>2</sub> nanotube solar cells. *RSC Adv.* **2020**, *10*, 28225–28231. [CrossRef]
17. Sadek, A.Z.; Zheng, H.; Latham, K.; Wlodarski, W.; Kalantar-zadeh, K. Anodization of Ti Thin Film Deposited on ITO. *Langmuir* **2009**, *25*, 509–514. [CrossRef] [PubMed]
18. Bhuvanewari, S.; Seetha, M.; Chandrasekaran, J.; Marnadu, R.; Masuda, Y.; Aldossary, O.M.; Ubaidullah, M. Fabrication and characterization of p-Si/n-In<sub>2</sub>O<sub>3</sub> and p-Si/n-ITO junction diodes for optoelectronic device applications. *Surf. Interfaces* **2021**, *23*, 100992. [CrossRef]
19. Tian, J.; Xu, C.; Cui, S.; Ma, L.; Fu, Y. A Photonic Crystal Fiber-Based Biosensor with Quasi-D-shaped Layout and ITO-Graphene Combination. *Plasmonics* **2021**, *16*, 1451–1460. [CrossRef]
20. Hsiao, P.-T.; Liou, Y.-J.; Teng, H. Electron Transport Patterns in TiO<sub>2</sub> Nanotube Arrays Based Dye-Sensitized Solar Cells under Frontside and Backside Illuminations. *J. Phys. Chem. C* **2011**, *115*, 15018–15024. [CrossRef]
21. Kim, M.; Yun, H.-G.; Jang, L.-W.; Jeon, D.-W.; Kang, M.G.; Yoon, J.-H.; Kim, J.-M.; Park, J.H.; Lee, I.-H.; Kim, J.J. Promising efficiency enhancement in cobalt redox couple-based back-illuminated dye-sensitized solar cells with titanium foil substrate. *J. Power Sources* **2015**, *278*, 32–37. [CrossRef]
22. Zhong, P.; Que, W.; Chen, J.; Hu, X. Elucidating the role of ultrathin Pt film in back-illuminated dye-sensitized solar cells using anodic TiO<sub>2</sub> nanotube arrays. *J. Power Sources* **2012**, *210*, 38–41. [CrossRef]
23. Wang, H.; Li, H.; Wang, J.; Wu, J. High aspect-ratio transparent highly ordered titanium dioxide nanotube arrays and their performance in dye sensitized solar cells. *Mater. Lett.* **2012**, *80*, 99–102. [CrossRef]



24. Kathirvel, S.; Su, C.; Yang, C.-Y.; Shiao, Y.-J.; Chen, B.-R.; Li, W.-R. The growth of TiO<sub>2</sub> nanotubes from sputter-deposited Ti film on transparent conducting glass for photovoltaic applications. *Vacuum* **2015**, *118*, 17–25. [\[CrossRef\]](#)
25. Lin, C.-J.; Yu, W.-Y.; Chien, S.-H. Transparent electrodes of ordered opened-end TiO<sub>2</sub>-nanotube arrays for highly efficient dye-sensitized solar cells. *J. Mater. Chem.* **2010**, *20*, 1073–1077. [\[CrossRef\]](#)
26. Lamberti, A.; Sacco, A.; Bianco, S.; Manfredi, D.; Armandi, M.; Quaglio, M.; Tresso, E.; Pirri, C.F. An easy approach for the fabrication of TiO<sub>2</sub> nanotube-based transparent photoanodes for Dye-sensitized Solar Cells. *Sol. Energy* **2013**, *95*, 90–98. [\[CrossRef\]](#)
27. Kim, J.Y.; Noh, J.H.; Zhu, K.; Halverson, A.F.; Neale, N.R.; Park, S.; Hong, K.S.; Frank, A.J. General Strategy for Fabricating Transparent TiO<sub>2</sub> Nanotube Arrays for Dye-Sensitized Photoelectrodes: Illumination Geometry and Transport Properties. *ACS Nano* **2011**, *5*, 2647–2656. [\[CrossRef\]](#)
28. Zelny, M.; Kment, S.; Ctvrtlik, R.; Pausova, S.; Kmentova, H.; Tomastik, J.; Hubicka, Z.; Rambabu, Y.; Krysa, J.; Naldoni, A.; et al. TiO<sub>2</sub> Nanotubes on Transparent Substrates: Control of Film Microstructure and Photoelectrochemical Water Splitting Performance. *Catalysts* **2018**, *8*, 25. [\[CrossRef\]](#)
29. Kumi-Barimah, E.; Penhale-Jones, R.; Salimian, A.; Upadhyaya, H.; Hasnath, A.; Jose, G. Phase evolution, morphological, optical and electrical properties of femtosecond pulsed laser deposited TiO<sub>2</sub> thin films. *Sci. Rep.* **2020**, *10*, 10144. [\[CrossRef\]](#)
30. Aiempnakit, M. Fabrication of Titanium Dioxide Nanotubes and their Photovoltaic Performance for Dye-sensitized Solar Cells. *Int. J. Electrochem. Sci.* **2020**, *15*, 10392–10405. [\[CrossRef\]](#)
31. Çırak, B.B. Fabrication and characterization of transparent Cr-decorated TiO<sub>2</sub> nanoporous electrode for enhanced photo-electrocatalytic performance. *Vacuum* **2020**, *177*, 109375. [\[CrossRef\]](#)
32. Krumpmann, A.; Dervaux, J.; Derue, L.; Douhéret, O.; Lazzaroni, R.; Snyders, R.; Decroly, A. Influence of a sputtered compact TiO<sub>2</sub> layer on the properties of TiO<sub>2</sub> nanotube photoanodes for solid-state DSSCs. *Mater. Des.* **2017**, *120*, 298–306. [\[CrossRef\]](#)
33. Krysa, J.; Lee, K.; Pausova, S.; Kment, S.; Hubicka, Z.; Ctvrtlik, R.; Schmuki, P. Self-organized transparent 1D TiO<sub>2</sub> nanotubular photoelectrodes grown by anodization of sputtered and evaporated Ti layers: A comparative photoelectrochemical study. *Chem. Eng. J.* **2017**, *308*, 745–753. [\[CrossRef\]](#)
34. Agarwal, R.; Himanshu; Patel, S.L.; Chander, S.; Ameta, C.; Dhaka, M.S. Vacuum annealing level evolution of titania thin films: Functionality as potential optical window in solar cells. *Mater. Lett.* **2020**, *277*, 128368. [\[CrossRef\]](#)
35. Zhukova, Y.; Hiepen, C.; Knaus, P.; Osterland, M.; Prohaska, S.; Dunlop, J.W.C.; Fratzl, P.; Skorb, E.V. The Role of Titanium Surface Nanostructuring on Preosteoblast Morphology, Adhesion, and Migration. *Adv. Healthc. Mater.* **2017**, *6*, 1601244. [\[CrossRef\]](#) [\[PubMed\]](#)
36. Kadri, L.; Bulai, G.; Carlescu, A.; George, S.; Gurlui, S.; Leontie, L.; Doroftei, C.; Adnane, M. Effect of Target Sintering Temperature on the Morphological and Optical Properties of Pulsed Laser Deposited TiO<sub>2</sub> Thin Films. *Coatings* **2021**, *11*, 561. [\[CrossRef\]](#)
37. David, T.M.; Dev, P.R.; Wilson, P.; Sagayaraj, P.; Mathews, T. A critical review on the variations in anodization parameters toward microstructural formation of TiO<sub>2</sub> nanotubes. *Electrochem. Sci. Adv.* **2021**, e202100083. [\[CrossRef\]](#)
38. Chong, B.; Yu, D.; Jin, R.; Wang, Y.; Li, D.; Song, Y.; Gao, M.; Zhu, X. Theoretical derivation of anodizing current and comparison between fitted curves and measured curves under different conditions. *Nanotechnology* **2015**, *26*, 145603. [\[CrossRef\]](#)
39. Hoar, T.P.; Mott, N.F. A mechanism for the formation of porous anodic oxide films on aluminium. *J. Phys. Chem. Solids* **1959**, *9*, 97–99. [\[CrossRef\]](#)
40. Shahzad, K.; Tsuji, E.; Aoki, Y.; Nagata, S.; Habazaki, H. Formation and field-assisted dissolution of anodic films on iron in fluoride-containing organic electrolyte. *Electrochim. Acta* **2015**, *151*, 363–369. [\[CrossRef\]](#)
41. Fu, Y.; Mo, A. A Review on the Electrochemically Self-organized Titania Nanotube Arrays: Synthesis, Modifications, and Biomedical Applications. *Nanoscale Res. Lett.* **2018**, *13*, 187. [\[CrossRef\]](#)
42. Liu, G.; Wang, K.; Hoivik, N.; Jakobsen, H. Progress on free-standing and flow-through TiO<sub>2</sub> nanotube membranes. *Sol. Energy Mater. Sol. Cells* **2012**, *98*, 24–38. [\[CrossRef\]](#)
43. Gong, T.; Li, C.; Li, X.; Yue, H.; Zhu, X.; Zhao, Z.; Lv, R.; Zhu, J. Evidence of oxygen bubbles forming nanotube embryos in porous anodic oxides. *Nanoscale Adv.* **2021**, *3*, 4659–4668. [\[CrossRef\]](#)
44. Fahim, N.F.; Sekino, T.; Morks, M.F.; Kusunose, T. Electrochemical Growth of Vertically-Oriented High Aspect Ratio Titania Nanotubes by Rapid Anodization in Fluoride-Free Media. *J. Nanosci. Nanotechnol.* **2009**, *9*, 1803–1818. [\[CrossRef\]](#) [\[PubMed\]](#)
45. Lu, N.; Zhang, J.; Dan, Y.; Sun, M.; Gong, T.; Li, X.; Zhu, X. Growth of porous anodic TiO<sub>2</sub> in silver nitrate solution without fluoride: Evidence against the field-assisted dissolution reactions of fluoride ions. *Electrochem. Commun.* **2021**, *126*, 107022. [\[CrossRef\]](#)
46. Zhou, Q.; Tian, M.; Ying, Z.; Dan, Y.; Tang, F.; Zhang, J.; Zhu, J.; Zhu, X. Dense films formed during Ti anodization in NH<sub>4</sub>F electrolyte: Evidence against the field-assisted dissolution reactions of fluoride ions. *Electrochem. Commun.* **2020**, *111*, 106663. [\[CrossRef\]](#)
47. Zhou, Q.; Niu, D.; Feng, X.; Wang, A.; Ying, Z.; Zhang, J.; Lu, N.; Zhu, J.; Zhu, X. Debunking the effect of water content on anodizing current: Evidence against the traditional dissolution theory. *Electrochem. Commun.* **2020**, *119*, 106815. [\[CrossRef\]](#)
48. Yu, M.; Chen, Y.; Li, C.; Yan, S.; Cui, H.; Zhu, X.; Kong, J. Studies of oxide growth location on anodization of Al and Ti provide evidence against the field-assisted dissolution and field-assisted ejection theories. *Electrochem. Commun.* **2018**, *87*, 76–80. [\[CrossRef\]](#)
49. Yu, M.; Cui, H.; Ai, F.; Jiang, L.; Kong, J.; Zhu, X. Terminated nanotubes: Evidence against the dissolution equilibrium theory. *Electrochem. Commun.* **2018**, *86*, 80–84. [\[CrossRef\]](#)
50. Qin, S.; Wu, L.; Zhang, J.; Han, Y.; Zheng, H.; Ma, J.; Ma, W. A novel elaboration for various morphologies of three-layer TiO<sub>2</sub> nanotubes by oxygen bubble mould. *Mater. Res. Bull.* **2018**, *106*, 220–227. [\[CrossRef\]](#)

51. LeClere, D.J.; Velota, A.; Skeldon, P.; Thompson, G.E.; Berger, S.; Kunze, J.; Schmuki, P.; Habazaki, H.; Nagata, S. Tracer Investigation of Pore Formation in Anodic Titania. *J. Electrochem. Soc.* **2008**, *155*, C487. [\[CrossRef\]](#)
52. Huang, W.; Xu, H.; Ying, Z.; Dan, Y.; Zhou, Q.; Zhang, J.; Zhu, X. Split TiO<sub>2</sub> nanotubes- Evidence of oxygen evolution during Ti anodization. *Electrochim. Commun.* **2019**, *106*, 106532. [\[CrossRef\]](#)
53. Zhang, Z.; Liu, Q.; He, M.; Tang, F.; Ying, Z.; Xu, H.; Song, Y.; Zhu, J.; Zhu, X. Quantitative Analysis of Oxide Growth During Ti Galvanostatic Anodization. *J. Electrochem. Soc.* **2020**, *167*, 113501. [\[CrossRef\]](#)
54. Garcia-Vergara, S.J.; Skeldon, P.; Thompson, G.E.; Habazaki, H. A flow model of porous anodic film growth on aluminium. *Electrochim. Acta* **2006**, *52*, 681–687. [\[CrossRef\]](#)
55. Capraz, Ö.Ö.; Shrotriya, P.; Skeldon, P.; Thompson, G.E.; Hebert, K.R. Role of Oxide Stress in the Initial Growth of Self-Organized Porous Aluminum Oxide. *Electrochim. Acta* **2015**, *167*, 404–411. [\[CrossRef\]](#)
56. Zhu, X.; Liu, L.; Song, Y.; Jia, H.; Xiao, X.; Yang, X. Oxygen bubble mould effect: Serrated nanopore formation and porous alumina growth. *Mon. Filt. Chem.-Chem. Mon.* **2008**, *139*, 999–1003. [\[CrossRef\]](#)
57. Zhang, W. An Oxygen-bubble-mould-effect Derived Model for Kinetics of Anodic TiO<sub>2</sub> Nanotubes under Constant Current. *J. Phys. Conf. Ser.* **2021**, *1893*, 012011. [\[CrossRef\]](#)
58. Petrisková, P.; Monfort, O.; Satrapinskyy, L.; Dobročka, E.; Plecenik, T.; Plesch, G.; Papšík, R.; Bermejo, R.; Lenčič, Z. Preparation and photocatalytic activity of TiO<sub>2</sub> nanotube arrays prepared on transparent spinel substrate. *Ceram. Int.* **2021**, *47*, 12970–12980. [\[CrossRef\]](#)
59. Shin, K.; Park, J.H. Highly Transparent Dual-Sensitized Titanium Dioxide Nanotube Arrays for Spontaneous Solar Water Splitting Tandem Configuration. *ACS Appl. Mater. Interfaces* **2015**, *7*, 18429–18434. [\[CrossRef\]](#)
60. Zafar, Z.; Kim, J.-O. Optimization of hydrothermal synthesis of Fe-TiO<sub>2</sub> nanotube arrays for enhancement in visible light using an experimental design methodology. *Environ. Res.* **2020**, *189*, 109908. [\[CrossRef\]](#)
61. Nematollahi, R.; Ghotbi, C.; Khorasheh, F.; Larimi, A. Ni-Bi co-doped TiO<sub>2</sub> as highly visible light response nano-photocatalyst for CO<sub>2</sub> photo-reduction in a batch photo-reactor. *J. CO<sub>2</sub> Util.* **2020**, *41*, 101289. [\[CrossRef\]](#)
62. Shipochka, M.; Eliyas, A.; Stambolova, I.; Blaskov, V.; Vassilev, S.; Simeonova, S.; Balashev, K. Synthesis of TiO<sub>2</sub> on SnO<sub>2</sub> bicomponent system and investigation of its structure and photocatalytic activity. *Mater. Chem. Phys.* **2018**, *220*, 249–259. [\[CrossRef\]](#)
63. Parida, B.; Iniyani, S.; Goic, R. A review of solar photovoltaic technologies. *Renew. Sustain. Energy Rev.* **2011**, *15*, 1625–1636. [\[CrossRef\]](#)
64. Husain, A.A.F.; Hasan, W.Z.W.; Shafie, S.; Hamidon, M.N.; Pandey, S.S. A review of transparent solar photovoltaic technologies. *Renew. Sustain. Energy Rev.* **2018**, *94*, 779–791. [\[CrossRef\]](#)
65. Gong, J.; Sumathy, K.; Qiao, Q.; Zhou, Z. Review on dye-sensitized solar cells (DSSCs): Advanced techniques and research trends. *Renew. Sustain. Energy Rev.* **2017**, *68*, 234–246. [\[CrossRef\]](#)
66. Chen, L.-S.; Sil, M.C.; Chang, C.-C.; Chen, C.-M. Optimization of photoelectrode by structural engineering for efficiency improvement of dye-sensitized solar cells at different light intensity. *J. Alloys Compd.* **2021**, *870*, 159478. [\[CrossRef\]](#)
67. Kakiage, K.; Aoyama, Y.; Yano, T.; Oya, K.; Fujisawa, J.; Hanaya, M. Highly-efficient dye-sensitized solar cells with collaborative sensitization by silyl-anchor and carboxy-anchor dyes. *Chem. Commun.* **2015**, *51*, 15894–15897. [\[CrossRef\]](#) [\[PubMed\]](#)
68. Galstyan, V.; Vomiero, A.; Concina, L.; Braga, A.; Brisotto, M.; Bontempi, E.; Faglia, G.; Sberveglieri, G. Vertically Aligned TiO<sub>2</sub> Nanotubes on Plastic Substrates for Flexible Solar Cells. *Small* **2011**, *7*, 2437–2442. [\[CrossRef\]](#)
69. Vomiero, A.; Galstyan, V.; Braga, A.; Concina, L.; Brisotto, M.; Bontempi, E.; Sberveglieri, G. Flexible dye sensitized solar cells using TiO<sub>2</sub> nanotubes. *Energy Environ. Sci.* **2011**, *4*, 3408. [\[CrossRef\]](#)
70. Elsanousi, A.; Elamin, N.; Abdallah, A. Highly Ordered TiO<sub>2</sub> Nanotubes and Their Application to Dye Sensitized Solar Cells. *J. Appl. Ind. Sci.* **2013**, *1*, 39–42.
71. Vadla, S.S.; Bandyopadhyay, P.; John, S.; Ghosh, P.; Roy, S.C. TiO<sub>2</sub> Nanotube Arrays on Flexible Kapton Substrates for Photo-Electrochemical Solar Energy Conversion. *ACS Appl. Nano Mater.* **2020**, *3*, 11715–11724. [\[CrossRef\]](#)
72. Li, P.; Wang, J.; Zu, G.; Jiao, P.; Liu, S.; Yang, Y.; Chen, S.; Li, H. Synergetic catalytic properties of gold nanoparticles planted on transparent titanium dioxide nanotube array bed. *Mater. Chem. Phys.* **2018**, *217*, 437–444. [\[CrossRef\]](#)
73. Wang, J.; Wang, H.; Li, H.; Wu, J. Synthesis and characterization of TiO<sub>2</sub> nanotube film on fluorine-doped tin oxide glass. *Thin Solid Films* **2013**, *544*, 276–280. [\[CrossRef\]](#)
74. Farsinezhad, S.; Mohammadpour, A.; Dalrymple, A.N.; Geisinger, J.; Kar, P.; Brett, M.J.; Shankar, K. Transparent Anodic TiO<sub>2</sub> Nanotube Arrays on Plastic Substrates for Disposable Biosensors and Flexible Electronics. *J. Nanosci. Nanotechnol.* **2013**, *13*, 2885–2891. [\[CrossRef\]](#) [\[PubMed\]](#)
75. Zhang, Q.; Myers, D.; Lan, J.; Jenekhe, S.A.; Cao, G. Applications of light scattering in dye-sensitized solar cells. *Phys. Chem. Chem. Phys.* **2012**, *14*, 14982. [\[CrossRef\]](#) [\[PubMed\]](#)
76. Adhikari, S.G.; Shamsaldeen, A.; Andersson, G.G. The effect of TiCl<sub>4</sub> treatment on the performance of dye-sensitized solar cells. *J. Chem. Phys.* **2019**, *151*, 164704. [\[CrossRef\]](#) [\[PubMed\]](#)
77. Li, D.; Jiang, Z.; Xia, Q.; Yao, Z. Pre- or post-TiCl<sub>4</sub> treated TiO<sub>2</sub> nano-array photoanode for QDSSC: Ti<sup>3+</sup> self-doping, flat-band level and electron diffusion length. *Appl. Surf. Sci.* **2019**, *491*, 319–327. [\[CrossRef\]](#)
78. Chen, C.; Li, F.; Li, G.; Tan, F.; Li, S.; Ling, L. Double-sided transparent electrodes of TiO<sub>2</sub> nanotube arrays for highly efficient CdS quantum dot-sensitized photoelectrodes. *J. Mater. Sci.* **2014**, *49*, 1868–1874. [\[CrossRef\]](#)

## 7.2 Anodization of Ti films sputtered onto the substrate of complex geometries

### A brief overview of the article A2

#### *Introduction*

Over the past decade, research on the growth and practical application of semitransparent photoelectrodes based on anodic titania nanotubes has focused on Ti films sputtered only on one side of planar substrates. Compared with the single-sided electrode, light harvesting and conversion can take place on both sides of the double-sided planar substrate. In addition, the double-sided electrode offers a large active surface, twice that of a single-sided one, available for further functionalization. However, until now, the study of titania nanotubes grown on both sides of planar substrates is still rather inadequate.

In the previous subsection, the anodization conditions were optimized to grow well-ordered nanotube layers on one side of the planar substrate. Two optimized anodization conditions were determined. One regarding the formation of the aligned nanotubes architecture and the other ensuring fabrication of the spaced nanotubes. The objective in this subsection is the use of these optimized anodization conditions for the fabrication of the semitransparent double-sided photoelectrode, namely where both sides of the planar substrate are overgrown by the nanotubes layer.

Semitransparent double-sided electrodes were obtained by successive anodization of the sides of the planar substrate arranged in the special holder. Two symmetric electrodes consisting of aligned (signed (A)) or spaced (signed (S)) nanotubes grown on both sides of ITO-glass were synthesized. As a result samples labelled as NT(A)-ITO-NT(A) and NT(S)-ITO-NT(S) were obtained. Moreover, one asymmetric electrode material was fabricated by growth of spaced nanotubes onto one side and aligned nanotubes onto the other one. This kind of material was labelled as NT(A)-ITO-NT(S). The synthesis methods, as well as the morphologies together with the electrochemical properties of the prepared electrodes are discussed in the article A2. This approach developed in this work is unique since such arrangement has not been reported in any work before, and it also allows for the effective control of the tubular architecture on the sides of the planar substrates.

#### *Optical and structural properties*

The measure of the absorbance on the sides of the double sided materials has shown that the recorded spectra overlap for the symmetric samples (**Figure 62 (a)**).



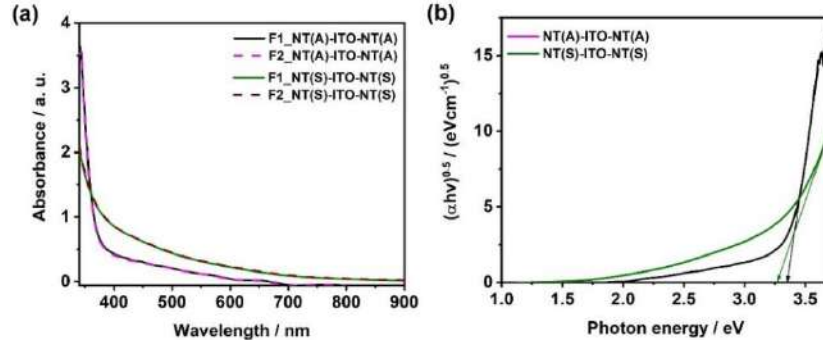


**Figure 62.** Absorption spectra of NT(A)-ITO-NT(A), NT(S)-ITO-NT(S) materials annealed at 450 °C for 1 h. (b)  $(\alpha h\nu)^{1/2}$  vs. photon energy (Reproduced from the article A2). F1 and F2 represent the sides 1 and 2, respectively of the electrodes.

The aligned NT sample exhibits high absorbance intensity in UV region. However, the absorbance intensity in the visible range of the spaced NT is relatively higher with respect to that of the aligned NT layer. The bandgaps determined on the basis of Tauc plots (**Figure 62 (b)**) for the aligned NT sample is 3.33 eV and 3.26 eV for the spaced NT.

After annealing the samples at 450 °C for 1 h, the crystallinity on the sides of the electrodes was verified in ten different places for each side of the sample (**Figure 63**).

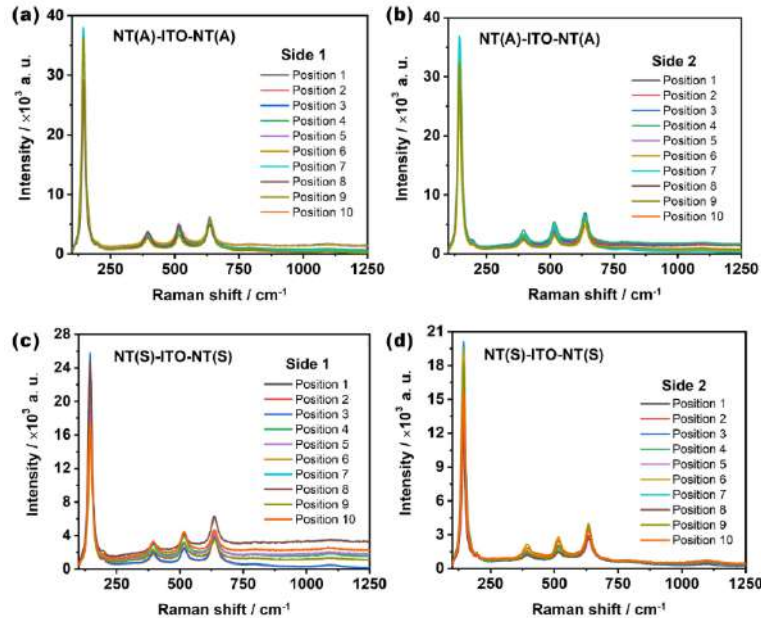


**Figure 63.** Raman spectra recorded at different positions on the (a) side 1, (b) side 2 of NT(A)-ITO-NT(A) and on the (c) side 1, (d) side 2 of NT(S)-ITO-NT(S) annealed at 450 °C for 1h.



**Figure 63** shows that the anatase is present over all the investigated anodized places. In fact, for all measurements, there are six (6) peaks in the recorded spectrum, as shown in **Figure 63**. The peaks located at 144, 197, 399, 516 and 639 $\text{cm}^{-1}$  are ascribed to  $E_{g(1)}$ ,  $E_{g(2)}$ ,  $B_{1g}$ ,  $A_{1g}+B_{1g}$  and  $E_{g(3)}$  active modes of the anatase phase of titanium dioxide.<sup>144</sup> The peak at 1050  $\text{cm}^{-1}$  results from the ITO-glass substrate.<sup>189</sup>

#### *Photoelectrochemical activity of the double-sided material*

Here, additional analysis of the linear sweep voltammetry curves is provided. The shapes of the LSV curves were examined to track the photocurrent generation of the double sided electrodes under interrupter irradiation. As was shown in article A2 for symmetric electrodes, regardless illuminated side, the generated photocurrent is nearly the same. Therefore, for each electrode only one LSV plot, shown in **Figure 64**, is considered for analysis.

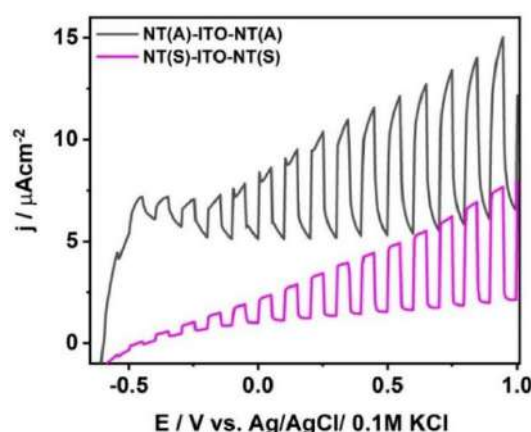


**Figure 64.** LSV curves recorded under chopped UV-vis light illumination (light/dark every 5 s) of NT(A)-ITO-NT(A) and NT(S)-ITO-NT(S).  
(Reproduced from the data collected for article A2).

For both photoelectrodes, when the light is turned on, there is a rapid increase followed by a slow raise in the photocurrent to reach their maximum values. Herein, the photocurrent response is not quasi-rectangular in shape. Such behaviour is more pronounced for the aligned nanotubes comparing the spaced one. The slow dynamic of the photocurrent to reach the steady state is associated with the presence of trap filling phenomena along the tubular layer.<sup>89,153</sup> In other words, the photogenerated electron undergoes several trapping and de-trapping processes (i.e. the trapped electron moves from one trap state to another after being detrapped) within the nanotubes before reaching the current collector. Those not desired processes hamper reaching

the maximum value of the photocurrent.<sup>190</sup> Additionally, when the light is turned off, the current recorded for the sample with spaced nanotubes drops sharply to its black current value, whereas the aligned nanotubes material exhibits a longer photocurrent tail (**Figure 64**). The occurrence of this long photocurrent tail is attributed to the slow detrapping of electrons.<sup>191</sup> This analysis of the shape of the photocurrent versus potential curve indicates that the transport of the photogenerated charge within the bare double-sided material predominantly occurs via electron hopping between localized trap states within the tubular layer.

### **Anodization of Ti film sputtered onto optical fiber**

In the first attempt, the fiber was anodized in a two-electrode setup using a platinum mesh as the cathode and the fiber as the anode. The distance between the fiber and the platinum mesh was 2 cm. The anodization was carried out in the mixture of ethylene glycol (95%) with water (5%) containing 1 M  $\text{H}_3\text{PO}_4$  and 0.27 M  $\text{NH}_4\text{F}$ , thermostated at 23 °C at the voltage of 60 V. The scheme of the experimental setup and the morphology of the anodized layer is shown in **Figure 65**.

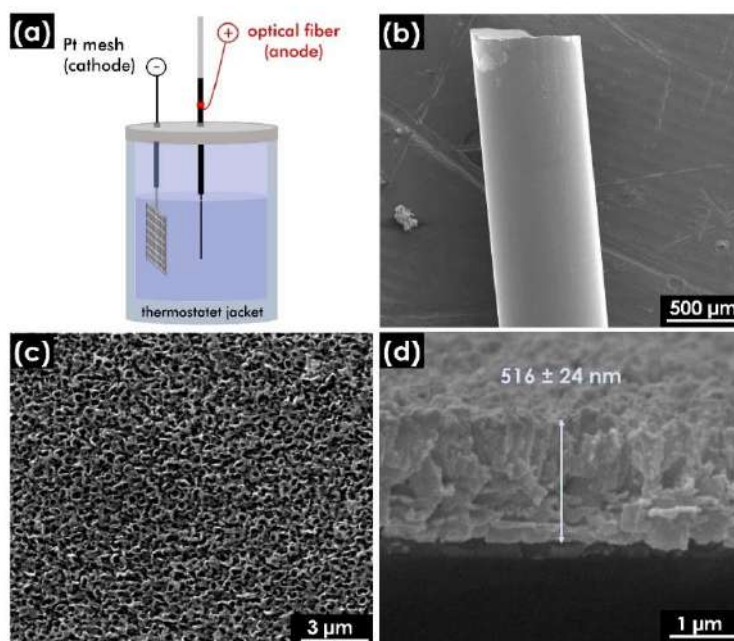


**Figure 65.** (a) Anodization setup for formation of titania nanotubes on the optical fiber (b) low resolution SEM image of the anodized region and high resolution SEM of (c) top image and (d) cross section image of the tubular oxide layer grown on the fiber.

Although a tubular layer was obtained, the top image shows an irregular morphology. The surface on top of the nanotubes is not ideally smooth, but rather looks as sponge-like, porous structure. Due to that, such nanostructure is not suitable for label-free sensing. A smooth and crack-free layer with well-open pores is required for this kind of application, according to the feedback from our partner from Warsaw University of Technology, experts in label-free optical sensing. In addition, according to Sun et al.<sup>192</sup>, the anodization of substrates with cylindrical geometry by using the traditional two electrode setup leads to a significant variation in the length of the nanotubes over the entire surface of the substrate. As illustrated in **Figure 66**, it is a consequence of the non-uniform distribution of the electric field on the surface of optical fiber substrate characterized by cylindrical geometry.<sup>192</sup> Following that, the growth rate of the nanotube gradually decreases along the surface being far from the side facing the platinum mesh, to its back.<sup>192</sup>

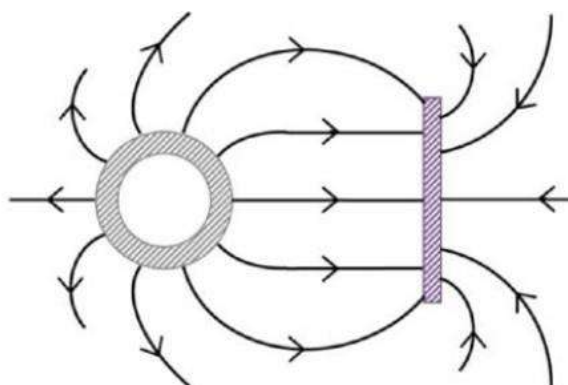


**Figure 66.** Scheme showing distribution of electric lines in the electrolyte for an anode with tubular geometry in a two electrode setup.  
(Reproduce with the permission from the reference<sup>192</sup>)

To uniform the electrochemically driven etching over the entire surface of the cylindrical fiber, another configuration, but still very simple was proposed. This time the fiber was placed in the center between two platinum meshes. In this configuration, the distance between the two platinum meshes was optimized to obtain the tubular morphology. Indeed, when the Pt meshes were relatively close to the fiber, any tubular nanostructure was obtained due to a strong chemical dissolution of the oxide layer. For each anodization trial, the distance between the Pt meshes are given in **Table 7**, while the scheme of the anodization setup together with SEM images are presented in **Figure 67**.

**Table 7.** Distance between the Pt meshes and the description of the morphology obtained for each anodized sample.

electrode	distance between Pt meshes / cm	obtained morphology
Fiber 1	2	porous layer
Fiber 2	2.5	porous layer
Fiber 3	3	porous layer
Fiber 4	3.5	tubular layer

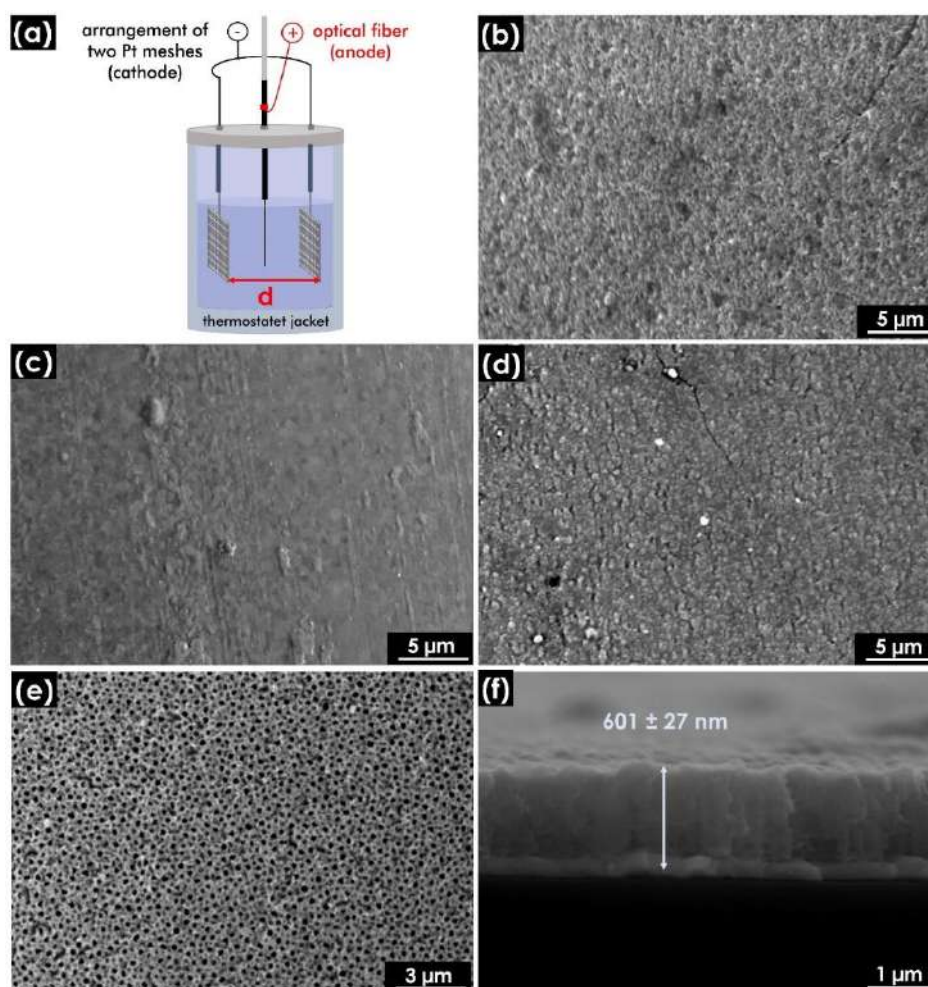


**Figure 67** (a) Experimental setup arrangement using two platinum meshes as the cathode dedicated for the anodization of the optical fiber. SEM images of the sample anodized using two platinum meshes being at the distance of (b) 2 cm (c) 2.5 cm (d) 3 cm (e) 3.5 cm. (f) Corresponding cross section image of the tubular layer obtained when the platinum meshes were 3.5 cm far from each other.

**Figure 67 (e)** shows image of uniform and smooth top of the fabricated material, which is adequate for application in label-free sensing. The tube growth as anodization proceeded was analysed through the current versus time profile depicted in **Figure 68**.

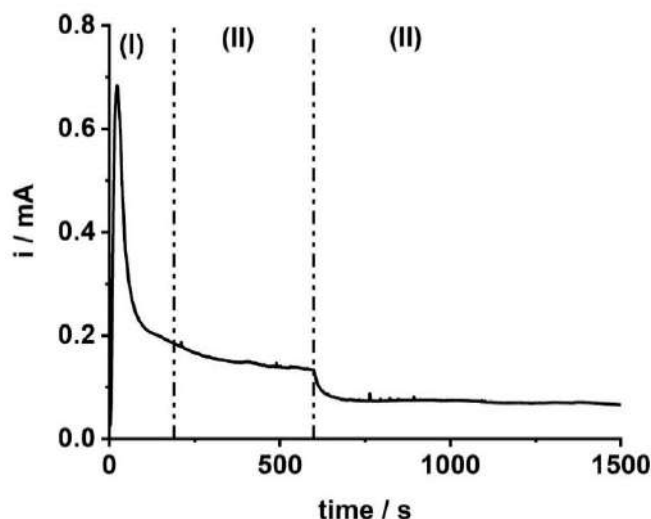


**Figure 68.** Current-time plot registered during anodization of Ti film deposited onto the optical fiber.

The current-time (i-t) profile recorded during anodization is similar to those already reported for the planar titanium substrate when only one Pt mesh was used as a cathode. Three stages can be distinguished along the i-t curve. The initial sharp increase in the anodization current (in stage I) is due to the increase in the ionic current occurring due to the decomposition of the water present in the electrolyte into  $2H^+$  and  $O^{2-}$ . This increase in current is followed by a sudden drop resulting from the growth of the  $TiO_2$  oxide barrier layer. In the stage II, the current undergoes a slow decrease to a steady state, followed by another sharp drop in current due to the continued growth of the oxide layer. The slow decrease in the current observed at this stage is due to the formation of pores within the oxide barrier layer. Finally, the current (in the stage III) reaches a steady state resulting from some kind of the competition between anodic oxide formation and chemical dissolution of the oxide as soluble fluoride complexes. Thus, in this stage the formation of the tubular morphology occurs.

#### *Optical fiber overgrown by titania nanotubes for label-free sensing*

It is well known that ITO-LMR (linear molecular resonance) i.e. optical fiber sensors make it possible to measure the refractive index of the medium. It has been observed

experimentally that when the optical fiber is covered with a Ti film, the fiber loses its sensing feature. Here, the Ti film is first sputtered onto the naked optical fiber (without cladding) and then anodized to form a semitransparent tubular oxide layer on the fiber. The objective is to study the influence of the presence of the tubular oxide layer on the detection properties of the sensor and this part was realized by the prof. Mateusz Śmietana group from Warsaw University of Technology. Herein just an example of the results collected by PhD student Emil Pitula is shown to indicate the potential application aspect. However, I would like to underline that those measurements were carried out by Mr E. Pitula and will become part of his PhD thesis. The fiber overgrown by the nanotubes that I prepared, was tested in five liquid media of different refractive index and the results are presented in **Figure 69**.

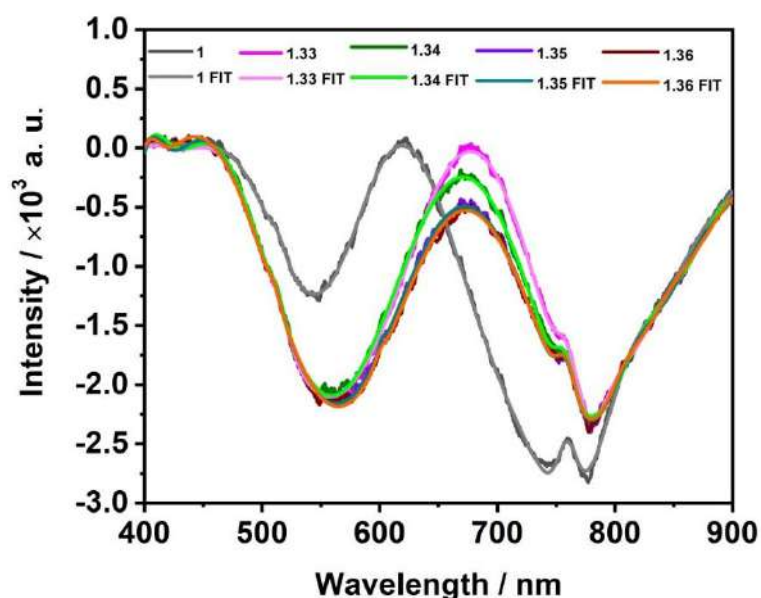


**Figure 69.** Optical measurements of the ITO-LMR sensor with nanotubes in solutions with different refractive index. (FIT: fitted curve).

Although a relatively thick tubular layer of about 500 nm was formed on the fiber, the presence of maxima is visible in the spectra recorded upon immersing the anodized part of the sensor in different liquid media. The first maxima can be clearly observed between 525 nm and 575 nm. In addition, there is an upward shift in resonance maxima with gradually increasing refractive index. The sensitivity to refractive index changes of the sensors in aqueous solutions was 260 nm/RIU. As it was mentioned, it is only a small part of the data gathered by other scientific group but it indicates the potential application of the unique coating of the optical fiber for sensing purpose.

## *Conclusion*

Aligned and spaced TNT were successfully grown on both sides of the planar substrate. Raman measurements revealed that anatase titanium oxide is present on the anodized area on both sides of the planar substrate after annealing at 450 °C for one hour. Although the spaced NT sample has a narrower bandgap (3.26 eV) compared to the aligned NT (3.33 eV), the LSV measurements indicate the larger photocurrent for the aligned NT material. This difference results from the higher amount of the photoactive material present on the surface, since in the case of the aligned arrangement more nanotubes cover particular area.

Regarding to the optical fiber, aligned titania nanotubes were grown over the whole anodized part of surface of the fibers owing to the new arrangement of traditional two-electrode anodization setup. Indeed, semitransparent uniform and smooth tubular layers were obtained by keeping the fibers at the center between two Pt meshes. Several samples were prepared using this same anodization conditions and setup configuration to check reproducibility and were sent to our partner in Warsaw University of Technology to perform label-free sensing of gases and liquids. Promising results were gathered when as-prepared fibers were used and additional tests and characterizations towards further investigations on the influence of nanotubular geometry of the optical fiber coating exhibiting different thickness on the sensing performance of the fiber are going on.

As the photoactivity of the bare semitransparent titania material is relatively low ( $4.6 \mu\text{Acm}^{-2}$ ), the modification of the tubular layer with a selected compound can raise its overall photoactivity. Before investigating the modification of the tubular layer grown onto the both sides of the planar substrate, the optimization of the surface functionalization was carried out using the single-sided electrode. Two different decorating agents were investigated in this work. First, the modification of the tubular layer with silver was explored (see subsection 7.3). The next subsection (i.e. 7.3) discusses the photoelectrochemical and electrochemical activity of semitransparent anodic aligned and spaced nanotubes formed out of TiAg film. Then, in the last subsection (see subsection 7.5), the feasibility to decorate the tubular layer with laser treated titanium carbide MXene ( $\text{Ti}_3\text{C}_2\text{T}_x$ ) was investigated as well, as a noble metal-free compound to improve the photoactivity of the metal oxide semiconductor.





## Double-sided semitransparent titania photoelectrode with enhanced light harvesting

Dujearic-Stephane Kouao<sup>a,\*</sup>, Jan Hanuš<sup>b</sup>, Ondřej Kylián<sup>b</sup>, Radka Simerova<sup>c</sup>, Petr Sezemsky<sup>c</sup>, Vitezslav Stranak<sup>c</sup>, Katarzyna Grochowska<sup>a</sup>, Katarzyna Siuzdak<sup>a</sup>

<sup>a</sup> Centre for Plasma and Laser Engineering, The Szwalski Institute of Fluid-Flow Machinery, Polish Academy of Sciences, 14 Fiszeru St, 80-231 Gdańsk, Poland

<sup>b</sup> Charles University, Faculty of Mathematics and Physics, V Holešovičkách 2, Prague 8, 180 00, Czech Republic

<sup>c</sup> University of South Bohemia, Faculty of Science, Bantsovská 1760, 37005 České Budějovice, Czech Republic

### ARTICLE INFO

#### Keywords:

Titania nanotubes  
Double-sided electrode  
ITO  
Anodizing  
Photoelectrochemical

### ABSTRACT

In this work, unique semitransparent electrodes were prepared by the anodization of titanium layers (540 nm thick) initially deposited on the both sides of glass substrates employing indium-tin oxide interface layers serving as a current collector for the induced photocurrent. The anodization strategy used in this study enables fabrication of semitransparent titanium dioxide nanotube arrays with either aligned or spaced architecture on the two sides of the planar substrate. This study aims to perform a detailed investigation of this novel photoelectrode system (crystal structure, morphology and optical properties) to reveal their photoelectrochemical features. It was found that the photoelectrode exhibits enhanced photocurrent density about 1.9 times higher ( $4.6 \mu\text{Acm}^{-2}$  at  $+0.5 \text{ V}$ ) for aligned nanotubes compared to a substrate overgrown symmetrically by separated nanotubes ( $2.4 \mu\text{Acm}^{-2}$  at  $+0.5 \text{ V}$ ). This can be effectively explained by the higher tube density in the case of aligned nanostructures, which provide more channels for charge percolation. In addition, both the high donor concentration ( $6.4 \times 10^{20} \text{ cm}^{-3}$ ) together with the low charge transfer resistance of the semitransparent electrode of the aligned nanotubes make the material promising for application in photoelectrochemical systems and smart light management.

### 1. Introduction

Photoactive semiconducting metal oxides are the vital components of a photoelectrochemical (PEC) system. Their optical and morphological properties rule both the charge carriers separation, and transport to the external circuit [1]. Among others, the nanotubular form of titania are still under intense investigation as a low-cost semiconducting material applicable in solar cells [2,3], photochromic devices [4,5], and photocatalysis [6,7]. The variety of possible applications derives not only from the properties of titania, since this material exhibits high photocorrosion resistance, photostability, and durability, but also from the unique tubular shape, which can provide facile transport of charges [8].

For the production of titania nanomaterials, many methods have been explored including hydrothermal [6], sol-gel [9], and also electrochemical routes [7]. However, most of them provide the reaction product in the form of a powder. Anodization is one of the latter routes and is considered a cost-efficient, relatively simple and highly

reproducible method, ensuring the uniformly of ordered, vertically oriented titania nanotube arrays (NT) [10]. As a substrate, titanium as a metallic foil [11], wire [12], mesh [13], or even deposited film onto a conducting substrate [14] is used while fluoride-ion-containing electrolytes provide a reactive environment. Compared to others, the reliability of the anodization method does not only lie in its effectiveness in controlling the geometric characteristics of the tube, namely the length of the tube, the wall thickness, the diameter of the pores, but also in the distribution of those hollow nanocylinders that grow out of the Ti substrate. The nanotube architecture plays an important role in the electrolyte diffusion through the tubular layer [15,16]. In general, two different tubular architectures are mostly reported, namely when nanotubes are vertically oriented and attach to each other (aligned nanotubes) or when some distance between the nanotubes (spaced nanotubes) is preserved. The spaced nanotube architecture have has the privilege to provide additional paths for the electrolyte penetration and ions storage through the active material by adjusting the gap between the tubes [17]. Related to this, spaced NT-based materials have been explored as a promising storage layer for supercapacitors [18]. In

\* Corresponding author.

E-mail address: [dkouao@imp.gda.pl](mailto:dkouao@imp.gda.pl) (D.-S. Kouao).

<https://doi.org/10.1016/j.rser.2024.114390>

Received 11 October 2022; Received in revised form 20 December 2023; Accepted 24 March 2024

Available online 28 March 2024

1364-0321/© 2024 Elsevier Ltd. All rights reserved.



Nomenclature			
<b>Abbreviation</b>			
AC	Alternating Current	$(N_D)$	Donor density [ $\text{cm}^{-3}$ ]
CV	Cyclic Voltammetry	N	Number of points in the Powell algorithm [–]
CPE	Constant phase element	$N_t$	Nanotubes per unit area [ $\text{cm}^{-2}$ ]
EIS	Electrochemical Impedance Spectroscopy	$P_M$	Parameters of the Powell algorithm [–]
ITO	Indium Tin Oxide	Q	Capacitance for $n = 1$ [ $\Omega^{-1}\text{cm}^{-2}\text{s}^n$ ]
NT	Nanotube	$r_a$	Amplitude weighting [–]
QCM	Quartz Crystal Microbalance	$r_c$	Constant parameter [–]
TCO	Transparent conducting oxide	$R_1$	Internal radius of the tube [m]
<b>Notations</b>		$R_2$	Distance between the tube centre and the centre of the tube wall [m]
FA	side overgrown with aligned nanotubes	$R_{ct}$	Charge transfer resistance at the semiconductor/electrolyte interface [ $\Omega$ ]
FS	side overgrown with spaced nanotubes	$R_s$	Series resistance [ $\Omega$ ]
F1	side 1 of the symmetric electrode	T	Temperature [K]
F2	side 2 of the symmetric electrode	$W_o$	Open Warburg element
NT(A)	aligned nanotubes	$W_{or}$	Warburg coefficient [ $\Omega\text{cm}^{-2}\text{s}^{0.5}$ ]
NT(S)	spaced nanotubes	$W_{oc}$	Warburg coefficient [ $\text{s}^{0.5}$ ]
NT-ITO-NT ITO	ITO overgrown with nanotubes on the both sides	Z	Impedance [ $\Omega$ ]
NT(A)-ITO-NT(A) ITO	ITO overgrown with aligned nanotubes on the both sides	$Z''$	Imaginary part of the impedance [ $\Omega$ ]
NT(S)-ITO-NT(S) ITO	ITO overgrown with spaced nanotubes on the both sides	$Z'$	Real part of the impedance [ $\Omega$ ]
NT(A)-ITO-NT(S)	one side of the ITO is overgrown with aligned nanotubes and the other with spaced nanotubes	y	Distance between two tubes [ $\Omega$ ]
PEC	Photoelectrochemical	<b>Subscript</b>	
UV-vis	Ultraviolet-visible	i	Corresponding measured values of impedance in the Powell algorithm
<b>Symbols and units</b>		$i_{calc}$	Corresponding calculated values of impedance in the Powell algorithm
C	Space charge capacitance [F]	<b>Superscript</b>	
e	Electron charge [C]	n	Frequency dispersion of the constant phase element
E	Applied potential [V]	<b>Greek</b>	
$E_g$	Band gap energy	$\epsilon$	Relative permittivity [–]
$E_{fb}$	Flat band potential [V]	$\epsilon_0$	Permittivity of the free space [ $\text{Fcm}^{-1}$ ]
F	Frequency of the AC signal [Hz]	$\omega$	Angular frequency [ $\text{rads}^{-1}$ ]
K	Boltzmann constant [ $\text{JK}^{-1}$ ]	$\chi^2$	fitting errors [–]
H	Planck constant [Js]	$\alpha$	Absorption coefficient
M	Number of parameters of the Powell algorithm [–]	$\nu$	photon frequency

addition, the control of the tube-to-tube spacing can facilitate the decoration of the outer surface of the nanotubes, since aligned and spaced architectures provide different spaces for further decoration with other nanomaterials. As evidence, the use of spaced NTs as catalyst supports in polymer electrolyte membrane fuel cells demonstrated superior performance compared to aligned NTs, which results from the tube-to-tube spacing that allows a significantly higher amount of platinum nanoparticles to be loaded onto the device's cathode [19]. However, there are also some drawbacks associated with this spaced NT architecture. Indeed, as the gaps between the tubes increase (loosely packed nanotubes), the tubular layer becomes less compact and, thus, with their increasing height, their mechanical stability worsens. The tube density, considered as the number of tubes per unit area, decreases, thus reducing the active surface area of the material. This will obviously lead to a reduction in the photoactivity of the electrode, since the photoresponse of the material is directly correlated to the total active surface area available for the photoelectrochemical process [20]. However, knowing that the photoactivity of titania is not particularly impressive, such an architecture provides both the internal and outer wall for modification with light absorbers. Although promising photoactivity has been reported by using nanotubes grown on Ti foil as a photoanode, the presence of the opaque metal foil which underlies the NT limits their potential applications, especially in PEC devices requiring

semitransparent electrodes. Moreover, the  $\text{TiO}_2/\text{Ti}$  interface cannot withstand the shocks caused by the mechanical instability of Ti foils at the microscale [21]. In consequence, the stress created at the oxide/metal interface may cause the formation of cracks and delamination of the NT layer from the foil [22]. Therefore, the mechanical stability at the Ti/NT interface is a concern for the practical use of photoanodes consisting of Ti foil overgrown with NT. In fact, from an industrial point of view, not only the solar conversion efficiency but also the long-term stability of the materials that compose the device is of fundamental importance [23]. The design of functional materials for use in micro- or nano-sized devices in solar energy conversion and storage systems is currently also of paramount interest in solar technologies [24]. Related to this, NTs grown on Ti foil are not suitable candidates for application in such advanced technologies, because the Ti foil used for the anodizing itself typically has a thickness between 0.1 and 1 mm [22]. Therefore, the facile development of NTs onto a transparent conducting oxide (TCO) substrate, including indium tin oxide (ITO) [2], fluorine-doped tin oxide [25], and aluminium zinc oxide [26], is needed, namely for technological application and practical usage. In fact, TCOs such as ITO exhibit good mechanical properties (even at a thickness of  $152 \pm 6$  nm), which can be even further improved by thermal treatment [27]. In general, two methods are used to form NTs on different TCOs. One is based on transferring NTs already grown out of the Ti foils

combined with their physical bonding onto the TCO [28,29], and the other option at first concerns the deposition of a Ti film onto a TCO by the magnetron sputtering technique [30]. The obtained substrates are then anodized and finally nanotubes are directly formed onto the TCO [3,7]. Both approaches have been successfully explored for the synthesis of semitransparent photoelectrodes based on NTs.

Planar substrates overgrown with NTs are considered as potential candidates for future industrial applications, especially in solar energy conversion technologies. Indeed, a front electrode of a solar water splitting tandem system consisting of semitransparent NT-based materials has demonstrated a promising ability to produce hydrogen (2.1% efficiency) [6]. The power conversion efficiency of dye-sensitized solar cells using a semitransparent anodic NT-based photoanode is about 7% [31]. From an industrial point of view, those technologies are not ready for market implementation due to their current inefficiency. Industry and academic researchers are working on improving the solar conversion efficiency of those semitransparent electrodes as a low-cost alternative to silicon-based materials. Another industrial interest for NTs formed out of Ti film deposited on planar substrates is their use in microdevices for chemoresistive sensors to detect toxic gases such as ammonia and carbon monoxide [32]. Indeed, a highly stable response that is reversible even under repetitive gas exposure at different  $\text{NH}_3$  or CO concentrations has already been achieved by using NTs formed out of Ti film deposited onto flexible planar substrates that can be easily incorporated in microdevices [32]. The semitransparent characteristic of NTs formed onto the TCO can be explored for live cell imaging applications. This technology allows the analysis of live cells using automated fluorescence microscopy systems. A live-cell imaging platform consisting of fluorescence microscopy with semitransparent NTs has been developed by Meyerink et al. [33] for capturing and quantifying intricate cellular responses in live cells in real-time. The industrial perspective of this application is summarised in the work of McCann et al. [34]. However, it is worth underlining that most works related to the growth and practical application of semitransparent anodic titania nanotubes have been focused on titanium deposited onto one side of the planar TCO substrates. This research highlights improvements of this concept. It should be noted that the specific surface area greatly affects the optical properties of the material [28]. In PEC systems, an increase in the active surface area of the photoanode provides both more space for, e.g., dye loading and channels for electron transport to the TCO, which are crucial for the efficiency of sensitising solar cells. As an innovative solution, double-sided electrodes were proposed where both the front and back sides of the electrode were responsible for light absorption and subsequently its conversion into a photocurrent. Such a strategy provides an increase of the materials surface area, thus improving the solar-to-electricity conversion efficiency. Moreover, double-sided electrodes can be used for fabricating bipolar devices where both sides take part in different electrochemical processes. Such an opportunity was the driving force behind this work.

The double-sided NT configuration can improve the conversion efficiency of the photoelectrode compared to the single-sided one since devices can take advantage of the two photoactive areas present on the same substrate. However, so far, research into the fabrication of an electrode material based on NTs grown on both sides of a planar substrate is still rather problematic. The first approach of Mor et al. [35] for producing double-sided semitransparent NT electrodes consisted of juxtaposing two different semitransparent electrodes back-to-back. In this approach, one is coated with aligned NTs and the other with copper-modified aligned NTs. The cost of this method is higher compared a double-sided semitransparent fabricated out of a single transparent conducting oxide. Another disadvantage of this back-to-back two glass slides arrangement is the loss of light by reflection at the air/glass interface due to Fresnel reflection [36]. With these two electrodes being placed back-to-back, the presence of air at the junction is obvious. A Fresnel reflection of about 3.37% has already been reported at the air/glass interface by Kim [36]. This loss in the incidence

light results from the large refractive index difference between the air and the glass. Since the refractive index of air is lower than that of the glass substrate, light will deviate from its initial path with a higher angle of refraction than the incident one. Additionally, if another material is used as a glue to hold the electrodes together at the junction, this connection may also absorb or disperse a part of the incident light. Overall, the structure of this double-sided electrode will reduce the transmission efficiency of the incident light to the entire solar cell.

Another approach, proposed by Cheng et al. [28], was based on the usage of a double-sided semitransparent NT electrode made out of a single transparent conduction oxide and was based on transferring nanotubes already grown on a Ti foil to double-sided ITO, achieving an NT-TCO-NT configuration. However, this method also has several drawbacks. Selective physical or chemical detachment of the tubular layer from the anodized Ti foil can lead to severe distortion of both the nanotube morphology and the titanium oxide microstructure. This method is time-consuming as it involves several steps, including (1) anodizing the Ti foil, (2) annealing the anodized sample, (3) detaching the tubular layer from the anodized Ti foil, (4) bonding the detached tubular layer onto the TCO using a titania-based slurry, and (5) annealing the TCO substrate overgrown with the nanotubes. For double-sided electrodes, step (4) should be done on both sides of the TCO. Another limitation of this method is the size of the tubular layer that can be transferred to the TCO. Indeed, the film composed of aligned titania nanotubes can be dislocated into several parts during its detachment from the Ti foil. The process of transferring the titania layer without causing any mechanical damage requires enormous effort, and can limit the large-scale production of the double-sided NT electrodes using this method [32]. It is worth mentioning that works have also been carried out to synthesize double-sided NTs out of Ti foil. For this type of substrate, Mohapata et al. [37] showed that nanotube arrays can be grown onto both sides of a Ti foil by keeping the Ti foil equidistant between two platinum meshes during its anodization. Later, works reported by Sun et al. [38] demonstrated that even using a single platinum mesh during anodizing leads to the formation of the tubular layers simultaneously on both sides of the titanium foil. However, the nanotube architecture is highly sensitive to the composition of the organic electrolyte used during the anodization. In fact, the aligned NTs are usually obtained using a mixture of organic solutions based on an electrolyte such as glycerol [39], ethylene glycol [39], sodium carboxymethylcellulose [40], and 1-butyl-3-methylimidazolium tetrafluoroborate [41] with fluorine salts, whereas the laterally spaced NT architecture has been synthesized in a diethylene glycol [16,42], triethylene glycol [15], and dimethyl sulfoxide solution [18,19]. Moreover, mostly the spaced nanotubes are formed when the anodization is performed when the electrolyte or anode is heated. Therefore, by leaving both sides of the substrate in contact with the same electrolyte and other parameters during the anodization, the architecture cannot be separately controlled on both sides of the substrate. In fact, so far, the synthesis of an asymmetric electrode consisting of aligned nanotubes on one side and spaced nanotubes on the other has not been reported using the approach of Mohapata et al. [37] or Sun et al. [38].

Even though both sides of planar transparent conducting oxides are available, the design and fabrication of double-sided electrodes by controlling the NT architectures (aligned NTs and spaced NTs) on the sides of a single planar TCO glass substrate have not been investigated so far. In this work, the formation of novel, double-sided semitransparent titania nanotube arrays onto ITO-coated glass were investigated. Unlike the approaches of Cheng et al. [28] and Mor et al. [35], a double-sided semitransparent NT electrode was synthesized using a single planar glass substrate coated on both sides with Ti films. A strategy based on the successive anodization of the sides of the substrate was employed. Effective control of the nanotubes' architecture on both sides of the planar substrate was possible through the usage of an anodization setup equipped with a suitable sample holder allowing each side to be anodized independently. As evidence, two symmetric and one asymmetric



double-sided NT-ITO-NT electrodes have been successfully synthesized. These series of electrodes consist of: (i) aligned nanotubes onto both sides NT(A)-ITO-NT(A), (ii) spaced nanotubes on both sides NT(S)-ITO-NT(S), and (iii) one side covered by aligned and the other by spaced nanotubes NT(A)-ITO-NT(S). It is worth emphasising that both the fabrication and physicochemical properties of semitransparent double-sided NT electrodes, especially NT(S)-ITO-NT(S) and NT(A)-ITO-NT(S) electrodes, have not been reported so far. The methodology adopted in this work is simple and reduces the cost of using two different TCO substrates held back to back. In addition, the easy control of the tubular morphology and oxide layer architectures developed on the sides of the substrate simply by optimising the anodization conditions open the way to broad possibilities of asymmetric and symmetric photoelectrodes that can be synthesized and explored for practical applications in PEC devices.

This work is structured as follows: a detailed description of the synthesis method, including the deposition of ITO and Ti films on the sides of the glass substrates followed by their anodization, is presented in section 2 'Experimental section'. This section discusses the reproducibility and homogeneity of the deposition method as well as the anodization strategy enabling the growth of aligned and spaced NTs on the sides of planar substrates. Then, the physicochemical characterizations and photoelectrochemical measurements carried out in this work are presented. Section 3 'Result' discusses the morphology, optical properties and structure of the prepared tubular oxide layers, with the aim of understanding the impact of the material architectures on the photoresponse of the electrodes. A critical analysis of the influence of the tubular oxide architecture on the overall performance of double-sided NT-ITO-NT photoelectrodes is discussed. Finally, the key findings and some probable limitation of the use of the double-sided electrodes in solar cells are summarised in section 4 'Conclusion'.

## 2. Experimental section

### 2.1. Deposition of Ti/ITO/Ti substrates

The Ti-ITO-glass-ITO-Ti structures were prepared by magnetron sputtering of ITO and Ti films, one on each side of the substrates. Silica glass (Menzel Glaeser) microscopic slides were used as substrates. The substrates were cut to dimensions of  $15 \times 10 \text{ mm}^2$  and cleaned in an ultrasonic bath in different solvents according to the following order: acetone, distilled water, isopropanol, distilled water, ethanol, deionised water. In the next step, the surfaces were plasma cleaned and plasma activated just before the deposition; the substrates were acting as rf-biased electrodes propagating a discharge for 10 min. The rf discharge was ignited in a reactive atmosphere:  $\text{Ar}/\text{O}_2 = 6/20$  at a pressure of 3.5 Pa, feeding the active electrode (substrate) by an rf power of 30 W (Advanced Energy Cesar, 13.56 MHz), with a corresponding negative self-bias of 200 V. The plasma cleaning and the deposition of the thin films were carried out in the same UHV chamber, equipped by magnetron sputtering gun(s) for the deposition of thin film. The vacuum chamber was evacuated by a primary dry scroll and secondary turbomolecular pumps down to a base-pressure of  $6 \cdot 10^{-5}$  Pa. The process gases were delivered to the vacuum system by mass flow controllers (MKS Instruments). The working pressure in the vacuum chamber was set by a gate valve installed between the pumping system and the chamber, as described in Fig. 1.

The double-side Ti-( $\text{TiO}_x$ )-ITO-glass-ITO-( $\text{TiO}_x$ )-Ti was prepared by a step-by-step process covering both sides of the substrate. A schematic view of the sandwich films is shown in Fig. 2.

The deposition parameters of the sandwich-like film were as follows:

- (i) ITO deposition on both sides of glass substrates was done by rf magnetron sputtering of the compound ITO target  $\text{In}_2\text{O}_3/\text{SnO}_2$  with a composition 90/10 wt% and a purity grade of 99.99% (Testbourne Ltd). The magnetron sputtering gun, with a diameter

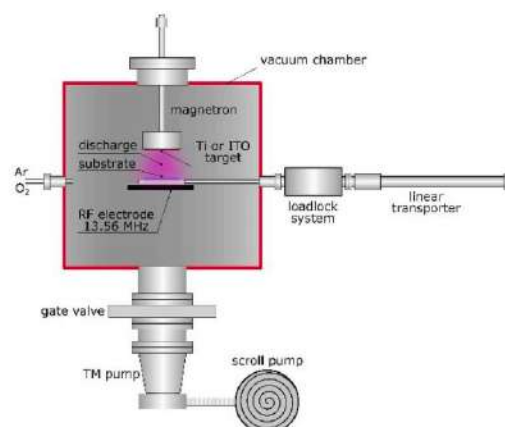


Fig. 1. Scheme of experimental arrangement for fabrication of double-side Ti-( $\text{TiO}_x$ )-ITO-glass-ITO-( $\text{TiO}_x$ )-Ti samples.

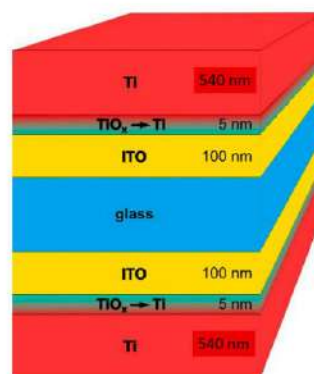


Fig. 2. Scheme of sandwich-like double-sided Ti-( $\text{TiO}_x$ )-ITO-glass-ITO-( $\text{TiO}_x$ )-Ti film for subsequent anodization and fabrication of NT arrays.

of 3 inches (Kurt J. Lesker Company) was driven by an rf power of 150 W with a negative bias of 160 V. The distance between the magnetron and the substrate was 160 mm. All experiments were performed in an Ar atmosphere at 1 Pa; the Ar flow rate was 25 sccm. The deposition process and the film growth were monitored in situ and in real time by quartz crystal microbalance (QCM) to reach a uniform thickness of 100 nm for all samples; the deposition time was about 11 min. After the deposition, the ITO-glass-ITO samples were thermally annealed at 500 °C for 1 h to improve their optical and electrical properties.

- (ii)  $\text{TiO}_x$  graded interface layer was deposited as a buffer between the ITO and Ti films. The gradient  $\text{TiO}_x \rightarrow \text{Ti}$  interface layer was deposited onto the ITO to form a transition layer between the metal-oxide and metal films to improve the adhesion. The inter-layer was deposited by dc magnetron sputtering of the Ti target (3 inches in diameter, thickness: 4 mm, produced by Bibus Metals, purity grade 99.3%), employing a custom-built planar magnetron. The magnetron was powered by a dc power supply (Kurt J. Lesker, DC01 BP) and was 60 mm from the substrate. The

deposition started in a reactive atmosphere  $\text{Ar}/\text{O}_2 = 6/20$  which gradually changed to a 6/0 ratio, at a constant pressure of 0.5 Pa, and constant discharge current of 600 mA. The graded  $\text{TiO}_x \rightarrow \text{Ti}$  interface was deposited for 1 min, which corresponds to a thickness of about 5 nm.

- (iii) Ti film was deposited by dc magnetron sputtering of the Ti target; the same as that produced in the previous step (ii). The sputtering process was driven in constant current mode of 600 mA, which corresponds to a cathode voltage of  $-377$  V and power of 226 W. The films were deposited in an Ar atmosphere (flow rate: 6 sccm) and pressure of 0.12 Pa. The film growth was monitored by quartz microbalance (QCM) with an estimated deposition rate of 45 nm/min. The film's thickness was 540 nm.

The samples were prepared in batches, each counting five samples to ensure the homogeneity of the deposited films. In the first phase of the research, the deposition process was optimised for all types of thin films (ITO,  $\text{TiO}_x \rightarrow \text{Ti}$ , Ti). The deposition rate was monitored in situ and in real time by QCM. Other film parameters, such as film thickness, crystallography, electrical conductivity etc., were measured after the deposition to tailor and optimise the sample fabrication. From the measured data, the standard deviation and subsequently the relative error  $<5\%$  was estimated for all monitored parameters if the samples were prepared under the same conditions. For that reason, the reproducibility of sample production is with a relative error  $<5\%$ , too. The films deposited onto the samples of  $15 \times 10 \text{ mm}^2$  were spatially homogeneous with relative error  $<3\%$ .

## 2.2. Synthesis of NT-ITO-NT materials

The NT-ITO-NT photoelectrodes were synthesized in a two-step anodization process. First, the Ti-ITO-glass-ITO-Ti substrates were placed into an appropriate holder, which made it possible to anodize only one side by isolating the other from the electrolyte. When the anodization of the first side was finished, the sides of the substrates were changed. Thus, both sides of the substrates were successively anodized. To obtain aligned nanotubes, the anodization was carried out in a two-electrode system in ethylene glycol containing 0.27 M  $\text{NH}_4\text{F}$ , 1 M  $\text{H}_3\text{PO}_4$  and 5 vol % deionised water at 60 V for 34 min. The temperature of the electrochemical cell was maintained at 23 °C using a thermostat (Julabo F-12). A platinum mesh acted as the cathode and one side of the Ti-ITO-glass-ITO-Ti substrate as the anode. Spaced nanotubes were prepared by using a diethylene glycol-based electrolyte mixed with 0.15 M  $\text{NH}_4\text{F}$ , 0.5 M hydrofluoric acid (HF) and 7 vol %  $\text{H}_2\text{O}$ , for 20 min at 40 °C, under a constant voltage of 40 V. Afterwards, the samples were annealed at 450 °C for 1 h in air with a heating rate of 2 °C min<sup>-1</sup> by using a tubular furnace (Nabertherm). The set of samples was composed of two symmetric electrodes consisting either of aligned or spaced NTs grown onto both sides of the substrate, (labelled by NT(A)-ITO-NT(A) and NT(S)-ITO-NT(S)) and one asymmetric material obtained by developing aligned NTs on one side and spaced NTs on the other one (labelled by NT(A)-ITO-NT(S)). For the symmetric NT arrangement, namely when the same morphology was grown on both sides, the labels F1 and F2 were used to denote the difference between the faces. For the asymmetric material, the labels FA and FS indicate which side is exposed to the radiation source (FA: side overgrown with aligned NTs, and FS: side overgrown with spaced NTs).

## 2.3. Characterisation

An FEI Quanta FEG 250 field emission scanning electron microscope (FE-SEM) was employed for the morphological characterisation of the prepared materials after annealing. The crystal structure of the samples was identified using a Raman spectrometer (Renishaw). The instrument was equipped with an argon ion laser (514 nm) as the excitation source and was operating at 10% of its total power. The optical properties were

investigated using a UV-vis spectrophotometer (PerkinElmer) operating at a scanning speed of 120 nm/min. The electrochemical and photoelectrochemical measurements were carried out on an Autolab PGSTAT302 N potentiostat-galvanostat system (Methrom, Autolab) in a three-electrode cell with a quartz window.

## 2.4. Photoelectrochemical measurements

The prepared substrates, platinum mesh, and Ag/AgCl were used as the working electrode, reference electrode, and counter electrode, respectively. Before each experiment, the electrolyte was deaerated by an argon flow for 30 min. During the measurements, the argon flow was maintained above the solution. All measurements proceeded in an electrolyte of 0.5 M  $\text{Na}_2\text{SO}_4$  under ambient conditions at room temperature. The NT-ITO-NT electrodes were immersed in the solution (both sides covered with NTs were in contact with the electrolyte), and the photoresponse was investigated under both UV-vis and visible illumination. A 150 W xenon lamp (Osram XBO 150) was used as the UV-vis light source. The light with wavelengths below 400 nm was subtracted using an optical filter for measurements in visible light. To assess the photoresponse of each side of the NT-ITO-NT photoanodes, first, one side of the electrode was irradiated by the light and the generated current from both sides of the NT-ITO-NT photoelectrode was recorded. Afterwards, the measurement was repeated while illuminating the other side of the materials. The cyclic voltammetry (CV) was performed in a potential window of  $-1$  to  $+1$  V at a scan rate of 50 mVs<sup>-1</sup>. Linear sweep voltammetry (LSV) was performed by recording the photocurrent under chopped light irradiation (light/dark every 5 s) in either UV-vis or visible light from  $-0.7$  to  $+1$  V at a scan rate of 10 mVs<sup>-1</sup>. The current density increased under light illumination and returned to its background value as the light was turned off. The photocurrent density was determined by subtracting the light current density and the dark current density at a given potential. The electrochemical impedance spectra (EIS) were measured either in dark or under UV-vis illumination, with frequencies varying from 0.1 to 20 kHz with a 10 mV amplitude of the AC signal. The impedance data were analysed on the basis of an electric equivalent circuit (EEQC) using the EIS Spectrum Analyser program. The modified Powell algorithm was used with amplitude weighting  $r_g$ :

$$r_g(\omega, P_1 \dots P_M) = r_c^2 / (N - M) \quad (1)$$

where N is the number of points, M is the number of parameters,  $\omega$  is the angular frequency, and  $P_1 \dots P_M$  are the parameters. Parameter  $r_c$  is defined as:

$$r_c^2 = \sum_{i=1}^N \frac{(Z_i' - Z_{\text{calc}}')^2 + (Z_i'' - Z_{\text{calc}}'')^2}{Z_i'^2 + Z_{\text{calc}}'^2} \quad (2)$$

where i corresponds to the measured values of impedance and  $i_{\text{calc}}$  is attributed to the calculated values, and N is the number of points. For the Mott-Schottky analysis, EIS spectra were recorded at a constant frequency of 1 kHz in the potential range of  $+0.1$  to  $-1.2$  V.

## 3. Results and discussion

### 3.1. Structural and optical characterisation

Fig. 3 (a)–(c) shows the prepared semitransparent NT(A)-ITO-NT(A), NT(S)-ITO-NT(S) and NT(A)-ITO-NT(S) materials. For each substrate, well-ordered semitransparent NTs were uniformly grown over a disk of 10.5 mm in diameter. No NTs were detected outside this area, since it was protected by the electrode holder. A slight difference in the transparency of the prepared materials can be observed by the naked eye depending on the NT architecture, as shown in Fig. 3 (a)–(c). Fig. 3 (d)–(g) shows the top and cross-section images of the aligned and spaced-NT



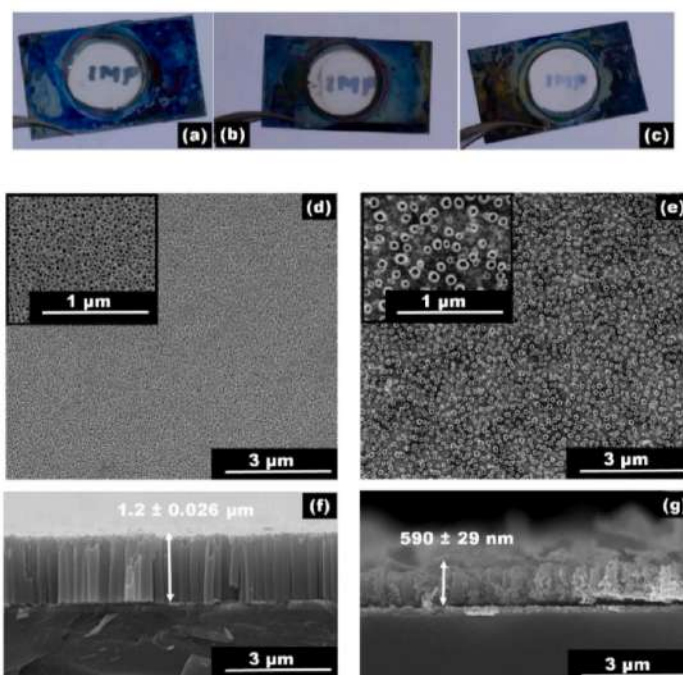


**Fig. 3.** (a–c) Photographs of the semitransparent substrates annealed at 450 °C, (a) NT(A)-ITO-NT(A), (b) NT(A)-ITO-NT(S) and (c) NT(S)-ITO-NT(S). (d–e) SEM top images of the (d) aligned NTs and (e) spaced NTs grown onto ITO-coated glass. (inset: higher magnifications of the obtained morphology). (f–g) SEM cross-section images of (f) aligned NTs and (g) spaced NTs grown on ITO-coated glass.

grown onto ITO-coated glass. The close-packed configuration of the NTs (shown in Fig. 3 (d)) had an average tube length of  $1.2 \mu\text{m} \pm 26 \text{ nm}$  and an outer diameter of  $(51 \pm 10) \text{ nm}$ . For the spaced structure, each tube was separated from the others, with an average tube-to-tube spacing of  $(380 \pm 56) \text{ nm}$  (Fig. 3 (e)). The average tube length and outer diameters were  $(590 \pm 29) \text{ nm}$  and  $(150 \pm 69) \text{ nm}$ , respectively. As can be noted, the aligned NTs have an average length 2 times greater than that of the spaced morphology. This can be ascribed to the synthesis conditions, mainly the electrolyte composition. The spaced NTs were obtained in an organic electrolyte containing hydrofluoric acid. According to Mor et al. [43] and Yoriya et al. [44], the HF content in the electrolyte is one of the main factors that limits the nanotube length. It is worth noting that nanotubes with a length on the order of micrometres can promote the visible light scattering of the photoactive material [10,31]. A good light-scattering ability of the material augments the probability of incident photons being effectively absorbed, thereby improving the photoresponse of the materials [43,45]. In addition, the average outer diameter of the aligned structures was found to be 3-fold smaller compared to the spaced one. The average tube diameter has a strong influence on the wettability and the roughness factor of the surface. According to Liu et al. [46], an increase of the tube diameter in the range from 30 to 190 nm provides more space for the electrolyte species transportation.

Anodization is one of the most reproducible methods used for the synthesis of tubular or porous layers from different metals. The morphologies produced in this work are repeatable. To show the reproducibility of the morphologies shown in Fig. 3, Ti films were deposited onto one side of eight ITO-coated glass substrates and were anodized according to the anodization conditions to obtain for the aligned or

spaced NT architecture described in the experimental section 2.2. The morphologies obtained out of various Ti films deposited onto the ITO substrates are shown: for aligned titania in Fig. 4, whereas for spaced titania in Fig. 5. The outer diameters of the samples were determined to evaluate the fluctuation from sample to sample after the anodization. The pore diameters of the aligned NT samples were between  $50 \pm 11 \text{ nm}$  and  $51 \pm 10 \text{ nm}$ , while those of the spaced NTs were between  $150 \pm 66 \text{ nm}$  and  $150 \pm 69 \text{ nm}$ . The shift in the standard deviation in the morphology from sample to sample anodized under the same conditions can be considered as negligible.

After annealing the anodized NTs at 450 °C in air, the crystallinity of the anodized materials was verified by Raman spectroscopy, as shown in Fig. 6. The Raman spectra of the aligned-NT and spaced-NT materials exhibit four bands of the anatase phase of titanium dioxide located at 144, 394, 516 and  $636 \text{ cm}^{-1}$ , respectively [47]. The modes at 144 ( $E_{1g}$ ) and  $394 (B_{1g}) \text{ cm}^{-1}$  are ascribed to Ti–O bending vibrations, whereas the bands at 516 ( $A_{1g}, B_{1g}$ ) and  $638 (E_{3g}) \text{ cm}^{-1}$  correspond to Ti–O stretching vibrations [48]. The weak peak located at  $1050 \text{ cm}^{-1}$  results from the ITO-coated glass substrate, as indicated in Fig. 6 (b). It can be observed (Fig. 6 (c)) that the signals of the aligned-NT materials are more intense compared to those of the spaced-NT (Fig. 6 (c)). In general, the variation in intensity of the most intense Raman peak ( $144 (E_{1g}) \text{ cm}^{-1}$  mode) is ascribed to changes in the crystalline size [49,50]. The probable reasons for the decrease in the intensities of the Raman peaks are the increase in grain boundaries due to the synthesis conditions [51] and the increase in the concentration of defects resulting from significant lattice distortion [49,52]. The reduction in the intensity of the  $144 \text{ cm}^{-1}$  band for the spaced-NT material indicates its low crystallinity with respect to that of the aligned structure [51,52].

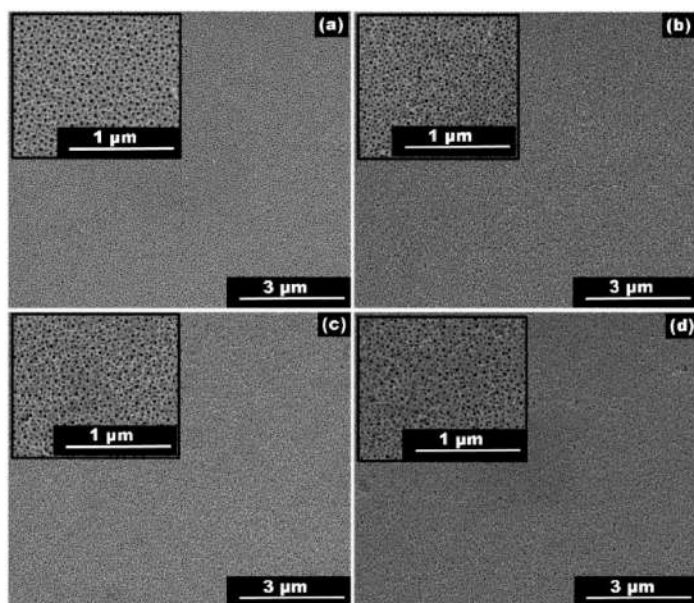


Fig. 4. SEM top images of aligned NTs grown on different ITO-coated glass substrates (a, b, c and d represent the substrates).

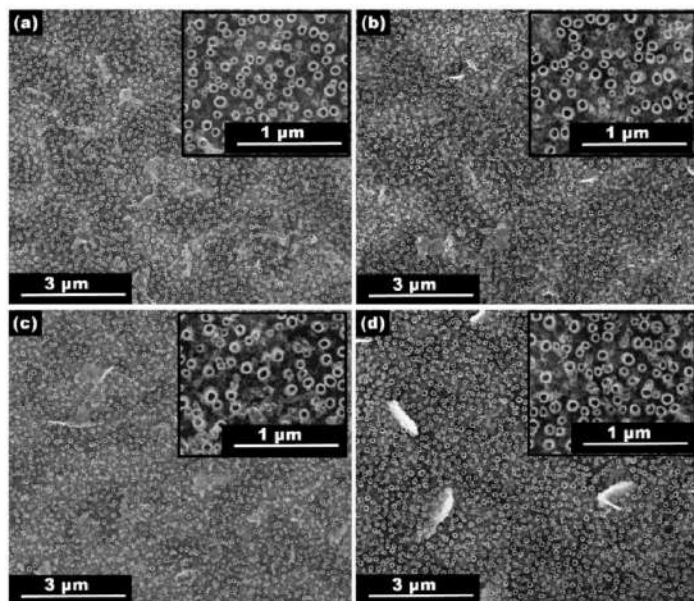


Fig. 5. SEM top images of spaced NTs grown on different ITO-coated glass substrates (a, b, c and d represent the substrates).

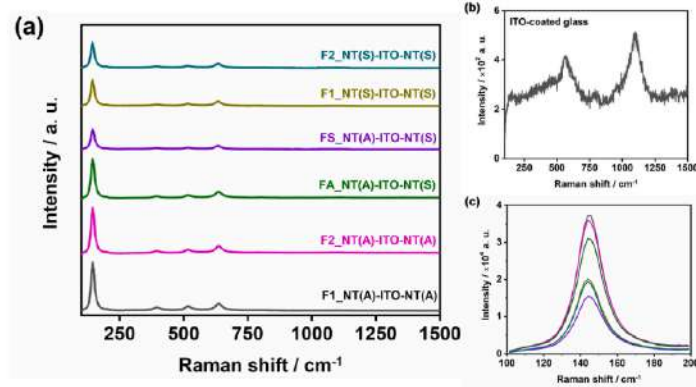


Fig. 6. (a) Raman spectra of the both sides of NT(A)-ITO-NT(A), NT(A)-ITO-NT(S) and NT(S)-ITO-NT(S) materials, annealed at 450 °C for 1 h. (b) Raman spectra of ITO-coated glass. (c) Raman spectra of the most intense anatase peak at 144  $\text{cm}^{-1}$ .

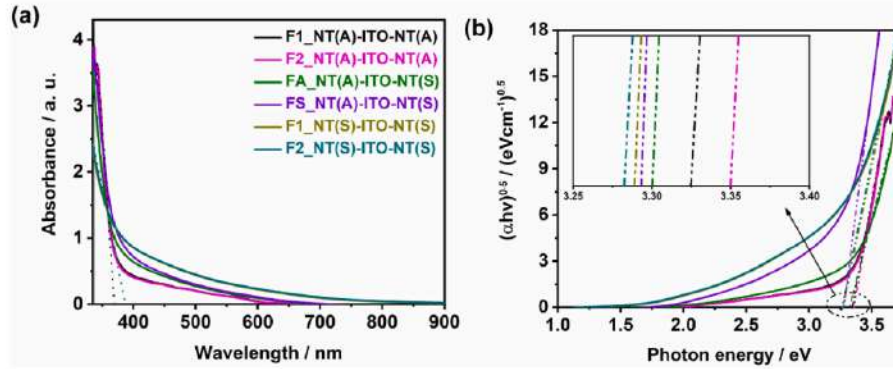


Fig. 7. (a) Absorption spectra of both sides of NT(A)-ITO-NT(A), NT(A)-ITO-NT(S) and NT(S)-ITO-NT(S) materials annealed at 450 °C for 1 h. (b)  $(\alpha h\nu)^{1/2}$  vs. photon energy.

To assess the effect of the nanotubes' architecture on the optical properties of the obtained NT(A)-ITO-NT(A), NT(A)-ITO-NT(S) and NT(S)-ITO-NT(S) materials, the absorption spectra of the aligned and spaced NTs were compared (Fig. 7). As shown in Fig. 7, the recorded absorption spectra on both sides of the symmetric materials, i.e. NT(A)-ITO-NT(A) and NT(A)-ITO-NT(S), almost overlap. The absorption edges were designated at the intersection of the tangent of the absorption curve and the x axis [10]. The absorption edges of the aligned and spaced NTs were found to be below 400 nm. This indicates that both architectures (aligned or spaced ones) mainly absorb light in the UV region of the entire spectrum. It can be noticed that the absorption edges of the spaced-NT sample are redshifted by about 20 nm with respect to the aligned one (Fig. 7). Such a shift in the absorption edge wavelength may result from the quantisation effect in the tubular morphology [53, 54]. As discussed in the Raman analysis, the low crystallinity of the spaced-NT materials, presumably resulting from the lattice distortion, can cause aggregation of oxygen vacancies [55]. Oxygen vacancies can generate defect levels about 0.75–1.18 eV below the  $\text{TiO}_2$  conduction band, causing the absorption edge to shift towards the longer wavelengths [56,57]. The calculated band gaps,  $E_g$ , are summarised in Table 1 with respect to Fig. 7. The relation between absorption

Table 1

Band gap energy values of the as-prepared materials.

Sample	$E_g$ (eV)
F1 <sub>NT</sub> (A)-ITO-NT(A)	3.33
F2 <sub>NT</sub> (A)-ITO-NT(A)	3.35
F1 <sub>NT</sub> (S)-ITO-NT(S)	3.29
F2 <sub>NT</sub> (S)-ITO-NT(S)	3.26
FA <sub>NT</sub> (A)-ITO-NT(S)	3.30
FS <sub>NT</sub> (A)-ITO-NT(S)	3.27

coefficient  $\alpha$  and band gap  $E_g$  of the semiconductor is given by:

$$(\alpha h\nu)^n = h\nu - E_g, \quad (3)$$

where  $h$  is the Planck constant,  $\nu$  is the frequency, and  $n$  takes the value 0.5 for an indirect band transition and 2 for a direct band transition. Singh et al. [58] demonstrated that titania-based materials can have either a direct or an indirect band gap structure depending on the temperature at which the materials are synthesized. They showed that titania-based materials prepared at a temperature of around 400 °C (anatase) have an indirect band gap, while materials synthesized at a



higher temperature of 900 °C (rutile), have a direct band gap structure [58,59]. Since all tubular layers exhibit the anatase phase of titania after their annealing at 450 °C, in this study,  $n = 0.5$  was used for the determination of the band gaps of the samples. The value of  $\alpha$  is determined according to Lambert's law,  $\alpha = 2.303 \frac{A}{d}$ , where  $A$  is the absorbance recorded by the UV-vis spectrophotometer and  $d$  is the thickness of the tubular layer. Plots in the Tauc coordinates for indirect bandgap semiconductors ( $(\alpha h\nu)^{0.5}$  versus  $h\nu$ ) are shown in Fig. 7. The band gaps of the samples were determined on the basis of the intersection of the extrapolation of the linear parts of the graphs with the x axis [55]. The band gap values for the spaced architectures are slightly smaller compared to the aligned ones. The change in the band gap value as compared to the bulk anatase titania (3.20 eV) results from the geometric features of the obtained electrodes [60].

### 3.2. Photoelectrochemical properties

The electrochemical properties of the annealed samples were first investigated by means of cyclic voltammetry. Fig. 8 (a) shows the voltammograms of the NT(A)-ITO-NT(A), NT(S)-ITO-NT(S) and NT(S)-ITO-NT(S) electrodes. The CV curve of the NT(S)-ITO-NT(S) does not show any redox peaks, while a reduction peak appears at  $-0.64$  V versus Ag/AgCl/0.1 M KCl for the NT(A)-ITO-NT(A) and NT(A)-ITO-NT(S) (slightly visible band) in the same potential range. These cathodic peaks are associated with the reduction of  $\text{Ti}^{4+}$  to  $\text{Ti}^{3+}$  combined with  $\text{H}^+$  intercalation on the anatase  $\text{TiO}_2$  layer surface ( $\text{Ti}^{4+} + \text{H}^+ + e^- \rightarrow \text{Ti}^{3+}\text{H}^+$ ) [61,62]. For all three electrodes, polarisation towards a more negative

direction ends with hydrogen evolution ( $2\text{H}^+ + 2e^- \rightarrow \text{H}_2$ ) [63]. However, no oxidation peaks are seen in the reverse scans. This indicates that the electrochemical reactions of the NT(A)-ITO-NT(S) and NT(S)-ITO-NT(S) electrodes are irreversible. The NT(A)-ITO-NT(A) electrode demonstrated a significant increase of the current density in both the anodic and cathodic directions, showing the good electrochemical performance of the aligned-NT-based materials. Obviously, the difference in the electrochemical activities of both the NT(A)-ITO-NT(A) and NT(S)-ITO-NT(S) materials results from their different morphological characteristics, namely tube diameter, and intertube spacing and length, respectively. As explained by both Sun et al. [64] and Zhuang et al. [65], an increase in the tube diameter and intertube spacing drastically reduced the active surface area of the materials. Hence, the large tube diameter ( $150 \pm 69$  nm) and intertube spacing ( $380 \pm 56$  nm) of the spaced-NT material as compared to the aligned one (tube diameter of  $51 \pm 10$  nm), which may explain its relatively low capacitive current.

The photoresponse of the as-synthesized materials was carefully investigated by means of linear sweep voltammetry under chopped light (light/dark every 5 s) in both UV-visible and visible irradiations. To assess the photoresponse of each side, a comparative study of the linear sweep voltammograms of both sides of the NT(A)-ITO-NT(A), NT(S)-ITO-NT(S) and NT(A)-ITO-NT(S) electrodes are shown in Fig. 8(b)–(d). The LV curves of the samples show that both sides of all investigated electrodes are photoactive under UV-visible light. For the symmetric electrodes, i.e. NT(A)-ITO-NT(A) or NT(S)-ITO-NT(S), regardless of the side exposed to light, the same activity was recorded. The NT(A)-ITO-NT(A) exhibited a photocurrent of  $4.6 \mu\text{Acm}^{-2}$  at  $0.5$  V, which is 1.9 times

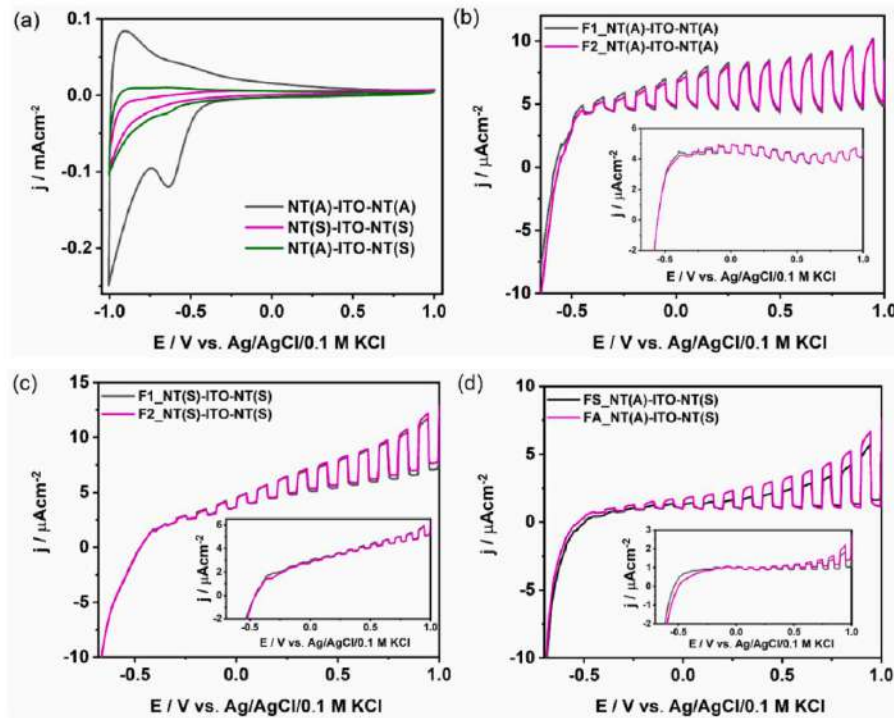


Fig. 8. (a) Cyclic voltammetry curves of NT(A)-ITO-NT(A), NT(S)-ITO-NT(S) and NT(A)-ITO-NT(S) based electrodes materials. Linear sweep voltammograms (light/dark every 5 s) of the both sides of (b) NT(A)-ITO-NT(A), (c) NT(S)-ITO-NT(S) and (d) NT(A)-ITO-NT(S) under UV-vis illumination (inset: Linear sweep voltammograms recorded under visible illumination).

larger than that of the NT(S)-ITO-NT(S) ( $2.4 \mu\text{Acm}^{-2}$  at 0.5 V). Since the prepared aligned-NT materials have slightly higher band gap energies than their spaced counterparts (Table 1), the high photocurrent of the aligned-NT photoanodes can be explained by their morphology, namely both the nanotube length and density, defined as the number of tubes per unit area. Long aligned NTs ( $1.2 \mu\text{m} \pm 26 \text{ nm}$ ) have a higher probability of capturing incident photons than spaced ones, which have shorter lengths ( $590 \pm 29 \text{ nm}$ ) [31]. It is well known that the photo-generated electrons move along the nanotubes towards the TCO, where they are collected and transferred to an external circuit. The tubes act as electric channels for electron transport [66]. Therefore, the decrease in the nanotube density will obviously drop the current density of the material. Assuming that both architectures, i.e. aligned NTs and spaced NTs, are regular arrays of tubes included in a hexagonal mesh, the nanotube densities ( $N_t$ ) can be calculated by using the formula proposed by Pu et al. [67]:

$$N_t = \frac{2}{\sqrt{3}(4R_2 - 2R_1 + y)^2} \quad (3)$$

where  $R_1$  and  $R_2$  are the internal radius and the distance between the tube centre and the centre of the tube wall, respectively. The distance between two tubes,  $y$ , is considered to be constant. The calculated values of the tube densities were found to be  $0.32 \times 10^{11} \text{ cm}^{-2}$  for NT(A)-ITO-NT(A) and  $0.36 \times 10^{10} \text{ cm}^{-2}$  for NT(S)-ITO-NT(S). The low tube density of the spaced-NT materials can explain its poor photocurrent density. Another reason for the good photoresponse of the aligned material is its higher level of crystallinity, as shown by their Raman patterns with

higher intensity (Fig. 6) [68,69]. Indeed, to obtain a high photocurrent, a large number of the photogenerated electrons need to be collected. Related to this, the increase in the crystallinity will reduce the amount of grain boundaries along the tubes, in turn enhancing the electron-hole separation [68]. The low intensities of the Raman peaks obtained for the spaced-NT materials may suggest the presence of numerous grain boundaries and defects, which act as electron-trapping sites along the tube walls [70], thus promoting electron-hole recombination. The asymmetric electrode (NT(A)-ITO-NT(S)) shows an increase in the photoresponse when illuminated from the side covered with spaced NTs ( $2.8 \mu\text{Acm}^{-2}$ ) as compared to the NT(S)-ITO-NT(S) ( $2.4 \mu\text{Acm}^{-2}$ ). This improvement can be attributed to the synergistic contribution of both architectures, i.e. aligned and spaced NTs. The prepared electrodes lose their photoresponsivity under visible light illumination due to their poor absorption properties in the visible region, i.e. 84.2% for the NT(A)-ITO-NT(A) and 81.6% for the NT(S)-ITO-NT(S).

Electrochemical impedance spectroscopy measurements were carried out to analyse the charge transport mechanisms through the tubular layers. Fig. 9 shows the Nyquist curves of the NT(A)-ITO-NT(A), NT(S)-ITO-NT(S) and NT(A)-ITO-NT(S). The spectra were measured in the dark and under UV-vis light illumination. For the aligned-NT materials, the Nyquist plots recorded in the dark and under UV-vis irradiation almost overlap (Fig. 9 (a)–(b)), whereas the curves registered for the spaced-NT materials under UV-vis illumination are clearly distinguishable from the spectra obtained in the dark (Fig. 9 (c)–(d)). The influence of UV-vis illumination on the electrical properties of both architectures, namely the aligned and spaced NTs, was examined using the electric equivalent circuit depicted in Fig. 9 (a) insert.  $R_s$  is the series resistance, which takes

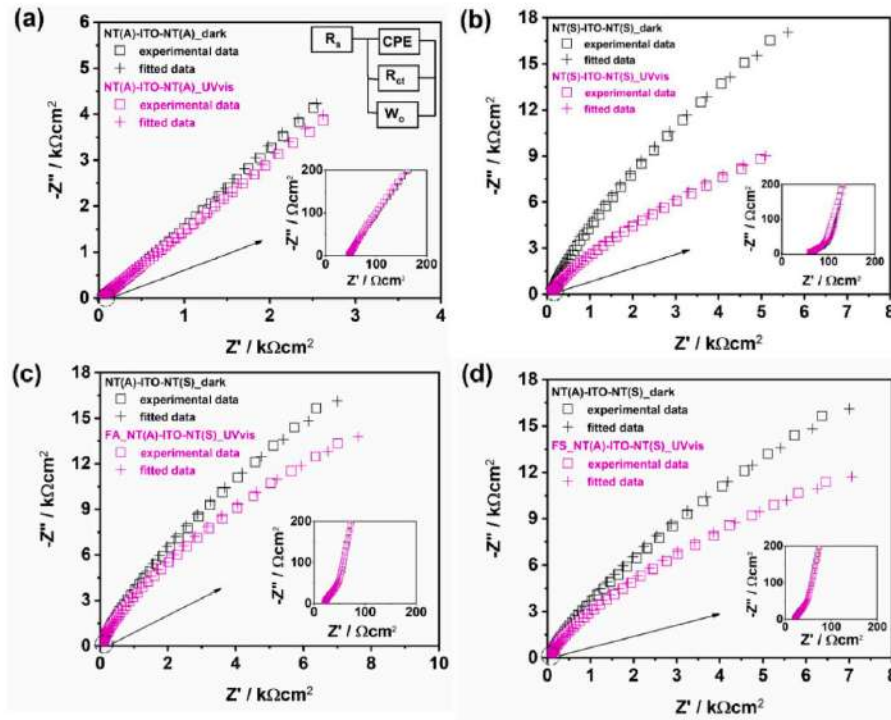


Fig. 9. Nyquist plots of EIS measurements of NT(A)-ITO-NT(A), NT(S)-ITO-NT(S) and NT(A)-ITO-NT(S) in the dark and under UV-vis illumination (insert: equivalent circuit used to fit the experimental impedance spectra recorded in the dark and under UV-vis and visible illumination of the prepared electrodes).



into account the intrinsic resistance of the NT layer, the contact resistance between the NT layer and the current collector (ITO), and the bulk resistance of the electrolyte;  $R_{ct}$  is the charge transfer resistance at the semiconductor/electrolyte interface; CPE is the constant phase element. The CPE is characterised by the impedance  $Z = Q^{-1}(i\omega)^{-n}$ , where a certain frequency dispersion is taken into account. The frequency dispersion is expressed in  $n$ , and  $\omega$  represents the angular frequency. When  $n = 1$ ,  $Q$  is identified with capacitance, while for the used procedure,  $n$  is below 1, which reflects both the porous nature of the working electrode and its heterogeneity. Open Warburg element (Wo) is attributed to the diffusion of electrolyte ions into the tubular structure [71]. The fitting errors ( $\chi^2$ ) are of the order of  $10^{-3}$ – $10^{-4}$  and the values of all the parameters are summarised in Table 2. The lower value of the series resistance of the aligned-NT material than the spaced one indicates the good electrical conductivity of the close-packed NTs compared to the spaced ones. The good conductivity of the tubular layer promotes the migration of the photogenerated electrons in the conduction band of the semiconductor towards the current collector, thus reducing the electron-hole recombination rate since more electrons can be collected. Moreover, the charge transfer resistance of the aligned-NT material is found to be smaller compared to that of the spaced-NT. This indicates that the charge separation is faster at the aligned-NT/electrolyte interface than at the spaced-NT/electrolyte interface. This rapid charge transfer across the aligned-NT/electrolyte interface can also explain the good photoresponse of the aligned NT-based material. As depicted in Table 2, the charge transfer resistances of the aligned-NT and spaced-NT dropped significantly under UV-vis illumination. This results from the improvement in the conductivity of titania materials due to the additional light-generated electrons in the conduction band. The increase in the material's conductivity will obviously raise the charge separation rate at the semiconductor/electrolyte interface [71].

Mott-Schottky plots of aligned and spaced NTs grown onto one side of ITO-coated glass were provided to conduct a qualitative investigation of the influence of the materials' architecture on the flat band potential position and the corresponding donor density. The Mott-Schottky relation for an n-type semiconductor is given as:

$$C^{-2} = \left( \frac{2}{\epsilon \epsilon_0 N_D} \right) \left( E - E_{fb} - \frac{kT}{e} \right) \quad (4)$$

where  $C$  is the space charge capacitance,  $\epsilon$  is the permittivity of the anatase titania ( $\epsilon = 38$ ) [72],  $\epsilon_0$  is the permittivity of the free space ( $8.85 \times 10^{-14}$  F/cm),  $e$  is the electron charge,  $N_D$  is the donor density,  $E$  is the applied potential,  $E_{fb}$  is the flat band potential,  $k$  is the Boltzmann constant, and  $T$  is the temperature. The capacitance of the space charge layer can be calculated using the following equation:

$$C = - \frac{1}{2\pi f Z'} \quad (5)$$

where  $f$  is the frequency of the AC signal, and  $Z'$  is the imaginary part of impedance [3]. The Mott-Schottky plots for both architectures have a positive slope, namely n-type semiconductor behaviour. Extrapolating the linear regions of the curve  $C^{-2}$  vs.  $E/V$  vs. Ag/AgCl/0.1 M KCl, as shown in Fig. 10, the flat band potential values ( $E_{fb}$ ) were found to be

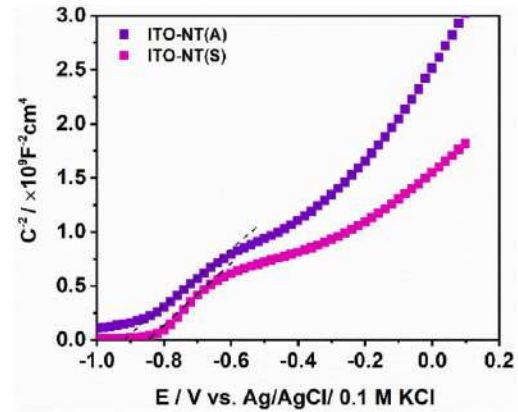


Fig. 10. Mott-Schottky curves of aligned and spaced NTs grown on ITO-coated glass.

−0.85 vs. Ag/AgCl/0.1 M KCl for the spaced-NT material and −0.96 V vs. Ag/AgCl/0.1 M KCl for the aligned-NT. There was a negative shift of the flat band potential position for the aligned-NT with respect to that of the spaced-NT. The more negative flat band potential value of the aligned-NT indicates greater accumulation of electrons in the titania structure and reflects a decrease in electron-hole pair recombination [73,74]. This is in agreement with the good electrical conductivity of the aligned-NT material compared to the spaced-NT, as discussed in the electrochemical impedance spectroscopy analysis. The shift between the flat band potentials of the aligned-NT and the spaced-NT is about 0.11 V vs. Ag/AgCl/0.1 M KCl. In general, the presence of surface states, defects and oxygen vacancies (owing to the charge compensation effect) in the semiconductor is the main reason for the shift in the flat band potential [71].

As compared to the flat band potential value of ca. −0.78 V vs Ag/AgCl reported by Vadla et al. [3] for pure anodic aligned NTs grown on a semitransparent substrate (Kapton HN polyimide sheet), the aligned-NT architectures synthesized in this work led to a cathodic shift of the flat band potential. This can be ascribed to the difference in the synthesis conditions. Indeed, in their work, a solvothermal process was carried out in an autoclave at 220 °C for 3 h to obtain the anatase TiO<sub>2</sub> instead of annealing the material in air.

By using the equation:

$$N_D = \left( \frac{2}{\epsilon \epsilon_0} \right) \left( \frac{dE}{dC^{-2}} \right) [14] \quad (6)$$

The calculated value of the donor density for the aligned-NT material ( $6.4 \times 10^{20}$  cm<sup>−3</sup>) was found to be greater than that of the spaced-NT ( $5.6 \times 10^{20}$  cm<sup>−3</sup>). This higher donor concentration for the aligned architecture is more evidence of its good electrical conductivity compared to the spaced-NT-based materials. In that case, more charge carriers are

Table 2

Values of fitting parameters obtained in the dark and under UV-vis illumination for NT(A)-ITO-NT(A), NT(S)-ITO-NT(S) and NT(A)-ITO-NT(S) electrodes.

	Sample	$R_s$ (kΩcm <sup>2</sup> )	$R_{ct}$ (kΩcm <sup>2</sup> )	$Q_{lin}$ (kΩ <sup>−1</sup> cm <sup>−2</sup> s <sup>−1</sup> )	$n$	$W_{ar}$ (kΩcm <sup>−2</sup> s <sup>0.5</sup> )	$W_{oc}$ (s <sup>0.5</sup> )
dark	NT(A)-ITO-NT(A)	0.026	42	0.203	0.69	10	1.08
	NT(S)-ITO-NT(S)	0.068	140	0.047	0.80	1.901	0.094
	NT(A)-ITO-NT(S)	0.020	91	0.058	0.80	2.446	0.074
UV-vis	NT(A)-ITO-NT(A)	0.026	19	0.119	0.73	6.602	1.163
	NT(S)-ITO-NT(S)	0.066	73	0.050	0.80	1.897	0.093
	FA <sub>NT</sub> (A)-ITO-NT(S)	0.02	58	0.063	0.78	2.306	0.071
	FS <sub>NT</sub> (A)-ITO-NT(S)	0.02	48	0.073	0.77	2.220	0.072

**Table 3**

Donor densities obtained from pure TiO<sub>2</sub> or TiO<sub>2</sub> modified with metal and non-metal nanoparticles obtained on conducting planar substrates.

Electrode material	Donor density/cm <sup>-3</sup>	Reference
TiO <sub>2</sub> (aligned NT)	$3.6 \times 10^{19}$	[14]
Ag-doped TiO <sub>2</sub> (aligned NT)	$3.93 \times 10^{20}$	
TiO <sub>2</sub> (aligned NT)	$8.9 \times 10^{19}$	[3]
TiO <sub>2</sub> (thin film)	$6.8 \times 10^{18}$	[71]
Cu-doped TiO <sub>2</sub> (thin film)	$9.0 \times 10^{18}$	
N-doped TiO <sub>2</sub> (thin film)	$12.4 \times 10^{18}$	
TiO <sub>2</sub> (thin film)	$3.83 \times 10^{20}$	[75]
TiO <sub>2</sub> (nanorods)	$1.4 \times 10^{22}$	[78]
Fe-doped TiO <sub>2</sub> (nanorods)	$4.1 \times 10^{22}$	
TiO <sub>2</sub> (thin film)	$4.5 \times 10^{20}$	[80]
TiO <sub>2</sub> (aligned NT)	$6.7 \times 10^{20}$	[76]
N-doped TiO <sub>2</sub> (aligned NT)	$3.9 \times 10^{20}$	
TiO <sub>2</sub> (aligned NT)	$4.5 \times 10^{19}$	[79]
TiO <sub>2</sub> -PbS heterostructure (aligned NT)	$2.3 \times 10^{20}$	
TiO <sub>2</sub> (nanoporous)	$1.99 \times 10^{19}$	[81]
One sheet TiO <sub>2</sub> (aligned NT)	$8.87 \times 10^{22}$	[77]
Two sheet TiO <sub>2</sub> (aligned NT)	$0.58 \times 10^{24}$	
Three sheet TiO <sub>2</sub> (aligned NT)	$1.7 \times 10^{24}$	
NT(S)	$5.6 \times 10^{20}$	This work
NT(A)	$6.4 \times 10^{20}$	This work

available to participate in the electrochemical process. As depicted in Table 3, the donor densities determined from the Mott-Schottky plots for the aligned and spaced NTs prepared are comparable in order of magnitude to the values reported by both Singh et al. [75] ( $3.83 \times 10^{20}$  cm<sup>-3</sup>) and Hanzu et al. [76] ( $6.7 \times 10^{20}$  cm<sup>-3</sup>) for pure TiO<sub>2</sub> materials. Comparing this to the values obtained for a pure NT layer developed by anodic oxidation of Ti films deposited onto other semitransparent substrates, namely a Kapton HN polyimide sheet ( $8.9 \times 10^{19}$  cm<sup>-3</sup>) [3] and soda-lime glass substrates ( $6.8 \times 10^{18}$  cm<sup>-3</sup>) [71], the synthesized NT (A) and NT(S) materials showed higher donor concentrations. However, the donor densities obtained by Mahmoud et al. [77] for pure NTs grown on Ti meshes with a wire diameter of 0.3 mm are four times higher in order of magnitude than that of NT(A). Excluding the results reported by Hanzu et al. [76], the modification of the TiO<sub>2</sub> material with metal or non-metal nanoparticle has led to an increase in the donor density with respect to their pristine TiO<sub>2</sub> counterpart, as shown in Table 3 for the work of Wang et al. [14], Garlisi et al. [71], Chakhari et al. [78] and Pathak et al. [79]. Similarly, modification of the aligned or spaced NTs formed on the two sides of planar substrates can be further modified with other heteroatoms to optimise the overall performance of the material.

#### 4. Conclusions

The work reports a novel concept of double-sided NT arrays with ITO collecting electrodes for light harvesting. An anodization method was adopted to successfully fabricate double-sided semitransparent photoanodes consisting of either aligned or spaced NTs; the nanotube arrays are grown on both sides of ITO-coated glass. A Raman study revealed that both the close- and loose-packed NTs exhibit the anatase phase after annealing. The spaced-NT material, with the largest average tube diameter (150 nm), provides a slightly redshifted absorption edge, by about 20 nm with respect to its aligned counterpart. Owing to its high tube density of ca.  $0.32 \times 10^{11}$  cm<sup>-2</sup> and larger average tube length (2 times longer than their spaced counterpart), NT(A)-ITO-NT(A) exhibited the largest photocurrent of  $4.6 \mu\text{Acm}^{-2}$  at 0.5 V. The good electrical properties of the aligned-NT material, indicated by its high donor concentration of  $6.4 \times 10^{20}$  cm<sup>-3</sup> and both its smaller series and charge transfer resistances, support the excellent photoelectrochemical properties of the NT(A)-ITO-NT(A) electrode. Even though the aligned nanostructures exhibited the best photoresponse, all the fabricated electrode materials can be used towards efficient light management after wall surface modification, e.g. deposition of a light absorber. The

elaborated synthesis route of NT(A)-ITO-NT(A), NT(A)-ITO-NT(S) and NT(S)-ITO-NT(S) is simple and reproducible. Further modifications, e.g. via deposition of some metal nanoparticles, organic molecules, or conducting polymers onto both sides of the proposed semitransparent NT electrodes, are currently under investigation. The modification of each side by different photoactive materials can lead to the formation a p-n heterojunction, where, for example, oxygen evolution will take place on one side while hydrogen generation occurs on the other. Such a tandem configuration can find also application in solar light-induced electrochemical sensing and catalysis of organics.

#### CRedit authorship contribution statement

**Dujeoric-Stephane Kouao:** Investigation, Writing – original draft, Conceptualization, Data curation. **Jan Hanus:** Investigation. **Ondrej Kylian:** Investigation. **Radka Simerova:** Investigation. **Petr Sezemsky:** Investigation. **Vitezslav Stranak:** Methodology, Writing – review & editing, Conceptualization. **Katarzyna Grochowska:** Methodology, Writing – review & editing, Conceptualization. **Katarzyna Siuzdak:** Funding acquisition, Methodology, Writing – review & editing, Project administration, Conceptualization.

#### Declaration of competing interest

The authors declare that they have no known competing financial interests or personal relationships that could have appeared to influence the work reported in this paper.

#### Data availability

Data will be made available on request.

#### Acknowledgements

This research was funded by the National Science Centre, Poland, grant number 2020/02/Y/ST8/00030 and Czech Science Foundation agency through the project 21-05030K.

#### References

- [1] Elumalai NK, Vijila C, Jose R, Uddin A, Ramakrishna S. Metal oxide semiconducting interfacial layers for photovoltaic and photocatalytic applications. *Mater Renew Sustain Energy* 2015;4:11. <https://doi.org/10.1007/s40243-015-0054-9>.
- [2] Büttner P, Döhler D, Korenko S, Möhrlein S, Bochmann S, Vogel N, Minguez-Bacho I, Bachmann J. Solid state interdigitated Sb<sub>2</sub>S<sub>3</sub> based TiO<sub>2</sub> nanotube solar cells. *RSC Adv* 2020;10:28225–31. <https://doi.org/10.1039/D0RA04123H>.
- [3] Vadla SS, Bandyopadhyay P, John S, Ghosh P, Roy SC. TiO<sub>2</sub> nanotube arrays on flexible Kapton substrates for photo-electrochemical solar energy conversion. *ACS Appl Nano Mater* 2020;3:11715–24. <https://doi.org/10.1021/acsann.0c02028>.
- [4] Naoi K, Ohko Y, Tatsuma T. TiO<sub>2</sub> films loaded with silver nanoparticles: control of multicolor photochromic behavior. *J Am Chem Soc* 2004;126:3664–8. <https://doi.org/10.1021/ja039474z>.
- [5] Biancardo M, Argazzi R, Bignozzi CA. Solid-State photochromic device based on nanocrystalline TiO<sub>2</sub> functionalized with electron Donor–Acceptor species. *Inorg Chem* 2005;44:9619–21. <https://doi.org/10.1021/ic0514593>.
- [6] Shin K, Park JH. Highly transparent dual-sensitized titanium dioxide nanotube arrays for spontaneous solar water splitting tandem configuration. *ACS Appl Mater Interfaces* 2015;7:18429–34. <https://doi.org/10.1021/acsami.5b04521>.
- [7] Petrisková P, Monfort O, Satrapinsky L, Dobročka E, Plecenik T, Plesch G, Papsík R, Bermejo R, Lencés Z. Preparation and photocatalytic activity of TiO<sub>2</sub> nanotube arrays prepared on transparent spinel substrate. *Ceram Int* 2021;47:12970–80. <https://doi.org/10.1016/j.ceramint.2021.01.160>.
- [8] Zheng Q, Kang H, Yun J, Lee J, Park JH, Baik S. Hierarchical construction of self-standing anodized titania nanotube arrays and nanoparticles for efficient and cost-effective front-illuminated dye-sensitized solar cells. *ACS Nano* 2011;5:5088–93. <https://doi.org/10.1021/nn201169u>.
- [9] Imran M, Riaz S, Naseem S. Synthesis and characterization of titania nanoparticles by sol-gel technique. *Mater Today Proc* 2015;2:5455–61. <https://doi.org/10.1016/j.matpr.2015.11.069>.
- [10] Bjelajac A, Petrović R, Djokic V, Matolin V, Vondraček M, Dembele K, Moldovan S, Ersen O, Socol G, Mihailescu IN, Janacković D. Enhanced absorption of TiO<sub>2</sub> nanotubes by N-doping and CdS quantum dots sensitization: insight into the structure. *RSC Adv* 2018;8:35073–82. <https://doi.org/10.1039/C8RA06341A>.



- [11] Tesler AB, Altomare M, Schmuki P. Morphology and optical properties of highly ordered TiO<sub>2</sub> nanotubes grown in NH<sub>4</sub>F/o -H<sub>3</sub>PO<sub>4</sub> electrolytes in view of light-harvesting and catalytic applications. *ACS Appl Nano Mater* 2020;3:10646–58. <https://doi.org/10.1021/acsanm.0c01859>.
- [12] Dong X, Li Y, Lin Z, Ge J, Qiu J. Oriented TiO<sub>2</sub> nanowire array grown on curved surface of Ti wire with superior photoelectrochemical properties. *Appl Surf Sci* 2013;270:457–61. <https://doi.org/10.1016/j.apsusc.2013.01.048>.
- [13] Luo D, Liu B, Fujishima A, Nakata K. TiO<sub>2</sub> nanotube arrays formed on Ti meshes with periodically arranged holes for flexible dye-sensitized solar cells. *ACS Appl Nano Mater* 2019;2:3943–50. <https://doi.org/10.1021/acsanm.9b00849>.
- [14] Wang S, Zhang Z, Huo W, Zhu K, Zhang X, Zhou X, Fang F, Xie Z, Jiang J. Preferentially oriented Ag-TiO<sub>2</sub> nanotube array film: an efficient visible-light-driven photocatalyst. *J Hazard Mater* 2020;399:123016. <https://doi.org/10.1016/j.jhazmat.2020.123016>.
- [15] Nguyen NT, Ozkan S, Tomanec O, Zboril R, Schmuki P. Spaced Titania Nanotube Arrays Allow the Construction of an Efficient N-Doped Hierarchical Structure for Visible-Light Harvesting. *ChemistryOpen* 2018;7:131–5. <https://doi.org/10.1002/open.201700199>.
- [16] Ozkan S, Nguyen NT, Mazare A, Hahn R, Cerri I, Schmuki P. Fast growth of TiO<sub>2</sub> nanotube arrays with controlled tube spacing based on a self-ordering process at two different scales. *Electrochim Commun* 2017;77:98–102. <https://doi.org/10.1016/j.elecom.2017.03.007>.
- [17] Zhang B, Sun S, Shi N, Liao X, Yin G, Huang Z, Chen X, Pu X. Spaced TiO<sub>2</sub> nanotube arrays for electrodeposition of MoO<sub>3</sub> to achieve high electrochemical performance. *J Alloys Compd* 2020;820:153066. <https://doi.org/10.1016/j.jallcom.2019.153066>.
- [18] Galstyan V, Macak JM, Djenzian T. Anodic TiO<sub>2</sub> nanotubes: A promising material for energy conversion and storage. *Appl Mater Today* 2022;29:101613. <https://doi.org/10.1016/j.apmt.2022.101613>.
- [19] Ozkan S, Valle F, Mazare A, Hwang I, Taccardi N, Zazpe R, Macak JM, Cerri I, Schmuki P. Optimized Polymer Electrolyte Membrane Fuel Cell Electrode Using TiO<sub>2</sub> Nanotube Arrays with Well-Defined Spacing. *ACS Appl Nano Mater* 2020;3:4157–70. <https://doi.org/10.1021/acsanm.0c00325>.
- [20] Yang H, Pan C. Diameter-controlled growth of TiO<sub>2</sub> nanotube arrays by anodization and its photoelectric property. *J Alloys Compd* 2010;492:133–5. <https://doi.org/10.1016/j.jallcom.2009.11.112>.
- [21] Wang S, Zhang Z, Huo W, Zhu K, Zhang X, Zhou X, Fang F, Xie Z, Jiang J. Preferentially oriented Ag-TiO<sub>2</sub> nanotube array film: An efficient visible-light-driven photocatalyst. *J Hazard Mater* 2020;399:123016. <https://doi.org/10.1016/j.jhazmat.2020.123016>.
- [22] Tang Y, Tao J, Dong Z, Oh JT, Chen Z. The formation of micrometer-long TiO<sub>2</sub> nanotube arrays by anodization of titanium film on conducting glass substrate. *Adv Nat Sci Nanosci Nanotechnol* 2011;2:045002. <https://doi.org/10.1088/2043-6262/2/4/045002>.
- [23] Matteucci F, Cinà L, Lamanna E, Cacovich S, Divitini G, Midgley PA, Ducati C, Di Carlo A. Encapsulation for long-term stability enhancement of perovskite solar cells. *Nano Energy* 2016;30:162–72. <https://doi.org/10.1016/j.nanoen.2016.09.041>.
- [24] Pan X, Hong X, Xu L, Li Y, Yan M, Mai L. On-chip micro/nano devices for energy conversion and storage. *Nano Today* 2019;28:100764. <https://doi.org/10.1016/j.nantod.2019.100764>.
- [25] Zelny M, Kment S, Cvrtilik R, Pausova S, Kmentova H, Tomastik J, Hubicka Z, Rambabu V, Krysa J, Naldoni A, Schmuki P, Zboril R. TiO<sub>2</sub> Nanotubes on Transparent Substrates: Control of Film Microstructure and Photoelectrochemical Water Splitting Performance. *Catalysts* 2018;8:25. <https://doi.org/10.3390/catal8010025>.
- [26] Mandić V, Plodinec M, Kereković I, Jurać K, Janicki V, Gracin D, Gajović A, Moguš-Milanković A, Willinger MG. Tailoring anatase nanotubes for the photovoltaic device by the anodization process on behalf of microstructural features of titanium thin film. *Sol Energy Mater Sol Cells* 2017;168:136–45. <https://doi.org/10.1016/j.solmat.2017.04.028>.
- [27] Oh SJ, Kwon JH, Lee S, Choi KC, Kim T-S. Unveiling the Annealing-Dependent Mechanical Properties of Freestanding Indium Tin Oxide Thin Films. *ACS Appl Mater Interfaces* 2021;13:16650–9. <https://doi.org/10.1021/acsami.0c23112>.
- [28] Chen C, Li F, Li G, Tan F, Li S, Ling L. Double-sided transparent electrodes of TiO<sub>2</sub> nanotube arrays for highly efficient CdS quantum dot-sensitized photoelectrodes. *J Mater Sci* 2014;49:1868–74. <https://doi.org/10.1007/s10853-013-7875-7>.
- [29] Motola M, Sopha H, Krbal M, Hromádka L, Zmrhalová Z, Plesch G, Macak JM. Comparison of photoelectrochemical performance of anodic single- and double-walled TiO<sub>2</sub> nanotube layers. *Electrochim Commun* 2018;97:1–5. <https://doi.org/10.1016/j.elecom.2018.09.015>.
- [30] Kathirvel S, Su C, Yang C-Y, Shiao Y-J, Chen B-R, Li W-R. The growth of TiO<sub>2</sub> nanotubes from sputter-deposited Ti film on transparent conducting glass for photovoltaic applications. *Vacuum* 2015;118:17–25. <https://doi.org/10.1016/j.vacuum.2014.12.024>.
- [31] Varghese OK, Paulose M, Grimes CA. Long vertically aligned titania nanotubes on transparent conducting oxide for highly efficient solar cells. *Nat Nanotechnol* 2009;4:592–7. <https://doi.org/10.1038/nnano.2009.226>.
- [32] Jang N-S, Kim MS, Kim S-H, Lee S-K, Kim J-M. Direct growth of titania nanotubes on plastic substrates and their application to flexible gas sensors. *Sensors Actuators B Chem* 2014;199:361–8. <https://doi.org/10.1016/j.smb.2014.03.113>.
- [33] Meyerink JG, Kota D, Wood ST, Crawford GA. Transparent titanium dioxide nanotubes: Processing, characterization, and application in establishing cellular response mechanisms. *Acta Biomater* 2018;79:364–74. <https://doi.org/10.1016/j.actbio.2018.08.039>.
- [34] McCann T. Live Cell Imaging: An Industrial Perspective 2010:47–66. [https://doi.org/10.1007/978-1-60761-404-3\\_3](https://doi.org/10.1007/978-1-60761-404-3_3).
- [35] Mor GK, Varghese OK, Wilke RHT, Sharma S, Shankar K, Latempa TJ, Choi K-S, Grimes CA. p-Type Cu–Ti–O Nanotube Arrays and Their Use in Self-Biased Heterojunction Photoelectrochemical Diodes for Hydrogen Generation. *Nano Lett* 2008;8:1906–11. <https://doi.org/10.1021/nl080572y>.
- [36] Kim H. Metallic triangular pillar grating arrays for high transmission polarizers for air/glass interfaces. *Jpn J Appl Phys* 2019;58:042001. <https://doi.org/10.7567/1347-4065/ab0274>.
- [37] Mohapatra SK, Mahajan VK, Misra M. Double-side illuminated titania nanotubes for high volume hydrogen generation by water splitting. *Nanotechnology* 2007;18:445705. <https://doi.org/10.1088/0957-4484/18/44/445705>.
- [38] Sun L, Zhang S, Sun XW, Wang X, Cai Y. Double-Sided Anodic Titania Nanotube Arrays: A Lopsided Growth Process. *Langmuir* 2010;26:18424–9. <https://doi.org/10.1021/la103390s>.
- [39] Niu D, Han A, Cheng H, Ma S, Tian M, Liu L. Effects of organic solvents in anodization electrolytes on the morphology and tube-to-tube spacing of TiO<sub>2</sub> nanotubes. *Chem Phys Lett* 2019;735:136776. <https://doi.org/10.1016/j.cpllet.2019.136776>.
- [40] Mohamed AER, Kasemphaibulsuk N, Rohani S, Barghi S. Fabrication of Titania Nanotube Arrays in Viscous Electrolytes. *J Nanosci Nanotechnol* 2010;10:1998–2008. <https://doi.org/10.1166/jnn.2010.2102>.
- [41] Paramasivam I, Macak JM, Selvam T, Schmuki P. Electrochemical synthesis of self-organized TiO<sub>2</sub> nanotubular structures using an ionic liquid (BMIM-BF<sub>4</sub>). *Electrochim Acta* 2008;54:643–8. <https://doi.org/10.1016/j.electacta.2008.07.031>.
- [42] Ozkan S, Nguyen NT, Mazare A, Cerri I, Schmuki P. Controlled spacing of self-organized anodic TiO<sub>2</sub> nanotubes. *Electrochim Commun* 2016;69:76–9. <https://doi.org/10.1016/j.elecom.2016.06.004>.
- [43] Mor GK, Shankar K, Paulose M, Varghese OK, Grimes CA. Enhanced photocleavage of Water Using Titania Nanotube Arrays. *Nano Lett* 2005;5:191–5. <https://doi.org/10.1021/nl048301k>.
- [44] Yoriya S, Paulose M, Varghese OK, Mor GK, Grimes CA. Fabrication of Vertically Oriented TiO<sub>2</sub> Nanotube Arrays Using Dimethyl Sulfoxide Electrolytes. *J Phys Chem C* 2007;111:13770–6. <https://doi.org/10.1021/jp074655e>.
- [45] Mohammadian-Sarcheshmeh H, Arazzi R, Mazloum-Ardakani M. Application of bifunctional photoanode materials in DSSCs: A review. *Renew Sustain Energy Rev* 2020;134:110249. <https://doi.org/10.1016/j.rser.2020.110249>.
- [46] Liu G, Du K, Wang K. Surface wettability of TiO<sub>2</sub> nanotube arrays prepared by electrochemical anodization. *Appl Surf Sci* 2016;388:313–20. <https://doi.org/10.1016/j.apsusc.2016.01.010>.
- [47] Ilie AG, Scarisoareanu M, Morjan I, Dutu E, Badiceanu M, Mihailescu I. Principal component analysis of Raman spectra for TiO<sub>2</sub> nanoparticle characterization. *Appl Surf Sci* 2017;417:93–103. <https://doi.org/10.1016/j.apsusc.2017.01.193>.
- [48] Durgam K, Eppa R. Effect of metal ions doping on structural, optical properties and photocatalytic activity of anatase TiO<sub>2</sub> thin films. *Surf Interface Anal* 2021;53:194–205. <https://doi.org/10.1002/sia.6901>.
- [49] Georgescu D, Baia L, Ersen O, Baia M, Simon S. Experimental assessment of the phonon confinement in TiO<sub>2</sub> anatase nanocrystallites by Raman spectroscopy. *J Raman Spectrosc* 2012;43:876–83. <https://doi.org/10.1002/jrs.3103>.
- [50] Mathpal MC, Tripathi AK, Singh MK, Gairola SP, Pandey SN, Agarwal A. Effect of annealing temperature on Raman spectra of TiO<sub>2</sub> nanoparticles. *Chem Phys Lett* 2013;555:182–6. <https://doi.org/10.1016/j.cpllet.2012.10.082>.
- [51] Charalambous H, Jha SK, Wang H, Phuah XL, Wang H, Tsakalakos T. Inhomogeneous reduction and its relation to grain growth of titania during flash sintering. *Scr Mater* 2018;155:37–40. <https://doi.org/10.1016/j.scriptamat.2018.06.017>.
- [52] Gao J, Xue J, Jia S, Shen Q, Zhang X, Jia H, Liu X, Li Q, Wu Y. Self-Doping Surface Oxygen Vacancy-Induced Lattice Strains for Enhancing Visible Light-Driven Photocatalytic H<sub>2</sub> Evolution over Black TiO<sub>2</sub>. *ACS Appl Mater Interfaces* 2021;13:18758–71. <https://doi.org/10.1021/acsami.1c01101>.
- [53] Lai YK, Sun L, Chen C, Nie CG, Zuo J, Lin CJ. Optical and electrical characterization of TiO<sub>2</sub> nanotube arrays on titanium substrate. *Appl Surf Sci* 2005;252:1101–6. <https://doi.org/10.1016/j.apsusc.2005.02.035>.
- [54] Ge R, Fu W, Yang H, Zhang Y, Zhao W, Liu Z, Wang C, Zhu H, Yu Q, Zou G. Fabrication and characterization of highly-ordered titania nanotubes via electrochemical anodization. *Mater Lett* 2008;62:2688–91. <https://doi.org/10.1016/j.matlet.2008.01.015>.
- [55] Mor GK, Varghese OK, Paulose M, Grimes CA. Transparent Highly Ordered TiO<sub>2</sub> Nanotube Arrays via Anodization of Titanium Thin Films. *Adv Funct Mater* 2005;15:1291–6. <https://doi.org/10.1002/adfm.200500096>.
- [56] Chen CH, Shieh J, Hsieh SM, Kuo CL, Liao HY. Architecture, optical absorption, and photocurrent response of oxygen-deficient mixed-phase titania nanostructures. *Acta Mater* 2012;60:6429–39. <https://doi.org/10.1016/j.actamat.2012.08.030>.
- [57] Peng Y-H, Huang G-F, Huang W-Q. Visible-light absorption and photocatalytic activity of Cr-doped TiO<sub>2</sub> nanocrystal films. *Adv Powder Technol* 2012;23:8–12. <https://doi.org/10.1016/j.apmt.2010.11.006>.
- [58] Singh MK, Mehata MS. Phase-dependent optical and photocatalytic performance of synthesized titanium dioxide (TiO<sub>2</sub>) nanoparticles. *Optik (Stuttgart)* 2019;193:163011. <https://doi.org/10.1016/j.ijleo.2019.163011>.
- [59] Welte A, Waldauf C, Bräbe C, Wellmann PJ. Application of optical absorbance for the investigation of electronic and structural properties of sol-gel processed TiO<sub>2</sub> films. *Thin Solid Films* 2008;516:7256–9. <https://doi.org/10.1016/j.tsf.2007.12.025>.

- [60] Freitas RG, Santana MA, Pereira EC. Dependence of TiO<sub>2</sub> nanotube microstructural and electronic properties on water splitting. *J Power Sources* 2014; 251:178–86. <https://doi.org/10.1016/j.jpowsour.2013.11.067>.
- [61] Ghicov A, Tsuchiya H, Hahn R, Macak JM, Muñoz AG, Schmuki P. TiO<sub>2</sub> nanotubes: H<sup>+</sup> insertion and strong electrochromic effects. *Electrochem Commun* 2006;8: 528–32. <https://doi.org/10.1016/j.elecom.2006.01.015>.
- [62] Xiao P, Liu D, Garcia BB, Sepehri S, Zhang Y, Cao G. Electrochemical and photoelectrical properties of titania nanotube arrays annealed in different gases. *Sensors Actuators B Chem* 2008;134:367–72. <https://doi.org/10.1016/j.snb.2008.05.005>.
- [63] Liao W, Yang J, Zhou H, Murugananthan M, Zhang Y. Electrochemically Self-Doped TiO<sub>2</sub> Nanotube Arrays for Efficient Visible Light Photoelectrocatalytic Degradation of Contaminants. *Electrochim Acta* 2014;136:310–7. <https://doi.org/10.1016/j.electacta.2014.05.091>.
- [64] Sun L, Zhang S, Sun X, He X. Effect of the Geometry of the Anodized Titania Nanotube Array on the Performance of Dye-Sensitized Solar Cells. *J Nanosci Nanotechnol* 2010;10:4551–61. <https://doi.org/10.1166/jnn.2010.1695>.
- [65] Zhuang H-F, Lin C-J, Lai Y-K, Sun L, Li J. Some Critical Structure Factors of Titanium Oxide Nanotube Array in Its Photocatalytic Activity. *Environ Sci Technol* 2007;41:4735–40. <https://doi.org/10.1021/es0702723>.
- [66] Pan T-C, Wang S-H, Lal Y-S, Jehng J-M, Huang S-J. Study of the silver modified TiO<sub>2</sub> nanotube array applied to hydrogen evolution. *Appl Surf Sci* 2014;296: 189–94. <https://doi.org/10.1016/j.apsusc.2014.01.077>.
- [67] Pu P, Cachet H, Sutter EMM. Electrochemical impedance spectroscopy to study photo - induced effects on self-organized TiO<sub>2</sub> nanotube arrays. *Electrochim Acta* 2010;55:5938–46. <https://doi.org/10.1016/j.electacta.2010.05.048>.
- [68] Paulose M, Mor GK, Varghese OK, Shankar K, Grimes CA. Visible light photoelectrochemical and water-photoelectrolysis properties of titania nanotube arrays. *J Photochem Photobiol A Chem* 2006;178:8–15. <https://doi.org/10.1016/j.jphotochem.2005.06.013>.
- [69] Wang Q, Yang X, Wang X, Huang M, Hou J. Synthesis of N-doped TiO<sub>2</sub> mesopore by solvothermal transformation of anodic TiO<sub>2</sub> nanotubes and enhanced photoelectrochemical performance. *Electrochim Acta* 2012;62:158–62. <https://doi.org/10.1016/j.electacta.2011.12.009>.
- [70] Wang J, Wang H, Li H, Wu J. Synthesis and characterization of TiO<sub>2</sub> nanotube film on fluorine-doped tin oxide glass. *Thin Solid Films* 2013;544:276–80. <https://doi.org/10.1016/j.tsf.2013.03.104>.
- [71] Garlisi C, Lai C-Y, George I, Chiesa M, Palmisano G. Relating Photoelectrochemistry and Wettability of Sputtered Cu- and N-Doped TiO<sub>2</sub> Thin Films via an Integrated Approach. *J Phys Chem C* 2018;122:12369–76. <https://doi.org/10.1021/acs.jpcc.8b03650>.
- [72] Park BH, Li LS, Gibbons BJ, Huang JY, Jia QX. Photovoltaic response and dielectric properties of epitaxial anatase-TiO<sub>2</sub> films grown on conductive La<sub>0.5</sub>Sr<sub>0.5</sub>CoO<sub>3</sub> electrodes. *Appl Phys Lett* 2001;79:2797–9. <https://doi.org/10.1063/1.1412822>.
- [73] Zhang J, Bang JH, Tang C, Kamat PV. Tailored TiO<sub>2</sub>–SrTiO<sub>3</sub> Heterostructure Nanotube Arrays for Improved Photoelectrochemical Performance. *ACS Nano* 2010;4:387–95. <https://doi.org/10.1021/nn901087c>.
- [74] Saha S, Victorious A, Soleymani L. Modulating the photoelectrochemical response of titanium dioxide (TiO<sub>2</sub>) photoelectrodes using gold (Au) nanoparticles excited at different wavelengths. *Electrochim Acta* 2021;380:138154. <https://doi.org/10.1016/j.electacta.2021.138154>.
- [75] Singh AP, Kodan N, Mehta BR. Enhancing the photoelectrochemical properties of titanium dioxide by thermal treatment in oxygen deficient environment. *Appl Surf Sci* 2016;372:63–9. <https://doi.org/10.1016/j.apsusc.2016.03.072>.
- [76] Hanzu I, Djenizian T, Knauth P. Electrical and Proton Conduction Properties of Amorphous TiO<sub>2</sub> Nanotubes Fabricated by Electrochemical Anodization. *ECS Trans* 2011;35:21–31. <https://doi.org/10.1149/1.3570842>.
- [77] Mahmoud M, El-Kalliny AS, Squadrito G. Stacked titanium dioxide nanotubes photoanode facilitates unbiased hydrogen production in a solar-driven photoelectrochemical cell powered with a microbial fuel cell treating animal manure wastewater. *Energy Convers Manag* 2022;254:115225. <https://doi.org/10.1016/j.enconman.2022.115225>.
- [78] Fe-doped TiO<sub>2</sub> nanorods with enhanced electrochemical properties as efficient photoanode materials Chakhari W, Ben Naceur J, Ben Taleb S, Ben Assaker I, Chetoui R, editors. *J Alloys Compd* 2017;708:862–70. <https://doi.org/10.1016/j.jallcom.2016.12.181>.
- [79] Pathak P, Podzorski M, Bahnemann D, Subramanian VR. One-Pot Fabrication of High Coverage PbS Quantum Dot Nanocrystal-Sensitized Titania Nanotubes for Photoelectrochemical Processes. *J Phys Chem C* 2018;122:13659–68. <https://doi.org/10.1021/acs.jpcc.8b00120>.
- [80] Kavan L, Zúkalova M, Vik O, Havlicek D. Sol–Gel Titanium Dioxide Blocking Layers for Dye-Sensitized Solar Cells: Electrochemical Characterization. *ChemPhysChem* 2014;15:1056–61. <https://doi.org/10.1002/cphc.201400026>.
- [81] Xie G, Chang X, Adhikari BR, Thind SS, Chen A. Photoelectrochemical degradation of acetaminophen and valacyclovir using nanoporous titanium dioxide. *Chinese J Catal* 2016;37:1062–9. [https://doi.org/10.1016/S1872-2067\(15\)61101-9](https://doi.org/10.1016/S1872-2067(15)61101-9).



### 7.3 Anodization of TiAg alloy films deposited onto ITO-glass

#### A brief overview of the article A3

##### *Introduction*

In the previous subsections the growth of the tubular structure out of Ti film deposited onto one side and the two sides of the planar substrate was described. In general, the photoactivity of the pure tubular layer is relatively low due to the absorbance of light in the UV region of solar radiation. The raise of the photoelectrochemical activity of those electrodes is mostly related with the modification of the nanotubes layer, that can be realized via doping of non-metal and metal atoms or formation of the heterojunction together with highly photoactive material. In this work, the growth of aligned and spaced nanotubes out of titanium-silver deposited onto ITO-glass was investigated. The feasibility to grow tubular structure out of various Ti alloys film has been investigated by different research groups. Indeed, the anodization of alloys film such as TiNb<sup>25</sup>, TiCo<sup>26</sup>, TiFe<sup>27,28</sup>, TiMo<sup>29</sup>, TiW<sup>30</sup>, TiCu<sup>31</sup>, TiAg<sup>32</sup> have been reported. However, among all of those reports only the architecture composed of aligned nanotubes has been fabricated out of the deposited alloy films. Moreover, the investigation on the influence of the heteroatom content on the formation of the spaced nanotubes architecture has not been provided so far. Here, the anodization procedure was optimized towards formation of the aligned and spaced arrangement of nanotubes using as a substrate the alloy films, and the influence of tubular architecture and presence of the heteroatom on the photoactivity was also studied.

##### *Processing conditions and morphology analysis of the anodized tubular layer*

Aligned and spaced nanotubes were grown after the anodization of the TiAg films obtained from the prof. Vitezslav Stranak group from Czech Republic. The prepared samples were labelled a-xAg-TNT (for aligned nanotubes) and s-xAg-TNT (for the spaced nanotubes) where x is defined as silver content in the initial deposited TiAg film ( $x = 1.7, 3.5$  and  $5\%$ ). The anodization conditions for the aligned and the spaced architecture optimized for pure Ti obtained in the first subsection (i.e. in paragraph 7.1) were used and the anodization was stopped when the substrates became transparent. The obtained tubular morphologies, i.e. the SEM top and cross section images, are shown in **Figure 70** and **Figure 71** for the aligned TNT samples and in **Figure 72** and **Figure 73** for the spaced TNT.

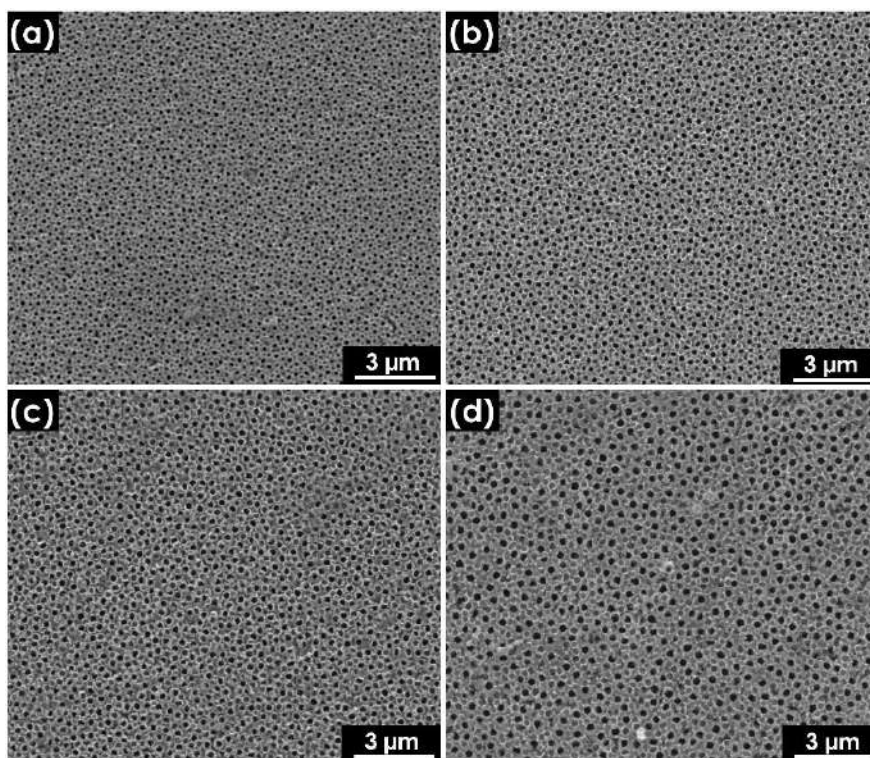


**Figure 70.** SEM top images of the anodized samples: (a) a-TNT, (b) a-1.7Ag-TNT, (c) a-3.5Ag-TNT and (d) a-5Ag-TNT. (Reproduced from article A3).

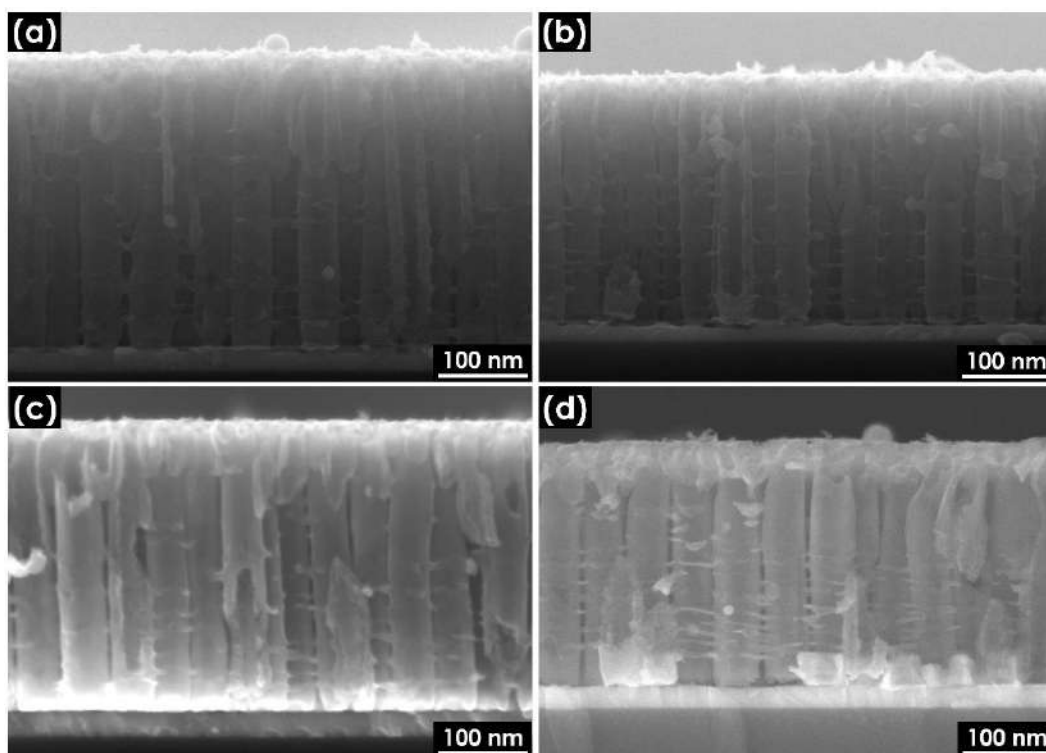


**Figure 71.** SEM cross-section images of the anodized samples: (a) a-TNT, (b) a-1.7Ag-TNT, (c) a-3.5Ag-TNT and (d) a-5Ag-TNT. (Reproduced from article A3).

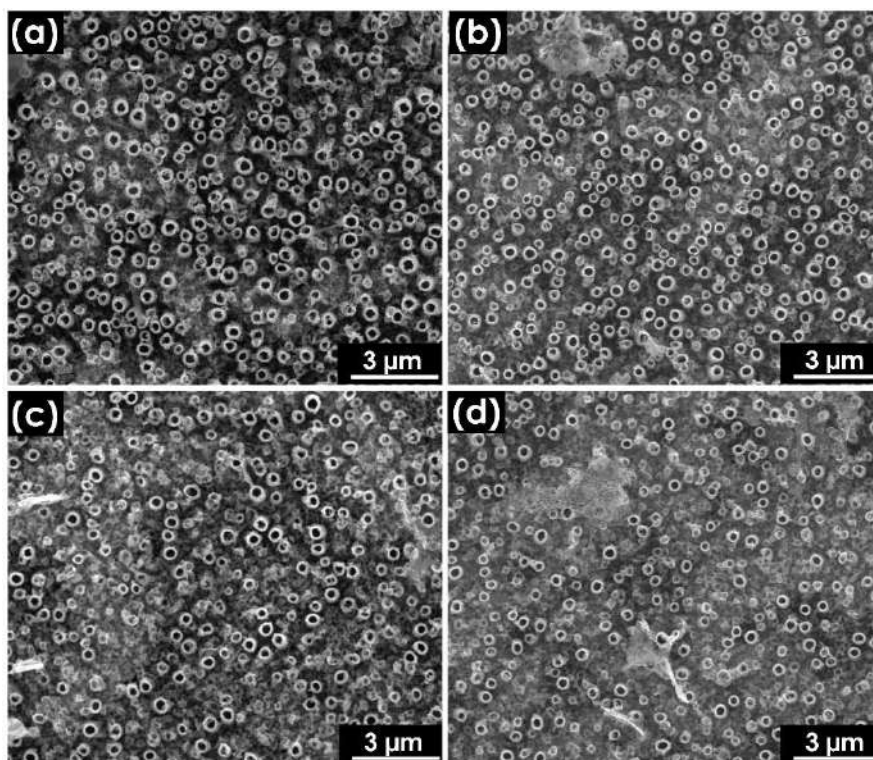


**Figure 72.** SEM images of the anodized samples: (a) s-TNT , (b) s-1.7Ag-TNT, (c) s-3.5Ag-TNT and (d) s-5Ag-TNT. (Reproduced from article A3).

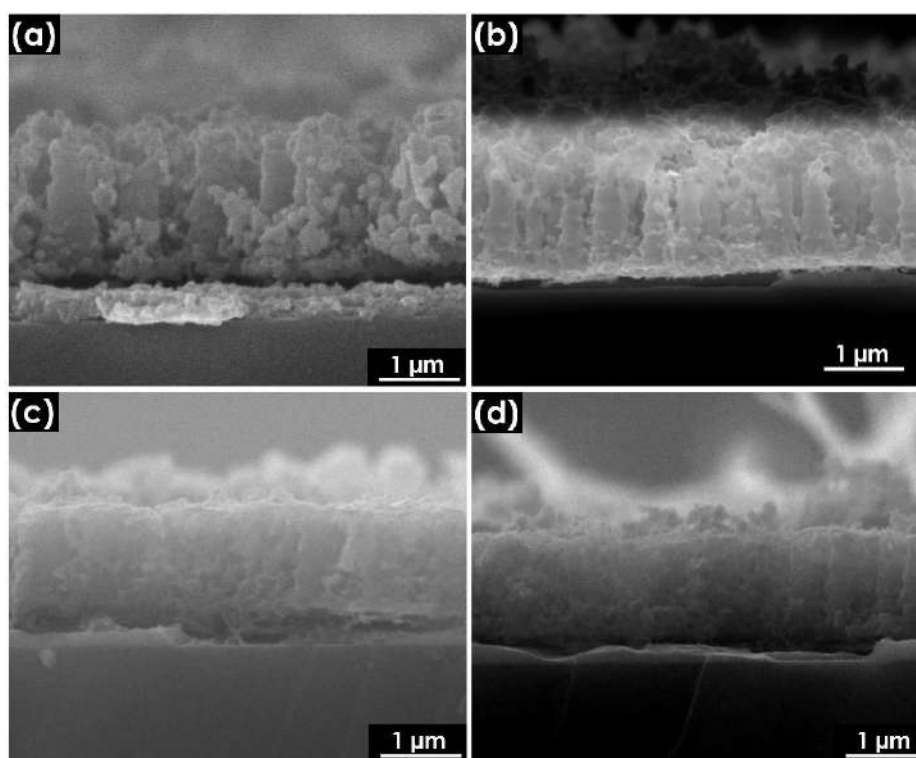


**Figure 73.** SEM cross-section images of the anodized samples: (a) s-TNT , (b) s-1.7Ag-TNT, (c) s-3.5Ag-TNT and (d) s-5Ag-TNT. (Reproduced from article A3).

Additional information about the geometry characteristics of the samples are provided. The geometrical features of the TNT are summarized in **Table 8**.

**Table 8.** Averaged inner diameters and lengths of as-prepared TNT.

aligned nanotubes			spaced nanotubes		
sample	inner diameter /nm	nanotube length/ nm	sample	inner diameter /nm	nanotube length /nm
<b>a-TNT</b>	$61 \pm 10$	$1200 \pm 26$	<b>s-TNT</b>	$129 \pm 13$	$590 \pm 29$
<b>a-1.7Ag-TNT</b>	$59 \pm 9$	$1127 \pm 23$	<b>s-1.7Ag-TNT</b>	$105 \pm 18$	$544 \pm 68$
<b>a-3.5Ag-TNT</b>	$60 \pm 10$	$1113 \pm 30$	<b>s-3.5Ag-TNT</b>	$110 \pm 20$	$494 \pm 51$
<b>a-5Ag-TNT</b>	$77 \pm 10$	$1049 \pm 30$	<b>s-5Ag-TNT</b>	$102 \pm 24$	$451 \pm 46$

There is no significant change in the pore diameters of the a-1.7Ag-TNT and a -3.5Ag-TNT samples, compared to the pure aligned TNT material (a-TNT). The increase of the Ag content to 5 % in the deposited film leads to an abrupt increase of the pore diameter of about 16 nm with respect to that of a-TNT. Although the tube length decreases slightly with the increase of Ag content in the deposited TiAg alloys, it is worth noting that the obtained average lengths for the a-TNT, a-1.7Ag-TNT, a -3.5Ag-TNT, and a-5Ag-TNT materials are roughly 2 times greater than the initial deposited TiAg film thickness (ca. 500 nm). As shown in **Table 8**, both the tube diameters and lengths of the s-1.7Ag-TNT, s-3.5Ag-TNT and a-5Ag-TNT materials are shorter comparing to s-TNT. Moreover, the average tube lengths of the s -3.5Ag -TNT and a-5Ag-TNT samples are found to be smaller than the deposited TiAg film thickness (**Table 8**). This may be related with the electrolyte composition, particularly the HF content in the electrolyte. Similar observations were reported by Premchand et al.<sup>193</sup> It was shown that a tube length of 560 nm was achieved when anodizing 1.92  $\mu\text{m}$  thick Ti film deposited onto Si substrates in an electrolyte containing 0.5 wt% HF. Yoriya et al.<sup>194</sup> also demonstrated that the presence of HF in the electrolyte results in relatively faster dissolution of the oxide layer forming at the top, thus limiting the nanotube length. This severe etching at the pore mouth can also explain the large pore diameters of the spaced TNT ( $102 \pm 24$  nm -  $129 \pm 13$  nm) comparing to the aligned materials ( $61 \pm 13$  nm -  $77 \pm 16$  nm).

### Structural properties

**Figure 74** depicts the Raman spectra of the prepared titania materials after annealing at 450 °C.

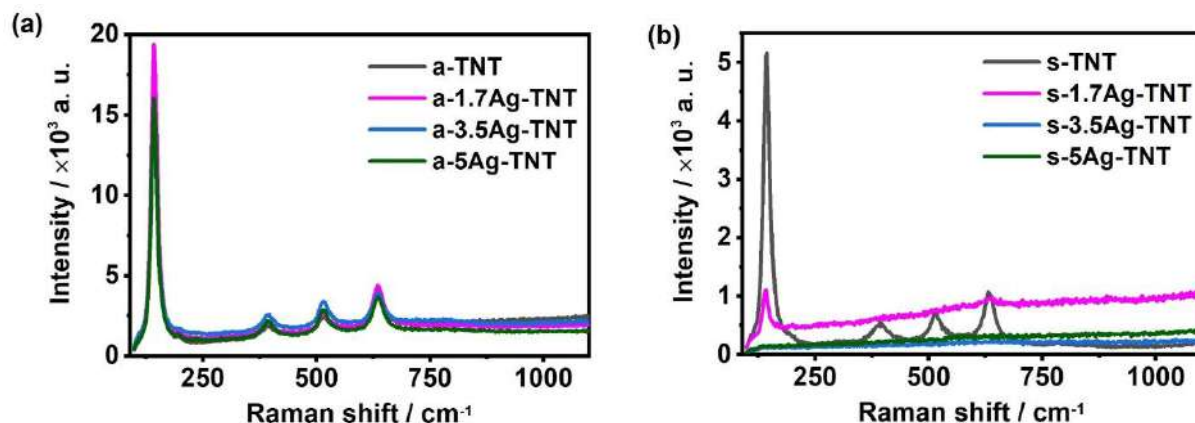


**Figure 74** Raman spectra recorded for: (a) a-TNT, a-1.7Ag-TNT, a-3.5Ag-TNT, a-5Ag-TNT, (b) s-TNT, s-1.7Ag-TNT, s-3.5Ag-TNT, s-5Ag-TNT. (Reproduced from article A3).

The spectra recorded for all aligned TNT samples show the series of peaks characteristic for anatase found at 144, 398, 515, and 640  $\text{cm}^{-1}$ , which are associated to the active vibrational modes of  $E_{1g}$ ,  $B_{1g}$ ,  $A_{1g}$ , and  $E_{3g}$ , respectively. In the case of the spaced titania, the Raman spectrum of s-1.7Ag-TNT shows only the most intense anatase peak at 143  $\text{cm}^{-1}$ . Raman spectra of the spaced TNT obtained for a Ag content above 1.7 % indicated that s-3.5Ag-TNT and s-5Ag-TNT samples are amorphous. In the article A3, XRD data were also given for the spaced TNT samples. The results indicated the presence of some trace amount of anatase titania in the s-3.5Ag-TNT and s-5Ag-TNT samples. This demonstrates that although all spaced TNT samples were calcined under the same conditions, s-3.5Ag-TNT and s-5Ag-TNT are not completely crystalline in the whole volume.

### Electrochemical response of the anodized alloy samples

Details of the investigation on the photoactivity of the anodized alloy films are discussed in **the article A3**. However, this subsection not only concerns the influence of the nanotube architecture and heterometal content on the photoactivity of the semitransparent material, but also the unique electrochemical response of the obtained tubular layer out of the alloy films, which are unknown for nanotubes developed from the pure Ti film. The ordered nanostructures obtained after anodizing the alloy films exhibit significantly higher voltammetric currents than the bare layers i.e. a-TNT and s-TNT. In addition, all active layers formed out of the alloys

exhibit redox peaks that are not observed for the tubular layer obtained with the pure Ti films. In agreement with the literature, namely Krysa et al.<sup>195</sup>, one can find the experimental evidence that the pure TiO<sub>2</sub> layer deposited onto TCO (i.e. FTO) does not exhibit redox peaks when the electrode is immersed in the neutral electrolyte i.e. KCl solution containing K<sub>3</sub>Fe(CN)<sub>6</sub>. Briefly, Krysa et al.<sup>195</sup> sputtered Ti film onto FTO substrate and then converted this Ti film into TiO<sub>2</sub> layer by thermal oxidation at different temperatures leading to formation of FTO/TiO<sub>2</sub>. The XRD analysis as well as semitransparency has confirmed the complete conversion of the titanium film into crystalline TiO<sub>2</sub> layer. Electrochemical tests performed in KCl based electrolyte containing a ferricyanide redox pair have shown that on the contrary to bare FTO electrode, the prepared FTO/TiO<sub>2</sub> does not exhibit any redox behaviour due to the semiconducting behaviour of titania. As discussed in the **article A2**, the TCO substrates such as ITO or FTO, exhibit the redox behaviour because they are characterized with very good conductivity (sheet resistance of  $\sim 10 \Omega$ ). For each architecture of titania nanotubes cyclic voltammetry curves were recorded and CV for a-TNT, a-5Ag-TNT, s-TNT and s-5Ag-TNT samples are presented in **Figure 75**.

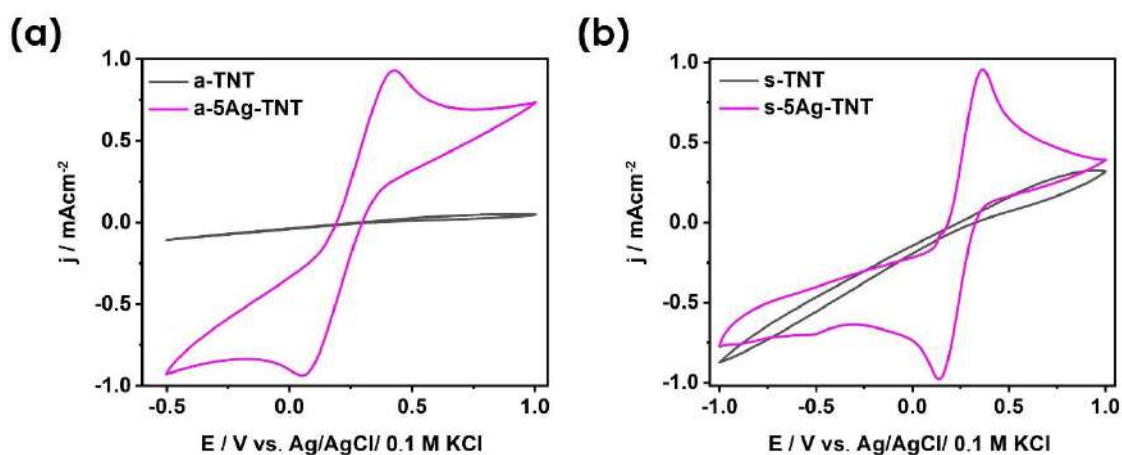


**Figure 75.** Cyclic voltammograms of (a) a-TNT and a-5Ag-TNT and (b) s-TNT and s-5Ag-TNT recorded in 0.5 M Na<sub>2</sub>SO<sub>4</sub> + 10 mM K<sub>3</sub>Fe(CN)<sub>6</sub> at 50 mVs<sup>-1</sup>. (Reproduced from article A3).

It should be mentioned that EDX elemental analysis showed that about 60 % of the initial Ag content is still present in the tubular layer of the aligned nanotube samples, while the Ag content in the spaced nanotube samples is out of detection limit. However, the peak-to-peak separation distance for the spaced nanotubes sample is 0.2 V vs. Ag/AgCl/0.1 M KCl, which is smaller comparing to that of the aligned nanotubes sample (0.3 V vs. Ag/AgCl/0.1 M KCl).



This indicated that s-5Ag-TNT exhibits high electrochemical reversibility, although no Ag was found in its nanotube layers. Therefore, the appearance of these peaks is associated rather with the redox reaction occurring on the ITO surface with the ferricyanide redox active species. Indeed, contact angle measurements have shown that the tubular layer produced out of the alloys films exhibits better wetting properties comparing to the bare TNT layers.

#### *Photoelectrochemical response of the anodized alloy samples*

In the next step, characterisation of the photoresponse of the fabricated electrode materials was carried out. The LSV curves recorded under chopped light are shown in **Figure 76**. Photoelectrode based on aligned TNT (i.e. 3.5 % of Ag content) exhibited about 3 times higher photocurrents than its counterpart formed out of pure Ti films. This is probably due to the fact that generated electrons resulting from the light-induced oxidation of Ag atoms are embedded within the tubular layer, namely  $\text{Ag} \rightarrow \text{Ag}^+ + \text{e}^-$ . In the case of spaced TNT, as shown on the LSV curve (**Figure 76 (b)**), for deposited TiAg films with Ag content above 1.7 %, the prepared TNT are no longer photoactive. As shown in Raman spectra given in **Figure 74**, this can be attributed to the presence of amorphous phase in s-3.5Ag-TNT and s-5Ag-TNT samples after their annealing. Indeed, disordered amorphous structure hamper the percolation of electrons leading to a substantial increase of the recombination rate of electron-hole pair.

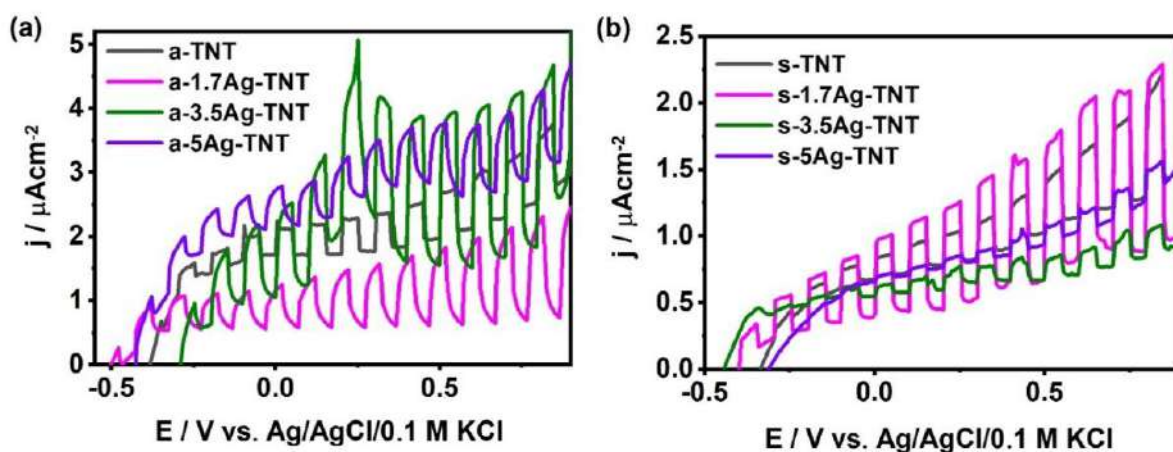


**Figure 76.** LSV curves registered under chopped UV-vis light illumination (light and dark periods last 5 s) of (a) a-TNT, a-1.7Ag-TNT, a-3.5Ag-TNT, a-5Ag-TNT; (b) s-TNT, s-1.7Ag-TNT, s-3.5Ag-TNT, s-5Ag-TNT in 0.5 M  $\text{Na}_2\text{SO}_4$ .

The quantum efficiency measurements for the photoactive materials have been also carried out. Three-fold increase in the incident photon-to-current conversion efficiency was reached for the most photoactive sample compared to the bare tubular layer. The recorded spectra are shown in **Figure 77**.

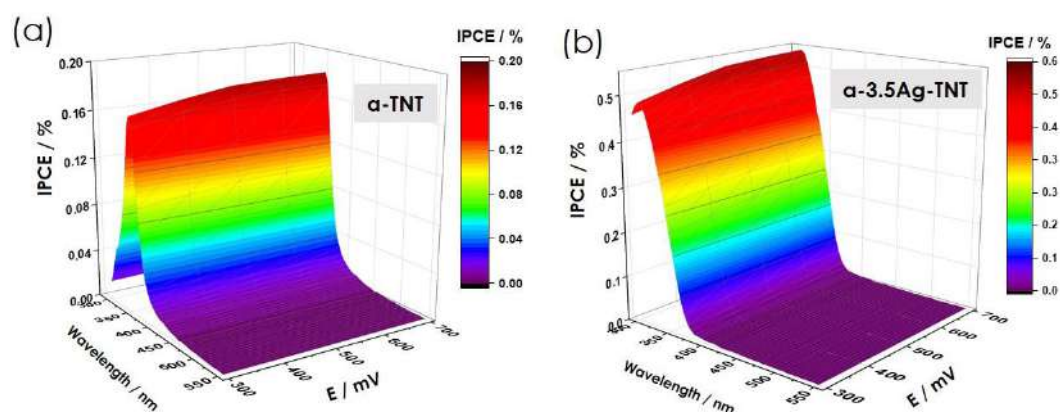


**Figure 77.** IPCE 3D map for (a) a-TNT and (b) a-3.5Ag-TNT. (Reproduced from article A3).

This increase in the IPCE can be associated to the presence of silver within the anodized tubular layer as mentioned in the discussion on the LSV. In fact, as shown in the article A3, there are shifts of the flat band potentials for all titania nanotubes prepared out of the TiAg alloys with respect to their pure counterparts. As discussed by Garlisi et al.<sup>159</sup> the presence of heteroatoms and the structural defects within the material are responsible for the shifting of its flat band potential. Although an increase in the photon-to electron conversion efficiency is achieved by anodizing the TiAg alloy films as compared to the bare material, its overall light harvesting efficiency was still below 1 %. This led our research group to explore other electrochemical decorating agents, namely the two-dimensional transition metal carbides and nitrides known as MXenes.  $\text{Ti}_3\text{C}_2\text{T}_x$  MXene was selected to avoid the widely used and expensive noble metals (i.e. Ag and Au).

### Conclusion

This subsection focuses on the synthesis and characterization of photoelectrochemical and electrochemical properties of the tubular layer formed out of the alloy metallic films. The results have shown that both aligned and spaced nanotubes can be grown out of the titanium - silver alloy layers containing up to 5 % of Ag in the initial deposited film. The obtained materials especially, a-3.5Ag-TNT sample exhibits a 3-fold increase in the photocurrent density

as compared to bare TNT. Investigation on the electrochemical activity of the prepared materials in the presence of ferricyanide redox species in the electrolyte has revealed that for some Ag content in TNT, reversible redox reaction occurs that was not found for bare TNT, exhibiting purely semiconducting activity that does not allow to rise both oxidation and reduction peak during cyclic voltammetry. This demonstrates that semitransparent TNT electrodes (i.e. aligned and spaced TNT) formed out of TiAg films exhibit unique features unknown for pure titania and they can be considered as a promising materials not only for solar-driven processes but also those where the ferriicyanide redox couple acts as a probe molecule. However, although an increase in the photoresponse can be noted for the tubular layer obtained out of the alloy film comparing to its counterpart obtained by anodizing the pure Ti film, the overall performance is still very low for practical application. Other chemical compound, namely transition-metal carbide MXenes was also investigated for the modification of the tubular layer and the obtained results are presented in the subsection **7.5**.

# Photoelectrochemical and Electrochemical Activity of Anodic Semitransparent Aligned and Spaced Titania Nanotubes Formed out of Titanium–Silver Alloys

Dujeiric-Stephane Kouao,\* Jan Hanuš, Ondřej Kylián, Radka Simerova, Petr Sezemsky, Vitezslav Stranak, Katarzyna Grochowska, and Katarzyna Siuzdak

Cite This: *ACS Appl. Nano Mater.* 2024, 7, 1548–1561

Read Online

ACCESS |

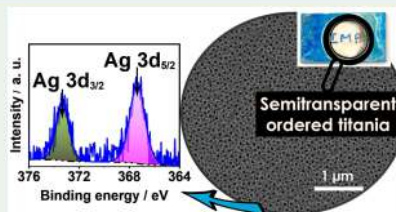
Metrics & More

Article Recommendations

Supporting Information

**ABSTRACT:** Two titania nanotube (TNT) architectures, namely, aligned and spaced, have been synthesized by anodizing titanium–silver (TiAg) alloy films (i.e., 1.7, 3.5, and 5% Ag content) sputtered onto indium–tin oxide. The Raman spectra showed that the anatase phase is obtained for the aligned TNT up to 5% Ag content, whereas no anatase peak is observed for the spaced TNT above 1.7% Ag content in the deposited TiAg alloys. The electrochemical studies carried out in the presence of redox species showed that, among others for 5% Ag content in the deposited TiAg alloy used for anodization, a reversible redox reaction of ferricyanide species occurs that was not found for bare TNT. Moreover, irrespective of the titania arrangement, an increase of the Ag content in the TiAg films to 5% leads to a very efficient electron-transfer rate of  $3.84 \times 10^{-3} \text{ cm s}^{-1}$  for aligned and  $7.98 \times 10^{-3} \text{ cm s}^{-1}$  for spaced titania. In addition, the photoelectrode based on aligned TNT grown out of the TiAg alloy films containing 3.5% Ag exhibited a photocurrent density of about 3 times higher with respect to the aligned TNT obtained from the pure titanium film.

**KEYWORDS:** titania nanotubes, titanium–silver alloys, indium–tin oxide, anodization, photoelectrochemical



## 1. INTRODUCTION

In recent years, semitransparent materials based on titania nanotube (TNT) arrays synthesized by anodizing titanium (Ti) films deposited onto transparent conducting oxides (TCOs) have received considerable attention and interest due to their potential applications as inexpensive and sustainable electrodes for photoelectrochemical (PEC) systems.<sup>1</sup> Such electrodes offer the possibility to promote electrolyte diffusion through the active material by controlling the geometrical features including the tube length, wall thickness, and roughness, pore diameter, and tube-to-tube spacing of the prepared TNT.<sup>2</sup> This can be realized simply by optimizing the anodization parameters including the applied voltage, anodization temperature, water content in the electrolyte, and fluorine ion concentration.<sup>3</sup>

Compared to TNT grown on the opaque Ti foil<sup>4</sup> or Ti alloys,<sup>5</sup> semitransparent materials made of TCOs overgrown with TNT have multiple advantages. First, the opaque metal foil that serves as a substrate for TNT limits their potential applications, especially in PEC and optoelectrochemical devices (e.g., dye-sensitized solar cells or electrochromic devices) requiring semitransparent electrodes.<sup>6,7</sup> In fact, materials exhibiting semitransparency allow the light to pass through the entire cell, thus increasing the number of photogenerated electron–hole pairs compared to the non-

transparent substrate.<sup>8</sup> In addition, the sustainability of electrodes made of TNT grown on Ti foil is another issue. As discussed by Tang et al.<sup>6</sup> and Lim et al.,<sup>7</sup> the TNT/Ti interface cannot withstand shocks due to the mechanical instability of Ti thin foils considered as microscale. As a result, the stress created at the oxide/Ti metal interface can cause cracks to form and the TNT layer to delaminate from the foil.<sup>6,7</sup> Moreover, the metallic Ti underneath the nanotubes can lead to electrical shorting.<sup>6,7</sup> It is worth noting that, in the case of semitransparent TNT-based materials, the adhesion of the deposited Ti film on TCO can be further improved to ensure better stability of TNT on TCO.<sup>9–11</sup> Among others, the most simple strategy consists of the introduction of either a titania<sup>10</sup> or a nanoparticle-doped titania<sup>9</sup> interlayer between the deposited Ti film and the TCO substrate. This strategy has been explored by Kim et al.,<sup>9</sup> Büttner et al.,<sup>11</sup> and Krumpmann et al.<sup>10</sup> to produce Ti/TCO substrates and is considered to be crucial in the fabrication of crack-free and more regular TNT

Received: September 3, 2023

Revised: December 12, 2023

Accepted: December 13, 2023

Published: January 8, 2024





with tunable geometry on TCO. In fact, this transition layer concatenates the sputtered film and substrate, which improves the adhesive forces between the coated film and the TCO.<sup>12</sup>

Although TNT grown by anodic oxidation onto TCO are regarded as promising electrodes for PEC devices, the poor absorption of titania in visible light due to the wide band gap limits their solar-to-electricity conversion efficiency (only 7%).<sup>13</sup> Two major approaches cover (i) broadening the titania absorption spectrum to the visible region and (ii) promoting the electron–hole separation through modification of the tubular structure with metal nanoparticles.<sup>14,15</sup> Related to this, the most utilized method consists of the decoration of already-grown TNT onto the TCO with an adequate amount of metal nanoparticles such as Au,<sup>15</sup> AuPt,<sup>16</sup> and Ru.<sup>17</sup> In general, the presence of metal nanoparticles can induce collective electronic excitations at the semiconductor (TiO<sub>2</sub>)/metal interfaces (i.e., surface plasmon resonance effect).<sup>18,19</sup> As a consequence, enhancement of the light absorption capacity of the materials can be expected.<sup>18,19</sup> This can increase the number of photogenerated electron–hole pairs, thereby improving the light-harvesting properties of photoelectrodes. However, the drawback of using the above-mentioned method to deposit nanoparticles on top of the TNT is accumulation of the nanoparticles mainly in the crown position.<sup>20</sup> Hence, the tubular structure can lose its regular distribution of nanotube arrays.<sup>20</sup> Moreover, as first discussed by Lamberti et al.<sup>20</sup> and later by Farkhondeh et al.,<sup>21</sup> the amount of metal deposited on top of the TNT must be carefully controlled. Indeed, for a relatively high amount of deposited metal, it can completely cover the entire surface on top of the TNT, thus blocking the pores.<sup>20,21</sup> This can make the application of the TNT almost useless because the electrolyte can no longer diffuse through the entire tubular layer. In addition, these opaque layers of nanoparticles deposited on top can prevent incident light from illuminating the TNT, thereby greatly reducing the number of photogenerated electrons. Another method consists of the synthesis of TNT out of alloy films uniformly deposited onto TCO by a simultaneous cosputtering technique from two targets, namely, Ti and heterometal sources (TiX, where X = heterometal). Such a strategy allows one to obtain uniform nanotube array layers with well-dispersed dopant atoms in the titania matrix.<sup>14,18,22–25</sup> Here the challenge is to achieve semitransparent and well-ordered TNT materials because both the transparency and tube growth can be strongly affected by the heterometal content in the deposited films. Moreover, a significant amount of heterometal can be lost during anodization due to the etching process.

Although two TNT architectures are generally investigated, i.e., aligned and spaced, so far only semitransparent aligned TNT formed out of TiNb,<sup>26</sup> TiCo,<sup>27</sup> TiFe,<sup>14,28</sup> TiMo,<sup>22</sup> TiW,<sup>23</sup> TiCu,<sup>29</sup> and TiAg<sup>18</sup> alloys have been reported. To the best of our knowledge, no work was conducted to investigate both the feasibility to grow spaced TNT by anodizing the deposited TiX films and the influence of the heteroatom concentration in the deposited films on the physicochemical properties of both TNT architectures. The works reported by Lui et al.<sup>19</sup> and Mohammadi et al.<sup>30</sup> have proven that, after modification of the TNT with silver (Ag) nanoparticles, the photoelectrodes have exhibited considerably higher photochemical activity, roughly 3 times greater than that of bare TiO<sub>2</sub> nanotubes. Wodka et al.<sup>31</sup> showed that the Fermi level of Ag nanoparticles is situated close to the conduction-band edge of the anatase titania. This can promote electron transfer

between the semiconductor (TiO<sub>2</sub>) and the metal (Ag).<sup>19</sup> These promising results show that TiO<sub>2</sub> modified with Ag nanoparticles can efficiently reduce the recombination of photogenerated electron–hole pairs and promote charge-transfer kinetics.<sup>19,30</sup> However, until now, the electrochemical performance was little explored, and no activity of the tubular layer prepared from a TiAg film in the presence of redox species in the electrolyte was verified.

In this work, semitransparent aligned and spaced TNT out of TiAg alloys (500 nm thick) with different Ag contents (1.7, 3.5, and 5%) deposited onto indium–tin oxide (ITO) have been synthesized by anodic oxidation. The crystallinity, morphology, and chemical bonds of the prepared materials were investigated using Raman spectroscopy, field-emission scanning electron microscopy, and X-ray photoelectron spectroscopy, respectively. Moreover, cyclic voltammetry and electrochemical impedance spectroscopy were performed in the presence of a ferricyanide redox pair electrolyte to study the electrochemical activity and kinetics of the obtained TNT materials. We show that not only does the Ag content affect the structure but also, as a consequence, the electrochemical performance of fabricated materials is significantly changed as well.

## 2. EXPERIMENTAL SECTION

**2.1. Deposition of TiAg Alloys onto ITO.** The fabrication of TiAg alloys for anodization employed magnetron sputtering in several steps of sample preparation. First, glass slides of rectangular shape with a size of 15 × 26 mm<sup>2</sup> were covered by a 100-nm-thick layer of ITO by radio-frequency (RF) sputtering of a 3-in. ITO target (Testbourne Ltd., In<sub>2</sub>O<sub>3</sub>/SnO<sub>2</sub> of composition 90/10 wt % and a declared purity of 99.99%) in a pure Ar atmosphere at a pressure of 0.1 Pa and 150 W of RF power delivered into the magnetron. Then the ITO films were annealed in air for 1 h at 500 °C. To improve adhesion between ITO and the Ti-based alloy, the ITO surface was biased by −190 V and treated by 30 W RF plasma discharge for 10 min in an atmosphere with an Ar/O<sub>2</sub> ratio of 6/20 and a pressure of 3.3 Pa. Moreover, a 5-nm-thick TiO<sub>2</sub> interlayer was deposited on top of the annealed ITO by direct-current (dc) sputtering of a 3-in. Ti target (Kurt J. Lesker, declared purity of 99.5%) in the atmosphere with the same Ar/O<sub>2</sub> ratio and a pressure of 0.5 Pa. Consecutively, deposition of the Ti or TiAg alloy continued without the presence of oxygen. A total of four sets of different metal films were fabricated, all with a thickness of 500 nm. For pure Ti films, the Ti target was sputtered in an Ar atmosphere with a pressure of 0.125 Pa and a dc power of 232 W. For TiAg alloys, a 3-in. Ag target (Kurt J. Lesker, declared purity 99.99%) in a second magnetron was used for cosputtering simultaneously with the Ti target. The composition of the TiAg alloys was controlled by dc power delivered to the magnetron sputtering of the Ag target. The Ag contents of 1.7, 3.5, and 5% were obtained from powers of 9, 20, and 30 W, respectively.

**2.2. Synthesis of Semitransparent Aligned and Spaced TNT Materials.** Substrates consisting of TiAg films (500 nm thick) with different Ag contents (1.7, 3.5, and 5%) deposited onto glass coated with ITO were anodized using a two-electrode cell. A platinum mesh acted as the cathode, whereas the substrate served as the anode. The distance between the electrodes was 2 cm, and the temperature of the electrochemical cell was controlled using a thermostat (Julabo F-12). The anodization was stopped when the substrate had become transparent. The sample holder used for the anodization of the substrates had a circular hole of 10.5 mm diameter. Such a construction enabled a particular area to be exposed to the electrolyte, while the other parts of the substrate were isolated from the electrolyte. As a result, in the area that did not have contact with the electrolyte, the nanotubes were not formed. For all samples, the symbol “IMP” (the abbreviation for the name of our Institute) written on the paper sheet on which the samples were placed can be seen by



naked eye only through this anodized area (i.e., a 10.5-mm-diameter disk), indicating their semitransparent feature (Figures S1–S3). To obtain aligned TNT, anodization was performed in an ethylene glycol bath containing 0.27 M  $\text{NH}_4\text{F}$ , 1 M  $\text{H}_3\text{PO}_4$ , and 5 vol %  $\text{H}_2\text{O}$  at 60 V. The temperature of the cell was 23 °C, and the obtained aligned TNT were labeled as a- $x\text{Ag-TNT}$ , where  $x$  is defined as the Ag content in the initial deposited TiAg film ( $x = 1.7, 3.5$ , and 5%). The spaced TNT materials were obtained by anodizing the substrates in a diethylene glycol-based electrolyte mixed with 0.15 M  $\text{NH}_4\text{F}$ , 0.5 M HF, and 7 vol %  $\text{H}_2\text{O}$  at 40 V. The temperature was fixed at 40 °C, and the prepared spaced TNT materials were labeled as s-1.7Ag-TNT, s-3.5Ag-TNT, and s-5Ag-TNT. The photographs of the obtained semitransparent materials are shown in Figures S1 and S2. We also tried to anodize TiAg films with a higher content of Ag (i.e., 6.8%), but as a result, no ordered tubular layer was obtained (Figures S3 and S4). For comparison, aligned and spaced TNT formed out of pure Ti films deposited onto ITO have been synthesized as well and labeled as a-TNT and s-TNT. Afterward, all prepared materials were annealed at 450 °C for 1 h in air with a heating rate of 2 °C  $\text{min}^{-1}$  by using a tubular furnace (Nabertherm). Annealing allows a phase transition from amorphous to crystalline because the as-anodized material exhibits amorphous nature. Moreover, the calcination process also leads to oxidation of the remaining metallic part into  $\text{TiO}_2$ . The different steps involved in the fabrication process of the semitransparent materials are listed in Figure 1. These steps include

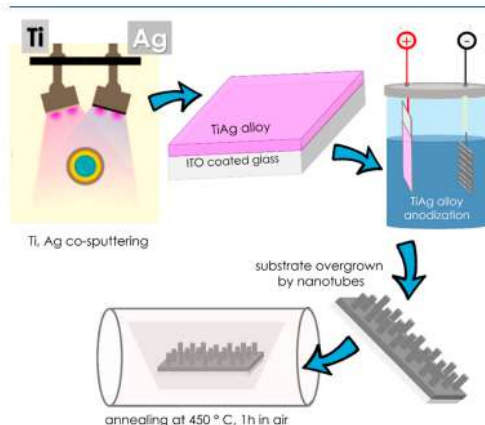


**Figure 1.** Schematic of the steps of the synthesis process: cosputtering of the TiAg film followed by anodization and subsequent annealing of the materials.

deposition by cosputtering (or sputtering) of TiAg alloys (or a pure Ti film) on ITO-coated glass, followed by anodization of the sputtered film according to anodizing conditions, allowing one to obtain the aligned or spaced TNT described above. Last, the sample was annealed in air for further characterizations.

**2.3. Analysis Instruments.** The morphological features of the synthesized materials were examined using field-emission scanning electron microscopy (SEM; FEI Quanta FEG 250). For both the top and cross-sectional views, the substrate was placed on the sample holder perpendicular to the scanning surface. For the morphology inspection of the sample surface, a piece of copper tape with conductive glue was attached on the bottom side, providing an electrical connection between the top surface of the sample and the stage. In the case of the cross-sectional view, a 10-nm-thick film of gold was sputtered to receive higher contrast images. Energy-dispersive X-ray (EDX) spectra were recorded using a JED-2300 detector (JEOL). A Raman spectrometer (Renishaw) equipped with an excitation source (wavelength of 514 nm) and operating at 10% of

its total power (50 mW) was used to identify the crystal structure of the samples. An X-ray diffractometer (Bruker D2 Phaser second generation) using  $\text{Cu K}\alpha$  radiation and a LynxEye XE-T detector was used to analyze the phase composition of the samples. An UV–vis spectrophotometer (PerkinElmer) operating at a scanning speed of 120  $\text{nm min}^{-1}$  was utilized to investigate the optical properties of the obtained samples in the wavelength range of 320–800 nm. X-ray photoelectron spectroscopy (XPS) spectra to identify the functional groups present for the aligned and spaced TNT were collected by an XPS spectrometer equipped with a hemispherical analyzer (Phoibos 100, Specs) and an Al  $\text{K}\alpha$  X-ray source (1486.6 eV, 200 W, Specs) at a constant takeoff angle of 90°. The electrochemical and PEC measurements were performed using an Autolab PGSTAT302N potentiostat–galvanostat system (Methrom, Autolab) in a three-electrode cell with a quartz window. A xenon lamp (Osram XBO 150) equipped with an AM 1.5 filter was used as a light source. Contact-angle measurements were performed using a DSA 100 drop shape analyzer (Krüss, Germany). A 4  $\mu\text{L}$  water droplet was placed at room temperature on the surface of the investigated materials. The contact angles were measured by using *Advance* software. All physicochemical characterizations described above were carried out only on the anodized semitransparent regions.

**2.4. Electrochemical and PEC Measurements.** All measurements were carried out in a three-electrode setup. The prepared samples were used as the working electrodes, a platinum mesh acted as the counter electrode, and  $\text{Ag/AgCl}/0.1 \text{ M KCl}$  served as the reference electrode. Before each experiment, the electrolyte was deaerated with an argon flow for 30 min. During the measurements, the argon flow was maintained above the solution. For both TNT architectures, cyclic voltammetry (CV) was first carried out in 0.5 M  $\text{Na}_2\text{SO}_4$  in the applied potential range of  $-1.0$  to  $+1.0 \text{ V}$  at a scan rate of  $50 \text{ mV s}^{-1}$ . Afterward, the measurements were carried out in 0.5 M  $\text{Na}_2\text{SO}_4 + 10 \text{ mM K}_3\text{Fe}(\text{CN})_6$  at scan rates of 10, 20, 50, 90, 120, and  $150 \text{ mV s}^{-1}$  in wide potential windows of  $-1.0$  to  $+1.0 \text{ V}$  for the spaced TNT and  $-0.5$  to  $+1.0 \text{ V}$  for the aligned TNT. The electrochemical impedance spectroscopy (EIS) spectra were measured at the formal potential with frequencies varying from 20 kHz to 0.1 Hz with a 10 mV amplitude of the alternating-current (ac) signal. The formal potential is a measure of the potential of a cell where both oxidized and reduced species are present at equal concentration, i.e., average midpoint potential of the cathodic and anodic peak potentials. The impedance data were analyzed on the basis of an electric equivalent circuit using an EIS Spectrum Analyzer program. The modified Powell algorithm used for analysis of the data is presented in eqs S1 and S2. Linear-sweep voltammetry (LSV) measurements for the aligned and spaced TNT materials were carried out in 0.5 M  $\text{Na}_2\text{SO}_4$  in the dark and under UV–vis- and visible-light illumination at  $10 \text{ mV s}^{-1}$  in the potential range from  $-0.7$  to  $+1.0 \text{ V}$ . Chronoamperometry measurements for photostability verification were performed by recording the current under chopped UV–vis-light irradiation for 2 h. The sequence of the irradiation/dark periods was as follows: first the sample was polarized in the dark, then the electrode was irradiated for 30 min, afterward the light was switched off for 1 min, then the working electrode was once again exposed to light for 1 h and kept in the dark for 1 min, and the final UV–vis radiation over the electrode lasted 30 min. For Mott–Schottky analysis, EIS spectra were recorded in 0.5 M  $\text{Na}_2\text{SO}_4$  at a constant frequency of 1 kHz, in the potential range from  $+0.1$  to  $-1.2 \text{ V}$  vs  $\text{Ag/AgCl}/0.1 \text{ M KCl}$ . The 3D map of the incident photon-to-electron conversion efficiency (IPCE) was recorded by a photoelectric spectrometer (Instytut Fotonowy) equipped with a 150 W xenon lamp. Measurements were performed in 0.5 M  $\text{Na}_2\text{SO}_4$  in the potential range of  $+0.3$  to  $+0.7 \text{ V}$  vs  $\text{Ag/AgCl}/0.1 \text{ M KCl}$  from 300 to 550 nm. During all electrochemical and PEC measurements, only the anodized area of the substrates was in contact with the electrolyte, while the remaining nonanodized titania were protected, not to have contact with an electrolyte.



### 3. RESULTS AND DISCUSSION

The current–transient curves of the TiAg alloy films containing 3.5% Ag are shown in Figure S5. The curves recorded during the anodization of a-3.5Ag-TNT and s-3.5Ag-TNT present three regimes. In the first stage, the current increases up to a maximum value followed by an exponential decay resulting from the formation of the  $\text{TiO}_2$  barrier layer.<sup>32</sup> In the second regime, the decay is followed by a short current increase due to the growth of embryo pores on the oxide surface.<sup>32</sup> Finally, the current undergoes a steady decrease, indicating the formation of the nanotubes.<sup>32</sup> The full transformation of the opaque metallic alloy film into an oxide tubular layer is reached when the substrate has become transparent, i.e., 25 min for a-3.5Ag-TNT and 16 min for s-3.5Ag-TNT.<sup>13,33</sup> Figure 2 shows the SEM images of the

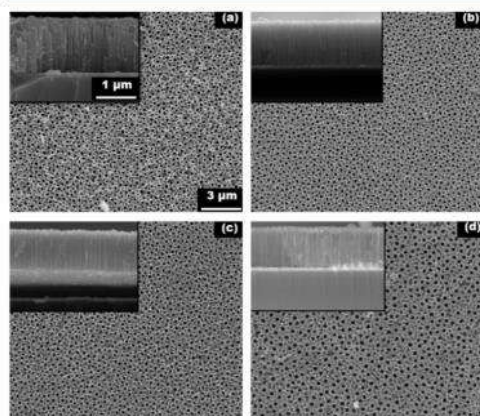


**Figure 2.** SEM top images of (a) a-TNT, (b) a-1.7Ag-TNT, (c) a-3.5Ag-TNT, and (d) a-5Ag-TNT. Inset: Corresponding cross-sectional images of the prepared materials. Scale bars given in part a are the same for all of the images.

obtained aligned TNT after annealing at 450 °C for 1 h. A smooth surface with well-ordered close-packed nanotubes has been synthesized out of TiAg alloys deposited onto ITO. As can be seen in the cross-sectional images (Figure 2, inset), there is no distortion of the tubular structure of the prepared materials up to 5% Ag content in the deposited film. The SEM top images of the spaced TNT materials show visible gaps between the tubes (Figure 3).

Elemental analysis from EDX presented in Figure S6 and Table S1 showed that after anodization the Ag content in the deposited films is reduced by approximately 40% for the aligned TNT, whereas for the spaced architecture, no Ag atom was detected in the anodized samples. During the anodization of the TiAg films, the silver species, i.e.,  $\text{Ag}^+$ , trapped inside the  $\text{TiO}_2$  layer migrate toward the electrolyte with the applied voltage.<sup>34</sup> This leach out of Ag ions resulting from the dissociation of the oxide layer by the fluorine (F) ions present in the electrolyte can explain the loss of Ag after the anodization.<sup>34</sup> In the case of the aligned TNT, because the nanotubes are closely packed, a relatively big amount of Ag can still be found in the tubular layer due to the Ag being trapped between the nanotube walls in this compact structure, as

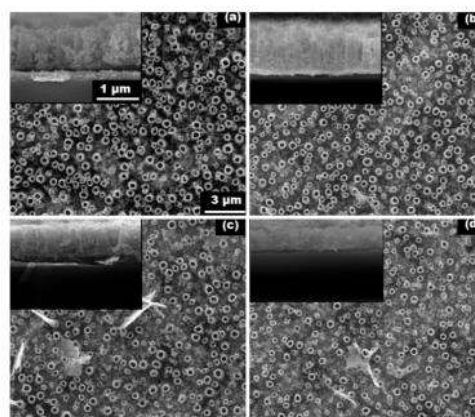


**Figure 3.** SEM top images of (a) s-TNT, (b) s-1.7Ag-TNT, (c) s-3.5Ag-TNT, and (d) s-5Ag-TNT. Inset: Cross-sectional images of the prepared materials. Scale bars given in part a are the same for all of the images.

detected by EDX measurement. However, with the gradual increase of the tube-to-tube spacing toward the loosely packed TNT (i.e., spaced TNT), one may observe substantial removal of the Ag content in the anodized layer. This may explain the fact that Ag is out of the detection limit for the spaced TNT.

The Raman spectra of the a-TNT, a-1.7Ag-TNT, s-3.5Ag-TNT, a-5Ag-TNT, and s-TNT materials show the characteristic peaks of the anatase phase of  $\text{TiO}_2$  at 144, 398, 515, and 640  $\text{cm}^{-1}$ , which are assigned to the active vibrational modes of  $E_{1g}$ ,  $B_{1g}$ ,  $A_{1g}$ , and  $E_{3g}$ , respectively (Figure 4a,b).<sup>35</sup> There are no additional visible signals related to any Ag species. This may be due to the very low Ag content that remains in the tubular layers after anodization of the TiAg films. Anatase titania were obtained with an increase in the Ag content in the deposited TiAg films up to 5%. This indicates the stability of the crystalline phases for the aligned TNT architecture. In fact, the presence of Ag in the TNT layers after anodization does not influence the crystallization of the aligned titania.

In the case of the spaced arrangement, the Raman spectrum of s-1.7Ag-TNT exhibits only one band at 143  $\text{cm}^{-1}$  ( $E_{1g}$ ). As shown in Figure 4d, this peak is broadened and slightly shifted to the lower-wavenumber region. Moreover, there are no signals detected on the Raman spectra of the s-3.5Ag-TNT and s-5Ag-TNT samples.

XRD measurements were performed for the spaced TNT-based materials to detect the presence of a trace of anatase titania in the s-3.5Ag-TNT and s-5Ag-TNT samples. The results have shown that the XRD patterns of s-3.5Ag-TNT and s-5Ag-TNT exhibit the broad diffraction peak at 25.57° characteristic of the (101) plane of anatase titania. In addition, the weak peak at 38.09° in the spectrum of s-3.5Ag-TNT also results from the (004) plane of anatase titania. As shown in Figure 5, the anatase peaks of s-TNT and s-1.7Ag-TNT are much more intense than those of the s-3.5Ag-TNT and s-5Ag-TNT samples. Moreover, compared to s-3.5Ag-TNT and s-5Ag-TNT, the presence of additional anatase peaks on the XRD patterns of the s-TNT and s-1.7Ag-TNT samples can be observed. For example, the signals at 48.30° and 54.18° (for s-TNT) and at 62.99° (for both s-TNT and s-1.7Ag-TNT) are

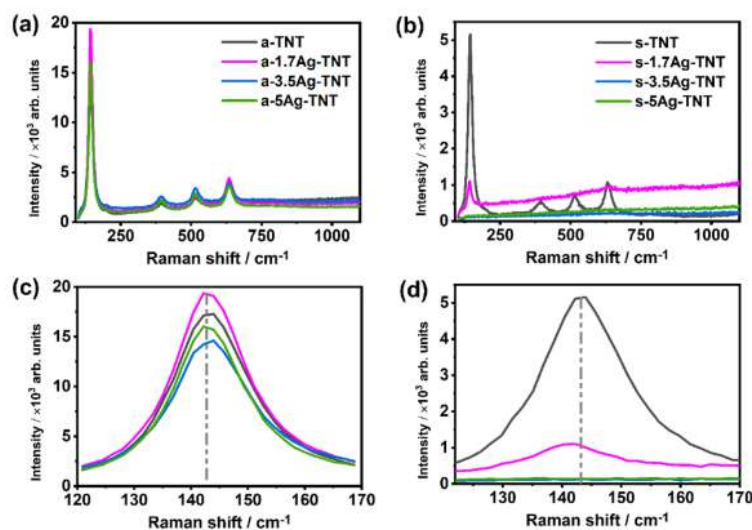


**Figure 4.** Raman spectra of (a) a-TNT, a-1.7Ag-TNT, a-3.5Ag-TNT, a-5Ag-TNT, (b) s-TNT, s-1.7Ag-TNT, s-3.5Ag-TNT, and s-5Ag-TNT. Magnification of the most intense anatase peak at  $144\text{ cm}^{-1}$  of (c) a-TNT, a-1.7Ag-TNT, a-3.5Ag-TNT, and a-5Ag-TNT and (d) s-TNT, s-1.7Ag-TNT, s-3.5Ag-TNT, and s-5Ag-TNT.

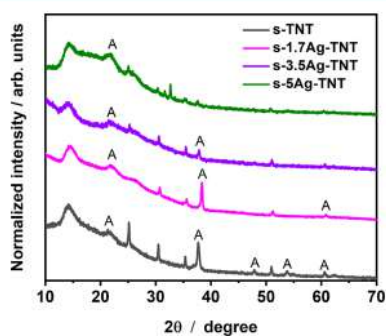


**Figure 5.** XRD patterns of s-TNT, s-1.7Ag-TNT, s-3.5Ag-TNT, and s-5Ag-TNT.

assigned to the (200), (105), and (204) planes of anatase  $\text{TiO}_2$ , respectively.

This indicates that, although all spaced TNT samples have been annealed in the same conditions, both s-3.5Ag-TNT and s-5Ag-TNT are not completely crystallized after 1 h of calcination at  $450^\circ\text{C}$  compared to the s-TNT and s-1.7Ag-TNT samples. Distortion of the lattice symmetry characteristic of the anatase phase resulting from the presence of structural defects (e.g., oxygen-deficient sites) can be responsible for inhibition of the transition from the amorphous to anatase phase.<sup>36–38</sup>

Parts a and b of Figure 6 show the absorption spectra of the prepared materials. It can be noticed that, for the aligned TNT, the presence of Ag in the TNT layers (Table S1) did not shift the absorption edge to the visible region. All prepared TNT materials out of the TiAg alloys, i.e., a-1.7Ag-TNT, a-3.5Ag-

TNT, a-5Ag-TNT, s-1.7Ag-TNT, s-3.5Ag-TNT, and s-5Ag-TNT, mainly absorb below 400 nm. Several less pronounced peaks are visible on the absorbance spectra of the a-1.7Ag-TNT, a-3.5Ag-TNT, and a-5Ag-TNT samples (Figure 6a, inset). These small and broad absorption peaks have already been observed by Lai et al.<sup>39</sup> when studying the optical properties of Ag-doped TNTs. As discussed above, EDX elemental analysis (Table S1) has shown that, after anodization, 60% of the initial Ag content in the deposited films was detected for the samples a-1.7Ag-TNT, a-3.5Ag-TNT, and a-5Ag-TNT. Therefore, the occurrence of these resonance absorption bands may be associated with the sub-band-gap states generated in the TNT structures resulting from the Ag atoms trapped inside the nanotube walls during anodization.<sup>39,40</sup> This phenomenon is not observed for the spaced architecture due to the absence of Ag in the titania matrix after anodization, as shown by the EDX results (Figure S6). The absorption peak at 430 nm obtained for s-5Ag-TNT can be ascribed to the trapped holes.<sup>40</sup> The values of the band-gap energies of the samples are summarized in Table 1. With the exception of the sample s-5Ag-TNT, an increase of the Ag content in the deposited alloy films leads for both architectures to an increase of the band gap of the prepared materials with respect to that of the pure sample. This can be explained by the Burstein–Moss shift.<sup>41</sup> The density of states near the titania conduction band has increased due to the presence of Ag content in the TNT layers (for the aligned TNT). Accordingly, the optical band gap increases when all states closer to the conduction band are saturated (get populated) by electrons from the donors. In the case of the spaced TNT materials, the increase in the density of states can be attributed to the presence of structural defects. In fact, the Burstein–Moss effect originating from defects in the titania matrix was reported by Ferrara et al.<sup>42</sup>



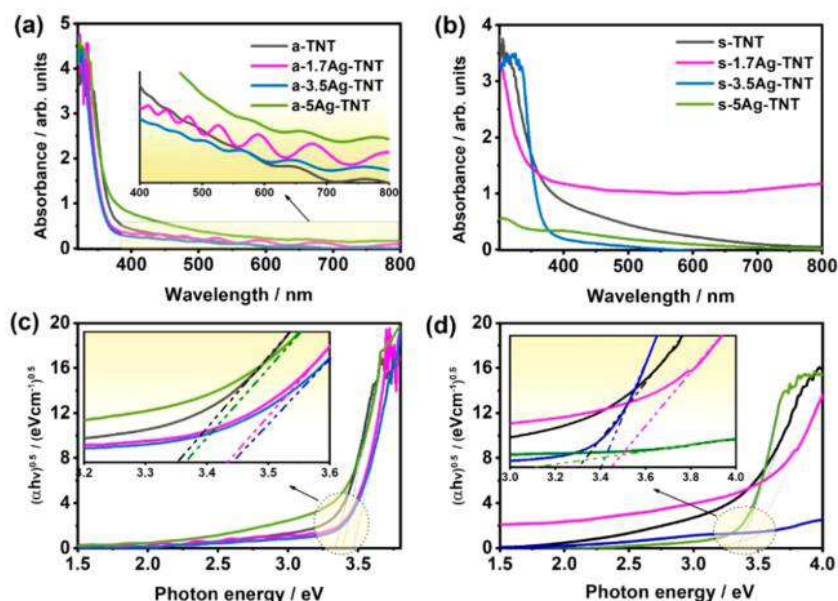


**Figure 6.** Absorption spectra of (a) a-TNT, a-1.7Ag-TNT, a-3.5Ag-TNT, and a-5Ag-TNT and (b) s-TNT, s-1.7Ag-TNT, s-3.5Ag-TNT, and s-5Ag-TNT.  $(\alpha h\nu)^{1/2}$  vs photon energy curves of (c) a-TNT, a-1.7Ag-TNT, a-3.5Ag-TNT, and a-5Ag-TNT and (d) s-TNT, s-1.7Ag-TNT, s-3.5Ag-TNT, and s-5Ag-TNT.

**Table 1.** Band-Gap-Energy ( $E_g$ ) Values of the As-Prepared Materials

aligned nanotubes		spaced nanotubes	
sample	$E_g$ /eV	sample	$E_g$ /eV
a-TNT	3.35	s-TNT	3.30
a-1.7Ag-TNT	3.43	s-1.7Ag-TNT	3.42
a-3.5Ag-TNT	3.44	s-3.5Ag-TNT	3.40
a-5Ag-TNT	3.37	s-5Ag-TNT	3.11

The overall chemical composition of the TNT materials prepared from the Ti and TiAg films was examined in detail by XPS analysis. There are no significant differences in the high-resolution XPS spectra of Ti 2p, O 1s, C 1s, F 1s, and Ag 3d

recorded for all of the prepared TNT materials out of the TiAg alloys. The spectra recorded for a-3.5Ag-TNT and s-3.5Ag-TNT are depicted in Figure S7. The XPS results for the a-TNT, a-1.7Ag-TNT, a-5Ag-TNT, s-TNT, s-1.7Ag-TNT, and s-5Ag-TNT materials are presented in Table S2.<sup>45–48</sup> As shown in Figure S7, contrary to the EDX results (Table S1), the XPS measurements revealed the presence of some traces of Ag on the surface of the s-3.5Ag-TNT sample. The Ag 3d spectra can be deconvoluted into two doublets, i.e., 3d<sub>5/2</sub> and 3d<sub>3/2</sub>, signals situated at the binding energies of 367.37 and 373.33 eV for a-3.5Ag-TNT and at 367.53 and 373.64 eV for s-3.5Ag-TNT. For both materials, the splitting of the 3d doublets is about 6.0 eV. According to Soliman et al.,<sup>43</sup> such a splitting energy indicates that the Ag is mainly present in the metallic Ag<sup>0</sup> state.

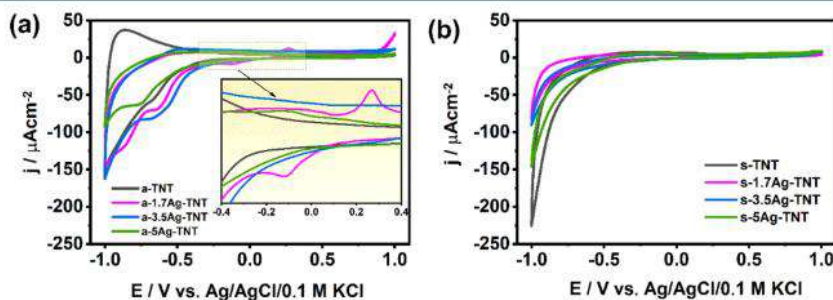


**Figure 7.** CV curves of (a) a-TNT, a-1.7Ag-TNT, a-3.5Ag-TNT, and a-5Ag-TNT and (b) s-TNT, s-1.7Ag-TNT, s-3.5Ag-TNT, and s-5Ag-TNT in 0.5 M Na<sub>2</sub>SO<sub>4</sub>.

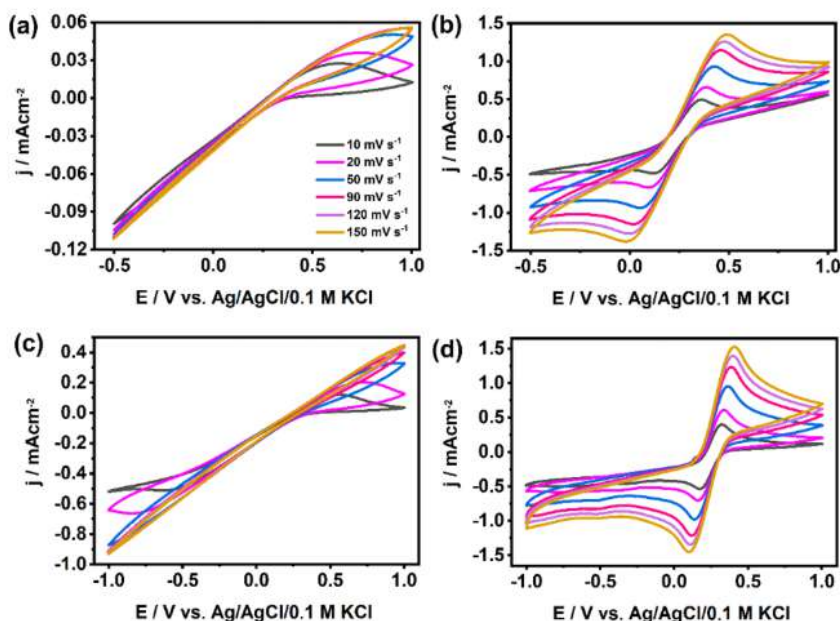


**Figure 8.** CV curves of (a) a-TNT, (b) a-5Ag-TNT, (c) s-TNT, and (d) s-5Ag-TNT recorded in 0.5 M Na<sub>2</sub>SO<sub>4</sub> + 10 mM K<sub>3</sub>Fe(CN)<sub>6</sub> at 10, 20, 50, 90, 120, and 150 mV s<sup>−1</sup>.

The two main peaks at 458.50 and 464.22 eV for a-3.5Ag-TNT and at 458.60 and 464.32 eV for s-3.5Ag-TNT on the Ti 2p spectra are assigned to Ti 2p<sub>1/2</sub> and Ti 2p<sub>3/2</sub>, respectively. For both materials, the splitting energy between the 2p<sub>3/2</sub> and 2p<sub>1/2</sub> signals is about 5.7 eV. This indicates that the state of Ti ions is Ti<sup>4+</sup>.<sup>43</sup> Regarding the binding energy typical for oxygen (O), in the case of s-3.5Ag-TNT and a-3.5Ag-TNT, the O 1s spectra can be fitted into three peaks located at 530.6, 532.4, and 535.42 eV, ascribed to Ti–O bonds,<sup>44</sup> O-deficient sites<sup>45</sup> and C–O bonds, respectively.<sup>46</sup> The obtained spectra of C 1s and F 1s shown in Figure S8 result from the F salt and the organic residues originating from the diethylene glycol- and ethylene glycol-based electrolytes, respectively. These two spectra (i.e., C 1s and F 1s) are usually present in the XPS survey of anodic TNT materials synthesized in the organic electrolyte containing F ions. For both a-3.5Ag-TNT and s-3.5Ag-TNT, the spectra of C 1s can be deconvoluted into four peaks at 285, 286.60, 288, and 290.87 eV. These signals can be attributed to C–C,<sup>47</sup> C–O,<sup>47</sup> C=O,<sup>47</sup> and C–F bonds,<sup>47</sup> respectively. The two signals at 684.6 and 688.7 eV in the F 1s spectra can be assigned to [TiF<sub>6</sub>]<sup>2−</sup><sup>48</sup> and C–F bonds.

CV was used to investigate the electrochemical activity of the prepared materials in two electrolytes, namely, in Na<sub>2</sub>SO<sub>4</sub> without and with [Fe(CN)<sub>6</sub>]<sup>3−/4−</sup> as a redox pair. Figure 7 shows the voltammograms of the prepared samples recorded in a 0.5 M Na<sub>2</sub>SO<sub>4</sub> solution at a scan rate of 50 mV s<sup>−1</sup>. The CV plots of the pure aligned TNT show a small reduction peak at −0.6 V vs Ag/AgCl/0.1 M KCl occurring due to the reduction of Ti<sup>4+</sup> to Ti<sup>3+</sup> according to eq 1:



This cathodic peak becomes more prominent for the a-1.7Ag-TNT, a-3.5Ag-TNT, and a-5Ag-TNT samples. This may be due to the reduction of oxygenated species of Ag.<sup>49</sup> Indeed, both the XPS and EDX spectra of the a-1.7Ag-TNT, a-3.5Ag-TNT, and a-5Ag-TNT have shown the presence of Ag. The CV curve of a-1.7Ag-TNT shows clear redox peaks at −0.11 and +0.27 V vs Ag/AgCl/0.1 M KCl, respectively. This can be associated with the reduction and oxidation of Ag.<sup>49,50</sup>

A similar behavior was reported by Amor et al.<sup>49</sup> when investigating the electrochemical activity of a Ag electrode in 0.5 M Na<sub>2</sub>SO<sub>4</sub>. However, this activity is no longer visible for the a-3.5Ag-TNT and a-5Ag-TNT samples in the same potential range. The distribution of Ag in the tubular layer is important as well. We regard that, as detected by EDX measurement, Ag species can be trapped between the nanotube walls in different positions, some on the outer and some on the inner tube wall, and some of them can be present inside the wall without any contact to any surface region. However, peaks found on the CV curves arise from the reaction taking place with the Ag species present at the electrolyte/electrode interface along the outer tube wall surface. The presumable reason for the decrease of the peaks of the surface electrochemistry can be attributed to the fact that there are not enough channels for the electrolyte ions to reach and react with the Ag atoms.<sup>51</sup> The CV curves of the spaced architecture do not show any peaks (Figure 7b).

Profound information about both the electrochemical activity and the kinetics of the prepared electrodes was further investigated by performing CV measurements in 0.5 M Na<sub>2</sub>SO<sub>4</sub> + 10 mM K<sub>3</sub>Fe(CN)<sub>6</sub> electrolyte at different scan rates from 10 to 150 mV s<sup>−1</sup>. The CV curves were collected for



**Table 2.** Values of the Fitting Parameters Obtained for the Prepared Electrodes Determined for Spectra Recorded at the Formal Potential of the Redox Reaction

sample	$R_s/\text{k}\Omega\text{ cm}^2$	$R_{ct}/\text{k}\Omega\text{ cm}^2$	$Q_{int}/\text{k}\Omega^{-1}\text{ cm}^{-2}\text{ s}^n$	$n$	$W_{ox}/\Omega\text{ cm}^2\text{ s}^{0.5}$	$W_{red}/\text{s}^{0.5}$
a-1.7Ag-TNT	0.325	0.280	0.02	0.812	2.63	8.873
a-3.5Ag-TNT	0.025	0.018	0.024	0.504	1.927	1.396
a-5Ag-TNT	0.062	0.014	0.024	0.782	1.172	1.240
s-1.7Ag-TNT	0.074	0.166	0.011	0.771	2.531	4.651
s-3.5Ag-TNT	0.46	0.01	0.013	0.714	0.278	0.606
s-5Ag-TNT	0.277	0.009	0.008	0.671	1.80	4.764

bare ITO and for the a-TNT, a-1.7Ag-TNT, a-3.5Ag-TNT, a-5Ag-TNT, s-TNT, s-1.7Ag-TNT, s-3.5Ag-TNT, and s-5Ag-TNT materials, where the ITO layer acts as the current collector to investigate the electron-transfer process at the current collector surface. The voltammograms of bare ITO show a pair of redox peaks (Figure S9). An increase in the scan rate from 10 to 150  $\text{mV s}^{-1}$  leads to both a positive shift in the oxidation peak potential and a negative shift in the reduction peak potential, thus causing the anodic/cathodic peak separation to increase with the scan rate. This indicates that the electron-transfer process of the ferro/ferricyanide reactions at the ITO surface is quasi-reversible.<sup>52</sup> Such behavior is typical for ITO because this layer is considered to be a very good semitransparent conducting electrode. However, nearly flat voltammograms with hardly visible anodic peaks are obtained for ITO substrates overgrown with aligned or spaced TNT, prepared by anodic oxidation of Ti films, i.e., a-TNT and s-TNT materials (Figure 8). This indicates that both TNT architectures behave as semiconductors with wide band gaps acting as compact blocking layers that inhibit the reversibility of the electron-transfer reaction on the current collector surface, i.e., ITO. Indeed, as was already discussed by both Lee et al.<sup>53</sup> and Ma et al.,<sup>54</sup> the voltammograms of the pure TNT layers in an aqueous electrolyte containing a  $[\text{Fe}(\text{CN})_6]^{3-/4-}$  redox couple do not exhibit any redox peak due to the poor electrical conductivity of titania materials.<sup>54</sup> Contrary to the TNT formed out of the pure Ti films, a pair of redox peaks appears on the CV curves of all aligned and spaced TNT materials grown out of TiAg films (1.7, 3.5, and 5% Ag content) deposited onto ITO. It should be underlined here that, according to XPS measurements, neither  $\text{Ti}^{3+}$  species nor Ag is present for spaced s-5Ag-TNT, exhibiting the most reversible behavior in the presence of redox species (Figure 8). The voltammograms of the a-1.7Ag-TNT, a-3.5Ag-TNT, s-1.7Ag-TNT, and s-3.5Ag-TNT samples are presented in Figure S10.

Because these reversible reactions take place at the ITO surface, for both architectures (spaced and aligned TNT), the occurrence of these redox peaks may be attributed to the improvement of the wettability of the developed TNT layers obtained after anodization of the deposited TiAg alloys. In fact, the wettability determines the ability of the electrolyte to seep through the TNT layer to the current collector, where the redox reaction takes place. For the aligned TNT materials, the presence of Ag atoms trapped inside the nanotube walls (detected by both XPS and EDX) can explain the enhancement of the wetting properties of the obtained TNT layers.<sup>55</sup> Moreover, according to the EDX data, no measurable Ag content was detected for the spaced TNT materials after anodization of the TiAg films. Following that, the tube-to-tube spacing acting as additional channels that promote infiltration of the electrolyte in the tubular layer is one of the main factors

influencing the wetting properties of the spaced TNT materials.

Water contact-angle measurements were performed to assess the wetting properties of the s-5Ag-TNT and a-5Ag-TNT samples. The cross-sectional images of the water droplet on the samples are shown in Figures S11 and S12. In the case of the spaced TNT materials, the contact angle drops abruptly from 110.7° for s-TNT to 42.8° for s-5Ag-TNT. For the aligned structure, a decrease in the contact angle from 7.4° (a-TNT) to 4.7° (a-5Ag-TNT) was also observed. Our results show that, regardless the nanotube architectures, the TNT prepared out of TiAg films (5% Ag content) exhibit better wettability compared to their counterparts formed out of pure Ti films, thus facilitating the infiltration of  $[\text{Fe}(\text{CN})_6]^{3-/4-}$  ions through the tubular layer to the ITO surface where the redox reaction takes place.

A linear dependence between the anodic and cathodic peak currents with respect to the square root of the scanning rate of 10–150  $\text{mV s}^{-1}$  was obtained for bare ITO (Figure S9), a-1.7Ag-TNT, a-3.5Ag-TNT, a-5Ag-TNT, s-1.7Ag-TNT, s-3.5Ag-TNT, and s-5Ag-TNT (Figure S13). This indicates that the transfer kinetics of the  $[\text{Fe}(\text{CN})_6]^{3-/4-}$  redox couple at these electrodes is predominantly under diffusion control.<sup>56</sup> The diffusion coefficients for the electrodes can be determined by substituting the slope of the peak current density vs scan rate curves into the Randles–Sevcik equation:

$$i_p = 2.686 \times 10^5 \times n^{3/2} A D^{1/2} C_0 \nu^{1/2} \quad (2)$$

where  $i_p$  is the peak current,  $n$  is the number of electrons transferred in the redox reaction,  $A$  is the electrode surface area ( $\text{cm}^2$ ),  $D$  is the diffusion coefficient ( $\text{cm}^2\text{ s}^{-1}$ ),  $C_0$  is the concentration of the redox species ( $\text{mol cm}^{-3}$ ),  $C_0 = C_{\text{red}} = C_{\text{ox}} = 10^{-5}\text{ mol cm}^{-3}$ , and  $\nu$  is the scan rate ( $\text{V s}^{-1}$ ).<sup>57</sup> The diffusion coefficient of the electrodes can be determined using the following equation:

$$D = \left( \frac{\text{slope}}{2.686 \times 10^5 \times n^{3/2} C_0} \right)^2 \quad (3)$$

The slopes and both the correlation and diffusion coefficients are presented in Table S3. The highest electron diffusion coefficient for the anodic peak (i.e.,  $1.60 \times 10^{-6}\text{ cm}^2\text{ s}^{-1}$ ) was obtained for the bare ITO electrode. This value is almost equal to that reported by Branch et al.<sup>58</sup> (i.e.,  $1.59 \times 10^{-6}\text{ cm}^2\text{ s}^{-1}$ ) for the ITO electrode immersed in aqueous electrolyte [0.1 M KCl + 10 mM  $\text{K}_3\text{Fe}(\text{CN})_6$ ]. Table S3 shows that, for both TNT architectures (i.e., aligned and spaced TNT), the presence of nanotubes on ITO has led to a slow electron transfer at the electrode surface. In fact, the electron-transfer reactions of the  $[\text{Fe}(\text{CN})_6]^{3-/4-}$  redox couple at the electrode surface strongly depend on the surface properties and the chemical composition of the electrode.<sup>59</sup>

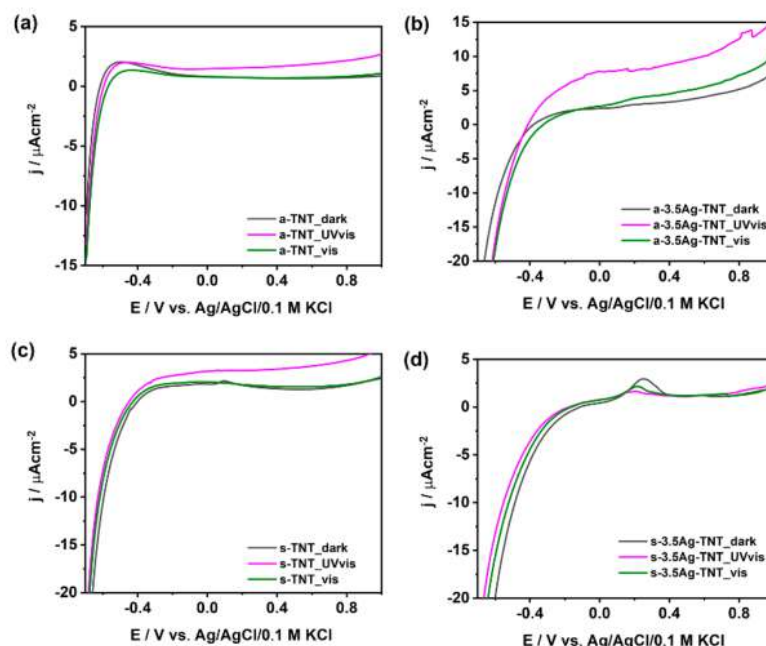


**Figure 9.** Linear-sweep voltammograms in the dark and under UV-vis- and visible-light illumination of (a) a-TNT, (b) a-3.5Ag-TNT, (c) s-TNT, and (d) s-3.5Ag-TNT in 0.5 M Na<sub>2</sub>SO<sub>4</sub>.

Investigation of the kinetics of the charge transfer at the semiconductor/electrolyte interfaces was carried out through EIS measurements. Figure S14 presents the impedance spectra in a Nyquist representation, recorded at the formal potential of the redox reaction. The formal potentials of the a-1.7Ag-TNT, a-3.5Ag-TNT, a-5Ag-TNT, s-1.7Ag-TNT, s-3.5Ag-TNT, and s-5Ag-TNT samples are 0.23, 0.24, 0.25, 0.22, 0.23, and 0.25 V vs Ag/AgCl/0.1 M KCl, respectively. The recorded data were fitted to the equivalent circuit shown in Figure S14b (inset). The goodness of fit ( $\chi^2$ ) is on the order of  $10^{-3}$ – $10^{-4}$ , and the values of the parameters are depicted in Table 2. The circuit is composed of a series resistance ( $R_s$ ), a charge-transfer resistance ( $R_{ct}$ ), a constant-phase element (CPE), which is attributed to the capacitance of the bulk semiconductor, and an open Warburg element ( $W_o$ ) associated with the diffusion of electrolyte ions through the tubular layer. For both TNT architectures, the smallest  $R_{ct}$  values were obtained for the TNT synthesized out of the highest, 5%, Ag content in the deposited TiAg film. The standard heterogeneous rate constant ( $k^0$ ) was determined for all samples to quantify the electron-transfer kinetics at the electrode/electrolyte interfaces.<sup>60</sup> The relationship between  $R_{ct}$  and  $k^0$  is given as follows:

$$k^0 = \frac{RT}{(nF)^2 A C_0 R_{ct}} \quad (4)$$

where  $R$  is the molar gas constant ( $8.32 \text{ J mol}^{-1} \text{ K}^{-1}$ ),  $T$  is the electrolyte temperature (296 K),  $n$  is the number of electrons transferred in the redox reaction ( $n = 1$ ),  $F$  is the Faraday constant ( $96500 \text{ C mol}^{-1}$ ),  $A$  is attributed to the geometric electrode area, and  $C_0 = C_{\text{red}} = C_{\text{ox}} = 10^{-5} \text{ mol cm}^{-3}$ .<sup>61</sup> The

calculated values for a-1.7Ag-TNT, a-3.5Ag-TNT, and a-5Ag-TNT are  $1.24 \times 10^{-4}$ ,  $2.76 \times 10^{-3}$ , and  $3.84 \times 10^{-3} \text{ cm s}^{-1}$ , respectively, and  $3.38 \times 10^{-4}$ ,  $7.15 \times 10^{-3}$ , and  $7.98 \times 10^{-3} \text{ cm s}^{-1}$  for the s-1.7Ag-TNT, s-3.5Ag-TNT, and s-5Ag-TNT samples. For both the aligned and spaced TNT, the greater value of  $k^0$  is obtained for the TNT developed out of the deposited films with the highest Ag content, i.e., 5%. Except for the a-1.7Ag-TNT and s-1.7Ag-TNT samples, the  $k^0$  values of a-3.5Ag-TNT, a-5Ag-TNT, s-3.5Ag-TNT, and s-5Ag-TNT are comparable to the values reported by both Zhao et al.<sup>56</sup> for TNT modified with a carbon nanofilm ( $1.4 \times 10^{-3} \text{ cm s}^{-1}$ ) and Xiao et al.<sup>62</sup> for TNT annealed under N<sub>2</sub> ( $2.18 \times 10^{-3} \text{ cm s}^{-1}$ ) and TNT annealed in CO ( $1.34 \times 10^{-3} \text{ cm s}^{-1}$ ) at 500 °C. This indicates that TNT formed out of TiAg alloys with relatively high Ag content (above 1.7%) can exhibit fast electron transfer at the electrode/electrolyte interface.

Other properties of TNT-based materials that should be considered in terms of their intended use in the PEC system are their light-harvesting ability and photostability. Taking into account the importance of those properties, we investigated the impact of the obtained TNT structures, and their chemical compositions on their photoresponse were investigated. The current of the electrode material exposed to visible and UV-vis radiation was tracked using LSV. For both TNT architectures, regardless of the Ag content in the TiAg films, the LSV curves recorded in the dark and under visible-light illumination overlap (Figures 9 and S15). Under visible-light illumination, there is not any improvement in the photo-response of the TNT grown out of TiAg alloys compared to that of the pure material. This may be due to the relatively



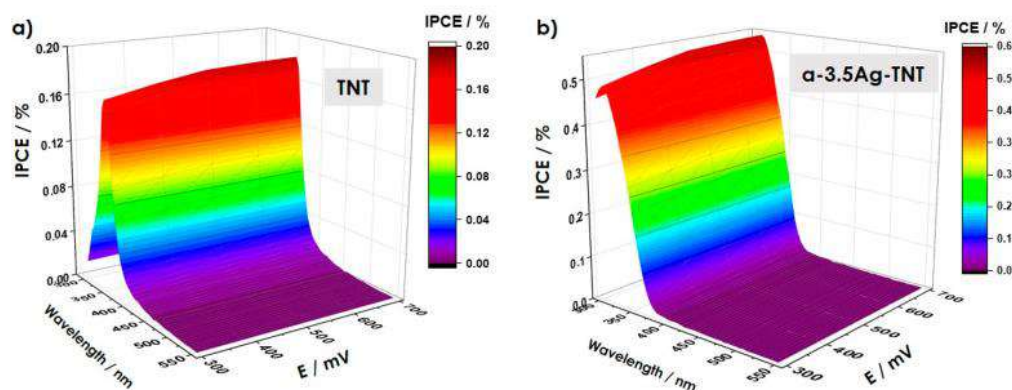


Figure 10. 3D IPCE maps recorded for (a) a-TNT and (b) a-3.5Ag-TNT.

large band-gap energies of the TNT materials formed from the alloy films. Under UV–vis illumination, the curves registered for a-TNT, a-1.7Ag-TNT, a-3.5Ag-TNT, s-TNT, and s-1.7Ag-TNT are clearly distinguishable from the plots obtained in the dark (Figures 9 and S15). However, the results show that the a-5Ag-TNT, s-3.5Ag-TNT, and s-5Ag-TNT samples do not exhibit satisfactory photoactivities even under UV–vis light (Figures 9 and S15).

The photostability of the electrodes was investigated by the chronoamperometry technique (Figure S16), while the whole measuring protocol was described in detail in the Experimental Section. After 60 s of polarization in the dark, when the electrode is irradiated, the current increases rapidly for both aligned and spaced titania and then decreases slowly. This rapid growth of the current is finished by the anodic spike that results from separation of the hole–electron pair generated at the titania/electrolyte interface. After this moment, the decay exhibiting exponential nature arises due to the recombination processes. It should be underlined here that for the semiconductor exhibiting n-type behavior, as in the case of titania, when the electrode is exposed to light of high energy (UV), it promotes the accumulation of electrons in the conduction band, and some of them are stored in the deep surface states.<sup>63</sup> Therefore, when the material is irradiated for the first time, those recombination centers are fulfilled and the next illumination periods are not finished with such a sharp anodic peak. Nevertheless, for all electrodes after 30 min of irradiation, the photocurrent remains the same value, indicating good stability of the TNT materials. The photocurrent densities of the s-3.5Ag-TNT and s-5Ag-TNT samples determined from the chronoamperometry curves (Figure S16c) after 2 h are less than  $0.3 \mu\text{A cm}^{-2}$ , which is an order of magnitude smaller compared to those of s-TNT ( $1.02 \mu\text{A cm}^{-2}$ ) and s-1.7Ag-TNT ( $1.08 \mu\text{A cm}^{-2}$ ). It should be reminded that, according to the recorded and already-analyzed Raman spectra, no signals characteristic for the anatase crystalline phase for the s-3.5Ag-TNT and s-5Ag-TNT samples were found after annealing. This can effectively explain the poor photoactivity of the two electrodes. In general, better photoresponses are reported for the anatase phase of titania.<sup>64</sup> Ghicov et al.<sup>64</sup> pointed out that the anatase titania can exhibit an enhancement of the photoresponse even ca. 100 times higher compared to the amorphous materials. In fact, the

photogenerated electrons must pass through the crystalline structure to be collected at the current collector.<sup>65</sup> Related to this, a nearly perfect structure is required to collect as many electrons as possible. The amorphous phases (as shown in Figure 4) of the s-3.5Ag-TNT and s-5Ag-TNT samples hamper the percolation of electrons; thus, a substantial increase of the recombination of electron–hole pairs occurs. In the case of the aligned TNT, the photocurrent densities recorded during the whole chronoamperometry test show an increase from  $0.5 \mu\text{A cm}^{-2}$  for a-TNT (Figure S16d) to  $1.7 \mu\text{A cm}^{-2}$  for a-3.5Ag-TNT (Figure S16f). This is probably due to the fact that electrons can also be the product of the light-induced oxidation of Ag atoms present in the nanotube walls, namely, according to eq 5



Among all samples, a-3.5Ag-TNT exhibits both good photostability and the highest photocurrent. For comparison with the already reported performance of semitransparent TNTs grown onto TCOs, IPCE maps of the most photoactive a-3.5Ag-TNT sample and bare titania (a-TNT) were recorded (Figure 10). The IPCE of a-3.5Ag-TNT is found to be about 0.6%, while for bare titania at the maximum point, it does not exceed 0.2%. It should be evoked here that the IPCE strongly depends on the TNT tubular length.<sup>15,66</sup> In the case of Ti foils, by increasing the anodization time (i.e., for some hours), several-micrometer-thick TNT layers can be grown and high IPCE values can be obtained. Regarding the semitransparent TNT electrodes, it is well-known that the length of the nanotubes increases with the deposited Ti layer. Thus, the length of the produced TNT onto TCOs is limited by the thickness of the initial sputtered Ti film. Also in the case of the semitransparent materials, anodizing the deposited Ti film for several hours can lead to complete etching of the Ti film, and no tubular layer will be obtained. Thus, the IPCE values reached by the particular materials should be analyzed, taking into account the morphology of the fabricated layer, especially its thickness. A comparison of the obtained IPCE for the 3.5Ag-TNT sample with those reported for only TNTs grown onto TCOs is provided in Table 3. Compared to the already-reported works, the performance of the fabricated materials is reasonable.

**Table 3.** Average Tube Length and IPCE of TNTs Grown on TCOs

electrode material	TCO	nanotube length/ $\mu\text{m}$	IPCE/%	ref
TNT	FTO	20.0	80	32
TiO <sub>2</sub> -nanorods-decorated TNT	FTO	2.0	2.95	8
TiO <sub>2</sub> -nanoparticles-decorated TNT	FTO	2.0	2.56	8
TNT	FTO	2.0	1.90	8
a-TNT	ITO	1.2	0.2	this work
a-3.5Ag-TNT	ITO	1.1	0.6	this work

Mott–Schottky analysis was conducted to determine both the donor concentration and the flat-band potential values of the anodized materials. The Mott–Schottky relationship for *n*-type semiconductors is given as

$$C^{-2} = \left( \frac{2}{\epsilon \epsilon_0 N_D} \right) \left( E - E_{fb} - \frac{kT}{e} \right) \quad (6)$$

where *C* is the space-charge capacitance,  $\epsilon$  is the permittivity of the anatase titania ( $\epsilon = 38$ ),  $\epsilon_0$  ( $8.85 \times 10^{-14} \text{ F cm}^{-1}$ ) is the permittivity of free space, *e* is the electron charge,  $N_D$  is the donor density, *E* is the applied potential,  $E_{fb}$  is the flat-band potential, *k* is the Boltzmann constant, and *T* is the temperature.<sup>68</sup> The capacitance of the space-charge layer can be calculated using the following equation:

$$C = -\frac{1}{2\pi f Z_{im}} \quad (7)$$

where *f* is the frequency of the ac signal and  $Z_{im}$  is the imaginary part of the impedance. Extrapolation of the linear regions of the  $C^{-2}$  vs *E* curve for each sample is provided in Figures S17 and S18. The donor density,  $N_D$ , can be derived from the slope of the Mott–Schottky plot and is calculated via the equation

$$N_D = \left( \frac{2}{\epsilon \epsilon_0} \right) \left( \frac{dE}{dC^{-2}} \right)^{-2} \quad (8)$$

where  $\frac{dE}{dC^{-2}}$  is the inverse of the slope of the  $C^{-2}$  vs *E* curve.<sup>68</sup>

The  $E_{fb}$  values were determined at the intersection of the tangent of the linear regions of the  $C^{-2}$  vs *E* curve. The  $E_{fb}$  and  $N_D$  values are given in Table 4. There are positive shifts of the  $E_{fb}$  values for all aligned and spaced TNT materials prepared out of the TiAg alloys with respect to their pure counterparts (i.e., a-TNT and s-TNT). However, as shown in Table 4, this

**Table 4.**  $E_{fb}$  and  $N_D$  Values of the Samples

aligned nanotubes			spaced nanotubes		
sample	$E_{fb}/V$ vs Ag/AgCl/0.1 M KCl	$N_D/\times 10^{20} \text{ cm}^{-3}$	sample	$E_{fb}/V$ vs Ag/AgCl/0.1 M KCl	$N_D/\times 10^{20} \text{ cm}^{-3}$
a-TNT	−0.85	6.4	s-TNT	−0.96	5.6
a-1.7Ag-TNT	−0.69	5.8	s-1.7Ag-TNT	−0.61	6.6
a-3.5Ag-TNT	−0.71	2.2	s-3.5Ag-TNT	−0.51	1.4
a-5Ag-TNT	−0.55	8.2	s-5Ag-TNT	−0.59	2.8

shift is not a linear function of the Ag content in the deposited TiAg films. In general, the origin of the shift in  $E_{fb}$  is due to not only the presence of heteroatoms but also the structural defects in the materials, i.e., O or cation vacancies in the semiconductor induced during the synthesis process.<sup>69</sup> Li et al.<sup>70</sup> pointed out that a positive shift of  $E_{fb}$  indicates a rise of the Fermi level near the conduction band, which can promote charge separation at the semiconductor/electrolyte interface, thereby improving the photoresponse of the materials.<sup>69</sup> In our case, the positive shifts of  $E_{fb}$  for the aligned TNT materials have led to an increase in the photocurrent density with respect to a-TNT for the a-3.5Ag-TNT (about 3 times) sample, which is in agreement with the results of Li et al.<sup>70</sup> In the case of the spaced TNT materials, the s-1.7Ag-TNT sample has almost the same photocurrent density ( $1.02 \mu\text{A cm}^{-2}$ ) as the s-TNT sample ( $1.08 \mu\text{A cm}^{-2}$ ), but no improvement in the photoresponse of the s-3.5Ag-TNT and s-5Ag-TNT samples was observed with an anodic shift of  $E_{fb}$ . This can be attributed to the obtained amorphous phase after annealing.

#### 4. CONCLUSIONS

TNT arrays with aligned and spaced architectures were prepared by the anodization of TiAg films deposited onto ITO. The physicochemical properties of the obtained semi-transparent materials and their electrochemical activities were investigated and discussed. The results show that the aligned TNT with the anatase phase can be synthesized out of the alloy films with up to 5% Ag content. For both TNT architectures, an increase in the band-gap energy values of the TNT has been observed. This can be explained by the Burstein–Moss effect due to the presence of Ag in the deposited alloys. Although some small amount of Ag is still present in the obtained aligned TNT layer after anodization, there is almost no Ag content in the spaced TNT layer according to the recorded EDX spectra due to the strong etching process by F ions during anodization. The increase of the Ag content in the TiAg films has led to high electron-transfer kinetics at the electrode/electrolyte interfaces. However, this can be effectively explained not only by the presence of Ag in the deposited films but also by the morphological features of the prepared TNT. The aligned TNT developed out of the TiAg films exhibits promising photoresponse and photostability tested for 2 h. Below 3.5% of the Ag content, a linear increase of the photocurrent density of up to 3 times with respect to that of the photoelectrode based on aligned TNT grown out of the pure Ti film was obtained. This may be attributed to the positive shift of  $E_{fb}$ , as discussed in the Mott–Schottky analysis. Indeed, the presence of Ag in the TNT matrix leads to an increase in the Fermi level near the conduction-band edge, which promotes electron–hole separation. This study provides evidence that semitransparent TNT materials (i.e., aligned and spaced TNT) formed out of TiAg films are promising materials for electrochemical devices due to their high electron-transfer rate. For the first time, both spaced and aligned TNT were successfully synthesized by anodizing TiAg films sputtered onto ITO. This work paves the way for the use of a tubular layer formed out of TiAg alloys as promising materials not only for solar-driven processes but also in which the ferri/ferrocyanide redox couple acts as a probe molecule, e.g., electrochemical sensors. In addition, because Ag is highly antibacterial, TNT can also be grown onto other



substrates (not only TCOs) that can then be used as antibacterial surfaces.

## ■ ASSOCIATED CONTENT

### ■ Supporting Information

The Supporting Information is available free of charge at <https://pubs.acs.org/doi/10.1021/acsnm.3c04186>.

Photographs of the semitransparent substrates overgrown with aligned TNT, overgrown with spaced TNT, and obtained by anodizing TiAg films containing 6.8% Ag; SEM top images of anodized TiAg films containing 6.8% Ag; potentiostatic current–time curves of the samples; EDX spectra of the samples; Ag and Ti atomic concentrations in the anodized samples; high-resolution XPS spectra of Ti 2p, O 1s, Ag 3d, C 1s, and F 1s for anodized TiAg films containing 3.5% Ag; XPS binding energies and corresponding chemical bonds of the sample; cyclic voltammograms at different scan rates recorded in 0.5 M Na<sub>2</sub>SO<sub>4</sub> + 10 mM K<sub>3</sub>Fe(CN)<sub>6</sub> and peak current density vs scan rate curves of ITO; cyclic voltammograms at different scan rates recorded in 0.5 M Na<sub>2</sub>SO<sub>4</sub> + 10 mM K<sub>3</sub>Fe(CN)<sub>6</sub> of anodized films containing 1.7% and 3.5% Ag; cross-sectional images of water droplets on anodized pure Ti films and an alloy film containing 5% Ag; peak current density vs scan rate curves of the anodized samples; Nyquist plots of EIS measurements performed at the formal potential of the redox reaction of the samples; linear-sweep voltammograms in the dark and under UV–vis- and visible-light illumination of anodized films containing 1.7% and 5% Ag; transient photocurrent curves recorded under chopped UV–vis-light illumination of the anodized samples; slope and correlation coefficient of the peak current density vs scan rate curves and the diffusion coefficients of the anodized samples; and Mott–Schottky curves of the anodized samples (PDF)

## ■ AUTHOR INFORMATION

### Corresponding Author

Dujearic-Stephane Kouao – Centre for Plasma and Laser Engineering, Institute of Fluid-Flow Machinery, Polish Academy of Sciences, 80-231 Gdańsk, Poland; [orcid.org/0000-0003-0649-1122](https://orcid.org/0000-0003-0649-1122); Email: [dkouao@imp.gda.pl](mailto:dkouao@imp.gda.pl)

### Authors

Jan Hanuš – Faculty of Mathematics and Physics, Charles University, 18000 Prague 8, Czech Republic  
Ondřej Kylián – Faculty of Mathematics and Physics, Charles University, 18000 Prague 8, Czech Republic  
Radka Šimerová – Faculty of Science, University of South Bohemia, 37005 České Budějovice, Czech Republic  
Petr Sezemsky – Faculty of Science, University of South Bohemia, 37005 České Budějovice, Czech Republic  
Vítězslav Stranák – Faculty of Science, University of South Bohemia, 37005 České Budějovice, Czech Republic  
Katarzyna Grochowska – Centre for Plasma and Laser Engineering, Institute of Fluid-Flow Machinery, Polish Academy of Sciences, 80-231 Gdańsk, Poland; [orcid.org/0000-0001-7577-3399](https://orcid.org/0000-0001-7577-3399)  
Katarzyna Siuzdak – Centre for Plasma and Laser Engineering, Institute of Fluid-Flow Machinery, Polish

Academy of Sciences, 80-231 Gdańsk, Poland; [orcid.org/0000-0001-7434-6408](https://orcid.org/0000-0001-7434-6408)

Complete contact information is available at:  
<https://pubs.acs.org/doi/10.1021/acsnm.3c04186>

### Notes

The authors declare no competing financial interest.

## ■ ACKNOWLEDGMENTS

This research was funded by the National Science Centre, Poland (Grant 2020/02/Y/ST8/00030), and Czech Science Foundation Agency through Project 21-05030K.

## ■ REFERENCES

- (1) Motola, M.; Satrapinsky, L.; Čaplovicová, M.; Roch, T.; Gregor, M.; Grančič, B.; Greguš, J.; Čaplovič, L.; Plesch, G. Enhanced Photocatalytic Activity of Hydrogenated and Vanadium Doped TiO<sub>2</sub> Nanotube Arrays Grown by Anodization of Sputtered Ti Layers. *Appl. Surf. Sci.* **2018**, *434*, 1257–1265.
- (2) Hejazi, S.; Altomare, M.; Nguyen, N. T.; Mohajernia, S.; Lickleder, M.; Schmuki, P. Intrinsic Au-Decoration on Anodic TiO<sub>2</sub> Nanotubes Grown from Metastable Ti–Au Sputtered Alloys–High Density Co-Catalyst Decoration Enhances the Photocatalytic H<sub>2</sub> Evolution. *Appl. Mater. Today* **2019**, *14*, 118–125.
- (3) Aguirre Ocampo, R.; Echeverría Echeverría, F. Effect of the Anodization Parameters on TiO<sub>2</sub> Nanotubes Characteristics Produced in Aqueous Electrolytes with CMC. *Appl. Surf. Sci.* **2019**, *469*, 994–1006.
- (4) Yu, Y.; Li, C.; Wang, H.; Chen, J.; Zhu, X.; Ying, Z.; Song, Y. High-Specific-Capacitance Electrolytic Capacitors Based on Anodic TiO<sub>2</sub> Nanotube Arrays. *Electrochim. Acta* **2022**, *429*, 140974.
- (5) Liu, R.; Jiang, L.; Li, C.; Li, P.; Zhang, Y.; Zhu, X.; Song, Y. Enhanced Supercapacitive Properties of Mixed Oxide Nanotubes Grown by Anodization of Ti–Fe Alloys. *Energy Technol.* **2022**, *10* (12). DOI: 10.1002/ente.202201128.
- (6) Tang, Y.; Tao, J.; Dong, Z.; Oh, J. T.; Chen, Z. The Formation of Micrometer-Long TiO<sub>2</sub> Nanotube Arrays by Anodization of Titanium Film on Conducting Glass Substrate. *Adv. Nat. Sci. Nanosci. Nanotechnol.* **2011**, *2* (4), 045002.
- (7) Lim, S. L.; Liu, Y.; Li, J.; Kang, E.-T.; Ong, C. K. Transparent Titania Nanotubes of Micrometer Length Prepared by Anodization of Titanium Thin Film Deposited on ITO. *Appl. Surf. Sci.* **2011**, *257* (15), 6612–6617.
- (8) Kathirvel, S.; Su, C.; Yang, C.-Y.; Shiao, Y.-J.; Chen, B.-R.; Li, W.-R. The Growth of TiO<sub>2</sub> Nanotubes from Sputter-Deposited Ti Film on Transparent Conducting Glass for Photovoltaic Applications. *Vacuum* **2015**, *118*, 17–25.
- (9) Kim, J. Y.; Noh, J. H.; Zhu, K.; Halverson, A. F.; Neale, N. R.; Park, S.; Hong, K. S.; Frank, A. J. General Strategy for Fabricating Transparent TiO<sub>2</sub> Nanotube Arrays for Dye-Sensitized Photoelectrodes: Illumination Geometry and Transport Properties. *ACS Nano* **2011**, *5* (4), 2647–2656.
- (10) Krumpmann, A.; Dervaux, J.; Derue, L.; Douhéret, O.; Lazzaroni, R.; Snyders, R.; Decroly, A. Influence of a Sputtered Compact TiO<sub>2</sub> Layer on the Properties of TiO<sub>2</sub> Nanotube Photoanodes for Solid-State DSSCs. *Mater. Des.* **2017**, *120*, 298–306.
- (11) Büttner, P.; Döhler, D.; Korenko, S.; Möhrlein, S.; Bochmann, S.; Vogel, N.; Minguez-Bacho, I.; Bachmann, J. Solid State Interdigitated Sb<sub>2</sub>S<sub>3</sub> Based TiO<sub>2</sub> Nanotube Solar Cells. *RSC Adv.* **2020**, *10* (47), 28225–28231.
- (12) Weicheng, K.; Kangmei, L.; Jun, H. TEM Structure, Nanomechanical Property, and Adhesive Force of Magnetron-Sputtered Cr-DLC Coating on a Nitrided Ti<sub>6</sub>Al<sub>4</sub>V Alloy. *J. Phys. Chem. C* **2021**, *125* (30), 16733–16745.
- (13) Varghese, O. K.; Paulose, M.; Grimes, C. A. Long Vertically Aligned Titania Nanotubes on Transparent Conducting Oxide for Highly Efficient Solar Cells. *Nat. Nanotechnol.* **2009**, *4* (9), 592–597.

- (14) Kyeremateng, N. A.; Hornebecq, V.; Martinez, H.; Knauth, P.; Djenizian, T. Electrochemical Fabrication and Properties of Highly Ordered Fe-Doped TiO<sub>2</sub> Nanotubes. *ChemPhysChem* **2012**, *13* (16), 3707–3713.
- (15) Li, P.; Wang, J.; Zu, G.; Jiao, P.; Liu, S.; Yang, Y.; Chen, S.; Li, H. Synergetic Catalytic Properties of Gold Nanoparticles Planted on Transparent Titanium Dioxide Nanotube Array Bed. *Mater. Chem. Phys.* **2018**, *217*, 437–444.
- (16) Sanabria-Arenas, B. E.; Mazare, A.; Yoo, J.; Nguyen, N. T.; Hejazi, S.; Bian, H.; Diamanti, M. V.; Pedferri, M. P.; Schmuki, P. Intrinsic AuPt-Alloy Particles Decorated on TiO<sub>2</sub> Nanotubes Provide Enhanced Photocatalytic Degradation. *Electrochim. Acta* **2018**, *292*, 865–870.
- (17) Kar, P.; Farsinezhad, S.; Mahdi, N.; Zhang, Y.; Obuekwe, U.; Sharma, H.; Shen, J.; Semagina, N.; Shankar, K. Enhanced CH<sub>4</sub> Yield by Photocatalytic CO<sub>2</sub> Reduction Using TiO<sub>2</sub> Nanotube Arrays Grafted with Au, Ru, and ZnPd Nanoparticles. *Nano Res.* **2016**, *9* (11), 3478–3493.
- (18) Wang, S.; Zhang, Z.; Huo, W.; Zhu, K.; Zhang, X.; Zhou, X.; Fang, F.; Xie, Z.; Jiang, J. Preferentially Oriented Ag-TiO<sub>2</sub> Nanotube Array Film: An Efficient Visible-Light-Driven Photocatalyst. *J. Hazard. Mater.* **2020**, *399*, 123016.
- (19) Liu, C.; Li, T.; Zhang, Y.; Kong, T.; Zhuang, T.; Cui, Y.; Fang, M.; Zhu, W.; Wu, Z.; Li, C. Silver Nanoparticle Modified TiO<sub>2</sub> Nanotubes with Enhanced the Efficiency of Dye-Sensitized Solar Cells. *Microporous Mesoporous Mater.* **2019**, *287*, 228–233.
- (20) Lamberti, A.; Virga, A.; Chiadò, A.; Chiodoni, A.; Bejtka, K.; Rivolo, P.; Giorgis, F. Ultrasensitive Ag-Coated TiO<sub>2</sub> Nanotube Arrays for Flexible SERS-Based Optofluidic Devices. *J. Mater. Chem. C* **2015**, *3* (26), 6868–6875.
- (21) Farkhondeh, M. A.; Hernández, S.; Rattalino, M.; Makkee, M.; Lamberti, A.; Chiodoni, A.; Bejtka, K.; Sacco, A.; Pirri, F. C.; Russo, N. Syngas Production by Electrochemical Reduction of CO<sub>2</sub> Using Ag-Decorated TiO<sub>2</sub> Nanotubes. *Int. J. Hydrogen Energy* **2020**, *45* (50), 26458–26471.
- (22) Habazaki, H.; Uozumi, M.; Konno, H.; Shimizu, K.; Nagata, S.; Asami, K.; Skeldon, P.; Thompson, G. E. Influence of Molybdenum Species on Growth of Anodic Titania. *Electrochim. Acta* **2002**, *47* (24), 3837–3845.
- (23) Gui, Y.; Blackwood, D. J. Honey-Comb Structured WO<sub>3</sub>/TiO<sub>2</sub> Thin Films with Improved Electrochromic Properties. *J. Electrochem. Soc.* **2015**, *162* (10), E205–E212.
- (24) Mor, G. K.; Varghese, O. K.; Wilke, R. H. T.; Sharma, S.; Shankar, K.; Latempa, T. J.; Choi, K.-S.; Grimes, C. A. P-Type Cu-Ti-O Nanotube Arrays and Their Use in Self-Biased Heterojunction Photoelectrochemical Diodes for Hydrogen Generation. *Nano Lett.* **2008**, *8* (7), 1906–1911.
- (25) Farsinezhad, S.; Banerjee, S. P.; Bangalore Rajeeva, B.; Wiltshire, B. D.; Sharma, H.; Sura, A.; Mohammadpour, A.; Kar, P.; Fedosejevs, R.; Shankar, K. Reduced Ensemble Plasmon Line Widths and Enhanced Two-Photon Luminescence in Anodically Formed High Surface Area Au-TiO<sub>2</sub> 3D Nanocomposites. *ACS Appl. Mater. Interfaces* **2017**, *9* (1), 740–749.
- (26) Bleckenwegner, P.; Mardare, C. C.; Cobet, C.; Kollender, J. P.; Hassel, A. W.; Mardare, A. I. Compositionally Dependent Nonlinear Optical Bandgap Behavior of Mixed Anodic Oxides in Niobium-Titanium System. *ACS Comb. Sci.* **2017**, *19* (2), 121–129.
- (27) Bohórquez, A. J.; Quiroz, H. P.; Dussan, A. Growth and Crystallization of Cobalt-Doped TiO<sub>2</sub> Alloys: Effect of Substrate and Annealing Temperature. *Appl. Surf. Sci.* **2019**, *474*, 97–101.
- (28) Mor, G. K.; Prakasam, H. E.; Varghese, O. K.; Shankar, K.; Grimes, C. A. Vertically Oriented Ti-Fe-O Nanotube Array Films: Toward a Useful Material Architecture for Solar Spectrum Water Photoelectrolysis. *Nano Lett.* **2007**, *7* (8), 2356–2364.
- (29) Hang, R.; Gao, A.; Huang, X.; Wang, X.; Zhang, X.; Qin, L.; Tang, B. Antibacterial Activity and Cytocompatibility of Cu-Ti-O Nanotubes. *J. Biomed. Mater. Res. Part A* **2014**, *102* (6), 1850–1858.
- (30) Mohammadi, K.; Moshai, A.; Azimzadehirani, M.; Pourbakhsh, Z.-S. Photoelectrochemical Activity of Ag Loaded TiO<sub>2</sub> Nanotube Arrays Produced by Sequential Chemical Bath Deposition for Water Splitting. *J. Mater. Sci. Mater. Electron.* **2019**, *30* (2), 1878–1884.
- (31) Wodka, D.; Bielańska, E.; Socha, R. P.; Elżbieciak - Wodka, M.; Gurgul, J.; Nowak, P.; Warszyński, P.; Kumakiri, I. Photocatalytic Activity of Titanium Dioxide Modified by Silver Nanoparticles. *ACS Appl. Mater. Interfaces* **2010**, *2* (7), 1945–1953.
- (32) Al-Abdullah, Z. T. Y.; Shin, Y.; Kler, R.; Perry, C. C.; Zhou, W.; Chen, Q. The Influence of Hydroxide on the Initial Stages of Anodic Growth of TiO<sub>2</sub> Nanotubular Arrays. *Nanotechnology* **2010**, *21* (50), S05601.
- (33) Bjelajac, A.; Petrović, R.; Vujanecic, J.; Veltruska, K.; Matolin, V.; Siketic, Z.; Provatas, G.; Jaksic, M.; Stan, G. E.; Socol, G.; Mihailescu, I. N.; Janačković, D. Sn-Doped TiO<sub>2</sub> Nanotubular Thin Film for Photocatalytic Degradation of Methyl Orange Dye. *J. Phys. Chem. Solids* **2020**, *147*, 109609.
- (34) Poddar, S.; Bit, A.; Sinha, S. K. A Study on Influence of Anodization on the Morphology of Titania Nanotubes over Ti<sub>6</sub>Al<sub>4</sub>V Alloy in Correlation to Hard Tissue Engineering Application. *Mater. Chem. Phys.* **2020**, *254*, 123457.
- (35) Ilie, A. G.; Scarisoareanu, M.; Morjan, I.; Dutu, E.; Badiceanu, M.; Mihailescu, I. Principal Component Analysis of Raman Spectra for TiO<sub>2</sub> Nanoparticle Characterization. *Appl. Surf. Sci.* **2017**, *417*, 93–103.
- (36) Mosquera, A. A.; Albella, J. M.; Navarro, V.; Bhattacharyya, D.; Endrino, J. L. Effect of Silver on the Phase Transition and Wettability of Titanium Oxide Films. *Sci. Rep.* **2016**, *6* (1), 32171.
- (37) Alamgir, Khan, W.; Ahmad, S.; Mehedi Hassan, M.; Naqvi, A. H. Structural Phase Analysis, Band Gap Tuning and Fluorescence Properties of Co Doped TiO<sub>2</sub> Nanoparticles. *Opt. Mater. (Amst.)* **2014**, *38*, 278–285.
- (38) Georgescu, D.; Baia, L.; Ersen, O.; Baia, M.; Simon, S. Experimental Assessment of the Phonon Confinement in TiO<sub>2</sub> Anatase Nanocrystallites by Raman Spectroscopy. *J. Raman Spectrosc.* **2012**, *43* (7), 876–883.
- (39) Lai, Y. K.; Sun, L.; Chen, C.; Nie, C. G.; Zuo, J.; Lin, C. J. Optical and Electrical Characterization of TiO<sub>2</sub> Nanotube Arrays on Titanium Substrate. *Appl. Surf. Sci.* **2005**, *252* (4), 1101–1106.
- (40) Mor, G. K.; Shankar, K.; Varghese, O. K.; Grimes, C. A. Photoelectrochemical Properties of Titania Nanotubes. *J. Mater. Res.* **2004**, *19* (10), 2989–2996.
- (41) Munir, S.; Shah, S. M.; Hussain, H.; Ali Khan, R. Effect of Carrier Concentration on the Optical Band Gap of TiO<sub>2</sub> Nanoparticles. *Mater. Des.* **2016**, *92*, 64–72.
- (42) Ferrara, M. C.; Mazzarelli, S.; Schioppa, M.; Piloni, L.; Tapfer, L. Growth, Optical, and Wettability Properties of Iron Modified Titania and Ferropseudobrookite Thin Films. *J. Appl. Phys.* **2021**, *130* (14), 145301.
- (43) Soliman, K. A.; Zedan, A. F.; Khalifa, A.; El-Sayed, H. A.; Aljaber, A. S.; AlQaradawi, S. Y.; Allam, N. K. Silver Nanoparticles-Decorated Titanium Oxynitride Nanotube Arrays for Enhanced Solar Fuel Generation. *Sci. Rep.* **2017**, *7* (1), 1913.
- (44) Surovčík, J.; Medvecká, V.; Greguš, J.; Gregor, M.; Roch, T.; Annušová, A.; Durina, P.; Vojteková, T. Characterization of TiO<sub>2</sub> Nanofibers with Enhanced Photocatalytic Properties Prepared by Plasma Assisted Calcination. *Ceram. Int.* **2022**, *48*, 37322.
- (45) Touni, A.; Liu, X.; Kang, X.; Carvalho, P. A.; Diplas, S.; Both, K. G.; Sotiropoulos, S.; Chatzidakis, A. Galvanic Deposition of Pt Nanoparticles on Black TiO<sub>2</sub> Nanotubes for Hydrogen Evolving Cathodes. *ChemSusChem* **2021**, *14* (22), 4993–5003.
- (46) Wang, R.; Sun, Q.; Gu, H.; Ye, W.; Yuan, G.; Yang, Z.; Long, X. Preparation and Electromagnetic-Wave-Absorption Properties of a Nitrogen-Doped Carbon-Supported Iron(II,III) Oxide Composite. *J. Mater. Sci. Mater. Electron.* **2022**, *33* (3), 1383–1394.
- (47) Fang, D.; He, F.; Xie, J.; Xue, L. Calibration of Binding Energy Positions with C1s for XPS Results. *J. Wuhan Univ. Technol. Sci. Ed.* **2020**, *35* (4), 711–718.
- (48) Regonini, D.; Satka, A.; Jaroenworarluck, A.; Allsopp, D. W. E.; Bowen, C. R.; Stevens, R. Factors Influencing Surface Morphology of Anodized TiO<sub>2</sub> Nanotubes. *Electrochim. Acta* **2012**, *74*, 244–253.



- (49) Amor, Y. B.; Sutter, E.; Takenouti, H.; Tribollet, B.; Boinet, M.; Faure, R.; Balencie, J.; Durieu, G. Electrochemical Study of the Tarnish Layer of Silver Deposited on Glass. *Electrochim. Acta* **2014**, *131*, 89–95.
- (50) Liu, B.; Ding, C.; Xiao, B.; Cui, L.; Wang, M. Electrocatalytic Dechlorination of Chloroacetic Acids on Silver Nanodendrites Electrode. *Mater. Sci. Eng., C* **2014**, *37*, 108–112.
- (51) Jiang, Y.; Zheng, B.; Du, J.; Liu, G.; Guo, Y.; Xiao, D. Electrophoresis Deposition of Ag Nanoparticles on TiO<sub>2</sub> Nanotube Arrays Electrode for Hydrogen Peroxide Sensing. *Talanta* **2013**, *112*, 129–135.
- (52) Gusmão, R.; López-Puente, V.; Yate, L.; Pastoriza-Santos, L.; Pérez-Juste, J.; González-Romero, E. Screen-Printed Carbon Electrodes Doped with TiO<sub>2</sub>-Au Nanocomposites with Improved Electrocatalytic Performance. *Mater. Today Commun.* **2017**, *11*, 11–17.
- (53) Lee, D. Y.; Kim, E.-K.; Yoon, S. J.; Lim, I.; Cho, K.; Shinde, D. V.; Patil, S. A.; Lee, W.; Nah, Y.-C.; Shrestha, N. K.; Lee, J. K.; Han, S.-H. A Facile Approach for Carburization of Anodically Grown Titania Nanotubes: Towards Metallization of Nanotubes. *RSC Adv.* **2014**, *4* (62), 32599.
- (54) Yu, H.; Ma, J.; Zhang, Y.; Zhang, X.; Shi, W. Cyclic Voltammetry Studies of TiO<sub>2</sub> Nanotube Arrays Electrode: Conductivity and Reactivity in the Presence of H<sup>+</sup> and Aqueous Redox Systems. *Electrochim. Acta* **2011**, *56* (18), 6498–6502.
- (55) Shivaram, A.; Bose, S.; Bandyopadhyay, A. Mechanical Degradation of TiO<sub>2</sub> Nanotubes with and without Nanoparticulate Silver Coating. *J. Mech. Behav. Biomed. Mater.* **2016**, *59*, 508–518.
- (56) Zhao, J.; Cheng, L.; Wang, J.; Liu, Y.; Yang, J.; Xu, Q.; Chen, R.; Ni, H. Heteroatom-Doped Carbon Nanofilm Embedded in Highly Ordered TiO<sub>2</sub> Nanotube Arrays by Thermal Nitriding with Enhanced Electrochemical Activity. *J. Electroanal. Chem.* **2019**, *852*, 113513.
- (57) Mishra, N. K.; Mondal, R.; Maiyalagan, T.; Singh, P. Synthesis, Characterizations, and Electrochemical Performances of Highly Porous, Anhydrous Co<sub>0.3</sub>Ni<sub>0.5</sub>C<sub>2</sub>O<sub>4</sub> for Pseudocapacitive Energy Storage Applications. *ACS Omega* **2022**, *7* (2), 1975–1987.
- (58) Branch, S. D.; Lines, A. M.; Lynch, J.; Bello, J. M.; Heineman, W. R.; Bryan, S. A. Optically Transparent Thin-Film Electrode Chip for Spectroelectrochemical Sensing. *Anal. Chem.* **2017**, *89* (14), 7324–7332.
- (59) Krishnaveni, P.; Ganesh, V. Electron Transfer Studies of a Conventional Redox Probe in Human Sweat and Saliva Bio-Mimicking Conditions. *Sci. Rep.* **2021**, *11* (1), 7663.
- (60) Fernández Macía, L.; Petrova, M.; Hubin, A. ORP-EIS to Study the Time Evolution of the [Fe (CN)<sub>6</sub>]<sup>3−</sup>/[Fe (CN)<sub>6</sub>]<sup>4−</sup> reaction due to adsorption at the electrochemical interface. *J. Electroanal. Chem.* **2015**, *737*, 46–53.
- (61) Siuzdak, K.; Ficek, M.; Sobaszek, M.; Ryl, J.; Gnyba, M.; Niedzialkowski, P.; Malinowska, N.; Karczewski, J.; Bogdanowicz, R. Boron-Enhanced Growth of Micron-Scale Carbon-Based Nanowalls: A Route toward High Rates of Electrochemical Biosensing. *ACS Appl. Mater. Interfaces* **2017**, *9* (15), 12982–12992.
- (62) Xiao, P.; Fang, H.; Cao, G.; Zhang, Y.; Zhang, X. Effect of Ti<sup>3+</sup> Defects on Electrochemical Properties of Highly-Ordered Titania Nanotube Arrays. *Thin Solid Films* **2010**, *518* (23), 7152–7155.
- (63) Spadavecchia, F.; Ardizzone, S.; Cappelletti, G.; Falcicola, L.; Ceotto, M.; Lotti, D. Investigation and Optimization of Photocurrent Transient Measurements on Nano-TiO<sub>2</sub>. *J. Appl. Electrochem.* **2013**, *43* (2), 217–225.
- (64) Ghicov, A.; Tsuchiya, H.; Macak, J. M.; Schmuki, P. Annealing Effects on the Photoresponse of TiO<sub>2</sub> Nanotubes. *Phys. Status Solidi* **2006**, *203* (4), R28–R30.
- (65) Nguyen, T.-V.; Yang, O.-B. Photoresponse and AC Impedance Characterization of TiO<sub>2</sub>-SiO<sub>2</sub> Mixed Oxide for Photocatalytic Water Decomposition. *Catal. Today* **2003**, *87* (1–4), 69–75.
- (66) Guo, F.; Liu, J.; Zhang, W.; Yu, Z.; Liu, Y.; Liang, W. Synthesis of Cu,N-Doped TiO<sub>2</sub> Nanotube by a Novel Magnetron Sputtering Method and Its Photoelectric Property. *Vacuum* **2019**, *165*, 223–231.
- (67) Park, B. H.; Li, L. S.; Gibbons, B. J.; Huang, J. Y.; Jia, Q. X. Photovoltaic Response and Dielectric Properties of Epitaxial Anatase-TiO<sub>2</sub> Films Grown on Conductive La<sub>0.5</sub>Sr<sub>0.5</sub>CoO<sub>3</sub> Electrodes. *Appl. Phys. Lett.* **2001**, *79* (17), 2797–2799.
- (68) Vadla, S. S.; Bandyopadhyay, P.; John, S.; Ghosh, P.; Roy, S. C. TiO<sub>2</sub> Nanotube Arrays on Flexible Kapton Substrates for Photo-Electrochemical Solar Energy Conversion. *ACS Appl. Nano Mater.* **2020**, *3* (12), 11715–11724.
- (69) Garlisi, C.; Lai, C.-Y.; George, L.; Chiesa, M.; Palmisano, G. Relating Photoelectrochemistry and Wettability of Sputtered Cu- and N-Doped TiO<sub>2</sub> Thin Films via an Integrated Approach. *J. Phys. Chem. C* **2018**, *122* (23), 12369–12376.
- (70) Li, Z.; Xin, Y.; Wu, W.; Fu, B.; Zhang, Z. Phosphorus Cation Doping: A New Strategy for Boosting Photoelectrochemical Performance on TiO<sub>2</sub> Nanotube Photonic Crystals. *ACS Appl. Mater. Interfaces* **2016**, *8* (45), 30972–30979.



### Supporting Information

Photoelectrochemical and Electrochemical Activity of Anodic Semitransparent Aligned and Spaced Titania Nanotubes Formed out of Titanium-Silver Alloys.

Dujearic-Stephane Kouao <sup>1, \*</sup>, Jan Hanuš <sup>2</sup>, Ondřej Kylián <sup>2</sup>, Radka Simerova <sup>3</sup>, Petr Sezemsky <sup>3</sup>, Vitezslav Stranak <sup>3</sup>, Katarzyna Grochowska <sup>1</sup>, Katarzyna Siuzdak <sup>1</sup>

<sup>1</sup> Centre for Plasma and Laser Engineering, Institute of Fluid-Flow Machinery, Polish Academy of Sciences, Fiszerka 14 st., 80-231 Gdańsk, Poland

<sup>2</sup> Faculty of Mathematics and Physics, Charles University, V Holešovičkách 2, 180 00 Prague 8, Czech Republic

<sup>3</sup> Faculty of Science, University of South Bohemia, Banisovska 1760, 37005 České Budejovice, Czech Republic

\*Corresponding author

E-mail address: dkouao@imp.gda.pl

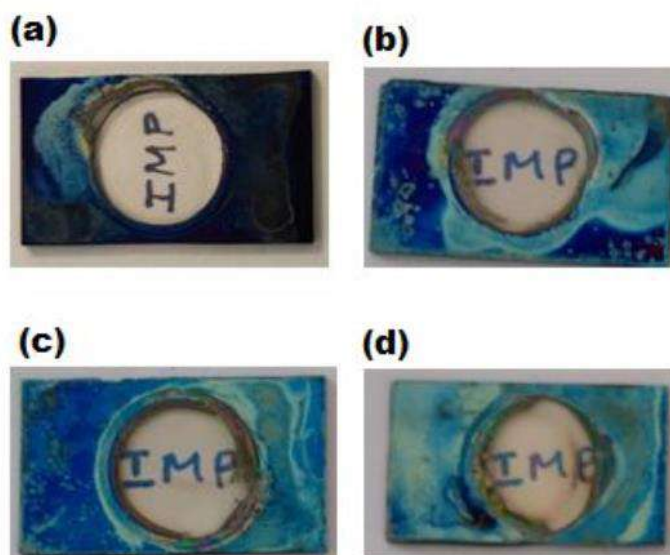


**Figure S1.** Photographs of the semitransparent ITO coated glass substrates overgrown with aligned TNT: (a) a-TNT, (b) a-1.7Ag-TNT, (c) a-3.5Ag-TNT, (d) a-5Ag-TNT annealed at 450 °C.

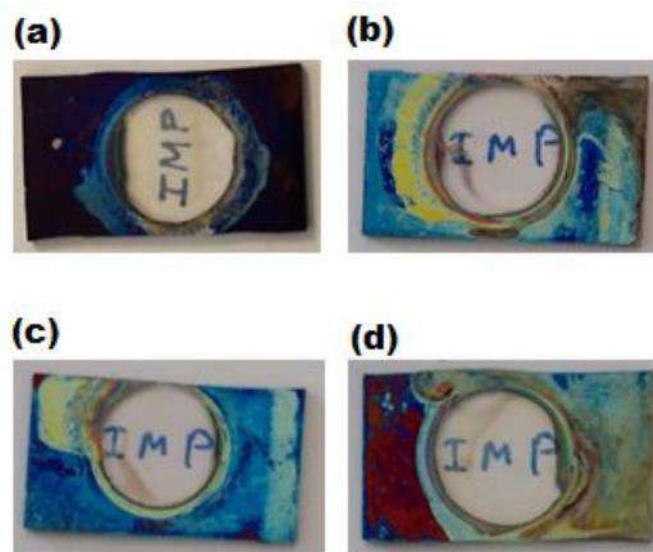


**Figure S2.** Photographs of the semitransparent ITO coated glass substrates overgrown with spaced TNT: (a) s-TNT, (b) s-1.7Ag-TNT, (c) s-3.5Ag-TNT, (d) s-5Ag-TNT annealed at 450 °C.

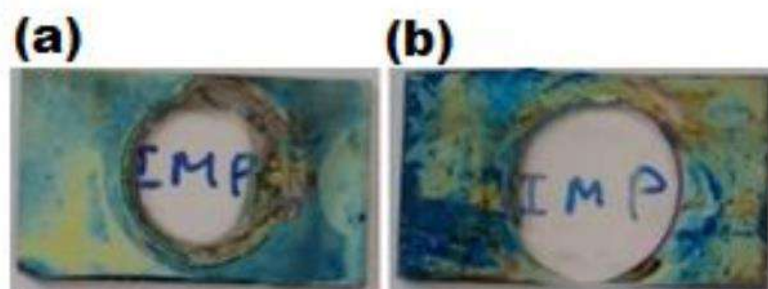


**Figure S3.** Photographs of the semitransparent substrates obtained by anodizing TiAg films containing 6.8 % of silver, using the anodization conditions to obtain (a) aligned TNT and (b) spaced TNT annealed at 450 °C.

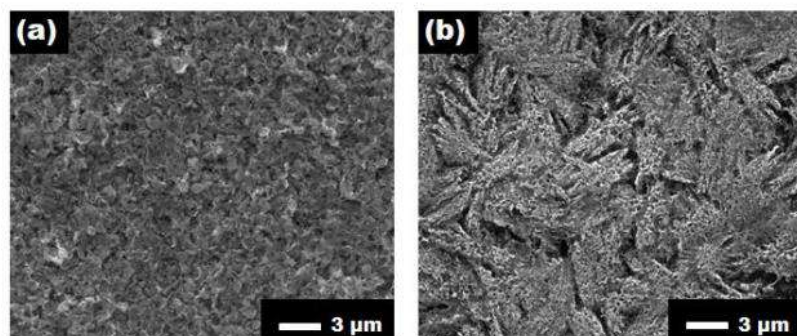


**Figure S4.** SEM top images of the anodized TiAg films containing 6.8 % of silver using the anodization conditions to obtain (a) aligned TNT and (b) spaced TNT annealed at 450 °C.

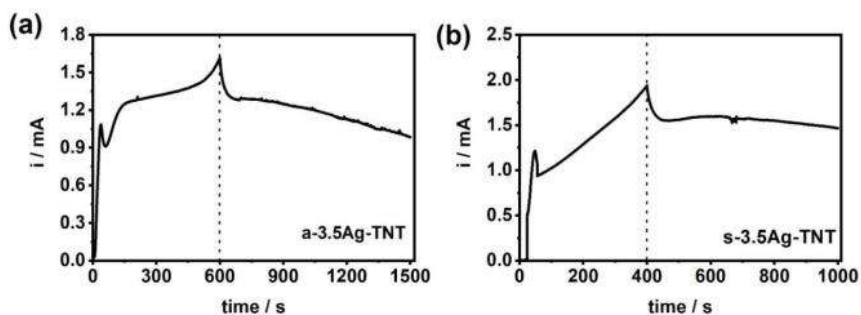


**Figure S5.** Anodization current as a function of time for (a) a-3.5Ag-TNT and (b) s-3.5Ag-TNT.

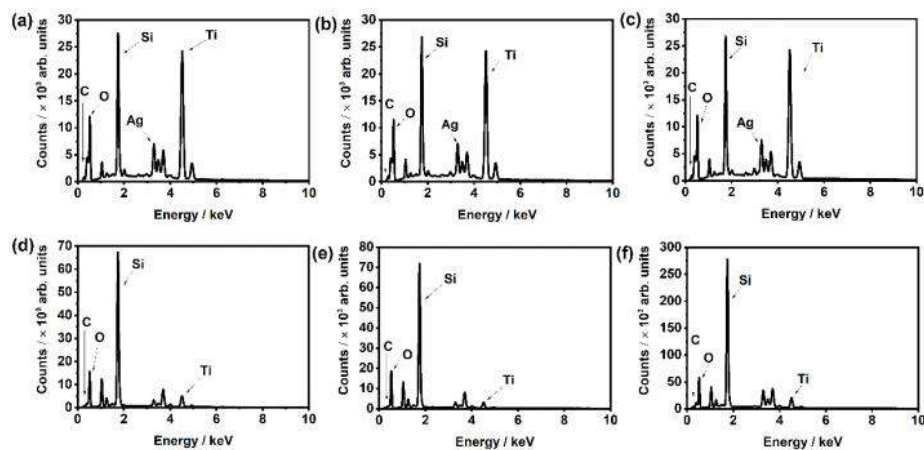


**Figure S6.** EDX spectra showing quantitative elemental distribution for (a) a-1.7Ag-TNT, (b) a-3.5Ag-TNT, (c) a-5Ag-TNT, (d) s-1.7Ag-TNT, (e) s-3.5Ag-TNT, (f) s-5Ag-TNT samples.

**Table S1.** Ag and Ti atomic concentration of the prepared TNT materials out of TiAg alloys measured by EDX.

aligned nanotubes			spaced nanotubes		
sample	Ag (at. %)	Ti (at. %)	sample	Ag (at. %)	Ti (at. %)
a-1.7Ag-TNT	1.09	98.91	s-1.7Ag-TNT	0	100
a-3.5Ag-TNT	2.03	97.97	s-3.5Ag-TNT	0	100
a-5Ag-TNT	3.13	96.87	s-5Ag-TNT	0	100

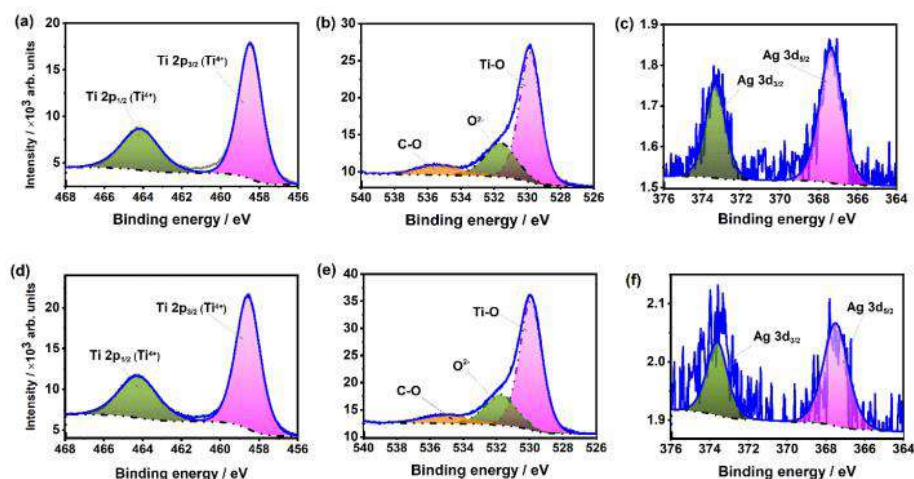


**Figure S7.** High-resolution XPS spectra of (a) Ti 2p, (b) O 1s, (c) Ag 3d for a-3.5Ag-TNT, and (e) Ti 2p, (f) O 1s, (g) Ag 3d for s-3.5Ag-TNT.

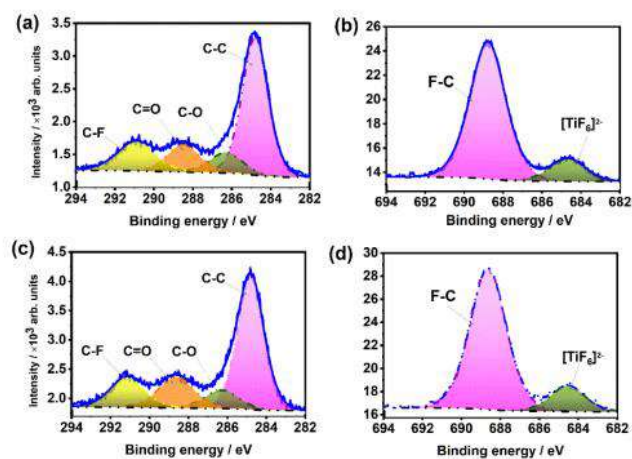


**Figure S8.** High-resolution XPS spectra of (a) C 1s, (b) F 1s for a-3.5Ag-TNT, and (c) C 1s, (d) F 1s for s-3.5Ag-TNT.

S4

**Table S2.** Binding energies and corresponding chemical bonds obtained from the high-resolution XPS spectra of Ti 2p, O 1s, C 1s, F 1s and Ag 3d for a-TNT, a-1.7Ag-TNT, a-5Ag-TNT, s-TNT, s-1.7Ag-TNT and s-5Ag-TNT samples.

Aligned nanotubes					Spaced nanotubes					
sample	spectra	binding energy (eV)	chemical bond / or state	reference	sample	spectra	binding energy (eV)	chemical bond / or state	reference	
a-TNT	Ti 2p	458.3	2p <sub>3/2</sub> (Ti <sup>4+</sup> )	[43]	s-TNT	Ti 2p	458.7	2p <sub>3/2</sub> (Ti <sup>4+</sup> )	[43]	
		464	2p <sub>1/2</sub> (Ti <sup>4+</sup> )	[43]			464.4	2p <sub>1/2</sub> (Ti <sup>4+</sup> )	[43]	
	O 1s	529.6	Ti-O	[44]		O 1s	530.1	Ti-O	[44]	
		532.1	O <sup>2-</sup>	[45]			531.9	C=O	[45]	
		535.3	C-O	[46]		C 1s	284.8	C-C	[47]	
	C 1s	284.8	C-C	[47]			286.4	C-O	[47]	
		286.4	C-O	[47]			288.8	C=O	[47]	
		288.6	C=O	[47]		F 1s	688.8	[TiF <sub>6</sub> ] <sup>2-</sup>	[48]	
	290.9	C-F	[47]	684.8			C-F	[48]		
	F 1s	688.5	[TiF <sub>6</sub> ] <sup>2-</sup>	[48]		s-1.7Ag-TNT	Ti 2p	458.4	2p <sub>3/2</sub> (Ti <sup>4+</sup> )	[43]
		684.3	C-F	[48]				464.2	2p <sub>1/2</sub> (Ti <sup>4+</sup> )	[43]
a-1.7Ag-TNT	Ti 2p	458.3	2p <sub>3/2</sub> (Ti <sup>4+</sup> )	[43]	O 1s		530.2	Ti-O	[44]	
		464	2p <sub>1/2</sub> (Ti <sup>4+</sup> )	[43]			532.1	O <sup>2-</sup>	[45]	
	O 1s	529.5	Ti-O	[44]			535.1	C-O	[46]	
		532.7	O <sup>2-</sup>	[45]			C 1s	284.8	C-C	[47]
		535.2	C-O	[46]				286.4	C-O	[47]
C 1s	284.8	C-C	[47]	288.7	C=O			[47]		
	286.4	C-O	[47]	F 1s	688.6		[TiF <sub>6</sub> ] <sup>2-</sup>			
	288.3	C=O	[47]		684.3		C-F			
F 1s	688.5	[TiF <sub>6</sub> ] <sup>2-</sup>	[48]	Ag 3d	367.1		3d <sub>5/2</sub> (Ag <sup>0</sup> )	[43]		
	684.1	C-F	[48]		373.1	3d <sub>1/2</sub> (Ag <sup>0</sup> )	[43]			
a-5Ag-TNT	Ti 2p	458.2	2p <sub>3/2</sub> (Ti <sup>4+</sup> )	[43]	s-5Ag-TNT	Ti 2p	458.1	2p <sub>3/2</sub> (Ti <sup>4+</sup> )	[43]	
		463.8	2p <sub>1/2</sub> (Ti <sup>4+</sup> )	[43]			463.7	2p <sub>1/2</sub> (Ti <sup>4+</sup> )	[43]	
	O 1s	529.4	Ti-O	[44]		O 1s	529.4	Ti-O	[44]	
		531.9	O <sup>2-</sup>	[45]			532.1	O <sup>2-</sup>	[45]	
		535.1	C-O	[46]			535.5	C-O	[46]	
	C 1s	284.8	C-C	[47]		C 1s	284.8	C-C	[47]	
		286.4	C-O	[47]			286.3	C-O	[47]	
		288.3	C=O	[47]			288.3	C=O	[47]	
	F 1s	688.4	[TiF <sub>6</sub> ] <sup>2-</sup>	[48]		F 1s	688.5	[TiF <sub>6</sub> ] <sup>2-</sup>	[48]	
		684.2	C-F	[48]			Ag 3d	684.4	C-F	[48]
	Ag 3d	366.9	3d <sub>5/2</sub> (Ag <sup>0</sup> )	[43]						
372.9		3d <sub>1/2</sub> (Ag <sup>0</sup> )	[43]							



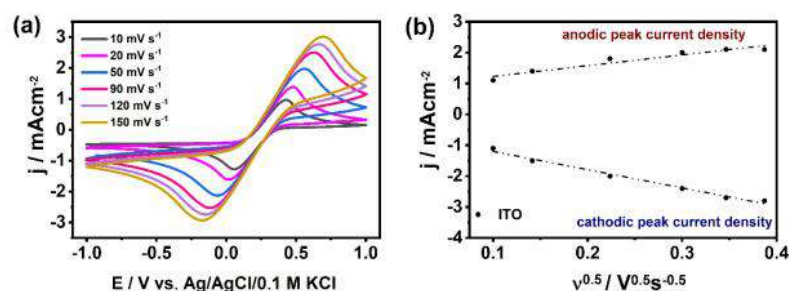


**Figure S9.** (a) Cyclic voltammograms of ITO recorded in 0.5 M Na<sub>2</sub>SO<sub>4</sub> + 10 mM K<sub>3</sub>Fe(CN)<sub>6</sub> at 10, 20, 50, 90, 120 and 150 mV s<sup>-1</sup>, and (b) plot of peak current density vs. scan rate of bare ITO.

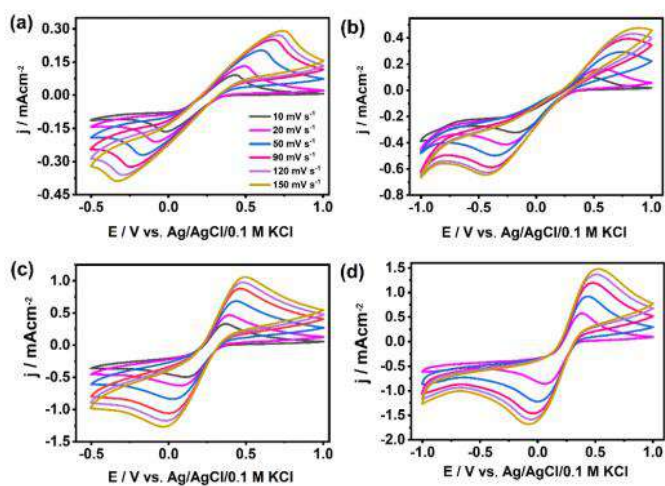


**Figure 10.** Cyclic voltammograms of (a) a-1.7Ag-TNT, (b) s-1.7Ag-TNT, (c) a-3.5Ag-TNT, (d) s-3.5Ag-TNT recorded in 0.5 M Na<sub>2</sub>SO<sub>4</sub> + 10 mM K<sub>3</sub>Fe(CN)<sub>6</sub> at 10, 20, 50, 90, 120 and 150 mV s<sup>-1</sup>.

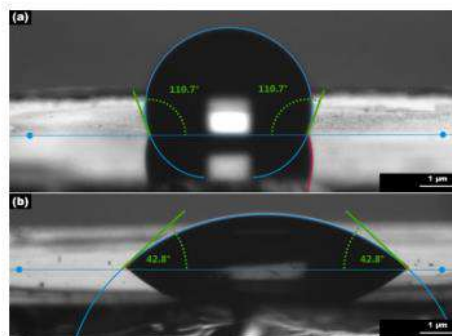


**Figure S11.** Cross-sectional images of water droplets on the grown TNT layers of (a) s-TNT and (b) s-5Ag-TNT.

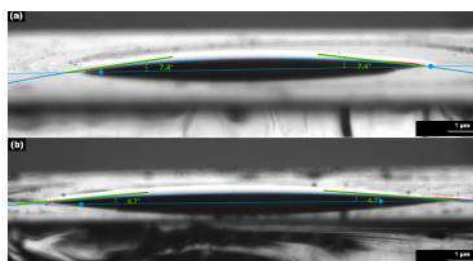


**Figure S12.** Cross-sectional images of water droplets on the grown TNT layers of (a) a-TNT and (b) a-5Ag-TNT.

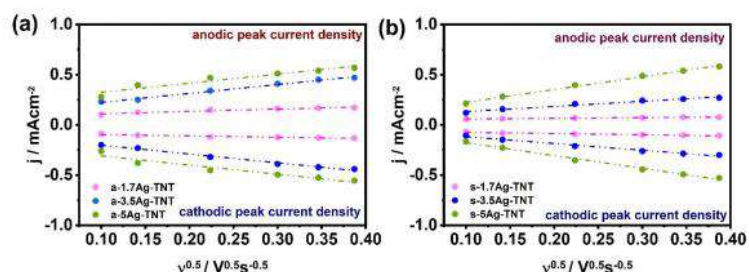


**Figure S13.** Plots of peak current density vs. scan rate of (a) a-TNT, a-1.7Ag-TNT, a-3.5Ag-TNT, a-5Ag-TNT, (b) s-TNT, s-1.7Ag-TNT, s-3.5Ag-TNT, s-5Ag-TNT in 0.5 M  $\text{Na}_2\text{SO}_4$  + 10 mM  $\text{K}_3\text{Fe}(\text{CN})_6$ .

The modified Powell algorithm was used for the analysis of the EIS data. The amplitude weighting  $r_a$  is given by the equation S1:

$$r_a(\omega, P_1 \dots P_M) = r_e^2 / (N - M) \quad (1)$$

where  $N$  is the number of points,  $M$  is the number of parameters,  $\omega$  is the angular frequency,  $P_1 \dots P_M$  are parameters. Parameter  $r_e$  is given by the equation S2:

$$r_e^2 = \sum_{i=1}^N \frac{(Z'_i - Z'_{i_{calc}})^2 + (Z''_i - Z''_{i_{calc}})^2}{Z'^2_i + Z'^2_{i_{calc}}} \quad (2)$$

where  $i$  corresponds to the measured values of impedance and  $i_{calc}$  is attributed to the calculated values;  $N$  is the number of points.

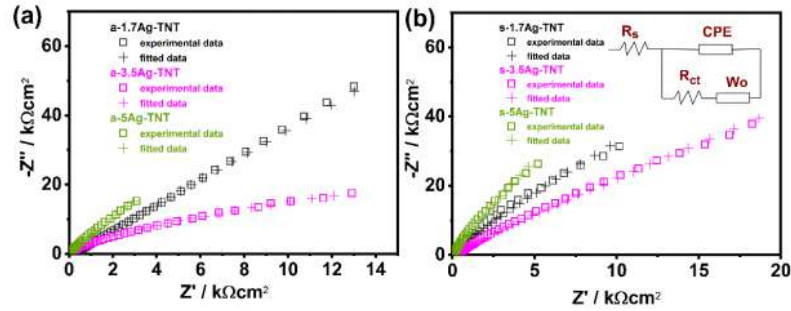


**Figure S14.** Nyquist plots of EIS measurements performed at the formal potential of redox reaction for (a) a-1.7Ag-TNT, a-3.5Ag-TNT, a-5Ag-TNT, (b) s-1.7Ag-TNT, s-3.5Ag-TNT, s-5Ag-TNT recorded in 0.5 M  $\text{Na}_2\text{SO}_4$  + 10 mM  $\text{K}_3\text{Fe}(\text{CN})_6$ .

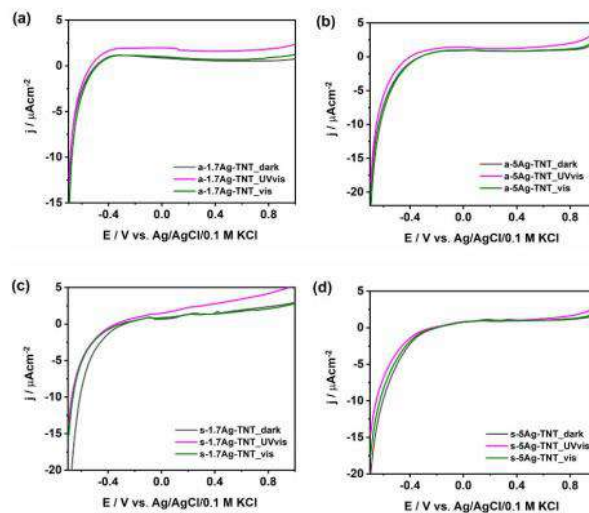


Figure S15. Linear sweep voltammograms in dark and under UV-vis and visible light illumination of (a) a-1.7Ag-TNT, (b) a-5Ag-TNT, (c) s-1.7Ag-TNT, (d) s-5Ag-TNT in 0.5 M Na<sub>2</sub>SO<sub>4</sub>.

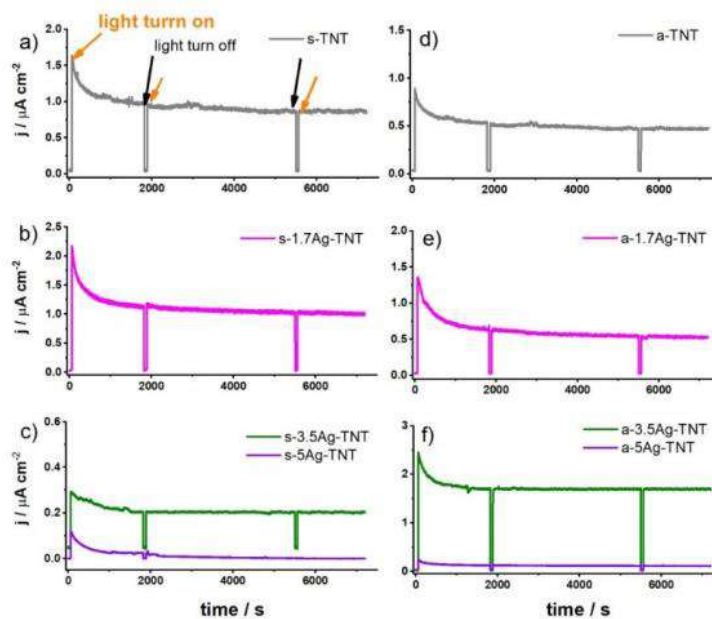
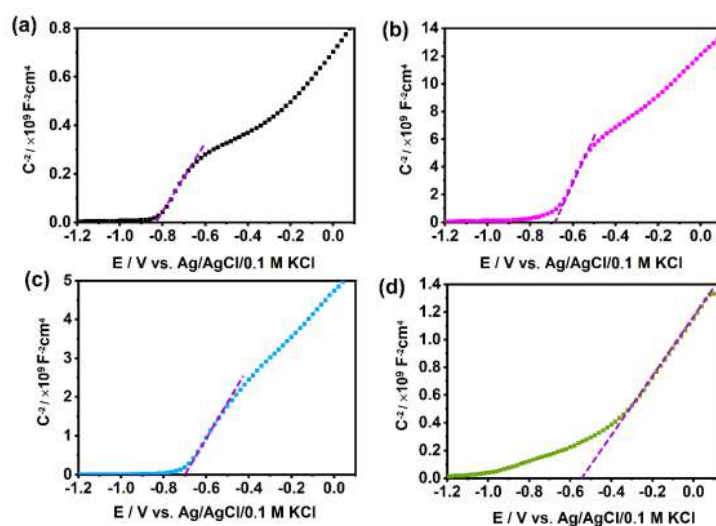


Figure S16. Transient photocurrent curves recorded under chopped UV-vis light illumination (information about the sequence of dark/light periods is provided in the experimental section) of (a) s-

TNT, (b) s-1.7Ag-TNT, (c) s-3.5Ag-TNT and s-5Ag-TNT, (d) a-TNT, (e) a-1.7Ag-TNT and (f) a-3.5Ag-TNT and a-5Ag-TNT in 0.5 M Na<sub>2</sub>SO<sub>4</sub> at the potential of +0.5 V vs. Ag/AgCl/0.1M KCl.

**Table S3.** Slope and correlation coefficient ( $r^2$ ) of the peak current density vs. scan rate curve and the diffusion coefficient of the prepared samples.

Sample	Anodic peaks			Cathodic peaks		
	Slope (mAcm <sup>2</sup> V <sup>-0.5</sup> s <sup>0.5</sup> )	$r^2$	Diffusion coefficient (cm <sup>2</sup> s <sup>-1</sup> )	Slope (mAcm <sup>2</sup> V <sup>-0.5</sup> s <sup>0.5</sup> )	$r^2$	Diffusion coefficient (cm <sup>2</sup> s <sup>-1</sup> )
ITO	3.48	0.93	$1.60 \times 10^{-6}$	-5.89	0.98	$4.80 \times 10^{-6}$
a-1.7Ag-TNT	0.23	0.91	$7.33 \times 10^{-9}$	-0.13	0.92	$2.34 \times 10^{-9}$
a-3.5Ag-TNT	0.88	0.99	$1.07 \times 10^{-7}$	-0.87	0.98	$1.05 \times 10^{-7}$
a-5Ag-TNT	0.89	0.92	$1.92 \times 10^{-7}$	-0.91	0.92	$1.44 \times 10^{-7}$
s-1.7Ag-TNT	0.24	0.91	$7.98 \times 10^{-9}$	-0.12	0.92	$1.99 \times 10^{-9}$
s-3.5Ag-TNT	0.51	0.97	$3.60 \times 10^{-8}$	-0.67	0.98	$6.22 \times 10^{-8}$
s-5Ag-TNT	1.27	0.99	$2.23 \times 10^{-7}$	-1.28	0.99	$2.27 \times 10^{-7}$



**Figure S17.** Mott-Schottky curves of (a) a-TNT, (b) a-1.7Ag-TNT, (c) a-3.5Ag-TNT, (d) a-5Ag-TNT in 0.5 M Na<sub>2</sub>SO<sub>4</sub>.



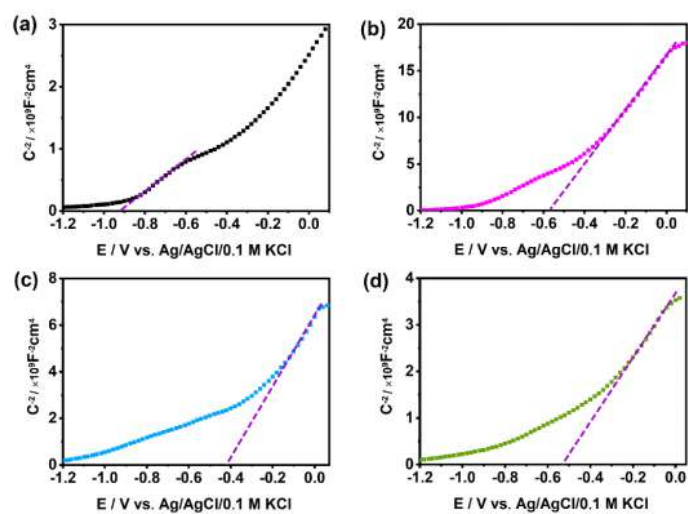


**Figure S18.** Mott-Schottky curves of (a) s-TNT, (b) s-1.7Ag-TNT, (c) s-3.5Ag-TNT, (d) s-5Ag-TNT in 0.5 M Na<sub>2</sub>SO<sub>4</sub>.

## 7.4 Semitransparent electrode based on aligned nanotubes for methylene blue sensing

### A brief overview of the article A4

#### *Introduction*

Surface-enhanced Raman scattering (SERS) is one of the widely used analytical spectroscopic techniques for organic chemicals, biomolecules and environmental pollutants sensing. The principle of this method is based on a huge enhancement of the Raman scattering of molecules situated in close proximity to a substrate. In this work the SERS activity of the anodic aligned tubular layer grown on ITO-glass towards methylene blue (MB) is investigated. A comparative study on the detection ability of ITO/TiO<sub>2</sub>/Ag coatings with three different TiO<sub>2</sub> morphologies i.e. planar, tubular and nanoparticle is carried out to understand the influence of TiO<sub>2</sub> morphology on its sensing performance.

#### *Fabrication of the sensors*

Three sensors were fabricated according to the procedure described in **Figure 78**.

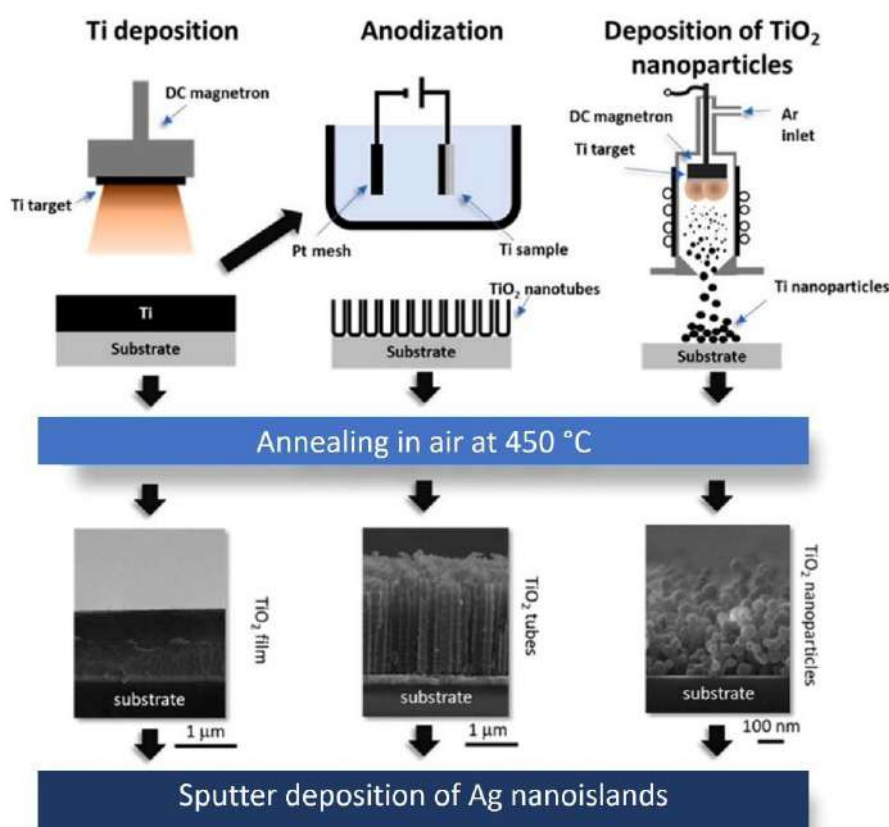


**Figure 78.** Schematic of the procedures for the fabrication of TiO<sub>2</sub> layer decorated by silver.

- (i) planar Ag/TiO<sub>2</sub> substrate (left), (ii) nanotubular Ag/TiO<sub>2</sub> substrate (middle) and (iii) nanoparticle-based Ag/TiO<sub>2</sub> substrate (right). (Reproduced from article A4).

There were prepared three different materials used later on in SERS measurements:

(i) The fabrication of the planar Ag/TiO<sub>2</sub> substrate was carried out first by depositing 1  $\mu\text{m}$  Ti film onto ITO-glass followed by the annealing of the deposited film at 450  $^{\circ}\text{C}$  for 1h. Then, the obtained layer was decorated with Ag nanoislands.

(ii) The fabrication of the nanotubular Ag/TiO<sub>2</sub> substrate was carried out first by depositing 1  $\mu\text{m}$  Ti film onto ITO-glass followed by anodizing of the Ti film using the anodization conditions optimized to obtain aligned nanotubes. Then, the obtained material was annealed at 450  $^{\circ}\text{C}$  for 1 h. In the last step, Ag was sputtered on top of the tubular layer forming silver nanoislands.

(iii) The fabrication of the nanoparticle Ag/TiO<sub>2</sub> substrate was carried out first by depositing 1  $\mu\text{m}$  layer of Ti nanoparticles onto ITO-glass followed by the annealing of the substrate at 450  $^{\circ}\text{C}$  for 1h. Then, the obtained layer was decorated with Ag nanoislands.

#### *Morphology of the prepared sensors*

The morphologies of the prepared materials are presented in **Figure 79**. **Figure 79 (a)**, shows the planar TiO<sub>2</sub> film decorated with Ag nanoparticles. The silver nanoislands deposited on top of the tubular layer (1.6  $\mu\text{m}$  long) are shown in **Figure 79 (b)**. This highly porous layer of spherical TiO<sub>2</sub> nanoparticles (with an average diameter of 50 nm) decorated with silver nanoislands is depicted in **Figure 79 (c)**.

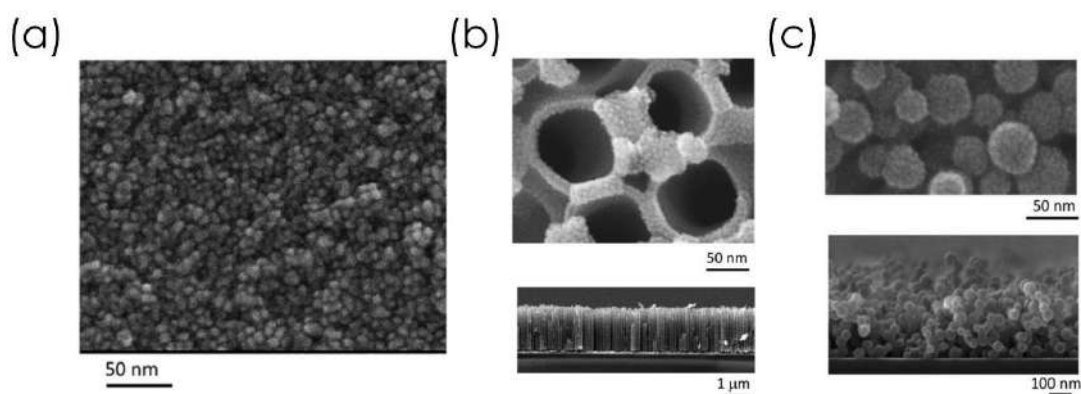


**Figure 79.** SEM images of the TiO<sub>2</sub> layer decorated by silver. (a) SEM top image of planar Ag/TiO<sub>2</sub> substrate. (b) SEM top and cross section images of nanotubular Ag/TiO<sub>2</sub> substrate. (c) SEM top images (low and high resolution images) of nanoparticle-based Ag/TiO<sub>2</sub> substrate. (Reproduced from article A4).

### *Sensing performance of the fabricated Ag/TiO<sub>2</sub> substrate*

During the test, methylene blue was used as the SERS probe. A given amount of MB aqueous solution was dropped on top of the Ag/TiO<sub>2</sub> substrates and dried at ambient temperature. Then, recording of Raman spectrum was carried out on the sample. In the article A4, it was shown that all three fabricated Ag/TiO<sub>2</sub> substrates are SERS active and can detect methylene blue molecules at the concentration of  $1 \times 10^{-6}$  M. It is well known that silver-free TiO<sub>2</sub> does not exhibit SERS activity towards MB sensing. Therefore, the enhancement of the SERS signal results from the localized plasmon resonance occurring due to the presence of silver nanoislands and the chemical enhancement mechanism is negligible. The different TiO<sub>2</sub> substrates only serve here as a nanostructured platform for the deposition of the Ag silver nanoislands. However, since all the fabricated titania substrates offer different surface area available for the Ag silver nanoislands deposition, the SERS signal intensities can be correlated with the TiO<sub>2</sub> morphology (as shown in **Figure 80**).

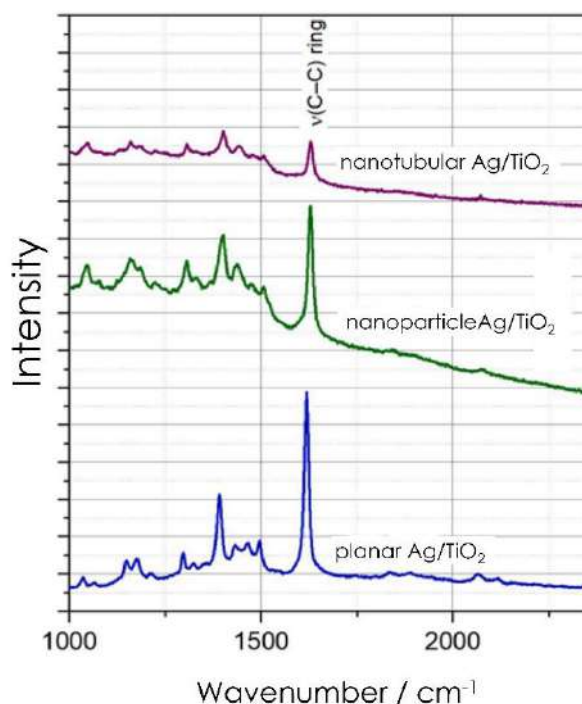


**Figure 80.** Dependence of SERS spectra on TiO<sub>2</sub> morphology ( $1 \times 10^{-6}$  M MB).

(Reproduced from article A4).

Among all prepared substrates, the nanotubular Ag/TiO<sub>2</sub> exhibits the lowest intensities of SERS signal. The main reason mentioned in article A4 is as follows: during the deposition of Ag nanoislands, the compact structure of the aligned TNT does not allow the deposition of Ag on

the outer surface of the nanotubes. In addition, the pore diameter is relatively small, around 100 nm. Those small pores do not allow efficient decoration of the interior of the nanotubes with Ag nanoislands. Thus, only the top surface of the tubular layer can be decorated effectively, as shown in the top SEM images.

After the SERS test, the possibility of recycling the SERS-active substrates was investigated. The recyclability test was performed by irradiating the substrates (i.e., nanotubular Ag/TiO<sub>2</sub>, planar Ag/TiO<sub>2</sub>, and nanoparticulate Ag/TiO<sub>2</sub>) in air by a UV lamp (SankyoDenki G15T8, Hg, 253.7 nm, 15 W, irradiation time up to 120 min) to clean them from the organic pollutant, i.e., MB. Subsequently, Raman spectra were recorded before and after adding new MB droplets onto the samples. The results indicate that despite the fact that the Ag/TiO<sub>2</sub> nanotubular substrate exhibits the lowest SERS signal intensities compared to the planar Ag/TiO<sub>2</sub> and nanoparticulate Ag/TiO<sub>2</sub> substrates, this tubular structure demonstrated superior recyclability by UV radiation.

### *Conclusion*

In the article A4, another method was employed for the modification of the semitransparent tubular layers and their further utilization. In this approach the silver nanoparticles were sputtered on top of the titania nanotubes. The resultant material was used for the surface-enhanced Raman scattering detection of methylene blue. The sample based on the tubular layer modified with Ag has a relatively lower SERS activity comparing to the nanoparticle one. However, this sample exhibited the superior recyclability by UV radiation over all prepared SERS active platforms.

It is worth mentioning that Ag is highly antibacterial therefore the nanotubular Ag/TiO<sub>2</sub> substrates can be also used as antibacterial surfaces for local therapy in biomedical implant. However this particular application is out of our research area.





## TiO<sub>2</sub>/Ag nanostructured coatings as recyclable platforms for surface-enhanced Raman scattering detection

Adéla Hanková<sup>a</sup>, Anna Kuzminova<sup>a</sup>, Jan Hanuš<sup>a</sup>, Petr Sezemský<sup>b</sup>, Radka Simerová<sup>b</sup>, Vítězslav Stranák<sup>b</sup>, Katarzyna Grochowska<sup>c</sup>, Dujearic-Stephane Kouao<sup>c</sup>, Katarzyna Siuzdak<sup>c</sup>, Marek Procházka<sup>d</sup>, Tereza Košutová<sup>a</sup>, Ondřej Kylián<sup>a,\*</sup>

<sup>a</sup> Charles University, Faculty of Mathematics and Physics, Department of Macromolecular Physics, V Holešovičkách 2, Prague 8, 18000, Czech Republic

<sup>b</sup> University of South Bohemia, Faculty of Science, Institute of Physics and Biophysics, Branislavská 1760, České Budějovice 37005, Czech Republic

<sup>c</sup> Centre for Plasma and Laser Engineering, The Szwedalski Institute of Fluid-Flow Machinery PASi, Fiszera 14, Gdańsk 80-231, Poland

<sup>d</sup> Charles University, Faculty of Mathematics and Physics, Institute of Physics, Ke Karlovu 5, Prague 121 16, Czech Republic

### ARTICLE INFO

#### Keywords:

Surface-enhanced Raman spectroscopy  
Nanostructured Ag/TiO<sub>2</sub> coatings  
Re-cyclability

### ABSTRACT

The surface-enhanced Raman scattering (SERS) has become irreplaceable for the direct detection of organic chemicals and biomolecules. However, the SERS-active platforms need to meet certain requirements for routine use. Among them, the most important are low detection limit, spectra reproducibility, and the possibility of being re-used. In this study, we investigate and compare the SERS performance of Ag/TiO<sub>2</sub> coatings with three different architectures - planar, tubular and nanoparticle-based - prepared by means of plasma-assisted techniques. In all three cases, the nanoislands, made of plasmonic Ag, enhance the SERS signal, while the TiO<sub>2</sub> provides degradation of surface contaminants after UV irradiation. The latter relates to the natural photoactivity of titania, which enables the recycling of the substrates. As shown, nanopatterning of surfaces offers a good compromise between the high detection limit and re-cyclability of those nanostructured Ag/TiO<sub>2</sub> coatings with larger active surface area; here, namely TiO<sub>2</sub> nanoparticle films decorated with silver nanoislands behave promisingly. Such nanostructured Ag/TiO<sub>2</sub> films allow not only the detection of methylene blue (MB) at concentrations down to  $5 \times 10^{-9}$  M, but also may be easily cleaned by UV radiation in a reasonable time scale.

### 1. Introduction

Since its discovery in the '70s of the last century [1], surface-enhanced Raman scattering (SERS) established itself as one of the most powerful analytical spectroscopic techniques for ultrasensitive direct detection of organic chemicals and biomolecules, food chemicals, environmental pollutants, etc. [2–7]. This detection method is based on a tremendous enhancement of Raman scattering of molecules situated in close proximity to an appropriate substrate [8]. Although different phenomena may cause the SERS activity of materials, it is generally recognized that the dominant one is an electromagnetic enhancement, which is connected with the resonance excitation of surface plasmons localized in the metallic nanostructures [8]. Because of this, the preparation of metallic nanostructured platforms, mainly based on noble metals that exhibit localized plasmon resonance in the visible spectral region (Ag, Au, Cu), with tailor-made properties (e.g., size and shape of

metallic nanostructures and their mutual distance) is an essential task for reliable SERS detection and corresponding applications.

The SERS-activity of metal-based platforms is, however, not the only parameter that has to be considered for possible applications; equally, and in some cases, even more critical for routine measurements is the assurance of good signal reproducibility, uniformity over macroscopic areas, spectral stability [9], as well as the simplicity of the fabrication process and the possibility to recycle the SERS substrates for their multiple usages.

Concerning the simplicity of the deposition procedure, spectral reproducibility and uniformity, low-pressure physical vapor deposition (PVD) techniques (e.g., vacuum evaporation, sputtering) have been recognized as an interesting and fully solvent-free alternative to other methods based on chemical synthesis. For instance, optimized sputtered arrays of silver nanoislands were recently reported to provide enhancement factor (EF) up to  $1 \times 10^7$  [10,11].

\* Corresponding author.

E-mail address: [ondrej.kylian@gmail.com](mailto:ondrej.kylian@gmail.com) (O. Kylián).

<https://doi.org/10.1016/j.surfin.2022.102441>

Received 3 August 2022; Received in revised form 15 October 2022; Accepted 22 October 2022

Available online 30 October 2022

2468-0230/© 2022 Elsevier B.V. All rights reserved.

The PVD low-pressure deposition techniques are furthermore suitable for coating various substrate materials, including photocatalytic semiconductors, such as  $\text{TiO}_2$ . This paves the way to combine the high SERS activity of sputtered metallic nanostructures and UV-induced photo-catalysis decomposition of organic molecules adsorbed on the  $\text{TiO}_2$  surface, enabling the SERS substrates' re-cyclability [12]. This approach represents an interesting alternative to other suggested strategies that are based, for instance, on the use of detergents [13] or on the application of oxygen plasma for cleaning of SERS-active platforms [14], as UV cleaning does not produce any waste or does not require costly vacuum equipment. The first attempts in this direction were made in 2016 by Kumar et al. [15] and Ling et al. [16]. Although the architecture of the supporting  $\text{TiO}_2$  substrates, decorated by sputtered or evaporated Ag, differed in these two studies (while the  $\text{TiO}_2$  nanorod arrays fabricated by glancing angle deposition were used in [15],  $\text{TiO}_2$  anodized nanotube arrays were employed in [16]), both groups proved that high SERS activity and re-cyclability of produced Ag/ $\text{TiO}_2$  surfaces under UV irradiation might be achieved. This is in agreement with other studies dealing with Ag/ $\text{TiO}_2$  heterogeneous nanostructured surfaces prepared by "wet" chemistry techniques for the decoration of  $\text{TiO}_2$  nanostructures with silver (e.g. [17–21]). However, the SERS enhancement and possibility to re-use UV cleaned substrates might be influenced by the architecture of Ag/ $\text{TiO}_2$  platforms which has not been studied so far. Hence, the main aim of this study is to fill the gap by investigating the performance of three Ag/ $\text{TiO}_2$  platforms with planar, nanotubular and nanoparticle-based architectures (Fig. 1) that were fabricated using plasma-assisted methods.

## 2. Experimental

### 2.1. Samples preparation

We study the effect of surface nanoarchitecture, of the films prepared in a similar way, on the SERS detection and UV decomposition. The fabrication procedures employed in this study for producing Ag/ $\text{TiO}_2$  substrates with three different morphologies are schematically depicted in Fig. 2. The studied architectures were based on (i) planar  $\text{TiO}_2$  film, (ii)  $\text{TiO}_2$  nanotubes, and (iii)  $\text{TiO}_2$  nanoparticle film that were all subsequently decorated by Ag nanoparticles.

The planar and nanotubular (NT)  $\text{TiO}_2$  films were initially prepared by deposition of homogeneous Ti films by direct current (DC) magnetron sputtering. The titanium deposition was performed in a high vacuum chamber using a planar magnetron with a 76 mm Ti target (Kurt J. Lesker, declared purity 99.5%). The magnetron was operated in pure Ar at the magnetron current of 600 mA and pressure of 0.1 Pa. The thickness of Ti films was 1  $\mu\text{m}$ .

To obtain highly ordered and vertically aligned  $\text{TiO}_2$  nanotube arrays, one set of Ti-coated samples was subjected to electrochemical anodization carried out in the two-electrode arrangement. A platinum mesh was used as a cathode and Ti sputtered film as an anode. The

electrodes were placed at a distance of 2 cm between them. The anodization process was carried out in ethylene glycol-based electrolyte (p.a. Chempur) containing 0.27 M  $\text{NH}_4\text{F}$  (p.a. Chempur), 1 M  $\text{H}_3\text{PO}_4$  (p.a. Chempur) and deionized water (5 vol %  $\text{H}_2\text{O}$ ) at 60 V. The temperature was kept at 23°C through a thermostat (Julabo F-12). After the anodization, the samples were rinsed with deionized water and left in the ambient atmosphere until dry. The final height of the formed nanotubes was 1.6  $\mu\text{m}$ .

Ti nanoparticles (NPs) were produced by a gas aggregation source of homemade construction that was described in detail in our previous study [22]. It consisted of a planar magnetron equipped with a 3-inch Ti target (Kurt J. Lesker, declared purity 99.995%) placed into stainless steel, water-cooled aggregation chamber (100 mm in diameter). A conical lid ended the aggregation chamber with a tubular exit orifice (diameter 3.5 mm, length 20 mm) that separated the aggregation chamber from the main deposition chamber. Ti NPs were produced using Ar, DC magnetron current of 400 mA, and pressures in the aggregation and main deposition chambers of 40 Pa and 0.1 Pa, respectively. The NPs were subsequently collected on a substrate located at a distance of 150 mm from the exit orifice of the aggregation chamber. The thickness of films of Ti NPs was approximately 350 nm in this study.

All three types of as-prepared materials, i.e., Ti films, the arrays of anodized nanotubes, and gas-phase synthesized Ti nanoparticles, were subsequently annealed in a laboratory furnace in the air to obtain crystalline  $\text{TiO}_2$  substrates. The temperature was increased from room temperature up to 450°C and then held at this temperature for 1 h. After the annealing period, the furnace cooled down freely to room temperature. Thermal annealing encourages crystallization and oxidation, which turns metallic Ti or amorphous  $\text{TiO}_2$  into the crystalline phases of  $\text{TiO}_2$  [23]. The XRD diffraction patterns of all three types of fabricated coatings, which were measured by Rigaku SmartLab diffractometer equipped with a 9 kW Cu rotating anode X-ray source and analysed using MStruct software [24], are presented in the Supplementary material (Fig. S1).

Finally, all three types of  $\text{TiO}_2$  coatings were decorated with Ag nanoislands. These were deposited using a 2-inch DC magnetron with a silver target (Kurt J. Lesker, declared purity 99.99%). The silver sputtering was performed in Ar atmosphere at the pressure of 3 Pa and the magnetron current of 300 mA. Under these conditions, the deposition rate of silver was 10 nm/min. Due to the low surface free energy of  $\text{TiO}_2$  surface, the Volmer-Weber growth [25] was dominant and 3D Ag nanoislands were formed. The deposition time in this study was kept constant and equal to 1 min. This deposition time was selected based on preliminary experiments as it assures the formation of a dense array of individual Ag nanoislands on a  $\text{TiO}_2$  planar surface (see later in the text).

### 2.2. Samples characterization

After each deposition step, the morphology of the samples was evaluated using Scanning Electron Microscope (SEM) using a field-

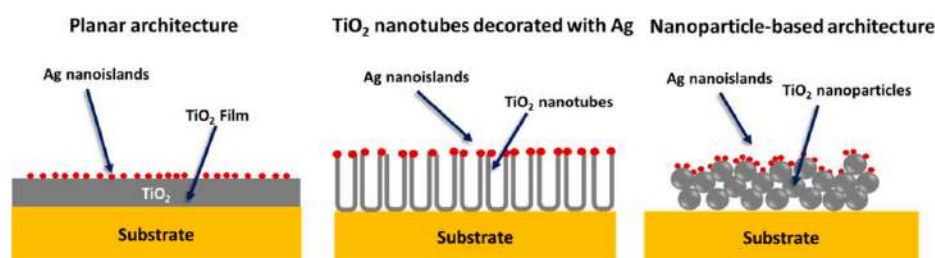


Fig. 1. Schematic representation of tested architectures: (i) planar  $\text{TiO}_2$ , (ii)  $\text{TiO}_2$  nanotubular, and (iii)  $\text{TiO}_2$  nanoparticle array, in all cases decorated by Ag nanoislands.



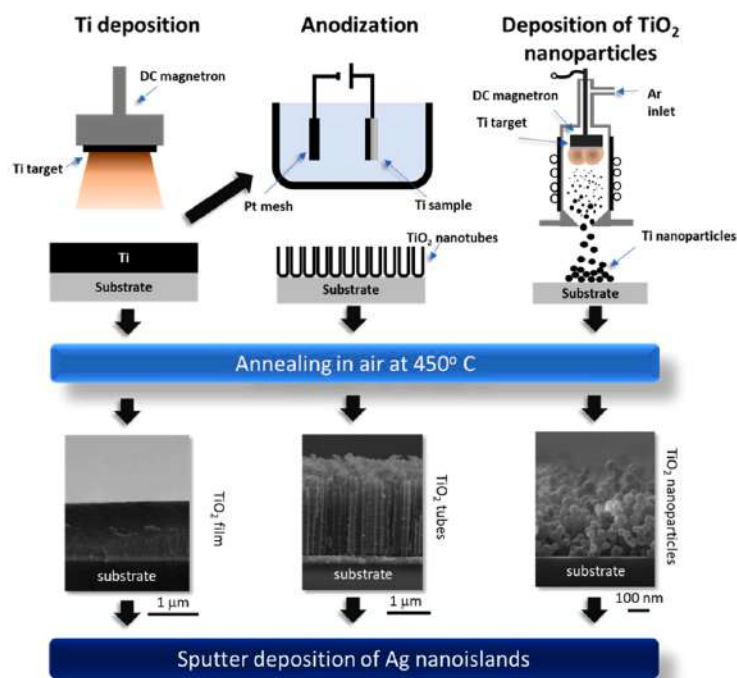


Fig. 2. Schematic procedures for the fabrication of (i) planar Ag/TiO<sub>2</sub> substrates (left), (ii) nanotubular Ag/TiO<sub>2</sub> substrates (middle) and (iii) nanoparticle-based Ag/TiO<sub>2</sub> substrates (right).

emission microscope JSM-7200F (JEOL). SEM was operated in secondary electron mode at an acceleration voltage of 15 kV and a working distance of 10 mm.

The SERS performance of produced materials was tested using methylene blue (MB, Sigma), as a SERS probe. The droplets of MB aqueous solution were spotted on the Ag/TiO<sub>2</sub> substrates and allowed to dry at ambient temperature. Raman spectra were subsequently collected by an integrated confocal Raman microscopic system (LabRam HR800, Horiba Jobin-Yvon) using as an excitation source of He-Ne laser (632.8 nm wavelength, power at the sample 0.02mW). This system was equipped with a diffraction grating (300 grooves/mm) and a CCD detector cooled with liquid nitrogen. The laser beam was focused onto the sample to a spot of approximately 1  $\mu\text{m}$  in diameter during the measurements.

To test the possibility of recycling the SERS-active Ag/TiO<sub>2</sub> substrates, additional tests were performed, in which the substrates with spotted MB were exposed to UV radiation in the air (SankyoDenki G15T8, Hg, 253.7nm, 15W, irradiation time up to 120 min). Subsequently, the Raman spectra were remeasured on such cleaned substrates before and after spotting fresh droplets of MB.

### 3. Results

In this section, the results reached on all three types of Ag/TiO<sub>2</sub> substrates will be one by one discussed, emphasizing their SERS activity and re-cyclability. However, before doing so, it is essential mentioning that none of the TiO<sub>2</sub> substrates without silver nanoislands used in this study exhibited measurable SERS signal, at least at a concentration  $1 \times 10^{-6}$  M of MB solution. Because of this, the appearance of the Raman

peaks that correspond to MB is supposed to be connected solely to the presence of plasmonic Ag nanostructures. In other words, the electromagnetic SERS enhancing mechanism dominates for all fabricated samples and the chemical enhancement mechanism is, in our case, negligible and does not contribute to the SERS signal.

#### 3.1. Planar TiO<sub>2</sub>/Ag substrates

The first type of studied Ag/TiO<sub>2</sub> SERS-active platforms, and also the simplest one, is planar TiO<sub>2</sub> film decorated with silver nanoislands. As shown in Fig. 3a, where an example of an SEM image of this kind of surface is presented, the size of individual Ag nanoislands for the selected Ag deposition time is less than 10 nm, and the formed nanoislands remain to be separated and without the direct mutual contact. The formation of such silver nanoisland arrays on TiO<sub>2</sub> substrate, i.e., a structure similar to the ones reported for Ag sputtered on different substrates at a low fluence of Ag [26], is consistent with the Volmer-Weber growth [25], i.e., a surface diffusion-mediated growth mode.

The analysis of the SERS spectra recorded immediately after the complete drying of the droplet of  $1 \times 10^{-6}$  M MB water solution revealed the presence of Raman peaks that are characteristic of MB [27,28]. Two intense peaks dominate the spectra at around  $1399\text{ cm}^{-1}$  and  $1624\text{ cm}^{-1}$ , which correspond to C-N symmetrical stretching and C-C ring stretching, respectively (Fig. 3b, top). Besides these intense peaks, it is possible to also detect the peaks at  $1154\text{ cm}^{-1}$  and  $1303\text{ cm}^{-1}$ , which are connected with the in-plane bending and ring deformation mode of C-H, and other relatively weak MB Raman peaks.

The planar Ag/TiO<sub>2</sub> substrate with dried MB spot was subsequently

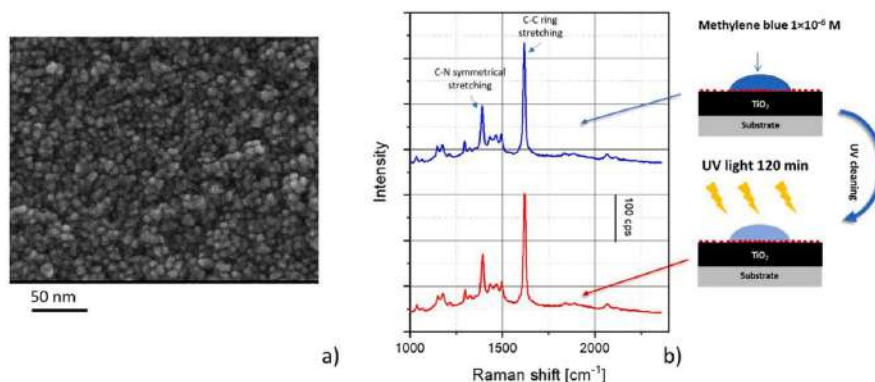


Fig. 3. (a) SEM image of planar Ag/TiO<sub>2</sub> substrates and (b) SERS spectra of freshly deposited and dried  $1 \times 10^{-6}$  M MB containing droplet (top) and SERS spectra recorded after 2 h of irradiation by UV light.

exposed to UV radiation for 2 h to test its re-cyclability. However, no change in the intensity of detected Raman peaks of MB and structure of recorded Raman spectra was observed, as depicted in Fig. 3b, bottom. This clearly shows that 2 h of UV radiation is not, in this case, sufficient to clean the substrate.

### 3.2. Nanotubular TiO<sub>2</sub>/Ag substrates

The second tested structure of Ag/TiO<sub>2</sub> surfaces, similar to the ones investigated in previous studies (e.g. [16,21,29–31]), is based on approximately 1.6  $\mu\text{m}$  long, closely packed TiO<sub>2</sub> nanotube array with small Ag nanoislands on the top. Based on the SEM analysis of produced NT samples (see Fig. 4a), it can be concluded that the Ag nanoislands have nanometric sizes and stay separated from each other also in this case. The SEM image shows that the silver nanoislands stay on the nanotube arrays' top rim. Concerning the SERS results, the spectral

peaks characteristic of MB molecule are again clearly visible in the recorded Raman spectra (Fig. 4b, top), with the most intense peak at  $1624\text{ cm}^{-1}$ . However, in contrast to planar Ag/TiO<sub>2</sub> surfaces, exposure of the dried MB spot for 2 h to UV radiation led to a complete disappearance of Raman peaks of MB (Fig. 4b, middle), indicating the self-cleaning effect of the TiO<sub>2</sub>. This effect may be attributed to the fact that the hydrophilic and photocatalytic anatase surface (see Fig. S1b) generates the electron-positive hole pairs in the presence of light with energy higher than the material band gap. The charge carriers then migrate towards the surface, where electrons can generate superoxide or hydroperoxyl radicals. These radical species can decompose the pollutants and clean the surface [32,33].

To further confirm the re-usability of such cleaned surfaces for SERS measurements, a new MB droplet was spotted on UV cleaned NT Ag/TiO<sub>2</sub> array, allowed to dry and remeasured. As seen in Fig. 4b, bottom, obtained SERS spectra are practically identical to the ones recorded on

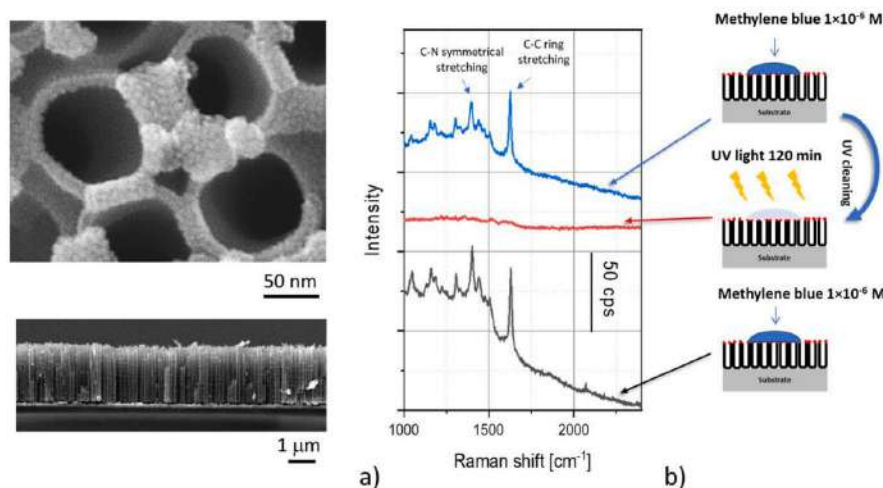


Fig. 4. (a) SEM images of top-view and cross-section of tubular Ag/TiO<sub>2</sub> substrates and (b) SERS spectra of  $1 \times 10^{-6}$  M MB on the as-deposited substrate (top), SERS spectra recorded after 2 h irradiation by UV light (middle), and SERS spectra acquired after spotting and drying fresh MB containing droplet on UV-cleaned substrate, i.e., re-cycling of the substrate (bottom).



as-prepared substrates, and no significant differences in the structure of the Raman spectra and intensities of individual peaks of MB molecule were observed.

### 3.3. Nanoparticle-based $\text{TiO}_2/\text{Ag}$ substrates

Finally,  $\text{Ag}/\text{TiO}_2$  surfaces based on  $\text{TiO}_2$  nanoparticles were studied, too. This highly porous  $\text{Ag}/\text{TiO}_2$  coatings are composed of  $\text{TiO}_2$  spherical nanoparticles (diameter  $\sim 50$  nm) homogeneously seeded from the top by the nanometer-sized and well-separated individual Ag nanoislands (for SEM image, see Fig. 5a). According to XRD (Fig. S1c), the  $\text{TiO}_2$  nanoparticles are characterized by the presence of mixed phases - rutile, brookite and anatase. The SERS spectra of dried  $1 \times 10^{-6}$  M MB on such substrate were found to be similar to the previous two cases, as it is evident from the comparison of Fig. 3b, top (planar  $\text{Ag}/\text{TiO}_2$ ), Fig. 4b, top (NT  $\text{Ag}/\text{TiO}_2$ ) and Fig. 5b, top, where Raman spectra measured on nanoparticle-based  $\text{Ag}/\text{TiO}_2$  surface are presented. Concerning the possibility of re-cycling NP  $\text{Ag}/\text{TiO}_2$  coatings by UV radiation, the same effect was observed as in the case of NT  $\text{Ag}/\text{TiO}_2$ : the Raman peaks of MB disappeared after UV irradiation (Fig. 5b, middle), and such cleaned surface may be re-used for new measurement providing again the SERS spectra comparable to the spectra acquired using as-deposited NP  $\text{Ag}/\text{TiO}_2$  surfaces (Fig. 5b, bottom). The 2D maps ( $40 \mu\text{m} \times 30 \mu\text{m}$ , step  $2 \mu\text{m}$ ) of the intensity of MB peak at  $1624 \text{ cm}^{-1}$  that show good reproducibility of the measurements performed both on the freshly deposited MB droplet and measurements on the UV-cleaned surfaces are presented in Supplementary material (Fig. S2).

## 4. Discussion

As shown in the previous section, all three types of  $\text{Ag}/\text{TiO}_2$  substrates are SERS active and allow for the detection of MB molecules at the concentration of  $1 \times 10^{-6}$  M. This result is in-line with previous studies performed on planar Ag nanoisland arrays [34]. Since no Raman signal originating from MB molecule was observed for silver-free  $\text{TiO}_2$  samples, the surface enhancement is connected with the localized plasmon resonance of Ag nanoislands. Despite the possibility of detecting MB, a direct comparison of the SERS spectra revealed that the intensities of MB peaks differ significantly depending on the architecture of produced SERS-active substrates. As can be seen in Fig. 6a, where

examples of MB SERS spectra recorded on different  $\text{Ag}/\text{TiO}_2$  surfaces are compared, the highest intensities of peaks belonging to MB were achieved on planar  $\text{Ag}/\text{TiO}_2$  surfaces, followed by NP  $\text{Ag}/\text{TiO}_2$  and, finally, by NT  $\text{Ag}/\text{TiO}_2$ . This ordering of SERS signal intensities may be explained by the different actual surface areas of the base titania layer. If one compares planar  $\text{TiO}_2$  substrates and  $\text{TiO}_2$  surfaces built from approximately 50 nm-sized NPs, the latter ones have, due to the spherical shape of NPs, considerably higher surface area that can accommodate incoming Ag atoms during the silver deposition. This means that for the fixed amount of deposited Ag (i.e., for the fixed deposition time used in this study), the number of Ag atoms per unit surface area accessible by silver is lower in the case of nanoparticle-based surface as compared to planar one. Because of this, it might be expected that effectively less material is available for the growth of Ag nanoislands per unit surface, which influences both their size and mutual distances between individual nanoislands. This may shift the position of localized plasmon resonance of Ag nanostructures slightly away from its optima concerning the used wavelength of the excitation laser and might cause the decrease of the detected Raman signal.

The role of surface architecture for SERS performance is even more crucial in the case of nanotubular  $\text{Ag}/\text{TiO}_2$ . As shown in Fig. 4a, the openings of vertically aligned  $\text{TiO}_2$  nanotubes have approximately 100 nm in diameter. The “holes” represent a significant fraction of the surface and Ag nanoparticles are solely deposited at the top and close to the top surface of the tubes. In other words, the actual  $\text{TiO}_2$  surface area that may be decorated with silver, i.e., the SERS-active area, is dramatically reduced (approximately 1/4 of the surface in our case). As a result, the smaller surface area where silver nanostructures come into direct contact with MB molecules during the SERS measurements naturally results in the lowering of the SERS signal, i.e., an effect experimentally observed in this study.

Despite the worse SERS activity of NT and NP  $\text{Ag}/\text{TiO}_2$  substrates compared to the coatings' planar architecture, both structured types of  $\text{Ag}/\text{TiO}_2$  surfaces exhibited superior re-cyclability by UV radiation. This fact is highlighted in Fig. 6b, where intensities of C-C ring stretching band of MB at  $1624 \text{ cm}^{-1}$  measured before and after the UV irradiation are presented. The reason for this is twofold. First, although the annealing step during  $\text{TiO}_2$  preparation was the same for all three substrates, the resulting  $\text{TiO}_2$  structure is different (Fig. S1). The cleaning

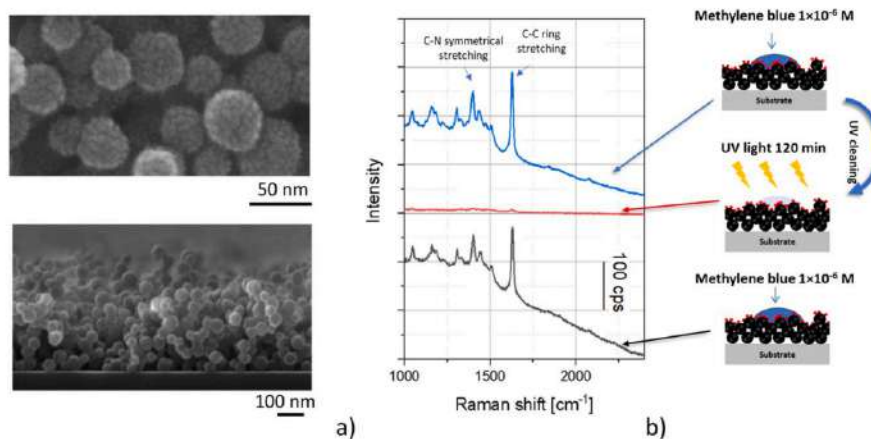


Fig. 5. (a) SEM images of top-view and cross-section of  $\text{Ag}/\text{TiO}_2$  substrates based on  $\text{TiO}_2$  nanoparticles decorated with Ag nanoislands and (b) SERS spectra of  $1 \times 10^{-6}$  M MB on the as-deposited substrate (top), SERS spectra recorded after 2 h irradiation by UV light (middle) and SERS spectra acquired after spotting and drying fresh MB containing droplet on UV-cleaned substrate (bottom).



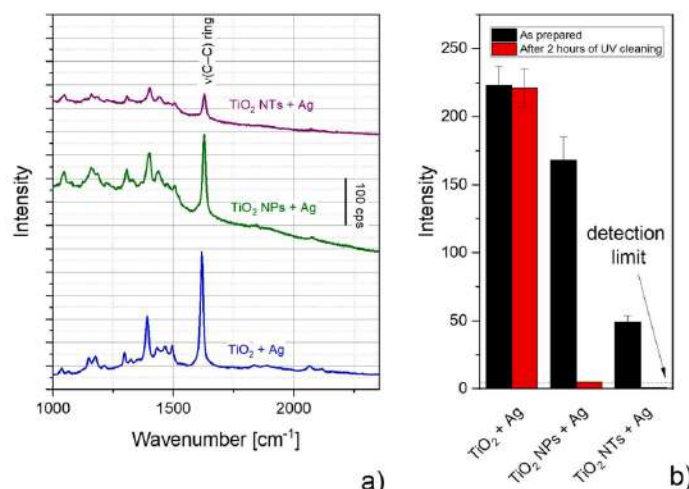


Fig. 6. (a) Comparison of SERS spectra of  $1 \times 10^{-6}$  M MB on the as-deposited substrates. (b) Intensities of C-C ring stretching band of MB at  $1624 \text{ cm}^{-1}$  measured before and after UV-cleaning step on different substrates.

activity and decomposition of the organic molecules can be achieved by photocatalytic properties of  $\text{TiO}_2$  after UV irradiation due to the bandgap that is larger than 3 eV depending on the crystallographic phase; the anatase is typically reported as the most photoactive structure because of the higher bandgap ( $\sim 3.2$  eV). The higher band gap reduces the light portion that can be absorbed, but it raises the valence band maximum to higher energy levels relative to the redox potential of adsorbed molecules [35]. Because of the relatively high thickness of planar Ti films, their phase transformation induced by the annealing in air might be limited only to their top-most layer. However, it was shown in [36] that catalytic properties are not determined only by the uppermost surface properties but also the bulk transport of charged carriers, which differs for different  $\text{TiO}_2$  phases, plays an important role. The vertical profile in the structure of annealed Ti films thus can cause a lowering of their photoactivity. One can expect that the  $\text{TiO}_2$  phases will crystalline on the surface top, being in close contact with oxygen-rich atmosphere (open air) during the annealing, while the bulk of the film is not fully transformed to crystalline  $\text{TiO}_2$ . The XRD indeed indicated a significant contribution of  $\text{Ti}_2\text{O}$  phase in the films as it is evident from Fig. S1a. In addition, the dominant phase in the planar  $\text{TiO}_2$  films was rutile, i.e., the less photoactive phase of titania (e.g. [37,38]). These two effects may explain the low and practically negligible photocatalytic effect measured on the planar Ag/ $\text{TiO}_2$  surface. As indicated by the preliminary tests, the improvements could be most probably achieved by lowering the thickness of deposited Ti film, significant prolongation of the annealing time or by using reactive sputtering of photocatalytic  $\text{TiO}_2$ . However, as the main intention was to compare the performance of the coatings prepared using similar protocols, no optimization was performed in the frame of this study and all substrates and nanostructures are prepared in principle by magnetron sputtering of metallic Ti in the inert Ar atmosphere and annealed at the same temperature for the same time. The aforementioned insufficient crystallization into photocatalytic  $\text{TiO}_2$  phases is significantly reduced in both types of nanostructured coatings as the mean size of Ti structures is dramatically reduced. Furthermore, the dominant phase in the tubular coatings is anatase, i.e., the phase with the strongest photocatalytic activity. This is consistent with the highest efficiency in the MB degradation observed for this type of film.

The second reason for the better re-cyclability of nanostructured Ag/

$\text{TiO}_2$  coatings is their larger surface area that boosts the photoactive performance of  $\text{TiO}_2$  and, hence, facilitates the degradation of bio-molecules. In this process, the electrons photogenerated under UV irradiation are captured by oxygen adsorbed on the surface of the nanocomposite and produce superoxide radicals, while interactions between the formed holes and the surface  $\text{H}_2\text{O}$  lead to the production of hydroxyl radicals. Such formed highly reactive radicals subsequently interact with organic molecules and decompose them into volatile inorganic compounds such as  $\text{CO}_2$  and  $\text{H}_2\text{O}$  [29]. Furthermore, the nanostructured character of the films reduces the volume electron-hole recombination in  $\text{TiO}_2$ , which increases the photoactivity of resulted coatings. It is important to stress that the UV cleaning step has been performed in the air, suggesting that air humidity is sufficient for effective cleaning of Ag/ $\text{TiO}_2$  nanostructured surfaces.

Considering all three types of Ag/ $\text{TiO}_2$  coatings, the one that represents the best compromise between high SERS activity and re-cyclability is the one composed of  $\text{TiO}_2$  NPs decorated with Ag. To further explore the applicability of such a SERS-active platform, additional tests were performed focused on evaluating the detection limit, spectral reproducibility, and kinetics of MB removal by photo-induced degradation. The intensities of C-C symmetrical stretching peak of MB molecule measured for different initial MB concentrations are presented in Fig. 7. It is evident that the intensity of the SERS signal of MB decreases with decreasing MB concentration. This lowering is more or less linear in the log-log plot and the lowest concentration at which MB was detectable was  $5 \times 10^{-9}$  M. The gradual decrease in MB concentration, and with it connected reduction of measured MB peak intensity, is also accompanied by increased spectral intensity variation. This effect is depicted in Fig. 7b, where intensities of C-C ring stretching band of MB at  $1624 \text{ cm}^{-1}$  measured at different positions on the samples for 3 different MB concentrations are presented. However, as can be seen, even at the concentration of  $1 \times 10^{-7}$  M the relative standard deviation is approximately 25% of the measured intensity, which is still acceptable for a plasmonic-based SERS platform.

Concerning the UV cleaning, the irradiation time employed in the previous experiments was 120 min. To investigate the kinetics of MB degradation induced by UV radiation, additional tests were performed for samples with the initial MB concentrations  $1 \times 10^{-6}$  M and  $1 \times 10^{-7}$  M. The results are summarized in Fig. 7c. It can be seen that the SERS

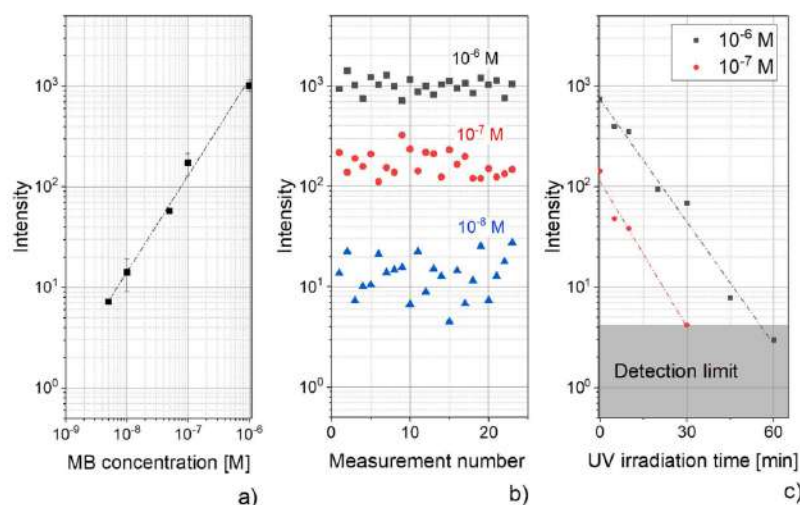


Fig. 7. (a) Dependence of the intensity the C–C ring stretching band on MB concentration. (b) Intensities of  $1624\text{ cm}^{-1}$  peak measured at different places on samples for three selected MB concentrations. (c) Evolution of the intensity of the C–C ring stretching band with UV irradiation time.

intensity exponentially decreases in both cases with increasing irradiation time. The complete disappearance of MB peak from the SERS spectra is then dependent on the initial amount of MB; while no MB SERS peaks were detectable after 30 min for  $1 \times 10^{-7}\text{ M}$ , 1 h of UV irradiation was necessary to clean the surface in the case of higher ( $1 \times 10^{-6}\text{ M}$ ) initial concentration of MB.

#### 4. Conclusions

We carried a study of Ag/TiO<sub>2</sub> nanostructured surfaces, which provide at the same time (i) SERS activity due to plasmonic Ag and (ii) TiO<sub>2</sub> induced self-cleaning that gives the potential of re-cyclability. The presented results may be summarized as follows.

First, the direct comparison of the SERS-activity of three different types of Ag/TiO<sub>2</sub> substrates, prepared by plasma-assisted techniques, revealed that all of them offer the possibility to detect MB, which was selected as a model biomolecule. The highest intensity of the SERS signal of MB was observed for planar TiO<sub>2</sub> film decorated with Ag, followed by a TiO<sub>2</sub> nanoparticle array coated with Ag nanoislands and TiO<sub>2</sub> nanotubes capped with silver nanoislands. As discussed, this difference in the SERS performance of studied architectures for the fixed deposited amount of Ag may be explained by the differences in the surface coverage by Ag nanoislands.

The second important finding is that while all studied architectures of TiO<sub>2</sub>/Ag substrates were proved to be SERS-active and usable for reliable detection of biomolecules, only the nanostructured ones (nanotubular and nanoparticle-based) provide an additional feature – the re-cyclability by UV irradiation. This effect highlights the enhanced photocatalytic performance of TiO<sub>2</sub> nanostructured surfaces as compared to planar TiO<sub>2</sub> surfaces. Here the effect of photocatalytic self-cleaning is attributed to TiO<sub>2</sub> crystallinity and enhanced effective surface area. Based on the presented results, the TiO<sub>2</sub> nanoparticle films decorated with Ag nanoislands offer the best trade-off between SERS enhancement comparable with the commonly used silver nanostructures and the possibility of multiple uses. Although the detection limit for MB is  $5 \times 10^{-9}\text{ M}$  in this case, further optimization of the performance of Ag/TiO<sub>2</sub> SERS-active platforms is still possible, e.g., by tuning the size and number of both TiO<sub>2</sub> and Ag NPs. The results of this study may thus

pave the way for the development of low-cost, easy-to-prepare recyclable, and highly efficient SERS-active platforms that may also use other plasmonic metals. From this point of view, an interesting option may represent Au as this metal possesses superior chemical stability as compared to Ag.

#### CRediT authorship contribution statement

Adéla Hanková: Investigation. Anna Kuzminova: Investigation. Jan Hanuš: Investigation. Petr Sezemsky: Investigation. Radka Simerova: Investigation. Vitezslav Stranek: Conceptualization, Funding acquisition, Writing – original draft, Writing – review & editing. Katarzyna Grochowska: Investigation. Dujearic-Stephane Kouao: Investigation. Katarzyna Siuzdak: Investigation, Investigation, Funding acquisition. Marek Procházka: Investigation, Methodology. Tereza Košutová: Investigation. Ondřej Kylián: Conceptualization, Funding acquisition, Writing – original draft, Writing – review & editing.

#### Declaration of Competing Interest

The authors declare that they have no known competing financial interests or personal relationships that could have appeared to influence the work reported in this paper.

#### Data Availability

Data will be made available on request.

#### Acknowledgments

This work was supported by the grant GAČR 21-05030K from the Grant Agency of the Czech Republic and by the National Science Centre, Poland via grant no 2020/02/Y/ST8/00030.

#### Supplementary materials

Supplementary material associated with this article can be found, in



the online version, at doi:[10.1016/j.surfin.2022.102441](https://doi.org/10.1016/j.surfin.2022.102441).

## References

- [1] M. Fleischmann, P.J. Hendra, A.J. McQuillan, Raman spectra of pyridine adsorbed at a silver electrode, *Chem. Phys. Lett.* 26 (1974) 163–166, <https://doi.org/10.1111/1541-4337.12062>.
- [2] D. Cialla, S. Pollok, C. Steinbrücker, K. Weber, J. Popp, SERS-based detection of biomolecules, *Nanophotonics* 3 (2014) 383–411, <https://doi.org/10.1515/nanoph-2013-0024>.
- [3] A. Szaniawska, A. Kudelski, Applications of surface-enhanced Raman scattering in biochemical and medical analysis, *Front. Chem.* 9 (2021) 1–7, <https://doi.org/10.3389/fchem.2021.664134>.
- [4] K.C. Bantz, A.F. Meyer, N.J. Wittenberg, H. Im, Ö. Kurtuluş, S.H. Lee, N. C. Lindquist, S.-H. Oh, C.L. Haynes, Recent progress in SERS biosensing, *Phys. Chem. Chem. Phys.* 13 (2011) 11551, <https://doi.org/10.1039/c0cp01841d>.
- [5] J. Zheng, L. He, Surface-enhanced Raman spectroscopy for the chemical analysis of food, *Comprehens. Rev. Food Sci. Food Safety* 13 (2014) 317–328, <https://doi.org/10.1111/1541-4337.12062>.
- [6] D.W. Li, W.L. Zhai, Y.T. Li, Y.T. Long, Recent progress in surface enhanced Raman spectroscopy for the detection of environmental pollutants, *Microchim. Acta* 181 (2014) 23–43, <https://doi.org/10.1007/s00604-013-1115-3>.
- [7] E.C. Le Ru, P.G. Etchegoin, Principles of Surface-Enhanced Raman Spectroscopy, Elsevier, 2009, <https://doi.org/10.1016/B978-0-444-52779-0.X0001-3>.
- [8] M. Procházka, Surface-Enhanced Raman Spectroscopy, Springer International Publishing, Cham, 2016, <https://doi.org/10.1007/978-3-319-23992-7>.
- [9] A.I. Pérez-Jiménez, D. Lyu, Z. Lu, G. Liu, B. Ren, Surface-enhanced Raman spectroscopy: benefits, trade-offs and future developments, *Chem. Sci.* 11 (2020) 4563–4577, <https://doi.org/10.1039/d0sc00809e>.
- [10] G. Santoro, S. Yu, M. Schwartzkopf, P. Zhang, S. Koyiloth Vayalil, J.F.H. Risch, M. A. Rübhausen, M. Hernández, C. Domingo, S.V. Roth, Silver substrates for surface enhanced Raman scattering: correlation between nanostructure and Raman scattering enhancement, *Appl. Phys. Lett.* 104 (2014), 243107, <https://doi.org/10.1063/1.4884423>.
- [11] M. Šubr, M. Petr, O. Kylián, J. Kratochvíl, M. Procházka, Large-scale Ag nanoislands stabilized by a magnetron-sputtered polytetrafluoroethylene film as substrates for highly sensitive and reproducible surface-enhanced Raman scattering (SERS), *J. Mater. Chem. C* 3 (2015) 11478–11485, <https://doi.org/10.1039/C5TC02919H>.
- [12] J. Jimenez-Cisneros, J.P. Galindo-Lazo, M.A. Mendez-Rojas, J.R. Campos-Delgado, M. Cerro-Lopez, Plasmonic spherical nanoparticles coupled with titania nanotube arrays prepared by anodization as substrates for surface-enhanced Raman spectroscopy applications: a review, *Molecules* 26 (2021), <https://doi.org/10.3390/molecules26247443>.
- [13] A. Garg, W. Nam, W. Zhou, Reusable surface-enhanced Raman spectroscopy membranes and textiles via template-assisted self-assembly and micro/nanoimprinting, *ACS Appl. Mater. Interfaces* 12 (2020) 56290–56299, <https://doi.org/10.1021/acsami.0c16351>.
- [14] J. Song, W. Nam, W. Zhou, Scalable high-performance nanolaminated SERS substrates based on Multistack vertically oriented plasmonic nanogaps, *Adv. Mater. Technol.* 4 (2019), 1800689, <https://doi.org/10.1002/admt.201800689>.
- [15] S. Kumar, D.K. Lodhi, J.P. Singh, Highly sensitive multifunctional recyclable Ag-TiO<sub>2</sub> nanorod SERS substrates for photocatalytic degradation and detection of dye molecules, *RSC Adv.* 6 (2016) 45120–45126, <https://doi.org/10.1039/C6RA06163J>.
- [16] Y. Ling, Y. Zhuo, L. Huang, D. Mao, Using Ag-embedded TiO<sub>2</sub> nanotubes array as recyclable SERS substrate, *Appl. Surface Sci.* 388 (2016) 169–173, <https://doi.org/10.1016/j.apsusc.2016.01.257>.
- [17] J. Chen, L. Yang, Synthesis and SERS performance of a recyclable SERS substrate based on Ag NPs Coated TiO<sub>2</sub> NT Arrays, *Integr. Ferroelectr.* 147 (2013) 17–23, <https://doi.org/10.1080/10584587.2013.790270>.
- [18] H. Fang, C.X. Zhang, L. Liu, Y.M. Zhao, H.J. Xu, Recyclable three-dimensional Ag nanoparticle-decorated TiO<sub>2</sub> nanorod arrays for surface-enhanced Raman scattering, *Biosens. Bioelectron.* 64 (2015) 434–441, <https://doi.org/10.1016/j.bios.2014.09.053>.
- [19] Y. Xie, Y. Jin, Y. Zhou, Y. Wang, SERS activity of self-cleaning silver/titania nanoray, *Appl. Surface Sci.* 313 (2014) 549–557, <https://doi.org/10.1016/j.apsusc.2014.06.020>.
- [20] Z. Zhang, J. Yu, J. Yang, X. Lv, T. Wang, Preparation of sensitive and recyclable porous Ag/TiO<sub>2</sub> composite films for SERS detection, *Appl. Surface Sci.* 359 (2015) 853–859, <https://doi.org/10.1016/j.apsusc.2015.10.197>.
- [21] T. Zhu, H. Wang, L. Zang, S. Jin, S. Guo, E. Park, Z. Mao, Y.M. Jung, Flexible and reusable Ag coated TiO<sub>2</sub> nanotube arrays for highly sensitive SERS detection of formaldehyde, *Molecules* (2020) 25, <https://doi.org/10.3390/molecules25051199>.
- [22] A. Hanková, A. Kuzminova, J. Hanuš, T. Košutová, P. Šolár, J. Kousal, O. Kylián, Nanostructured and columnar vanadium and vanadium oxides films synthesized by means of magnetron-based gas aggregation source, *Surf. Coat. Technol.* 431 (2022), 128015, <https://doi.org/10.1016/j.surfcoat.2021.128015>.
- [23] N. Martin, C. Rousselot, D. Rondot, F. Palmirio, R. Mercier, Microstructure modification of amorphous titanium oxide thin films during annealing treatment, *Thin Solid Films* 300 (1997) 113–121, [https://doi.org/10.1016/S0040-6090\(96\)09510-7](https://doi.org/10.1016/S0040-6090(96)09510-7).
- [24] Z. Matěj, R. Kužel, L. Nichtová, XRD total pattern fitting applied to study of microstructure of TiO<sub>2</sub> films, *Powder Diffract.* 25 (2010) 125–131, <https://doi.org/10.1154/1.3392371>.
- [25] M. Ohring, Materials Science of Thin Films, Elsevier, 2002, <https://doi.org/10.1016/B978-0-12-524975-1.X5000-9>.
- [26] J. Kratochvíl, A. Kuzminova, O. Kylián, H. Biederman, Comparison of magnetron sputtering and gas aggregation nanoparticle source used for fabrication of silver nanoparticle films, *Surf. Coat. Technol.* 275 (2015) 296–302, <https://doi.org/10.1016/j.surfcoat.2015.05.003>.
- [27] G.-N. Xiao, S.-Q. Man, Surface-enhanced Raman scattering of methylene blue adsorbed on cap-shaped silver nanoparticles, *Chem. Phys. Lett.* 447 (2007) 305–309, <https://doi.org/10.1016/j.cplett.2007.09.045>.
- [28] R.R. Naujok, R.V. Duevel, R.M. Corn, Fluorescence and Fourier transform surface-enhanced Raman scattering measurements of methylene blue adsorbed onto a sulfur-modified gold electrode, *Langmuir* 9 (1993) 1771–1774, <https://doi.org/10.1021/la00031a026>.
- [29] Y. Zhou, J. Chen, L. Zhang, L. Yang, Multifunctional TiO<sub>2</sub>-coated Ag nanowire arrays as recyclable SERS substrates for the detection of organic pollutants, *Eur. J. Inorg. Chem.* 2012 (2012) 3176–3182, <https://doi.org/10.1002/ejic.201200009>.
- [30] A. Roguska, A. Kudelski, M. Pisarek, M. Opara, M. Janik-Czacher, Raman investigations of SERS activity of Ag nanoclusters on a TiO<sub>2</sub>-nanotubes/Ti substrate, *Vibrat. Spectrosc.* 55 (2011) 38–43, <https://doi.org/10.1016/j.vibspec.2010.07.003>.
- [31] Y. Xie, Enhancement effect of silver nanoparticles decorated Titania nanotube array acting as active SERS substrate, *Inorg. Nano-Metal. Chem.* 0 (2021) 1–7, doi: 10.1080/24701556.2021.1984533.
- [32] S. Banerjee, D.D. Dionysiou, S.C. Pillai, Self-cleaning applications of TiO<sub>2</sub> by photo-induced hydrophilicity and photocatalysis, *Appl. Catal. B Environ.* 176–177 (2015) 396–428, <https://doi.org/10.1016/j.apcatb.2015.03.058>.
- [33] R. Wang, K. Hashimoto, A. Fujishima, M. Chikuni, E. Kojima, A. Kitamura, M. Shimohigoshi, T. Watanabe, Light-induced amphiphilic surfaces, *Nature* 388 (1997) 431–432, <https://doi.org/10.1038/41233>.
- [34] A. Kuzminova, M. Šubr, O. Kylián, P. Kůs, J. Hanuš, M. Procházka, Nanostructured metal coatings for surface-enhanced Raman spectroscopy (SERS) prepared by means of low-pressure plasma, *Vacuum* (2019) 170, <https://doi.org/10.1016/j.vacuum.2019.108951>.
- [35] T. Ohno, K. Sarukawa, K. Tokieda, M. Matsumura, Morphology of a TiO<sub>2</sub> photocatalyst (Degussa, P-25) consisting of anatase and rutile crystalline phases, *Journal of Catalysis* 203 (2001) 82–86, <https://doi.org/10.1006/jcat.2001.3316>.
- [36] T. Luttrell, S. Halpegamage, J. Tao, A. Kramer, E. Sutter, M. Batzill, Why is anatase a better photocatalyst than rutile? - Model studies on epitaxial TiO<sub>2</sub> films, *Sci. Rep.* 4 (2015) 1–8, <https://doi.org/10.1038/srep04043>.
- [37] M. Addamo, M. Bellardita, A. Di Paola, L. Palmisano, Preparation and photoactivity of nanostructured anatase, rutile and brookite TiO<sub>2</sub> thin films, *Chem. Commun.* (2006) 4943–4945, <https://doi.org/10.1039/b612172a>.
- [38] G. Zerjav, K. Zizek, J. Zavasknik, A. Pintar, Brookite vs. rutile vs. anatase: what's behind their various photocatalytic activities? *J. Environ. Chem. Eng.* 10 (2022) <https://doi.org/10.1016/j.jece.2022.107722>.

# Supplementary material

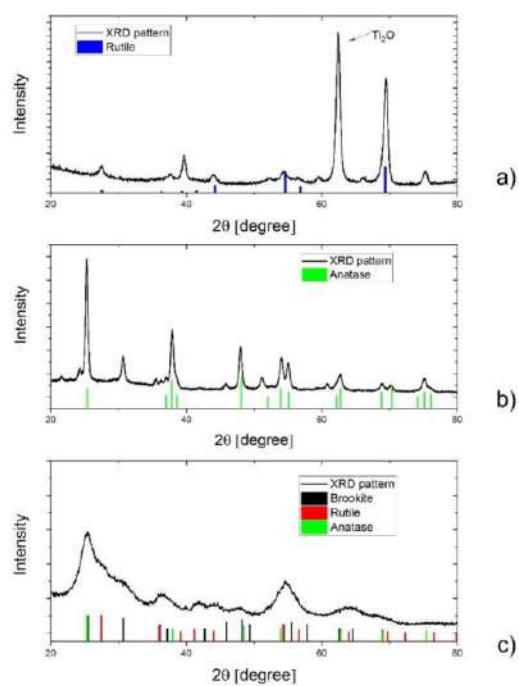


**Figure S1.** XRD diffraction patterns of a) planar  $\text{TiO}_2$  films, b) tubular arrays, and c) nanoparticle film. The different crystalline phases are indicated in the figures by vertical lines.

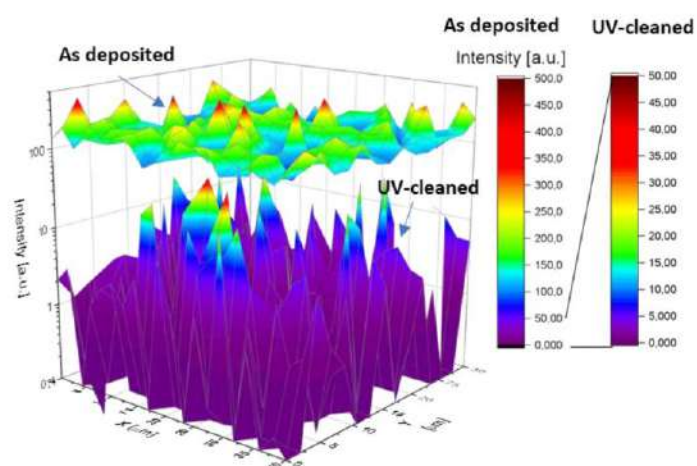


**Figure S2.** 2D maps of the intensity of MB peak at  $1624\text{ cm}^{-1}$  measured on the nanoparticle-based coatings before and after the UV-cleaning step. For better clarity of the figure, the colour scales have different ranges.



## 7.5 Functionalization of semitransparent tubular layer with laser-treated MXene

### A brief overview of the article A5

#### *Introduction*

Recently, the usage of the two-dimensional transition metal carbide MXene to improve photoconversion of the  $\text{TiO}_2$  photoanode for direct applications in dye-sensitized solar cells and photochemistry was initiated by He et al.<sup>37</sup>, Lemos et al.<sup>36</sup> and Khatun et al.<sup>38</sup> Those pioneering works are encouraging in terms of increasing the photoactivity of the bare  $\text{TiO}_2$ . Indeed, a 30 % increase in photocurrent density compared to that of the bare  $\text{TiO}_2$  sample was reported for 150  $\mu\text{L}$  dispersed solution of  $\text{Ti}_3\text{C}_2\text{T}_x$  MXene spin coated on  $\text{TiO}_2$  material.<sup>38</sup> It was shown that bringing together titania nanotubes and MXene increases the value of donor density of the whole nanostructure while during the sample irradiation MXene exhibit surface plasmon resonance effect that via injection of electrons to the titania conduction band leads to the improved photoresponse. However, during using the spin-coating method for the decoration of the highly porous, tubular-like morphology, the problem of the uniform distribution of the catalyst particles in the tubular layer may arise. Typically authors provide only SEM images of a small surface area indicating particles accumulated in some parts of the porous material that suggests that the deposition stage requires optimization. Additionally, it should be evoked that the catalytic properties of  $\text{Ti}_3\text{C}_2\text{T}_x$  MXene can be further increased by appropriate heat treatment through the conversion of as-synthesized  $\text{Ti}_3\text{C}_2\text{T}_x$  into  $\text{Ti}_3\text{C}_2\text{T}_x/\text{TiO}_2$  heterostructure, but continuous heat delivery can lead to complete oxidation to titania. Therefore, it seemed reasonable to take the advantage from the synergistic effect between the outstanding electrical conductivity of  $\text{Ti}_3\text{C}_2\text{T}_x$  and the photostability of  $\text{TiO}_2$  material that can be modified via different approaches, to produce an efficient noble metal-free photoelectrode. On the other hand, there are known methods basing on the  $\text{TiCl}_4$  hydrothermal treatment of titania nanotubes<sup>196</sup> leading to the increased surface area supporting the improvement of the photoconversion efficiency. This kind of surface engineering could be considered as a way to bring together small amount of nano- and microparticles together with the nanostructured substrate leading to their homogenous distribution.

Taking into account promising achievements already reported in the literature regarding MXene as a decorating agent and realising that the elaboration of the modification procedure is crucial to take advantage from the product of such process, I put my efforts trying to both integrate MXene and titania nanotubes and reach the uniform composite photoelectrode. The obtained results are discussed in the **article A5**.

### *Synthesis of $\text{Ti}_3\text{C}_2\text{T}_x/\text{TiO}_2$ heterostructure*

Details of all the steps involved in the synthesis of the  $\text{Ti}_3\text{C}_2\text{T}_x/\text{TiO}_2$  heterostructure are provided in the experimental part of the **article A5**. Herein, the scheme of the laser ablation process employed in this work is provided together with a brief description of the whole synthesis method.

In order to obtain the  $\text{Ti}_3\text{C}_2\text{T}_x/\text{TiO}_2$  heterojunction,  $\text{Ti}_3\text{C}_2\text{T}_x$  was first synthesized by the etching of the Al layers out of the MAX phase in a mixed solution of 2 mL HF/18 mL HCl for 24 h to produce  $\text{Ti}_3\text{C}_2\text{T}_x$  MXene multilayer. Then, the multilayered material was delaminated in 0.5 M  $\text{Na}_2\text{SO}_4$ . The SEM image of the as-prepared material before laser annealing is presented in **Figure 15** (in the subsection 4.6.1). The  $\text{Ti}_3\text{C}_2\text{T}_x/\text{TiO}_2$  heterostructure was obtained by laser ablation method. Briefly, 400 mg of  $\text{Ti}_3\text{C}_2\text{T}_x$  MXene powder was mixed with 1 mL of water and frozen using liquid nitrogen. 15 mL of isopropanol was poured onto the frozen material, and then the material was ablated by a laser beam of 1064 nm wavelength. The steps involved in the laser treatment of the  $\text{Ti}_3\text{C}_2\text{T}_x$  material, and the laser parameters are shown in **Figure 81**.

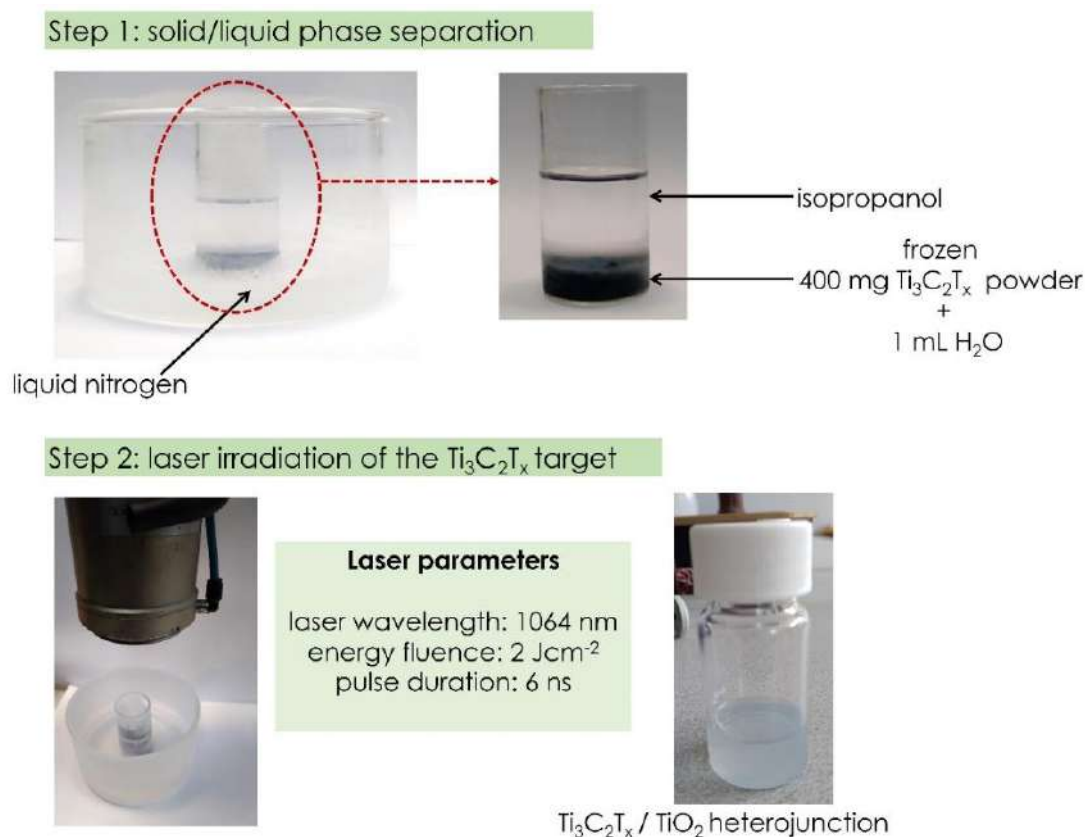


**Figure. 81.** Schematic of the steps of the synthesis method for  $\text{Ti}_3\text{C}_2\text{T}_x/\text{TiO}_2$

*Morphology and chemical composition of the  $Ti_3C_2T_x/TiO_2$  heterostructure*

The morphology of the prepared sample was examined by TEM (**Figure 82**).

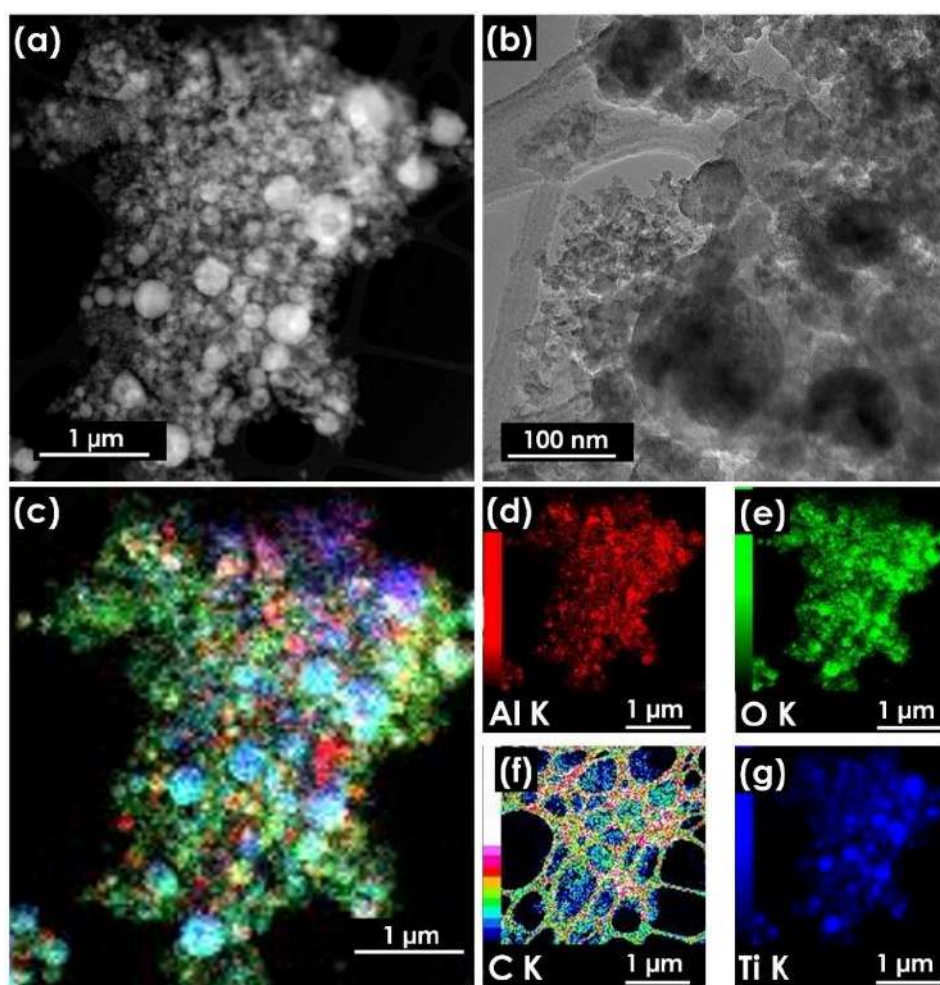


**Figure. 82.** (a) Low resolution and (b) high resolution TEM images of the laser treated  $Ti_3C_2T_x$  MXene. (c) EDX elemental mapping for all the selected elements, (d-e) distribution mapping recorded for (d) Al, (e) O, (f) C, and (g) Ti of the laser annealed  $Ti_3C_2T_x$ . (Reproduced from the data collected for article A5).

The high resolution TEM images show the presence of spherical particles in the material after the laser treatment of the frozen MXene pellet. The high resolution TEM image shows the impact of the laser beam on the MXene surface, namely one can observe spherical particles that arise due to the laser-matter interaction out of the initially layered

nanostructure. The chemical composition of the resultant material was analysed by energy dispersive X-ray technique. As shown in **Figure 82 (c-g)**, the EDX mapping indicates that the spherical particles included in the obtained material after the laser annealing are mainly composed of titanium oxides. It is also worth mentioning that all elements initially present in the sample before the laser treatment, i.e. carbon and titanium, were detected in the laser ablated sample. Different diagnostics methods, such as Raman and X-ray photoelectron spectroscopies as well as X-ray diffractometry studies performed before and after the laser treatment of  $\text{Ti}_3\text{C}_2\text{T}_x$  revealed that the product of laser treatment is a mixture of crystallized  $\text{TiO}_2$  and MXene phase.

*Structural properties of the as-synthesis  $\text{Ti}_3\text{C}_2\text{T}_x/\text{TiO}_2$  heterostructure*

The XRD patterns of  $\text{Ti}_3\text{AlC}_2$  MAX phase and  $\text{Ti}_3\text{C}_2\text{T}_x$  before and after laser ablation are shown in **Figure 83**.

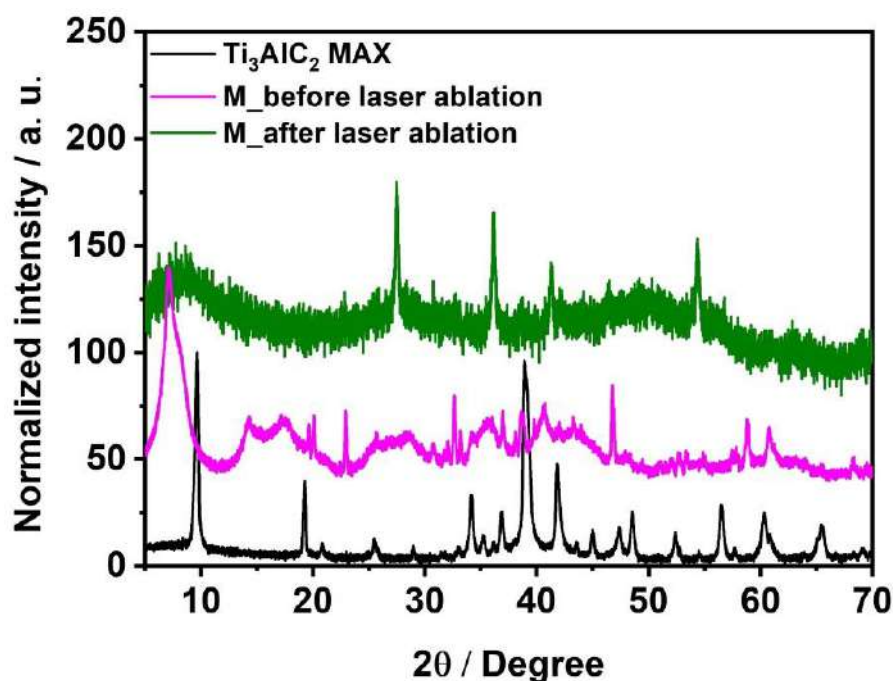


**Figure 83.** XRD patterns of  $\text{Ti}_3\text{AlC}_2$  MAX phase and  $\text{Ti}_3\text{C}_2\text{T}_x$  before and after laser ablation (M:  $\text{Ti}_3\text{C}_2\text{T}_x$  MXene). (Reproduced from the data collected for article A5).

The XRD pattern of the  $\text{Ti}_3\text{AlC}_2$  MAX phase exhibits peaks at  $9.77^\circ$ ,  $19.34^\circ$ ,  $34.24^\circ$ ,  $36.98^\circ$ ,  $39.01^\circ$ ,  $41.77^\circ$ ,  $48.60^\circ$ ,  $52.41^\circ$ ,  $56.54^\circ$ , and  $60.32^\circ$ . The recorded pattern is in the accordance with XRD standard JCPDS card no. 52-0875 for titanium aluminium carbide.

The sharp decrease of the diffraction signal at  $39.01^\circ$  in the diffractogram registered for  $\text{Ti}_3\text{C}_2\text{T}_x$  confirms that the most of Al species were removed from the MAX phase.<sup>197,198</sup> The peak at  $9.20^\circ$  was shifted towards  $7^\circ$  and became relatively broad, confirming the enlargement of the lattice spacing after the etching process.<sup>197,198</sup> Due to the laser annealing five peaks appeared on the recorded XRD pattern. The three peaks found at  $27.71^\circ$ ,  $36.24^\circ$  and  $41.85^\circ$  are associated with the planes (110), (101) and (111) of the rutile phase of  $\text{TiO}_2$  (JCPDS 21-1276), while that at  $54.30^\circ$  corresponds to the plane (105) of the anatase phase (JCPDS 21-1272). This result confirms the presence of a mixture of anatase and rutile crystalline phases of titania in the annealed sample. The peak at  $7^\circ$  present in the XRD pattern of  $\text{Ti}_3\text{C}_2\text{T}_x$  before its laser ablation is still visible in the diffractogram of the laser-treated sample. Since the XRD patterns of anatase and rutile titania do not exhibit diffraction peaks below  $20^\circ$  according to the data in JCPDS card no. 21-1272 (anatase) and 21-1276 (rutile) the presence of this peak confirms the presence of  $\text{Ti}_3\text{C}_2\text{T}_x$  in the final product after laser annealing.

*Decoration of semitransparent anodic nanotubes with the obtained  $\text{Ti}_3\text{C}_2\text{T}_x/\text{TiO}_2$  heterostructure*

A mixed solution of  $x \mu\text{L}$  ( $x = 100, 200$  and  $300 \mu\text{L}$ ) of the  $\text{Ti}_3\text{C}_2\text{T}_x/\text{TiO}_2$  heterostructure suspension in water and  $25 \text{ mL}$  of  $0.1 \text{ M}$   $\text{TiCl}_4$  in water was stored in an ice bath.  $5 \text{ mL}$  of this solution was dropped gently onto the top of the nanotubular layer previously placed in a beaker. The beaker was kept on the hot plate at  $100^\circ\text{C}$ . After  $30 \text{ min}$  the substrate was rinsed with deionized water. This procedure was repeated four more times, giving in total 5 cycles, and finally the materials were calcined in air at  $450^\circ\text{C}$  for one hour. Afterwards the morphology diagnostics was carried out and the top SEM images of the modified tubular layer with  $\text{Ti}_3\text{C}_2\text{T}_x/\text{TiO}_2$  taken at different resolutions are provided in **Figure 84**. The modified samples were labelled 1M- $\text{TiCl}_4$ @TNT, 2M- $\text{TiCl}_4$ @TNT and 3M- $\text{TiCl}_4$ @TNT corresponding to the tubular layers modified with  $0.1 \text{ M}$   $\text{TiCl}_4$  containing  $100 \mu\text{L}$ ,  $200 \mu\text{L}$  and  $300 \mu\text{L}$  of the  $\text{Ti}_3\text{C}_2\text{T}_x/\text{TiO}_2$  (suspension in water), respectively. The SEM images of the samples show that at relatively low  $\text{Ti}_3\text{C}_2\text{T}_x/\text{TiO}_2$  amount i.e.  $100 \mu\text{L}$  and  $200 \mu\text{L}$  any nano- or microparticles are hardly visible on top of the decorated samples.



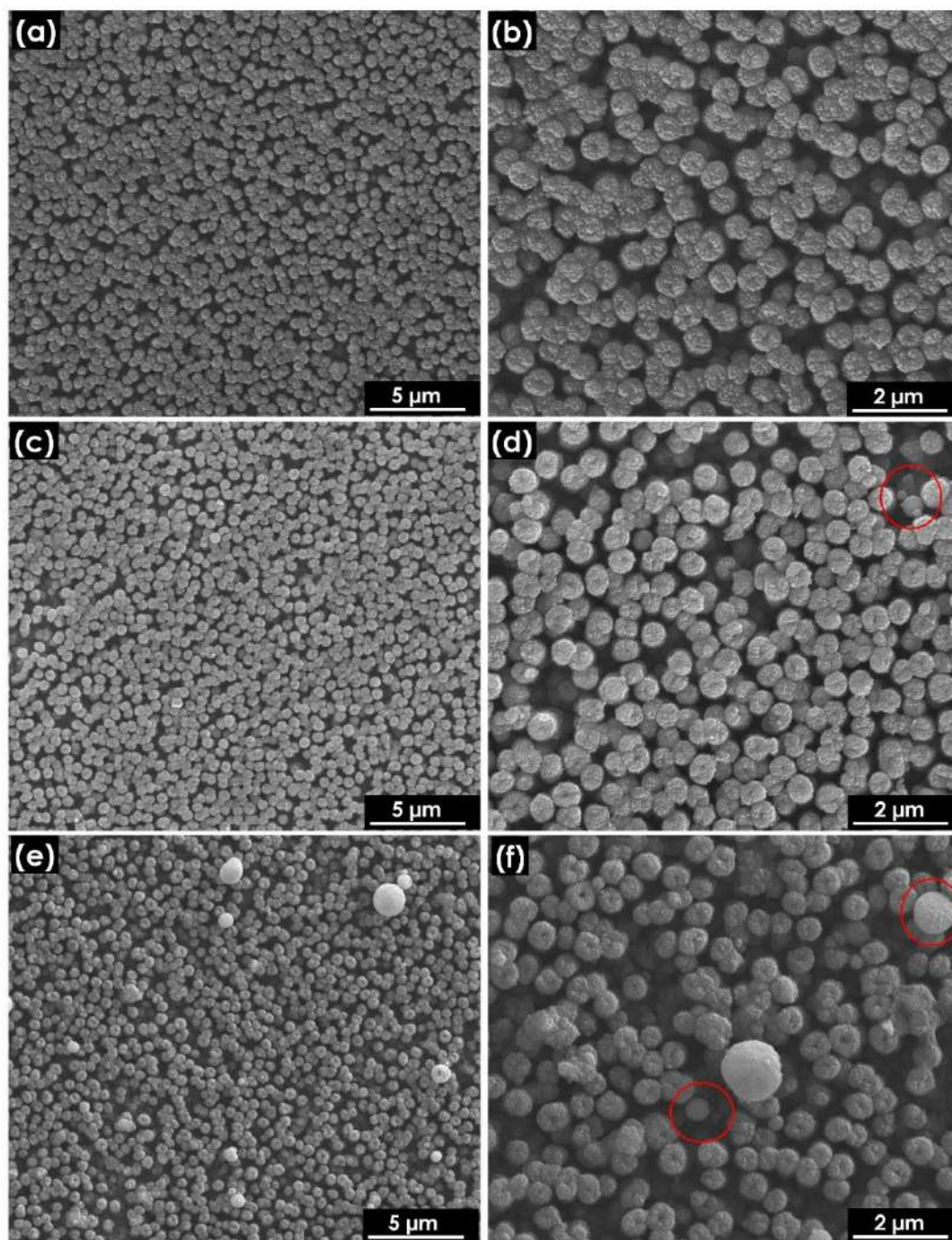


**Figure 84.** SEM images of the modified tubular layer with  $\text{Ti}_3\text{C}_2\text{T}_x/\text{TiO}_2$  taken at different resolution for (a) and (b) 1M-TiCl<sub>4</sub>@TNT, (c) and (d) 2M-TiCl<sub>4</sub>@TNT and (e) and (f) 3M-TiCl<sub>4</sub>@TNT. Spongy spherical particles are indicated in the red circle for the high resolution SEM images. (Reproduced from the data collected for article A5).

The presence of spherical particles trapped between the walls of the nanotubes can be seen in the relatively low resolution SEM images for 2M-TiCl<sub>4</sub>@TNT (i.e. **Figure. 84 (d)**).

Further increase of the amount of the solution with spherical heterostructures to 300  $\mu\text{L}$  led to the presence of the spongy spherical particles, both between the walls of the nanotubes and on top of the tubular layer. The diagnostics of the morphology of obtained materials indicated that the developed decoration method is effective in controlling the presence of decorating compound only between the tubular walls. This way, any agglomerated structures does not inhibit interaction between the incident light and the tubular surface, since having an opaque particles layer on top of the nanotubes can reduce the accessibility of light to the nanotubes. The cross-section images of the samples are provided in **Figure 85** and the geometrical features of the samples are depicted in **Table 9**.

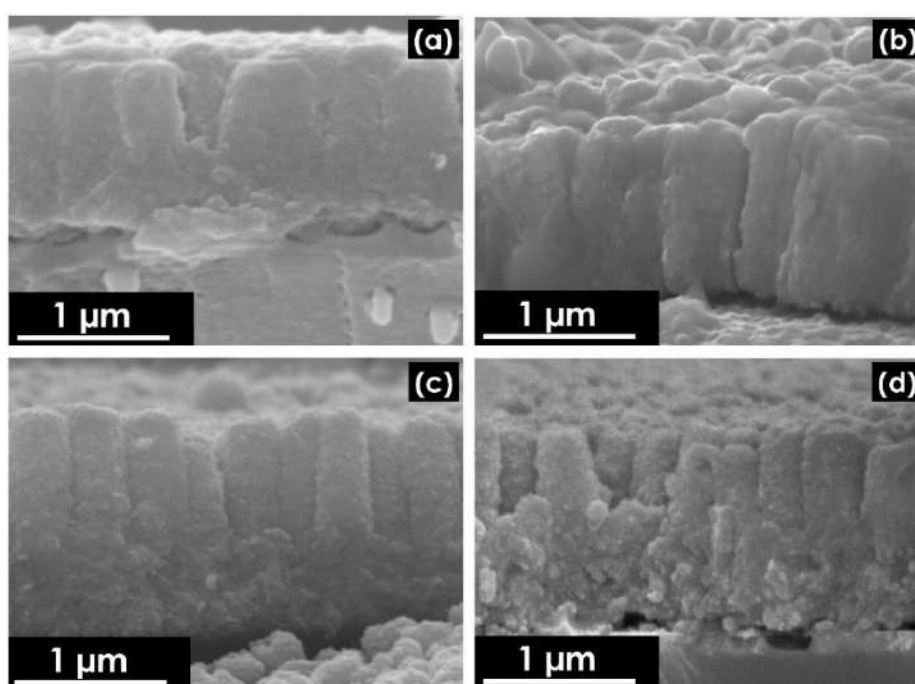


**Figure 85.** SEM cross-section images of (a)  $\text{TiCl}_4\text{@TNT}$ , (b)  $1\text{M-TiCl}_4\text{@TNT}$ , (c)  $2\text{M-TiCl}_4\text{@TNT}$  and (d)  $3\text{M-TiCl}_4\text{@TNT}$ . (Reproduced from the data collected for article A5).

**Table 9.** Averaged nanotube wall thicknesses and lengths of as-prepared TNT.

sample	nanotube wall thickness [nm]	nanotube length [nm]
TNT	$32 \pm 4$	$906 \pm 42$
$\text{TiCl}_4\text{@TNT}$	$126 \pm 14$	$953 \pm 50$
$1\text{M-TiCl}_4\text{@TNT}$	$133 \pm 16$	$955 \pm 42$
$2\text{M-TiCl}_4\text{@TNT}$	$141 \pm 15$	$963 \pm 50$
$3\text{M-TiCl}_4\text{@TNT}$	$150 \pm 18$	$967 \pm 53$

The LSV measurement recorded under chopped light indicates that the most photoactive tubular layer modified with  $\text{Ti}_3\text{C}_2\text{T}_x/\text{TiO}_2$  exhibits five-fold increase in the photocurrent compared to the bare  $\text{TiO}_2$  layer (**Figure 86**). The LSV curves of all samples are provided in the article A5.

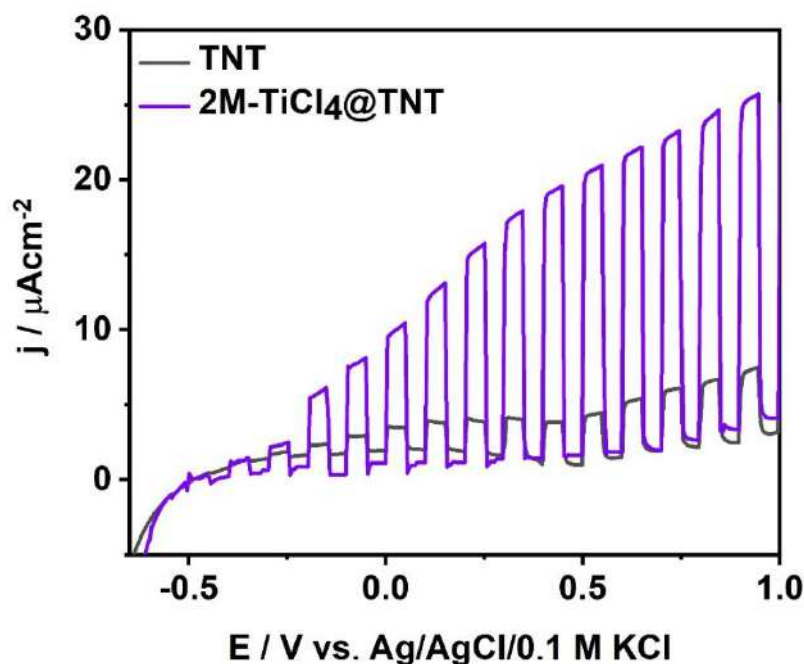


**Figure 86.** Linear sweep voltammetry in chopped UV-vis light (light/dark changes every 5 s) recorded for TNT and 2M-TiCl<sub>4</sub>@TNT.

Mott-Schottky measurements were conducted to analyse in detail the electrical properties of the samples. The plotted data have revealed the presence of two flat band potentials for 1M-TiCl<sub>4</sub>@TNT and 2M-TiCl<sub>4</sub>@TNT samples. These results indicate the presence of sub-band levels within the semiconductor bandgap. Consideration of the Mott-Schottky analysis in explaining the photoactivity enhancement can be understood through the electron-hole separation mechanism shown in **Figure 87**.

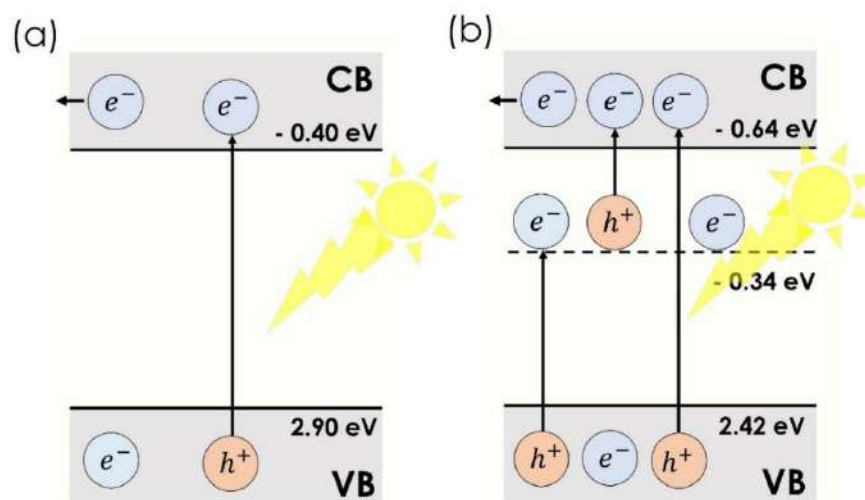


**Figure 87.** Mechanism of the electron-hole separation in the semiconductor (a) without sub-band levels in the bandgap and (b) with the presence of sub-band levels in the bandgap.

(Reproduced from the data collected for article A5).

The photocurrent increases when the photogenerated electrons are efficiently collected at ITO acting here as a current collector. Related to this, a strategy to increase the photoexcited electrons within the conduction band and then their facilitated transfer to the current collector is of fundamental importance.<sup>199</sup> In the case of the unmodified samples i.e. TNT and  $\text{TiCl}_4\text{@TNT}$  only one flat band potential was found by the Mott-Schottky analysis with the donor density of  $0.7 \times 10^{20} \text{ cm}^{-3}$  and  $1.1 \times 10^{20} \text{ cm}^{-3}$ , respectively. For those two samples, under light illumination the conduction band is enriched only by the photogenerated electrons from the valance band as illustrated in **Figure 87 (a)**. However, in the case of the modified samples two flat band potentials were found with donor densities of  $2.5 \times 10^{20} \text{ cm}^{-3}$  and  $0.9 \times 10^{20} \text{ cm}^{-3}$  for 1M- $\text{TiCl}_4\text{@TNT}$  sample, and with donor densities of  $3.2 \times 10^{20} \text{ cm}^{-3}$  and  $1.7 \times 10^{20} \text{ cm}^{-3}$  for 2M- $\text{TiCl}_4\text{@TNT}$  sample. For those two samples, as explained by both Fang et al.<sup>199</sup> and Nishikawa et al.<sup>200</sup>, under illumination not only the electron from the valence band but also the electrons accumulated in the sub-band level are injected in their conduction bands. The electron-hole separation mechanism under light illumination is illustrated in **Figure 87 (b)**. In this case more photoelectrons are available in the conduction band of titania that can be transferred to the current collector. In consequence, increase in photocurrent density of the material can be observed.

The investigation of the quantum efficiency of the samples was carried out as well. 2M- $\text{TiCl}_4\text{@TNT}$  sample exhibits an IPCE of 13.3 %, which is an order of magnitude higher

comparing to that of TNT (1.7 %) and  $\text{TiCl}_4\text{@TNT}$  (2.0 %). The photoluminescence measurements provided in the article A5, have shown that the PL signal intensities of all modified samples with  $\text{Ti}_3\text{C}_2\text{T}_x/\text{TiO}_2$  are lower than those of TNT and  $\text{TiCl}_4\text{@TNT}$  samples. This indicates that the tubular layer exhibits a low electron-hole recombination rate after its modification with the  $\text{Ti}_3\text{C}_2\text{T}_x/\text{TiO}_2$  heterojunction. Moreover, the recorded electrochemical impedance spectra of the samples show a substantial decrease in the charge transfer resistance in dark conditions as well as under visible light illumination for 1M- $\text{TiCl}_4\text{@TNT}$  and 2M- $\text{TiCl}_4\text{@TNT}$  samples compared to TNT and  $\text{TiCl}_4\text{@TNT}$  (see **Table S3** in the supporting information file linked to article A5). In addition, all modified samples with  $\text{Ti}_3\text{C}_2\text{T}_x/\text{TiO}_2$  exhibit enhanced light absorption capacity in both UV and visible regions. This improvement in both the conductivity and the absorbance properties of the tubular layer after its modification with the  $\text{Ti}_3\text{C}_2\text{T}_x/\text{TiO}_2$  heterostructure can effectively explain the increase of the IPCE recorded for the modified samples, presented in **Figure 88**.

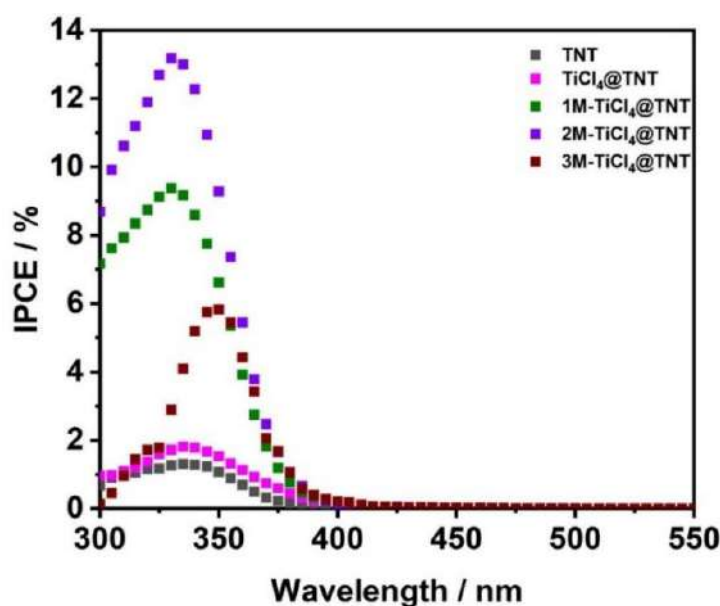


**Figure 88.** IPCE curves of the samples: bare titania and those modified with laser treated MXene, recorded at +0.5 V vs.  $\text{Ag}/\text{AgCl}/0.1 \text{ M KCl}$  in  $0.5 \text{ M Na}_2\text{SO}_4$ .  
(Reproduced from the data collected for article A5).

### Conclusions

Laser ablation of the frozen MXene powder leads to the formation of  $\text{TiO}_2$  sphere/ $\text{Ti}_3\text{C}_2\text{T}_x$  that was captured in the isopropanol present in the liquid form above the frozen target. In order to integrate spherical heterojunction with titania nanotubes, the  $\text{TiCl}_4$ -assisted hydrothermal



approach has been proposed. Elaborated functionalization strategy of semitransparent anodic titania nanotubes with the laser prepared heterostructures led to remarkably improved photoelectrochemical performance of nanotubular platform while its semitransparency was preserved. Indeed, the IPCE measurement of the fabricated TNT modified with  $\text{TiO}_2$  sphere/ $\text{Ti}_3\text{C}_2\text{T}_x$  heterostructures has revealed an increase in the photon to electron conversion efficiency of about one order of magnitude comparing to the bare TNT. This change results from the improvement of both the electrical and optical properties of the sample after its modification with the  $\text{Ti}_3\text{C}_2\text{T}_x/\text{TiO}_2$  heterostructure as discussed in the Article A5. It was also demonstrated that all samples exhibit good photostability under visible illumination without significant decay up to 300 s. These results show the great potential of the  $\text{TiO}_2$  sphere/ $\text{Ti}_3\text{C}_2\text{T}_x$  as a novel decorating agent to increase the photoconversion efficiency of semiconducting nanostructures with limited photoresponse. This can also arouse much interest in exploring not only MXene itself, but  $\text{TiO}_2/\text{Ti}_3\text{C}_2\text{T}_x$  heterostructure as a noble metal-free material towards photoelectrochemical applications.

# Laser-Treated MXene as an Electrochemical Agent to Boost Properties of Semitransparent Photoelectrode Based on Titania Nanotubes

Dujeanic-Stephane Kouao,\* Katarzyna Grochowska, Vitezslav Stranak, Petr Sezemsky, Justyna Gumieniak, Agnieszka Kramek, Jakub Karczewski, Emerson Coy, Jan Hanus, Ondrej Kylian, Mirosław Sawczak, and Katarzyna Siuzdak\*

Cite This: *ACS Nano* 2024, 18, 10165–10183

Read Online

ACCESS |

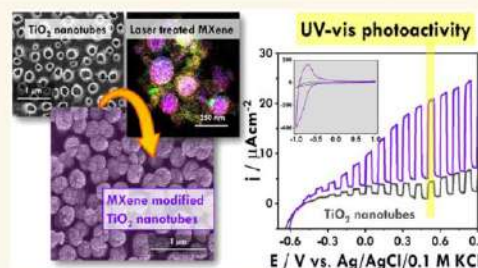
Metrics & More

Article Recommendations

Supporting Information

**ABSTRACT:** In this study,  $\text{Ti}_3\text{C}_2\text{T}_x$  underwent laser treatment to reshape it, resulting in the formation of a  $\text{TiO}_2/\text{Ti}_3\text{C}_2\text{T}_x$  heterojunction. The interaction with laser light induced the formation of spherical  $\text{TiO}_2$  composed of an anatase–rutile phase on the  $\text{Ti}_3\text{C}_2\text{T}_x$  surface. Such a heterostructure was loaded over a titania nanotube (TNT) layer, and the surface area was enhanced through immersion in a  $\text{TiCl}_3$  solution followed by thermal treatment. Consequently, the photon-to-electron conversion efficiency exhibits a 10-fold increase as compared to bare TNT. Moreover, for the sample produced with optimized conditions, five times higher photoactivity is observed in comparison to bare TNT. It was shown that under visible light irradiation the most photoactive heterojunction based on the tubular layer reveals a substantial drop in the charge transfer resistance of about 32% with respect to the dark condition. This can be attributed to the narrower band gaps of the modified material and improvement of the separation efficiency of the photogenerated electron–hole pairs. Overall results suggest that this investigation underscores  $\text{TiO}_2/\text{Ti}_3\text{C}_2\text{T}_x$  as a promising noble-metal-free material that enhances both the electrochemical and photoelectrochemical performances of electrode materials based on TNT that can be further used in light-harvesting applications.

**KEYWORDS:** titania nanotubes, MXene, photoactivity, semitransparent electrode, laser



## 1. INTRODUCTION

The increasing interest in the fabrication of high-efficiency semitransparent electrodes at low manufacturing cost for practical application in photoelectrochemical and optoelectrochemical devices has initiated fundamental research in the field of semiconductors.<sup>1–3</sup> Among others, titania is undoubtedly the most investigated semiconductor metal oxide, owing to its outstanding photoactivity under UV light.<sup>4,5</sup> In addition, semitransparent materials based on titania can be fabricated simply by anodizing Ti film sputtered onto transparent conducting oxides (TCO).<sup>1,2</sup> Highly ordered titania nanotubes (TNTs) with both tunable tube-to-tube spacing and large surface area available for photoelectrochemical processes can be produced directly on TCO by optimizing the anodization conditions<sup>1</sup> and can provide an ordered platform for further modifications. However, several issues associated with  $\text{TiO}_2$  materials still need to be addressed. For example, titania mainly absorbs light in the UV region ( $\lambda < 400$

nm).<sup>6,7</sup> Therefore, the light absorption range of this material must be extended to the entire visible range. In addition, the high recombination rate of the photogenerated electron–hole pairs along the tubular layer drops drastically the light conversion efficiency of TNTs.<sup>8</sup> Attempts have been made to improve the charge separation rate either through the decoration of the tubular layer with an adequate amount of metallic nanoparticles such as Au,<sup>9</sup> AuPt,<sup>10</sup> and Ru<sup>11</sup> or by anodizing Ti alloys films such as TiNb,<sup>12</sup> TiCo,<sup>13</sup> TiFe,<sup>14,15</sup> TiMo,<sup>16</sup> TiW,<sup>17</sup> TiCu,<sup>18</sup> and TiAg<sup>19</sup> sputtered onto the TCO. Significant improvement in the photoactivity with respect to

Received: January 3, 2024

Revised: March 16, 2024

Accepted: March 22, 2024

Published: March 27, 2024



pure TNTs has been reported using Au and Ag as decorating agents due to their plasmonic features.<sup>10,19</sup> However, due to the cost of noble metals and somewhat limited range of their properties, other electrochemically active agents should be explored.

Following this, it is worth focusing onto titanium carbide ( $\text{Ti}_3\text{C}_2\text{T}_x$  MXene) synthesized by selective etching of Al layers from the  $\text{Ti}_3\text{AlC}_2$  MAX phase. This compound has been widely investigated as 2D materials for electrochemical systems<sup>20,21</sup> since it combines properties such as outstanding electrical conductivity, high hydrophilicity, low cost, and good electrochemical and structural stability.<sup>22</sup> Recently, both Khatun et al.<sup>22</sup> and El-Demellawi et al.<sup>23</sup> have shown that  $\text{Ti}_3\text{C}_2\text{T}_x$  MXene exhibits even surface plasmon excitation under light illumination. Moreover, Colin-Ulloa et al.<sup>24</sup> have reported that titanium carbide MXene exhibits intense plasmonic effects under visible and near-IR light. Therefore,  $\text{Ti}_3\text{C}_2\text{T}_x$  can be used as a counterpart for the fabrication of a  $\text{TiO}_2/\text{Ti}_3\text{C}_2\text{T}_x$  heterojunction to improve the performance of the  $\text{TiO}_2$  material, especially its photoresponse. In addition, Shahzad et al.,<sup>25</sup> Zheng et al.,<sup>26</sup> and Zhang et al.<sup>27</sup> have investigated the absorption properties of  $\text{TiO}_2/\text{Ti}_3\text{C}_2\text{T}_x$  heterojunction prepared simply by oxidation of  $\text{Ti}_3\text{C}_2\text{T}_x$ . Their results have shown that  $\text{TiO}_2/\text{Ti}_3\text{C}_2\text{T}_x$  heterostructure materials exhibit narrower band gaps than the pristine  $\text{TiO}_2$ . This results from the presence of  $\text{Ti}^{3+}$  donor sites and  $\text{Ti}^{2+}$  acceptor sites in  $\text{Ti}_3\text{C}_2\text{T}_x$  due to its semimetallic nature.<sup>22</sup> In fact, regardless the synthesis method used for the fabrication of  $\text{Ti}_3\text{C}_2\text{T}_x$ , almost all reported X-ray photoelectron spectroscopy (XPS) data in the literature for titania carbide MXene revealed the presence of both of  $\text{Ti}^{3+}$  donor and  $\text{Ti}^{2+}$  acceptor densities in the Ti 2p spectrum.<sup>28–30</sup>

The above discussion demonstrates that the  $\text{TiO}_2/\text{Ti}_3\text{C}_2\text{T}_x$  heterojunction is a suitable material for practical application in photoelectrochemical devices. Indeed, investigations on the photoelectrocatalytic activity of materials based on  $\text{TiO}_2/\text{Ti}_3\text{C}_2\text{T}_x$  heterojunctions have revealed promising performances. For example,  $\text{Cu}_2\text{O}$ -doped  $\text{TiO}_2/\text{Ti}_3\text{C}_2\text{T}_x$  prepared by a hydrothermal method has demonstrated high photocatalytic  $\text{H}_2$  production, approximately  $3677 \mu\text{mol g}^{-1}$ .<sup>31</sup> The  $\text{TiO}_2/\text{Ti}_3\text{C}_2\text{T}_x$  heterojunction prepared by Li et al.<sup>32</sup> by adding 5 wt %  $\text{Ti}_3\text{C}_2\text{T}_x$  to rutile  $\text{TiO}_2$  has shown 400% improvement in the photocatalytic hydrogen production compared to the pure rutile  $\text{TiO}_2$  sample. Liu et al.<sup>33</sup> reported that the close contact between  $\text{Ti}_3\text{C}_2$  and  $\text{TiO}_2$  in the  $\text{TiO}_2/\text{Ti}_3\text{C}_2\text{T}_x$  heterostructure can facilitate the photoinduced electron–hole separation rate and lead to higher hydrogen production performance of  $2520.4 \mu\text{mol g}^{-1} \cdot \text{h}^{-1}$ .  $\text{TiO}_2/\text{Ti}_3\text{C}_2\text{T}_x$ -based photoelectrodes exhibited highly improved performance in  $\text{CO}_2$  reduction in comparison to bare titania.<sup>34</sup> The photocatalytic reduction of  $\text{CO}_2$  to  $\text{CH}_4$  fuels carried out by Song et al.<sup>35</sup> showed that  $\text{TiO}_2/\text{Ti}_3\text{C}_2\text{T}_x$  photocatalytic electrodes exhibit photocatalytic  $\text{CH}_4$  production higher than that of the photoelectrode based on titania (P25) material.<sup>35</sup> Moreover the performance of photocatalytic  $\text{CO}_2$  reduction to  $\text{CH}_4$  of  $\text{TiO}_2/\text{Ti}_3\text{C}_2\text{T}_x$  material was approximately 3.7 times higher compared to commercial  $\text{TiO}_2$  (P25).<sup>36</sup> Recently, the performance of  $\text{TiO}_2/\text{Ti}_3\text{C}_2\text{T}_x$  materials in dye-sensitized solar cells (DSSCs) has been investigated by Lemos et al.<sup>37</sup> and He et al.<sup>38</sup> Briefly, Lemos et al.<sup>37</sup> reported an increase in the power conversion efficiency of dye-sensitized solar cells of about 20% when only 0.075 wt %  $\text{Ti}_3\text{C}_2\text{T}_x$  was added to  $\text{TiO}_2$ . They showed that the presence of  $\text{Ti}_3\text{C}_2\text{T}_x$  MXene in the  $\text{TiO}_2/\text{Ti}_3\text{C}_2\text{T}_x$  heterostructure

promotes the migration of the photogenerated electrons in  $\text{TiO}_2$  toward the output terminal of the device, thus raising the electron–hole separation rate of  $\text{TiO}_2$ . Similarly, He et al.<sup>38</sup> have shown that DSSCs fabricated using a photoelectrode based on  $\text{TiO}_2/\text{Ti}_3\text{C}_2\text{T}_x$  deliver high power conversion efficiency of about 29.68% under UV–vis light. The photoelectrochemical performance of titania nanotubes (grown on Ti foil) modified with  $\text{Ti}_3\text{C}_2\text{T}_x$  by using spin coating method has been reported by Khatun et al.<sup>22</sup> In their work, they demonstrated that  $\text{Ti}_3\text{C}_2\text{T}_x$  behaves as a plasmonic material. Hence, under light irradiation collective electron excitation occurs in  $\text{Ti}_3\text{C}_2\text{T}_x$  and these electrons are injected into the conduction bands of  $\text{TiO}_2$  to compensate for the high electron loss during the recombination process. An increase in the photocurrent density of about 30% higher with respect to that of the pure TNT layer has been achieved by the TNT/ $\text{Ti}_3\text{C}_2\text{T}_x$  photoelectrode. Although the results of Khatun et al.<sup>22</sup> are encouraging, since the surface of the substrate is not flat but highly porous, concerns about the uniformity of the distribution of the  $\text{Ti}_3\text{C}_2\text{T}_x$  particles in the tubular layer using the spin coating method may arise. The method for the integration of  $\text{Ti}_3\text{C}_2\text{T}_x$  particles with  $\text{TiO}_2$  material is important as well. For example, the drop-casting of a  $\text{Ti}_3\text{C}_2\text{T}_x$  dispersed solution onto a  $\text{TiO}_2$  film was explored by He et al.<sup>38</sup> *In situ* strategies consisting of the direct conversion of  $\text{Ti}_3\text{C}_2\text{T}_x$  powder used as the starting materials into  $\text{TiO}_2/\text{Ti}_3\text{C}_2\text{T}_x$  have also been reported, including laser ablation treatment,<sup>30,39</sup> plasma treatment,<sup>40</sup> hydrothermal treatment,<sup>25,26,41,42</sup> or even high-temperature annealing.<sup>43</sup> In these methods, the resultant  $\text{TiO}_2/\text{Ti}_3\text{C}_2\text{T}_x$  heterostructure obtained after an appropriate processing of the  $\text{Ti}_3\text{C}_2\text{T}_x$  MXene is dispersed in a solvent and then drop coated<sup>44</sup> or spin coated<sup>45</sup> onto a substrate for further investigations.

Among others, the laser ablation technique, which consists of generating nanoparticles by light ablation of a solid target in a liquid or gaseous environment, is an easy, fast, and straightforward method for synthesis/production of nanoparticles.<sup>45</sup> It is worth mentioning that materials other than MXenes have also been used as targets and subjected to a laser beam, and the obtained nanostructures were further used for applications in energy storage and energy conversion devices. For example, an electrocatalyst based on AuPt alloys fabricated by laser ablation of a Au/Pt mixture suspended in a mixed methanol/water solution exhibited a low overpotential of 26 mV to drive the water splitting process toward the production of hydrogen.<sup>46</sup> Naik Shreyanka et al.<sup>47</sup> reported the synthesis of various architectures of three-dimensional metal–organic framework (MOF) materials, namely, Cu–BTC, Co–BTC, and Ni–BTC, by pulsed laser ablation performed in dimethylformamide. Particularly, Co–BTC exhibited promising electrocatalytic activity in water splitting. The laser-induced oxidation of  $\text{Ti}_3\text{C}_2\text{T}_x$  has been investigated by different scientific groups. In general, two methods have been reported to date for the laser annealing of  $\text{Ti}_3\text{C}_2\text{T}_x$  MXene. One of the already used approaches is based on the laser ablation of a  $\text{Ti}_3\text{C}_2\text{T}_x$  pellet<sup>30,48</sup> or  $\text{Ti}_3\text{C}_2\text{T}_x$  thin film coated onto a flat substrate such as glass,<sup>49,50</sup> sapphire,<sup>49</sup> or silicon.<sup>49</sup> However, because the spot size of the laser beam is smaller than the entire surface of the target material, the laser beam can only focus on some limited area. In the other method, first  $\text{Ti}_3\text{C}_2\text{T}_x$  is dispersed in organic solvent (e.g., in methanol<sup>44</sup> or ethanol<sup>51</sup>) or in water,<sup>52</sup> and then the suspension is irradiated with a laser for the oxidation of the  $\text{Ti}_3\text{C}_2\text{T}_x$  MXene.<sup>44,51,52</sup>



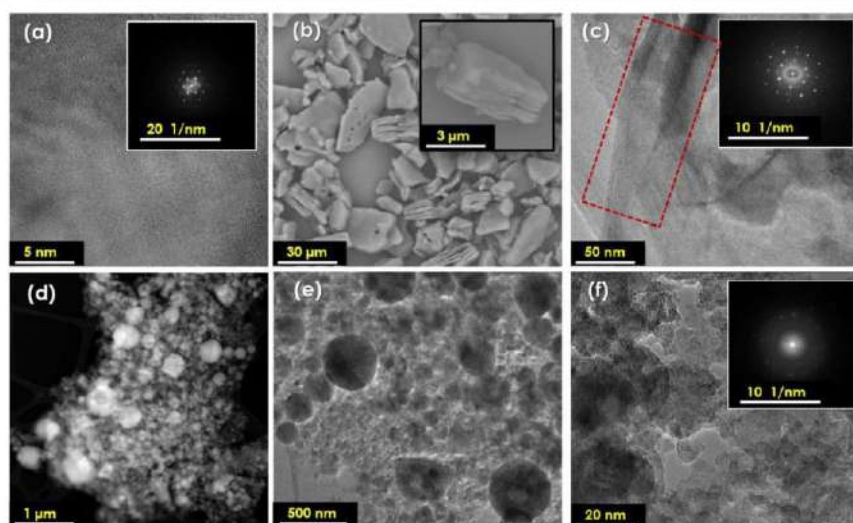


Figure 1. (a) TEM image (inset: corresponding SAED patterns) of  $\text{Ti}_3\text{AlC}_2$  MAX phase. (b) SEM image (inset: single MXene particle) and (c) high-resolution TEM image (inset: corresponding SAED patterns) of  $\text{Ti}_3\text{C}_2\text{T}_x$  before laser ablation. (d and e) Low-resolution TEM image and (f) high-resolution TEM image (inset: corresponding SAED patterns) of  $\text{Ti}_3\text{C}_2\text{T}_x$  after laser ablation.

However, in this method only suspended  $\text{Ti}_3\text{C}_2\text{T}_x$  particles in the path of the ablating laser beam can interact with the beam and oxidize. Even if a change in color of the irradiated solution is observed after a particular time, this does not guarantee that all particles have been oxidized. Hence, the resulting active material after laser ablation can be composed of a mixture of oxidized  $\text{Ti}_3\text{C}_2\text{T}_x$  and nonoxidized  $\text{Ti}_3\text{C}_2\text{T}_x$ . Therefore, if one would like to work only with the synthesis product, a highly selective and efficient separation process should be elaborated. However, structural characterizations performed through X-ray diffraction and Raman measurements of the ablated  $\text{Ti}_3\text{C}_2\text{T}_x$  dispersed in methanol with a 532 nm laser wavelength reported by Park et al.<sup>44</sup> have shown complete destruction of the  $\text{Ti}_3\text{C}_2\text{T}_x$  crystalline structure resulting from its total transformation into  $\text{TiO}_2$  and  $\text{TiC}$ , after only 5 min of laser illumination, indicating that those conditions were highly aggressive toward the fine nanostructure of MXenes.

In this work the feasibility of transformation of  $\text{Ti}_3\text{C}_2\text{T}_x$  into a  $\text{TiO}_2/\text{Ti}_3\text{C}_2\text{T}_x$  heterostructure material via laser ablation without complete destruction of the  $\text{Ti}_3\text{C}_2\text{T}_x$  crystal structure is investigated. Indeed, the  $\text{TiO}_2/\text{Ti}_3\text{C}_2\text{T}_x$  heterostructure can combine the photoactive features of titania with the outstanding electrical conductivity as well as the good light absorption ability of MXenes<sup>53</sup> and acts as an efficient noble metal free decorating agent for semiconductor modification. For example, investigations on the photoactivity of partially oxidized  $\text{Ti}_3\text{C}_2\text{T}_x$  into a  $\text{TiO}_2/\text{Ti}_3\text{C}_2\text{T}_x$  heterostructure conducted by Chertopalov et al.<sup>54</sup> have revealed consistent photoresponse; that is, a photocurrent of about 12  $\mu\text{A}$  was recorded under UV light illumination. Since no photocurrent was recorded under UV light irradiation for the nonoxidized  $\text{Ti}_3\text{C}_2\text{T}_x$  material, the plausible explanation for the observed photocurrent for the  $\text{TiO}_2/\text{Ti}_3\text{C}_2\text{T}_x$  heterostructure provided by Chertopalov et al.<sup>54</sup> is that electrons from both the valence band of  $\text{TiO}_2$  and the defect levels of  $\text{Ti}_3\text{C}_2\text{T}_x$  MXene are

injected into the conductive band of  $\text{TiO}_2$ , which is responsible for the high photocurrent detected in the partially oxidized MXene material. However, unlike the work of Chertopalov et al.,<sup>54</sup> My Tran et al.<sup>55</sup> have recorded a photocurrent density of 0.1  $\mu\text{A}\cdot\text{cm}^{-2}$  in the dark and about 1.46  $\mu\text{A}\cdot\text{cm}^{-2}$  under UV light irradiation for pure  $\text{Ti}_3\text{C}_2\text{T}_x$  MXene. The  $\text{TiO}_2/\text{Ti}_3\text{C}_2\text{T}_x$  heterostructure prepared by hydrothermal synthesis by using pure  $\text{Ti}_3\text{C}_2\text{T}_x$  as starting material has exhibited a rise in the photocurrent density 10 times (16.2  $\mu\text{A}\cdot\text{cm}^{-2}$ ) higher than that of the pure  $\text{Ti}_3\text{C}_2\text{T}_x$  photoelectrodes. Although consistent photocurrents were reported using these *in situ* synthesized  $\text{TiO}_2/\text{Ti}_3\text{C}_2\text{T}_x$  heterostructures,<sup>46,54–59</sup> no work was conducted to investigate the feasibility of using those heterostructures as a decorating agent for the modification of other semiconducting materials to enhance their photoactivities.

Taking into account the promising results reported by both Chertopalov et al.<sup>54</sup> and Tran et al.,<sup>55</sup> our study aims to investigate the partially oxidized  $\text{Ti}_3\text{C}_2\text{T}_x$  MXene obtained via laser processing. The resulting  $\text{TiO}_2/\text{Ti}_3\text{C}_2\text{T}_x$  has been used as decorating agent to boost the photoactivity of anodic titania nanotubes. In this regard, in contrast to the already reported methods, herein the laser-induced oxidation of  $\text{Ti}_3\text{C}_2\text{T}_x$  was carried out when the substrate temperature was significantly lowered to minimize thermally induced destruction of the crystal structure of  $\text{Ti}_3\text{C}_2\text{T}_x$ . The strategy was based on the freezing of the as-prepared water suspension of  $\text{Ti}_3\text{C}_2\text{T}_x$  MXene using liquid nitrogen and maintaining the temperature of the solidified medium below the freezing point of the isopropanol phase located above the solid one. This approach hampers the thermal effect arising due to laser interaction with matter. During the ablation, generated products were caught in the liquid phase that ensures also separation between the solid substrate and the ablated particles that were suspended in isopropanol. Physicochemical characterizations using transmission electron microscopy (TEM), Raman and X-ray

photoelectron (XPS) spectroscopies, as well as X-ray diffractometry (XRD) carried out before and after the laser ablation of  $\text{Ti}_3\text{C}_2\text{T}_x$  revealed that the  $\text{TiO}_2/\text{Ti}_3\text{C}_2\text{T}_x$  heterostructure was obtained after the laser treatment. It is also important to mention that this work reports not only the strategy developed for the synthesis of the  $\text{TiO}_2$  sphere/ $\text{Ti}_3\text{C}_2\text{T}_x$  heterostructure but also the applicability to integrate the modified MXenes within the tubular nanostructures. In addition, to the best of our knowledge, so far no report was released to evaluate the light-harvesting performance of semitransparent TNTs modified by a  $\text{TiO}_2$  sphere/ $\text{Ti}_3\text{C}_2\text{T}_x$  heterostructure. Investigation of the electrochemical and photoelectrochemical properties of the fabricated materials has revealed significant improvement in the performance of the TNT electrodes after the modification with  $\text{TiO}_2/\text{Ti}_3\text{C}_2\text{T}_x$ .

## 2. RESULTS AND DISCUSSION

**2.1. Characterization of  $\text{Ti}_3\text{C}_2\text{T}_x$  before and after Laser Treatment.** Since the  $\text{Ti}_3\text{C}_2\text{T}_x$  MXene material exhibits fine nanostructure morphology, inspection was carried out with transmission electron microscopy together with characterization of the elemental composition. Figure 1a presents a high-resolution TEM image and the corresponding SAED (selected area electron diffraction) pattern (inset) of the  $\text{Ti}_3\text{AlC}_2$  MAX phase. The as-prepared material according to the procedure given in the Experimental Section (i.e., section 4.2) presents the typical loosely packed accordion-like multilayered morphology of titania carbide MXenes (Figure 1b). A similar open stacked sheet-like morphology was reported by Wei et al.<sup>60</sup> for  $\text{Ti}_3\text{C}_2\text{T}_x$  delaminated also by alkali salt (i.e., Li, Na, and K salts). The high-resolution TEM image in Figure 1c shows clear evidence of the presence of a layered structure in the  $\text{Ti}_3\text{C}_2\text{T}_x$  sample. The SAED pattern (inset Figure 1c) confirms that the prepared  $\text{Ti}_3\text{C}_2\text{T}_x$  has retained the hexagonal symmetry structure of the parent  $\text{Ti}_3\text{AlC}_2$  MAX phase (inset Figure 1a).<sup>28</sup> Moreover, the determined interplane spacing corresponding to the (1010) crystal plane was found to be 0.257 nm, which overlaps the value reported by Schen et al. for  $\text{Ti}_3\text{C}_2\text{T}_x$  MXene.<sup>61</sup>

After the laser treatment, the material changes its morphology, and Figure 1d shows that spherical particles have been formed. The TEM image given in Figure 1e indicates that the spherical particles are formed on the  $\text{Ti}_3\text{C}_2\text{T}_x$  surface. Similar reshaping was observed by Park et al.<sup>44</sup> after irradiating the as-synthesized  $\text{Ti}_3\text{C}_2\text{T}_x$  MXene (50 mg) dispersed in methanol by using a 532 nm wavelength laser with pulse width of 10 ns and pulse repetition of 10 Hz. This relatively short wavelength has led to the complete degradation of the MXene into the  $\text{TiO}_2/\text{TiC}$  heterostructure after only 5 min of laser illumination. The high energy provided by the laser beam has resulted in the collapse of the 2D layered structure of MXene and further formation of the spherical particles. Taking into account those results, to limit the thermal effect arising due to laser interaction with matter, a low-temperature synthesis method was adopted. In this approach, the dispersed  $\text{Ti}_3\text{C}_2\text{T}_x$  MXene particles were first mixed with water and then frozen by nitrogen liquid before the laser processing by applying a laser wavelength of 1064 nm with pulse width of 6 ns and pulse repetition of 60 Hz. The spherical particles formed due to the interaction of the laser beam with the  $\text{Ti}_3\text{C}_2\text{T}_x$  target material after 30 min of irradiation are visible in Figure 1d,f. The high-resolution TEM image (Figure 1f) shows large polycrystallinity with a rough

surface after the laser treatment. The symmetrical diffraction points in the corresponding SAED pattern show the hexagonal crystal structure typical for the  $\text{Ti}_3\text{C}_2\text{T}_x$  phase. This indicates that although laser treatment was applied, one can still find  $\text{Ti}_3\text{C}_2\text{T}_x$  MXene in the final product.

Additionally, high-resolution TEM imaging and corresponding EDX mapping were performed to identify the chemical composition of the formed spherical-like particles (Figure 2).

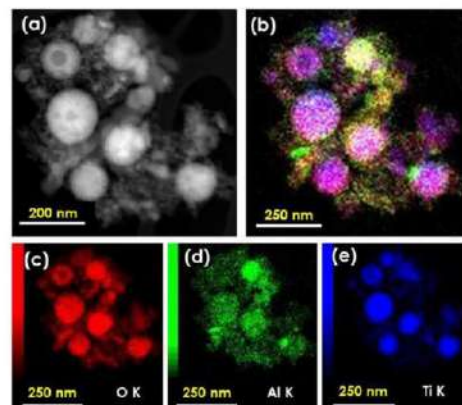


**Figure 2.** (a) High-resolution TEM image and (b) elemental mapping for all the selected elements, (c–e) distribution mapping recorded for (c) O, (d) Al, and (e) Ti of the  $\text{Ti}_3\text{C}_2\text{T}_x$  after laser ablation.

The EDX elemental mapping obtained from the distribution mapping of Ti, Al, and O elements revealed that those spherical particles consist mainly of titanium oxides, thus indicating that the heterostructure of  $\text{TiO}_2/\text{Ti}_3\text{C}_2\text{T}_x$  arises after the laser treatment of  $\text{Ti}_3\text{C}_2\text{T}_x$ . It can be concluded that  $\text{Ti}_3\text{C}_2\text{T}_x$  acts as both Ti source and support for the formation of the  $\text{TiO}_2$  nanospheres. In addition, some areas of Al oxides were also detected, indicating that traces of aluminum were still present in the  $\text{Ti}_3\text{C}_2\text{T}_x$  sample before the laser ablation and get oxidized due to the laser treatment. This situation when some Al residues are present in  $\text{Ti}_3\text{C}_2\text{T}_x$  is not exceptional. In fact, substantial decrease, but not complete removal, of the Al content was reported also after the etching of the Al layers out of the  $\text{Ti}_3\text{AlC}_2$  MAX phase.<sup>62,63</sup>

The FTIR spectra of the samples are presented in Figure S1. The broad and strong absorption bands below  $1000\text{ cm}^{-1}$  in the FTIR spectrum of  $\text{Ti}_3\text{C}_2\text{T}_x$  after the laser annealing correspond to Ti–O and O–Ti–O vibration, confirming the presence of  $\text{TiO}_2$ .<sup>64</sup>

The crystalline structures of the prepared samples were analyzed by X-ray diffraction. The XRD patterns of  $\text{Ti}_3\text{AlC}_2$  MAX phase and  $\text{Ti}_3\text{C}_2\text{T}_x$  MXene both before and after laser treatment are presented in Figure 3a. According to the JCPDS card no. 52-0875, the intense peaks in the XRD pattern of the  $\text{Ti}_3\text{AlC}_2$  MAX phase at  $9.77^\circ$ ,  $19.34^\circ$ ,  $34.24^\circ$ ,  $36.98^\circ$ ,  $39.01^\circ$ ,  $41.77^\circ$ ,  $48.60^\circ$ ,  $52.41^\circ$ ,  $56.54^\circ$ , and  $60.32^\circ$  are indexed to (002), (004), (101), (103), (008), (104), (105), (107), (108), (109), and (110) diffraction planes.<sup>65,66</sup> The formation of  $\text{Ti}_3\text{C}_2\text{T}_x$  from the  $\text{Ti}_3\text{AlC}_2$  MAX phase is confirmed on the XRD spectrum of  $\text{Ti}_3\text{C}_2\text{T}_x$  by the abrupt decrease of the



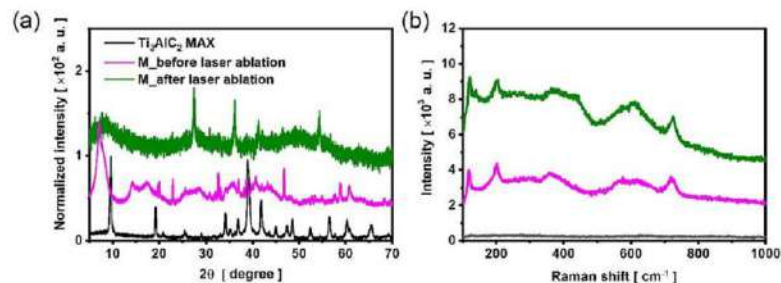


Figure 3. (a) XRD patterns and (b) Raman spectra of  $\text{Ti}_3\text{AlC}_2$  MAX phase and  $\text{Ti}_3\text{C}_2\text{T}_x$  before and after laser ablation (M:  $\text{Ti}_3\text{C}_2\text{T}_x$  MXene).

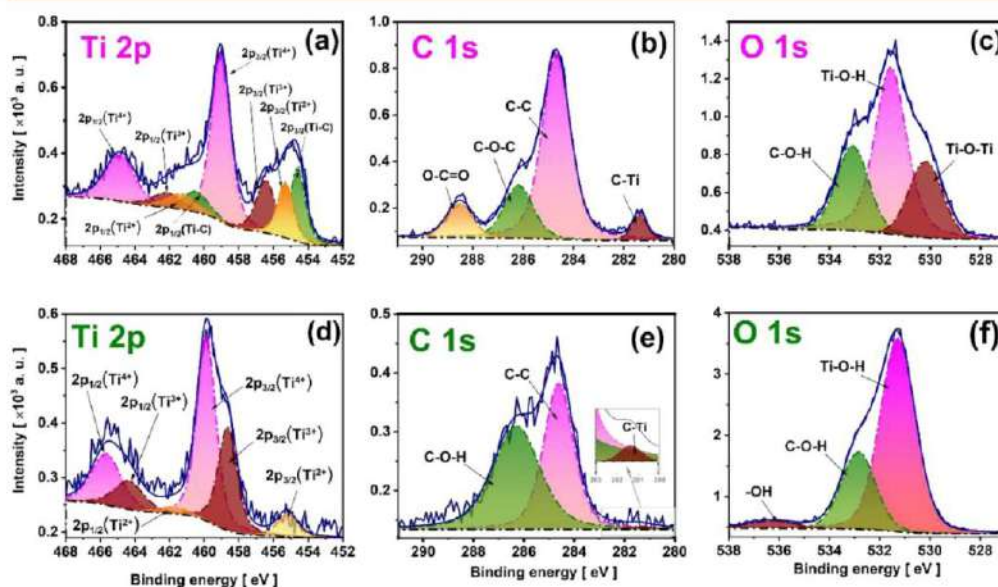


Figure 4. High-resolution XPS spectra of Ti 2p for  $\text{Ti}_3\text{C}_2\text{T}_x$  (a) before and (d) after laser ablation, C 1s for  $\text{Ti}_3\text{C}_2\text{T}_x$  (b) before and (e) after laser ablation, and O 1s for  $\text{Ti}_3\text{C}_2\text{T}_x$  (c) before and (f) after laser ablation.

characteristic diffraction signal at  $39.01^\circ$ .<sup>65–67</sup> This indicates that most of the Al layers were removed.<sup>65,66</sup> In addition, the diffraction peak at  $9.20^\circ$  corresponding to the (002) plane has become relatively broad and shifted to  $7^\circ$ , indicating the enlargement of the lattice spacing after the etching process.<sup>65,66</sup> However, knowing that both titania phases, namely, anatase and rutile, according to data in JCPDS card nos. 21-1272 and 21-1276 do not exhibit any signal below  $20^\circ$ , the presence of the wide peak at  $7.20^\circ$  in the XRD pattern after the laser annealing indicates the presence of  $\text{Ti}_3\text{C}_2\text{T}_x$ .<sup>62</sup> Indeed, the XRD pattern of the  $\text{TiO}_2/\text{TiC}$  heterostructure obtained by Park et al.<sup>44</sup> after the complete destruction of the  $\text{Ti}_3\text{C}_2\text{T}_x$  crystal structure does not exhibit any diffraction peak below  $20^\circ$ . As explained by Hu et al.,<sup>67</sup> the broadening of this signal results from the substitution of the Al atoms by the functional groups (i.e., OH $^-$ , F, and Na) in the interlayer of  $\text{Ti}_3\text{C}_2\text{T}_x$ . After the laser treatment, the appearance of the characteristic

diffraction peaks at  $27.71^\circ$ ,  $36.24^\circ$ , and  $41.85^\circ$  corresponding to the (110), (101), and (111) planes of the rutile phase of  $\text{TiO}_2$  (JCPDS 21-1276) and the peak at  $54.30^\circ$  corresponding to the (105) plane of the anatase phase of  $\text{TiO}_2$  (JCPDS 21-1272) confirms the presence of titania particles in the final product.<sup>68</sup>

Further analysis of the crystalline phase of the  $\text{Ti}_3\text{AlC}_2$  MAX phase and the prepared  $\text{Ti}_3\text{C}_2\text{T}_x$  before and after the laser treatment was conducted using Raman spectroscopy. The Raman spectra of the samples are shown in Figure 3b. It can be noticed that the spectrum recorded for the MAX phase exhibits signals of low intensity. A similar result has been reported by Sarycheva et al.<sup>69</sup> using the same excitation laser wavelength, namely, 785 nm. This can be explained by the metallic nature of the  $\text{Ti}_3\text{AlC}_2$  MAX phase.<sup>69</sup> The Raman spectra of  $\text{Ti}_3\text{C}_2\text{T}_x$  before and after laser treatment exhibit three peaks located at 120, 201, and  $726\text{ cm}^{-1}$ , respectively. The resonant peak at 120

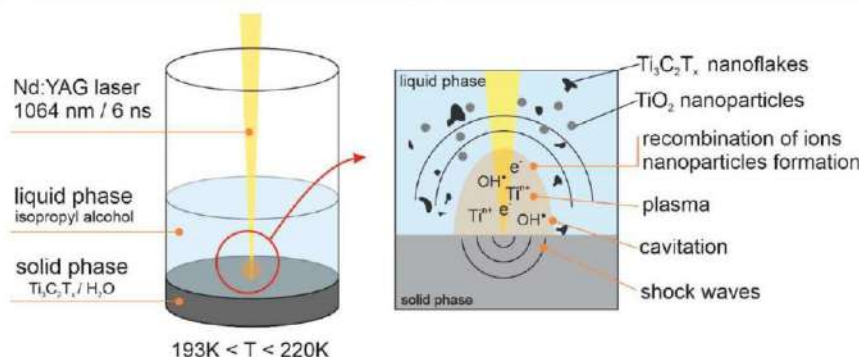


Figure 5. Mechanism of the formation of the  $\text{TiO}_2/\text{Ti}_3\text{C}_2\text{T}_x$  heterojunction.

$\text{cm}^{-1}$  corresponds to the  $E_g$  in-plane shear about the midplane of titanium atoms,<sup>69,70</sup> and the two characteristic sharp peaks at 201 and  $726\text{ cm}^{-1}$  are assigned to the  $A_{1g}$  out-of-plane vibration of the surface functional groups attached to titanium atoms and the  $A_{1g}$  out-of-plane vibration of carbon atoms, respectively. The additional broad peak at  $610\text{ cm}^{-1}$  in the Raman spectrum of  $\text{Ti}_3\text{C}_2\text{T}_x$  after the laser annealing is assigned to the  $A_{1g}$  vibration mode of the  $\text{TiO}_2$  rutile phase.<sup>71</sup> This result indicates that in situ formation of  $\text{TiO}_2$  from  $\text{Ti}_3\text{C}_2\text{T}_x$  MXene has been achieved through the laser treatment process.

The changes in the chemical composition and oxidation states of the prepared  $\text{Ti}_3\text{C}_2\text{T}_x$  MXene materials before and after laser ablation were examined by XPS analysis (Figure 4). The analysis concerns the binding energy regions typical for titanium Ti 2p, oxygen O 1s, and carbon C 1s.

The Ti 2p spectrum of the  $\text{Ti}_3\text{C}_2\text{T}_x$  sample before the laser ablation (Figure 4a) can be deconvoluted into four sets of spin-orbit doublets corresponding to  $2p_{3/2}$  and  $2p_{1/2}$  components. The splitting energies of each doublet is 5.7 eV, and the  $2p_{3/2}$  components at 454.6, 455.3, 456.6, and 459 eV are assigned to Ti–C bonds,<sup>28,72</sup> titanium (in the  $\text{Ti}^{2+}$  chemical state) bonded to three oxygen atoms and one carbon atom,<sup>28,40</sup> titanium (in the  $\text{Ti}^{3+}$  chemical state) bonded to two oxygen atoms, one carbon and one fluorine atom,<sup>28,40</sup> and  $\text{TiO}_2$  ( $\text{Ti}^{4+}$ ),<sup>28,73</sup> respectively. However, after the laser ablation of  $\text{Ti}_3\text{C}_2\text{T}_x$ , the doublet corresponding to the Ti–C bonds completely disappears in the Ti 2p spectrum (Figure 4d). This results from the breaking of the Ti–C bonds, accompanied by the partial oxidation of  $\text{Ti}_3\text{C}_2\text{T}_x$  leading to the growth of  $\text{TiO}_2$  spheres as observed in the TEM images.<sup>30,41,74</sup>

The mechanism driving the formation of the  $\text{TiO}_2$  particles was proposed by Li et al.<sup>52</sup> when investigating the laser-induced degradation of  $\text{Ti}_3\text{C}_2\text{T}_x$  dispersed in water. Briefly, when  $\text{Ti}_3\text{C}_2\text{T}_x$  particles are irradiated with a laser, collective electron excitation occurs at the  $\text{Ti}_3\text{C}_2\text{T}_x$  surface (i.e., plasmonic excitation).<sup>52</sup> Those electrons generated at the MXene surface are captured by the oxygen molecules originating from water.<sup>52</sup> The continuous attack of oxygen would lead to the breaking of the C–Ti bonds and the formation of the  $\text{TiO}_2$ .<sup>52</sup> It should be kept in mind that  $\text{Ti}_3\text{C}_2\text{T}_x$  particles were in contact with water since the powder was first dispersed in water and then frozen for the laser annealing. Hence, the proposed mechanism can also explain

the growth of the  $\text{TiO}_2$  observed in the EDX map in Figure 2b. The presence of the doublets associated with  $\text{Ti}^{2+}$  and  $\text{Ti}^{3+}$  chemical states confirms that the  $\text{Ti}_3\text{C}_2\text{T}_x$  is not completely oxidized into  $\text{TiO}_2$  after the laser ablation.<sup>30</sup> In this study the formation of  $\text{TiO}_2/\text{Ti}_3\text{C}_2\text{T}_x$  heterostructure can be explained as follows: During laser ablation, several phenomena occur that contribute to the formation of nanoparticles and exfoliation of MXene. As a result of the absorption of the laser pulse energy, a shock wave is created in the material, which may cause fragmentation of the solid phase. Additionally, due to the absorption of radiation energy, the phenomenon of laser ablation occurs, during which chemical bonds are broken and ions are created. As plasma recombination occurs, ions become trapped in the liquid phase, resulting in the formation of nanoparticles. The process of mechanical and thermal shock wave exfoliation of MXenes under pulsed laser irradiation was reported by Ramírez et al.,<sup>75</sup> where the laser was used for production of quantum dots (QD) from MAX phase suspended in aqueous solution. The shock wave is responsible for production of small particles and flakes of MXene since the thermal energy is not sufficient to break all chemical bonds. Ions arising during laser ablation can create chemical compounds during recombination. In addition to the formation of MXenes QDs, Ramírez et al.<sup>75</sup> have also reported the formation of  $\text{Ti}_3\text{C}_2/\text{Ti}_3\text{C}$  QDs. The chemical composition of nanoparticles formed under laser-induced plasma is determined by composition of a plasma plume as well as liquid-phase composition where ablation occurs. According to Golightly et al.,<sup>76</sup> during laser ablation of a metallic titanium target immersed in an aqueous solution, titanium dioxide nanoparticles were formed and metallic nanoparticles arise when ethanol is used as a medium, while TiC nanoparticles were detected during ablation in isopropanol. In our experiment the target is formed by MXene suspended in water and afterward solidified at a temperature below 220 K. Isopropyl alcohol was used as a liquid phase whose main function is to trap nanoparticles generated during ablation. Since the laser ablation occurs at the liquid/solid interface, except MXene nanoflakes,  $\text{TiO}_2$  nanoparticles will be produced (according to the formation mechanism proposed by Li et al.<sup>52</sup>). However,  $\text{Ti}_3\text{C}_2\text{T}_x$  particles trapped in the isopropanol solution may act also as a carbon source and can induce formation of titanium carbide (Figure 5).



The C 1s spectra of  $\text{Ti}_3\text{C}_2\text{T}_x$  samples recorded before the laser treatment (Figure 4b) present four peaks at 281.4, 284.7, 286.2, and 288.5 eV corresponding to C–Ti bonds,<sup>77</sup> C–C bonds,<sup>78</sup> C–O bonds,<sup>79</sup> and C=O bonds,<sup>80</sup> respectively. As one can see in Figure 4e, the disappearance of the band corresponding to C=O bonds after the laser ablation indicates the reduction of the surface group functionalities anchored to carbon atoms. The reduction of the C=O group can occur according to the mechanism for reduction of a carbonyl group in the presence of hydrogen to give an alcohol group: C–OH. In fact, the presence of C–OH bonds was detected on the basis of the interpretation of signals forming the C 1s spectrum after the laser treatment. Since the  $\text{Ti}_3\text{C}_2\text{T}_x$  MXene was mixed with water before it was frozen, the hydrogen can come from water decomposition upon laser annealing, i.e.,  $\text{C}=\text{O} + \text{H}_2\text{O} \rightarrow \text{OH}-\text{C}-\text{OH}$  (nucleophilic addition of water to C=O).<sup>81</sup> Finally, the C 1s spectrum after the laser ablation also shows the presence of residual C–Ti bonds.

The O 1s spectrum of the  $\text{Ti}_3\text{C}_2\text{T}_x$  sample before the laser ablation exhibits three peaks at 530.2 eV, 531.6 and 533.1 eV which are attributed to Ti–O–Ti,<sup>82,83</sup> Ti–OH,<sup>83,84</sup> and C–OH,<sup>85</sup> respectively (Figure 4c). After the  $\text{Ti}_3\text{C}_2\text{T}_x$  laser annealing, only the peaks corresponding to the Ti–OH and C–OH bonds are present in the XPS spectrum. In addition, as one can see in Figure 4f, the intensities of these two peaks significantly increased after the laser processing. Moreover, the oxygen atomic content determined by the XPS measurements have shown an increase from 30% for the pristine  $\text{Ti}_3\text{C}_2\text{T}_x$  sample to about 68% in the laser-treated sample. As discussed by Kuang et al.,<sup>86</sup> this significant rise in the oxygen content together with the increase in intensity of the peak corresponding to the Ti–O bands (Figure 4f) is additional evidence that titanium dioxide is formed through the partial oxidation of the pristine MXene. The peak at 536.6 eV in the O 1s spectrum (Figure 4f) is attributed to chemisorbed oxygen and water.<sup>87</sup>

In summary, TEM, XRD, and XPS analyses of the prepared samples have demonstrated that the  $\text{TiO}_2/\text{Ti}_3\text{C}_2\text{T}_x$  heterostructure in which  $\text{TiO}_2$  exhibits a nanosphere-like morphology has been successfully synthesized after the laser annealing.

**2.2. Investigation of  $\text{TiO}_2$  Sphere/ $\text{Ti}_3\text{C}_2\text{T}_x$  Heterojunction as Decorating Agent for the Functionalization of Semitransparent TNT-Based Materials.** The prepared  $\text{TiO}_2/\text{Ti}_3\text{C}_2\text{T}_x$  is for further modification of semitransparent spaced titania nanotubes. The whole route of the modification process of the TNTs is described in detail in the Experimental Section (section 4.6). First, changes in the morphology and structural and optical properties were studied. The as-anodized TNT sample has an average tube length of  $906 \pm 42$  nm (Figure S2). Although the anodization was carried out at constant voltage (i.e., 40 V) the cross-sectional image of the pristine tubular layer exhibits spaced  $\text{TiO}_2$  bamboo-type nanotubes. Albu et al.<sup>88</sup> pointed out that the nanotubes with bamboo-like morphologies are obtained only if the anodization was performed under alternating voltage conditions (AC). The anodization carried out under constant voltage conditions (DC) would lead to tubular layers with smooth tubes.<sup>88</sup> Xie et al.<sup>89</sup> have also synthesized bamboo-shaped nanotube arrays via both alternating voltage and alternating current anodization processes. Our results show that the bamboo-type morphology is not only sensitive to the AC or DC voltage mode. The electrolyte composition that rules the ion-diffusion gradient

during the formation of the nanotubes must be taken into account as well.

Figure 6 shows the top and cross-sectional images of  $\text{TiCl}_4$ @TNT, 1M- $\text{TiCl}_4$ @TNT, 2M- $\text{TiCl}_4$ @TNT, and 3M- $\text{TiCl}_4$ @TNT.

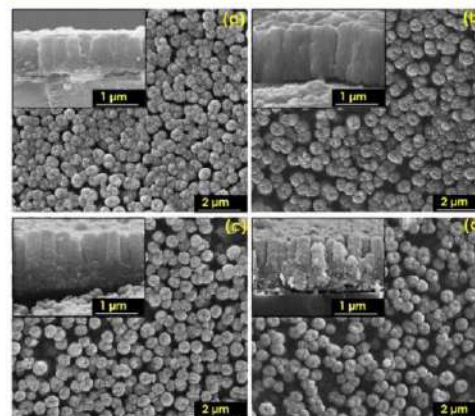


Figure 6. SEM top images of (a)  $\text{TiCl}_4$ @TNT, (b) 1M- $\text{TiCl}_4$ @TNT, (c) 2M- $\text{TiCl}_4$ @TNT, and (d) 3M- $\text{TiCl}_4$ @TNT (Insets: corresponding cross-sectional images of the prepared materials).

TNT samples. The modification of TNTs with  $\text{TiCl}_4$  has led to the increase of the tube wall thickness to about  $126 \pm 14$  nm. This change in the tubular wall thickness after the modification of TNTs by  $\text{TiCl}_4$  has been also reported by Javed et al.<sup>90</sup> They also demonstrated that the modification of TNTs by  $\text{TiCl}_4$  can lead to formation of titania nanoparticles over the upper surface of the nanotubes. The increase of the  $\text{TiO}_2/\text{Ti}_3\text{C}_2\text{T}_x$  amount (i.e., 100, 200, and 300  $\mu\text{L}$ ) resulted in further enlargement of the thickness of the tube walls as depicted in Table 1.

Table 1. Averaged Nanotube Wall Thicknesses and Lengths of As-Prepared TNTs

sample	nanotube wall thickness [nm]	nanotube length [nm]
TNT	$32 \pm 4$	$906 \pm 42$
$\text{TiCl}_4$ @TNT	$126 \pm 14$	$953 \pm 50$
1M- $\text{TiCl}_4$ @TNT	$133 \pm 16$	$955 \pm 42$
2M- $\text{TiCl}_4$ @TNT	$141 \pm 15$	$963 \pm 50$
3M- $\text{TiCl}_4$ @TNT	$150 \pm 18$	$967 \pm 53$

The Raman spectra of the TNT materials modified with M- $\text{TiCl}_4$  are shown in Figure 7. All spectra present the five characteristic peaks of anatase titania located at 144, 197, 399, 516, and 639  $\text{cm}^{-1}$ , which correspond to the active  $E_{g(1)}$ ,  $E_{g(2)}$ ,  $B_{1g}$ ,  $A_{1g} + B_{1g}$ , and  $E_{g(3)}$  vibrational modes, respectively. The additional peak at 720  $\text{cm}^{-1}$  in the recorded spectra for 1M- $\text{TiCl}_4$ @TNT, 2M- $\text{TiCl}_4$ @TNT, and 3M- $\text{TiCl}_4$ @TNT results from  $\text{Ti}_3\text{C}_2\text{T}_x$  that was also loaded in the tubular nanostructure. In comparison to TNT and  $\text{TiCl}_4$ @TNT samples, the spectra of the TNTs modified with M- $\text{TiCl}_4$  exhibit a pronounced peak at 197  $\text{cm}^{-1}$ . This can result from the contribution of the signal at 201  $\text{cm}^{-1}$  present in the Raman spectrum of  $\text{Ti}_3\text{C}_2\text{T}_x$  MXene. As shown in Figure 7b,

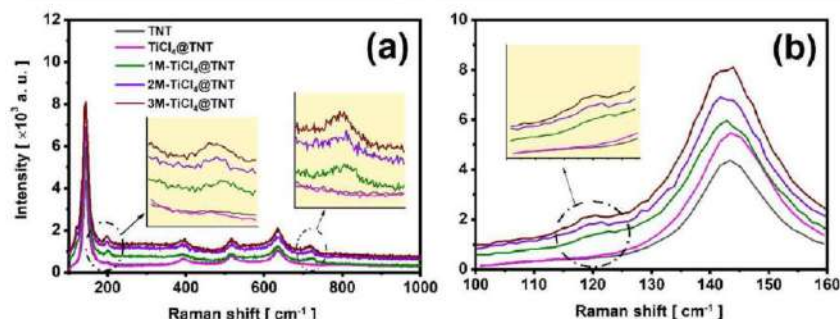


Figure 7. (a) Raman spectra recorded for bare TNTs,  $\text{TiCl}_4$ @TNT,  $1\text{M-TiCl}_4$ @TNT,  $2\text{M-TiCl}_4$ @TNT, and  $3\text{M-TiCl}_4$ @TNT. (b) Magnification of the Raman spectra in the wavenumber at ca.  $144\text{ cm}^{-1}$ .

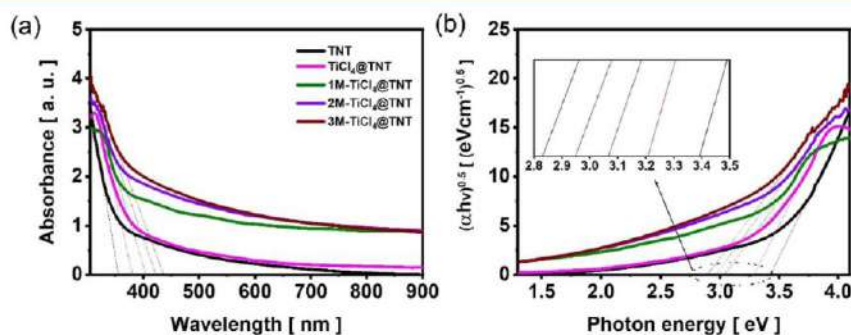


Figure 8. (a) Absorbance spectra of TNT,  $\text{TiCl}_4$ @TNT,  $1\text{M-TiCl}_4$ @TNT,  $2\text{M-TiCl}_4$ @TNT, and  $3\text{M-TiCl}_4$ @TNT. (b) Tauc plots of the prepared samples.

the resonant peak at  $120\text{ cm}^{-1}$  of  $\text{Ti}_3\text{C}_2\text{T}_x$  is visible in the spectra of all TNTs modified with  $\text{M-TiCl}_4$ .

The absorbance spectra of the prepared materials are presented in Figure 8. As is typical for titania material, TNTs absorb mostly in the UV range due to the wide band gap. After titania treatment with  $\text{TiCl}_4$  solution, the absorption edge shifts from 365 to 383 nm, but still mostly ultraviolet light is absorbed. The improvement in the absorption properties of the tubular layer can be attributed to the increase of the wall thickness of titania nanotubes as can be observed in the SEM images (Figure 6).<sup>91,92</sup> The absorption edges have shifted even above 400 nm after the modification of the nanotubes when  $\text{TiCl}_4$  laser-treated MXene material was used. Moreover, the absorption intensity in the visible range of the samples treated with  $\text{M-TiCl}_4$  is relatively higher with respect to those of TNT and  $\text{TiCl}_4$ @TNT samples. Similar results have been reported by both Lemos et al.<sup>37</sup> and Zheng et al.<sup>26</sup> when investigating the absorption properties of the  $\text{TiO}_2/\text{Ti}_3\text{C}_2\text{T}_x$  heterojunction. This increase in the photon-harvesting capability results from the fact that the part of the incident radiation that is absorbed by  $\text{Ti}_3\text{C}_2\text{T}_x$  is then trapped in the tubular nanostructure. This shift in absorption edges toward longer wavelengths is an indicator of narrower band gaps for all modified materials as compared to TNT and  $\text{TiCl}_4$ @TNT samples.

The calculated band gap energy values were found to be 3.39, 3.26, 3.06, 2.95, and 2.82 eV for TNT,  $\text{TiCl}_4$ @TNT,  $1\text{M-TiCl}_4$ @TNT,  $2\text{M-TiCl}_4$ @TNT, and  $3\text{M-TiCl}_4$ @TNT samples, respectively.

The presence of  $\text{Ti}^{3+}$  donor states in the synthesized  $\text{TiO}_2/\text{Ti}_3\text{C}_2\text{T}_x$  heterostructure (Figure 4b) can effectively explain the narrowing of the band gap.<sup>93,94</sup>

Figure 9 shows the photoluminescence (PL) spectra of the prepared samples. PL measurements were performed to provide information about the rate of electron–hole recombination in the prepared semiconductor materials. Electrons are excited from lower energy levels to the upper energy levels with an excitation wavelength of 365 nm, and the PL spectrum is recorded within the wavelength range of 400–750 nm. These electrons excited into the higher energy levels will then get de-excited to different lower energy levels (where the transition probability is allowed) and recombine with holes. Those transitions are detected in the photoluminescence spectrum of the semiconductor owing to the fitting analysis, indicating the presence of several peaks corresponding to different energy level transitions.<sup>95</sup>

Since the intensity of the photoluminescence peak is proportional to the rate of the radiative electron–hole recombination, one can describe in detail the fate of photogenerated charges. As shown in the Figure 9, all modified tubular layers with  $\text{TiO}_2$  sphere/ $\text{Ti}_3\text{C}_2\text{T}_x$  exhibit a broad PL spectrum with lower signal intensities in comparison to bare TNT and  $\text{TiCl}_4$ @TNT samples. This shows that the modification of the titania by the  $\text{TiO}_2/\text{Ti}_3\text{C}_2\text{T}_x$  hetero-



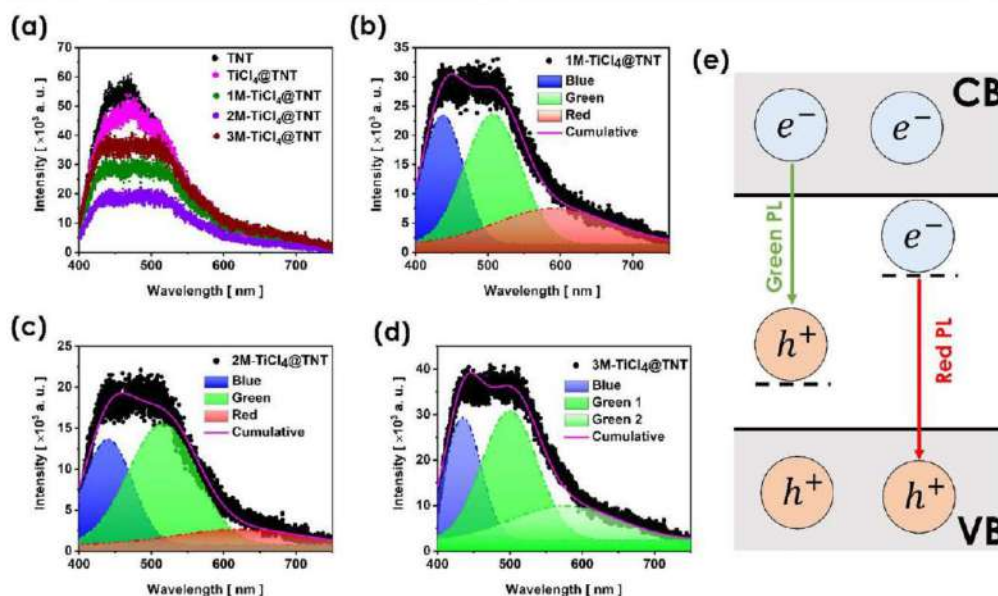


Figure 9. Photoluminescence of the (a) as-prepared samples. Deconvoluted photoluminescence spectra of (b) 1M-TiCl<sub>4</sub>@TNT, (c) 2M-TiCl<sub>4</sub>@TNT, and (d) 3M-TiCl<sub>4</sub>@TNT. (e) Photoluminescence mechanism for green emission (i.e., band in the range from 435 to 600 nm) and red emission (i.e., band in the range from 600 to 750 nm).

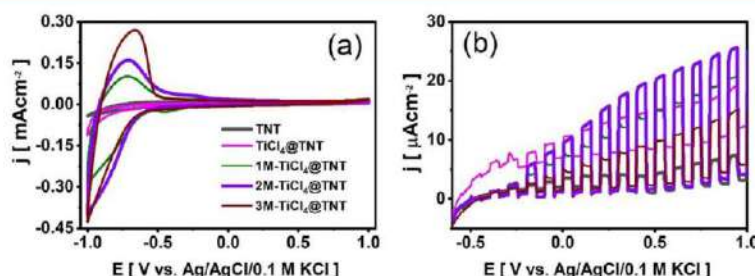


Figure 10. (a) Cyclic voltammetry curves and (b) linear sweep voltammetry in chopped UV-vis light (light/dark changes every 5 s) recorded for TNT, TiCl<sub>4</sub>@TNT, 1M-TiCl<sub>4</sub>@TNT, 2M-TiCl<sub>4</sub>@TNT, and 3M-TiCl<sub>4</sub>@TNT in 0.5 M Na<sub>2</sub>SO<sub>4</sub>.

structure inhibits the radiative recombination of electron–hole pairs. The PL spectra were fitted with a Gaussian function, and the goodness of the fit is 0.99. The fitting parameters are summarized in Table S1. The deconvoluted spectra for both TNT and TiCl<sub>4</sub>@TNT are presented in Figure S3. The band in the range from 435 to 500 nm, with a maximum at 450 nm (TNT), 448 nm (TiCl<sub>4</sub>@TNT), 440 nm (1M-TiCl<sub>4</sub>@TNT), 441 nm (2M-TiCl<sub>4</sub>@TNT), and 437 nm (3M-TiCl<sub>4</sub>@TNT) is attributed to the radiative recombination in the shallow trap levels near the band edges.<sup>96</sup> The other band in the range from 500 to 600 nm, with a maximum at 511 nm (TNT), 513 nm (TiCl<sub>4</sub>@TNT), 506 nm (1M-TiCl<sub>4</sub>@TNT), 515 nm (2M-TiCl<sub>4</sub>@TNT), and 501 nm (3M-TiCl<sub>4</sub>@TNT) is ascribed to the radiative recombination of electrons with trapped holes ( $e^-_{CB} + h^+_{trapped} \rightarrow h\nu$ ).<sup>97</sup> As shown in Figure 9, among other materials only the spectra recorded for 1M-TiCl<sub>4</sub>@TNT (part

b) and 2M-TiCl<sub>4</sub>@TNT (part c) samples exhibit a band, with a maximum at 601 nm (1M-TiCl<sub>4</sub>@TNT) and at 620 nm (2M-TiCl<sub>4</sub>@TNT). This band results from the radiative recombination of trapped electrons present on the Ti<sup>3+</sup> or Ti<sup>4+</sup> sites (below the conduction bands) with holes in the valence band ( $e^-_{CB} + h^+_{trapped} \rightarrow h\nu$ ).<sup>97</sup>

The electrochemical performance of the prepared electrodes was tested at the beginning via cyclic voltammetry measurements performed in 0.5 M Na<sub>2</sub>SO<sub>4</sub> electrolyte. 1M-TiCl<sub>4</sub>@TNT, 2M-TiCl<sub>4</sub>@TNT, and 3M-TiCl<sub>4</sub>@TNT electrodes exhibit significantly larger CV loops with respect to TNT and TiCl<sub>4</sub>@TNT samples (Figure 10a). This can be explained by the significant increase of the density of surface functional groups of the loaded TiO<sub>2</sub>/Ti<sub>3</sub>C<sub>2</sub>T<sub>x</sub> on the TNTs, i.e., increased abundance of –OH termination as confirmed by XPS (O 1s spectrum, Figure 4f). The improvement of the



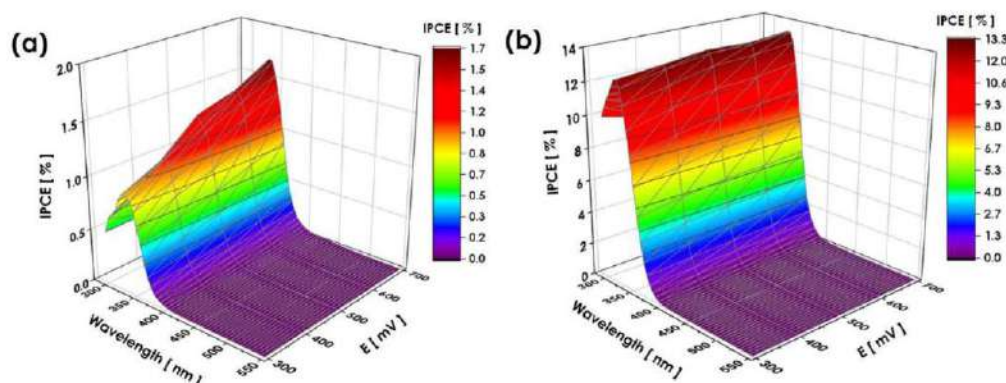


Figure 11. IPCE 3D maps recorded for (a) TNTs and (b) 2M-TiCl<sub>4</sub>@TNT in 0.5 M Na<sub>2</sub>SO<sub>4</sub>.

electrochemical activity of TiO<sub>2</sub>/Ti<sub>3</sub>C<sub>2</sub>T<sub>x</sub> material by the –OH surface termination groups is explained as follows: The higher content of hydrophilic –OH groups increases the ability of the aqueous electrolyte to infiltrate through the porous active material, which facilitates the ion transport across the tubular oxide layer during the electrochemical process. As a result, more active sites are exposed for the electrolyte penetration.<sup>98,99</sup> In that way more Na<sup>+</sup> cations can be intercalated as well into the interlayer spacing of MXenes, thereby increasing the current density. The reduction observed at the cathodic limit can be associated with the reduction of different titanium states: Ti<sup>4+</sup> + e<sup>−</sup> → Ti<sup>3+</sup> and Ti<sup>3+</sup> + e<sup>−</sup> → Ti<sup>2+</sup>, detected by XPS measurements, with concomitant hydrogen evolution from water in the electrolyte.

The photoresponse of the electrodes was investigated by linear sweep voltammetry measurements under chopped UV–vis light. The photocurrent density ( $\Delta j$ ) is determined as the difference between current density recorded under light and in the dark when samples were polarized at +0.5 V vs Ag | AgCl | 0.1 M KCl (Figure 10b). The photocurrent densities of the samples are found to be 4.0, 6.4, 14.0, 19.7, and 9.1  $\mu\text{A cm}^{-2}$  for TNT, TiCl<sub>4</sub>@TNT, 1M-TiCl<sub>4</sub>@TNT, 2M-TiCl<sub>4</sub>@TNT, and 3M-TiCl<sub>4</sub>@TNT samples, respectively. As discussed by Javed et al.<sup>90</sup> and Charoensirithavorn et al.,<sup>91</sup> the increase of the photocurrent density after the modification of TNTs by TiCl<sub>4</sub> can be explained by both the increase of the active surface area (Figure 6) and the generation of TiO<sub>2</sub> nanoparticles over the upper surface of the nanotubes depending on the concentration of the TiCl<sub>4</sub> solution. In comparison to both TNT and TiCl<sub>4</sub>@TNT samples, further increase in the photocurrent density was noted for all tubular layers modified with M-TiCl<sub>4</sub>. This can be ascribed to both the low electron–hole recombination rate (as discussed in PL analysis) and the smaller band gaps of 1M-TiCl<sub>4</sub>@TNT, 2M-TiCl<sub>4</sub>@TNT, and 3M-TiCl<sub>4</sub>@TNT samples. 2M-TiCl<sub>4</sub>@TNT presents the best photoactivity, with a photocurrent density approximately 5 times higher than that of the TNT sample. This increase in the photocurrent density can be also attributed to the improvement of the separation efficiency of the photogenerated electron–hole pairs due to the good conductivity of Ti<sub>3</sub>C<sub>2</sub>T<sub>x</sub> from the TiO<sub>2</sub>/Ti<sub>3</sub>C<sub>2</sub>T<sub>x</sub> heterostructure present in the tubular layers that promotes the electron transport in the tubular layer. The induced electron–

hole pair separation mechanism in the TiO<sub>2</sub>/Ti<sub>3</sub>C<sub>2</sub>T<sub>x</sub> heterojunction has been discussed by both Hieu et al.<sup>100</sup> and Li et al.<sup>101</sup> In our case, it is worth noting that TNTs consist of TiO<sub>2</sub> in a tubular arrangement so the tubular layer (i.e., TNT + TiO<sub>2</sub>/Ti<sub>3</sub>C<sub>2</sub>T<sub>x</sub>) is only composed of TiO<sub>2</sub>/Ti<sub>3</sub>C<sub>2</sub>T<sub>x</sub> material. Briefly, under light illumination of TiO<sub>2</sub>/Ti<sub>3</sub>C<sub>2</sub>T<sub>x</sub>, the photoexcited electrons in the TiO<sub>2</sub> conduction band rapidly migrate to the energy levels of Ti<sub>3</sub>C<sub>2</sub>T<sub>x</sub> due to its semimetallic properties (high conductivity).<sup>100,101</sup> Ti<sub>3</sub>C<sub>2</sub>T<sub>x</sub> acts as an electron sink and prevents the recombination of photo-generated electron–hole pairs.<sup>100,101</sup> This improves the electron–hole pair separation in the TiO<sub>2</sub> material.<sup>100,101</sup> In addition, as discussed by Lemos et al.,<sup>37</sup> the good conductivity of Ti<sub>3</sub>C<sub>2</sub>T<sub>x</sub> can also facilitate the electron transportation in the tubular layer toward the current collector. It is also possible that TiO<sub>2</sub> spheres/Ti<sub>3</sub>C<sub>2</sub>T<sub>x</sub> used as decorating agent for the modification of the tubular layers induced impurity levels with relatively high donor density within the structure of the final product after the modification. These donors contribute to the improvement of the overall conductivity of the modified materials. This is discussed below where the Mott–Schottky analysis will be presented. The photocurrent densities already reported for TiO<sub>2</sub>/Ti<sub>3</sub>C<sub>2</sub>T<sub>x</sub> or TiO<sub>2</sub>/C heterojunctions obtained by oxidation of Ti<sub>3</sub>C<sub>2</sub>T<sub>x</sub> using techniques other than laser treatment are presented in Table S2.

For more detailed inspection of the photoresponse, 3D maps of the IPCE of the fabricated heterojunction were recorded. The IPCE measurements for TNT and 2M-TiCl<sub>4</sub>@TNT samples are presented in Figure 11. The recorded maps for TiCl<sub>4</sub>@TNT, 1M-TiCl<sub>4</sub>@TNT, and 3M-TiCl<sub>4</sub>@TNT are shown in the Supporting Information in Figures S4–S6. The IPCE of the TNT (1.7%) is comparable to the value reported by Kathirvel et al.<sup>2</sup> (1.90%) for 2  $\mu\text{m}$ -thick an aligned titania nanotubes layer grown by anodic oxidation of Ti film deposited onto fluorine-doped tin oxide. However, this value is low compared to the value reported by Valota et al.<sup>102</sup> (5.2%) for the tubular layer grown by galvanostatic anodization of a Ti film deposited onto fluorine-doped tin oxide. It should be noted here that the IPCE values reported by both Valota et al.<sup>102</sup> and Kathirvel et al.<sup>2</sup> were measured with TNT loaded with N719 dye. Since the dye in such an arrangement is mainly responsible for light absorption, the measured IPCE value reflects the overall performance of both TNTs and N719 dye

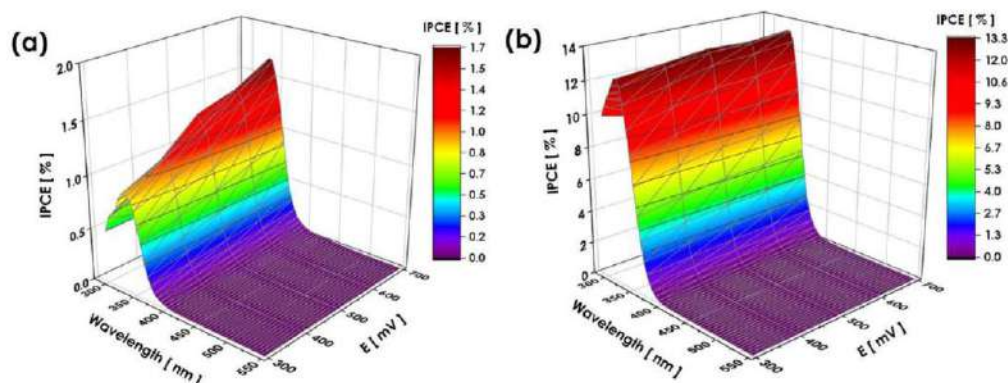


Figure 11. IPCE 3D maps recorded for (a) TNTs and (b) 2M-TiCl<sub>4</sub>@TNT in 0.5 M Na<sub>2</sub>SO<sub>4</sub>.

electrochemical activity of TiO<sub>2</sub>/Ti<sub>3</sub>C<sub>2</sub>T<sub>x</sub> material by the –OH surface termination groups is explained as follows: The higher content of hydrophilic –OH groups increases the ability of the aqueous electrolyte to infiltrate through the porous active material, which facilitates the ion transport across the tubular oxide layer during the electrochemical process. As a result, more active sites are exposed for the electrolyte penetration.<sup>98,99</sup> In that way more Na<sup>+</sup> cations can be intercalated as well into the interlayer spacing of MXenes, thereby increasing the current density. The reduction observed at the cathodic limit can be associated with the reduction of different titanium states: Ti<sup>4+</sup> + e<sup>−</sup> → Ti<sup>3+</sup> and Ti<sup>3+</sup> + e<sup>−</sup> → Ti<sup>2+</sup>, detected by XPS measurements, with concomitant hydrogen evolution from water in the electrolyte.

The photoresponse of the electrodes was investigated by linear sweep voltammetry measurements under chopped UV–vis light. The photocurrent density ( $\Delta j$ ) is determined as the difference between current density recorded under light and in the dark when samples were polarized at +0.5 V vs Ag | AgCl | 0.1 M KCl (Figure 10b). The photocurrent densities of the samples are found to be 4.0, 6.4, 14.0, 19.7, and 9.1  $\mu\text{A cm}^{-2}$  for TNT, TiCl<sub>4</sub>@TNT, 1M-TiCl<sub>4</sub>@TNT, 2M-TiCl<sub>4</sub>@TNT, and 3M-TiCl<sub>4</sub>@TNT samples, respectively. As discussed by Javed et al.<sup>90</sup> and Charoensirithavorn et al.,<sup>91</sup> the increase of the photocurrent density after the modification of TNTs by TiCl<sub>4</sub> can be explained by both the increase of the active surface area (Figure 6) and the generation of TiO<sub>2</sub> nanoparticles over the upper surface of the nanotubes depending on the concentration of the TiCl<sub>4</sub> solution. In comparison to both TNT and TiCl<sub>4</sub>@TNT samples, further increase in the photocurrent density was noted for all tubular layers modified with M-TiCl<sub>4</sub>. This can be ascribed to both the low electron–hole recombination rate (as discussed in PL analysis) and the smaller band gaps of 1M-TiCl<sub>4</sub>@TNT, 2M-TiCl<sub>4</sub>@TNT, and 3M-TiCl<sub>4</sub>@TNT samples. 2M-TiCl<sub>4</sub>@TNT presents the best photoactivity, with a photocurrent density approximately 5 times higher than that of the TNT sample. This increase in the photocurrent density can be also attributed to the improvement of the separation efficiency of the photogenerated electron–hole pairs due to the good conductivity of Ti<sub>3</sub>C<sub>2</sub>T<sub>x</sub> from the TiO<sub>2</sub>/Ti<sub>3</sub>C<sub>2</sub>T<sub>x</sub> heterostructure present in the tubular layers that promotes the electron transport in the tubular layer. The induced electron–

hole pair separation mechanism in the TiO<sub>2</sub>/Ti<sub>3</sub>C<sub>2</sub>T<sub>x</sub> heterojunction has been discussed by both Hieu et al.<sup>100</sup> and Li et al.<sup>101</sup> In our case, it is worth noting that TNTs consist of TiO<sub>2</sub> in a tubular arrangement so the tubular layer (i.e., TNT + TiO<sub>2</sub>/Ti<sub>3</sub>C<sub>2</sub>T<sub>x</sub>) is only composed of TiO<sub>2</sub>/Ti<sub>3</sub>C<sub>2</sub>T<sub>x</sub> material. Briefly, under light illumination of TiO<sub>2</sub>/Ti<sub>3</sub>C<sub>2</sub>T<sub>x</sub>, the photoexcited electrons in the TiO<sub>2</sub> conduction band rapidly migrate to the energy levels of Ti<sub>3</sub>C<sub>2</sub>T<sub>x</sub> due to its semimetallic properties (high conductivity).<sup>100,101</sup> Ti<sub>3</sub>C<sub>2</sub>T<sub>x</sub> acts as an electron sink and prevents the recombination of photo-generated electron–hole pairs.<sup>100,101</sup> This improves the electron–hole pair separation in the TiO<sub>2</sub> material.<sup>100,101</sup> In addition, as discussed by Lemos et al.,<sup>37</sup> the good conductivity of Ti<sub>3</sub>C<sub>2</sub>T<sub>x</sub> can also facilitate the electron transportation in the tubular layer toward the current collector. It is also possible that TiO<sub>2</sub> spheres/Ti<sub>3</sub>C<sub>2</sub>T<sub>x</sub> used as decorating agent for the modification of the tubular layers induced impurity levels with relatively high donor density within the structure of the final product after the modification. These donors contribute to the improvement of the overall conductivity of the modified materials. This is discussed below where the Mott–Schottky analysis will be presented. The photocurrent densities already reported for TiO<sub>2</sub>/Ti<sub>3</sub>C<sub>2</sub>T<sub>x</sub> or TiO<sub>2</sub>/C heterojunctions obtained by oxidation of Ti<sub>3</sub>C<sub>2</sub>T<sub>x</sub> using techniques other than laser treatment are presented in Table S2.

For more detailed inspection of the photoresponse, 3D maps of the IPCE of the fabricated heterojunction were recorded. The IPCE measurements for TNT and 2M-TiCl<sub>4</sub>@TNT samples are presented in Figure 11. The recorded maps for TiCl<sub>4</sub>@TNT, 1M-TiCl<sub>4</sub>@TNT, and 3M-TiCl<sub>4</sub>@TNT are shown in the Supporting Information in Figures S4–S6. The IPCE of the TNT (1.7%) is comparable to the value reported by Kathirvel et al.<sup>2</sup> (1.90%) for 2  $\mu\text{m}$ -thick an aligned titania nanotubes layer grown by anodic oxidation of Ti film deposited onto fluorine-doped tin oxide. However, this value is low compared to the value reported by Valota et al.<sup>102</sup> (5.2%) for the tubular layer grown by galvanostatic anodization of a Ti film deposited onto fluorine-doped tin oxide. It should be noted here that the IPCE values reported by both Valota et al.<sup>102</sup> and Kathirvel et al.<sup>2</sup> were measured with TNT loaded with N719 dye. Since the dye in such an arrangement is mainly responsible for light absorption, the measured IPCE value reflects the overall performance of both TNTs and N719 dye



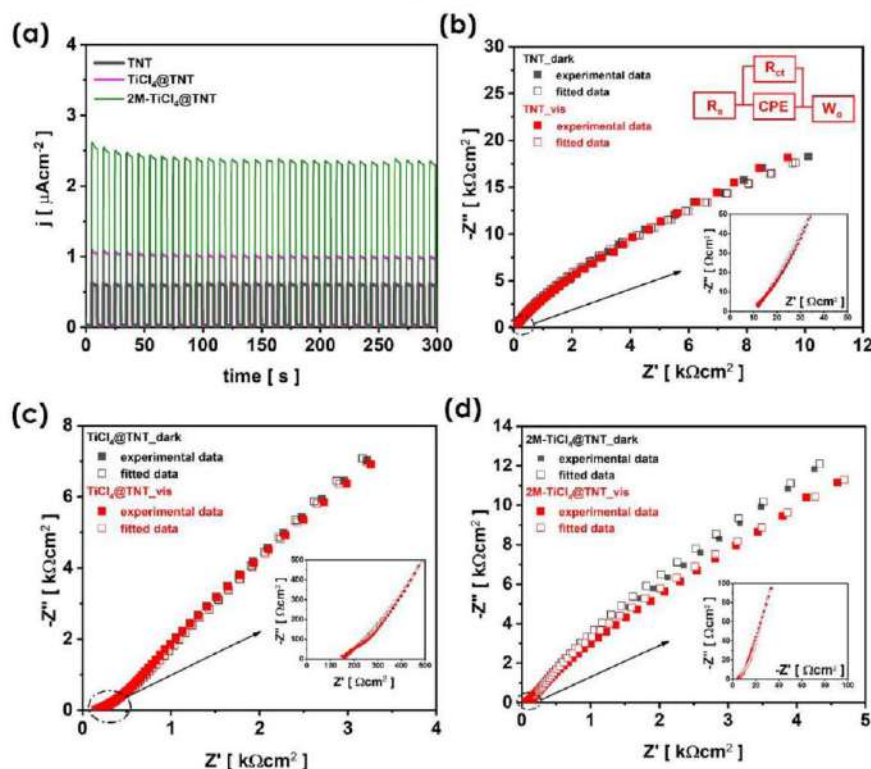


Figure 12. (a) Transient photocurrent curves recorded at +0.5 V vs Ag/AgCl/0.1 M KCl (visible light/dark every 5 s) of TNT,  $\text{TiCl}_4$ @TNT, and  $2\text{M-TiCl}_4$ @TNT. Nyquist plots of EIS measurements of (b) TNTs, (c)  $\text{TiCl}_4$ @TNT, and (d)  $2\text{M-TiCl}_4$ @TNT in the dark and under visible light illumination (Inset: equivalent circuit used to fit the experimental impedance spectra recorded in the dark and under visible light).

(i.e., not only the tubular layer). In this study, the IPCE measurements were carried out with samples without any adsorbed dye. The modification of TNTs with  $\text{M-TiCl}_4$  allowed an order of magnitude increase in the IPCE for  $1\text{M-TiCl}_4$ @TNT (10.75%) and  $2\text{M-TiCl}_4$ @TNT (13.30%) samples. Figure S7 shows that  $2\text{M-TiCl}_4$ @TNT exhibits higher conversion efficiency above 400 nm with respect to TNTs and  $\text{TiCl}_4$ @TNT.

Equation 3 indicates that the IPCE value increases with increasing both the light-harvesting efficiency  $\eta_{\text{LH}}$  and the charge separation efficiency  $\eta_{\text{SP}}$  of the semiconductor. The light-harvesting efficiency provides information regarding the fraction of light intensity absorbed by the materials. The absorption spectra recorded for the synthesized samples (Figure 7) have revealed higher ability to absorb light in the UV–vis range for  $1\text{M-TiCl}_4$ @TNT,  $2\text{M-TiCl}_4$ @TNT, and  $3\text{M-TiCl}_4$ @TNT samples as compared to TNTs and  $\text{TiCl}_4$ @TNT. This can indicate better photoactivity of the material due to the modification with  $\text{TiO}_2$  sphere/ $\text{Ti}_3\text{C}_2\text{T}_x$  heterojunction. In addition, the photoluminescence analysis (Figure 9) has revealed low radiative electron–hole recombination for all tubular layers after the modification with the  $\text{TiO}_2$  sphere/

$\text{Ti}_3\text{C}_2\text{T}_x$  heterojunction. Those data justified the higher IPCE values recorded for  $1\text{M-TiCl}_4$ @TNT,  $2\text{M-TiCl}_4$ @TNT, and  $3\text{M-TiCl}_4$ @TNT. The charge transfer resistance ( $R_{ct}$ ) of the samples was further investigated by means of impedance spectroscopy measurements, as presented in the next section.

To study the photoresponse and the charge-transfer properties at the semiconductor/electrolyte interfaces, the samples were investigated under visible light by chronoamperometry and electrochemical impedance spectroscopy techniques. The  $2\text{M-TiCl}_4$ @TNT sample shows a relatively high photocurrent of about  $2.5 \mu\text{A cm}^{-2}$ , without significant decay over 300 s in comparison to TNTs and  $\text{TiCl}_4$ @TNT (Figure 12). The Nyquist plots recorded for TNTs,  $\text{TiCl}_4$ @TNT, and  $2\text{M-TiCl}_4$ @TNT are shown in Figure 12 (the plots for  $1\text{M-TiCl}_4$ @TNT and  $3\text{M-TiCl}_4$ @TNT are provided in Figure S8). The proposed electrical equivalent circuit used for the modeling of the EIS data is shown in Figure 12b (inset), and the goodness of the fit ( $\chi^2$ ) is of the order of  $10^{-3}$ – $10^{-4}$ . This equivalent circuit is composed of a series resistance ( $R_s$ ) corresponding the bulk resistance taking into account the intrinsic resistance of the tubular layer, the contact resistance at the TNT layer and the current collector (ITO), and the

electrolyte resistance; a charge transfer resistance at the semiconductor/electrolyte interface ( $R_{ct}$ ); a constant phase element (CPE) corresponding to the ability of storing ions at the semiconductor/electrolyte interface; and an open Warburg element ( $W_o$ ) characterizing the diffusion of ions from the electrolyte into the TNT layer. The CPE element is used instead of pure capacitance due to the surface roughness of the electrode material. Table S2 presents the fitting parameters obtained for all prepared electrodes. For all samples the series resistance is not sensitive to the UV–vis light. In the dark, except 3M-TiCl<sub>4</sub>@TNT the modification of the TNT with M-TiCl<sub>4</sub> led to a decrease in the charge transfer resistance. The drop in the  $R_{ct}$  under visible light is depicted in Table 2. The results show that 2M-TiCl<sub>4</sub>@TNT exhibits good photo-sensitivity in visible light in comparison to TNT and TiCl<sub>4</sub>@TNT samples.

**Table 2. Drop in the Charge Transfer Resistance<sup>a</sup> of the Samples under Visible Light**

sample	decrease in $R_{ct}$ [%]
TNT	5.0
TiCl <sub>4</sub> @TNT	6.3
1M-TiCl <sub>4</sub> @TNT	10.9
2M-TiCl <sub>4</sub> @TNT	32.2
3M-TiCl <sub>4</sub> @TNT	28.9

$$\frac{\alpha R_{ct}(\text{dark}) - R_{ct}(\text{vis})}{R_{ct}(\text{dark})} \times 100$$

The electron transport properties of the prepared samples were further investigated by intensity-modulated photocurrent spectroscopy measurements. Figure S9 shows the IMPS Nyquist plots of the photoelectrodes, where  $Q'$  and  $Q''$  represent the real and imaginary part of the  $Q$  function (current). Compared to the TNT and TiCl<sub>4</sub>@TNT samples, the curves of all tubular oxide layers modified with TiO<sub>2</sub>/Ti<sub>3</sub>C<sub>2</sub>T<sub>x</sub> are composed of two clearly visible semicircles. The presence of two semicircles indicates transport of electrons with two different diffusion modes, namely, the semicircle located in the low-frequency region (below 10 Hz) is associated with the trap limited transport mode near the surface of the material, while the other semicircle present in the high-frequency region (above 100 Hz) corresponds to the trap-free transport mode at the core.<sup>103–105</sup> Two semicircles in the IMPS Nyquist plot were also obtained by Chen et al.<sup>103</sup> after introducing oxygen vacancies in titania. As already discussed by Chen et al.,<sup>103</sup> the trap-free transport mode at the core indicates the presence of sub-band levels in the electronic band structure of the materials.<sup>103</sup> As shown in Figure 13, regardless of the amount of TiO<sub>2</sub>/Ti<sub>3</sub>C<sub>2</sub>T<sub>x</sub> loaded into the tubular layers, the value of the minimum frequency of the semicircle in the highest-frequency region remains unchanged and corresponds to an electron transport time ( $\frac{1}{2\pi f_{\min}}$ ) of 864  $\mu$ s. Since this

mode of electron transport occurs at the core of the materials and was only observed for all oxide layers modified with M-TiCl<sub>4</sub> it can be interpreted as the electrons transfer at the TiO<sub>2</sub>/Ti<sub>3</sub>C<sub>2</sub>T<sub>x</sub> interface.

Mott–Schottky plots of all prepared samples are presented in Figures S10–S14. The Mott–Schottky plots of 1M-TiCl<sub>4</sub>@TNT and 2M-TiCl<sub>4</sub>@TNT samples present two distinct linear regions, indicating the presence of both shallow and deep energy levels.<sup>106</sup> In general, the main reasons for the appearance of two linear regions in Mott–Schottky plots are

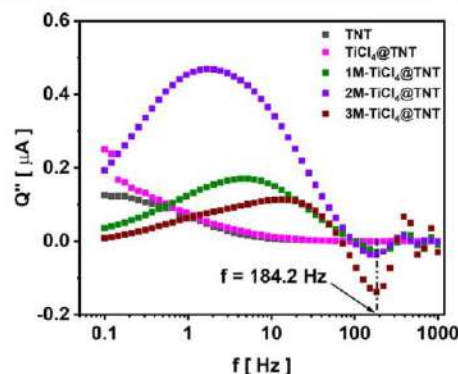


**Figure 13.** Plot of the imaginary part of the  $Q$  function versus irradiation frequency.

(i) the presence of surface states, (ii) the inhomogeneous donor distribution, and (iii) the presence of a second donor level in the band gap.<sup>107</sup> The flat band potentials ( $V_{fb}$ ) and the donor densities calculated from the slopes of the linear regions are shown in Table 3. Taking into account the smaller band

**Table 3. Flat Band Potential ( $V_{fb}$ ) and Donor Concentration ( $N_D$ ) of the Samples**

sample	$V_{fb}/V$ vs Ag/AgCl/0.1 M KCl	$N_D/\times 10^{20} \text{ cm}^{-3}$	$V_{fb}/V$ vs Ag/AgCl/0.1 M KCl	$N_D/\times 10^{20} \text{ cm}^{-3}$
TNT	−0.54	0.7	no slope	
TiCl <sub>4</sub> @TNT	−0.65	1.1	no slope	
1M-TiCl <sub>4</sub> @TNT	−0.78	2.5	−0.48	0.9
2M-TiCl <sub>4</sub> @TNT	−0.85	3.2	−0.6	1.7
3M-TiCl <sub>4</sub> @TNT	−0.75	2.8	no slope	

gaps of the 1M-TiCl<sub>4</sub>@TNT, 2M-TiCl<sub>4</sub>@TNT, and 3M-TiCl<sub>4</sub>@TNT materials, in our case the presence of a second donor level in the band gaps can effectively explain the two linear regions in the Mott–Schottky plots for 1M-TiCl<sub>4</sub>@TNT and 2M-TiCl<sub>4</sub>@TNT samples. In the case of the 3M-TiCl<sub>4</sub>@TNT sample, the absence of the other slope may be explained by the fact that the second donor level overlaps with the conduction band minimum. The connection between the sub-band levels and the enhancement of the photocurrent density can be explained as follows:

To obtain high photocurrent density, the photoexcited electrons in the conduction band of TiO<sub>2</sub> should be efficiently collected at the ITO acting here as a current collector. In this regard, a strategy to increase the electron–hole separation efficiency and then facilitate charge transfer is of fundamental importance.<sup>108</sup> The donor level detected in the forbidden band plays an essential role in the increase of photoelectron injection in the conduction band of the semiconductor. As shown in Table 3, there is a relatively high donor density in the sub-band levels of the 1M-TiCl<sub>4</sub>@TNT ( $0.9 \times 10^{20} \text{ cm}^{-3}$ ) and



2M-TiCl<sub>4</sub>@TNT ( $1.7 \times 10^{20} \text{ cm}^{-3}$ ) samples. As explained by both Fang et al.<sup>108</sup> and Nishikawa et al.,<sup>109</sup> under illumination not only are electrons in the valence band of TiO<sub>2</sub> injected in the conduction band but also those electrons accumulate in the sub-band level. In comparison to the unmodified semiconductor oxide, i.e., TNTs and TiCl<sub>4</sub>@TNT, which do not have any donor level within the band gap, under light irradiation the conduction bands of 1M-TiCl<sub>4</sub>@TNT and 2M-TiCl<sub>4</sub>@TNT samples gain electrons from two sources, namely, from their valence bands as well as from their sub-band levels (as shown in Figure 14).<sup>108</sup> According to the mechanism

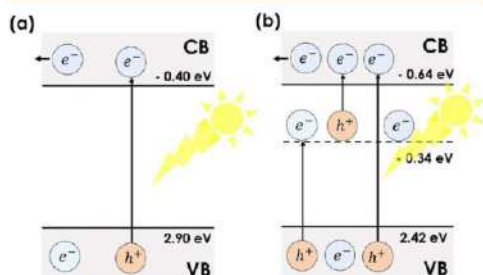


**Figure 14.** Mechanism of the charge separation in TiO<sub>2</sub> (a) without donor level in the band gap and (b) with the presence of donor level in the band gap.

illustrated in Figure 14, more photoelectrons are available in the conduction band of titania that can participate in the interfacial charge transfer toward the current collector. In consequence, we observe an increase in the photocurrent density of the material.

All modified TNTs with M-TiCl<sub>4</sub> exhibit more negative flat band potentials with respect to both TNT and TiCl<sub>4</sub>@TNT samples. The more negative potential is an indicator of larger accumulation of electrons in the heterostructure and reflects a decrease in the rate of recombination of electron–hole pairs.<sup>110,111</sup> As depicted in Table 3, the functionalization of the tubular oxide layer with the TiO<sub>2</sub> sphere/Ti<sub>3</sub>C<sub>2</sub>T<sub>x</sub> has led to the significant increase in the donor density of the photoelectrodes. The high donor density means that more charge carriers are available to participate in the photoelectrochemical and electrochemical processes.<sup>112,113</sup>

However, as shown in Table 3, the flat band potential of the 3M-TiCl<sub>4</sub>@TNT sample is positively shifted in comparison to 1M-TiCl<sub>4</sub>@TNT and 2M-TiCl<sub>4</sub>@TNT. This indicates a decrease in the overall capacitance (i.e., charge carrier) of the sample.<sup>114</sup> In fact, the donor density for 3M-TiCl<sub>4</sub>@TNT ( $2.8 \times 10^{20} \text{ cm}^{-3}$ ) is smaller as compared to 1M-TiCl<sub>4</sub>@TNT ( $2.5 \times 10^{20} \text{ cm}^{-3} + 0.9 \times 10^{20} \text{ cm}^{-3}$ ) and 2M-TiCl<sub>4</sub>@TNT ( $3.2 \times 10^{20} \text{ cm}^{-3} + 1.7 \times 10^{20} \text{ cm}^{-3}$ ) samples. In addition, conducted analysis has revealed that 3M-TiCl<sub>4</sub>@TNT presents high photoluminescence intensity compared to 1M-TiCl<sub>4</sub>@TNT and 2M-TiCl<sub>4</sub>@TNT. This indicates that the electron–hole recombination rate is higher for 3M-TiCl<sub>4</sub>@TNT than for the two other modified samples. The worsened electrical properties, namely, relatively poor electrical conductivity and high radiative electron–hole recombination rate, for 3M-TiCl<sub>4</sub>@TNT compared to 1M-TiCl<sub>4</sub>@TNT and 2M-TiCl<sub>4</sub>@TNT samples can effectively explain the drop in the recorded photocurrent (i.e., for 3M-TiCl<sub>4</sub>@TNT).

### 3. CONCLUSIONS

Laser treatment of Ti<sub>3</sub>C<sub>2</sub>T<sub>x</sub> was proven to be effective in reshaping the material and forming a TiO<sub>2</sub>/Ti<sub>3</sub>C<sub>2</sub>T<sub>x</sub> heterojunction. The resulting TiO<sub>2</sub> on the Ti<sub>3</sub>C<sub>2</sub>T<sub>x</sub> surface exhibited a distinctive spherical morphology with a combination of anatase and rutile phases. Highly ordered titania nanotube layers, which were prepared through anodizing Ti films sputtered onto indium tin oxide, were then modified using a mixture of the synthesized TiO<sub>2</sub>/Ti<sub>3</sub>C<sub>2</sub>T<sub>x</sub> material dispersed in a TiCl<sub>4</sub> solution. Electrode materials obtained that way exhibit narrower band gaps in comparison to bare TNTs as well as an increased photoactivity (5 times for the best sample). This enhanced photoactivity under visible light was attributed to an 11%, 32%, and 29% reduction in charge transfer resistance for 1M-TiCl<sub>4</sub>@TNT, 2M-TiCl<sub>4</sub>@TNT, and 3M-TiCl<sub>4</sub>@TNT, respectively, compared to dark conditions. Moreover, XPS data of postlaser treated TiO<sub>2</sub>/Ti<sub>3</sub>C<sub>2</sub>T<sub>x</sub> revealed the presence of oxidation states, specifically Ti<sup>3+</sup> and Ti<sup>2+</sup> that play a crucial role in increasing the separation of photogenerated electron–hole pairs. The more negative potential for M-TiCl<sub>4</sub>@TNT materials indicates the decrease of recombination rate of electron–hole pairs.

This study highlights the TiO<sub>2</sub>/Ti<sub>3</sub>C<sub>2</sub>T<sub>x</sub> heterojunction as a promising alternative to noble metal-based treatments, improving the light-harvesting performance of semitransparent TNT photoelectrodes.

### 4. EXPERIMENTAL SECTION

**4.1. Materials and Reagents.** Hydrofluoric acid (40%, Chempur), hydrochloric acid (99.7%, Chempur), sodium chloride (Prolab), ammonium fluoride (99.7%, Chempur), sodium sulfate (99.9%, Chempur), diethylene glycol (99.6%, Chempur), Ti<sub>3</sub>AlC<sub>2</sub> MAX powder (>90%, < 40 μm particle size, Sigma-Aldrich), and titanium tetrachloride (Sigma-Aldrich) were used.

**4.2. Synthesis of Ti<sub>3</sub>C<sub>2</sub>T<sub>x</sub> MXene.** Ti<sub>3</sub>AlC<sub>2</sub> powder (1 g) was added to (20 mL) of a mixed solution of HF and HCl in the volumetric ratio (HF:HCl) equal to (1:9) and stirred at 300 rpm for 24 h at 35 °C. The suspension was centrifuged at 3500 rpm for 5 min. The obtained sediment present at the bottom was washed with water until neutral pH was reached and dried under vacuum in a desiccator overnight. The prepared Ti<sub>3</sub>C<sub>2</sub>T<sub>x</sub> MXene multilayer was delaminated with NaCl. The dried Ti<sub>3</sub>C<sub>2</sub>T<sub>x</sub> powder (0.5 g) was stirred in (50 mL) of (0.5 M) NaCl aqueous solution overnight. The dispersed solution was centrifuged at 3500 rpm (MPW-251, MPW MED. INSTRUMENTS) for 5 min, and the material collected at the bottom was redispersed in 20 mL of water. This procedure was repeated for five centrifugation cycles to remove impurities. The sediment at the bottom was collected and dried overnight in a desiccator under vacuum to obtain MXene powder.

**4.3. Laser Treatment of MXene.** The prepared Ti<sub>3</sub>C<sub>2</sub>T<sub>x</sub> powder (40 mg) was dispersed in (1 mL) of deionized water and poured into a (15 mL) glass bottle. The bottle was placed in a cuvette containing liquid nitrogen to freeze the obtained Ti<sub>3</sub>C<sub>2</sub>T<sub>x</sub> suspension. Then (10 mL) of isopropanol was poured on the top of the frozen material (Ti<sub>3</sub>C<sub>2</sub>T<sub>x</sub>). The temperature of the glass bottle was maintained above the freezing point of isopropanol. The solidified water suspension of Ti<sub>3</sub>C<sub>2</sub>T<sub>x</sub> was ablated by a 1064 nm laser (Laser blast 500, Quantel) with an energy density of 2 J cm<sup>-2</sup>, a pulse width of 6 ns, and a pulse repetition of 60 Hz. During the irradiation process, material ablated from the solid phase was trapped in the liquid isopropanol, forming white stable suspension. After 30 min of ablation the dispersed solution above the frozen material was collected and centrifuged at 14000 rpm for 30 min. The obtained sediment was dried overnight in a desiccator under vacuum. Then (8 mg) of the dried powder was dispersed in (15 mL) of deionized water (i.e., 0.53 g L<sup>-1</sup>) and stirred for 15 min to obtain a dispersed solution for further processing.



**4.4. Deposition of ITO.** The first step of TNT electrode fabrication was to deposit transparent and conductive indium tin oxide (ITO) films with a thickness of 100 nm on clean glass slides. This was done in a UHV chamber using radio frequency (RF, 13.56 MHz) magnetron sputtering of an ITO target 76 mm in diameter. The working pressure of the Ar atmosphere was kept at 0.2 Pa with the Ar flow rate of 21 sccm. The magnetron was operated at a constant RF power of 150 W delivered into the discharge with a cathode bias of 140 V. The samples were placed 16 cm from the sputtering gun. To optimize their quality and performance, the deposited ITO films were subsequently annealed at 500 °C for 1 h in air.

**4.5. Deposition of Ti onto ITO.** A Ti target (76 mm in diameter) was used for deposition of Ti films onto ITO by means of DC magnetron sputtering. The working pressure of Ar was set to 0.12 Pa (Ar flow rate 6 sccm) to receive smooth and compact Ti coatings, which is a crucial parameter for successful anodization. The magnetron current was fixed at 600 mA with corresponding power of 224 W. The deposition rate reached at this condition was 45 nm min<sup>-1</sup>. Ar/O<sub>2</sub> radio frequency (RF, 13.56 MHz) plasma with the Ar/O<sub>2</sub> ratio of 3/10 (flow rates) and power of 30 W at the pressure of 3.3 Pa was applied to pre-clean the ITO substrates. The substrates were in this case placed directly on the RF electrode. The 10 min pre-cleaning was followed by deposition of thin 4 nm TiO<sub>2</sub> interlayer which improved the adhesion of the final Ti film. The TiO<sub>2</sub> film was deposited by DC reactive magnetron sputtering at 600 mA in the mixture of Ar and O<sub>2</sub> (3/10 flow rates) and total pressure of 0.5 Pa.

**4.6. Fabrication of Semitransparent Spaced Titania Nanotube Materials.** Anodization was carried out in a two-electrode cell with ITO glass coated with 1 μm thick Ti film and platinum mesh acting as an anode and a cathode, respectively. A thermostat (Julabo F-12, JULABO GmbH) was used to maintain the temperature of the cell at 40 °C, and the anodization was performed in diethylene glycol-based electrolyte mixed with (0.15 M) NH<sub>4</sub>F, (0.5 M) HF, and (7 vol %) H<sub>2</sub>O at 40 V for 20 min. The sample obtained after anodization was labeled as TNTs.

**4.7. Modification of TNTs with Laser-Treated MXene.** *x* μL (*x* = 100, 200, and 300 μL) of the dispersed laser-treated MXene particles was mixed in (25 mL) of (0.1 M) TiCl<sub>4</sub> (TiCl<sub>4</sub> was dispersed in water) and stored in an ice bath. The resultant solution was labeled as M-TiCl<sub>4</sub> to make the name of the samples more concise. The TNT electrode was placed in a beaker, and (5 mL) of M-TiCl<sub>4</sub> was poured on the top of the tubular layer. Then, the beaker was left to rest for 30 min on a hot plate (CAT H 17.5) at 100 °C. This process allows the infiltration of the laser-treated MXene particles through the nanotube layer, and at the same time it leads to the widening of the tube walls. Afterward, the electrode was rinsed with deionized water to remove the excess of the nonadsorbed species. The first cycle included the steps from the immersion in M-TiCl<sub>4</sub> solution to the rinsing with the deionized water. This procedure was repeated 5 times, and for each cycle (5 mL) of M-TiCl<sub>4</sub> solution was used. The electrodes were labeled 1M-TiCl<sub>4</sub>@TNT, 2M-TiCl<sub>4</sub>@TNT and 3M-TiCl<sub>4</sub>@TNT for (100 μL), (200 μL) and (300 μL) of M-TiCl<sub>4</sub> solution, respectively. For comparison, a pristine TNT layer and TNTs modified only with 0.1 M TiCl<sub>4</sub> (TiCl<sub>4</sub>@TNT), using the same above protocol, were fabricated as well. Then all the obtained materials were annealed in air at 450 °C for an hour in a tubular furnace (RI20/1000/12-P330, Nabertherm GmbH) with a thermal ramp of 2 °C min<sup>-1</sup>.

**4.8. Characterization Methods.** Transmission electron microscopy (TEM) pictures were obtained using an ARM 200F instrument (JEOL, 200 eV) equipped with an energy-dispersive X-ray spectrometer (EDX).

X-ray photoelectron spectroscopy (XPS) measurements of Ti<sub>2</sub>C<sub>2</sub>T<sub>x</sub> powder before and after the laser treatment were performed using a Thermo Scientific K-Alpha X-ray Photoelectron Spectrometer. The samples were irradiated with low-energy X-ray radiation (Al Kα = 1486.7 eV). Measurements were carried out under pressure of 10<sup>-9</sup> to 10<sup>-8</sup> mbar. Survey spectra were registered using a pass energy of 150 eV and a step size of 1 eV. The equipment was calibrated using C 1s (284.5 eV). In turn, high-resolution spectra were recorded in the

oxygen O 1s, titanium Ti 2p, and carbon C 1s binding energy ranges using a pass energy of 20 eV and step size of 0.1 eV.

Surface morphology of the electrodes was investigated by means of a Quanta FEG 250 (FEI) Schottky field-emission scanning electron microscopy (SEM) instrument equipped with a secondary Everhart-Thornley electron detector with a beam accelerating voltage of 10 kV.

The phase composition of the samples was analyzed by X-ray diffractometer (Bruker D2 Phaser second generation) using Cu Kα radiation and a LynxEye XE-T detector at room temperature.

Raman measurements were carried out at room temperature using a Raman spectrometer (Renishaw) equipped with a 785 nm red diode laser used as the excitation source and operating at 1% of its total power. Raman spectra were registered in the wavenumber range from 100 to 1000 cm<sup>-1</sup> using the 20X objective.

Absorbance measurements were conducted with an ultraviolet-visible (UV-vis) spectrophotometer (PerkinElmer) in the wavelength range of 310–950 nm operating at a scanning speed of 120 nm min<sup>-1</sup>.

Photoluminescence (PL) measurements were carried out at room temperature using a SHAMROCK-SR-3031-A Spectrograph (Andor Technology). The active material is illuminated with a 450 mW LED excitation light source (λ = 365 nm), and an ICCD camera records the fluorescence spectra of the samples within the wavelength range of 400–750 nm. Optical filters, FGUV-11 (Thorlabs) and GG 400 (Schott AG), were used to eliminate undesired light modes during measurements of the PL excitation spectra.

**4.9. Electrochemical and Photoelectrochemical Measurements.** Electrochemical and photoelectrochemical measurements were carried out using (0.5 M) Na<sub>2</sub>SO<sub>4</sub> as an electrolyte. All the electrochemical measurements were carried out using an Autolab PGSTAT302N potentiostat-galvanostat system (Metrohm) in a three-electrode cell with a quartz window. The three-electrode system consisted of a Pt mesh (counter electrode), Ag | AgCl | 0.1 M KCl (reference electrode) and the prepared modified or unmodified TNTs (working electrodes). The electrolyte was purged with argon flow for 30 min before starting the electrochemical tests. During the experiment the argon flow was maintained above the electrolyte. A xenon lamp (Osram XBO 150) equipped with an AM 1.5 filter was used as a light source. The electrochemical cell was equipped with a quartz window enabling the irradiation of the working electrode with the whole solar spectrum. Cyclic voltammetry (CV) was performed in the potential range from -1.0 to +1.0 V at a scan rate of 50 mV s<sup>-1</sup>. Linear sweep voltammetry (LSV) measurements were carried out when the working electrode was exposed to chopped UV-vis light illumination. The scans were recorded at 10 mV s<sup>-1</sup> in the potential range from -0.55 to +1.0 V. Chronoamperometry was performed by recording the photocurrent under chopped visible light irradiation for 300 s. Each light and dark period lasted 5 s, and the access to light was controlled by the automated shutter. The electrochemical impedance spectra (EIS) were recorded in the frequency range from 20 kHz to 0.1 Hz with 10 mV amplitude of the AC signal in the dark and under visible light illumination. The EIS data was fitted with the electric equivalent circuit using an EIS Spectrum Analyzer program. The modified Powell algorithm was used with amplitude weighting *r*<sub>s</sub>:

$$r_s(\omega, P_1, \dots, P_M) = r_c^2 / (N - M) \quad (1)$$

where *N* is the number of points, *M* is the number of parameters, *ω* is the angular frequency, and *P*<sub>1</sub>, ..., *P*<sub>*M*</sub> are parameters. Parameter *r*<sub>c</sub> is defined as

$$r_c^2 = \sum_{i=1}^N \frac{(Z'_i - Z'_{i,calc})^2 + (Z''_i - Z''_{i,calc})^2}{Z'^2_{i,calc} + Z''^2_{i,calc}} \quad (2)$$

Photocurrent action maps were measured with a photoelectric spectrometer for quantum efficiency measurements (Instytut Fotonyki, Poland) equipped with a solar simulator, Czerny–Turner monochromator, and potentiostat. The illumination source was calibrated using the silicon photodiode to calculate light intensities. The wavelength range was set from 300 to 550 nm, and the potential range was from 300 to 700 mV vs Ag | AgCl | 3 M KCl reference

electrode. Measurement points were taken with 5 nm and 100 mV steps.

Basically, for a given wavelength, IPCE( $\lambda$ ) is defined as the ratio of the effective electrons excited ( $\Delta N$ ) by the photons and incident photons ( $\Delta P$ ) of the excitation source, which is given by the following formula:<sup>115</sup>

$$\text{IPCE}(\lambda) = \frac{\Delta N}{\Delta P} = \eta_{\text{LH}} \times \eta_{\text{SP}} \quad (3)$$

where  $\eta_{\text{LH}}$  is the light-harvesting efficiency and  $\eta_{\text{SP}}$  is the charge separation efficiency.<sup>115</sup> It can be rewritten as

$$\text{IPCE}(\lambda) = \frac{j}{P} \hbar \omega \quad (4)$$

where  $j$  is the photocurrent,  $P$  is light intensity, and  $\hbar \omega$  is photon energy.

The intensity-modulated photocurrent spectroscopy (IMPS) measurement was conducted by using electrochemical spectrometer (Instytut Fotonowy, Poland) connected to a 373 nm LED and a potentiostat. An anodic bias voltage of +500 mV with respect to the Ag | AgCl | 3 M KCl reference electrode was applied to the sample, and measurements were recorded in the light frequency range from 1000 to 0.1 Hz. Typically the data are represented either in the form of a  $Q$ -plane plot, which is a plot of the real part of the IMPS transfer function of the negative imaginary part  $-Q''(\omega)$  versus the real part  $Q'(\omega)$ , or in terms of the evolution of  $Q'(\omega)$  versus frequency. Real ( $Q'(\omega)$ ) and imaginary ( $Q''(\omega)$ ) parts of the  $Q$ -function are defined as

$$Q'(\omega) = \frac{\int_0^T I(t) \cos \omega t \, dt}{T} \quad (5)$$

$$Q''(\omega) = \frac{\int_0^T I(t) \sin \omega t \, dt}{T} \quad (6)$$

where  $T$  is a period of the light intensity stimulus and  $I(t)$  is the recorded time-dependent current.

For Mott–Schottky analysis, EIS spectra were recorded in 0.5 M  $\text{Na}_2\text{SO}_4$  at a constant frequency of 1 kHz, in the potential range from +0.1 to  $-1.2$  V Ag/AgCl/0.1 M KCl.

The flat band potential ( $V_{\text{fb}}$ ) and the donor concentration ( $N_{\text{D}}$ ) of a semiconductor can be evaluated based on a Mott–Schottky plot. The Mott–Schottky relation for  $n$ -type semiconductors is given as

$$C^{-2} = \left( \frac{2}{ee\epsilon_0 N_{\text{D}}} \right) \left( V - V_{\text{fb}} - \frac{kT}{e} \right) \quad (7)$$

where  $C$  is the space charge capacitance,  $e$  is the permittivity of the anatase titania ( $\epsilon = 38$ ),<sup>116</sup>  $\epsilon_0$  ( $8.85 \times 10^{-14}$  F  $\text{cm}^{-1}$ ) is the permittivity of free space,  $e$  is the electron charge,  $N_{\text{D}}$  is the donor density,  $V$  is the applied potential,  $V_{\text{fb}}$  is the flat band potential,  $k$  is the Boltzmann constant, and  $T$  is the temperature.<sup>117</sup> The capacitance of the space charge layer can be calculated using the following equation:

$$C = -\frac{1}{2\pi f Z_{\text{im}}} \quad (8)$$

where  $f$  is the frequency of the AC signal and  $Z_{\text{im}}$  is the imaginary part of the impedance. The donor density,  $N_{\text{D}}$ , can be derived from the slope of the Mott–Schottky plot and is calculated via the equation

$$N_{\text{D}} = \left( \frac{2}{ee\epsilon_0} \right) \left( \frac{dE}{dC^2} \right) \quad (9)$$

where  $\frac{dE}{dC^2}$  is the inverse of the slope of the  $C^{-2}$  vs  $E$  curve.<sup>117</sup>

The potential values of the bottom of the conduction band ( $V_{\text{CBM}}$ ) and the top of the valence band ( $V_{\text{VBM}}$ ) are determined according to the values of the flat band potentials, and the potentials are recalculated against NHE at pH 7 according to the equations<sup>118</sup>

$$V_{\text{CBM}} = V_{\text{fb}} + \Delta V - 0.059(7 - \text{pH}) \quad (10)$$

$$V_{\text{VBM}} = V_{\text{CB}} + \frac{E_{\text{g}}}{e} \quad (11)$$

The corresponding values of the energy levels are determined as follows:

$$E_{\text{CBM}} = eV_{\text{CBM}} \quad (12)$$

$$E_{\text{VBM}} = eV_{\text{VBM}} \quad (13)$$

where  $\Delta V = 0.21$  V is the Ag/AgCl potential against NHE,<sup>118</sup>  $e$  is the electron charge, and  $E_{\text{g}}$  the band gap of the materials (pH 5.9).

## ASSOCIATED CONTENT

### Supporting Information

The Supporting Information is available free of charge at <https://pubs.acs.org/doi/10.1021/acsnano.4c00092>.

FTIR spectra of  $\text{Ti}_3\text{AlC}_2$  MAX phase and  $\text{Ti}_3\text{C}_2\text{T}_x$  before and after laser ablation; SEM top and cross section images of bare TNT; photoluminescence spectra of TNT and  $\text{TiCl}_4$ @TNT; fitting parameters of the deconvoluted photoluminescence spectra of the titania based electrode materials; IPCE 3D maps recorded for  $\text{TiCl}_4$ @TNT, 1 M- $\text{TiCl}_4$ @TNT, and 3M- $\text{TiCl}_4$ @TNT in 0.5 M  $\text{Na}_2\text{SO}_4$ ; IPCE curve of the samples registered at +500 mV vs Ag/AgCl/0.1 M KCl; comparison of the IMPS Nyquist plots; table with photocurrent densities for other  $\text{TiO}_2/\text{Ti}_3\text{C}_2\text{T}_x$  or  $\text{TiO}_2/\text{C}$  heterojunctions; Nyquist plots of EIS measurements of 1M- $\text{TiCl}_4$ @TNT and 3M- $\text{TiCl}_4$ @TNT in the dark and under visible light illumination; values of fitting parameters obtained in dark and under visible light for the prepared electrodes; Mott–Schottky curves of samples in 0.5 M  $\text{Na}_2\text{SO}_4$  (PDF)

## AUTHOR INFORMATION

### Corresponding Authors

Dujejarc-Stephane Kouao – Centre for Plasma and Laser Engineering, Institute of Fluid-Flow Machinery, Polish Academy of Sciences, 80-231 Gdańsk, Poland; [orcid.org/0000-0003-0649-1122](https://orcid.org/0000-0003-0649-1122); Email: [dkouao@imp.gda.pl](mailto:dkouao@imp.gda.pl)

Katarzyna Siuzdak – Centre for Plasma and Laser Engineering, Institute of Fluid-Flow Machinery, Polish Academy of Sciences, 80-231 Gdańsk, Poland; [orcid.org/0000-0001-7434-6408](https://orcid.org/0000-0001-7434-6408); Email: [ksiuzdak@imp.gda.pl](mailto:ksiuzdak@imp.gda.pl)

### Authors

Katarzyna Grochowska – Centre for Plasma and Laser Engineering, Institute of Fluid-Flow Machinery, Polish Academy of Sciences, 80-231 Gdańsk, Poland; [orcid.org/0000-0001-7577-3399](https://orcid.org/0000-0001-7577-3399)

Vitezslav Stranak – Faculty of Science, University of South Bohemia, 37005 České Budějovice, Czech Republic

Petr Sezemsky – Faculty of Science, University of South Bohemia, 37005 České Budějovice, Czech Republic; [orcid.org/0000-0002-7648-9960](https://orcid.org/0000-0002-7648-9960)

Justyna Gumieniak – The Faculty of Mechanics and Technology, Rzeszów University of Technology, 37-450 Stalowa Wola, Poland

Agnieszka Kramek – The Faculty of Mechanics and Technology, Rzeszów University of Technology, 37-450 Stalowa Wola, Poland



**Jakub Karczewski** – Faculty of Applied Physics and Mathematics, Institute of Nanotechnology and Materials Engineering, Gdańsk University of Technology, 80-233 Gdańsk, Poland

**Emerson Coy** – NanoBioMedical Centre, Adam Mickiewicz University, 61-614 Poznań, Poland; [orcid.org/0000-0002-4149-9720](https://orcid.org/0000-0002-4149-9720)

**Jan Hanus** – Faculty of Mathematics and Physics, Charles University, 180 00 Praha, Czech Republic

**Ondrej Kylian** – Faculty of Mathematics and Physics, Charles University, 180 00 Praha, Czech Republic; [orcid.org/0000-0001-6115-3471](https://orcid.org/0000-0001-6115-3471)

**Mirosław Sawczak** – Centre for Plasma and Laser Engineering, Institute of Fluid-Flow Machinery, Polish Academy of Sciences, 80-231 Gdańsk, Poland; [orcid.org/0000-0002-1365-5351](https://orcid.org/0000-0002-1365-5351)

Complete contact information is available at:  
<https://pubs.acs.org/10.1021/acsnano.4c00092>

## Notes

The authors declare no competing financial interest.

## ACKNOWLEDGMENTS

The work was financially supported by the National Science Centre (Poland) within project no. 2020/02/Y/ST8/00030 and Czech Science Foundation within grant 21-05030K.

## REFERENCES

- (1) Varghese, O. K.; Paulose, M.; Grimes, C. A. Long vertically aligned titania nanotubes on transparent conducting oxide for highly efficient solar cells. *Nat. Nanotechnol.* **2009**, *4* (9), 592–597.
- (2) Kathirvel, S.; Su, C.; Yang, C.-Y.; Shiao, Y.-J.; Chen, B.-R.; Li, W.-R. The growth of TiO<sub>2</sub> nanotubes from sputter-deposited Ti film on transparent conducting glass for photovoltaic applications. *Vacuum* **2015**, *118*, 17–25.
- (3) Kim, J. Y.; Noh, J. H.; Zhu, K.; Halverson, A. F.; Neale, N. R.; Park, S.; Hong, K. S.; Frank, A. J. General Strategy for Fabricating Transparent TiO<sub>2</sub> Nanotube Arrays for Dye-Sensitized Photoelectrodes: Illumination Geometry and Transport Properties. *ACS Nano* **2011**, *5* (4), 2647–2656.
- (4) Wang, Y.-Y.; Chen, Y.-X.; Barakat, T.; Zeng, Y.-J.; Liu, J.; Siffert, S.; Su, B.-L. Recent Advances in Non-Metal Doped Titania for Solar-Driven Photocatalytic/Photoelectrochemical Water-Splitting. *J. Energy Chem.* **2022**, *66*, 529–559.
- (5) Wang, K.; Kowalska, E. Property-Governed Performance of Platinum-Modified Titania Photocatalysts. *Front. Chem.* **2022**, *10*, 01 DOI: 10.3389/fchem.2022.972494.
- (6) Liu, X.; Yang, Y.; Li, H.; Yang, Z.; Fang, Y. Visible Light Degradation of Tetracycline Using Oxygen-Rich Titanium Dioxide Nanosheets Decorated by Carbon Quantum Dots. *Chem. Eng. J.* **2021**, *408*, 127259.
- (7) Ruqin, G.; Pan, L.; Zichang, Z.; Yingli, Y.; Heng, L.; Youyin, L.; Guoting, L. Photocatalytic Performance of Nitrogen-Doped Titanium Dioxide Nanostructures Prepared by Sol-Gel Method. *Inorg. Nano-Metal Chem.* **2023**, 1–8.
- (8) Sun, L.; Zhang, S.; Sun, X.; He, X. Effect of the Geometry of the Anodized Titania Nanotube Array on the Performance of Dye-Sensitized Solar Cells. *J. Nanosci. Nanotechnol.* **2010**, *10* (7), 4551–4561.
- (9) Li, P.; Wang, J.; Zu, G.; Jiao, P.; Liu, S.; Yang, Y.; Chen, S.; Li, H. Synergetic Catalytic Properties of Gold Nanoparticles Planted on Transparent Titanium Dioxide Nanotube Array Bed. *Mater. Chem. Phys.* **2018**, *217*, 437–444.
- (10) Sanabria-Arenas, B. E.; Mazare, A.; Yoo, J.; Nguyen, N. T.; Hejazi, S.; Bian, H.; Diamanti, M. V.; Pedferri, M. P.; Schmuki, P. Intrinsic AuPt-alloy particles decorated on TiO<sub>2</sub> nanotubes provide enhanced photocatalytic degradation. *Electrochim. Acta* **2018**, *292*, 865–870.
- (11) Kar, P.; Farsinezhad, S.; Mahdi, N.; Zhang, Y.; Obuekwe, U.; Sharma, H.; Shen, J.; Semagina, N.; Shankar, K. Enhanced CH<sub>4</sub> yield by photocatalytic CO<sub>2</sub> reduction using TiO<sub>2</sub> nanotube arrays grafted with Au, Ru, and ZnPd nanoparticles. *Nano Res.* **2016**, *9* (11), 3478–3493.
- (12) Bleckenwegner, P.; Mardare, C. C.; Cobet, C.; Kollender, J. P.; Hassel, A. W.; Mardare, A. I. Compositionally Dependent Nonlinear Optical Bandgap Behavior of Mixed Anodic Oxides in Niobium-Titanium System. *ACS Comb. Sci.* **2017**, *19* (2), 121–129.
- (13) Bohórquez, A. J.; Quiroz, H. P.; Dussan, A. Growth and crystallization of Cobalt-doped TiO<sub>2</sub> alloys: Effect of substrate and annealing temperature. *Appl. Surf. Sci.* **2019**, *474*, 97–101.
- (14) Mor, G. K.; Prakasham, H. E.; Varghese, O. K.; Shankar, K.; Grimes, C. A. Vertically Oriented Ti-Fe-O Nanotube Array Films: Toward a Useful Material Architecture for Solar Spectrum Water Photoelectrolysis. *Nano Lett.* **2007**, *7* (8), 2356–2364.
- (15) Kyeremateng, N. A.; Hornebecq, V.; Martinez, H.; Knauth, P.; Djenizian, T. Electrochemical Fabrication and Properties of Highly Ordered Fe-Doped TiO<sub>2</sub> Nanotubes. *ChemPhysChem* **2012**, *13* (16), 3707–3713.
- (16) Habazaki, H.; Uozumi, M.; Konno, H.; Shimizu, K.; Nagata, S.; Asami, K.; Skeldon, P.; Thompson, G. E. Influence of Molybdenum Species on Growth of Anodic Titania. *Electrochim. Acta* **2002**, *47* (24), 3837–3845.
- (17) Gui, Y.; Blackwood, D. J. Honey-Comb Structured WO<sub>3</sub>/TiO<sub>2</sub> Thin Films with Improved Electrochromic Properties. *J. Electrochem. Soc.* **2015**, *162* (10), E205–E212.
- (18) Mor, G. K.; Varghese, O. K.; Wilke, R. H. T.; Sharma, S.; Shankar, K.; Latempa, T. J.; Choi, K.-S.; Grimes, C. A. P-Type Cu-Ti-O Nanotube Arrays and Their Use in Self-Biased Heterojunction Photoelectrochemical Diodes for Hydrogen Generation. *Nano Lett.* **2008**, *8* (7), 1906–1911.
- (19) Wang, S.; Zhang, Z.; Huo, W.; Zhu, K.; Zhang, X.; Zhou, X.; Fang, F.; Xie, Z.; Jiang, J. Preferentially oriented Ag-TiO<sub>2</sub> nanotube array film: An efficient visible-light-driven photocatalyst. *J. Hazard. Mater.* **2020**, *399*, 123016.
- (20) Jiang, Y.; Sun, T.; Xie, X.; Jiang, W.; Li, J.; Tian, B.; Su, C. Oxygen-Functionalized Ultrathin Ti<sub>3</sub>C<sub>2</sub>T<sub>x</sub> MXene for Enhanced Electrochemical Hydrogen Evolution. *ChemSusChem* **2019**, *12* (7), 1368–1373.
- (21) Bat-Erdene, M.; Batmunkh, M.; Sainbileg, B.; Hayashi, M.; Bati, A. S. R.; Qin, J.; Zhao, H.; Zhong, Y. L.; Shapter, J. G. Highly Dispersed Ru Nanoparticles on Boron-Doped Ti<sub>3</sub>C<sub>2</sub>T<sub>x</sub> (MXene) Nanosheets for Synergistic Enhancement of Electrochemical Hydrogen Evolution. *Small* **2021**, *17* (38), 2102218.
- (22) Khatun, N.; Dey, S.; Behera, G. C.; Roy, S. C. Ti<sub>3</sub>C<sub>2</sub>T<sub>x</sub> MXene functionalization induced enhancement of photoelectrochemical performance of TiO<sub>2</sub> nanotube arrays. *Mater. Chem. Phys.* **2022**, *278*, 125651.
- (23) El-Demellawi, J. K.; Lopatin, S.; Yin, J.; Mohammed, O. F.; Alshareef, H. N. Tunable Multipolar Surface Plasmons in 2D Ti<sub>3</sub>C<sub>2</sub>T<sub>x</sub> MXene Flakes. *ACS Nano* **2018**, *12* (8), 8485–8493.
- (24) Colin-Ulloa, E.; Fitzgerald, A.; Montazeri, K.; Mann, J.; Natu, V.; Ngo, K.; Uzarski, J.; Barsoum, M. W.; Titova, L. V. Ultrafast Spectroscopy of Plasmons and Free Carriers in 2D MXenes. *Adv. Mater.* **2023**, *35* (8), 2208659.
- (25) Shahzad, A.; Rasool, K.; Nawaz, M.; Miran, W.; Jang, J.; Moztahida, M.; Mahmoud, K. A.; Lee, D. S. Heterostructural TiO<sub>2</sub>/Ti<sub>3</sub>C<sub>2</sub>T<sub>x</sub> (MXene) for photocatalytic degradation of antiepileptic drug carbamazepine. *Chem. Eng. J.* **2018**, *349*, 748–755.
- (26) Zheng, H.; Meng, X.; Chen, J.; Que, M.; Wang, W.; Liu, X.; Yang, L.; Zhao, Y. *In situ* phase evolution of TiO<sub>2</sub>/Ti<sub>3</sub>C<sub>2</sub>T<sub>x</sub> heterojunction for enhancing adsorption and photocatalytic degradation. *Appl. Surf. Sci.* **2021**, *545*, 149031.
- (27) Zhang, H.; Zhang, X.; Xie, C.; Shi, W.; Yang, P. Composite nanoarchitectonics with TiO<sub>2</sub> nanocrystals and superior thin Ti<sub>3</sub>C<sub>2</sub>T<sub>x</sub>

nanosheets towards efficient NO removal. *Environ. Res.* **2023**, *227*, 115793.

(28) Peng, Y.; Cai, P.; Yang, L.; Liu, Y.; Zhu, L.; Zhang, Q.; Liu, J.; Huang, Z.; Yang, Y. Theoretical and Experimental Studies of  $\text{Ti}_3\text{C}_2$  MXene for Surface-Enhanced Raman Spectroscopy-Based Sensing. *ACS Omega* **2020**, *5* (41), 26486–26496.

(29) Ghosh, K.; Ghosh, J.; Giri, P. K. Accordion-like Multilayered Two-Dimensional  $\text{Ti}_3\text{C}_2\text{T}_x$  MXenes for Catalytic Elimination of Organic Dyes from Wastewater via the Fenton Reaction. *ACS Appl. Nano Mater.* **2022**, *5* (11), 16451–16461.

(30) Liu, C.; Zhang, H.; Li, R.; Li, X.; Tang, P.; Wang, Y.; Yang, B.; Qiao, Z.; Gao, G. Laser triggered exothermic chemical reaction in Au nanoparticle@ $\text{Ti}_3\text{C}_2$  MXene membrane: A route toward efficient light to high-temperature pulse conversion. *Chem. Eng. J.* **2021**, *420*, 127672.

(31) Peng, C.; Xu, W.; Wei, P.; Liu, M.; Guo, L.; Wu, P.; Zhang, K.; Cao, Y.; Wang, H.; Yu, H.; Peng, F.; Yan, X. Manipulating Photocatalytic Pathway and Activity of Ternary  $\text{Cu}_2\text{O}/(001)\text{TiO}_2@ \text{Ti}_3\text{C}_2\text{T}_x$  Catalysts for  $\text{H}_2$  Evolution: Effect of Surface Coverage. *Int. J. Hydrogen Energy* **2019**, *44* (57), 29975–29985.

(32) Wang, H.; Peng, R.; Hood, Z. D.; Naguib, M.; Adhikari, S. P.; Wu, Z. Titania Composites with 2 D Transition Metal Carbides as Photocatalysts for Hydrogen Production under Visible-Light Irradiation. *ChemSusChem* **2016**, *9* (12), 1490–1497.

(33) Liu, Z.; Zhou, Y.; Yang, L.; Yang, R. Green Preparation of In-Situ Oxidized  $\text{TiO}_2/\text{Ti}_3\text{C}_2$  Heterostructure for Photocatalytic Hydrogen Production. *Adv. Powder Technol.* **2021**, *32* (12), 4857–4861.

(34) Li, J.; Li, K.; Tan, Q.; Li, Q.; Fan, J.; Wu, C.; Lv, K. Facile Preparation of Highly Active  $\text{CO}_2$  Reduction  $(001)\text{TiO}_2/\text{Ti}_3\text{C}_2\text{T}_x$  Photocatalyst from  $\text{Ti}_3\text{AlC}_2$  with Less Fluorine. *Catalysts* **2022**, *12* (7), 785.

(35) Song, Q.; Shen, B.; Yu, J.; Cao, S. A 3D Hierarchical  $\text{Ti}_3\text{C}_2\text{T}_x/\text{TiO}_2$  Heterojunction for Enhanced Photocatalytic  $\text{CO}_2$  Reduction. *ChemNanoMat* **2021**, *7* (8), 910–915.

(36) Low, J.; Zhang, L.; Tong, T.; Shen, B.; Yu, J.  $\text{TiO}_2/\text{MXene}$   $\text{Ti}_3\text{C}_2$  Composite with Excellent Photocatalytic  $\text{CO}_2$  Reduction Activity. *J. Catal.* **2018**, *361*, 255–266.

(37) Lemos, H. G.; Ronchi, R. M.; Portugal, G. R.; Rossato, J. H. H.; Selopal, G. S.; Barba, D.; Nancio, E. C.; Rosei, F.; Arantes, J. T.; F. Santos, S. Efficient  $\text{Ti}_3\text{C}_2\text{T}_x/\text{TiO}_2$  Hybrid Photoanodes for Dye-Sensitized Solar Cells. *ACS Appl. Energy Mater.* **2022**, *5* (12), 15928–15938.

(38) He, S.; Lan, Z.; Zhang, B.; Gao, Y.; Shang, L.; Yue, G.; Chen, S.; Shen, Z.; Tan, F.; Wu, J. Holistically Optimizing Charge Carrier Dynamics Enables High-Performance Dye-Sensitized Solar Cells and Photodetectors. *ACS Appl. Mater. Interfaces* **2022**, *14* (38), 43576–43585.

(39) Yuan, Y.; Jiang, L.; Li, X.; Zuo, P.; Zhang, X.; Lian, Y.; Ma, Y.; Liang, M.; Zhao, Y.; Qu, L. Ultrafast Shaped Laser Induced Synthesis of MXene Quantum Dots/Graphene for Transparent Supercapacitors. *Adv. Mater.* **2022**, *34* (12), 2110013.

(40) Vida, J.; Gemeiner, P.; Pavličková, M.; Mazalová, M.; Souček, P.; Plašienka, D. Nanocrystalline  $\text{TiO}_2/\text{Ti}_3\text{C}_2\text{T}_x$  MXene composites with a tunable work function prepared using atmospheric pressure oxygen plasma. *Nanoscale* **2023**, *15* (3), 1289–1298.

(41) Chen, J.; Zheng, H.; Zhao, Y.; Que, M.; Lei, X.; Zhang, K.; Luo, Y. Preparation of facet exposed  $\text{TiO}_2/\text{Ti}_3\text{C}_2\text{T}_x$  composites with enhanced photocatalytic activity. *J. Phys. Chem. Solids* **2020**, *145*, 109565.

(42) Chen, Y.; Li, X.; Cai, G.; Li, M.; Tang, D. In situ formation of  $(0\ 0\ 1)\text{TiO}_2/\text{Ti}_3\text{C}_2\text{T}_x$  heterojunctions for enhanced photoelectrochemical detection of dopamine. *Electrochem. commun.* **2021**, *125*, 106987.

(43) Zhou, S.; Jiang, L.; Wang, H.; Yang, J.; Yuan, X.; Wang, H.; Liang, J.; Li, X.; Li, H.; Bu, Y. Oxygen Vacancies Modified  $\text{TiO}_2/\text{O}$ -Terminated  $\text{Ti}_3\text{C}_2\text{T}_x$  Composites: Unravelling the Dual Effects between Oxygen Vacancy and High-Work-Function Titanium Carbide. *Adv. Funct. Mater.* **2023**, 2307702.

(44) Park, C. E.; Jeong, G. H.; Theerthagiri, J.; Lee, H.; Choi, M. Y. Moving beyond  $\text{Ti}_2\text{C}$  to  $\text{Ti}_3\text{C}_2$  MXene to Pt-Decorated  $\text{TiO}_2$ @ $\text{TiC}$  Core-Shell via Pulsed Laser in Reshaping Modification for Accelerating Hydrogen Evolution Kinetics. *ACS Nano* **2023**, *17* (8), 7539–7549.

(45) Semaltianos, N. G. Nanoparticles by Laser Ablation. *Crit. Rev. Solid State Mater. Sci.* **2010**, *35* (2), 105–124.

(46) Yu, Y.; Lee, S. J.; Theerthagiri, J.; Lee, Y.; Choi, M. Y. Architecting the AuPt Alloys for Hydrazine Oxidation as an Anolyte in Fuel Cell: Comparative Analysis of Hydrazine Splitting and Water Splitting for Energy-Saving  $\text{H}_2$  Generation. *Appl. Catal. B Environ.* **2022**, *316*, 121603.

(47) Naik Shreyanka, S.; Theerthagiri, J.; Lee, S. J.; Yu, Y.; Choi, M. Y. Multiscale Design of 3D Metal-Organic Frameworks (M-BTC, M: Cu, Co, Ni) via PLAL Enabling Bifunctional Electrocatalysts for Robust Overall Water Splitting. *Chem. Eng. J.* **2022**, *446*, 137045.

(48) Yuan, Y.; Jiang, L.; Li, X.; Zuo, P.; Zhang, X.; Lian, Y.; Ma, Y.; Liang, M.; Zhao, Y.; Qu, L. Ultrafast Shaped Laser Induced Synthesis of MXene Quantum Dots/Graphene for Transparent Supercapacitors. *Adv. Mater.* **2022**, *34* (12), 2110013 DOI: 10.1002/adma.202110013.

(49) Guzelurk, B.; Kamysbayev, V.; Wang, D.; Hu, H.; Li, R.; King, S. B.; Reid, A. H.; Lin, M.-F.; Wang, X.; Walko, D. A.; Zhang, X.; Lindenberg, A.; Talapin, D. V. Understanding and Controlling Photothermal Responses in MXenes. *Nano Lett.* **2023**, *23* (7), 2677–2686.

(50) Zang, X.; Jian, C.; Zhu, T.; Fan, Z.; Wang, W.; Wei, M.; Li, B.; Follmar Diaz, M.; Ashby, P.; Lu, Z.; Chu, Y.; Wang, Z.; Ding, X.; Xie, Y.; Chen, J.; Hohman, J. N.; Sanghadasa, M.; Grossman, J. C.; Lin, L. Laser-Sculptured Ultrathin Transition Metal Carbide Layers for Energy Storage and Energy Harvesting Applications. *Nat. Commun.* **2019**, *10* (1), 3112.

(51) Qin, W.-W.; Hu, X.-F.; Fan, J.-L.; Liu, Y.-S.; Tan, L.-P.; Zhou, M.; Wu, C.-Q.; Ge, B.-H.; Gao, S.-J.; Qian, J.; Zhang, W. One-Step Laser Ablation of Fe Clusters Supported on  $\text{Ti}_3\text{C}_2\text{T}_x$  Nanosheets for Enhanced  $\text{NH}_3$  Sensing at Room Temperature. *Ceram. Int.* **2023**, *49* (11), 18353–18362.

(52) Li, J.; Qin, R.; Yan, L.; Chi, Z.; Yu, Z.; Li, N.; Hu, M.; Chen, H.; Shan, G. Plasmonic Light Illumination Creates a Channel To Achieve Fast Degradation of  $\text{Ti}_3\text{C}_2\text{T}_x$  Nanosheets. *Inorg. Chem.* **2019**, *58* (11), 7285–7294.

(53) Li, R.; Zhang, L.; Shi, L.; Wang, P. MXene  $\text{Ti}_3\text{C}_2$ : An Effective 2D Light-to-Heat Conversion Material. *ACS Nano* **2017**, *11* (4), 3752–3759.

(54) Chertopalov, S.; Mochalin, V. N. Environment-Sensitive Photoresponse of Spontaneously Partially Oxidized  $\text{Ti}_3\text{C}_2$  MXene Thin Films. *ACS Nano* **2018**, *12* (6), 6109–6116.

(55) My Tran, N.; Thanh Hoai Ta, Q.; Noh, J.-S. Unusual Synthesis of Safflower-Shaped  $\text{TiO}_2/\text{Ti}_3\text{C}_2$  Heterostructures Initiated from Two-Dimensional  $\text{Ti}_3\text{C}_2$  MXene. *Appl. Surf. Sci.* **2021**, *538*, 148023.

(56) Soomro, R. A.; Kumar, J.; Neiber, R. R.; Sirajuddin; Alotaibi, A. M.; Shaikh, S. F.; Ahmed, N.; Nafady, A. Natural Oxidation of  $\text{Ti}_3\text{C}_2\text{T}_x$  to Construct Efficient  $\text{TiO}_2/\text{Ti}_3\text{C}_2\text{T}_x$  Photoactive Heterojunctions for Advanced Photoelectrochemical Biosensing of Folate-Expressing Cancer Cells. *Anal. Chim. Acta* **2023**, *1251*, 341016.

(57) Yuan, W.; Cheng, L.; An, Y.; Lv, S.; Wu, H.; Fan, X.; Zhang, Y.; Guo, X.; Tang, J. Laminated Hybrid Junction of Sulfur-Doped  $\text{TiO}_2$  and a Carbon Substrate Derived from  $\text{Ti}_3\text{C}_2$  MXenes: Toward Highly Visible Light-Driven Photocatalytic Hydrogen Evolution. *Adv. Sci.* **2018**, *5* (6), 1700870.

(58) Qin, X.; Ji, L.; Zhu, A. Construction of Rutile/Anatase Ohmic Heterojunction of  $\text{TiO}_2/\text{Ti}_3\text{C}_2$  with Robust Built-in Electric Field for Boosting Photocatalytic Organic Pollutant and Hydrogen Evolution. *Appl. Surf. Sci.* **2024**, *652*, 159338.

(59) Chen, L.; Ye, X.; Chen, S.; Ma, L.; Wang, Z.; Wang, Q.; Hua, N.; Xiao, X.; Cai, S.; Liu, X.  $\text{Ti}_3\text{C}_2$  MXene Nanosheet/ $\text{TiO}_2$  Composites for Efficient Visible Light Photocatalytic Activity. *Ceram. Int.* **2020**, *46* (16), 25895–25904.

(60) Wei, Z.; Peigen, Z.; Wubian, T.; Xia, Q.; Yamei, Z.; ZhengMing, S. Alkali treated  $\text{Ti}_3\text{C}_2\text{T}_x$  MXenes and their dye



adsorption performance, *Mater. Chem. Mater. Chem. Phys.* **2018**, *206*, 270–276.

(61) Shen, B.; Huang, H.; Liu, H.; Jiang, Q.; He, H. Bottom-up construction of three-dimensional porous MXene/nitrogen-doped graphene architectures as efficient hydrogen evolution electrocatalysts. *Int. J. Hydrogen Energy* **2021**, *46* (58), 29984–29993.

(62) Chen, Y.; Gu, W.; Tan, L.; Ao, Z.; An, T.; Wang, S. Photocatalytic H<sub>2</sub>O<sub>2</sub> production using Ti<sub>3</sub>C<sub>2</sub> MXene as a non-noble metal cocatalyst. *Appl. Catal. A Gen.* **2021**, *618*, 118127.

(63) Mičušák, M.; Šlouf, M.; Štepan, A.; Šoyka, Y.; Ovodok, E.; Procházka, M.; Omastová, M. Aging of 2D MXene Nanoparticles in Air: An XPS and TEM Study. *Appl. Surf. Sci.* **2023**, *610*, 155351.

(64) Li, J.; Zhen, D.; Sui, G.; Zhang, C.; Deng, Q.; Jia, L. Nanocomposite of Cu-TiO<sub>2</sub>-SiO<sub>2</sub> with High Photoactive Performance for Degradation of Rhodamine B Dye in Aqueous Wastewater. *J. Nanosci. Nanotechnol.* **2012**, *12* (8), 6265–6270.

(65) Wen, Y.; Rufford, T. E.; Chen, X.; Li, N.; Lyu, M.; Dai, L.; Wang, L. Nitrogen-doped Ti<sub>3</sub>C<sub>2</sub>T<sub>x</sub> MXene electrodes for high-performance supercapacitors. *Nano Energy* **2017**, *38*, 368–376.

(66) Gasso, S.; Sohal, M. K.; Mahajan, A. MXene modulated SnO<sub>2</sub> gas sensor for ultra-responsive room-temperature detection of NO<sub>2</sub>. *Sensors Actuators B Chem.* **2022**, *357*, 131427.

(67) Hu, K.; Wang, H.; Zhang, X.; Huang, H.; Qiu, T.; Wang, Y.; Zhang, C.; Pan, L.; Yang, J. Ultralight Ti<sub>3</sub>C<sub>2</sub>T<sub>x</sub> MXene foam with superior microwave absorption performance. *Chem. Eng. J.* **2021**, *408*, 127283.

(68) Reddy, G. T.; Kumar, G.; Reddy, N. C. G. Water-Mediated One-pot Three-Component Synthesis of Hydrazinyl-Thiazoles Catalyzed by Copper Oxide Nanoparticles Dispersed on Titanium Dioxide Support: A Green Catalytic Process. *Adv. Synth. Catal.* **2018**, *360* (5), 995–1006.

(69) Sarycheva, A.; Gogotsi, Y. Raman Spectroscopy Analysis of the Structure and Surface Chemistry of Ti<sub>3</sub>C<sub>2</sub>T<sub>x</sub> MXene. *Chem. Mater.* **2020**, *32* (8), 3480–3488.

(70) Lioi, D. B.; Neher, G.; Heckler, J. E.; Back, T.; Mehmood, F.; Nepal, D.; Pachter, R.; Vaia, R.; Kennedy, W. J. Electron-Withdrawing Effect of Native Terminal Groups on the Lattice Structure of Ti<sub>3</sub>C<sub>2</sub>T<sub>x</sub> MXenes Studied by Resonance Raman Scattering: Implications for Embedding MXenes in Electronic Composites. *ACS Appl. Nano Mater.* **2019**, *2* (10), 6087–6091.

(71) Ilie, A. G.; Scarisoareanu, M.; Morjan, I.; Dutu, E.; Badiceanu, M.; Mihailescu, I. Principal component analysis of Raman spectra for TiO<sub>2</sub> nanoparticle characterization. *Appl. Surf. Sci.* **2017**, *417*, 93–103.

(72) Lee, D. K.; Ahn, C. W.; Lee, J. W. TiO<sub>2</sub>/Carbon Nanosheets Derived from Delaminated Ti<sub>3</sub>C<sub>2</sub> MXenes as an Ultralong-Lifespan Anode Material in Lithium-Ion Batteries. *Adv. Mater. Interfaces* **2022**, *9* (10), 2102375.

(73) Kim, S. J.; Koh, H.-J.; Ren, C. E.; Kwon, O.; Maleski, K.; Cho, S.-Y.; Anasori, B.; Kim, C.-K.; Choi, Y.-K.; Kim, J.; Gogotsi, Y.; Jung, H.-T. Metallic Ti<sub>3</sub>C<sub>2</sub>T<sub>x</sub> MXene Gas Sensors with Ultrahigh Signal-to-Noise Ratio. *ACS Nano* **2018**, *12* (2), 986–993.

(74) Bao, X.; Li, H.; Wang, Z.; Tong, F.; Liu, M.; Zheng, Z.; Wang, P.; Cheng, H.; Liu, Y.; Dai, Y.; Fan, Y.; Li, Z.; Huang, B. TiO<sub>2</sub>/Ti<sub>3</sub>C<sub>2</sub> as an efficient photocatalyst for selective oxidation of benzyl alcohol to benzaldehyde. *Appl. Catal. B Environ.* **2021**, *286*, 119885.

(75) Ramirez, R.; Melillo, A.; Osella, S.; Asiri, A. M.; Garcia, H.; Primo, A. Green, HF-Free Synthesis of MXene Quantum Dots and Their Photocatalytic Activity for Hydrogen Evolution. *Small Methods* **2023**, *7* (6), 2300063.

(76) Golightly, J. S.; Castleman, A. W. Analysis of Titanium Nanoparticles Created by Laser Irradiation under Liquid Environments. *J. Phys. Chem. B* **2006**, *110* (40), 19979–19984.

(77) Li, X.; Zhu, J.; Zhang, B.; Jiao, Y.; Huang, J.; Wang, F. Manganese Dioxide Nanosheets Decorated on MXene (Ti<sub>3</sub>C<sub>2</sub>T<sub>x</sub>) with Enhanced Performance for Asymmetric Supercapacitors. *Ceram. Int.* **2021**, *47* (9), 12211–12220.

(78) Wang, S.; Ma, Z.; Lü, Q.; Yang, H. Manganese dioxide nanosheets decorated on MXene (Ti<sub>3</sub>C<sub>2</sub>T<sub>x</sub>) with enhanced performance for asymmetric supercapacitors. *ChemElectroChem.* **2019**, *6* (10), 2748–2754.

ance for asymmetric supercapacitors. *ChemElectroChem.* **2019**, *6* (10), 2748–2754.

(79) Lv, Z.; Ma, W.; Wang, M.; Dang, J.; Jian, K.; Liu, D.; Huang, D. Co-Constructing Interfaces of Multiheterostructure on MXene (Ti<sub>3</sub>C<sub>2</sub>T<sub>x</sub>)-Modified 3D Self-Supporting Electrode for Ultraefficient Electrocatalytic HER in Alkaline Media. *Adv. Funct. Mater.* **2021**, *31* (29), 2102576.

(80) Li, A.; Wang, X.; Chen, J.; Dong, C.; Wang, D.; Mao, Z. Surface-Termination Groups' Tuning to Improve the Lithium-Ion-Storage Performance of Ti<sub>3</sub>C<sub>2</sub>T<sub>x</sub> MXene. *Coatings* **2022**, *12* (7), 1005.

(81) Liu, B.; Liu, Y.; Chen, H.; Yang, M.; Li, H. Oxygen and Nitrogen Co-Doped Porous Carbon Nanosheets Derived from Perilla Frutescens for High Volumetric Performance Supercapacitors. *J. Power Sources* **2017**, *341*, 309–317.

(82) Jiang, H.; Sheng, M.; Li, Y.; Kong, S.; Bian, F. Photocatalytic one-pot multidirectional N-alkylation over Pt/D-TiO<sub>2</sub>/Ti<sub>3</sub>C<sub>2</sub>T<sub>x</sub> Ti<sub>3</sub>C<sub>2</sub>-based short-range directional charge transmission. *Appl. Organomet. Chem.* **2021**, *35* (8), e6291.

(83) Wen, M.; Xing, Y.; Liu, G.; Hou, S.; Hou, S. Electrochemical sensor based on Ti<sub>3</sub>C<sub>2</sub> membrane doped with UiO-66-NH<sub>2</sub> for dopamine. *Microchim. Acta* **2022**, *189* (4), 141.

(84) Huang, L.; Ai, L.; Wang, M.; Jiang, J.; Wang, S. Hierarchical MoS<sub>2</sub> nanosheets integrated Ti<sub>3</sub>C<sub>2</sub> MXenes for electrocatalytic hydrogen evolution. *Int. J. Hydrogen Energy* **2019**, *44* (2), 965–976.

(85) Kadja, G. T. M.; Natalya, S. A. C.; Khalil, M.; Iwanti, P. K.; Hermawati, E.; Nurfani, E. Unique TiO<sub>2</sub>-enveloped Ti<sub>3</sub>C<sub>2</sub> composites for efficient visible light-assisted photoreduction of bicarbonate. *Chem. Phys. Lett.* **2023**, *823*, 140541.

(86) Kuang, D.; Wang, L.; Guo, X.; She, Y.; Du, B.; Liang, C.; Qu, W.; Sun, X.; Wu, Z.; Hu, W.; He, Y. Facile hydrothermal synthesis of Ti<sub>3</sub>C<sub>2</sub>T<sub>x</sub>-TiO<sub>2</sub> nanocomposites for gaseous volatile organic compounds detection at room temperature. *J. Hazard. Mater.* **2021**, *416*, 126171.

(87) Wang, D.; He, N.; Xiao, L.; Dong, F.; Chen, W.; Zhou, Y.; Chen, C.; Wang, S. Coupling Coupling Electrocatalytic Nitric Oxide Oxidation over Carbon Cloth with Hydrogen Evolution Reaction for Nitrate Synthesis. *Angew. Chemie Int. Ed.* **2021**, *60* (46), 24605–24611.

(88) Albu, S. P.; Kim, D.; Schmuki, P. Growth of Aligned TiO<sub>2</sub> Bamboo-Type Nanotubes and Highly Ordered Nanolace. *Angew. Chemie Int. Ed.* **2008**, *47* (10), 1916–1919.

(89) Xie, Y.-L.; Li, Z.-X.; Xu, H.; Xie, K.-F.; Xu, Z.-G.; Zhang, H.-L. Fabrication of TiO<sub>2</sub> nanotubes with extended periodical morphology by alternating-current anodization. *Electrochem. commun.* **2012**, *17*, 34–37.

(90) Javed, H. M. A.; Que, W.; Shahid, M.; Qureshi, A. A.; Afzaal, M.; Mustafa, M. S.; Hussain, S.; Alsabaie, A. S.; Mahmoud, K. H.; El-Bahy, Z. M.; Kong, L. B. Investigations of anodization parameters and TiCl<sub>4</sub> treatments on TiO<sub>2</sub> nanostructures for highly optimized dye-sensitized solar cells. *Surfaces and Interfaces* **2021**, *27*, 101578.

(91) Charoensirithavorn, P.; Ogomi, Y.; Sagawa, T.; Hayase, S.; Yoshikawa, S. Improvement of Dye-Sensitized Solar Cell Through TiCl<sub>4</sub>-Treated TiO<sub>2</sub> Nanotube Arrays. *J. Electrochem. Soc.* **2010**, *157* (3), B354.

(92) Paulose, M.; Shankar, K.; Varghese, O. K.; Mor, G. K.; Grimes, C. A. Application of highly-ordered TiO<sub>2</sub> nanotube-arrays in heterojunction dye-sensitized solar cells. *J. Phys. D: Appl. Phys.* **2006**, *39* (12), 2498–2503.

(93) Ainouche, L.; Hamadou, L.; Kadri, A.; Benbrahim, N.; Bradai, D. T<sup>3+</sup> states induced band gap reduction and enhanced visible light absorption of TiO<sub>2</sub> nanotube arrays: Effect of the surface solid fraction factor. *Sol. Energy Mater. Sol. Cells* **2016**, *151*, 179–190.

(94) Ferrara, M. C.; Mazzarelli, S.; Schioppa, M.; Pilloni, L.; Tapfer, L. Growth, Optical, and Wettability Properties of Iron Modified Titania and Ferropseudobrookite Thin Films. *J. Appl. Phys.* **2021**, *130* (14), 145301.

(95) Bhandarkar, S. A.; Prathvi; Kompa, A.; Murari, M. S.; Kekuda, D.; Mohan, R. K. Investigation of Structural and Optical Properties of

- Spin Coated  $\text{TiO}_2/\text{Mn}$  Thin Films. *Opt. Mater. (Amst)*. **2021**, *118*, 111254.
- (96) Saini, C. P.; Barman, A.; Banerjee, D.; Grynk, O.; Prucnal, S.; Gupta, M.; Phase, D. M.; Sinha, A. K.; Kanjilal, D.; Skorupa, W.; Kanjilal, A. Impact of Self-Trapped Excitons on Blue Photoluminescence in  $\text{TiO}_2$  Nanorods on Chemically Etched Si Pyramids. *J. Phys. Chem. C* **2017**, *121* (21), 11448–11454.
- (97) Knorr, F. J.; McHale, J. L. Spectroelectrochemical Photoluminescence of Trap States of Nanocrystalline  $\text{TiO}_2$  in Aqueous Media. *J. Phys. Chem. C* **2013**, *117* (26), 13654–13662.
- (98) Zheng, H.; Meng, X.; Liu, D.; Wu, J.; Huo, S. Self-Cleaning Photoelectrocatalytic Filtration Based on  $\text{Ca}(\text{OH})_2/\text{Ti}_3\text{C}_2\text{T}$  Composite Nanofiltration Membranes for Synergistically Enhanced Separation and Degradation of Phenolic Compounds. *J. Water Process Eng.* **2023**, *55*, 104084.
- (99) Liu, N.; Yu, L.; Liu, B.; Yu, F.; Li, L.; Xiao, Y.; Yang, J.; Ma, J.  $\text{Ti}_3\text{C}_2$ -MXene Partially Derived Hierarchical 1D/2D  $\text{TiO}_2/\text{Ti}_3\text{C}_2$  Heterostructure Electrode for High-Performance Capacitive Deionization. *Adv. Sci.* **2023**, *10* (2), 2204041.
- (100) Hieu, V. Q.; Phung, T. K.; Nguyen, T.-Q.; Khan, A.; Doan, V. D.; Tran, V. A.; Le, V. T. Photocatalytic Degradation of Methyl Orange Dye by  $\text{Ti}_3\text{C}_2/\text{TiO}_2$  Heterojunction under Solar Light. *Chemosphere* **2021**, *276*, 130154.
- (101) Li, Y.; Deng, X.; Tian, J.; Liang, Z.; Cui, H.  $\text{Ti}_3\text{C}_2$  MXene-Derived  $\text{Ti}_3\text{C}_2/\text{TiO}_2$  Nanoflowers for Noble-Metal-Free Photocatalytic Overall Water Splitting. *Appl. Mater. Today* **2018**, *13*, 217–227.
- (102) Stergiopoulos, T.; Valota, A.; Likodimos, V.; Speliotis, T.; Niarchos, D.; Skeldon, P.; Thompson, G. E.; Falaras, P. Dye-Sensitization of Self-Assembled Titania Nanotubes Prepared by Galvanostatic Anodization of Ti Sputtered on Conductive Glass. *Nanotechnology* **2009**, *20* (36), 365601.
- (103) Chen, H.; Wei, Z.; Yan, K.; Bai, Y.; Yang, S. Unveiling Two Electron-Transport Modes in Oxygen-Deficient  $\text{TiO}_2$  Nanowires and Their Influence on Photoelectrochemical Operation. *J. Phys. Chem. Lett.* **2014**, *5* (16), 2890–2896.
- (104) Wang, C.-T.; Wu, S.-W.; Kuo, C.-C. Silver Nanoparticle-Embedded Titania Nanobelts with Tunable Electronic Band Structures and Plasmonic Resonance for Photovoltaic Application. *Mater. Sci. Semicond. Process.* **2022**, *138*, 106317.
- (105) Hsiao, P.-T.; Tung, Y.-L.; Teng, H. Electron Transport Patterns in  $\text{TiO}_2$  Nanocrystalline Films of Dye-Sensitized Solar Cells. *J. Phys. Chem. C* **2010**, *114* (14), 6762–6769.
- (106) Rekeb, L.; Hamadou, L.; Kadri, A.; Benbrahim, N.  $\text{Bi}/\alpha\text{-Bi}_2\text{O}_3/\text{TiO}_2$  Nanotubes Heterojunction with Enhanced UV and Visible Light Activity: Role of Bismuth. *Electrochim. Acta* **2017**, *256*, 162–171.
- (107) Ainouche, L.; Hamadou, L.; Kadri, A.; Benbrahim, N.; Bradai, D. Interfacial Barrier Layer Properties of Three Generations of  $\text{TiO}_2$  Nanotube Arrays. *Electrochim. Acta* **2014**, *133*, 597–609.
- (108) Fang, L.; Chen, J.; Zhang, M.; Jiang, X.; Sun, Z. Introduction of  $\text{Ti}^{3+}$  Ions into Heterostructured  $\text{TiO}_2$  Nanotree Arrays for Enhanced Photoelectrochemical Performance. *Appl. Surf. Sci.* **2019**, *490*, 1–6.
- (109) Nishikawa, M.; Shiroishi, W.; Honghao, H.; Suizu, H.; Nagai, H.; Saito, N. Probability of Two-Step Photoexcitation of Electron from Valence Band to Conduction Band through Doping Level in  $\text{TiO}_2$ . *J. Phys. Chem. A* **2017**, *121* (32), 5991–5997.
- (110) Saha, S.; Victorious, A.; Soleymani, L. Modulating the Photoelectrochemical Response of Titanium Dioxide ( $\text{TiO}_2$ ) Photoelectrodes Using Gold (Au) Nanoparticles Excited at Different Wavelengths. *Electrochim. Acta* **2021**, *380*, 138154.
- (111) Zhang, J.; Bang, J. H.; Tang, C.; Kamat, P. V. Tailored  $\text{TiO}_2$ - $\text{SrTiO}_3$  Heterostructure Nanotube Arrays for Improved Photoelectrochemical Performance. *ACS Nano* **2010**, *4* (1), 387–395.
- (112) Kolaei, M.; Tayebi, M.; Lee, B.-K. The Synergistic Effects of Acid Treatment and Silver (Ag) Loading for Substantial Improvement of Photoelectrochemical and Photocatalytic Activity of  $\text{Na}_2\text{Ti}_3\text{O}_7/\text{TiO}_2$  Nanocomposite. *Appl. Surf. Sci.* **2021**, *540*, 148359.
- (113) Su, T.; Yang, Y.; Shi, Y.; Zhang, X.; Jiang, Y.; Fan, R.; Cao, W. 40% Enhanced Photocurrent of Dye Sensitized Solar Cells Using Lotus-Shaped  $\text{H}_2$ -Treated Anatase  $\text{TiO}_2$  with {0 0 1} Dominated Facets. *Chem. Eng. J.* **2017**, *316*, 534–543.
- (114) Matsumoto, Y.; Miura, Y.; Takata, S. Thickness-Dependent Flat Band Potential of Anatase  $\text{TiO}_2$  (001) Epitaxial Films on Nb:SrTiO<sub>3</sub> (001) Investigated by UHV-Electrochemistry Approach. *J. Phys. Chem. C* **2016**, *120* (3), 1472–1477.
- (115) Li, H.; Xie, C.; Liao, Y.; Liu, Y.; Zou, Z.; Wu, J. Characterization of Incidental Photon-to-Electron Conversion Efficiency (IPCE) of Porous  $\text{TiO}_2/\text{SnO}_2$  Composite Film. *J. Alloys Compd.* **2013**, *569*, 88–94.
- (116) Park, B. H.; Li, L. S.; Gibbons, B. J.; Huang, J. Y.; Jia, Q. X. Photovoltaic response and dielectric properties of epitaxial anatase- $\text{TiO}_2$  films grown on conductive  $\text{La}_{0.5}\text{Sr}_{0.5}\text{CoO}_3$  electrodes. *Appl. Phys. Lett.* **2001**, *79* (17), 2797–2799.
- (117) Vadla, S. S.; Bandyopadhyay, P.; John, S.; Ghosh, P.; Roy, S. C.  $\text{TiO}_2$  Nanotube Arrays on Flexible Kapton Substrates for Photo-Electrochemical Solar Energy Conversion. *ACS Appl. Nano Mater.* **2020**, *3* (12), 11715–11724.
- (118) Giannakopoulou, T.; Papailias, I.; Todorova, N.; Boukos, N.; Liu, Y.; Yu, J.; Trapalis, C. Tailoring the energy band gap and edges' potentials of  $\text{g-C}_3\text{N}_4/\text{TiO}_2$  composite photocatalysts for  $\text{NO}_x$  removal. *Chem. Eng. J.* **2017**, *310*, 571–580.

## Supporting Information

### **Laser-treated MXene as an Electrochemical Agent to Boost Properties of Semitransparent Photoelectrode-based on Titania nanotubes**

*Dujearic-Stephane Kouao<sup>1\*</sup>, Katarzyna Grochowska<sup>1</sup>, Vitezslav Stranak<sup>2</sup>, Petr Sezemsky<sup>2</sup>, Justyna Gumieniak<sup>3</sup>, Agnieszka Kramek<sup>3</sup>, Jakub Karczewski<sup>4</sup>, Emerson Coy<sup>5</sup>, Jan Hanus<sup>6</sup>, Ondrej Kylian<sup>6</sup>, Mirosław Sawczak<sup>1</sup>, Katarzyna Siuzdak<sup>\*1</sup>*

<sup>1</sup> Centre for Plasma and Laser Engineering, Institute of Fluid-Flow Machinery, Polish Academy of Sciences, Fiszer 14 St., 80-231 Gdańsk, Poland

<sup>2</sup> Faculty of Science, University of South Bohemia, Branišovská 1760, 37005 České Budějovice, Czech Republic

<sup>3</sup> The Faculty of Mechanics and Technology, Rzeszów University of Technology, Kwiatkowskiego 4 St., 37-450 Stalowa Wola, Poland

<sup>4</sup> Faculty of Applied Physics and Mathematics, Institute of Nanotechnology and Materials Engineering, Gdańsk University of Technology, Narutowicza 11/12 St., 80-233 Gdańsk, Poland

<sup>5</sup> NanoBioMedical Centre, Adam Mickiewicz University, Wszechnicy Piastowskiej 3 St., 61-614 Poznań, Poland

<sup>6</sup> Faculty of Mathematics and Physics, Charles University, V Holesovickach 2, 180 00 Praha 8, Czech Republic

\*Corresponding author contact: [dkouao@imp.gda.pl](mailto:dkouao@imp.gda.pl); [ksiuzdak@imp.gda.pl](mailto:ksiuzdak@imp.gda.pl)



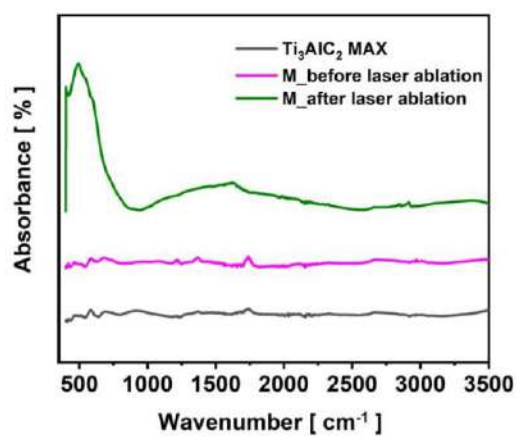


**Figure S1.** FTIR spectra of  $\text{Ti}_3\text{AlC}_2$  MAX phase and  $\text{Ti}_3\text{C}_2\text{T}_x$  before and after laser ablation. M:  $\text{Ti}_3\text{C}_2\text{T}_x$  MXene.

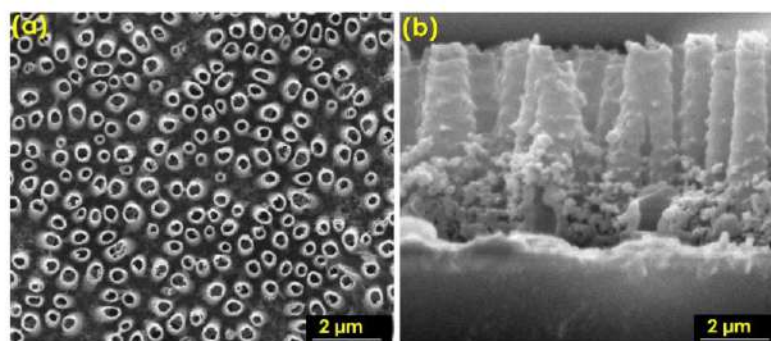


**Figure S2.** SEM top images of (a) TNT, (b) corresponding cross-section image of TNT.

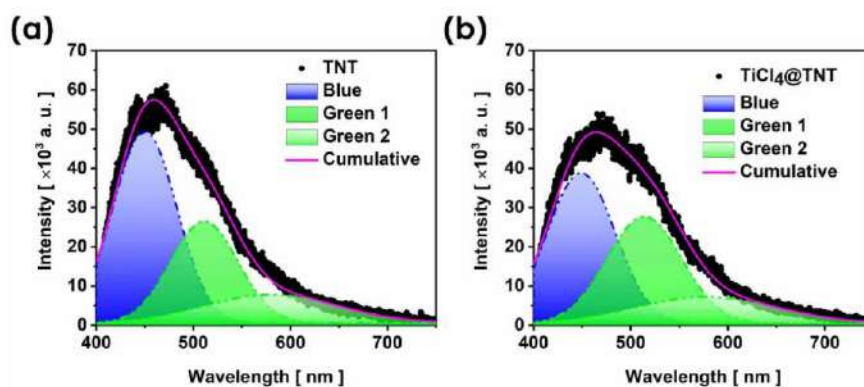


**Figure S3.** Deconvoluted photoluminescence spectrum of (a) TNT and (b)  $\text{TiCl}_4$ @TNT.



**Table S1.** Fitting parameters of the deconvoluted photoluminescence spectra of the titania based electrode materials.

sample	Peak 1		Peak 2		Peak 3	
	Position (nm)	FWHM (nm)	Position (nm)	FWHM (nm)	Position (nm)	FWHM (nm)
<b>TNT</b>	450 ± 1.2	65 ± 0.9	511 ± 2.2	69 ± 3.2	580 ± 1.1	135 ± 1.2
<b>TiCl<sub>4</sub>@TNT</b>	448 ± 1.6	70 ± 1.1	513 ± 2.6	77 ± 4.1	577 ± 2.2	143 ± 2.1
<b>1M-TiCl<sub>4</sub>@TNT</b>	440 ± 0.5	56 ± 0.6	506 ± 0.8	78 ± 2.1	601 ± 1.3	196 ± 2.9
<b>2M-TiCl<sub>4</sub>@TNT</b>	441 ± 1.5	66 ± 1.6	515 ± 1.8	94 ± 3.3	620 ± 2.2	170 ± 3.1
<b>3M-TiCl<sub>4</sub>@TNT</b>	437 ± 1.4	50 ± 0.5	501 ± 0.6	76 ± 2.0	586 ± 1.1	147 ± 1.9

**Table S2.** Photocurrent densities of TiO<sub>2</sub>/Ti<sub>3</sub>C<sub>2</sub>T<sub>x</sub> or TiO<sub>2</sub>/C heterojunctions synthesized by oxidation of Ti<sub>3</sub>C<sub>2</sub>T<sub>x</sub> MXenes.

sample	photocurrent density recorded under UV-vis light	synthesis method	reference
TiO <sub>2</sub> /Ti <sub>3</sub> C <sub>2</sub> T <sub>x</sub>	16.2 $\mu\text{Acm}^{-2}$	annealing of Ti <sub>3</sub> C <sub>2</sub> T <sub>x</sub> in air at 550 ° for 6 h	[55]
TiO <sub>2</sub> /Ti <sub>3</sub> C <sub>2</sub> T <sub>x</sub>	15.6 $\mu\text{Acm}^{-2}$	Ti <sub>3</sub> C <sub>2</sub> T <sub>x</sub> oxidized in open air for 6 days	[56]
L-TiO <sub>2</sub> /C	14 $\mu\text{Acm}^{-2}$	annealing of Ti <sub>3</sub> C <sub>2</sub> T <sub>x</sub> at 700 ° for 2 h in CO <sub>2</sub> atmosphere	[57]
TiO <sub>2</sub> /Ti <sub>3</sub> C <sub>2</sub> T <sub>x</sub>	12 $\mu\text{Acm}^{-2}$	interfacial film assembly deposition	[54]
TiO <sub>2</sub> /Ti <sub>3</sub> C <sub>2</sub> T <sub>x</sub>	6 $\mu\text{Acm}^{-2}$	annealing of Ti <sub>3</sub> C <sub>2</sub> T <sub>x</sub> in air at 550 °	[36]
TiO <sub>2</sub> /Ti <sub>3</sub> C <sub>2</sub> T <sub>x</sub>	1.5 $\mu\text{Acm}^{-2}$ (3.1 times higher than that of pure TiO <sub>2</sub> )	annealing of Ti <sub>3</sub> C <sub>2</sub> T <sub>x</sub> in air at 700 ° for 1 h	[58]
TiO <sub>2</sub> /Ti <sub>3</sub> C <sub>2</sub> T <sub>x</sub>	7 $\mu\text{Acm}^{-2}$ (3-times higher than that of pure TiO <sub>2</sub> nanoparticles)	solvothelmal method with Ti <sub>3</sub> C <sub>2</sub> T <sub>x</sub> in ethanol at 80 °C for 24 h	[59]
2M-TiCl <sub>4</sub> @TNT	19.7 $\mu\text{Acm}^{-2}$ (5 times higher than that of TNT)	TNT decorated with laser annealed Ti <sub>3</sub> C <sub>2</sub> T <sub>x</sub>	This work

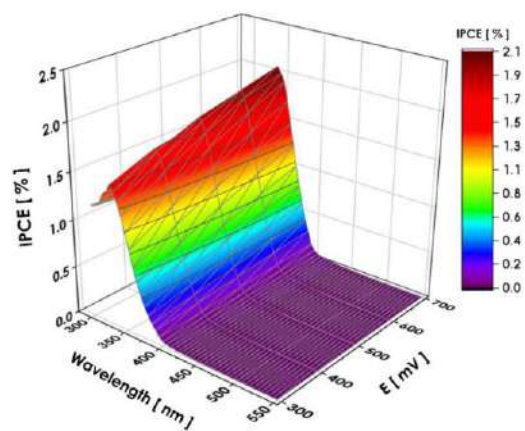


**Figure S4.** IPCE 3D maps recorded for TiCl<sub>4</sub>@TNT in 0.5 M Na<sub>2</sub>SO<sub>4</sub>.

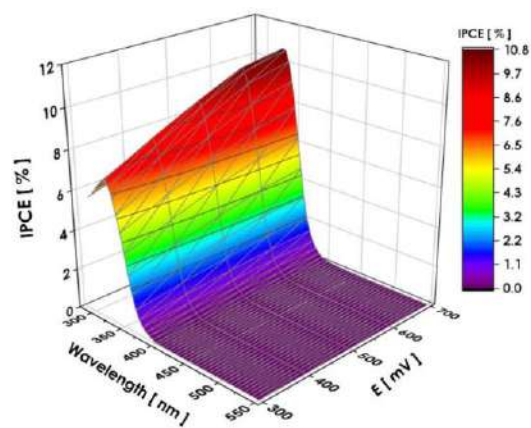


**Figure S5.** IPCE 3D maps recorded for 1M-TiCl<sub>4</sub>@TNT in 0.5 M Na<sub>2</sub>SO<sub>4</sub>.

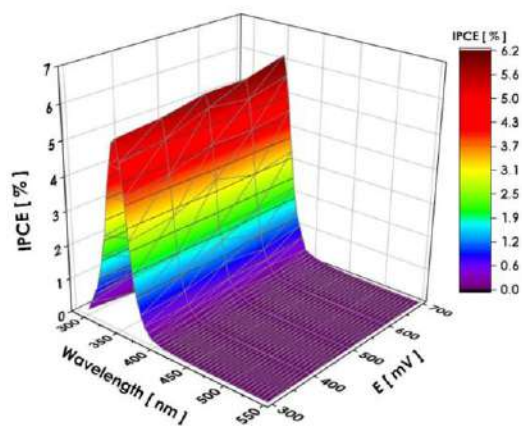


Figure S6. IPCE 3D maps recorded for 3M-TiCl<sub>4</sub>@TNT in 0.5 M Na<sub>2</sub>SO<sub>4</sub>.

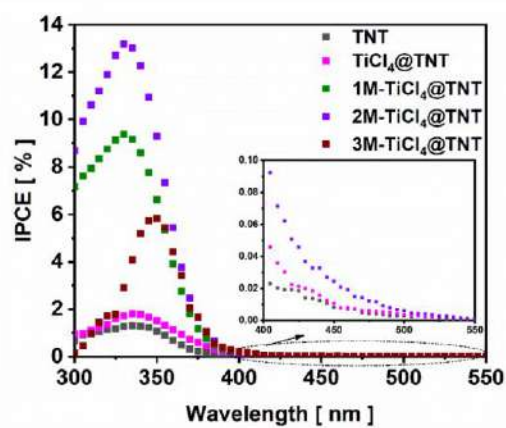
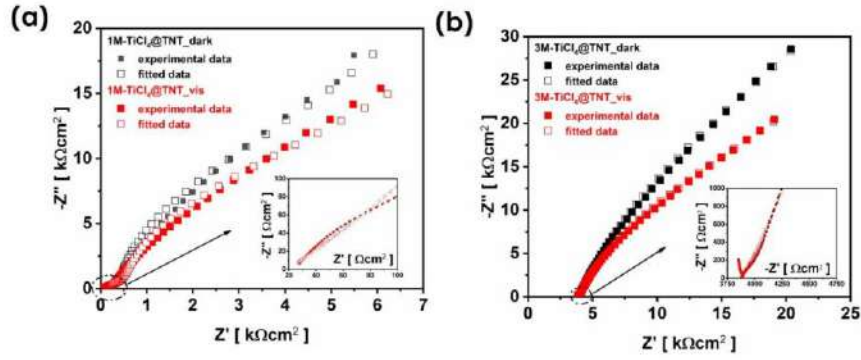


Figure S7. IPCE curve of the samples registered at +500 mV vs. Ag/AgCl/0.1M KCl.



**Figure S8.** Nyquist plots of EIS measurements of (a) 1M-TiCl<sub>4</sub>@TNT and (b) 3M-TiCl<sub>4</sub>@TNT in dark and under visible light illumination. Equivalent circuit used to fitting of the experimental impedance spectra are given in Fig. 12 b) in the main manuscript.

**Table S3.** Values of fitting parameters obtained in dark and under visible light for the prepared electrodes.

	sample	TNT	TiCl <sub>4</sub> @TNT	1M- TiCl <sub>4</sub> @TNT	2M-TiCl <sub>4</sub> @TNT	3M-TiCl <sub>4</sub> @TNT
<b>dark</b>	R <sub>s</sub> [kΩcm <sup>2</sup> ]	0.01	0.15	0.20	0.40	3.87
	R <sub>ct</sub> [kΩcm <sup>2</sup> ]	22.67	21.11	10.14	15.07	43.32
	Q <sub>in</sub> [kΩ <sup>-1</sup> cm <sup>-2</sup> s <sup>u</sup> ]	0.06	0.20	0.09	0.13	0.035
	n	0.83	0.99	0.97	0.82	0.78
	W <sub>or</sub> [Ωcm <sup>2</sup> s <sup>0.5</sup> ]	0.57	1.86	2.62	0.89	1.05
	W <sub>oc</sub> [s <sup>0.5</sup> ]	0.10	2	0.32	0.20	0.12
<b>vis</b>	R <sub>s</sub> [kΩcm <sup>2</sup> ]	0.01	0.15	0.02	0.40	3.87
	R <sub>ct</sub> [kΩcm <sup>2</sup> ]	21.53	19.77	9.03	10.21	30.79
	Q <sub>in</sub> [kΩ <sup>-1</sup> cm <sup>-2</sup> s <sup>u</sup> ]	0.59	0.20	0.09	0.12	0.036
	n	0.83	0.99	0.97	0.84	0.77
	W <sub>or</sub> [Ωcm <sup>2</sup> s <sup>0.5</sup> ]	0.61	1.86	2.69	0.94	0.68
	W <sub>oc</sub> [s <sup>0.5</sup> ]	0.10	2	0.31	0.21	0.11



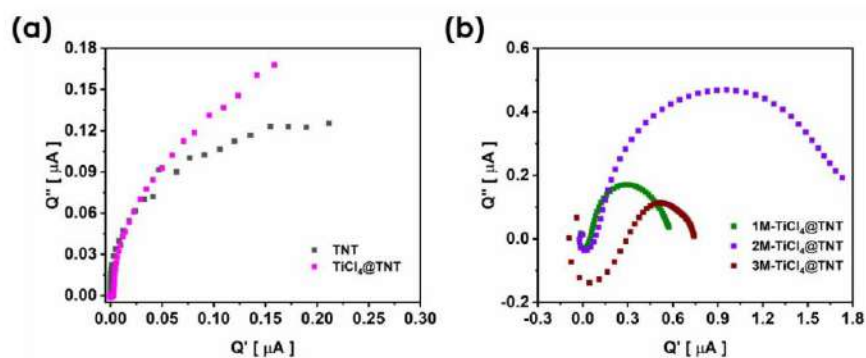


**Figure S9.** Comparison of the IMPS Nyquist plots of (a) TNT and  $TiCl_4@TNT$  (b). 1M- $TiCl_4@TNT$ , 2M- $TiCl_4@TNT$  and 3M- $TiCl_4@TNT$ .

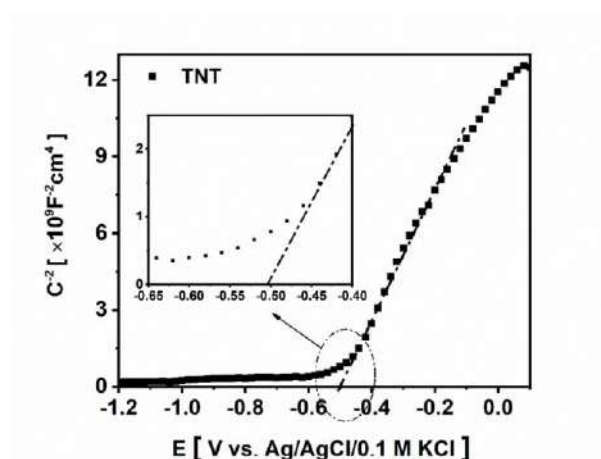


**Figure S10.** Mott-Schottky plot of TNT in 0.5 M  $Na_2SO_4$ .

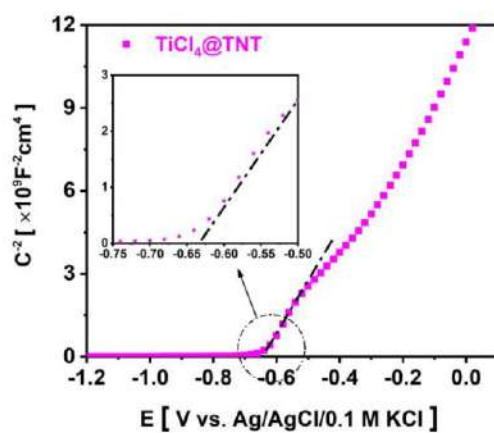


Figure S11. Mott-Schottky plot of  $\text{TiCl}_4@\text{TNT}$  in 0.5 M  $\text{Na}_2\text{SO}_4$ .

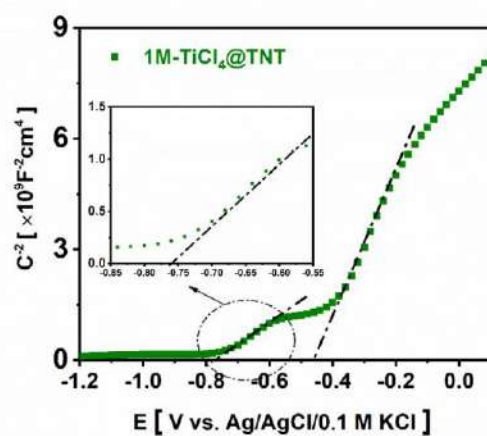


Figure S12. Mott-Schottky plot of 1M- $\text{TiCl}_4@\text{TNT}$  in 0.5 M  $\text{Na}_2\text{SO}_4$ .

## 8 General conclusion

This PhD dissertation consists of three parts namely, the theoretical section, then the section dedicated to methods used for synthesis and characterisation and finally the part describing gathered results with attached published articles. The theoretical part includes the description of the main aim of undertaken studies and state of art regarding the areas where research works were carried out. In the introduction I focused on the fabrication procedures of highly organised nanostructures on the semitransparent substrates for light conversion application. Such semitransparent electrode materials but able for efficient photoconversion can be especially useful to provide renewable energy electronic wearables. In particular, since the photoactivity depends on both morphology and structure of nanomaterials, different nanotubular architectures of titania were described here. The literature studies provide information about the fabrication steps of the semitransparent material consisting of the titania anodically developed onto the transparent conducting oxides including (a) deposition techniques of the thin films (i.e. magnetron sputtering) and (b) the anodization process. In this part, the challenges associated with use of this type of photoelectrodes as well as the already reported modification techniques of the tubular layers intended to raise their performance are also discussed. In the section dedicated to various methods, the experimental setups and working principles of the different equipment used in this work for characterization of fabricated materials are presented. Since numerous physicochemical characterization techniques were carried out, I described briefly scanning electron microscopy and transmission electron microscopy for morphology inspection, energy dispersive X-rays for elemental analysis, X-ray photoelectron spectroscopy providing information about surface chemistry, X-ray diffraction and Raman spectroscopy for verification of the crystal structure, UV-vis spectrophotometry to gain information about optical properties and the Fourier transform infrared spectroscopy that enables me to study surface species, particularly chemical bonds. The part of this paragraph was dedicated also to the electrochemical and photoelectrochemical characterization techniques such as cyclic voltammetry, linear sweep voltammetry, and electrochemical impedance spectroscopy and intensity-modulated photocurrent spectroscopy that provide a lot of data important for analysis of the stability of the material immersed in the electrolyte as well as its response to light. In addition, the working principle of experimental setup dedicated for the quantum efficiency (i.e. IPCE) and the photoluminescence measurements were discussed as well. The experimental section is subdivided into five

subsections. In each subsection, the published article as well as some of the unpublished data are presented.

Taking into account the comment and advices discussed in the review article A1. The first subsection focusses on the optimization of the anodization process of Ti film sputtered onto ITO coated glass substrate resulting in highly ordered and crack-free semitransparent tubular layers characterized with aligned and spaced arrangement. Titanium film sputtered on one side of ITO-glass was anodized in ethylene glycol based electrolyte to grow aligned nanotubes and in diethylene glycol electrolyte, to obtain tubular layer where some distance between tubes is ensured. The composition of the electrolyte used for anodization, such as water content (crucial to obtain aligned nanotubes) and the concentration of the hydrofluoric acid (important in the case of the spaced nanotubes) are adjusted to produce highly ordered semitransparent tubular layers out of the deposited Ti film. The results obtained during this stage indicate that to reach well aligned nanotubes, a water content less than or equal to 10 vol% in the electrolyte is required. Above this threshold value (i.e. 10 vol%), either an irregular morphology is formed or any single nanotube is grown. In the case of the spaced nanotubes, 0.5 M is found to be the optimal concentration of hydrofluoric acid resulting in well-ordered separated nanotubes out of the sputtered Ti film.

Since the selection of the optimal anodization conditions leading to the aligned and spaced nanotubes on the one side of the planar substrate was discussed, the second article A2 describes the methodology resulting in uniform growth of the ordered tubular structures on both sides of the planar substrate. The double-sided electrode was fabricated through the anodization of the both sides of the planar substrate coated with Ti film independently owing to the specially designed sample holder. This approach enabled effective control of the tubular architecture on the sides of the planar substrate, each side independently. In result two symmetric and one asymmetric double-sided electrodes have been successfully obtained. Owing to the fabrication procedure the unique combinations were achieved: (i) aligned nanotubes onto both sides, (ii) spaced nanotubes on both sides, and (iii) one side covered by aligned and the other by spaced nanotubes. The photoelectrochemical measurements showed that the photoelectrode overgrown by aligned nanotubes on its both sides exhibits a photocurrent density approximatively 2 times higher comparing to the substrate overgrown symmetrically by spaced nanotubes. Such performance is the consequence of the large tubes density, identified as the number of nanotubes per unit area, for the aligned nanotubes ( $0.32 \times 10^{11}$  nanotubes per  $\text{cm}^2$ ) comparing to



spaced counterpart ( $0.36 \times 10^{10}$  nanotubes per  $\text{cm}^{-2}$ ), providing higher surface area and more channels for charge percolation.

Elaboration of anodization strategy enabling the formation of tubular layer on optical fiber was also achieved. The experimental setup designed for the anodization of the fiber is composed of two platinum meshes connected together and acting as the cathode. The fiber with titanium coating acting as an anode was placed in the centre between those Pt meshes, while the distance between them has been optimized via diagnostics of the morphology of as-anodized substrate. The results indicated that 3.5 cm is the appropriate distance between the Pt meshes that results in the formation of semitransparent tubular layer on the surface of optical fiber. Such unique, nanostructured morphology has never been achieved for that kind of substrate like optical fiber. The fabricated sensor exhibits a sensitivity to refractive index changes in aqueous solutions of about 260 nm/RIU and is utilized by the prof. Mateusz Śmietana group from Warsaw University of Technology for opto-electrochemical sensing.

In the section dedicated to the article A3, investigation on the improvement of the electrochemical and photoelectrochemical performance of the semitransparent tubular layers via introduction of heteroatoms was described. The next type of semitransparent photoelectrode material, namely tubular layer modified with silver was fabricated by anodizing TiAg alloy films with different Ag content. Elemental analysis performed using Energy dispersive X-ray showed that in the case of aligned nanotubes, about 60 % of the initial Ag content present in deposited TiAg alloy is preserved after anodization. However, when it comes to the spaced nanotubes the Ag content is below the detection limit. Despite no Ag species were detected, the cyclic voltammograms of the spaced nanotube layers obtained after the anodization of the alloy films exhibit higher voltammetric current with the reversible behaviour in presence of redox species in the electrolyte. Such electrochemical performance is unusual for the bare tubular titania layer that due to the position of the valence and conduction bands does not show reversible behaviour. In addition, a three-fold increase in the incident photon-to-current conversion efficiency (IPCE) for the aligned nanotubes grown out of the TiAg alloy films containing 3.5 % of Ag was obtained with the respect to bare oxide layer of the same tubular architecture. It is worth to underline that all tubular layers prepared out of the TiAg alloys exhibit good photostability up to 2 h exposure to illumination. In fact, chronoamperometry curves given in supporting information file of article A3 showed that after an exponential decay (about 500 s) due to recombination processes, the current density holds stable value.

The article A4 discusses the applicability of the tubular layer decorated with Ag nanoislands for the SERS detection of methylene blue. The sensing surface was fabricated by sputtering of Ag onto the top of the semitransparent aligned nanotubes. The obtained material exhibits the highest recyclability among all the fabricated materials.

In the last article A5, the feasibility to raise the IPCE of the semitransparent electrode material through the modification by  $\text{Ti}_3\text{C}_2\text{T}_x/\text{TiO}_2$  heterostructure was briefly described. The heterostructure was obtained by the laser ablation of the  $\text{Ti}_3\text{C}_2\text{T}_x$  solid target being in contact with the liquid isopropanol. The integration of this noble metal free, laser treated catalyst with the highly organised tubular titania layer results in lower intensity of signals contributing to the photoluminescence spectra compared to bare titania sample. This indicates that the presence of the  $\text{Ti}_3\text{C}_2\text{T}_x/\text{TiO}_2$  in the titania based photoanode inhibits the radiative recombination of the photoinduced electron-hole pairs. In addition, modified oxide layer has smaller charge transfer resistance compared to the bare sample that was confirmed by the analysis of the collected electrochemical impedance spectra. The improvement of the electrical properties recorded for the tubular oxide based heterojunction resulted in a substantial, nearly ten time increase in the IPCE value compared to the bare substrate.

In summary, the results gathered in this PhD work provide a set of processing parameters that enable formation of unique, semitransparent electrode materials and their complex diagnostics covering morphology, structure, optical properties, chemical nature of elements, possibility of modification to provide new functionalities, as well as electrochemical and photoelectrochemical testing enabling the verification of photoactivity and sensing features. This study contributes to the fundamental research towards fabrication and improved performance of semitransparent photoanodes based on titania nanotubes applicable for light-driven processes and crucial for novel generations of solar cells, especially important for smart wearables where semitransparent display can also be the source of renewable energy used for charging purposes.

## 9 Scientific achievements

### List of published articles

1. **Kouao, D.-S.**; Hanuš, J.; Kylián, O.; Simerova, R.; Sezemsky, P.; Stranak, V.; Grochowska, K.; Siuzdak, K. *Double-Sided Semitransparent Titania Photoelectrode with Enhanced Light Harvesting*. Renewable and Sustainable Energy Reviews 2024, 197, 114390. <https://doi.org/10.1016/j.rser.2024.114390>. **IF = 16.79 / 200 points** (mechanical engineering)
2. **Kouao, D.-S.**; Grochowska, K.; Stranak, V.; Sezemsky, P.; Gumieniak, J.; Kramek, A.; Karczewski, J.; Coy, E.; Hanus, J.; Kylian, O.; Sawczak, M.; Siuzdak, K. *Laser-Treated MXene as an Electrochemical Agent to Boost Properties of Semitransparent Photoelectrode Based on Titania Nanotubes*. ACS Nano 2024, 18 (14), 10165–10183. <https://doi.org/10.1021/acsnano.4c00092>. **IF = 17.1 / 200 points**. (mechanical engineering)
3. **Kouao, D.-S.**; Hanuš, J.; Kylián, O.; Simerova, R.; Sezemsky, P.; Stranak, V.; Grochowska, K.; Siuzdak, K. *Photoelectrochemical and Electrochemical Activity of Anodic Semitransparent Aligned and Spaced Titania Nanotubes Formed out of Titanium–Silver Alloys*. ACS Applied Nano Materials. 2024, 7 (2), 1548–1561. <https://doi.org/10.1021/acsanm.3c04186>. **IF = 5.90 / 20 points**. (mechanical engineering)
4. Mehrotra, S; Gupta, M, **Kouao, D.-S**; Kumar, A; Singh, P; Bharti, B; Mathuriya, A-S; Bocchetta, P; Kumar, K. *Functional biochar derived from Desmostachya Bipinnata for the Application in Energy Storage/Conversion Devices*. Biomass Conversion and Biorefinery 2024, 14, 17263-17275. <https://doi.org/10.1007/s13399-023-03991-7>. **IF = 3.5 / 70 points**.
5. Taneja, N; **Kouao, D.-S**; Agrawal, N; Kumar, A; Singh, P; Bharti, B; Gupta, M; Kumar, Y. *Biodegradable and Highly Conductive Polymeric Blend based on the Latex of Calotropis gigantea as Solid Electrolyte in Energy Storage Applications*. High Performance Polymers 2023, 35, 16-27. <https://doi.org/10.1177/09540083221122675>. **IF = 1.8 / 40 points**. (mechanical engineering)
6. Hanková, A.; Kuzminova, A.; Hanuš, J.; Sezemsky, P.; Simerova, R.; Stranak, V.; Grochowska, K.; **Kouao, D.-S.**; Siuzdak, K.; Procházka, M.; Košutová, T.; Kylián, O. *TiO<sub>2</sub>/Ag Nanostructured Coatings as Recyclable Platforms for Surface-Enhanced Raman Scattering Detection*. Surfaces and Interfaces 2022, 35, 102441.

<https://doi.org/10.1016/j.surfin.2022.102441>. **IF = 6.20 / 70 points.** (mechanical engineering)

7. **Kouao, D.-S.**; Grochowska, K.; Siuzdak, K. *The Anodization of Thin Titania Layers as a Facile Process towards Semitransparent and Ordered Electrode Material*. *Nanomaterials* 2022, 12 (7) 1131.

<https://doi.org/10.3390/nano12071131>. **IF = 5.30 / 100 points.** (mechanical engineering)

8. Piłula, E; **Kouao, D.-S.**; Grochowska, K.; Sezemsky, P.; Simerova, R.; Dominguez, I; Siuzdak, K.; Villar, I-D; Stranak, V.; Śmietana, M. *Ordered Titanium Dioxide Nanotubes for Lossy-mode Resonance-based Humidity Sensing. In Optical Fiber Sensors*. Optica Publishing Group 2022, 4-62

<https://doi.org/10.1364/OFS.2022.W4.62>. (Conference paper)

9. **Kouao, D.-S.**; Gupta, M; Kumar, A; Sharma, V; Pandit, S; Bocchetta, P; Kumar. Y. *The Effect of Modifications of Activated Carbon Materials on the Capacitive Performance: Surface, Microstructure, and Wettability*. *Journal of Composites Science* 2021, 5(3), 66.

<https://doi.org/10.3390/jcs5030066>. **IF = 3.0 / 20 points.**

10. **Kouao, D.-S.**; Panta, P; Shulga, Y-M; Kumar, A; Gupta, M; Kumar, Y. *Physico-chemical Characterization of Activated Carbon Synthesized from Datura Metel's Peels and Comparative Capacitive Performance Analysis in Acidic Electrolytes and Ionic Liquids*. *Bioresource Technology Reports* 2020, 11, 100516.

<https://doi.org/10.1016/j.biteb.2020.100516>. **IF = no IF / 20 points.** (mechanical engineering)

**Total sum of IF: 59.59**

**Total sum of point: 740**

## **Monographs and Chapters**

1. **Kouao, D.-S.**; Siuzdak K. *MXenes electrocatalysts for water splitting* – chapter 5 in book: “Water Splitting: Production of Hydrogen”, **Wiley-Scrivener 2024, editor: Dr Inamuddin**, accepted and currently under editorial work

2. **Kouao, D.-S.** *Semitransparent aligned and spaced titania nanotubes materials formed out of TiAg alloys with unique photoelectrochemical activities*, **monograph, TSD PAN, 2023.** (Submitted)



3. **Kouao, D.-S.** *Synthesis of semitransparent titania nanotubes formed out of Cu-doped Ti film and study on photoelectrochemical properties*, **monograph, TSD PAN, 2022**. Accepted and currently under editorial work.

4. **Kouao, D.-S.** *Semitransparent layer of aligned titania nanotubes formed out of thin Ti film*, **monograph, TSD PAN, 2021**. Published, ISBN: 978-83-66928-00-8.

### **Presentations (conferences, seminars)**

1. **Kouao, D.-S.**; Grochowska, K.; Stranak, V.; Sezemsky, P.; Gumieniak, J.; Kramek, A.; Karczewski, J.; Coy, E.; Hanus, J.; Kylian, O.; Sawczak, M.; Siuzdak, K. *Laser Treatment of MXene Towards its Incorporation in Titania Nanotubes for Improved Light Conversion*. The 2024 Fall Meeting of the European Materials Research Society (E-MRS), 2024 (poster).

16.09.2024 - 19.09.2024

2. **Kouao, D.-S.**; Grochowska, K.; Bogdanowicz, R.; Siuzdak, K. *Towards sustainable fabrication of MXenes - electrochemically assisted etching performed in diluted HBF<sub>4</sub> based electrolyte*. The 2024 Fall Meeting of the European Materials Research Society (E-MRS), 2024 (poster). 16.09.2024 - 19.09.2024

3. **Kouao, D.-S.** *Electrochemical performance of semitransparent titania nanotubes functionalized with laser-treated MXene*. The Young Seminar of the Advanced Materials Center of Modern Material Technologies for Electrochemical and Sensing Applications, 2024 (oral presentation given by D.-S. Kouao). 10.09.2024

4. **Kouao, D.-S.**; Hanus, J.; Kylian, O.; Simerova, R.; Sezemsky, P.; Stranak, V.; Grochowska, K.; Siuzdak, K. *Semitransparent Aligned and Spaced Titania Nanotubes Materials Formed out of TiAg alloys with Unique Electrochemical Activities*. The 2023 Spring Meeting of the European Materials Research Society (E-MRS), 2023 (oral presentation given by D.-S. Kouao). 29.05.2023 – 02.06.2023.

5. **Kouao, D.-S.** *Development of the fabrication process of semitransparent electrodes for the light harvesting and advanced optical diagnostic*. TSD PAN Doctoral seminar, 2023. (oral presentation given by D.-S. Kouao). 12.06.2023 – 14.06.2023

6. **Kouao, D.-S.**; Sezemsky, P.; Śmietana, M.; Kylian, O.; Bogdanowicz, R.; Hanus, J.; Simerova, R.; Stranak, V.; Grochowska, K.; Siuzdak, K. *Double-sided Semitransparent Photoelectrodes based on Titania Nanotube Arrays*. 14th International Conference on Nanomaterials - Research & Application, NANOCON 2022 (poster). 19.10.2023 – 21.10.2023.

7. Hanus, J; **Kouao, D.-S**; Siuzdak, K; Simerova, R; Kosutova, T; Stranak, V; Sezemsky, P; Grochowska, K; Kylian, O. *Plasma assisted deposition of TiO<sub>2</sub> nanotubes doped by Ag and Cu*. International Conference on Laser, Plasma and Radiation Science and Technology, 2022 (oral presentation given by J. Hanus). 07.06.2023 – 10.06.2022.
8. Hanková, A.; Kuzminova, A.; Hanuš, J.; Sezemsky, P.; Simerova, R.; Stranak, V.; Grochowska, K.; **Kouao, D.-S**; Siuzdak, K.; Procházka, M.; Košutová, T.; Kylián, O. *Plasma-assisted production of sensitive and recyclable nanostructured TiO<sub>2</sub>/Ag SERS-active platforms*. 18th International Conference on Plasma Surface Engineering, 2022 (oral presentation by O. Kylian). 12.09.2022 – 15.09.2022.
9. **Kouao, D.-S**; *Developement of the semitransparent electrodes out of Cu-doped Ti film and their diagnostics*. TSD PAN Doctoral seminar, 2022. (oral presentation given by D.-S. Kouao). 13.06.2022 – 14.06.2022.
10. **Kouao, D.-S**; *Preparation Of Semitransparent Electrode For Enhanced Light Harvesting*. TSD PAN Doctoral seminar, 2021. (oral presentation given by D.-S. Kouao). 17.06.2021.
11. **Kouao, D.-S**; Sezemsky, P; Śmietana, M; Kylian, O; Bogdanowicz, R; Hanus, J; Simerova, R; Stranak, V; Grochowska, K; Siuzdak, K. *Semitransparent layer of aligned and separated titania nanotubes formed out of thin Ti film*. 3rd International Workshop on Functional Nanostructured Materials - FUNAM-3, 2021 (oral presentation given by D.-S. Kouao). 06.10.2021 – 08.10.2021.
12. Siuzdak, K; Sezemsky, P; Śmietana, M; Kylian, O; Bogdanowicz, R; Hanus, J; Simerova, R; Stranak, V; **Kouao, D.-S**; Grochowska, K. *Anodization of thin titanium films – challenges and opportunities*. 3rd International Workshop on Functional Nanostructured Materials - FUNAM-3, 2021 (oral presentation given by K. Siuzdak). 06.10.2021 – 08.10.2021.
13. Grochowska, K; Sezemsky, P; Śmietana, M; Kylian, O; Bogdanowicz, R; Hanus, J; Simerova, R; Stranak, V; **Kouao, D.-S**; Siuzdak, K. *Low-temperature plasma-assisted deposition of transparent conductive oxide-titanium thin films: towards semitransparent anodic titania fabrication*. 3rd International Workshop on Functional Nanostructured Materials - FUNAM-3, 2021 (poster). 06.10.2021 – 08.10.2021.

## Awards

Best poster award for the poster presentation in the Symposium O “MXenes and related materials” during the 2024 Fall Meeting of the European Materials Research Society (E-MRS), 2024.

## Other scientific activities

1. Participation in training in hydrothermal synthesis of nanomaterial under the supervision of PhD DSc Agata Szczeszak, Department of Rare Earths, Faculty of Chemistry, Adam Mickiewicz University, Poznań . 11.03.2024 – 16.03.2024.

2. Participation in *Advances in Functional Materials Summer School*, organized by Gdańsk University of Technology, Gdańsk . 26.07.2023 – 28.07.2023.

3. Photocatalytic measurements for samples obtained from the Sobex company. Tests performed under the supervision of PhD DSc Eng. Katarzyna Siuzdak, 2023

4. Participation in e-SPARK: *International Summer School on Experimental Electrochemistry*, organized by Institute of Physical Chemistry Polish Academy of Sciences, Warsaw . 05.05.2022 – 11.05.2022.

## Scientific project

PhD student in the international project CEUS-UNISONO (2020/02/Y/ST8/00030) *Semitransparent titania nanostructures on complex geometry surfaces for enhanced light harvesting and sensing* financed by National Science Centre in Poland, PI: PhD DSc Eng. Katarzyna Siuzdak, 05.2021 – present.

## Patent

Co-author of invention entitled: *Oxygen enriched plant based activated carbon composition and method of preparation thereof* (application No.202111007490 A; date of filling of Application: 23.02.2021).

Name of Applicant: Sharda University

Address of Applicant: Plot No. 32 & 34, Knowledge Park III, Greater Noida, Uttar Pradesh, 201310, India. Uttar Pradesh India

Name of Inventors: Dr. Meenal Gupta; Dr. Yogesh Kumar; Dr. Ashwani Kumar; Purushottam Panta; Kouao Dujearic-Stephane

### Scientific activity in numbers

Name	Dujearic-Stephane Kouao
h-index (Web of Science, 12.09.2024)	4
Citations (Web of Science, 04.09.2024)	90
Conference activities	4 posters, 9 oral presentations
Number of articles	10
Participation in scientific projects	1



## 10 Authors contribution statement

M.Sc. Dujearic-Stephane Kouao  
Department of Physical Aspects of Ecoenergy  
Centre of Plasma and Laser Engineering  
Institute of Fluid-Flow Machinery  
Polish Academy of Sciences  
Fiszera 14, 80-231 Gdańsk

25.06.2024

[dkouao@imp.gda.pl](mailto:dkouao@imp.gda.pl)

### Statement of contribution

In the article A1:

- **Kouao, D.-S.**; Grochowska, K.; Siuzdak, K. The Anodization of Thin Titania Layers as a Facile Process towards Semitransparent and Ordered Electrode Material. **Nanomaterials** **2022**, 12 (7), 1131. <https://doi.org/10.3390/nano12071131>. **IF = 5.30 / 100 points.**

I wrote the major part of the original draft and I was responsible for the preparation of the most of responses to the reviewers comments. I also took part in the literature analysis that was used for the preparation of the review paper.

In the article A2:

- **Kouao, D.-S.**; Hanuš, J.; Kylián, O.; Simerova, R.; Sezemsky, P.; Stranak, V.; Grochowska, K.; Siuzdak, K. Double-Sided Semitransparent Titania Photoelectrode with Enhanced Light Harvesting. **Renewable and Sustainable Energy Reviews** **2024**, 197, 114390. <https://doi.org/10.1016/j.rser.2024.114390>. **IF = 16.79 / 200 points.**

I was responsible for the optimization of the anodization procedure and the fabrication of semitransparent electrodes by growing the tubular layers on the ITO-glass substrates obtained from the research groups from Czech Republic. I performed measurements including Raman, UV-vis spectroscopies together with electrochemical and photoelectrochemical measurements (i.e. CV, LSV, EIS). I was involved in analysis of the spectra collected from the above

mentioned measurements as well as the characterization of morphological features of the tubular architectures. I wrote the most of the original draft and I took major role in preparation of the response to the reviewers comments.

In the article A3:

- Hanková, A.; Kuzminova, A.; Hanuš, J.; Sezemsky, P.; Simerova, R.; Stranak, V.; Grochowska, K.; **Kouao, D.-S.**; Siuzdak, K.; Procházka, M.; Košutová, T.; Kylián, O. TiO<sub>2</sub>/Ag Nanostructured Coatings as Recyclable Platforms for Surface-Enhanced Raman Scattering Detection. **Surfaces and Interfaces** **2022**, *35*, 102441. <https://doi.org/10.1016/j.surfin.2022.102441>. **IF = 6.20 / 70 points.**

I was responsible for the fabrication of semitransparent electrodes by growing the tubular layers on the ITO-glass substrates obtained from the research groups from Czech Republic. I also wrote the part of the experimental part related to anodization of the Ti film and take part in the reviewing of the original draft.

In the article A4:

- **Kouao, D.-S.**; Hanuš, J.; Kylián, O.; Simerova, R.; Sezemsky, P.; Stranak, V.; Grochowska, K.; Siuzdak, K. Photoelectrochemical and Electrochemical Activity of Anodic Semitransparent Aligned and Spaced Titania Nanotubes Formed out of Titanium–Silver Alloys. **ACS Applied Nano Materials**. **2024**, *7* (2), 1548–1561. <https://doi.org/10.1021/acsanm.3c04186>. **IF = 5.90 / 20 points.**

I was responsible for the optimization of the anodization procedure and the fabrication of the semitransparent electrodes by growing the tubular layers on the ITO-glass substrates. I performed measurements including Raman, UV-vis spectroscopies together with electrochemical and photoelectrochemical measurements (i.e. CV, LSV, EIS, IPCE). I was involved in the analysis of the spectra collected from the above mentioned measurements as well as the morphological features of the tubular architectures. I wrote the most of the original draft and I took major role in preparation of the response to the reviewers comments.

In the article A5:

- **Kouao, D.-S.**; Grochowska, K.; Stranak, V.; Sezemsky, P.; Gumieniak, J.; Kramek, A.; Karczewski, J.; Coy, E.; Hanus, J.; Kylian, O.; Sawczak, M.; Siuzdak, K. Laser-Treated MXene as an Electrochemical Agent to Boost Properties of Semitransparent Photoelectrode Based on Titania Nanotubes. **ACS Nano** **2024**, 18 (14), 10165–10183. <https://doi.org/10.1021/acsnano.4c00092>. **IF = 17.1 / 200 points.**

I fabricated the semitransparent electrodes by growing the tubular layers on the substrates. I took part in the laser ablation of the  $\text{Ti}_3\text{AlC}_2$ . I took part in the photoluminescence measurements. I performed the functionalization of the tubular layer with the laser ablated material. I performed measurements including Raman, UV-vis spectroscopy together with electrochemical and photoelectrochemical measurements (i.e. CV, LSV, EIS, IPCE, IMPS). I analyzed the spectra collected from the above mentioned measurements as well as the SEM, TEM and SAED measurements. I wrote the original draft and response to the reviewers comments.



PhD DSc Eng. Katarzyna Siuzdak, Prof. IMP PAN

25.06.2024

Department of Physical Aspects of Ecoenergy

Centre of Plasma and Laser Engineering

Institute of Fluid-Flow Machinery

Polish Academy of Sciences

Fiszera 14, 80-231 Gdańsk

ksiuzdak@imp.gda.pl

#### Statement of contribution

In the article A1:

- Kouao, D.-S.; Grochowska, K.; **Siuzdak, K.** The Anodization of Thin Titania Layers as a Facile Process towards Semitransparent and Ordered Electrode Material. **Nanomaterials** **2022**, 12 (7), 1131. <https://doi.org/10.3390/nano12071131>. **IF = 5.30 / 100 points.**

I initiated the idea of preparation of this kind of review, planned the parts of the draft and was involved in its writing. I also took part in preparation of the responses to the reviewers comments. I supported PhD student in every step of the writing: helped him with literature analysis and corrected his part as well.

In the article A2:

- Kouao, D.-S.; Hanuš, J.; Kylián, O.; Simerova, R.; Sezemsky, P.; Stranak, V.; Grochowska, K.; **Siuzdak, K.** Double-Sided Semitransparent Titania Photoelectrode with Enhanced Light Harvesting. **Renewable and Sustainable Energy Reviews** **2024**, 197, 114390. <https://doi.org/10.1016/j.rser.2024.114390>. **IF = 16.79 / 200 points.**

I initiated the research topic and as a PI of the CEUS-UNISONO project, I was responsible for the coordination of the works and contacts with the foreign research groups. I was significantly involved in the planning process of all the carried out experiments. I took part in the analysis of the electrochemical and photoelectrochemical measurements as well as I verified the results



describing morphology and structure of the material. I revised the whole manuscript and supervised the preparation of the responses to the reviewers comments. I supported PhD student at every stage of the realisation of his works.

In the article A3:

- Hanková, A.; Kuzminova, A.; Hanuš, J.; Sezemsky, P.; Simerova, R.; Stranak, V.; Grochowska, K.; Kouao, D.-S.; **Siuzdak, K.**; Procházka, M.; Košutová, T.; Kylián, O. TiO<sub>2</sub>/Ag Nanostructured Coatings as Recyclable Platforms for Surface-Enhanced Raman Scattering Detection. **Surfaces and Interfaces** **2022**, 35, 102441. **IF = 6.20 / 70 points.**

I was involved in the fabrication of the semitransparent titania nanotubes modified with silver, optimization of this process leading to the organized nanostructures. I also take part in the preparation of the original related with the discussion on the morphology of the prepared samples.

In the article A4:

- Kouao, D.-S.; Hanuš, J.; Kylián, O.; Simerova, R.; Sezemsky, P.; Stranak, V.; Grochowska, K.; **Siuzdak, K.** Photoelectrochemical and Electrochemical Activity of Anodic Semitransparent Aligned and Spaced Titania Nanotubes Formed out of Titanium–Silver Alloys. **ACS Applied Nano Materials**. **2024**, 7 (2), 1548–1561. <https://doi.org/10.1021/acsanm.3c04186>. **IF = 5.90 / 20 points.**

I initiated the research topic and as a PI of the CEUS-UNISONO project, I was responsible for the coordination of the works and contacts with the foreign research groups. I was significantly involved in the planning process of all the carried out experiments. I took part in the analysis of the electrochemical and photoelectrochemical measurements as well as I verified the results describing morphology and structure of the material. I revised the whole manuscript and supervised the preparation of the responses to the reviewers comments. I supported PhD student at every stage of the realisation of his works.



In the article A5:

- Kouao, D.-S.; Grochowska, K.; Stranak, V.; Sezemsky, P.; Gumieniak, J.; Kramek, A.; Karczewski, J.; Coy, E.; Hanus, J.; Kylian, O.; Sawczak, M.; **Siuzdak, K.** Laser-Treated MXene as an Electrochemical Agent to Boost Properties of Semitransparent Photoelectrode Based on Titania Nanotubes. **ACS Nano** **2024**, 18 (14), 10165–10183. <https://doi.org/10.1021/acsnano.4c00092>. **IF = 17.1 / 200 points.**

I initiated the research topic and as a PI of the CEUS-UNISONO project, I was responsible for the coordination of the works and contacts with the foreign research groups. I was significantly involved in the planning process of all the carried out experiments. I took part in the analysis of the electrochemical and photoelectrochemical measurements as well as I verified the results describing morphology and structure of the material. I revised the whole manuscript and supervised the preparation of the responses to the reviewers comments. I supported PhD student at every stage of the realisation of his works.

dr hab. inż. Katarzyna Siuzdak  
prof. IMP PAN

Kierownik  
Pracowni Materiałów Funkcjonalnych



PhD DSc Katarzyna Grochowska  
Department of Physical Aspects of Ecoenergy  
Centre of Plasma and Laser Engineering  
Institute of Fluid-Flow Machinery  
Polish Academy of Sciences  
Fiszera 14 st.  
80-231 Gdańsk

Gdańsk, 25.06.2024

kgrochowska@imp.gda.pl

#### Statement of contribution

In the article A1:

- Kouao, D.-S.; **Grochowska, K.**; Siuzdak, K. The Anodization of Thin Titania Layers as a Facile Process towards Semitransparent and Ordered Electrode Material. **Nanomaterials** **2022**, 12 (7), 1131. <https://doi.org/10.3390/nano12071131>. **IF = 5.30 / 100 points.**

I took part in the preparation of the original draft and response to the reviewers comments.

In the article A2:

- Kouao, D.-S.; Hanuš, J.; Kylián, O.; Simerova, R.; Sezemsky, P.; Stranak, V.; **Grochowska, K.**; Siuzdak, K. Double-Sided Semitransparent Titania Photoelectrode with Enhanced Light Harvesting. **Renewable and Sustainable Energy Reviews** **2024**, 197, 114390. <https://doi.org/10.1016/j.rser.2024.114390>. **IF = 16.79 / 200 points.**

I took part in the analysis of the UV-vis and Raman spectroscopy measurements. I was involved in the revision of the manuscript and response to the reviewers comments.

In the article A3:

- Hanková, A.; Kuzminova, A.; Hanuš, J.; Sezemsky, P.; Simerova, R.; Stranak, V.; **Grochowska, K.**; Kouao, D.-S.; Siuzdak, K.; Procházka, M.; Košutová, T.; Kylián, O. TiO<sub>2</sub>/Ag Nanostructured Coatings as Recyclable Platforms for Surface-Enhanced

Raman Scattering Detection. **Surfaces and Interfaces** 2022, 35, 102441.  
<https://doi.org/10.1016/j.surfin.2022.102441>. **IF = 6.20 / 70 points.**

I took part in discussion regarding planning of SERS activity measurements and analysis of obtained SERS results. I also took part in writing of the original draft.

In the article A4:

- Kouao, D.-S.; Hanuš, J.; Kylián, O.; Simerova, R.; Sezemsky, P.; Stranak, V.; **Grochowska, K.**; Siuzdak, K. Photoelectrochemical and Electrochemical Activity of Anodic Semitransparent Aligned and Spaced Titania Nanotubes Formed out of Titanium–Silver Alloys. **ACS Applied Nano Materials**. 2024, 7 (2), 1548–1561.  
<https://doi.org/10.1021/acsanm.3c04186>. **IF = 5.90 / 20 points.**

I took part in the analysis of the data obtained from UV-vis and Raman spectroscopy measurements. I was also involved in the revision of the first draft and response to the reviewers comments.

In the article A5:

- Kouao, D.-S.; **Grochowska, K.**; Stranak, V.; Sezemsky, P.; Gumieniak, J.; Kramek, A.; Karczewski, J.; Coy, E.; Hanus, J.; Kylian, O.; Sawczak, M.; Siuzdak, K. Laser-Treated MXene as an Electrochemical Agent to Boost Properties of Semitransparent Photoelectrode Based on Titania Nanotubes. **ACS Nano** 2024, 18 (14), 10165–10183.  
<https://doi.org/10.1021/acsnano.4c00092>. **IF = 17.1 / 200 points.**

I took part in the analysis of the UV-vis and Raman spectroscopy measurements for collected samples. I was also involved in the revision of the manuscript and response to the reviewers.



Prof. RNDr. Vítězslav Straňák, Ph.D.  
Faculty of Science  
University of South Bohemia  
Branišovská 1760 České Budějovice  
Czech Republic

24.06.2024

[stranak@prf.jcu.cz](mailto:stranak@prf.jcu.cz)

### Statement of contribution

In the article A2:

- Kouao, D.-S.; Hanuš, J.; Kylián, O.; Simerova, R.; Sezemsky, P.; **Stranak, V.**; Grochowska, K.; Siuzdak, K. Double-Sided Semitransparent Titania Photoelectrode with Enhanced Light Harvesting. **Renewable and Sustainable Energy Reviews** 2024, 197, 114390. <https://doi.org/10.1016/j.rser.2024.114390>. **IF = 16.79 / 200 points.**

Together with the PI from Polish side PhD DSc Katarzyna Siuzdak, I initiated the research topic. I also took part in the revision process of the first draft and responses to the reviewer's comments.

In the article A3:

- Hanková, A.; Kuzminova, A.; Hanuš, J.; Sezemsky, P.; Simerova, R.; **Stranak, V.**; Grochowska, K.; Kouao, D.-S.; Siuzdak, K.; Procházka, M.; Košutová, T.; Kylián, O. TiO<sub>2</sub>/Ag Nanostructured Coatings as Recyclable Platforms for Surface-Enhanced Raman Scattering Detection. **Surfaces and Interfaces** 2022, 35, 102441. <https://doi.org/10.1016/j.surfin.2022.102441>. **IF = 6.20 / 70 points.**

In this work, I have participated in sample preparation, deposition of thin film and their characterization. I also took part in the revision process of the first draft and responses to the reviewer's comments.

In the article A4:

- Kouao, D.-S.; Hanuš, J.; Kylián, O.; Simerova, R.; Sezemsky, P.; **Stranak, V.**; Grochowska, K.; Siuzdak, K. Photoelectrochemical and Electrochemical Activity of

Anodic Semitransparent Aligned and Spaced Titania Nanotubes Formed out of Titanium-Silver Alloys. **ACS Applied Nano Materials**. 2024, 7 (2), 1548–1561. <https://doi.org/10.1021/acsanm.3c04186>. IF = 5.90 / 20 points.

Together with the PI from the Polish side PhD DSc Katarzyna Siuzdak, I initiated the research topic. I also took part in the revision process of the first draft and responses to the reviewer's comments.

In the article A5:

- Kouao, D.-S.; Grochowska, K.; **Stranak, V.**; Sezemsky, P.; Gumieniak, J.; Kramek, A.; Karczewski, J.; Coy, E.; Hanus, J.; Kylian, O.; Sawczak, M.; Siuzdak, K. Laser-Treated MXene as an Electrochemical Agent to Boost Properties of Semitransparent Photoelectrode Based on Titania Nanotubes. **ACS Nano** 2024, 18 (14), 10165–10183. <https://doi.org/10.1021/acsnano.4c00092>. IF = 17.1 / 200 points.

Together with the PI of CEUS-UNISONO project from the Polish side PhD DSc Katarzyna Siuzdak, I initiated the research topic. I also took part in the revision of the first draft of the manuscript





Mgr. Radka Šimerová  
Faculty of Science  
University of South Bohemia  
Branišovská 1760 České Budějovice  
Czech Republic

25.06.2024

rsimerova@seznam.cz

#### Statement of contribution

In the article A2:

- Kouao, D.-S.; Hanuš, J.; Kylián, O.; **Simerova, R.**; Sezemsky, P.; Stranak, V.; Grochowska, K.; Siuzdak, K. Double-Sided Semitransparent Titania Photoelectrode with Enhanced Light Harvesting. **Renewable and Sustainable Energy Reviews** **2024**, 197, 114390. <https://doi.org/10.1016/j.rser.2024.114390>. **IF = 16.79 / 200 points.**

I performed the deposition of the ITO and TiO<sub>x</sub> interlayer film onto the glass substrates and revised the manuscript.

In the article A3:

- Hanková, A.; Kuzminova, A.; Hanuš, J.; Sezemsky, P.; **Simerova, R.**; Stranak, V.; Grochowska, K.; Kouao, D.-S.; Siuzdak, K.; Procházka, M.; Košutová, T.; Kylián, O. TiO<sub>2</sub>/Ag Nanostructured Coatings as Recyclable Platforms for Surface-Enhanced Raman Scattering Detection. **Surfaces and Interfaces** **2022**, 35, 102441. <https://doi.org/10.1016/j.surfin.2022.102441>. **IF = 6.20 / 70 points.**

I performed sample preparation and investigation.

In the article A4:

- Kouao, D.-S.; Hanuš, J.; Kylián, O.; **Simerova, R.**; Sezemsky, P.; Stranak, V.; Grochowska, K.; Siuzdak, K. Photoelectrochemical and Electrochemical Activity of

*Radka Šimerová*

Anodic Semitransparent Aligned and Spaced Titania Nanotubes Formed out of Titanium–Silver Alloys. **ACS Applied Nano Materials**. 2024, 7 (2), 1548–1561. <https://doi.org/10.1021/acsanm.3c04186>. IF = 5.90 / 20 points.

I performed the deposition of the ITO and TiO<sub>x</sub> interlayer film onto the glass substrates and revised the manuscript.

*Radha Jimeera*

Mgr. Petr Sezemský, Ph.D.  
Faculty of Science  
University of South Bohemia  
Braňšovská 1760 České Budějovice  
Czech Republic

24.06.2024

sezemskypetr@gmail.com

#### Statement of contribution

In the article A2:

- Kouao, D.-S.; Hanuš, J.; Kylián, O.; Simerova, R.; **Sezemsky, P.**; Stranak, V.; Grochowska, K.; Siuzdak, K. Double-Sided Semitransparent Titania Photoelectrode with Enhanced Light Harvesting. **Renewable and Sustainable Energy Reviews** **2024**, 197, 114390. <https://doi.org/10.1016/j.rser.2024.114390>. **IF = 16.79 / 200 points.**

I performed the deposition and optimization of the ITO, TiO<sub>x</sub> interlayer and Ti film onto the glass substrates and revised the manuscript and response to the reviewers comments.

In the article A3:

- Hanková, A.; Kuzminova, A.; Hanuš, J.; **Sezemsky, P.**; Simerova, R.; Stranak, V.; Grochowska, K.; Kouao, D.-S.; Siuzdak, K.; Procházka, M.; Košutová, T.; Kylián, O. TiO<sub>2</sub>/Ag Nanostructured Coatings as Recyclable Platforms for Surface-Enhanced Raman Scattering Detection. **Surfaces and Interfaces** **2022**, 35, 102441. <https://doi.org/10.1016/j.surfin.2022.102441>. **IF = 6.20 / 70 points.**

I performed the deposition and optimization of the ITO, TiO<sub>x</sub> interlayer and Ti film onto the glass substrates and revised the manuscript.

In the article A4:

- Kouao, D.-S.; Hanuš, J.; Kylián, O.; Simerova, R.; **Sezemsky, P.**; Stranak, V.; Grochowska, K.; Siuzdak, K. Photoelectrochemical and Electrochemical Activity of

Anodic Semitransparent Aligned and Spaced Titania Nanotubes Formed out of Titanium–Silver Alloys. **ACS Applied Nano Materials**. 2024, 7 (2), 1548–1561. <https://doi.org/10.1021/acsanm.3c04186>. **IF = 5.90 / 20 points**.

I performed the deposition of the ITO film onto the glass substrates and revised the manuscript.

In the article A5:

- Kouao, D.-S.; Grochowska, K.; Stranak, V.; **Sezemsky, P.**; Gumieniak, J.; Kramek, A.; Karczewski, J.; Coy, E.; Hanus, J.; Kylian, O.; Sawczak, M.; Siuzdak, K. Laser-Treated MXene as an Electrochemical Agent to Boost Properties of Semitransparent Photoelectrode Based on Titania Nanotubes. **ACS Nano** 2024, 18 (14), 10165–10183. <https://doi.org/10.1021/acsnano.4c00092>. **IF = 17.1 / 200 points**.

I performed the deposition of the ITO film onto the glass substrates and revised the manuscript.

  
.....  
Petr Sezemský

doc. Mgr. Jan Hanuš, Ph.D.  
Department of Macromolecular Physics  
Faculty of Mathematics and Physics  
Charles University  
V Holešovičkách 2/747  
180 00 Praha 8  
Czech Republic

24.06.2024

jan.hanus@gmail.com

#### Statement of contribution

In the article A2:

- Kouao, D.-S.; **Hanuš, J.**; Kylián, O.; Simerova, R.; Sezemsky, P.; Stranak, V.; Grochowska, K.; Siuzdak, K. Double-Sided Semitransparent Titania Photoelectrode with Enhanced Light Harvesting. **Renewable and Sustainable Energy Reviews** **2024**, 197, 114390. <https://doi.org/10.1016/j.rser.2024.114390>. **IF = 16.79 / 200 points.**

I performed the deposition of the TiO<sub>x</sub> interlayer and Ti film onto the ITO/glass substrates and revised the manuscript and response to the reviewers comments.

In the article A3:

- Hanková, A.; Kuzminova, A.; **Hanuš, J.**; Sezemsky, P.; Simerova, R.; Stranak, V.; Grochowska, K.; Kouao, D.-S.; Siuzdak, K.; Procházka, M.; Košutová, T.; Kylián, O. TiO<sub>2</sub>/Ag Nanostructured Coatings as Recyclable Platforms for Surface-Enhanced Raman Scattering Detection. **Surfaces and Interfaces** **2022**, 35, 102441. <https://doi.org/10.1016/j.surfin.2022.102441>. **IF = 6.20 / 70 points.**

I performed the deposition of the TiO<sub>x</sub> interlayer and Ti film onto the ITO/glass substrates.

In the article A4:

- Kouao, D.-S.; **Hanuš, J.**; Kylián, O.; Simerova, R.; Sezemsky, P.; Stranak, V.; Grochowska, K.; Siuzdak, K. Photoelectrochemical and Electrochemical Activity of Anodic Semitransparent Aligned and Spaced Titania Nanotubes Formed out of



Titanium–Silver Alloys. **ACS Applied Nano Materials**. 2024, 7 (2), 1548–1561.  
<https://doi.org/10.1021/acsanm.3c04186>. **IF = 5.90 / 20 points.**

I performed the deposition of the TiO<sub>x</sub> interlayer and TiAg film onto the ITO/glass substrates and revised the manuscript. Performed SEM and XPS measurements.

In the article A5:

- Kouao, D.-S.; Grochowska, K.; Stranak, V.; Sezemsky, P.; Gumieniak, J.; Kramek, A.; Karczewski, J.; Coy, E.; **Hanus, J.**; Kylian, O.; Sawczak, M.; Siuzdak, K. Laser-Treated MXene as an Electrochemical Agent to Boost Properties of Semitransparent Photoelectrode Based on Titania Nanotubes. **ACS Nano** 2024, 18 (14), 10165–10183.  
<https://doi.org/10.1021/acsnano.4c00092>. **IF = 17.1 / 200 points.**

I performed the deposition of the TiO<sub>x</sub> interlayer and Ti film onto the ITO/glass substrates and I was involved in the revision of the manuscript.



doc. RNDr. Ondřej Kylián, Ph.D.  
Department of Macromolecular Physics  
Faculty of Mathematics and Physics  
Charles University  
V Holešovičkách 2/747  
180 00 Praha 8  
Czech Republic

24.06.2024

ondrej.kylian@matfyz.cuni.cz

### Statement of contribution

In the article A2:

- Kouao, D.-S.; Hanuš, J.; **Kylián, O.**; Simerova, R.; Sezemsky, P.; Stranak, V.; Grochowska, K.; Siuzdak, K. Double-Sided Semitransparent Titania Photoelectrode with Enhanced Light Harvesting. **Renewable and Sustainable Energy Reviews** 2024, 197, 114390. <https://doi.org/10.1016/j.rser.2024.114390>. **IF = 16.79 / 200 points.**

I performed the deposition of the ITO, TiO<sub>x</sub> interlayer and Ti film onto the glass substrates and revised the manuscript and response to the reviewer's comments.

In the article A3:

- Hanková, A.; Kuzminova, A.; Hanuš, J.; Sezemsky, P.; Simerova, R.; Stranak, V.; Grochowska, K.; Kouao, D.-S.; Siuzdak, K.; Procházka, M.; Košutová, T.; **Kylián, O.** TiO<sub>2</sub>/Ag Nanostructured Coatings as Recyclable Platforms for Surface-Enhanced Raman Scattering Detection. **Surfaces and Interfaces** 2022, 35, 102441. <https://doi.org/10.1016/j.surfin.2022.102441>. **IF = 6.20 / 70 points.**

I defined the study's objectives, coordinated the work activities, prepared the original manuscript draft and response to the reviewer's comments.

In the article A4:

- Kouao, D.-S.; Hanuš, J.; **Kylián, O.**; Simerova, R.; Sezemsky, P.; Stranak, V.; Grochowska, K.; Siuzdak, K. Photoelectrochemical and Electrochemical Activity of Anodic Semitransparent Aligned and Spaced Titania Nanotubes Formed out of Titanium–Silver Alloys. **ACS Applied Nano Materials**. 2024, 7 (2), 1548–1561. <https://doi.org/10.1021/acsanm.3c04186>. **IF = 5.90 / 20 points.**

I performed the deposition of the ITO, TiO<sub>x</sub> interlayer and TiAg film onto the glass substrates and revised the manuscript.

In the article A5:

- Kouao, D.-S.; Grochowska, K.; Stranak, V.; Sezemsky, P.; Gumieniak, J.; Kramek, A.; Karczewski, J.; Coy, E.; Hanus, J.; **Kylian, O.**; Sawczak, M.; Siuzdak, K. Laser-Treated MXene as an Electrochemical Agent to Boost Properties of Semitransparent Photoelectrode Based on Titania Nanotubes. **ACS Nano** 2024, 18 (14), 10165–10183. <https://doi.org/10.1021/acsnano.4c00092>. **IF = 17.1 / 200 points.**

I performed the deposition of the ITO, TiO<sub>x</sub> interlayer and Ti film onto the glass substrates and I was involved in the revision of the manuscript.

In Prague 24.06.2024

  
Ondřej Kylián

PhD Agnieszka Kramek  
Faculty of Mechanics and Technology  
Rzeszów University of Technology  
Kwiatkowskiego 4  
37-450 Stalowa Wola

24.06.2024

a.kramek@prz.edu.pl

#### Statement of contribution

In the article A5:

- Kouao, D.-S.; Grochowska, K.; Stranak, V.; Sezemsky, P.; Gumieniak, J.; **Kramek, A.**; Karczewski, J.; Coy, E.; Hanus, J.; Kylian, O.; Sawczak, M.; Siuzdak, K. Laser-Treated MXene as an Electrochemical Agent to Boost Properties of Semitransparent Photoelectrode Based on Titania Nanotubes. **ACS Nano** **2024**, 18 (14), 10165–10183. <https://doi.org/10.1021/acsnano.4c00092>. **IF = 17.1 / 200 points.**

I was responsible for performing of XPS measurements of the obtained samples, the fitting procedure and contribution in the analysis of the spectra.



PhD DSc Eng Mirosław Sawczak, Prof. IMP PAN

24.06.2024

Department of Physical Aspects of Ecoenergy

Centre of Plasma and Laser Engineering

Institute of Fluid-Flow Machinery

Polish Academy of Sciences

Fiszera 14

80-231 Gdańsk

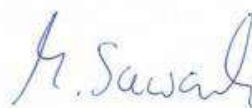
mireks@imp.gda.pl

#### Statement of contribution

In the article A5:

- Kouao, D.-S.; Grochowska, K.; Stranak, V.; Sezemsky, P.; Gumieniak, J.; Kramek, A.; Karczewski, J.; Coy, E.; Hanus, J.; Kylian, O.; **Sawczak, M.**; Siuzdak, K. Laser-Treated MXene as an Electrochemical Agent to Boost Properties of Semitransparent Photoelectrode Based on Titania Nanotubes. **ACS Nano** **2024**, 18 (14), 10165–10183. <https://doi.org/10.1021/acsnano.4c00092>. **IF = 17.1 / 200 points.**

I was responsible for developing the concept of an experiment using laser ablation in low temperature and preparation of the experimental data for laser treatment of the material. I performed the laser ablation of the  $\text{Ti}_3\text{AlC}_2$  and photoluminescence measurements. Moreover, I took part in the analysis of the photoluminescence measurements.





PhD DSc Eng Emerson Coy, Prof. UAM  
NanoBioMedical Centre  
Adam Mickiewicz University  
Wszechnicy Piastowskiej 3  
61-614 Poznań  
coy.emerson@amu.edu.pl

24.06.2024

#### Statement of contribution

In the article A5:

- Kouao, D.-S.; Grochowska, K.; Stranak, V.; Sezemsky, P.; Gumieniak, J.; Kramek, A.; Karczewski, J.; Coy, E.; Hanus, J.; Kylian, O.; Sawczak, M.; Siuzdak, K. Laser-Treated MXene as an Electrochemical Agent to Boost Properties of Semitransparent Photoelectrode Based on Titania Nanotubes. *ACS Nano* **2024**, 18 (14), 10165–10183. <https://doi.org/10.1021/acsnano.4c00092>. IF = 17.1 / 200 points.

I performed TEM and SAED measurements for the obtained samples. I provided the report with the analysis of the collected data that supported the description of the features of the material provided in the manuscript.



Signed by /  
Podpisano przez:  
Luis Emerson Coy  
Romero  
Date / Data:  
2024-06-24 10:50

dr hab. Emerson Coy, Prof UAM

M.Sc. Justyna Gumieniak  
Faculty of Mechanics and Technology  
Rzeszów University of Technology, Poland  
Kwiatkowskiego 4  
37-450 Stalowa Wola

24.06.2024

j.gumieniak@prz.edu.pl

#### Statement of contribution

In the article A5:

- Kouao, D.-S.; Grochowska, K.; Stranak, V.; Sezemsky, P.; **Gumieniak, J.**; Kramck, A.; Karczewski, J.; Coy, E.; Hanus, J.; Kylian, O.; Sawczak, M.; Siuzdak, K. Laser-Treated MXene as an Electrochemical Agent to Boost Properties of Semitransparent Photoelectrode Based on Titania Nanotubes. **ACS Nano** **2024**, 18 (14), 10165–10183. <https://doi.org/10.1021/acsnano.4c00092>. **IF = 17.1 / 200 points.**

I was responsible for performing of XPS measurements of the obtained samples, the fitting procedure and contribution in the analysis of the spectra.

*Justyna Gumieniak*

PhD DSc Eng Jakub Karczewski, prof. PG  
Faculty of Applied Physics and Mathematics  
Institute of Nanotechnology and Materials Engineering  
Gdańsk University of Technology  
Narutowicza 11/12  
80-233 Gdańsk  
jakub.karczewski@pg.edu.pl

24.06.2024

#### Statement of contribution

In the article A5:

- Kouao, D.-S.; Grochowska, K.; Stranak, V.; Sezemsky, P.; Gumieniak, J.; Kramek, A.; **Karczewski, J.**; Coy, E.; Hanus, J.; Kylian, O.; Sawczak, M.; Siuzdak, K. Laser-Treated MXene as an Electrochemical Agent to Boost Properties of Semitransparent Photoelectrode Based on Titania Nanotubes. **ACS Nano** **2024**, 18 (14), 10165–10183. <https://doi.org/10.1021/acsnano.4c00092>. **IF = 17.1 / 200 points.**

I was responsible for performing SEM and XRD measurements on the obtained samples.



## 11 Bibliography

- (1) Wiltshire, A.; Bernie, D.; Gohar, L.; Lowe, J.; Mathison, C.; Smith, C. Post COP26 : Does the 1.5°C Climate Target Remain Alive? *Weather* **2022**, 77 (12), 412–417. <https://doi.org/10.1002/wea.4331>.
- (2) Vekariya, Y.; Chopde, S.; Kathiriya, M.; Halder, K. Renewable Horizons: Solar Power and Dairy Industry in India. *Asian Res. J. Agric.* **2024**, 17 (2), 140–146. <https://doi.org/10.9734/arja/2024/v17i2432>
- (3) Grätzel, M. Mesoscopic Solar Cells for Electricity and Hydrogen Production from Sunlight. *Chem. Lett.* **2005**, 34 (1), 8–13. <https://doi.org/10.1246/cl.2005.8>.
- (4) Wang, Y.-Y.; Chen, Y.-X.; Barakat, T.; Zeng, Y.-J.; Liu, J.; Siffert, S.; Su, B.-L. Recent Advances in Non-Metal Doped Titania for Solar-Driven Photocatalytic/Photoelectrochemical Water-Splitting. *J. Energy Chem.* **2022**, 66, 529–559. <https://doi.org/10.1016/j.jechem.2021.08.038>.
- (5) Hou, X.; Li, Z.; Fan, L.; Yuan, J.; Lund, P. D.; Li, Y. Effect of Ti Foil Size on the Micro Sizes of Anodic TiO<sub>2</sub> Nanotube Array and Photoelectrochemical Water Splitting Performance. *Chem. Eng. J.* **2021**, 425, 131415. <https://doi.org/10.1016/j.cej.2021.131415>
- (6) Zheng, Q.; Kang, H.; Yun, J.; Lee, J.; Park, J. H.; Baik, S. Hierarchical Construction of Self-Standing Anodized Titania Nanotube Arrays and Nanoparticles for Efficient and Cost-Effective Front-Illuminated Dye-Sensitized Solar Cells. *ACS Nano* **2011**, 5 (6), 5088–5093. <https://doi.org/10.1021/nn201169u>
- (7) Vadla, S. S.; Bandyopadhyay, P.; John, S.; Ghosh, P.; Roy, S. C. TiO<sub>2</sub> Nanotube Arrays on Flexible Kapton Substrates for Photo-Electrochemical Solar Energy Conversion. *ACS Appl. Nano Mater.* **2020**, 3 (12), 11715–11724. <https://doi.org/10.1021/acsanm.0c02028>.
- (8) Kathirvel, S.; Su, C.; Yang, C.-Y.; Shiao, Y.-J.; Chen, B.-R.; Li, W.-R. The Growth of TiO<sub>2</sub> Nanotubes from Sputter-Deposited Ti Film on Transparent Conducting Glass for

- Photovoltaic Applications. *Vacuum* **2015**, *118*, 17–25.  
<https://doi.org/10.1016/j.vacuum.2014.12.024>.
- (9) Chen, Y.-L.; Chang, Y.-H.; Huang, J.-L.; Chen, I.; Kuo, C. Light Scattering and Enhanced Photoactivities of Electrospun Titania Nanofibers. *J. Phys. Chem. C* **2012**, *116* (5), 3857–3865.  
<https://doi.org/10.1021/jp2117246>.
- (10) Wu, J.-M.; Xue, H.-X. Photocatalytic Active Titania Nanowire Arrays on Ti Substrates. *J. Am. Ceram. Soc.* **2009**, *92* (9), 2139–2143.  
<https://doi.org/10.1111/j.1551-2916.2009.03153.x>.
- (11) Wu, J.-M.; Zhang, T.-W.; Zeng, Y.-W.; Hayakawa, S.; Tsuru, K.; Osaka, A. Large-Scale Preparation of Ordered Titania Nanorods with Enhanced Photocatalytic Activity. *Langmuir* **2005**, *21* (15), 6995–7002.  
<https://doi.org/10.1021/la0500272>.
- (12) Shin, K.; Park, J. H. Highly Transparent Dual-Sensitized Titanium Dioxide Nanotube Arrays for Spontaneous Solar Water Splitting Tandem Configuration. *ACS Appl. Mater. Interfaces* **2015**, *7* (33), 18429–18434.  
<https://doi.org/10.1021/acsami.5b04521>.
- (13) Lynch, R. P.; Ghicov, A.; Schmuki, P. A Photo-Electrochemical Investigation of Self-Organized TiO<sub>2</sub> Nanotubes. *J. Electrochem. Soc.* **2010**, *157* (3), G76.  
<https://doi.org/10.1149/1.3276455>.
- (14) Roy, P.; Kim, D.; Lee, K.; Spiecker, E.; Schmuki, P. TiO<sub>2</sub> Nanotubes and Their Application in Dye-Sensitized Solar Cells. *Nanoscale* **2010**, *2* (1), 45–59.  
<https://doi.org/10.1039/B9NR00131J>.
- (15) Sun, L.; Zhang, S.; Sun, X.; He, X. Effect of the Geometry of the Anodized Titania Nanotube Array on the Performance of Dye-Sensitized Solar Cells. *J. Nanosci. Nanotechnol.* **2010**, *10* (7), 4551–4561.  
<https://doi.org/10.1166/jnn.2010.1695>.
- (16) Assefpour-Dezfuly, M.; Vlachos, C.; Andrews, E. H. Oxide Morphology and Adhesive Bonding on Titanium Surfaces. *J. Mater. Sci.* **1984**, *19* (11), 3626–3639.



<https://doi.org/10.1007/BF00552275>.

- (17) Zhang, Y.; Farsinezhad, S.; D Wiltshire, B.; Kisslinger, R.; Kar, P.; Shankar, K. Optical Anisotropy in Vertically Oriented TiO<sub>2</sub> Nanotube Arrays. *Nanotechnology* **2017**, 28 (37), 374001.

<https://doi.org/10.1088/1361-6528/aa7d9d>.

- (18) Lee, K.; Mazare, A.; Schmuki, P. One-Dimensional Titanium Dioxide Nanomaterials: Nanotubes. *Chem. Rev.* **2014**, 114 (19), 9385–9454.

<https://doi.org/10.1021/cr500061m>.

- (19) Zhang, B.; Sun, S.; Shi, N.; Liao, X.; Yin, G.; Huang, Z.; Chen, X.; Pu, X. Spaced TiO<sub>2</sub> Nanotube Arrays for Electrodeposition of MoO<sub>3</sub> to Achieve High Electrochemical Performance. *J. Alloys Compd.* **2020**, 820, 153066.  
<https://doi.org/10.1016/j.jallcom.2019.153066>.

- (20) Ozkan, S.; Valle, F.; Mazare, A.; Hwang, I.; Taccardi, N.; Zazpe, R.; Macak, J. M.; Cerri, I.; Schmuki, P. Optimized Polymer Electrolyte Membrane Fuel Cell Electrode Using TiO<sub>2</sub> Nanotube Arrays with Well-Defined Spacing. *ACS Appl. Nano Mater.* **2020**, 3 (5), 4157–4170.

<https://doi.org/10.1021/acsanm.0c00325>.

- (21) Varghese, O. K.; Paulose, M.; Grimes, C. A. Long Vertically Aligned Titania Nanotubes on Transparent Conducting Oxide for Highly Efficient Solar Cells. *Nat. Nanotechnol.* **2009**, 4 (9), 592–597.

<https://doi.org/10.1038/nnano.2009.226>.

- (22) Mor, G. K.; Varghese, O. K.; Wilke, R. H. T.; Sharma, S.; Shankar, K.; Latempa, T. J.; Choi, K.-S.; Grimes, C. A. P-Type Cu–Ti–O Nanotube Arrays and Their Use in Self-Biased Heterojunction Photoelectrochemical Diodes for Hydrogen Generation. *Nano Lett.* **2008**, 8 (7), 1906–1911.

<https://doi.org/10.1021/nl080572y>.

- (23) Chen, C.; Li, F.; Li, G.; Tan, F.; Li, S.; Ling, L. Double-Sided Transparent Electrodes of TiO<sub>2</sub> Nanotube Arrays for Highly Efficient CdS Quantum Dot-Sensitized Photoelectrodes. *J. Mater. Sci.* **2014**, 49 (4), 1868–1874.

<https://doi.org/10.1007/s10853-013-7875-7>.

- (24) Jang, N.-S.; Kim, M. S.; Kim, S.-H.; Lee, S.-K.; Kim, J.-M. Direct Growth of Titania Nanotubes on Plastic Substrates and Their Application to Flexible Gas Sensors. *Sensors Actuators B Chem.* **2014**, *199*, 361–368.  
<https://doi.org/10.1016/j.snb.2014.03.113>.
- (25) Bleckenwegner, P.; Mardare, C. C.; Cobet, C.; Kollender, J. P.; Hassel, A. W.; Mardare, A. I. Compositionally Dependent Nonlinear Optical Bandgap Behavior of Mixed Anodic Oxides in Niobium–Titanium System. *ACS Comb. Sci.* **2017**, *19* (2), 121–129.  
<https://doi.org/10.1021/acscombsci.6b00162>.
- (26) Bohórquez, A. J.; Quiroz, H. P.; Dussan, A. Growth and Crystallization of Cobalt-Doped TiO<sub>2</sub> Alloys: Effect of Substrate and Annealing Temperature. *Appl. Surf. Sci.* **2019**, *474*, 97–101.  
<https://doi.org/10.1016/j.apsusc.2018.04.177>.
- (27) Mor, G. K.; Prakasam, H. E.; Varghese, O. K.; Shankar, K.; Grimes, C. A. Vertically Oriented Ti–Fe–O Nanotube Array Films: Toward a Useful Material Architecture for Solar Spectrum Water Photoelectrolysis. *Nano Lett.* **2007**, *7* (8), 2356–2364.  
<https://doi.org/10.1021/nl0710046>.
- (28) Kyeremateng, N. A.; Hornebecq, V.; Martinez, H.; Knauth, P.; Djenizian, T. Electrochemical Fabrication and Properties of Highly Ordered Fe-Doped TiO<sub>2</sub> Nanotubes. *ChemPhysChem* **2012**, *13* (16), 3707–3713.  
<https://doi.org/10.1002/cphc.201200406>
- (29) Habazaki, H.; Uozumi, M.; Konno, H.; Shimizu, K.; Nagata, S.; Asami, K.; Skeldon, P.; Thompson, G. E. Influence of Molybdenum Species on Growth of Anodic Titania. *Electrochim. Acta* **2002**, *47* (24), 3837–3845.  
[https://doi.org/10.1016/S0013-4686\(02\)00319-5](https://doi.org/10.1016/S0013-4686(02)00319-5).
- (30) Gui, Y.; Blackwood, D. J. Honey-Comb Structured WO<sub>3</sub> /TiO<sub>2</sub> Thin Films with Improved Electrochromic Properties. *J. Electrochem. Soc.* **2015**, *162* (10), E205–E212.  
<https://doi.org/10.1149/2.0031510jes>.
- (31) Arsha, A. S.; Raja, D. H. Generation Honeycomb-Structure of Titania Nanotubes and

- their Characterization. *nanosci. technol. an int. j.* **2024**, *15* (1), 27–37.  
<https://doi.org/10.1615/NanoSciTechnolIntJ.2023045069>.
- (32) Wang, S.; Zhang, Z.; Huo, W.; Zhu, K.; Zhang, X.; Zhou, X.; Fang, F.; Xie, Z.; Jiang, J. Preferentially Oriented Ag-TiO<sub>2</sub> Nanotube Array Film: An Efficient Visible-Light-Driven Photocatalyst. *J. Hazard. Mater.* **2020**, *399*, 123016.  
<https://doi.org/10.1016/j.jhazmat.2020.123016>.
- (33) Li, P.; Wang, J.; Zu, G.; Jiao, P.; Liu, S.; Yang, Y.; Chen, S.; Li, H. Synergetic Catalytic Properties of Gold Nanoparticles Planted on Transparent Titanium Dioxide Nanotube Array Bed. *Mater. Chem. Phys.* **2018**, *217*, 437–444.  
<https://doi.org/10.1016/j.matchemphys.2018.06.045>.
- (34) Sanabria-Arenas, B. E.; Mazare, A.; Yoo, J.; Nguyen, N. T.; Hejazi, S.; Bian, H.; Diamanti, M. V.; Pedferri, M. P.; Schmuki, P. Intrinsic AuPt-Alloy Particles Decorated on TiO<sub>2</sub> Nanotubes Provide Enhanced Photocatalytic Degradation. *Electrochim. Acta* **2018**, *292*, 865–870.  
<https://doi.org/10.1016/j.electacta.2018.09.206>.
- (35) Kar, P.; Farsinezhad, S.; Mahdi, N.; Zhang, Y.; Obuekwe, U.; Sharma, H.; Shen, J.; Semagina, N.; Shankar, K. Enhanced CH<sub>4</sub> Yield by Photocatalytic CO<sub>2</sub> Reduction Using TiO<sub>2</sub> Nanotube Arrays Grafted with Au, Ru, and ZnPd Nanoparticles. *Nano Res.* **2016**, *9* (11), 3478–3493.  
<https://doi.org/10.1007/s12274-016-1225-4>.
- (36) Lemos, H. G.; Ronchi, R. M.; Portugal, G. R.; Rossato, J. H. H.; Selopal, G. S.; Barba, D.; Venancio, E. C.; Rosei, F.; Arantes, J. T.; F. Santos, S. Efficient Ti<sub>3</sub>C<sub>2</sub>T<sub>x</sub> MXene/TiO<sub>2</sub> Hybrid Photoanodes for Dye-Sensitized Solar Cells. *ACS Appl. Energy Mater.* **2022**, *5* (12), 15928–15938.  
<https://doi.org/10.1021/acsaem.2c03474>.
- (37) He, S.; Lan, Z.; Zhang, B.; Gao, Y.; Shang, L.; Yue, G.; Chen, S.; Shen, Z.; Tan, F.; Wu, J. Holistically Optimizing Charge Carrier Dynamics Enables High-Performance Dye-Sensitized Solar Cells and Photodetectors. *ACS Appl. Mater. Interfaces* **2022**, *14* (38), 43576–43585.  
<https://doi.org/10.1021/acsaem.2c03474>.

- (38) Khatun, N.; Dey, S.; Behera, G. C.; Roy, S. C.  $\text{Ti}_3\text{C}_2\text{T}$  MXene Functionalization Induced Enhancement of Photoelectrochemical Performance of  $\text{TiO}_2$  Nanotube Arrays. *Mater. Chem. Phys.* **2022**, 278, 125651.  
<https://doi.org/10.1016/j.matchemphys.2021.125651>.
- (39) Yuan, Y.; Jiang, L.; Li, X.; Zuo, P.; Zhang, X.; Lian, Y.; Ma, Y.; Liang, M.; Zhao, Y.; Qu, L. Ultrafast Shaped Laser Induced Synthesis of MXene Quantum Dots/Graphene for Transparent Supercapacitors. *Adv. Mater.* **2022**, 34 (12).  
<https://doi.org/10.1002/adma.202110013>.
- (40) Liu, C.; Zhang, H.; Li, R.; Li, X.; Tang, P.; Wang, Y.; Yang, B.; Qiao, Z.; Yang, G. Laser Triggered Exothermic Chemical Reaction in Au Nanoparticle@  $\text{Ti}_3\text{C}_2$  MXene Membrane: A Route toward Efficient Light to High-Temperature Pulse Conversion. *Chem. Eng. J.* **2021**, 420, 127672.  
<https://doi.org/10.1016/j.cej.2020.127672>.
- (41) Vida, J.; Gemeiner, P.; Pavličková, M.; Mazalová, M.; Souček, P.; Plašienka, D.; Homola, T. Nanocrystalline  $\text{TiO}_2/\text{Ti}_3\text{C}_2\text{T}_x$  MXene Composites with a Tunable Work Function Prepared Using Atmospheric Pressure Oxygen Plasma. *Nanoscale* **2023**, 15 (3), 1289–1298.  
<https://doi.org/10.1039/D2NR04465J>.
- (42) Zheng, H.; Meng, X.; Chen, J.; Que, M.; Wang, W.; Liu, X.; Yang, L.; Zhao, Y. In Situ Phase Evolution of  $\text{TiO}_2/\text{Ti}_3\text{C}_2\text{T}$  Heterojunction for Enhancing Adsorption and Photocatalytic Degradation. *Appl. Surf. Sci.* **2021**, 545, 149031.  
<https://doi.org/10.1016/j.apsusc.2021.149031>.
- (43) Zhou, S.; Jiang, L.; Wang, H.; Yang, J.; Yuan, X.; Wang, H.; Liang, J.; Li, X.; Li, H.; Bu, Y. Oxygen Vacancies Modified  $\text{TiO}_2/\text{O}$ -Terminated  $\text{Ti}_3\text{C}_2$  Composites: Unravelling the Dual Effects between Oxygen Vacancy and High-Work-Function Titanium Carbide. *Adv. Funct. Mater.* **2023**.  
<https://doi.org/10.1002/adfm.202307702>.
- (44) Li, R.; Zhang, L.; Shi, L.; Wang, P. MXene  $\text{Ti}_3\text{C}_2$ : An Effective 2D Light-to-Heat Conversion Material. *ACS Nano* **2017**, 11 (4), 3752–3759.  
<https://doi.org/10.1021/acsnano.6b08415>.

- (45) Galstyan, V.; Vomiero, A.; Concina, I.; Braga, A.; Brisotto, M.; Bontempi, E.; Faglia, G.; Sberveglieri, G. Vertically Aligned TiO<sub>2</sub> Nanotubes on Plastic Substrates for Flexible Solar Cells. *Small* **2011**, 7 (17), 2437–2442.  
<https://doi.org/10.1002/sml.201101356>.
- (46) Weicheng, K.; Kangmei, L.; Jun, H. TEM Structure, Nanomechanical Property, and Adhesive Force of Magnetron-Sputtered Cr-DLC Coating on a Nitrided Ti<sub>6</sub>Al<sub>4</sub>V Alloy. *J. Phys. Chem. C* **2021**, 125 (30), 16733–16745.  
<https://doi.org/10.1021/acs.jpcc.1c03987>.
- (47) Kim, J. Y.; Noh, J. H.; Zhu, K.; Halverson, A. F.; Neale, N. R.; Park, S.; Hong, K. S.; Frank, A. J. General Strategy for Fabricating Transparent TiO<sub>2</sub> Nanotube Arrays for Dye-Sensitized Photoelectrodes: Illumination Geometry and Transport Properties. *ACS Nano* **2011**, 5 (4), 2647–2656.  
<https://doi.org/10.1021/nn200440u>.
- (48) Krumpmann, A.; Dervaux, J.; Derue, L.; Douhéret, O.; Lazzaroni, R.; Snyders, R.; Decroly, A. Influence of a Sputtered Compact TiO<sub>2</sub> Layer on the Properties of TiO<sub>2</sub> Nanotube Photoanodes for Solid-State DSSCs. *Mater. Des.* **2017**, 120, 298–306.  
<https://doi.org/10.1016/j.matdes.2017.02.028>.
- (49) Mor, G. K.; Varghese, O. K.; Paulose, M.; Grimes, C. A. Transparent Highly Ordered TiO<sub>2</sub> Nanotube Arrays via Anodization of Titanium Thin Films. *Adv. Funct. Mater.* **2005**, 15 (8), 1291–1296.  
<https://doi.org/10.1002/adfm.200500096>.
- (50) Kim, S. W.; Kim, H. K.; Yun, J. W.; Kim, E. J.; Hahn, S. H. Wetting and Photocatalytic Properties of TiO<sub>2</sub> Nanotube Arrays Prepared via Anodic Oxidation of E-Beam Evaporated Ti Thin Films. *Int. J. Photoenergy* **2015**, 2015, 1–6.  
<https://doi.org/10.1155/2015/320625>.
- (51) Krysa, J.; Lee, K.; Pausova, S.; Kment, S.; Hubicka, Z.; Ctvrtlik, R.; Schmuki, P. Self-Organized Transparent 1D TiO<sub>2</sub> Nanotubular Photoelectrodes Grown by Anodization of Sputtered and Evaporated Ti Layers: A Comparative Photoelectrochemical Study. *Chem. Eng. J.* **2017**, 308, 745–753.  
<https://doi.org/10.1016/j.cej.2016.09.112>.



- (52) Heljo, P. S.; Wolff, K.; Lahtonen, K.; Valden, M.; Berger, P. R.; Majumdar, H. S.; Lupo, D. Anodic Oxidation of Ultra-Thin Ti Layers on ITO Substrates and Their Application in Organic Electronic Memory Elements. *Electrochim. Acta* **2014**, *137*, 91–98. <https://doi.org/10.1016/j.electacta.2014.05.157>.
- (53) Kim, D. H.; Shim, Y.-S.; Moon, H. G.; Chang, H. J.; Su, D.; Kim, S. Y.; Kim, J.-S.; Ju, B. K.; Yoon, S.-J.; Jang, H. W. Highly Ordered TiO<sub>2</sub> Nanotubes on Patterned Substrates: Synthesis-in-Place for Ultrasensitive Chemiresistors. *J. Phys. Chem. C* **2013**, *117* (34), 17824–17831. <https://doi.org/10.1021/jp405150b>.
- (54) Chappanda, K. N.; Smith, Y. R.; Misra, M.; Mohanty, S. K. Site-Specific and Patterned Growth of TiO<sub>2</sub> Nanotube Arrays from e-Beam Evaporated Thin Titanium Film on Si Wafer. *Nanotechnology* **2012**, *23* (38), 385601. <https://doi.org/10.1088/0957-4484/23/38/385601>.
- (55) Büttner, P.; Döhler, D.; Korenko, S.; Möhrlein, S.; Bochmann, S.; Vogel, N.; Mínguez-Bacho, I.; Bachmann, J. Solid State Interdigitated Sb<sub>2</sub>S<sub>3</sub> Based TiO<sub>2</sub> Nanotube Solar Cells. *RSC Adv.* **2020**, *10* (47), 28225–28231. <https://doi.org/10.1039/D0RA04123H>.
- (56) Arshi, N.; LU, J.; Lee, C. G.; Yoon, J. H.; Koo, B. H.; Ahmed, F. Thickness Effect on Properties of Titanium Film Deposited by d.c. Magnetron Sputtering and Electron Beam Evaporation Techniques. *Bull. Mater. Sci.* **2013**, *36* (5), 807–812. <https://doi.org/10.1007/s12034-013-0552-2>.
- (57) Lee, C.-C.; Chen, C.-W.; Lin, J.-S.; Wang, S. H.; Lee, C.-S.; Chen, C.-C.; Lin, Y.-H.; Chen, C.-Y. Effect of Anodization Treatment on the Thickness, Hardness, and Microstructural Characterization of Anodic Aluminum Oxide Film on AA 6061 and Critical Patent Analysis. *J. Mater. Eng. Perform.* **2022**, *31* (1), 667–681. <https://doi.org/10.1007/s11665-021-06205-1>.
- (58) Lee, W.; Park, S.-J. Porous Anodic Aluminum Oxide: Anodization and Templated Synthesis of Functional Nanostructures. *Chem. Rev.* **2014**, *114* (15), 7487–7556. <https://doi.org/10.1021/cr500002z>.
- (59) Runge, J. M. A Brief History of Anodizing Aluminum. In *The Metallurgy of Anodizing*

- Aluminum*; Springer International Publishing: Cham, 2018; pp 65–148.  
[https://doi.org/10.1007/978-3-319-72177-4\\_2](https://doi.org/10.1007/978-3-319-72177-4_2).
- (60) Zhou, Q.; Tian, M.; Ying, Z.; Dan, Y.; Tang, F.; Zhang, J.; Zhu, J.; Zhu, X. Dense Films Formed during Ti Anodization in  $\text{NH}_4\text{F}$  Electrolyte: Evidence against the Field-Assisted Dissolution Reactions of Fluoride Ions. *Electrochem. commun.* **2020**, *111*, 106663. <https://doi.org/10.1016/j.elecom.2020.106663>.
- (61) Bjelajac, A.; Petrović, R.; Vujancevic, J.; Veltruska, K.; Matolin, V.; Siketic, Z.; Provatas, G.; Jaksic, M.; Stan, G. E.; Socol, G.; Mihailescu, I. N.; Janačković, D. Sn-Doped  $\text{TiO}_2$  Nanotubular Thin Film for Photocatalytic Degradation of Methyl Orange Dye. *J. Phys. Chem. Solids* **2020**, *147*, 109609. <https://doi.org/10.1016/j.jpcs.2020.109609>.
- (62) Macak, J. M.; Schmuki, P. Anodic Growth of Self-Organized Anodic  $\text{TiO}_2$  Nanotubes in Viscous Electrolytes. *Electrochim. Acta* **2006**, *52* (3), 1258–1264. <https://doi.org/10.1016/j.electacta.2006.07.021>.
- (63) Zhao, Y.; Hoivik, N.; Wang, K. Recent Advance on Engineering Titanium Dioxide Nanotubes for Photochemical and Photoelectrochemical Water Splitting. *Nano Energy* **2016**, *30*, 728–744. <https://doi.org/10.1016/j.nanoen.2016.09.027>.
- (64) Gong, D.; Grimes, C. A.; Varghese, O. K.; Hu, W.; Singh, R. S.; Chen, Z.; Dickey, E. C. Titanium Oxide Nanotube Arrays Prepared by Anodic Oxidation. *J. Mater. Res.* **2001**, *16* (12), 3331–3334. <https://doi.org/10.1557/JMR.2001.0457>.
- (65) Mor, G. K.; Varghese, O. K.; Paulose, M.; Mukherjee, N.; Grimes, C. A. Fabrication of Tapered, Conical-Shaped Titania Nanotubes. *J. Mater. Res.* **2003**, *18* (11), 2588–2593. <https://doi.org/10.1557/JMR.2003.0362>.
- (66) Cai, Q.; Paulose, M.; Varghese, O. K.; Grimes, C. A. The Effect of Electrolyte Composition on the Fabrication of Self-Organized Titanium Oxide Nanotube Arrays by Anodic Oxidation. *J. Mater. Res.* **2005**, *20* (1), 230–236. <https://doi.org/10.1557/JMR.2005.0020>.
- (67) Padiyan, D. P.; Raja, D. H. Synthesis of Various Generations Titania Nanotube Arrays

- by Electrochemical Anodization for H<sub>2</sub> Production. *Energy Procedia* **2012**, 22, 88–100.  
<https://doi.org/10.1016/j.egypro.2012.05.215>.
- (68) Paulose, M.; Prakasam, H. E.; Varghese, O. K.; Peng, L.; Popat, K. C.; Mor, G. K.; Desai, T. A.; Grimes, C. A. TiO<sub>2</sub> Nanotube Arrays of 1000 Mm Length by Anodization of Titanium Foil: Phenol Red Diffusion. *J. Phys. Chem. C* **2007**, 111 (41), 14992–14997.  
<https://doi.org/10.1021/jp075258r>.
- (69) Hoar, T. P.; Mott, N. F. A Mechanism for the Formation of Porous Anodic Oxide Films on Aluminium. *J. Phys. Chem. Solids* **1959**, 9 (2), 97–99.  
[https://doi.org/10.1016/0022-3697\(59\)90199-4](https://doi.org/10.1016/0022-3697(59)90199-4).
- (70) David, T. M.; Dev, P. R.; Wilson, P.; Sagayaraj, P.; Mathews, T. A Critical Review on the Variations in Anodization Parameters toward Microstructural Formation of TiO<sub>2</sub> Nanotubes. *Electrochem. Sci. Adv.* **2021**.  
<https://doi.org/10.1002/elsa.202100083>.
- (71) Sulka, G. D. Introduction to Anodization of Metals. In *Nanostructured Anodic Metal Oxides*; Elsevier, 2020; pp 1–34.  
<https://doi.org/10.1016/B978-0-12-816706-9.00001-7>.
- (72) Li, X.; Zhang, Y.; Gao, L.; Ma, J.; Qiu, Y.; Xu, X.; Ou, J.; Ma, W. The Growth Rate of Nanotubes and the Quantity of Charge during Anodization. *Electrochem. commun.* **2022**, 135, 107184.  
<https://doi.org/10.1016/j.elecom.2021.107184>.
- (73) Sieber, I.; Hildebrand, H.; Friedrich, A.; Schmuki, P. Formation of Self-Organized Niobium Porous Oxide on Niobium. *Electrochem. commun.* **2005**, 7 (1), 97–100.  
<https://doi.org/10.1016/j.elecom.2004.11.012>.
- (74) Gong, T.; Li, C.; Li, X.; Yue, H.; Zhu, X.; Zhao, Z.; Lv, R.; Zhu, J. Evidence of Oxygen Bubbles Forming Nanotube Embryos in Porous Anodic Oxides. *Nanoscale Adv.* **2021**, 3 (16), 4659–4668.  
<https://doi.org/10.1039/D1NA00389E>.
- (75) Yu, M.; Cui, H.; Ai, F.; Jiang, L.; Kong, J.; Zhu, X. Terminated Nanotubes: Evidence against the Dissolution Equilibrium Theory. *Electrochem. commun.* **2018**, 86, 80–84.

<https://doi.org/10.1016/j.elecom.2017.11.025>.

- (76) Lu, N.; Zhang, J.; Dan, Y.; Sun, M.; Gong, T.; Li, X.; Zhu, X. Growth of Porous Anodic TiO<sub>2</sub> in Silver Nitrate Solution without Fluoride: Evidence against the Field-Assisted Dissolution Reactions of Fluoride Ions. *Electrochem. commun.* **2021**, *126*, 107022. <https://doi.org/10.1016/j.elecom.2021.107022>.
- (77) Fahim, N. F.; Sekino, T.; Morks, M. F.; Kusunose, T. Electrochemical Growth of Vertically-Oriented High Aspect Ratio Titania Nanotubes by Rapid Anodization in Fluoride-Free Media. *J. Nanosci. Nanotechnol.* **2009**, *9* (3), 1803–1818. <https://doi.org/10.1166/jnn.2009.440>.
- (78) Zhu, X.; Liu, L.; Song, Y.; Jia, H.; Yu, H.; Xiao, X.; Yang, X. Oxygen Bubble Mould Effect: Serrated Nanopore Formation and Porous Alumina Growth. *Monatshefte für Chemie - Chem. Mon.* **2008**, *139* (9), 999–1003. <https://doi.org/10.1007/s00706-008-0893-5>.
- (79) Niu, D.; Han, A.; Cheng, H.; Ma, S.; Tian, M.; Liu, L. Effects of Organic Solvents in Anodization Electrolytes on the Morphology and Tube-to-Tube Spacing of TiO<sub>2</sub> Nanotubes. *Chem. Phys. Lett.* **2019**, *735*, 136776. <https://doi.org/10.1016/j.cplett.2019.136776>.
- (80) Mohamed, A. E. R.; Kasemphaibulsuk, N.; Rohani, S.; Barghi, S. Fabrication of Titania Nanotube Arrays in Viscous Electrolytes. *J. Nanosci. Nanotechnol.* **2010**, *10* (3), 1998–2008. <https://doi.org/10.1166/jnn.2010.2102>.
- (81) Paramasivam, I.; Macak, J. M.; Selvam, T.; Schmuki, P. Electrochemical Synthesis of Self-Organized TiO<sub>2</sub> Nanotubular Structures Using an Ionic Liquid (BMIM-BF<sub>4</sub>). *Electrochim. Acta* **2008**, *54* (2), 643–648. <https://doi.org/10.1016/j.electacta.2008.07.031>.
- (82) S, A. A.; Raja, D. H. Optical and Morphological Studies of Titania Nanotubes by Varying Anodization Parameters. *Next Mater.* **2024**, *4*, 100215. <https://doi.org/10.1016/j.nxmater.2024.100215>.
- (83) Ozkan, S.; Nguyen, N. T.; Mazare, A.; Cerri, I.; Schmuki, P. Controlled Spacing of Self-Organized Anodic TiO<sub>2</sub> Nanotubes. *Electrochem. commun.* **2016**, *69*, 76–79.

<https://doi.org/10.1016/j.elecom.2016.06.004>.

- (84) Ozkan, S.; Nguyen, N. T.; Mazare, A.; Hahn, R.; Cerri, I.; Schmuki, P. Fast Growth of TiO<sub>2</sub> Nanotube Arrays with Controlled Tube Spacing Based on a Self-Ordering Process at Two Different Scales. *Electrochem. commun.* **2017**, *77*, 98–102. <https://doi.org/10.1016/j.elecom.2017.03.007>.
- (85) Nguyen, N. T.; Ozkan, S.; Tomanec, O.; Zboril, R.; Schmuki, P. Spaced Titania Nanotube Arrays Allow the Construction of an Efficient N-Doped Hierarchical Structure for Visible-Light Harvesting. *ChemistryOpen* **2018**, *7* (2), 131–135. <https://doi.org/10.1002/open.201700199>.
- (86) Ruiquan, Y.; Longfei, J.; Xufei, Z.; Ye, S.; Dongliang, Y.; Aijun, H. Theoretical Derivation of Ionic Current and Electronic Current and Comparison between Fitting Curves and Measured Curves. *RSC Adv.* **2012**, *2* (32), 12474. <https://doi.org/10.1039/c2ra22124a>.
- (87) Aiempnakit, M. Fabrication of Titanium Dioxide Nanotubes and Their Photovoltaic Performance for Dye-Sensitized Solar Cells. *Int. J. Electrochem. Sci.* **2020**, 10392–10405. <https://doi.org/10.20964/2020.10.43>.
- (88) Bjelajac, A.; Petrović, R.; Djokic, V.; Matolin, V.; Vondraček, M.; Dembele, K.; Moldovan, S.; Ersen, O.; Socol, G.; Mihailescu, I. N.; Janačković, D. Enhanced Absorption of TiO<sub>2</sub> Nanotubes by N-Doping and CdS Quantum Dots Sensitization: Insight into the Structure. *RSC Adv.* **2018**, *8* (61), 35073–35082. <https://doi.org/10.1039/C8RA06341A>
- (89) Ghicov, A.; Tsuchiya, H.; Macak, J. M.; Schmuki, P. Annealing Effects on the Photoresponse of TiO<sub>2</sub> Nanotubes. *Phys. status solidi* **2006**, *203* (4), R28–R30. <https://doi.org/10.1002/pssa.200622041>.
- (90) Wang, Z.; Chen, K.; Xue, D. Crystallization of Amorphous Anodized TiO<sub>2</sub> Nanotube Arrays. *RSC Adv.* **2024**, *14* (12), 8195–8203. <https://doi.org/10.1039/D4RA00852A>
- (91) Tarjányi, T.; Bogár, F.; Minárovits, J.; Gajdács, M.; Tóth, Z. Interaction of Biomolecules with Anatase, Rutile and Amorphous TiO<sub>2</sub> Surfaces: A Molecular Dynamics Study.



*PLoS One* **2023**, 18 (9), e0289467.

<https://doi.org/10.1371/journal.pone.0289467>.

- (92) Nguyen, T.-V.; Yang, O.-B. Photoresponse and AC Impedance Characterization of TiO<sub>2</sub>–SiO<sub>2</sub> Mixed Oxide for Photocatalytic Water Decomposition. *Catal. Today* **2003**, 87 (1–4), 69–75.  
<https://doi.org/10.1016/j.cattod.2003.10.014>.
- (93) Mo, S.-D.; Ching, W. Y. Electronic and Optical Properties of Three Phases of Titanium Dioxide: Rutile, Anatase, and Brookite. *Phys. Rev. B* **1995**, 51 (19), 13023–13032.  
<https://doi.org/10.1103/PhysRevB.51.13023>.
- (94) Cromer, D. T.; Herrington, K. The Structures of Anatase and Rutile. *J. Am. Chem. Soc.* **1955**, 77 (18), 4708–4709.  
<https://doi.org/10.1021/ja01623a004>.
- (95) Wu, J.-M.; Hayakawa, S.; Tsuru, K.; Osaka, A. Crystallization of Anatase from Amorphous Titania in Hot Water and In Vitro Biomineralization. *J. Ceram. Soc. Japan* **2002**, 110 (1278), 78–80.  
<https://doi.org/10.2109/jcersj.110.78>.
- (96) Benavides, J. A.; Trudeau, C. P.; Gerlein, L. F.; Cloutier, S. G. Laser Selective Photoactivation of Amorphous TiO<sub>2</sub> Films to Anatase and/or Rutile Crystalline Phases. *ACS Appl. Energy Mater.* **2018**, 1 (8), 3607–3613.  
<https://doi.org/10.1021/acsaem.8b00171>.
- (97) Koparde, V. N.; Cummings, P. T. Phase Transformations during Sintering of Titania Nanoparticles. *ACS Nano* **2008**, 2 (8), 1620–1624.  
<https://doi.org/10.1021/nn800092m>.
- (98) Lebedev, V. A.; Kozlov, D. A.; Kolesnik, I. V.; Poluboyarinov, A. S.; Becerikli, A. E.; Grünert, W.; Garshev, A. V. The Amorphous Phase in Titania and Its Influence on Photocatalytic Properties. *Appl. Catal. B Environ.* **2016**, 195, 39–47.  
<https://doi.org/10.1016/j.apcatb.2016.05.010>.
- (99) Shivaram, A.; Bose, S.; Bandyopadhyay, A. Thermal Degradation of TiO<sub>2</sub> Nanotubes on Titanium. *Appl. Surf. Sci.* **2014**, 317, 573–580.

<https://doi.org/10.1016/j.apsusc.2014.08.107>.

- (100) Nachit, W.; Ait Ahsaine, H.; Ramzi, Z.; Touhtouh, S.; Goncharova, I.; Benkhoucha, K. Photocatalytic Activity of Anatase-Brookite TiO<sub>2</sub> Nanoparticles Synthesized by Sol Gel Method at Low Temperature. *Opt. Mater. (Amst)*. **2022**, *129*, 112256. <https://doi.org/10.1016/j.optmat.2022.112256>.
- (101) Zhang, H.; Banfield, J. F. Kinetics of Crystallization and Crystal Growth of Nanocrystalline Anatase in Nanometer-Sized Amorphous Titania. *Chem. Mater.* **2002**, *14* (10), 4145–4154. <https://doi.org/10.1021/cm020072k>.
- (102) Hu, Z.; Chen, S.; Shi, Y.; Yuan, F.; Yu, F.; Fang, J.; Yang, Y. Regulating Thermal Diffusion of Gold Thin Films at Solid-State Interfaces for Site-Selective Decoration of Gold Nanoparticles on Titania Nanotubes as an Efficient SERS Sensing Platform. *J. Mater. Chem. C* **2024**, *12* (1), 170–176. <https://doi.org/10.1039/D3TC03702A>.
- (103) Vasudevan, S.; Banu, F. S.; Nallaiyan, R. Evaluation of Electrochemical and Bioactive Performance of Tailored TiO<sub>2</sub> Nanotubes for Orthopaedic Application. *Surf. Coatings Technol.* **2024**, *480*, 130506. <https://doi.org/10.1016/j.surfcoat.2024.130506>
- (104) Lamberti, A.; Virga, A.; Chiadò, A.; Chiodoni, A.; Bejtka, K.; Rivolo, P.; Giorgis, F. Ultrasensitive Ag-Coated TiO<sub>2</sub> Nanotube Arrays for Flexible SERS-Based Optofluidic Devices. *J. Mater. Chem. C* **2015**, *3* (26), 6868–6875. <https://doi.org/10.1039/C5TC01154J>.
- (105) Farkhondehfal, M. A.; Hernández, S.; Rattalino, M.; Makkee, M.; Lamberti, A.; Chiodoni, A.; Bejtka, K.; Sacco, A.; Pirri, F. C.; Russo, N. Syngas Production by Electrocatalytic Reduction of CO<sub>2</sub> Using Ag-Decorated TiO<sub>2</sub> Nanotubes. *Int. J. Hydrogen Energy* **2020**, *45* (50), 26458–26471. <https://doi.org/10.1016/j.ijhydene.2019.04.180>.
- (106) Huang, J.; Feng, M.; Peng, Y.; Huang, C.; Yue, X.; Huang, S. Encapsulating Ni Nanoparticles into Interlayers of Nitrogen-Doped Nb<sub>2</sub> CT<sub>x</sub> MXene to Boost Hydrogen Evolution Reaction in Acid. *Small* **2023**, *19* (8).

<https://doi.org/10.1002/sml.202206098>.

- (107) Sokol, M.; Natu, V.; Kota, S.; Barsoum, M. W. On the Chemical Diversity of the MAX Phases. *Trends Chem.* **2019**, *1* (2), 210–223. <https://doi.org/10.1016/j.trechm.2019.02.016>.
- (108) Lim, K. R. G.; Shekhirev, M.; Wyatt, B. C.; Anasori, B.; Gogotsi, Y.; Seh, Z. W. Fundamentals of MXene Synthesis. *Nat. Synth.* **2022**, *1* (8), 601–614. <https://doi.org/10.1038/s44160-022-00104-6>.
- (109) Naguib, M.; Kurtoglu, M.; Presser, V.; Lu, J.; Niu, J.; Heon, M.; Hultman, L.; Gogotsi, Y.; Barsoum, M. W. Two-Dimensional Nanocrystals Produced by Exfoliation of  $\text{Ti}_3\text{AlC}_2$ . *Adv. Mater.* **2011**, *23* (37), 4248–4253. <https://doi.org/10.1002/adma.201102306>.
- (110) Zhu, X.; Cao, Z.; Wang, W.; Li, H.; Dong, J.; Gao, S.; Xu, D.; Li, L.; Shen, J.; Ye, M. Superior-Performance Aqueous Zinc-Ion Batteries Based on the In Situ Growth of  $\text{MnO}_2$  Nanosheets on  $\text{V}_2\text{CT}_x$  MXene. *ACS Nano* **2021**, *15* (2), 2971–2983. <https://doi.org/10.1021/acsnano.0c09205>.
- (111) Li, Z.; Dall’Agnese, Y.; Guo, J.; Huang, H.; Liang, X.; Xu, S. Flexible Freestanding All-MXene Hybrid Films with Enhanced Capacitive Performance for Powering a Flex Sensor. *J. Mater. Chem. A* **2020**, *8* (32), 16649–16660. <https://doi.org/10.1039/D0TA05710J>.
- (112) Ghidui, M.; Naguib, M.; Shi, C.; Mashtalir, O.; Pan, L. M.; Zhang, B.; Yang, J.; Gogotsi, Y.; Billinge, S. J. L.; Barsoum, M. W. Synthesis and Characterization of Two-Dimensional  $\text{Nb}_4\text{C}_3$  (MXene). *Chem. Commun.* **2014**, *50* (67), 9517–9520. <https://doi.org/10.1039/C4CC03366C>.
- (113) Liu, M.-C.; Zhang, Y.-S.; Zhang, B.-M.; Zhang, D.-T.; Tian, C.-Y.; Kong, L.-B.; Hu, Y.-X. Large Interlayer Spacing 2D  $\text{Ta}_4\text{C}_3$  Matrix Supported 2D  $\text{MoS}_2$  Nanosheets: A 3D Heterostructure Composite towards High-Performance Sodium Ions Storage. *Renew. Energy* **2021**, *169*, 573–581. <https://doi.org/10.1016/j.renene.2021.01.051>.
- (114) Hakim, M. W.; Fatima, S.; Tahir, R.; Iqbal, M. Z.; Li, H.; Rizwan, S. Ni-Intercalated  $\text{Mo}_2\text{TiC}_2\text{T}_x$  Free-Standing MXene for Excellent Gravimetric Capacitance Prepared via

- Electrostatic Self-Assembly. *J. Energy Storage* **2023**, *61*, 106662.  
<https://doi.org/10.1016/j.est.2023.106662>.
- (115) Deysher, G.; Shuck, C. E.; Hantanasirisakul, K.; Frey, N. C.; Foucher, A. C.; Maleski, K.; Sarycheva, A.; Shenoy, V. B.; Stach, E. A.; Anasori, B.; Gogotsi, Y. Synthesis of  $\text{Mo}_4\text{VAlC}_4$  MAX Phase and Two-Dimensional  $\text{Mo}_4\text{VC}_4$  MXene with Five Atomic Layers of Transition Metals. *ACS Nano* **2020**, *14* (1), 204–217.  
<https://doi.org/10.1021/acsnano.9b07708>.
- (116) Xue, N.; Li, X.; Zhang, M.; Han, L.; Liu, Y.; Tao, X. Chemical-Combined Ball-Milling Synthesis of Fluorine-Free Porous MXene for High-Performance Lithium Ion Batteries. *ACS Appl. Energy Mater.* **2020**, *3* (10), 10234–10241.  
<https://doi.org/10.1021/acsaem.0c02081>.
- (117) Gentile, A.; Marchionna, S.; Balordi, M.; Pagot, G.; Ferrara, C.; Di Noto, V.; Ruffo, R. Critical Analysis of MXene Production with In-Situ HF Forming Agents for Sustainable Manufacturing. *ChemElectroChem* **2022**, *9* (23).  
<https://doi.org/10.1002/celec.202200891>.
- (118) Xie, X.; Xue, Y.; Li, L.; Chen, S.; Nie, Y.; Ding, W.; Wei, Z. Surface Al Leached  $\text{Ti}_3\text{AlC}_2$  as a Substitute for Carbon for Use as a Catalyst Support in a Harsh Corrosive Electrochemical System. *Nanoscale* **2014**, *6* (19), 11035–11040.  
<https://doi.org/10.1039/C4NR02080D>.
- (119) Li, T.; Yao, L.; Liu, Q.; Gu, J.; Luo, R.; Li, J.; Yan, X.; Wang, W.; Liu, P.; Chen, B.; Zhang, W.; Abbas, W.; Naz, R.; Zhang, D. Fluorine-Free Synthesis of High-Purity  $\text{Ti}_3\text{C}_2\text{T}_x$  (T=OH, O) via Alkali Treatment. *Angew. Chemie Int. Ed.* **2018**, *57* (21), 6115–6119.  
<https://doi.org/10.1002/anie.201800887>.
- (120) Yang, S.; Zhang, P.; Wang, F.; Ricciardulli, A. G.; Lohe, M. R.; Blom, P. W. M.; Feng, X. Fluoride-Free Synthesis of Two-Dimensional Titanium Carbide (MXene) Using A Binary Aqueous System. *Angew. Chemie* **2018**, *130* (47), 15717–15721.  
<https://doi.org/10.1002/ange.201809662>.
- (121) Lukatskaya, M. R.; Halim, J.; Dyatkin, B.; Naguib, M.; Buranova, Y. S.; Barsoum, M. W.; Gogotsi, Y. Room-Temperature Carbide-Derived Carbon Synthesis by Electrochemical Etching of MAX Phases. *Angew. Chemie* **2014**, *126* (19), 4977–4980.

<https://doi.org/10.1002/ange.201402513>.

- (122) Sun, W.; Shah, S. A.; Chen, Y.; Tan, Z.; Gao, H.; Habib, T.; Radovic, M.; Green, M. J. Electrochemical Etching of  $\text{Ti}_2\text{AlC}$  to  $\text{Ti}_2\text{CT}_x$  (MXene) in Low-Concentration Hydrochloric Acid Solution. *J. Mater. Chem. A* **2017**, *5* (41), 21663–21668. <https://doi.org/10.1039/C7TA05574A>.
- (123) Pang, S.-Y.; Wong, Y.-T.; Yuan, S.; Liu, Y.; Tsang, M.-K.; Yang, Z.; Huang, H.; Wong, W.-T.; Hao, J. Universal Strategy for HF-Free Facile and Rapid Synthesis of Two-Dimensional MXenes as Multifunctional Energy Materials. *J. Am. Chem. Soc.* **2019**, *141* (24), 9610–9616. <https://doi.org/10.1021/jacs.9b02578>.
- (124) VahidMohammadi, A.; Kayali, E.; Orangi, J.; Beidaghi, M. Techniques for MXene Delamination into Single-Layer Flakes. In *2D Metal Carbides and Nitrides (MXenes)*; Springer International Publishing: Cham, 2019; pp 177–195. [https://doi.org/10.1007/978-3-030-19026-2\\_11](https://doi.org/10.1007/978-3-030-19026-2_11).
- (125) Anasori, B.; Gogotsi, Y. MXenes: Trends, Growth, and Future Directions. *Graphene 2D Mater.* **2022**, *7* (3–4), 75–79. <https://doi.org/10.1007/s41127-022-00053-z>.
- (126) Colin-Ulloa, E.; Fitzgerald, A.; Montazeri, K.; Mann, J.; Natu, V.; Ngo, K.; Uzarski, J.; Barsoum, M. W.; Titova, L. V. Ultrafast Spectroscopy of Plasmons and Free Carriers in 2D MXenes. *Adv. Mater.* **2023**, *35* (8). <https://doi.org/10.1002/adma.202208659>.
- (127) El-Demellawi, J. K.; Lopatin, S.; Yin, J.; Mohammed, O. F.; Alshareef, H. N. Tunable Multipolar Surface Plasmons in 2D  $\text{Ti}_3\text{C}_2\text{T}_x$  MXene Flakes. *ACS Nano* **2018**, *12* (8), 8485–8493. <https://doi.org/10.1021/acsnano.8b04029>.
- (128) Zhang, H.; Zhang, X.; Xie, C.; Shi, W.; Yang, P. Composite Nanoarchitectonics with  $\text{TiO}_2$  Nanocrystals and Superior Thin  $\text{Ti}_3\text{C}_2\text{T}_x$  Nanosheets towards Efficient NO Removal. *Environ. Res.* **2023**, *227*, 115793. <https://doi.org/10.1016/j.envres.2023.115793>.



- (129) Semaltianos, N. G. Nanoparticles by Laser Ablation. *Crit. Rev. Solid State Mater. Sci.* **2010**, *35* (2), 105–124.  
<https://doi.org/10.1080/10408431003788233>.
- (130) Guzelturk, B.; Kamysbayev, V.; Wang, D.; Hu, H.; Li, R.; King, S. B.; Reid, A. H.; Lin, M.-F.; Wang, X.; Walko, D. A.; Zhang, X.; Lindenberg, A.; Talapin, D. V. Understanding and Controlling Photothermal Responses in MXenes. *Nano Lett.* **2023**, *23* (7), 2677–2686.  
<https://doi.org/10.1021/acs.nanolett.2c05001>.
- (131) Zang, X.; Jian, C.; Zhu, T.; Fan, Z.; Wang, W.; Wei, M.; Li, B.; Follmar Diaz, M.; Ashby, P.; Lu, Z.; Chu, Y.; Wang, Z.; Ding, X.; Xie, Y.; Chen, J.; Hohman, J. N.; Sanghadasa, M.; Grossman, J. C.; Lin, L. Laser-Sculptured Ultrathin Transition Metal Carbide Layers for Energy Storage and Energy Harvesting Applications. *Nat. Commun.* **2019**, *10* (1), 3112.  
<https://doi.org/10.1038/s41467-019-10999-z>.
- (132) Park, C. E.; Jeong, G. H.; Theerthagiri, J.; Lee, H.; Choi, M. Y. Moving beyond  $\text{Ti}_2\text{C}_3\text{T}_x$  MXene to Pt-Decorated  $\text{TiO}_2@\text{TiC}$  Core–Shell via Pulsed Laser in Reshaping Modification for Accelerating Hydrogen Evolution Kinetics. *ACS Nano* **2023**, *17* (8), 7539–7549.  
<https://doi.org/10.1021/acsnano.2c12638>.
- (133) Qin, W.-W.; Hu, X.-F.; Fan, J.-L.; Liu, Y.-S.; Tan, L.-P.; Zhou, M.; Wu, C.-Q.; Ge, B.-H.; Gao, S.-J.; Qian, J.; Zhang, W. One-Step Laser Ablation of Fe Clusters Supported on  $\text{Ti}_3\text{C}_2\text{T}_x$  Nanosheets for Enhanced  $\text{NH}_3$  Sensing at Room Temperature. *Ceram. Int.* **2023**, *49* (11), 18353–18362.  
<https://doi.org/10.1016/j.ceramint.2023.02.207>.
- (134) Li, J.; Qin, R.; Yan, L.; Chi, Z.; Yu, Z.; Li, N.; Hu, M.; Chen, H.; Shan, G. Plasmonic Light Illumination Creates a Channel To Achieve Fast Degradation of  $\text{Ti}_3\text{C}_2\text{T}_x$  Nanosheets. *Inorg. Chem.* **2019**, *58* (11), 7285–7294.  
<https://doi.org/10.1021/acs.inorgchem.9b00329>
- (135) Yang, G. W. Laser Ablation in Liquids: Applications in the Synthesis of Nanocrystals.

*Prog. Mater. Sci.* **2007**, 52 (4), 648–698.

<https://doi.org/10.1016/j.pmatsci.2006.10.016>.

- (136) Kurdesau, F.; Khripunov, G.; da Cunha, A. F.; Kaelin, M.; Tiwari, A. N. Comparative Study of ITO Layers Deposited by DC and RF Magnetron Sputtering at Room Temperature. *J. Non. Cryst. Solids* **2006**, 352 (9–20), 1466–1470. <https://doi.org/10.1016/j.jnoncrysol.2005.11.088>.
- (137) Kim, H. J. High Mobility Si<sub>0.15</sub>Ge<sub>0.85</sub> Growth by Using the Molten Target Sputtering (MTS) within Heteroepitaxy Framework. *Sci. Rep.* **2019**, 9 (1), 11555. <https://doi.org/10.1038/s41598-019-47723-2>.
- (138) Maurya, D.; Sardarinejad, A.; Alameh, K. Recent Developments in R.F. Magnetron Sputtered Thin Films for PH Sensing Applications—An Overview. *Coatings* **2014**, 4 (4), 756–771. <https://doi.org/10.3390/coatings4040756>.
- (139) Paschotta, R. Microscopes - an Encyclopedia Article. In *RP Photonics Encyclopedia*; RP Photonics AG, 2019. <https://doi.org/10.61835/ctx>.
- (140) Inkson, B. J. Scanning Electron Microscopy (SEM) and Transmission Electron Microscopy (TEM) for Materials Characterization. In *Materials Characterization Using Nondestructive Evaluation (NDE) Methods*; Elsevier, 2016; pp 17–43. <https://doi.org/10.1016/B978-0-08-100040-3.00002-X>.
- (141) Zupanič, F. Extracting Electron Backscattering Coefficients from Backscattered Electron Micrographs. *Mater. Charact.* **2010**, 61 (12), 1335–1341. <https://doi.org/10.1016/j.matchar.2010.09.004>.
- (142) Cohen Hyams, T.; Mam, K.; Killingsworth, M. C. Scanning Electron Microscopy as a New Tool for Diagnostic Pathology and Cell Biology. *Micron* **2020**, 130, 102797. <https://doi.org/10.1016/j.micron.2019.102797>.
- (143) Al-Abdullah. The Study of the Growth Mechanism of TiO<sub>2</sub> Nanotubes and Their Applications. Diss. University of Sussex, 2013.
- (144) Ilie, A. G.; Scarisoareanu, M.; Morjan, I.; Dutu, E.; Badiceanu, M.; Mihailescu, I.

- Principal Component Analysis of Raman Spectra for TiO<sub>2</sub> Nanoparticle Characterization. *Appl. Surf. Sci.* **2017**, *417*, 93–103.  
<https://doi.org/10.1016/j.apsusc.2017.01.193>.
- (145) Klingler, R. J.; Kochi, J. K. Electron-Transfer Kinetics from Cyclic Voltammetry. Quantitative Description of Electrochemical Reversibility. *J. Phys. Chem.* **1981**, *85* (12), 1731–1741.  
<https://doi.org/10.1021/j150612a028>.
- (146) Yamada, H.; Yoshii, K.; Asahi, M.; Chiku, M.; Kitazumi, Y. Cyclic Voltammetry Part 1: Fundamentals. *Electrochemistry* **2022**, *90* (10), 22–66082.  
<https://doi.org/10.5796/electrochemistry.22-66082>.
- (147) Zhao, G.-C.; Zhang, L.; Wei, X.-W.; Yang, Z.-S. Myoglobin on Multi-Walled Carbon Nanotubes Modified Electrode: Direct Electrochemistry and Electrocatalysis. *Electrochem. commun.* **2003**, *5* (9), 825–829.  
<https://doi.org/10.1016/j.elecom.2003.07.006>.
- (148) Elgrishi, N.; Rountree, K. J.; McCarthy, B. D.; Rountree, E. S.; Eisenhart, T. T.; Dempsey, J. L. A Practical Beginner's Guide to Cyclic Voltammetry. *J. Chem. Educ.* **2018**, *95* (2), 197–206.  
<https://doi.org/10.1021/acs.jchemed.7b00361>.
- (149) Syedvali, P.; Rajeshkhanna, G.; Umeshbabu, E.; Kiran, G. U.; Rao, G. R.; Justin, P. In Situ Fabrication of Graphene Decorated Microstructured Globe Artichokes of Partial Molar Nickel Cobaltite Anchored on a Ni Foam as a High-Performance Supercapacitor Electrode. *RSC Adv.* **2015**, *5* (48), 38407–38416.  
<https://doi.org/10.1039/C5RA03463A>.
- (150) Zhao, J.; Cheng, L.; Wang, J.; Liu, Y.; Yang, J.; Xu, Q.; Chen, R.; Ni, H. Heteroatom-Doped Carbon Nanofilm Embedded in Highly Ordered TiO<sub>2</sub> Nanotube Arrays by Thermal Nitriding with Enhanced Electrochemical Activity. *J. Electroanal. Chem.* **2019**, *852*, 113513.  
<https://doi.org/10.1016/j.jelechem.2019.113513>.
- (151) Berger, T.; Monllor-Satoca, D.; Jankulovska, M.; Lana-Villarreal, T.; Gómez, R. The

- Electrochemistry of Nanostructured Titanium Dioxide Electrodes. *ChemPhysChem* **2012**, *13* (12), 2824–2875.  
<https://doi.org/10.1002/cphc.201200073>.
- (152) Khan, S.; Santos, M. J. L.; Dupont, J.; Teixeira, S. R. Photoelectrochemical Study of Ta<sub>3</sub>N<sub>5</sub> Nanotubes for Water Splitting. *IOP Conf. Ser. Mater. Sci. Eng.* **2015**, *97*, 012007.  
<https://doi.org/10.1088/1757-899X/97/1/012007>.
- (153) Li, Z.; Gao, F.; Greenham, N. C.; McNeill, C. R. Comparison of the Operation of Polymer/Fullerene, Polymer/Polymer, and Polymer/Nanocrystal Solar Cells: A Transient Photocurrent and Photovoltage Study. *Adv. Funct. Mater.* **2011**, *21* (8), 1419–1431.  
<https://doi.org/10.1002/adfm.201002154>.
- (154) Hwang, I.; McNeill, C. R.; Greenham, N. C. Drift-Diffusion Modeling of Photocurrent Transients in Bulk Heterojunction Solar Cells. *J. Appl. Phys.* **2009**, *106* (9).  
<https://doi.org/10.1063/1.3247547>.
- (155) Careem, M. A.; Noor, I. S. M.; Arof, A. K. Impedance Spectroscopy in Polymer Electrolyte Characterization. In *Polymer Electrolytes*; Wiley, 2020; pp 23–64.  
<https://doi.org/10.1002/9783527805457.ch2>.
- (156) Laschuk, N. O.; Easton, E. B.; Zenkina, O. V. Reducing the Resistance for the Use of Electrochemical Impedance Spectroscopy Analysis in Materials Chemistry. *RSC Adv.* **2021**, *11* (45), 27925–27936.  
<https://doi.org/10.1039/D1RA03785D>.
- (157) Mei, B.-A.; Munteshari, O.; Lau, J.; Dunn, B.; Pilon, L. Physical Interpretations of Nyquist Plots for EDLC Electrodes and Devices. *J. Phys. Chem. C* **2018**, *122* (1), 194–206.  
<https://doi.org/10.1021/acs.jpcc.7b10582>.
- (158) Li, Y.; Wang, C.; Li, Z.; Wang, M.; He, L.; Zhang, Z. Zirconium-Porphyrin Complex as Novel Nanocarrier for Label-Free Impedimetric Biosensing Neuron-Specific Enolase. *Sensors Actuators B Chem.* **2020**, *314*, 128090.  
<https://doi.org/10.1016/j.snb.2020.128090>.

- (159) Garlisi, C.; Lai, C.-Y.; George, L.; Chiesa, M.; Palmisano, G. Relating Photoelectrochemistry and Wettability of Sputtered Cu- and N-Doped TiO<sub>2</sub> Thin Films via an Integrated Approach. *J. Phys. Chem. C* **2018**, *122* (23), 12369–12376. <https://doi.org/10.1021/acs.jpcc.8b03650>.
- (160) Bredar, A. R. C.; Chown, A. L.; Burton, A. R.; Farnum, B. H. Electrochemical Impedance Spectroscopy of Metal Oxide Electrodes for Energy Applications. *ACS Appl. Energy Mater.* **2020**, *3* (1), 66–98. <https://doi.org/10.1021/acsaem.9b01965>.
- (161) X. A.S. Bondarenko, G. A. Ragoisha, In Progress in Chemometrics Research. A. L. Pomerantsev, Ed. Nova Science Publishers: New York. 2005, 89, 102 (the program is available online at <http://www.abc.chemistry.bsu.by/vi/analyser/>).
- (162) Azlan, M. N.; Azlina, Y.; Shaari, H. R.; Hisam, R.; Al-Hada, N. M.; Umar, S. A.; Kenzhaliyev, B. K. Extinction Coefficient and Fermi Energy of Zinctellurite Glass Doped with Neodymium Nanoparticles; 2023; p 070017. <https://doi.org/10.1063/5.0148528>.
- (163) Zhang, Z.; Yates, J. T. Band Bending in Semiconductors: Chemical and Physical Consequences at Surfaces and Interfaces. *Chem. Rev.* **2012**, *112* (10), 5520–5551. <https://doi.org/10.1021/cr3000626>.
- (164) Gomes, W. P.; Cardon, F. Electron Energy Levels in Semiconductor Electrochemistry. *Prog. Surf. Sci.* **1982**, *12* (2), 155–215. [https://doi.org/10.1016/0079-6816\(82\)90002-8](https://doi.org/10.1016/0079-6816(82)90002-8).
- (165) Zalnezhad, E.; Maleki, E.; Banihashemian, S. M.; Park, J. W.; Kim, Y. B.; Sarraf, M.; Sarhan, A. A. D. M.; Ramesh, S. Wettability, Structural and Optical Properties Investigation of TiO<sub>2</sub> Nanotubular Arrays. *Mater. Res. Bull.* **2016**, *78*, 179–185. <https://doi.org/10.1016/j.materresbull.2016.01.035>.
- (166) Park, B. H.; Li, L. S.; Gibbons, B. J.; Huang, J. Y.; Jia, Q. X. Photovoltaic Response and Dielectric Properties of Epitaxial Anatase-TiO<sub>2</sub> Films Grown on Conductive La<sub>0.5</sub>Sr<sub>0.5</sub>CoO<sub>3</sub> Electrodes. *Appl. Phys. Lett.* **2001**, *79* (17), 2797–2799. <https://doi.org/10.1063/1.1412822>.
- (167) Ershov, M.; Liu, H. C.; Li, L.; Buchanan, M.; Wasilewski, Z. R.; Jonscher, A. K.



- Negative Capacitance Effect in Semiconductor Devices. *IEEE Trans. Electron Devices* **1998**, *45* (10), 2196–2206.
- <https://doi.org/10.1109/16.725254>.
- (168) Giannakopoulou, T.; Papailias, I.; Todorova, N.; Boukos, N.; Liu, Y.; Yu, J.; Trapalis, C. Tailoring the Energy Band Gap and Edges' Potentials of g-C<sub>3</sub>N<sub>4</sub>/TiO<sub>2</sub> Composite Photocatalysts for NO<sub>x</sub> Removal. *Chem. Eng. J.* **2017**, *310*, 571–580.
- <https://doi.org/10.1016/j.cej.2015.12.102>.
- (169) Byers, J. C.; Ballantyne, S.; Rodionov, K.; Mann, A.; Semenikhin, O. A. Mechanism of Recombination Losses in Bulk Heterojunction P3HT:PCBM Solar Cells Studied Using Intensity Modulated Photocurrent Spectroscopy. *ACS Appl. Mater. Interfaces* **2011**, *3* (2), 392–401.
- <https://doi.org/10.1021/am100998t>.
- (170) Adhitya, K.; Alsulami, A.; Buckley, A.; Tozer, R. C.; Grell, M. Intensity-Modulated Spectroscopy on Loaded Organic Photovoltaic Cells. *IEEE J. Photovoltaics* **2015**, *5* (5), 1414–1421.
- <https://doi.org/10.1109/JPHOTOV.2015.2447838>.
- (171) Adhitya, Krisna. Intensity-Modulated Spectroscopy Instrument and its Applications. Diss. University of Sheffield, 2016.
- (172) Rodríguez-Gutiérrez, I.; Djatoubai, E.; Su, J.; Vega-Poot, A.; Rodríguez-Gattorno, G.; Souza, F. L.; Oskam, G. An Intensity-Modulated Photocurrent Spectroscopy Study of the Charge Carrier Dynamics of WO<sub>3</sub>/BiVO<sub>4</sub> Heterojunction Systems. *Sol. Energy Mater. Sol. Cells* **2020**, *208*, 110378.
- <https://doi.org/10.1016/j.solmat.2019.110378>.
- (173) Li, L.; Liang, J.; Qin, L.; Chen, D.; Huang, Y. In Situ Growth of a P-Type CuSCN/Cu<sub>2</sub>O Heterojunction to Enhance Charge Transport and Suppress Charge Recombination. *J. Mater. Chem. C* **2019**, *7* (23), 6872–6878.
- <https://doi.org/10.1039/C9TC02147G>.
- (174) Li, H.; Xie, C.; Liao, Y.; Liu, Y.; Zou, Z.; Wu, J. Characterization of Incidental Photon-to-Electron Conversion Efficiency (IPCE) of Porous TiO<sub>2</sub>/SnO<sub>2</sub> Composite Film. *J.*

*Alloys Compd.* **2013**, 569, 88–94.

<https://doi.org/10.1016/j.jallcom.2013.03.126>.

- (175) Wierzbicka, E.; Schultz, T.; Syrek, K.; Sulka, G. D.; Koch, N.; Pinna, N. Ultra-Stable Self-Standing Au Nanowires/TiO<sub>2</sub> Nanoporous Membrane System for High-Performance Photoelectrochemical Water Splitting Cells. *Mater. Horizons* **2022**, 9 (11), 2797–2808.

<https://doi.org/10.1039/D2MH00718E>.

- (176) Ahmad Abuilaiwi, F.; Awais, M.; Qazi, U. Y.; Ali, F.; Afzal, A. Al<sup>3+</sup> Doping Reduces the Electron/Hole Recombination in Photoluminescent Copper Ferrite (CuFe<sub>2</sub>–Al O<sub>4</sub>) Nanocrystallites. *Boletín la Soc. Española Cerámica y Vidr.* **2022**, 61 (3), 252–262. <https://doi.org/10.1016/j.bsecv.2020.11.007>.

- (177) Bhandarkar, S. A.; Prathvi; Kompa, A.; Murari, M. S.; Kekuda, D.; Mohan, R. K. Investigation of Structural and Optical Properties of Spin Coated TiO<sub>2</sub>:Mn Thin Films. *Opt. Mater. (Amst)*. **2021**, 118, 111254.

<https://doi.org/10.1016/j.optmat.2021.111254>.

- (178) Knorr, F. J.; McHale, J. L. Spectroelectrochemical Photoluminescence of Trap States of Nanocrystalline TiO<sub>2</sub> in Aqueous Media. *J. Phys. Chem. C* **2013**, 117 (26), 13654–13662.

<https://doi.org/10.1021/jp402264p>.

- (179) Wawrzyniak, J.; Karczewski, J.; Kupracz, P.; Grochowska, K.; Coy, E.; Mazikowski, A.; Ryl, J.; Siuzdak, K. Formation of the Hollow Nanopillar Arrays through the Laser-Induced Transformation of TiO<sub>2</sub> Nanotubes. *Sci. Rep.* **2020**, 10 (1), 20235. <https://doi.org/10.1038/s41598-020-77309-2>.

- (180) Chen, H.; Li, N.; Wu, Y.-H.; Shi, J.-B.; Lei, B.-X.; Sun, Z.-F. A Novel Cheap, One-Step and Facile Synthesis of Hierarchical TiO<sub>2</sub> Nanotubes as Fast Electron Transport Channels for Highly Efficient Dye-Sensitized Solar Cells. *Adv. Powder Technol.* **2020**, 31 (4), 1556–1563.

<https://doi.org/10.1016/j.appt.2020.01.020>.

- (181) Beranek, R.; Macak, J. M.; Gärtner, M.; Meyer, K.; Schmuki, P. Enhanced Visible Light

- Photocurrent Generation at Surface-Modified TiO<sub>2</sub> Nanotubes. *Electrochim. Acta* **2009**, *54* (9), 2640–2646.
- <https://doi.org/10.1016/j.electacta.2008.10.063>.
- (182) Jeong, H. W.; Park, K. J.; Han, D. S.; Park, H. High Efficiency Solar Chemical Conversion Using Electrochemically Disordered Titania Nanotube Arrays Transplanted onto Transparent Conductive Oxide Electrodes. *Appl. Catal. B Environ.* **2018**, *226*, 194–201.
- <https://doi.org/10.1016/j.apcatb.2017.12.043>.
- (183) Tesler, A. B.; Altomare, M.; Schmuki, P. Morphology and Optical Properties of Highly Ordered TiO<sub>2</sub> Nanotubes Grown in NH<sub>4</sub>F/ o -H<sub>3</sub>PO<sub>4</sub> Electrolytes in View of Light-Harvesting and Catalytic Applications. *ACS Appl. Nano Mater.* **2020**, *3* (11), 10646–10658.
- <https://doi.org/10.1021/acsanm.0c01859>.
- (184) Fraoucene, H.; Hatem, D.; Vacandio, F.; Pasquinelli, M. TiO<sub>2</sub> Nanotubes with Nanoglass Structure: The Effect of the Anodizing Voltage on the Formation Mechanism and Structure Properties. *J. Electron. Mater.* **2019**, *48* (4), 2046–2054.
- <https://doi.org/10.1007/s11664-019-06951-y>.
- (185) Broens, M. I.; Ramos Cervantes, W.; Oyarzún Jerez, D.; López Teijelo, M.; Linarez Pérez, O. E. The Keys to Avoid Undesired Structural Defects in Nanotubular TiO<sub>2</sub> Films Prepared by Electrochemical Anodization. *Ceram. Int.* **2020**, *46* (9), 13599–13606.
- <https://doi.org/10.1016/j.ceramint.2020.02.145>.
- (186) Naduvath, J.; Bhargava, P.; Mallick, S. Mechanism of Titania Nanoglass Formation during Anodization. *Chem. Phys. Lett.* **2015**, *626*, 15–19.
- <https://doi.org/10.1016/j.cplett.2015.03.011>.
- (187) Seçkin, E.; Ürgen, M. A Kinetic Model for Determining Morphology Transitions and Growth Kinetics of Titania Nanotubes during Anodization of Titanium in Ethylene Glycol Based Electrolytes. *Surf. Coatings Technol.* **2021**, *409*, 126840.
- <https://doi.org/10.1016/j.surfcoat.2021.126840>.
- (188) Likodimos, V.; Stergiopoulos, T.; Falaras, P.; Kunze, J.; Schmuki, P. Phase Composition, Size, Orientation, and Antenna Effects of Self-Assembled Anodized

- Titania Nanotube Arrays: A Polarized Micro-Raman Investigation. *J. Phys. Chem. C* **2008**, *112* (33), 12687–12696.
- <https://doi.org/10.1021/jp8027462>.
- (189) Pandey, R. K.; Upadhyay, C.; Prakash, R. Pressure Dependent Surface Morphology and Raman Studies of Semicrystalline Poly(Indole-5-Carboxylic Acid) by the Langmuir–Blodgett Technique. *RSC Adv.* **2013**, *3* (36), 15712.
- <https://doi.org/10.1039/c3ra41895b>.
- (190) Choudhury, B.; Bayan, S.; Choudhury, A.; Chakraborty, P. Narrowing of Band Gap and Effective Charge Carrier Separation in Oxygen Deficient TiO<sub>2</sub> Nanotubes with Improved Visible Light Photocatalytic Activity. *J. Colloid Interface Sci.* **2016**, *465*, 1–10.
- <https://doi.org/10.1016/j.jcis.2015.11.050>.
- (191) Zhang, Q.; Celorrio, V.; Bradley, K.; Eisner, F.; Cherns, D.; Yan, W.; Fermín, D. J. Density of Deep Trap States in Oriented TiO<sub>2</sub> Nanotube Arrays. *J. Phys. Chem. C* **2014**, *118* (31), 18207–18213.
- <https://doi.org/10.1021/jp505091t>.
- (192) Sun, L.; Wang, X.; Li, M.; Zhang, S.; Wang, Q. Anodic Titania Nanotubes Grown on Titanium Tubular Electrodes. *Langmuir* **2014**, *30* (10), 2835–2841.
- <https://doi.org/10.1021/la500050q>.
- (193) Premchand, Y. D.; Djenizian, T.; Vacandio, F.; Knauth, P. Fabrication of Self-Organized TiO<sub>2</sub> Nanotubes from Columnar Titanium Thin Films Sputtered on Semiconductor Surfaces. *Electrochem. commun.* **2006**, *8* (12), 1840–1844.
- <https://doi.org/10.1016/j.elecom.2006.08.028>.
- (194) Yoriya, S.; Paulose, M.; Varghese, O. K.; Mor, G. K.; Grimes, C. A. Fabrication of Vertically Oriented TiO<sub>2</sub> Nanotube Arrays Using Dimethyl Sulfoxide Electrolytes. *J. Phys. Chem. C* **2007**, *111* (37), 13770–13776.
- <https://doi.org/10.1021/jp074655z>.
- (195) Krýsa, J.; Krýsová, H.; Hubička, Z.; Kment, Š.; Maixner, J.; Kavan, L. Transparent Rutile TiO<sub>2</sub> Films Prepared by Thermal Oxidation of Sputtered Ti on FTO Glass. *Photochem. Photobiol. Sci.* **2019**, *18* (4), 891–896.

<https://doi.org/10.1039/c8pp00313k>.

- (196) Akilavasan, J.; Wijeratne, K.; Gannoruwa, A.; Alamoud, A. R. M.; Bandara, J. Significance of  $\text{TiCl}_4$  Post-Treatment on the Performance of Hydrothermally Synthesized Titania Nanotubes-Based Dye-Sensitized Solar Cells. *Appl. Nanosci.* **2014**, *4* (2), 185–188.

<https://doi.org/10.1007/s13204-012-0187-4>

- (197) Wen, Y.; Rufford, T. E.; Chen, X.; Li, N.; Lyu, M.; Dai, L.; Wang, L. Nitrogen-Doped  $\text{Ti}_3\text{C}_2\text{T}_x$  MXene Electrodes for High-Performance Supercapacitors. *Nano Energy* **2017**, *38*, 368–376.

<https://doi.org/10.1016/j.nanoen.2017.06.009>.

- (198) Gasso, S.; Sohal, M. K.; Mahajan, A. MXene Modulated  $\text{SnO}_2$  Gas Sensor for Ultra-Responsive Room-Temperature Detection of  $\text{NO}_2$ . *Sensors Actuators B Chem.* **2022**, *357*, 131427.

<https://doi.org/10.1016/j.snb.2022.131427>.

- (199) Fang, L.; Chen, J.; Zhang, M.; Jiang, X.; Sun, Z. Introduction of  $\text{Ti}^{3+}$  Ions into Heterostructured  $\text{TiO}_2$  Nanotree Arrays for Enhanced Photoelectrochemical Performance. *Appl. Surf. Sci.* **2019**, *490*, 1–6.  
<https://doi.org/10.1016/j.apsusc.2019.05.326>.

- (200) Nishikawa, M.; Shiroishi, W.; Honghao, H.; Suizu, H.; Nagai, H.; Saito, N. Probability of Two-Step Photoexcitation of Electron from Valence Band to Conduction Band through Doping Level in  $\text{TiO}_2$ . *J. Phys. Chem. A* **2017**, *121* (32), 5991–5997.  
<https://doi.org/10.1021/acs.jpca.7b05214>.